frontiers | Research Topics

Chemical and biogeochemical processes at methane and other cold seeps

Edited by
Davide Oppo, Dong Feng, Jörn Peckmann,
Jennifer Zwicker and Samantha Joye

Published in
Frontiers in Marine Science
Frontiers in Earth Science

ISSN 1664-8714
ISBN 978-2-8325-3785-5
DOI 10.3389/978-2-8325-3785-5

About Frontiers

Frontiers is more than just an open access publisher of scholarly articles: it is a pioneering approach to the world of academia, radically improving the way scholarly research is managed. The grand vision of Frontiers is a world where all people have an equal opportunity to seek, share and generate knowledge. Frontiers provides immediate and permanent online open access to all its publications, but this alone is not enough to realize our grand goals.

Frontiers journal series

The Frontiers journal series is a multi-tier and interdisciplinary set of open-access, online journals, promising a paradigm shift from the current review, selection and dissemination processes in academic publishing. All Frontiers journals are driven by researchers for researchers; therefore, they constitute a service to the scholarly community. At the same time, the *Frontiers journal series* operates on a revolutionary invention, the tiered publishing system, initially addressing specific communities of scholars, and gradually climbing up to broader public understanding, thus serving the interests of the lay society, too.

Dedication to quality

Each Frontiers article is a landmark of the highest quality, thanks to genuinely collaborative interactions between authors and review editors, who include some of the world's best academicians. Research must be certified by peers before entering a stream of knowledge that may eventually reach the public - and shape society; therefore, Frontiers only applies the most rigorous and unbiased reviews. Frontiers revolutionizes research publishing by freely delivering the most outstanding research, evaluated with no bias from both the academic and social point of view. By applying the most advanced information technologies, Frontiers is catapulting scholarly publishing into a new generation.

What are Frontiers Research Topics?

Frontiers Research Topics are very popular trademarks of the *Frontiers journals series*: they are collections of at least ten articles, all centered on a particular subject. With their unique mix of varied contributions from Original Research to Review Articles, Frontiers Research Topics unify the most influential researchers, the latest key findings and historical advances in a hot research area.

Find out more on how to host your own Frontiers Research Topic or contribute to one as an author by contacting the Frontiers editorial office: frontiersin.org/about/contact

Chemical and biogeochemical processes at methane and other cold seeps

Topic editors
Davide Oppo — University of Louisiana at Lafayette, United States
Dong Feng — Shanghai Ocean University, China
Jörn Peckmann — University of Hamburg, Germany
Jennifer Zwicker — University of Vienna, Austria
Samantha Joye — University of Georgia, United States

Citation
Oppo, D., Feng, D., Peckmann, J., Zwicker, J., Joye, S., eds. (2023). *Chemical and biogeochemical processes at methane and other cold seeps*. Lausanne: Frontiers Media SA. doi: 10.3389/978-2-8325-3785-5

Table of contents

frontiers
in Marine Science

ORIGINAL RESEARCH
published: 14 March 2022
doi: 10.3389/fmars.2022.857413

A Numerical Model for Determining Deep Methane Flux Linked to the Free Gas Zone: Application to the Ocean Drilling Program Site 995 and Implications for Regional Deep Methane Flux at the Blake Ridge

Zihan Zheng[1]*, Yuncheng Cao*[1]**, Wenyue Xu*[2] *and Duofu Chen*[1]***

[1] Shanghai Engineering Research Center of Hadal Science and Technology, College of Marine Sciences, Shanghai Ocean University, Shanghai, China, [2] Independent Consultant, Medford, MA, United States

The lack of the quantification of deep dissolved methane flux prevents us from accurately understanding hydrate accumulation and distribution at a given geologic setting where vertically upward methane advection dominates the hydrate system. The upward deep methane flux was usually applied as an assumed value in many previous studies. Considering the deep methane flux changes the methane concentration in the pore water and further affects the phase transfer between the gas and aqueous phases depending on the *in situ* methane concentration, we link gas bubbles distribution to deep dissolved methane flux. Here, we constructed a numerical model to quantify the dissolved methane flux from depth based on the parameters related to gas bubble distribution, including the residual gas saturation in sediments and the free gas zone (FGZ) thickness. We then applied our model to ODP Site 995 at the Blake Ridge where methane was sourced from deep layers. Our model results predict an upward deep methane flux of 0.0231 mol/m^2/a and the occurrence of another gas interval in deeper sediments, which are consistent with seismic data. We further explored the influence of upward methane flux on hydrate accumulation and found that the thin hydrate occurrence zone at nearby Site 994 likely resulted from a small deep methane flux. Combined with the previous conclusion of high deep methane flux at Site 997, we showed that along the Blake Ridge drilling transect the estimated deep methane fluxes decrease with increasing distance from the crest of the ridge. This approach for quantifying deep methane flux is complementary to the current hydrate accumulation model and provides new insights into the regional methane flux estimation at the Blake Ridge.

Keywords: methane flux, numerical simulation, methane gas, gas hydrate, Blake Ridge

Edited by:
Davide Oppo,
University of Louisiana at Lafayette,
United States

Reviewed by:
Ewa Burwicz-Galerne,
University of Bremen, Germany
Li Wei,
Columbia University, United States

****Correspondence:***
Yuncheng Cao
yccao@shou.edu.cn
Duofu Chen
dfchen@shou.edu.cn

Specialty section:
This article was submitted to
Marine Biogeochemistry,
a section of the journal
Frontiers in Marine Science

Received: *18 January 2022*
Accepted: *22 February 2022*
Published: *14 March 2022*

Citation:
Zheng Z, Cao Y, Xu W and Chen D (2022) A Numerical Model for Determining Deep Methane Flux Linked to the Free Gas Zone: Application to the Ocean Drilling Program Site 995 and Implications for Regional Deep Methane Flux at the Blake Ridge.
Front. Mar. Sci. 9:857413.
doi: 10.3389/fmars.2022.857413

INTRODUCTION

Natural gas hydrates precipitate in submarine sediments under suitable thermodynamic conditions of low temperature and high pressure (Kvenvolden, 1993; Sloan and Koh, 2008). These factors restrict a maximum suitable interval for hydrate stability, which is called the gas hydrate stability zone (GHSZ) (Xu and Ruppel, 1999). However, the amount of methane in the GHSZ limits the methane hydrate occurrence to a finite region below the seafloor, often referred to as the actual hydrate occurrence zone (GHOZ) (Zatsepina and Buffett, 1997; Bhatnagar et al., 2007; Malinverno, 2010; Malinverno and Goldberg, 2015. Methane can be generated by such as *in situ* methanogenesis, or supplied by upward advection of methane-bearing fluids and free gas flow (Chen and Cathles, 2003, 2005; Cao et al., 2013; Vanderbeek and Rempel, 2018; Dhakal and Gupta, 2021). The mode of methane supply by the advection of methane-bearing fluids has been demonstrated in various hydrate deposits globally, such as the Blake Ridge (Hyndman and Davis, 1992; Liu and Flemings, 2007; Malinverno et al., 2008; You et al., 2019). This deep methane source is produced in the deep subsurface sediments and subsequently migrated into the GHSZ by upward fluid flow. Numerous studies confirmed the existence of an external dissolved methane source at the Blake Ridge through porosity and capillary pressure analyses as well as the calculation of *in situ* methane production and geochemical data simulations (Davie and Buffett, 2003a,b; Flemings et al., 2003; Wallmann et al., 2006). In addition, the age of the pore fluids dated via radioisotope ^{129}I was significantly older than the surrounding sediments. The older age and the elevated bromide and iodide concentrations also suggest a deep fluid source at the Blake Ridge (Egeberg and Dickens, 1999; Fehn et al., 2000).

The effect of these deep methane-bearing fluids on hydrate formation depends on the flow velocity and the methane concentration in rising fluids. The velocity of the fluid flow can be estimated by investigating the measured pore water chloride profiles (Davie and Buffett, 2003a,b; Torres et al., 2004; Bhatnagar et al., 2008, 2011). However, the composition of this deep methane source is not well constrained. For simplification, numerous quantitative studies assumed the methane solubility at the BHSZ (base of the GHSZ) or a certain value inferred from gas distribution characteristics as the methane concentration in the rising fluids (Davie and Buffett, 2003b; Torres et al., 2004; Garg et al., 2008; Haacke et al., 2008). The model developed by Bhatnagar et al. (2007) has emphasized the significance of an accurate methane flux value for quantifying methane hydrate accumulation. Results suggest that a certain minimum methane flux is required to form hydrates in a hydrate system which is dominated by a deep methane source (Xu and Ruppel, 1999; Bhatnagar et al., 2007). If methane supplied from depth exceeds this minimum value, methane hydrate would extend to the BHSZ at a steady state due to the sedimentation (Burwicz and Haeckel, 2020). But more time is required to achieve this steady state if the methane concentration in the rising fluids is low. Therefore, the evolution of the methane hydrate deposits can be observed only if an accurate deep-sourced methane flux is obtained.

In addition to its influence on hydrate accumulation and distribution, this deep methane source significantly affects the formation and properties of the free-gas zone (FGZ) beneath the BHSZ (Pecher et al., 2001; Haacke et al., 2008). Haacke et al. (2007, 2008) adopted an methane concentration of the rising fluid that is approximately equivalent to the half the equilibrium solubility at the BHSZ to model the evolution of FGZ in the west Svalbard and suggested that the deep dissolved methane flux was a primary factor in controlling the gaseous methane occurrence and distribution in the FGZ (Haacke et al., 2007, 2008). Upward methane flux from depth toward the BHSZ affects pore-water methane concentration and resulting inter-conversion between the gaseous methane and dissolved methane as it moves upwards. Therefore, the deep dissolved methane flux is closely linked to gas bubbles distribution in the FGZ.

Here, a numerical model was constructed to quantify the upward methane flux based on methane mass conservation in the FGZ. This model was then applied to ODP Site 995 at the Blake Ridge where methane sourced from depth dominates the hydrate accumulation. Unlike previous work, our model established a relationship between the deep dissolved methane flux and gas bubbles saturation (gas volume fraction) and provides an approach for calculating the flux of deep methane. We subsequently combined our results at Site 995 with previous results about methane flux at nearby sites and yielded an integrated picture of regional methane flux patterns along the Blake Ridge drilling transect. This model for quantifying deep methane flux is complementary to the current hydrate accumulation model.

MODEL FORMULATION

Conceptual Model

In porous media of the GHSZ, methane can be present in aqueous, gaseous and hydrate phases (You et al., 2019). A Bottom Simulating Reflector (BSR) often marks the boundary between the base of the GHSZ and the underlying FGZ (Stoll et al., 1971; Shipley et al., 1979; Wood and Ruppel, 2000; Westbrook and Thatcher, 2009). The model domain in this study extended from the BHSZ to a few hundred meters below the BHSZ. Two spatial domains below the BHSZ were defined: the free gas domain (Domain 1) and the methane undersaturated domain (Domain 2). This conceptual model was illustrated in **Figure 1**. Domain 1 extended from the BHSZ to the base of the FGZ (BFGZ), and Domain 2 represented the section below the BFGZ (**Figure 1**). In Domain 1 where gas bubbles existed, gas and water were in equilibrium. The methane concentration in Domain 1 was equal to the gas-liquid solubility, which was regulated by local thermodynamic conditions (Duan et al., 1992; Davie et al., 2004). In contrast, in Domain 2, the dissolved methane concentration in pore water is less than its solubility. Therefore, only dissolved methane was expected (**Figure 1**).

The methane hydrate tended to dissociate and produce free gas and water when being buried out of the GHSZ (Xu, 2004; **Figure 1**). The hydrate burial may result in a thin region with three-phase coexisting beneath the BHSZ

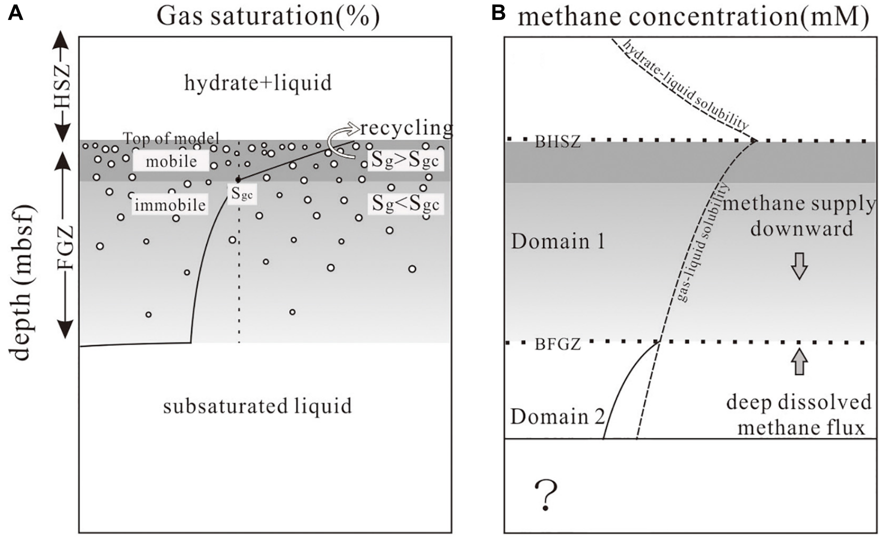

FIGURE 1 | Conceptual illustration of the free gas system below the BHSZ. **(A)** The region below the top of model (BHSZ) is divided into two domains. The mobile free gas shown in shaded dark gray was produced through hydrate dissociation, accumulated at the BHSZ or moved upward due to the buoyancy and left a certain gas which equals to the residual gas saturation (S_{gc}). These mobile gas bubbles occupy an extremely thin layer compared with the large gas distribution zone that controlled by the sedimentation and shown in shaded light gray. This model neglects the upward gas bubbles. **(B)** Dotted lines represent the BHSZ and BFGZ. Dashed lines represent hydrate-liquid and gas-liquid solubility curves. The downward gaseous methane and diffused methane and the upward flow of unsaturated fluid collectively affect the amount of methane in pore water, which results in inter-conversion between the gaseous methane and dissolved methane. The gas bubbles no longer exist below the BFGZ because gaseous methane at the BFGZ compensates the deep unsaturated dissolved methane. The methane concentration profile represented by black solid line in Domain 2 is plotted according to the deep methane flux. The question mark represents the possibility of the gas bubble occurrence beneath Domain 2 since the gas-liquid solubility tends to decrease with depth. The gas bubbles would exist if the methane concentration exceeds the gas-liquid solubility.

(Liu and Flemings, 2011). A fraction of the gas bubbles moved upwards due to buoyancy. They were recycled into the GHSZ through overcoming the capillary forces or accumulated below the BHSZ as a thin horizon (Haacke et al., 2008; **Figure 1**). We did not take into account these migrating gas bubbles toward the BHSZ since they appeared to be only important in hydrate accumulation which was dominated by gaseous methane recycling (Mogollon et al., 2009). Besides these mobile gas, there are some gases trapped in sediments which are unable to migrate freely. In fact, these residual gas bubbles exerted a significant control on the characteristics of the FGZ (Haacke et al., 2008). We focused on these residual gas bubbles that moved downward with sedimentation and their behavior within the sediment column which was influenced by the deep methane flux (Minshull and White, 1989; Haacke et al., 2008; **Figure 1**). As gas bubbles move downward via sedimentation, the mass transfer between gas and aqueous phases occurred. Because the methane concentration in the pore water is affected by the advection of methane-carrying pore fluids and diffusion of dissolved methane. This methane phase transfer is dependent on the *in situ* methane concentration: if unsaturated, gas bubbles represent a methane source for the aqueous phase; and if oversaturated, gas bubbles represents a methane sink (Mogollon et al., 2009). Therefore, the deep methane-carrying fluids controls the methane concentration in the pore water and further affects gas dissolution and formation (Su and Chen, 2007; Archer et al., 2012). The characteristics of gas bubbles distribution can be visualized through seismic imaging. Hence, the relationship between the gas bubbles distribution and the deep methane-carrying fluids enables the calculation of the deep methane flux as a function of gas bubble saturation and the depth of BFGZ.

The gaseous methane profile was controlled by physical processes including advection of methane-carrying pore fluids, diffusion of dissolved methane, and burial of the gas bubbles. We derived the gas control equation in the FGZ based on conservation of methane mass and obtained the gas distribution characteristics (**Figure 1**). Under the steady-state condition, the gaseous methane at the BFGZ exactly compensates the upward unsaturated dissolved methane, rendering the absence of gas below the BFGZ. Therefore, the mass balance of methane at the BFGZ can be used to calculate the deep methane flux. Furthermore, we established the methane mass balance equation to generate the dissolved methane profile in Domain 2 using the computed dissolved methane flux from depth. The curvature of the methane concentration profile in Domain 2 could reflect the flux of this deep methane.

Before introducing the numerical representations, several assumptions need to be made to build the mass balance equations: (1) the residual gas bubbles are trapped at the BHSZ and transported downwards with sediment burial (Davie and Buffett, 2003b); (2) the immobile gas is assumed to be distributed in a homogeneous mixture of water and gas, and (3) *in-situ* methanogenesis is neglected considering its extremely low contribution where FGZ develops (Haacke et al., 2008); (4) the salinity remains constant (3.5% seawater value), and its influence on solubility is neglected (Davie and Buffett, 2001); (5) the sediment-grain density and porosity are assumed to be constant (Wallmann et al., 2006).

Numerical Model

Domain 1: Existence of Interval With Free Gas

In Domain 1, the governing equation of the free gas is constructed. Fluid advection and diffusion are two mechanisms of dissolved methane transport through the liquid phase, which are represented by two terms on the right-hand side of Equation 1. This aqueous transport controls the gas bubble distribution in Domain 1 as discussed before. Simultaneously, the formed gas bubbles are transported by sedimentation, which is represented by the second term in Equation 1 (Xu and Ruppel, 1999; Davie and Buffett, 2001). The phase transfer occurs during this process. The volume fraction of methane gas becomes the primary dependent variable across Domain 1. The two-phase mass balance equation for gas bubbles in Domain 1 is as follows:

$$\frac{\partial}{\partial t}\left[\phi\rho_g S_g\right]+\frac{\partial}{\partial z}\left[u_s\phi\rho_g S_g\right]=\frac{\partial}{\partial z}\left[\frac{D_m}{\theta^2}\rho_w\phi\frac{\partial C_m^w}{\partial z}M_g\right]-\frac{\partial}{\partial z}\left[q_w C_m^w M_g\right] \quad (1)$$

where t is time; z (mbsf) is the depth below the seafloor defined as positive downwards;ρ_w (kg/m^3) (1,030 kg/m^3) and ρ_g (kg/m^3) are the densities of pore water and methane in the immobile gaseous phase, respectively; S_g denotes gaseous methane saturation (volume fraction of pore space); D_m(m^2/a) (0.028 m^2/a) is the diffusion coefficient of methane in free water; ϕ is porosity; θ is tortuosity, which can be calculated using Archie's law: $\theta^2=\phi^{-1}$ (Torres et al., 2004); C_m^w (mol/kg) is the concentration of aqueous methane; M_g is the relative molecular mass of methane (16 g/mol); q_w is the mass flux of pore water; and u_s (m/a) is the burial rate of gas bubbles with sediments, given in terms of u_0 (sedimentation rate at the seafloor) by Equation (2) (Davie and Buffett, 2001):

$$u_s=\frac{1-\phi_0}{1-\phi}u_0 \quad (2)$$

where ϕ_0 is the porosity of the seafloor. The sedimentation rate in Domains 1 and 2 remains constant, considering assumption (6). The influence of this simplification on the results will be assessed in the "Discussion" section.

The density of gaseous methane is calculated using Duan et al. (1992) and can be written as:

$$\rho_g=\frac{P}{ZRT}M_g \quad (3)$$

where P and T are the pressure and temperature at depth z, R is the universal gas constant (8.314 J/mol/k), and Z is the compressibility factor, which can be calculated using Duan et al. (1992).

Equation (1) can be rearranged to:

$$\frac{d}{dt}\left[\phi\rho_g S_g\right]=\frac{\partial}{\partial z}\left[\frac{D_m}{\theta^2}\rho_w\phi\frac{\partial C_m^w}{\partial z}M_g\right]-\frac{\partial}{\partial z}\left[q_w C_m^w M_g\right]=A_g \quad (4)$$

where $\frac{d(\phi\rho_g S_g)}{dt}$ represents the gas mass growth rate of a specific layer and is marked as A_g (kg/m^3/a). Integrating Equation (4) yields

$$\phi\rho_g S_g=\int_{t_0}^{0}A_g dt+\phi\rho_g S_{g,t=t_0,z=z_0}$$

$$=\int_{t_0}^{0}\frac{A_g}{u_s}dz+\phi\rho_g S_{g,t=t_0,z=z_0} \quad (z\le BEGZ) \quad (5)$$

where $\phi\rho_g S_{g,t=t_0,z=z_0}$ is the initial gaseous methane mass of a specific layer at the initial depth z_0 (BHSZ) and the initial time t_0. $S_{g,t=t_0,z=z_0}$ is the residual gas beneath the BHSZ that transported downwards with sediments, and its saturation is a boundary condition in this model (Firoozabadi et al., 1992; Haacke et al., 2008). $\int_{t_0}^{0}A_g dt$ represents the change in gaseous methane mass in the pore media of a specific layer from t_0 (initial time) to 0 (present time), that is, from z_0 (initial depth) to$z$ (present depth), $\phi\rho_g S_g$ is the present mass of methane gas in a specific layer. Rearranging Equation (5), the gas saturation profile in Domain 1 is obtained as follows:

$$S_g=\frac{M_g}{u_s\phi\rho_g}\left[F(z)-F(BHSZ)\right]+S_{g\,t=t_0},\ z=z_0 \quad (6)$$

where

$$F(\nu)=-q_w C_m^w(\nu)+\frac{D_m}{\theta^2}\phi\rho_w\frac{\partial C_m^w(\nu)}{\partial\nu} \quad (7)$$

Boundary Between Domains 1 and 2

In the steady state, the flux value of the unsaturated dissolved methane migrating to the BFGZ from below can be calculated through the methane flux above the BFGZ. The downward gas bubbles at the BFGZ is compensated exactly by the deep unsaturated methane-bearing fluid. Therefore, methane mass conservation is carried out in two vanishingly thin volumes above and below the BFGZ, respectively. These two flux values are equal in these two volumes. The methane flux in the upper thin volume includes contributions from advection of methane in the fluid, the diffusion of methane through the pore fluid, and the gaseous phases. For a unit surface area, the flux from the upper volume is:

$$F_{m,z=BFGZ}^{+}=-\frac{D_m}{\theta^2}\phi\rho_w\frac{\partial C_m^{w+}}{\partial z}+q_w C_m^{w+}+\frac{u_s\phi\rho_g S_g^{+}}{Mg} \quad (8)$$

where $F_{m,z=BFGZ}^{+}$ is the methane flux in the upper volume (positive downward) and C_m^{w+} denotes the methane concentration in the pore water at the BFGZ. S_g^{+} is the gas volume fraction of the pore space at the BFGZ which can be calculated through Equation (6).

Simultaneously, the value of methane flux in the lower volume that is transported toward the BFGZ is:

$$F_{m,z=BFGZ}^{-}=-\frac{D_m}{\theta^2}\phi\rho_w\frac{\partial C_m^{w-}}{\partial z}+q_w C_m^{w-} \quad (9)$$

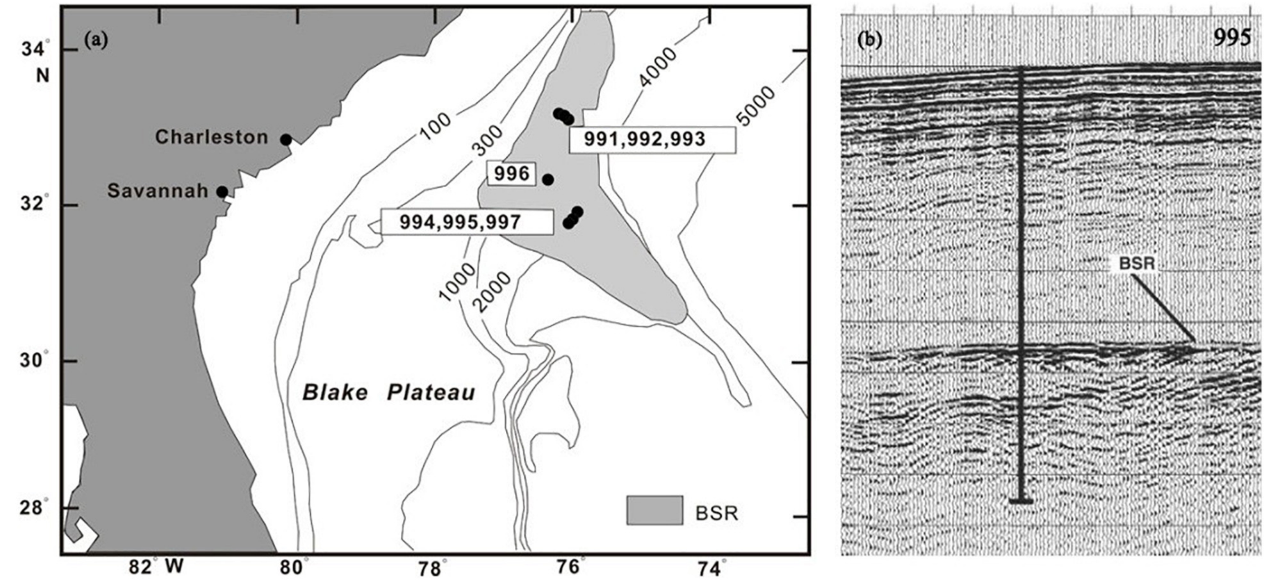

FIGURE 2 | (a) Map showing the location of the ODP Leg 164 and the BSR area in gray. **(b)** Seismic reflection profile across Site 995 showing the location of BSR (Paull et al., 1996).

where $F^-_{m,z=BFGZ}$ is the flux value of methane bearing fluid that migrating upward to the BFGZ. For a vanishingly thin volume, $F^-_{m,z=BFGZ}$ is equal to$F^+_{m,z=BFGZ}$. Of note, the methane concentration in pore water C^{w-}_{m} is equal to the value of C^{w+}_{m}. So far, the deep methane flux has been obtained.

Domain 2: Interval With Only Dissolved Methane

$F^-_{m,z=BFGZ}$ was performed using the above analysis. No free gas exists in Domain 2. The dissolved methane profile in the steady state here can be calculated according to the $F^-_{m,z=BFGZ}$ (Equation 9). Therefore, the dissolved methane profiles in Domain 2 could reflect the value of the $F^-_{m,z=BFGZ}$. If the methane fluxes from depth ($F^-_{m,z=BFGZ}$) were different, the methane profiles in Domain 2 would also be different. As only dissolved methane exists here, the transport of dissolved methane by the advection-dispersion equation can be described:

$$\frac{\partial}{\partial t}\left[\phi\rho_w C^w_m\right] = \frac{\partial}{\partial z}\left[\frac{D_m}{\theta^2}\rho_w\phi\frac{\partial C^w_m}{\partial z}\right] - \frac{\partial}{\partial z}\left[q_w C^w_m\right] \qquad (10)$$

The dissolved methane curve in Domain 2 in the steady state is obtained by assuming the time derivative of Equation (10) to zero and proceeding with the boundary conditions (the deep methane flux) obtained above.

APPLICATION TO BLAKE RIDGE OCEAN DRILLING PROGRAM SITE 995

Background

The Blake Ridge, located offshore in the southeast United States, contains abundant methane and gas hydrate (Paull et al., 1996; Dickens et al., 1997). The Ocean Drilling Program (ODP) Leg 164 drilled at the Blake Ridge has greatly enhanced our understanding of the effect of deep methane sources on methane hydrate accumulation (Bhatnagar et al., 2007; Frederick and Buffett, 2011; Burwicz and Rüpke, 2019). Three sites were drilled along the Blake Ridge transect with distinct BSR characteristics: the edge flank site without a BSR (Site 994), the flank site with a BSR (Site 995), and the site located on the crest of the drift deposit with a well-developed BSR (Site 997) (**Figure 2a**; Paull et al., 1996, 2000). The gas saturation at Site 995 is smaller than 1%, which is close to that of the residual gas bubbles in sediments (Paull et al., 1996, 2000; Holbrook, 2001; Reagan and Moridis, 2007). The occurrence of thick gas layer with low gas saturation made Site 995 appropriate for our model application because the gas bubble distribution here is obviously not affected by migrating gas bubbles formed by rapid hydrate dissociation. In addition, Site 995 is characterized by two gas-bearing zones that are detected by seismic profiles and downhole logging data (**Figure 2b**; Paull et al., 1996, 2000; Holbrook, 2001). The results computed from the upper gas interval could be verified through the lower gas interval. This is because that the second gas interval would be reproduced if the methane concentration beneath the BFGZ deriving from Equation 10 is reliable (**Figure 1**; Xu and Ruppel, 1999). Therefore, applying to Site 995 made the model convenient to be verified.

Parameterization

The basic parameters used in this model have been listed in **Table 1**. Some site-specific parameters needed to be stated before application to Site 995 include the fluid flow rate, the porosity, the sedimentation rate and the density of the gas bubbles. The rate of upward fluid flow was predicted by fitting the computed chloride profiles to the chloride measurements at ODP Site 995

(Paull et al., 1996; Dickens, 2001; Zheng et al., 2020). Accordingly, the value of the flow rate was determined to be 0.125 kg/m^2/a, which was described as the mass flux. This result is roughly consistent with the interstitial fluid velocity at the nearby Site 997 which was obtained by Davie and Buffett (2003b). The porosity profile (ϕ) as a function of depth was determined by fitting an empirical exponential function to the measurement data (Zheng et al., 2020). Finally, the porosity exhibits a limited variation in Domains 1 and 2, which represents a nearly complete compaction below BHSZ. Therefore, we assume a constant porosity value beneath the BHSZ (**Table 1**). Another parameter of particular importance is the sedimentation rate. Nannofossil biostratigraphy at Site 995 indicated that the recovered sequence was mainly continuous. An average sedimentation rate of 60 m/Ma at the seafloor was documented using log and core data (Paull et al., 1996). Combing with the assumption of a constant porosity, the burial velocity of the gas bubbles beneath the BHSZ was calculated as 28 m/Ma by Equation 2. The density of the gas bubbles (ρ_g) was calculated using Equation 3 on the basis of parameters in **Table 1** and finally it showed few changes in Domains 1 and 2. Meanwhile, the minor influence of the density value on gas saturation results has been mentioned before (Haacke et al., 2007, 2008; Mogollon et al., 2009). Therefore, the bubble density in this study was assumed to be constant (**Table 1**).

TABLE 1 | Site-specific parameters used for the ODP Site 995 and fitted values.

Parameters	Symbol	Value	Unit	References
Water depth	Dep	2,776	M	Paull et al., 1996
Seafloor temperature	T_0	3.75	°C	Paull et al., 1996
Geothermal gradient	G	0.0345	°C/m	Paull et al., 1996
Bottom simulating reflector	BSR	450	mbsf	Paull et al., 1996
Porosity in Domain 1 and Domain 2	ϕ	0.52	—	Paull et al., 1996
In situ sedimentation rate	u_s	28	m/Ma	Paull et al., 1996, 2000
Porosity at the seafloor	ϕ_0	0.77	—	Paull et al., 1996, 2000
The density of sediment	ρ_s	2,700	kg/m^3	Paull et al., 1996, 2000
The density of pore water	ρ_w	1,030	kg/m^3	Torres et al., 2004
The density of methane gas	ρ_g	226	kg/m^3	Duan et al., 1992
External fluid flux in deeper sediments	q_w	–0.125	kg/m^2-a	Calculated in this paper
Diffusion coefficient of dissolved methane in free water	D_m	0.028	m^2/a	Davie and Buffett, 2001, 2003b
Mole mass for methane gas	M_g	16	g/mol	Duan et al., 1992
The universal gas constant	R	8.314	J/mol/k	Duan et al., 1992
The density of bulk hydrate	ρ_h	925	kg/m^3	Daigle et al., 2020
Mole mass for methane hydrate	M_h	119.2	g/mol	Daigle et al., 2020

The numerical model relates the deep dissolved methane flux to the residual methane gas distribution characteristics in the FGZ. The residual gas saturation and the depth of BFGZ are another two important gas distribution related parameters. Below, we opted to discuss their effects on the deep methane flux. With the exception of these two values, all model parameters required for the simulation are listed in **Table 1**.

RESULTS AND DISCUSSION

Relationship Between Free Gas Distribution and Methane Flux

For the results that will be presented, the depth of BSR is assumed as where the top of the free gas interval occurs (Paull et al., 1996, 2000). And the influence of two parameters describing the free gas properties on results have been explored. Three BFGZ depths of 470, 480, and 490 mbsf were simulated to explore their effects on the model results (**Figure 3A**). The residual gas saturation is defined as 0.5%, given the local amount of gas bubbles. The gas is transported downwards with sediments and ceases at the BFGZ where the deep unsaturated methane compensates, as discussed in the *Conceptual Model*. The results show that a shallower BFGZ depth corresponds to more gas bubbles being buried (higher gas saturation) at the BFGZ, as well as a more unsaturated methane-bearing fluid migrating upward from the deep source (**Figures 3A,B**). The computed upward methane fluxes were 0.0229, 0.0230, and 0.0231 mol/m^2/a in these three scenarios. These unequal dissolved methane fluxes from deep can be distinguished by three methane concentration profiles with different gradients in Domain 2 (Equation 10) (**Figure 3A**).

We next considered the impact of the residual gas saturation in sediments on the calculation results, with BFGZ assumed to be 490 mbsf. Unequal residual gas bubbles beneath the BHSZ are transported downwards with sediments and are trapped at the BFGZ with different amounts of gas bubbles. A larger residual gas saturation at the top of model corresponds to more gas bubbles (higher gas saturation) at the BFGZ (**Figures 3C,D**). The computed upward methane fluxes were 0.0231, 0.0227, and 0.0221 mol/m^2/a when the residual gas saturations were defined as 0.5, 0.7, and 1%, respectively.

Site-Specific Results

The above analysis show that the amount of gas bubbles in the sediments could reflect the flux of deep dissolved methane. The gas bubble distribution at Site 995 need to be constrained first to quantify the deep dissolved methane flux here. In this study, the average gas hydrate saturation at the BHSZ at Site 995 was estimated to be 5% of the pore volume (Holbrook et al., 1996; Paull et al., 1996). The methane hydrate in this saturation would produce a maximum amount of gaseous methane in approximately 2.7% of the pore volume if it is completely dissociated (Haacke et al., 2008; Daigle et al., 2020). However, any gas in excess of the residual gas saturation tends to migrate upward into the GHSZ (Claypool and Kvenvolden, 1983;

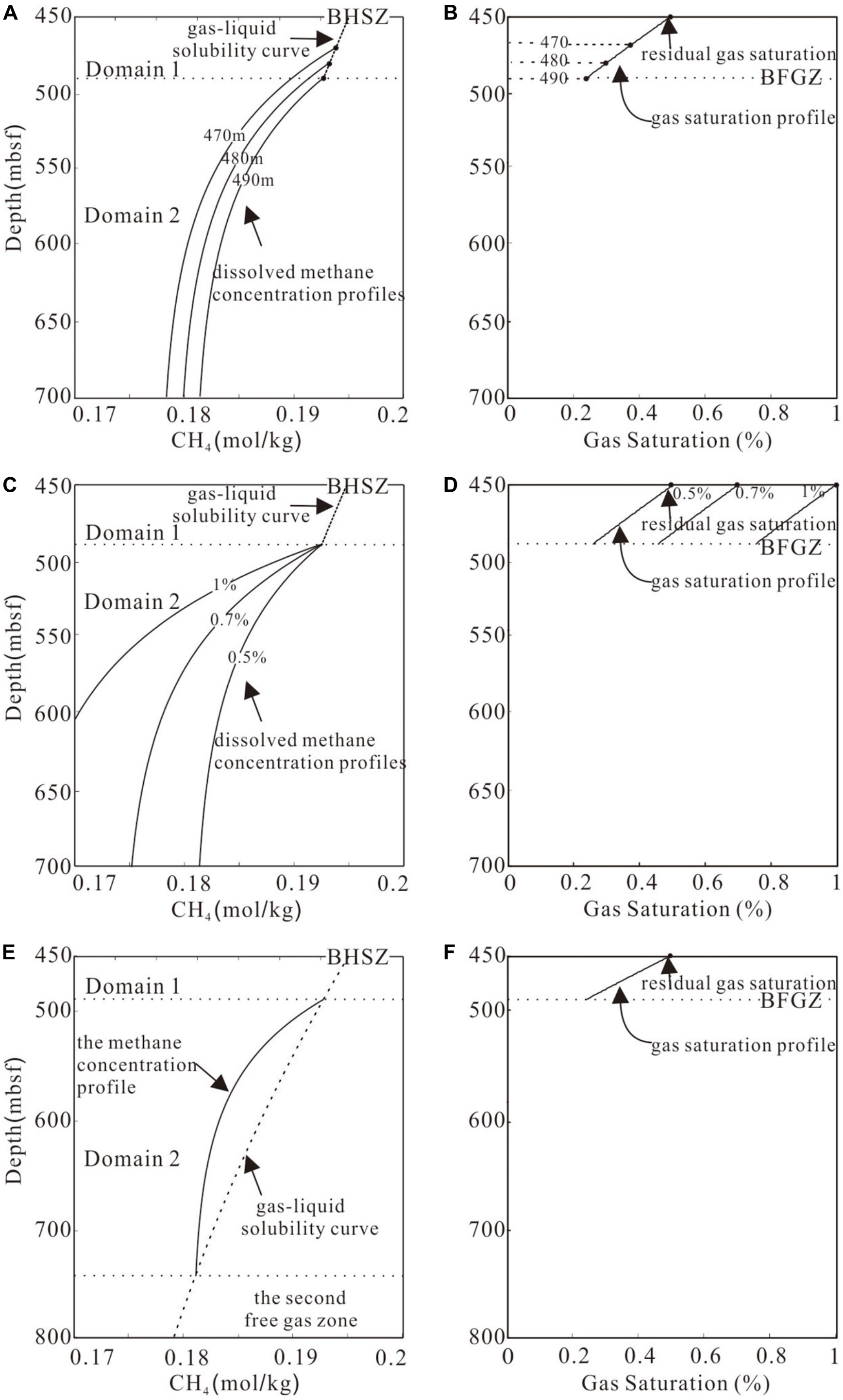

FIGURE 3 | (A) Black solid dots in Domain 1 correspond to BFGZ depth of 470, 480, and 490 mbsf, respectively. Dashed line in Domain 1 depicts the methane gas–liquid solubility curve. Three different FGZ thicknesses correspond to three methane concentration profiles, which indicate different values of methane fluxes from depth. **(B)** Methane gas saturation profiles according to the same residual gas saturation but different BFGZ depths. **(C)** Different dissolved methane fluxes from deep are represented by three lines with different slopes in Domain 2, corresponding to three distinct residual gas saturations of 0.5, 0.7, and 1%, respectively. **(D)** Three gas bubble profiles based on different residual gas saturations but the same BFGZ depth. **(E)** The dissolved methane concentration in Domain 2 is computed through the deep dissolved methane flux at Site 995 (Equation 10). The methane concentration is lower than the gas-liquid solubility in Domain 2. The deep methane flux satisfies a second gas interval occurs, which begins at approximately 740 mbsf. **(F)** Gas bubbles saturation profile at Blake Ridge Site 995.

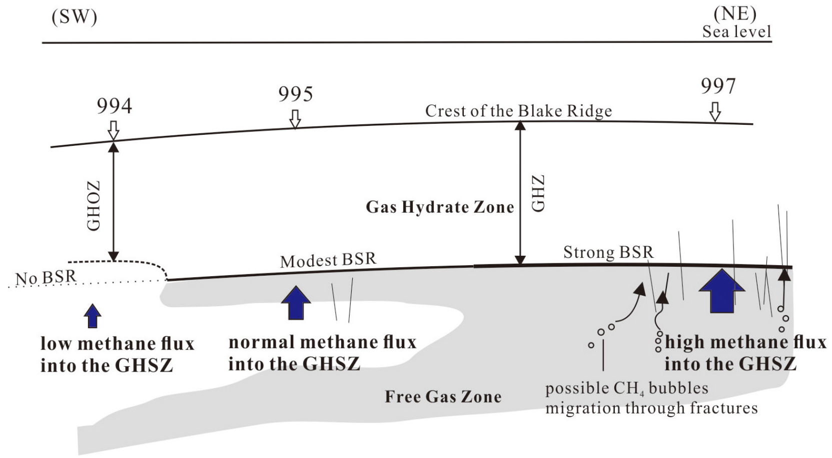

FIGURE 4 | Conceptual representation of the methane hydrate reservoir system at the Blake Ridge. From flank Site 994 to flank Site 995 and finally to crest Site 997, the deep methane flux (dark blue arrow) is changeable from low to high, corresponding to no BSR to strong BSR occurrence. FGZ (light gray) is beneath the BSRs. The methane hydrate-bearing zone at Site 994 (GHOZ) does not extend to the BSRs depth. However, thicker hydrate occurrences (GHZ) appear at Sites 995 and 997, which both extend to the BSRs.

Haacke et al., 2008). In other words, the residual gas that moves with sediments from the BHSZ is estimated to be less than 2.7% (Daigle et al., 2020). The values of the residual volume fraction of methane gas are often assumed to be about 1% in modeling studies (Firoozabadi et al., 1992; Reagan and Moridis, 2007; Archer et al., 2012). For example, Haacke et al. (2007, 2008) assumed a value of 0.4% as the residual gas volume in sediments to investigate the free gas evolution in the west Svalbard. Consequently, we assumed a low residual gas saturation of 0.5% in this model, which is in agreement with drilling data and previous investigations (Holbrook et al., 1996; Paull et al., 1996; Holbrook, 2001). Furthermore, the layer occupied by recycling gas bubbles with a high gas saturation has not been observed neither by downhole log-inferred nor seismic analysis (Paull et al., 1996; Holbrook, 2001). Therefore, it can be concluded that the recycling gas bubbles occupy a thin region comparing with the immobile free gas beneath the GHSZ at Site 995. The influence of the recycling gas thickness on the entire free gas thickness has been neglected. Analyses of seismic studies by Holbrook (2001) and downhole log inference by Paull et al. (2000) suggest that the depth of BFGZ at ODP Site 995 is approximately 490 mbsf. Therefore, 490 mbsf was adopted as the BFGZ depth, which was another parameter that characterizes gas distribution.

The obtained dissolved methane flux from deep at Site 995 was 0.0231 mol/m^2/a (**Figures 3E,F**), which resulted in a second free-gas interval that occurs at approximately 740 mbsf. This depth is in agreement with those reported by Paull et al. (1996, 2000) and Holbrook (2001). The occurrence of second gas layer at 740 mbsf predicted by our model confirmed the reliability of the estimated deep methane flux.

Influence of Sedimentation Rate Variation

The sedimentation rate was assumed to be constant in Domains 1 and 2 (**Table 1**). Therefore, we opted to discuss the influence of this assumption. The second term on the left of Equation (1) ($\frac{\partial}{\partial z}\left[u_s\phi\rho_g S_g\right]$) can be divided into two parts and expressed as $u_s\frac{\partial}{\partial z}\left[\phi\rho_g S_g\right]+\phi\rho_g S_g\frac{\partial u_s}{\partial z}$. In the conversion from Equations (1) to (4), the latter phase ($\phi\rho_g S_g\frac{\partial u_s}{\partial z}$) was ignored because of the assumption of a constant sedimentation rate. Hence, we should compare the values of $\frac{\partial}{\partial z}\left[u_s\phi\rho_g S_g\right]$ and $\phi\rho_g S_g\frac{\partial u_s}{\partial z}$. The magnitude of $\phi\rho_g S_g\frac{\partial u_s}{\partial z}$ is computed using the porosity function (Equation 2) and the parameters listed in **Table 1**. However, the value of $\frac{\partial}{\partial z}\left[u_s\phi\rho_g S_g\right]$ should be computed indirectly. The variation in the $u_s\phi\rho_g S_g$ value through Domain 1 is equivalent to the methane flux variation between the top and bottom of Domain 1, which can be calculated using Equation 8. Eventually, the value of $\frac{\partial}{\partial z}\left[u_s\phi\rho_g S_g\right]$ is proven to be several orders of magnitude greater than that of $\phi\rho_g S_g\frac{\partial u_s}{\partial z}$. Therefore, the change in the sedimentation rate has only a minor influence on the simulation results.

Regional Upward Methane Flux

Previously, the methane concentration in deep rising fluids was commonly assumed to be the methane concentration at BHSZ. In fact, the methane concentration in the deep fluid is lower than this value; otherwise, the pores of the sediments below BHSZ would all be occupied by gas bubbles as methane solubility decreases with depth beneath the BHSZ. Therefore, we first quantified the deep dissolved methane flux and applied the model at Site 995. We also explored the influence of a low deep methane flux on hydrate accumulation. A minimum methane flux from depth is required for hydrate formation in hydrate systems with deep methane sources (Xu and Ruppel, 1999; Bhatnagar et al., 2007). A larger deep methane flux causes the hydrate system to reach steady-state more rapidly. However, we applied a lower upward methane flux (0.015 mol/m^2/a) comparing with that at Site 995 on hydrate accumulation and found that the methane hydrate occurrence was extremely difficult to extend to the

BHSZ, despite the evolution time is long enough. The detailed model system for hydrate accumulation is described by Zheng et al. (2020). Finally, the actual hydrate occurrence thickness was thinner than that of the GHSZ. Site 994, a hydrate system with a thin zone of hydrate occurrence, might be attributed to the low methane flux from deep. This finding explains the discrepancy in hydrate distribution between Sites 994 and 995. Meanwhile, ODP Site 997 is located on the topographic crest of the Blake Ridge, 6.7 km northeast of Site 995. Numerous studies have shown that the methane hydrate deposit at Site 997 may be attributed to methane bubble migration along the fractured regions, suggesting a large deep methane flux (Flemings et al., 2003; Wallmann et al., 2006; Bhaumik and Gupta, 2007). Comparisons among Sites 994, 995, and 997 demonstrate that the deep methane flux is likely to increase along this drilling transect. Notably, the drilling report has also indicated that the hydrate occurrence discrepancy may be caused by variations in fluid composition (Paull et al., 1996). Therefore, we showed that along the Blake Ridge drilling transect the estimated deep methane fluxes decrease with increasing distance from the crest of the ridge (**Figure 4**). Previous studies have shown that a strong BSR is linked to elevated methane flux in deep layers (Pecher et al., 2001). Therefore, the regularly variable BSR characteristics at the Blake Ridge correspond well with our speculation.

In general, our numerical model provides a simple tool for estimating the value of deep methane flux. However, some caveats must be noted before the application. Our new approach is applicable to the system where the residual gas saturation has been determined or a low gas saturation is detected below the BHSZ. In such cases, methane gas originating from hydrate dissociation does not interfere with the FGZ.

CONCLUSION

With the aim of determining the deep dissolved methane flux transported into the GHSZ, we developed a numerical model based on the one-dimensional mass balance for methane to relate the characteristics of gas bubble distribution to the deep upward unsaturated methane-bearing fluid. Our calculations show that the methane flux in deep-sourced systems could be reflected by the volume fraction of residual methane gas in sediments and the FGZ thickness.

To the best of our knowledge, this is the first study that quantified the deep dissolved methane flux in a gas hydrate system with well-characterized FGZ beneath the BGHZ. The model-derived upward methane flux at Site 995 was 0.0231 mol/m^2/a. This result indicates the existence of a second free-gas interval at approximately 740 mbsf, which is consistent with the seismic data and further verifies our results. The hydrate occurrence is extremely difficult to extend to the BHSZ in a low methane flux scenario, such as Blake Ridge Site 994. Therefore, by combining these results and previous estimation of high deep methane flux at nearby Site 997, we showed that along the Blake Ridge drilling transect the estimated deep methane fluxes decrease with increasing distance from the crest of the ridge.

DATA AVAILABILITY STATEMENT

Publicly available datasets were analyzed in this study. This data can be found here: http://www-odp.tamu.edu/publications/pubs.htm.

AUTHOR CONTRIBUTIONS

ZZ: conceptualization, methodology, data analysis, and writing-original manuscript. YC: conceptualization, methodology, funding acquisition, writing-review and editing. WX: methodology and writing-review. DC: writing-review and funding acquisition. All authors contributed to manuscript preparation.

FUNDING

This work was supported by the National Key Research and Development Program of China (No. 2018YFC0310001), the NSF of China (Nos. 41776050, 91858208, and 41730528), and the China Geological Survey Project (No. DD20190230).

REFERENCES

Archer, D. E., Buffett, B. A., and Mcguire, P. C. (2012). A two-dimensional model of the passive coastal margin deep sedimentary carbon and methane cycles. *Biogeosciences* 9, 2921–2966. doi: 10.5194/bg-9-2859-2012

Bhatnagar, G., Chatterjee, S., Chapman, W. G., Dugan, B., Dickens, G., and Hirasaki, G. J. (2011). Analytical theory relating the depth of the sulfate-methane transition to gas hydrate distribution and saturation. *Geochem. Geophys. Geosys.* 12:Q03003. doi: 10.1029/2010GC003397

Bhatnagar, G., Chapman, W. G., Dickens, G. R., Dugan, B., and Hirasaki, G. J. (2007). Generalization of gas hydrate distribution and saturation in marine sediments by scaling of thermodynamic and transport processes. *Am. J. Sci.* 307, 861–900. doi: 10.2475/06.2007.01

Bhatnagar, G., Chapman, W. G., Dickens, G. R., Dugan, B., and Hirasaki, G. J. (2008). Sulfate-methane transition as a proxy for average methane hydrate saturation in marine sediments. *Geophys. Res. Lett.* 35:L03611. doi: 10.1029/2007gl032500

Bhaumik, A. K., and Gupta, A. K. (2007). Evidence of methane release from blake ridge ODP hole 997A during the plio-pleistocene: benthic foraminifer fauna and total organic carbon. *Curr. Sci.* 92, 192–199. doi: 10.1126/science.1135926

Burwicz, E., and Rüpke, L. (2019). Thermal state of the blake ridge gas hydrate stability zone (GHSZ)—insights on gas hydrate dynamics from a new multi-phase numerical model. *Energies* 12:3403. doi: 10.3390/en12173403

Burwicz, E., and Haeckel, M. (2020). Basin-scale estimates on petroleum components generation in the western black sea basin based on 3-D numerical modelling. *Mar. Pet. Geol.* 113:104122. doi: 10.1016/j.marpetgeo.2019.104122

Cao, Y., Chen, D. F., and Cathles, L. M. (2013). A kinetic model for the methane hydrate precipitated from venting gas at cold seep sites at hydrate ridge, cascadia margin, oregon *J. Geophys. Res. Solid Earth* 118, 1-13. doi: 10.1007/s11430-012-4553-6

Chen, D. F., and Cathles, L. M. (2003). A kinetic model for the pattern and amounts of hydrate precipitated from a gas stream: application to the bush hill vent site, green canyon block 185, Gulf of Mexico. *J. Geophys. Res. Solid Earth* 108:2058. doi: 10.1029/2001jb001597

Chen, D. F., and Cathles, L. M. (2005). On the thermal impact of gas venting and hydrate crystallization. *J. Geophys. Res. Solid Earth* 110:204. doi: 10.1029/2004JB003533

Claypool, G., and Kvenvolden, K. A. (1983). Methane and other hydrocarbon gases in marine sediment. *Ann. Rev. Earth Planet. Sci.* 11, 299–327. doi: 10.1146/annurev.ea.11.050183.001503

Daigle, H., Cook, A., Fang, Y., Bihani, A., Song, W., and Flemings, P. B. (2020). Gas-driven tensile fracturing in shallow marine sediments. *J. Geophys. Res. Solid Earth* 125, 1–19. doi: 10.1029/2020JB020835

Davie, M. K., and Buffett, B. A. (2001). A numerical model for the formation of gas hydrate below the seafloor. *J. Geophys. Res. Solid Earth* 106, 497–513. doi: 10.1029/2000jb900363

Davie, M. K., and Buffett, B. A. (2003a). Sources of methane for marine gas hydrate: inferences from a comparison of observations and numerical models. *Earth Planet. Sci. Lett.* 206, 51–63. doi: 10.1016/s0012-821x(02)01064-6

Davie, M. K., and Buffett, B. A. (2003b). A steady state model for marine hydrate formation: constraints on methane supply from pore water sulfate profiles. *J. Geophys. Res. Solid Earth* 108:2495. doi: 10.1029/2002jb002300

Davie, M. K., Zatsepina, O. Y., and Buffett, B. A. (2004). Methane solubility in marine hydrate environments. *Mar. geol.* 203, 177–184. doi: 10.1016/S0025-3227(03)00331-1

Dhakal, S., and Gupta, I. (2021). Simulating gas hydrate formation in the southern hydrate ridge. cascadia margin. *J. Nat. Gas Sci. Eng.* 88:103845. doi: 10.1016/j.jngse.2021.103845

Dickens, G. R., Paull, C. K., and Wallace, P. (1997). Direct measurement of in situ methane quantities in a large gas-hydrate reservoir. *Nature* 385, 426–428. doi: 10.1038/385426a0

Dickens, G. R. (2001). Sulfate profiles and barium fronts in sediment on the blake ridge: present and past methane fluxes through a large gas hydrate reservoir. *Geochim. Cosmochim. Acta.* 65, 529–543. doi: 10.1016/S0016-7037(00)00556-1

Duan, Z., Moller, N., Greenberg, J., and Weare, J. H. (1992). The prediction of methane solubility in natural waters to high ionic strength: from 0 to 250? and from 0 to 1600 bar. *Geochim. Cosmochim. Acta.* 56, 1451–1460. doi: 10.1016/0016-7037(92)90215-5

Egeberg, P. K., and Dickens, G. R. (1999). Thermodynamic and pore water halogen constraints on gas hydrate distribution at ODP Site 997 (Blake Ridge). *Chem. Geol.* 153, 53–79. doi: 10.1016/S0009-2541(98)00152-1

Fehn, U., Snyder, G., and Egeberg, P. K. (2000). Dating of pore waters with 129I: relevance for the origin of marine gas hydrates. *Science* 289, 2332–2335. doi: 10.1126/science.289.5488.2332

Firoozabadi, A., Ottesen, B., and Mikkelsen, M. (1992). Measurements of supersaturation and critical gas saturation. *SPE Form. Eval.* 7, 337–344. doi: 10.2118/19694-PA

Flemings, P. B., Liu, X., and Winters, W. J. (2003). Critical pressure and multiphase flow in Blake Ridge gas hydrates. *Geology* 31, 1057–1060. doi: 10.1130/g19863.1

Frederick, J. M., and Buffett, B. A. (2011). Topography and fracture-driven fluid focusing in layered ocean sediments. *Geophys. Res. Lett.* 38:L08614. doi: 10.1029/2010GL0460272011

Garg, S. K., Pritchett, J. W., Katoh, A., Baba, K., and Fujii, T. (2008). A mathematical model for the formation and dissociation of methane hydrates in the marine environment. *J. Geophys. Res.* 113:B01201. doi: 10.1029/2006JB004768

Haacke, R., Westbrook, G. K., and Hyndman, R. D. (2007). Gas hydrate, fluid flow and free gas: formation of the bottom-simulating reflector. *Earth Planet. Sci. Lett.* 261, 407–420. doi: 10.1016/j.epsl.2007.07.008

Haacke, R. R., Westbrook, G. K., and Riley, M. S. (2008). Controls on the formation and stability of gas hydrate-related bottom-simulating reflectors (BSRs): a case study from the west Svalbard continental slope. *J. Geophys. Res.* 113:B05104. doi: 10.1029/2007JB005200

Holbrook, W. S., Hoskins, H., and Wood, W. T. (1996). Methane hydrate and free gas on the Blake Ridge from vertical seismic profiling. *Science* 273, 1840–1843. doi: 10.1126/science.273.5283.1840

Holbrook, W. S. (2001). "Seismic studies of the blake ridge: implications for hydrate distribution, methane expulsion and free gas studies," in *Natural Gas hydrates: Occurrence, Distribution and Detection*, eds K. P. Charles and P. D. William (Washington, D.C: American Geophysical Union).

Hyndman, R. D., and Davis, E. E. (1992). A mechanism for the formation of methane hydrate and sea floor bottom-simulated reflectors by vertical fluid expulsion. *J. Geophy. Res.* 97, 7025–7041. doi: 10.1029/91JB03061

Kvenvolden, K. A. (1993). Gas hydrates: geological perspective and global change. *Rev. Geophy.* 31, 173–187. doi: 10.1029/93rg00268

Liu, X., and Flemings, P. B. (2007). Dynamic multiphase flow model of hydrate formation in marine sediments. *J. Geophys. Res.* 112:B03101. doi: 10.1029/2005jb004227

Liu, X., and Flemings, P. B. (2011). Capillary effects on hydrate stability in marine sediments. *J. Geophys. Res.* 116:B07102. doi: 10.1029/2010JB008143

Malinverno, A., Kastner, M., Torres, M. E., and Wortmann, U. G. (2008). Gas hydrate occurrence from pore water chlorinity and downhole logs in a transect across the northern cascadia margin (integrated ocean drilling program expedition 311). *J. Geophys. Res.* 113:B8. doi: 10.1029/2008JB005702

Malinverno, A. (2010). Marine gas hydrates in thin sand layers that soak up microbial methane. *Earth Planet. Sci. Lett.* 292, 399–408. doi: 10.1016/j.epsl.2010.02.008

Malinverno, A., and Goldberg, D. S. (2015). Testing short-range migration of microbial methane as a hydrate formation mechanism: results from andaman sea and kumano basin drill sites and global implications. *Earth Planet. Sci. Lett.* 422, 105–114. doi: 10.1016/j.epsl.2015.04.019

Minshull, T., and White, R. (1989). Sediment compaction and fluid migration in the Makran accretionary prism. *J. Geophys. Res.* 94, 7387–7402. doi: 10.1029/JB094iB06p07387

Mogollon, J. M., Heureux, I. L., Dale, A. W., and Regnier, P. (2009). Methane gas-phase dynamics in marine sediments: a model study. *Am. J. Sci.* 309, 189–220. doi: 10.2475/03.2009.01

Paull, C. K., Matsumoto, R., and Wallace, P. J. (1996). *Proceedings of the Ocean Drilling Program, Initial Reports*, 164.

Paull, C. K., Matsumoto, R., and Wallace, P. J. (2000). *Proceedings of the Ocean Drilling Program, Scientific Results*, 164.

Pecher, I. A., Kukowski, N., Huebscher, C., Greinert, J., and Bialas, J. (2001). The link between bottom-simulating reflections and methane flux into the gas hydrate stability zone – new evidence from lima basin. Peru Margin. *Earth Planet. Sci. Lett.* 185, 343–354. doi: 10.1016/S0012-821X(00)00376-9

Reagan, M. T., and Moridis, G. J. (2007). Oceanic gas hydrate instability and dissociation under climate change scenarios. *Geophys. Res. Lett.* 34:L22709. doi: 10.1029/2007GL031671

Shipley, T. H., Houston, M. H., Buffler, R. T., Shaub, F. J., McMillen, K. J., Ladd, J. W., et al. (1979). Seismic reflection evidence for the widespread occurrence of possible gas hydrate horizons on continental slopes and rises. *Am. Assoc. Pet. Geol. Bul.* 63, 2204–2213. doi: 10.1306/2f91890a-16ce-11d7-8645000102c1865d

Sloan, D. E., and Koh, C. A. (2008). *Clathrate Hydrates of Natural Gases*, 3rd Edn. New York, NY: CRC Press.

Stoll, R. D., Ewing, J., and Bryan, G. M. (1971). Anomalous wave velocities in sediments containing gas hydrates. *J. Geophys. Res.* 76, 2090–2094. doi: 10.1029/jb076i008p02090

Su, Z., and Chen, D. F. (2007). Calculation of methane hydrate solubility in marine environment and its constraints on gas hydrate occurrence. *Chin. J. Geophys.* 50, 1518–1526. doi: 10.1002/cjg2.1152

Torres, M. E., Wallmann, K., Tre´hu, A. M., Bohrmann, G., Borowski, W. S., and Tomaru, H. (2004). Gas hydrate growth, methane transport, and chloride enrichment at the southern summit of hydrate ridge, cascadia margin off oregon. *Earth Planet. Sci. Lett.* 226, 225–241. doi: 10.1016/j.epsl.2004.07.029

Vanderbeek, B. P., and Rempel, A. W. (2018). On the importance of advective versus diffusive transport in controlling the distribution of methane hydrate in heterogeneous marine sediments. *J. Geophys. Res. Solid Earth* 123, 5394–5411. doi: 10.1029/2017JB015298

Wallmann, K., Aloisi, G., and Haeckel, M. (2006). Kinetics of organic matter degradation, microbial methane generation, and gas hydrate formation in anoxic marine sediments. *Geochim. Cosmochim. Acta.* 70, 3905–3927. doi: 10.1016/j.gca.2006.06.003

Westbrook, G. K., and Thatcher, K. E. (2009). Escape of methane gas from the seabed along the West Spitsbergen continental margin. *Geophys. Res. Lett.* 36:L15608. doi: 10.1029/2009GL039191

Wood, W. T., and Ruppel, C. (2000). Seismic and thermal investigation of the Blake Ridge gas hydrate area: a synthesis. *Proc. Ocean. Drill. Prog. Sci. Results* 164, 253–264.

Xu, W., and Ruppel, C. (1999). Predicting the occurrence, distribution, and evolution of methane gas hydrate in porous marine sediments. *J. Geol. Res.* 104, 5081–5095. doi: 10.1029/1998JB900092

Xu, W. (2004). Modeling dynamic marine gas hydrate systems. *Am. Mineral.* 89, 1271–1279. doi: 10.2138/am-2004-8-916

You, K., Flemings, P. B., Malinverno, A., Collett, T. S., and Darnell, K. (2019). Mechanisms of methane hydrate formation in geological systems. *Rev. Geophys.* 57, 1–51. doi: 10.1029/2018RG000638

Zatsepina, O. Y., and Buffett, B. A. (1997). Phase equilibrium of gas hydrate: implications for the formation of hydrate in the deep sea floor. *Geophys. Res. Lett.* 24, 1567–1570. doi: 10.1029/97gl01599

Zheng, Z. H., Cao, Y. C., Xu, W. Y., and Chen, D. F. (2020). A numerical model to estimate the effects of variable sedimentation rates on methane hydrate formation-application to the ODP Site 997 on blake ridge, southeastern North American continental margin. *J. Geol. Res. Solid Earth* 125, 1–17. doi: 10.1029/2019jb018851

Conflict of Interest: WX was employed by the Independent Consultant.

The remaining authors declare that the research was conducted in the absence of any commercial or financial relationships that could be construed as a potential conflict of interest.

frontiers in Marine Science

ORIGINAL RESEARCH
published: 29 March 2022
doi: 10.3389/fmars.2022.858860

Magnesium Isotopes in Pore Water of Active Methane Seeps of the South China Sea

Meng Jin[1,2,3], Dong Feng[2,4*], Kangjun Huang[5], Shanggui Gong[4], Min Luo[4], Jörn Peckmann[6], Xudong Wang[4], Yu Hu[4] and Duofu Chen[3,4]

[1] Key Laboratory of Ocean and Marginal Sea Geology, South China Sea Institute of Oceanology, Innovation Academy of South China Sea Ecology and Environmental Engineering, Chinese Academy of Sciences, Guangzhou, China, [2] Laboratory for Marine Mineral Resources, Qingdao National Laboratory for Marine Science and Technology, Qingdao, China, [3] University of Chinese Academy of Sciences, Beijing, China, [4] Shanghai Engineering Research Center of Hadal Science and Technology, College of Marine Sciences, Shanghai Ocean University, Shanghai, China, [5] State Key Laboratory of Continental Dynamics and Shanxi Key Laboratory of Early Life and Environment, Department of Geology, Northwest University, Xi'an, China, [6] Institute for Geology, Center for Earth System Research and Sustainability, Universität Hamburg, Hamburg, Germany

OPEN ACCESS

Edited by:
Ed Hathorne,
Helmholtz Association of German Research Centres (HZ), Germany

Reviewed by:
Philip Pogge von Strandmann,
University College London,
United Kingdom
Zhilei Sun,
Qingdao Institute of Marine Geology (QIMG), China

***Correspondence:**
Dong Feng
dfeng@shou.edu.cn

Specialty section:
This article was submitted to Marine Biogeochemistry, a section of the journal Frontiers in Marine Science

Received: 20 January 2022
Accepted: 08 March 2022
Published: 29 March 2022

Citation:
Jin M, Feng D, Huang K, Gong S, Luo M, Peckmann J, Wang X, Hu Y and Chen D (2022) Magnesium Isotopes in Pore Water of Active Methane Seeps of the South China Sea. Front. Mar. Sci. 9:858860. doi: 10.3389/fmars.2022.858860

The magnesium (Mg) isotopic composition of marine authigenic carbonates is considered as promising archive of ancient seawater geochemistry and paleoenvironments. Previous experimental and theoretical work has shown that Mg isotope fractionation during carbonate mineral formation is a function of mineralogy and precipitation rate. However, information on Mg isotope fractionation is limited for well-defined precipitation rates in natural settings. Here, we investigate pore waters from sediments of an area of active methane seepage in the South China Sea. Low δ^{13}C values (< –48.3‰ VPDB) of dissolved inorganic carbon (DIC) near the sulfate-methane transition zone (SMTZ) indicate that sulfate-driven anaerobic oxidation of methane (SD-AOM) is the predominant biogeochemical process. Pore water composition of dissolved Mg, calcium (Ca), and strontium (Sr) agrees with aragonite as the dominant carbonate mineral at the site ROV1, and high Mg-calcite at sites ROV2 and ROV4. Calculated carbonate precipitation rates are 0.92 μmol cm^{-2} yr^{-1} for site ROV2 and 1.24 μmol cm^{-2} yr^{-1} for site ROV4; these estimates are similar to previous calculations for seeps from other areas. The pore water δ^{26}Mg values (–0.88‰ to –0.71‰) obtained for the three study sites are similar to those of seawater, in accord with a minor effect of Rayleigh fractionation due to abundant supply of Mg from seawater and insignificant consumption of Mg during carbonate precipitation. The modeled Mg isotope fractionation (ϵ = –2.0‰ to –1.0‰ for core ROV2; ϵ = –1.3‰ to –0.3‰ for core ROV4) can be explained by kinetic isotope fractionation during carbonate precipitation. The calculated carbonate precipitation rates and the degree of fractionation of Mg isotopes support the notion that fractionation is small at high precipitation rates. However, the carbonate precipitation rates calculated for the studied seep environments are much smaller than those in laboratory experiments, documenting a discrepancy of isotopic fractionation between carbonate authigenesis in laboratory experiments and natural environments. These results, including the modeled precipitation rates, provide new constraints for Mg isotope fractionation in natural settings.

Keywords: Mg isotopes, authigenic carbonate, pore water geochemistry, methane seep, South China Sea

1 INTRODUCTION

Carbonate precipitation, representing a sink of Mg in the ocean, is an important part of the oceanic Mg cycle (Higgins and Schrag, 2015). The Mg isotopic composition of marine carbonates is used as a proxy to constrain the composition of seawater on geological timescales and to trace the global Mg cycle (e.g. Tipper et al., 2006; Fantle and Higgins, 2014; Kasemann et al., 2014; Pogge von Strandmann et al., 2014; Higgins and Schrag, 2015; Gothmann et al., 2017). A large number of theoretical calculations and laboratory experiments have been conducted to determine the fractionation of Mg isotopes during precipitation of different types of carbonate minerals (e.g. Saenger and Wang, 2014; Li et al., 2015; Pinilla et al., 2015; Wang et al., 2017). Fractionation exhibits a temperature dependence of only approximately 0.01‰ $°C^{-1}$ (Li et al., 2012; Pearce et al., 2012; Wang et al., 2013), while it largely depends on carbonate mineralogy and precipitation rate (Immenhauser et al., 2010; Mavromatis et al., 2013; Wang et al., 2013). The mineralogical control is expressed in a general trend toward the enrichment of heavy Mg isotopes from calcite over magnesite over dolomite to aragonite (Wang et al., 2013). Moreover, small fractionation of Mg isotopes was observed in laboratory experiments with high carbonate precipitation rates (Immenhauser et al., 2010; Wombacher et al., 2011; Mavromatis et al., 2013), opposite to trends reported for Ca isotopes in carbonate minerals (Tang et al., 2008; DePaolo, 2011). This was attributed to the high free energy of hydration of Mg^{2+} ions (Mavromatis et al., 2013). However, such rate-dependent Mg isotope fractionation was not observed in some other calcite precipitation experiments, although precipitation rates varied over a wide range (Li et al., 2012; Chen et al., 2020). It follows that the influence of carbonate precipitation rate on fractionation of Mg isotopes may not be straightforward. Remarkably, research on the effect of precipitation rate on Mg isotope fractionation was mostly based on laboratory experiments to date. Yet, the conditions of carbonate precipitation in the environment are more complex than conditions during laboratory experiments (Li et al., 2015; Jin et al., 2021). Research investigating Mg isotope fractionation during carbonate precipitation in the environment is still limited (e.g. Lu et al., 2017; Pogge von Strandmann et al., 2019). Such discrepancy adds to the uncertainties in our understanding of the behavior of Mg isotopes during carbonate precipitation.

Organoclastic sulfate reduction (OSR) and sulfate-driven anaerobic oxidation of methane (SD-AOM) are two widespread biogeochemical processes in marine sediments commonly favoring carbonate precipitation (Jørgensen and Kasten, 2006; Schrag et al., 2013). It has been proposed that the rates of carbonate precipitation during SD-AOM are generally faster than those during OSR, owing to the higher rate of SD-AOM and the resulting higher alkalinity compared to OSR (Karaca et al., 2010). High rates of SD-AOM result in high precipitation rates of methane-derived seep carbonates, making these authigenic carbonates a significant component of overall marine sedimentary carbonates (Bradbury and Turchyn, 2019). Previously, Mg isotope fractionation during precipitation has been deduced from the analysis of the mineral products, i.e., seep carbonates (Lu et al., 2017; Jin et al., 2021). These studies suggested that besides precipitation rate, hydrogen sulfide produced by SD-AOM may also affect the fractionation of Mg isotopes (Lu et al., 2017; Jin et al., 2021). However, precipitation rate, which is believed to have a major influence on Mg isotope fractionation based on previous laboratory experiments, cannot be accurately constrained using rock samples. The lack of documented Mg isotope fractionation at well-constrained natural precipitation rates limits our understanding of Mg isotope variability in ancient carbonate rocks (cf. Blättler et al., 2021).

This study presents Mg isotope compositions of pore fluid from the Haima methane seeps of the South China Sea, a well-studied area where seep carbonate is forming today. The precipitation rate of the authigenic seep carbonate was constrained by pore fluid measurements and by the use of a diffusion-advection-reaction (DAR) model. Obtained precipitation rates are significantly lower than those observed in laboratory experiments (Immenhauser et al., 2010; Li et al., 2012; Mavromatis et al., 2013; Chen et al., 2020). The Sr/Ca and Mg/Ca ratios of pore water were used to constrain carbonate mineralogy (Nöthen and Kasten, 2011). Since the mineralogy of the nodules does not necessarily reflect today's pore water composition – the nodules may have formed in the past under a different pore water regime (cf. Blättler et al., 2021) – we decided to assess the current diagenetic environment from the cation composition of pore waters. For one core, aragonite was found to be the dominate calcium carbonate mineral, for the other two cores it was high-Mg calcite. These results were then used to evaluate the degree of fractionation, enabling us to provide new constraints on the extent of Mg isotope fractionation during carbonate mineral formation in natural environments.

2 MATERIALS AND METHODS

2.1 Sampling

Three gravity piston cores (ROV1, ROV2, and ROV4; water depth approximately 1300 to 1400 m) were collected at the Haima seeps from the northwest South China Sea during the Haiyang-6 cruise in 2020 (**Figure 1**). The presence of gas hydrates is inferred from

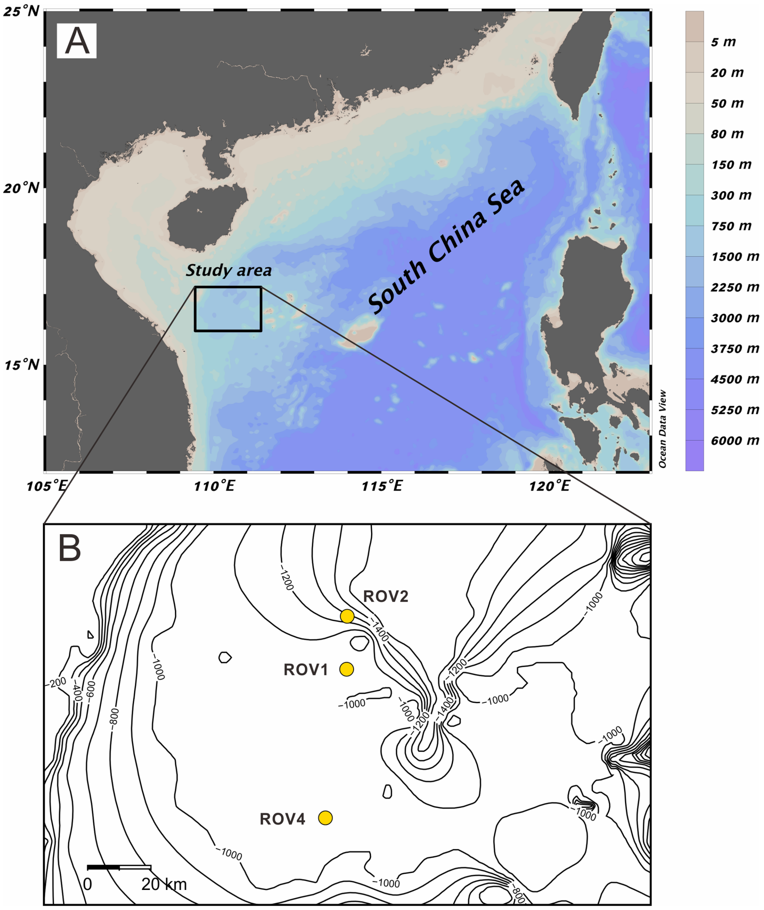

FIGURE 1 | Map showing the location of study area (Schlitzer, Reiner, Ocean Data View, https://odv.awi.de, 2021) **(A)** and sampling sites **(B)**.

widely distributed bottom simulating reflectors and gas chimneys (Hui et al., 2016). Gas hydrates, authigenic carbonates, and living chemosynthesis-based communities were recovered from the study area (Liang et al., 2017).

Immediately after recovery, the retrieved cores were brought to the onboard laboratory for pore water extraction. Pore water was collected at 5 to 20 cm intervals using Rhizon samplers with pore size of 0.28 μm. Subsamples for pore water DIC concentration were preserved with saturated $HgCl_2$ solution. For ions, dissolved elements, and Mg isotope analyses, subsamples were acidified with ultrapure concentrated HNO_3. All pore water subsamples were stored at 4°C. Carbonate nodules ranging in size from about 5 mm to 35 mm were distributed throughout the core ROV1, but were limited to the upper 230 cm in core ROV2. No nodules were observed in core ROV4.

2.2 Analysis of Dissolved Species in Pore Water

Sulfate (SO_4^{2-}) concentrations were measured on a Dionex ICS-5000 ion chromatograph with an analytical precision of < 2%. Calcium (Ca^{2+}), magnesium (Mg^{2+}), and strontium (Sr^{2+}) concentrations were determined by ICP-OES. The analytical precision was better than 3%. Concentration and isotope composition of DIC was determined with a Gas-bench continuous flow Delta-V Plus mass spectrometer after acidifying the sample with pure H_3PO_4. About 0.5 ml pore water was treated with 6 drops of pure H_3PO_4 in a glass vial at 25°C. After reacting for 18 h, the produced CO_2 was separated through a gas chromatographic column and was transferred to the mass spectrometer for $\delta^{13}C$ measurement. The isotopic ratio is expressed relative to the Vienna-Pee Dee Belemnite (V-PDB) standard and the analytical precision was better than ±0.1‰. $NaHCO_3$ lab-standard samples with concentration ranges from 1 to 30 mM were prepared for the determination of DIC concentration. Calculation of DIC concentration was based on the excellent linear correlation (R^2>0.999, N=7) between the intensity of CO_2 gas produced and the DIC concentration of the $NaHCO_3$ lab-standard samples. The analytical precision of the DIC concentration was <2%. The analyses were conducted at Shanghai Ocean University.

2.3 Mg Isotope Analysis of Pore Water

The analytical procedure for Mg isotope analysis was based on Bao et al. (2019). Two columns were used to purify Mg from other matrix metals. Column #1 (loaded with 2 ml of Bio-Rad 200–400 mesh AG50W-X12 resin) was designated to separate Mg from Ca. Column #2 (loaded with 0.5 ml of Bio-Rad 200–400 mesh AG50W-X12 resin) was used to separate Mg from all other matrices (Na, Al, Fe, Ti). To acquire a pure Mg fraction, each sample was passed through column #1 twice, followed by two passages through column #2. The recovery of Mg after the whole procedure of column chemistry was better than 99%, and the total blank for the complete analysis was <10 ng Mg, which is insignificant compared to the mass of the sample. One in-house standard Alfa Mg, one USGS standard (BCR-2), and seawater from the South China Sea were processed with samples for the whole procedure of column chemistry to assess the accuracy of column chemistry. Magnesium isotope ratios were measured with a Thermo Scientific Neptune Plus high-resolution MC-ICPMS at Northwest University, China. Measurements were conducted with the standard-sample bracketing method to correct for the instrumental mass bias and drift. Analyses were performed in low mass resolution mode, simultaneously measuring ^{26}Mg, ^{25}Mg, and ^{24}Mg. The measured Mg isotope ratios are reported in the delta notation as per mil (‰) deviation relative to the DSM3 standard (Young and Galy, 2004): δ^{x}Mg = [(^{x}Mg/^{24}Mg) sample/(^{x}Mg/^{24}Mg) DSM3] × 10^3, where x refers to 25 or 26. All samples were analyzed three times within an analytical session. The internal precision determined on the basis of ≥3 repeated runs of the same sample solution during a single analytical session was better than ±0.10‰ (2SD). Analyses of the Alfa Mg, BCR-2, and seawater standards yielded δ^{26}Mg values of –3.92 ± 0.09‰ (2SD), –0.22 ± 0.07‰ (2SD), and –0.86 ± 0.04‰ (2SD), respectively. When the equivalent 2SD uncertainties are considered, the Mg isotopic compositions reported herein are consistent with previously published values (Foster et al., 2010; Huang et al., 2015; Teng, 2017).

3 RESULTS

3.1 Dissolved Species of Pore Water

Depth profiles of dissolved sulfate, DIC concentrations, and $\delta^{13}C_{DIC}$ values are shown in **Figure 2**. Sulfate concentrations remain unchanged from 0 to 28 cm depth and linearly decrease to 140 cm for core ROV1, while sulfate concentrations decline from the topmost sediments to 200 cm below the seafloor for core ROV2. At site ROV4, sulfate reveals bottom-water concentration down to 240 cm below the seafloor and then linearly decreases to a depth of 460 cm. The approximate depths of the SMTZ at sites ROV1, ROV2, and ROV4 are 140 cm, 200 cm, and 460 cm below the seafloor, respectively. Concentrations of DIC steadily increase from 4 mM at 20 cm depth to 18 mM at the SMTZ at site ROV1, while rising from 3.3 mM in the topmost sediments to 18 mM at the SMTZ at site ROV2. For core ROV4, concentrations of DIC increase from 3.8 mM at 210 cm to 21 mM at the SMTZ. The $\delta^{13}C_{DIC}$ values decrease with depth toward the SMTZ. The lowest $\delta^{13}C_{DIC}$ values for the ROV1, ROV2, and ROV4 study sites are –48.3‰, –54.1‰, and –50.6‰, respectively.

Depth profiles of Ca^{2+}, Mg^{2+}, and Sr^{2+} concentrations are presented in **Figure 3**. Calcium concentration drops rapidly from the surface layer to the SMTZ at sites ROV1 and ROV2, while Ca concentration remains constant down to 240 cm below the seafloor before declining toward the SMTZ at the ROV4 site. Magnesium concentrations decline from 52.2 mM to 49.9 mM and from 53.9 mM to 48.2 mM with depth in the measured profiles at the ROV1 and ROV2 sites, respectively. For core ROV4, Mg^{2+} exhibits bottom water concentration down to a depth of 240 cm below the seafloor and before concentration decreases by 7 mM toward the base of the profile. For Sr^{2+} concentrations, only pore water at the ROV1 site shows a significant decline of approximately 70 μM within the upper 150 cm. Strontium concentrations at sites ROV2 and ROV4 decrease only little with depth (< 20 μM).

3.2 Mg Isotopic Composition of Pore Water

Depth profiles of δ^{26}Mg values are represented in **Figure 3**. The δ^{26}Mg and δ^{25}Mg values are converted to δ^{26}Mg′ and δ^{25}Mg′ values (Young and Galy, 2004), which are then presented in a δ^{25}Mg′ vs. δ^{26}Mg′ plot (**Figure 4**). All samples and standards analyzed in this study fall on a single mass-dependent fractionation line with a slope of 0.5169. The Mg isotopic composition of pore water from the three sites is close to seawater composition. The Mg isotopic composition of pore water from core ROV1 remains almost constant, ranging from −0.87‰ to −0.82‰. The δ^{26}Mg values of pore water extracted from the ROV2 and ROV4 cores increase with depth from −0.88‰ to −0.71‰, and −0.87‰ to −0.73‰, respectively.

4 DISCUSSION

4.1 Environmental Conditions and Carbonate Mineralogy

The δ^{13}C values of DIC generated from SD-AOM and OSR are close to δ^{13}C values of parent methane and organic matter, respectively (cf. Whiticar, 1999). The δ^{13}C values of methane in the study area range from −72.3‰ to −71.5‰ (Wei et al., 2020). The δ^{13}C value of South China Sea organic matter is approximately −20‰ (Chen et al., 2012). Therefore, the low $\delta^{13}C_{DIC}$ values of pore water from the study sites (**Figure 2**) indicates that SD-AOM is the dominant biogeochemical process. This is confirmed by the observed rapid depletion of sulfate and the shallow depth of the SMTZ. Intense SD-AOM resulted in a DIC concentration, which is known to facilitate carbonate precipitation at methane seeps (Berner, 1980; Aloisi et al., 2000; Naehr et al., 2007). The decrease of Ca^{2+}, Mg^{2+}, and Sr^{2+} concentrations with depth agrees with carbonate authigenesis in the local sedimentary environment (**Figure 3**), with the decline of Sr concentration best explained by aragonite formation (Snyder et al., 2007).

Changes of Ca^{2+}, Mg^{2+}, and Sr^{2+} concentrations in pore water can be used to identify the mineralogy of the carbonate minerals deemed to precipitate under current conditions (e.g. Nöthen and Kasten, 2011). Formation of high-Mg calcite, which has lower Sr/Ca ratios than seawater, results in an increase of the Sr/Ca ratios in pore water. Conversely, aragonite has higher Sr/Ca ratios but lower

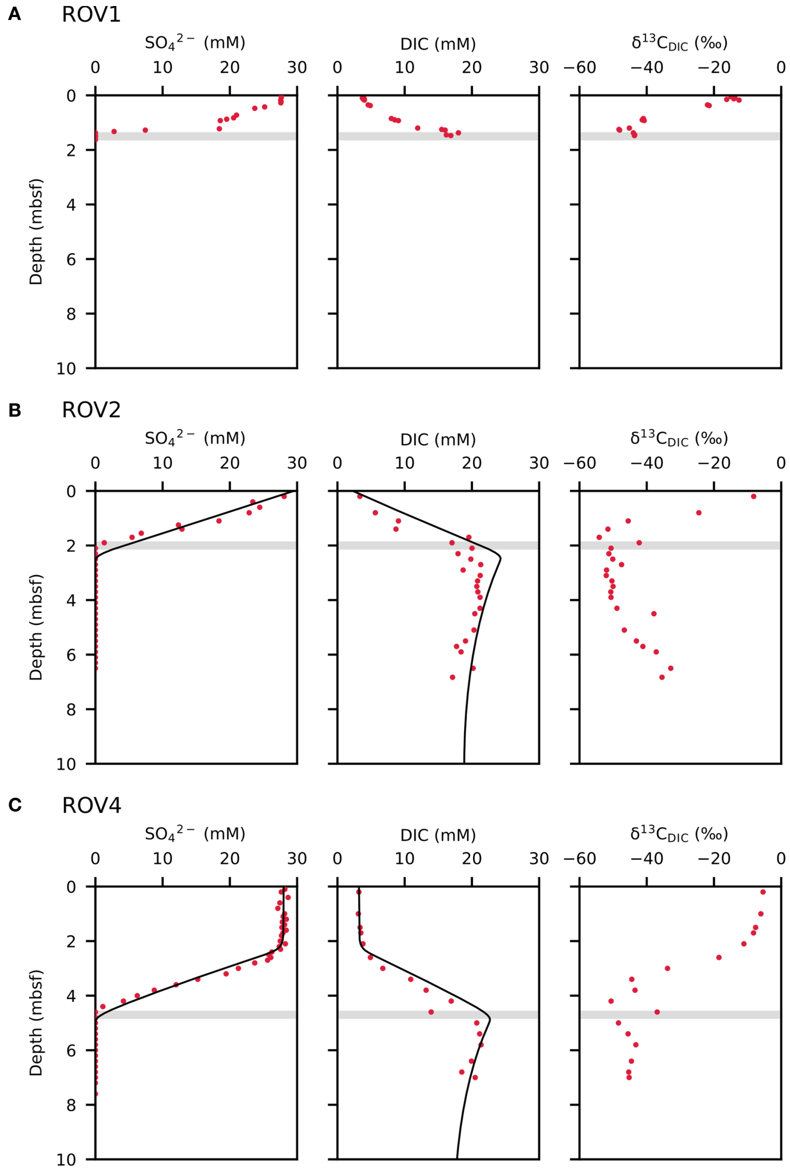

FIGURE 2 | Pore water profiles of sulfate (SO_4^{2-}) and dissolve inorganic carbon (DIC) concentrations and $\delta^{13}C_{DIC}$ values for cores ROV1 **(A)**, ROV2 **(B)**, and ROV4 **(C)**. Dots are measured data and solid lines are model results. The "mbsf" refers to meters below seafloor. The shaded bar marks the sulfate-methane transition zone (SMTZ).

Mg/Ca ratios than seawater; its removal from pore water will lead to the decrease of Sr/Ca ratios and the increase of Mg/Ca ratios in pore water. Accordingly, the current pore water conditions favor aragonite formation at the ROV1 site, but high-Mg calcite formation at the ROV2 and ROV4 sites (**Figure 5**).

4.2 Numerical Modeling of Carbonate Precipitation Rates and Mg Isotope Composition

4.2.1 Model Description

The one-dimensional, steady state, diffusion-advection-reaction (1D-DAR) model was applied to quantify the geochemical profiles of sediment pore water. This model has been widely used in simulations of early diagenetic processes (e.g. Wallmann et al., 2006; Fantle and DePaolo, 2007; Higgins and Schrag, 2010; Hu et al., 2018).

The simplified 1D-DAR model is expressed as:

$$\phi\cdot\frac{\partial C}{\partial t}=\frac{\partial}{\partial z}\left(\phi\cdot D\cdot\frac{\partial C}{\partial z}\right)-\frac{\partial}{\partial z}(\phi\cdot\omega\cdot C)+\phi\cdot\Sigma R$$

where C (mol m^{-3}) is the concentration of a certain element, Φ is porosity, z (m) is the depth below the seafloor, ω (m yr^{-1}) corresponds to advective velocities, D (m^2 yr^{-1}) is the vertical

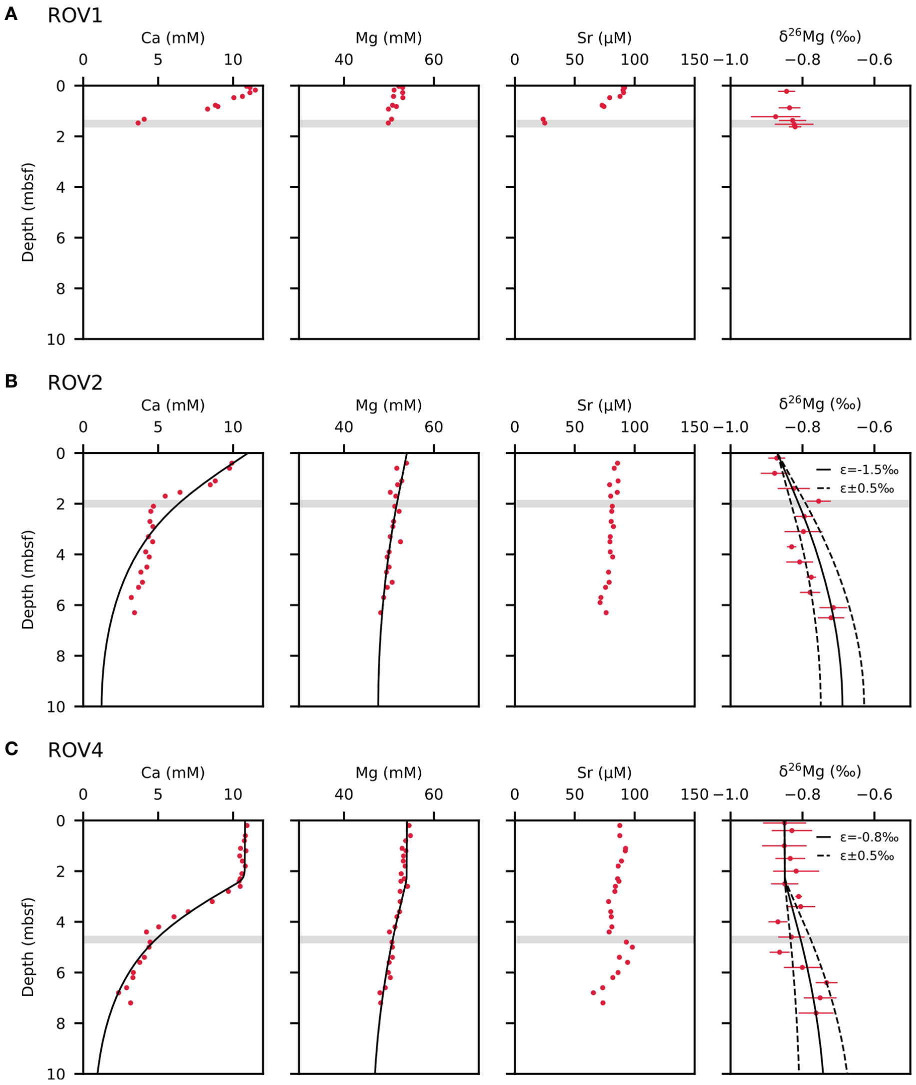

FIGURE 3 | Pore water profiles of calcium (Ca^{2+}), magnesium (Mg^{2+}), strontium (Sr^{2+}) concentrations, and $\delta^{26}Mg$ values for cores ROV1 **(A)**, ROV2 **(B)**, and ROV4 **(C)**. Dots are measured data and solid lines are model results. Uncertainties in modeled fractionation factors (ε) are calculated by varying fractionation factors by ±0.5‰ indicated by the dotted lines. The "mbsf" refers to meters below seafloor. The shaded bar marks the sulfate-methane transition zone (SMTZ).

diffusivity coefficient of bulk sediment, and ΣR is the first-order rate constant for chemical reactions that remove elements from pore water.

Depth-dependent molecular diffusion coefficients of dissolved species were calculated after Oelkers and Helgeson (1991) and corrected for the effect of tortuosity:

$$D = \frac{D_0}{1 - \ln(\Phi^2)}$$

where D_0 is the molecular diffusion coefficient in free seawater at the *in-situ* temperature, salinity, and pressure.

Since porosity and sedimentation rate data are not known, we assume a constant porosity and adopt the sedimentation rate of Wang et al. (2000) within the modeled domain. As a result, in the current absence of externally imposed fluid advection at the seafloor, the advective velocities of pore water are equivalent to the sedimentation rate, s (m yr^{-1}), at the seafloor.

Gas bubble irrigation is considered in the model to fit the obtained pore water data for the ROV4 site above 240 cm. Similar to bioirrigation, gas bubble irrigation promotes the exchange of pore water and bottom water, but its influence may extend to greater depth than bioirrigation (e.g. Haeckel et al., 2007; Hu et al., 2019). According to previous studies (Haeckel et al., 2007; Chuang et al., 2013; Hu et al., 2019), gas bubble irrigation is described by parameters α_1 (yr^{-1}) and α_2 (cm) that define the irrigation intensity and its attenuation below the irrigation depth L_{irr} (cm), respectively. The variable α_1 is a model fitting parameter, and irrigation depth can be determined with the aid of pore water data. For simplification, α_2 is assumed to be a constant value.

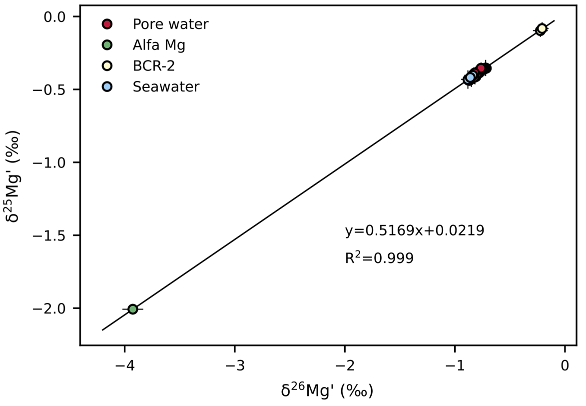

FIGURE 4 | Plot of δ^{25}Mg' vs. δ^{26}Mg' illustrating Mg isotopic composition of pore water and standards (Alfa Mg, BCR-2, seawater). Solid line represents the regression line of all data.

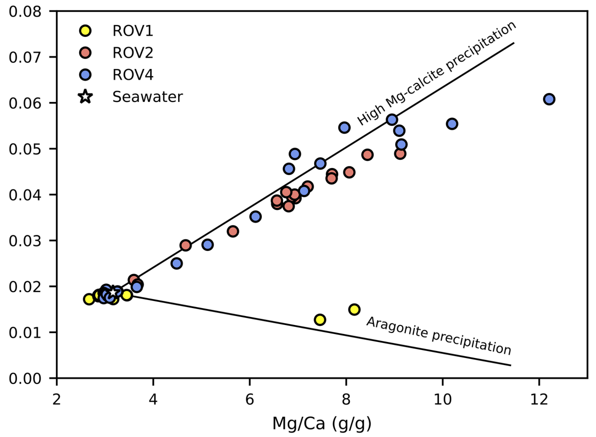

FIGURE 5 | Plot of Sr/Ca versus Mg/Ca (weight ratios) in pore water of cores ROV1, ROV2, and ROV4 as well as in seawater (de Villiers, 1999). The two bold lines indicate changes in the Sr/Ca to Mg/Ca relationship in pore water with respect to the composition of seawater that occur during precipitation of either aragonite or high Mg-calcite. The Sr/Ca and Mg/Ca ratios of the precipitating aragonite and high Mg-calcite were taken from Bayon et al. (2007) and Nöthen and Kasten (2011).

Given that SD-AOM is the dominant biogeochemical process at the study sites, carbonate precipitation driven by SD-AOM is assumed to explain the consumption of Mg^{2+} and Ca^{2+}:

$$\mathbf{x\,Ca^{2+}+(1-x)\,Mg^{2+}+CO_3^{2-}=Ca_xMg_{(1-x)}CO_3^{2-}}$$

Thus, it is inapplicable to calculate the reaction rate of Mg independently. Precipitation rates (R_P) of carbonate were calculated by saturation state and kinetic constant (k_{Ca}) in previous studies (e.g. Luff and Wallmann, 2003; Hu et al., 2019):

$$\mathbf{R_p=k_{Ca}\left(\frac{[Ca^{2+}][CO_3^{2-}]}{K_{sp}}-1\right)}$$

where K_{sp} refers to the solubility product of pure calcite for simplification, ignoring Mg contained in carbonate. The reaction rate of Mg was tuned to fit the concentration profiles in Higgins and Schrag (2010). In this study, we calculated the reaction rate of Ca and Mg respectively in order to model the fractionation of Mg isotopes during carbonate precipitation at the ROV2 and ROV4 study sites:

$$\mathbf{R_{Ca}=k_{Ca}\left(\frac{[Ca^{2+}][CO_3^{2+}]}{K_{sp1}}-1\right)}$$

$$\mathbf{R_{Mg}=k_{Mg}\left(\frac{[Mg^{2+}][CO_3^{2+}]}{K_{sp2}}-1\right)}$$

where K_{sp1} and K_{sp2} refers to the solubility product of $CaCO_3$ and $MgCO_3$, respectively, and k_{Ca} and k_{Mg} are tuned to fit the measured data. A typical pore water pH value of 7.6 was used to calculate CO_3^{2-} from the modeled DIC concentration (Zeebe and Wolf-Gladrow, 2001).

To model the Mg isotopic profiles (i.e. δ^{26}Mg) of pore water, we treat the isotopes ^{24}Mg and ^{26}Mg separately. Eq. (1) can be re-expressed as follows:

$$\mathbf{\phi\cdot\frac{\partial({}^{i}Mg)}{\partial t}=\frac{\partial}{\partial z}\left(\phi\cdot D_{Mg}\cdot\frac{\partial\,{}^{i}Mg}{\partial z}\right)-\frac{\partial}{\partial z}\left(\phi\cdot s\cdot{}^{i}Mg\right)+\phi\cdot R_{i_{Mg}}}$$

where ^{i}Mg is the concentration of ^{24}Mg or ^{26}Mg. We use the same diffusion coefficient (D_{Mg}) for both ^{24}Mg and ^{26}Mg owing to limited fractionation of Mg isotopes during diffusion ($\alpha^{26/24}_{diffusion}$ = 1.00003 ± 0.00006; Richter et al., 2006). Here, carbonate precipitation is the chemical reaction involving Mg ions.

The fractionation of Mg isotopes is represented as:

$$\mathbf{\epsilon^{26/24}=(\alpha^{26/24}-1)\times 1000}$$

where $\alpha^{26/24}=\frac{R_{^{26}Mg}}{R_{^{24}Mg}}$

The length of the simulated model domain was set to 1000 cm and 1200 cm for cores ROV2 and ROV4, respectively. Upper boundary conditions for all species were imposed as fixed concentrations (Dirichlet boundary), using measured values for the uppermost sediment layer where available. A zero-concentration gradient (Neumann-type boundary) was imposed at the lower boundary for all species. Model parameters are listed in **Table 1**.

4.2.2 Rates of Carbonate Precipitation and Mg Isotope Composition

The calculated reaction rates of Ca and Mg reach a peak near the SMTZ, owing to the highest DIC concentrations and the highest carbonate saturation in pore water. The depth-integrated rates and converted carbonate precipitation rates are listed in **Table 2**. The depth-integrated rates refer to the downward fluxes of Ca or Mg per unit surface area. Both the fluxes of Ca and Mg for the study sites are much higher than those calculated for ODP Site 1082, where SD-AOM-driven carbonate precipitation occurs in shallow sediments (Moore et al., 2004). R_{Mg} calculated in this study is also higher than that of ODP Site 1082 given by

TABLE 1 | Parameters used in the model to assess Mg isotope fractionation.

Parameter	ROV2	ROV4	Unit
Temperature (T)	4	4	°C
Salinity (S)	35	35	–
Pressure (P)	14.4	13.6	Mpa
Density of dry solids (ρ_s)	2.65	2.65	g cm^{-3}
Sedimentation rate (s)[a]	0.03	0.03	cm yr^{-1}
Porosity (Φ)[b]	0.7	0.7	–
Kinetic constant of SD-AOM ($k_{SD\text{-}AOM}$)	0.5	0.5	$cm^3\ yr^{-1}\ mmol^{-1}$
Kinetic constant for calcite precipitation (k_{Ca})	10^{-9}	1.5×10^{-9}	yr^{-1}
Kinetic constant for Mg calcite precipitation (k_{Mg})	3×10^{-10}	4×10^{-10}	yr^{-1}
Kinetic constant of methane gas bubble dissolution (k_{GD})	–	10^{-4}	yr^{-1}
Kinetic constant of methane gas bubble formation (k_{GF})	–	0.2	yr^{-1}
Depth of gas bubble irrigation (L_{irr})	–	230	cm
Irrigation coefficient at the surface (α_1)	–	0.4	yr^{-1}
Attenuation coefficient for decrease in bubble irrigation (α_2)[c]	–	5	cm
Upper boundary condition for SO_4^{2-}	29.5	28	mM
Upper boundary condition for DIC	2.3	3.2	mM
Upper boundary condition for CH_4	0	0	mM
Upper boundary condition for Ca^{2+}	11	10.8	mM
Upper boundary condition for Mg^{2+}	54	54	mM
Upper boundary condition for $\delta^{26}Mg$	–0.87	–0.85	‰ (DSM3)

[a] *Mean value derived from six ODP184 drillings in South China Sea (Wang et al., 2000).*

[b] *Modified after Wang et al. (2000).*

[c] *Huang et al. (1997).*

TABLE 2 | Depth-integrated rates of downward flux of Ca and Mg and converted carbonate precipitation rates.

Sites	Depth-integrated rates (μmol cm^{-2} yr^{-1})		Carbonate precipitation rate [a](μmol cm^{-2} yr^{-1})
	R_{Ca}	R_{Mg}	R_p (factor = 0.4[b])
ROV2	1.6	0.7	0.92
ROV4	2.2	0.9	1.24

[a] *Carbonate precipitation rate = (R_{Ca} + R_{Mg}) × factor.*

[b] *A conversion factor defined in Blättler et al. (2021) to relate fluxes to estimated precipitation rates of carbonate per unit reactive surface area at methane seeps.*

Higgins and Schrag (2010). The SMTZ at ODP Site 1082 is situated between 18 to 24 mbsf (meters below seafloor; Moore et al., 2004), which is much deeper than the position of the SMTZ at our study sites. Higher fluxes of Ca and Mg at the South China Sea sites agree with higher carbonate precipitation rates than those at ODP Site 1082.

Note that R_{Ca} and R_{Mg} are in the same order of magnitude, which is consistent with the consumption of Ca and Mg apparent in the depth profiles (**Figure 3**). A similar situation has been reported by Blättler et al. (2021), who observed a 26% decrease of Mg within 1.7 m of sediment depth. In case of aragonite precipitation, the consumption of Mg in pore water can be neglected owing to the small amount of Mg in aragonite compared to high-Mg calcite (Bayon et al., 2007). Carbonate precipitation rates were typically calculated from the depth profiles of Ca concentrations in previous studies (e.g. Luff and Wallmann, 2003; Karaca et al., 2010). However, in cases of high-Mg calcite precipitation with significant decrease of Mg in depth profiles, carbonate precipitation rates may be underestimated when based on the flux of Ca alone. In this study, R_{Ca} and R_{Mg} were therefore added up to calculate carbonate precipitation rates. In order to compare the carbonate precipitation rates in this study to that obtained from laboratory experiments, the sum of fluxes of Ca and Mg were converted into the precipitation rate of carbonate per unit reactive surface area. This requires several assumptions and rough estimates relevant to a roughness factor and a surface reactivity factor (Beckingham et al., 2016). A factor of 0.4 was yielded in Blättler et al. (2021) to convert Ca fluxes to carbonate precipitation rates on available mineral surface areas at methane seeps, which was adopted in this study (see **Table 2**). The resultant carbonate precipitation rates for sites ROV2 and ROV4 are 0.92 μmol cm^{-2} yr^{-1} and 1.24 μmol cm^{-2} yr^{-1}, respectively (**Table 2**). Uncertainties on estimating were considered to be an order of magnitude in either direction according to Blättler et al. (2021). The intensity of seepage in this study is similar to that in Blättler et al. (2021), and the calculated carbonate precipitation rates are in the same order of magnitude too.

The modeled Mg isotopic compositions of pore water are represented in **Figure 3**. The model was run with a constant seawater Mg isotopic composition and a varying Mg isotope fractionation factor (α = 0.998 to 0.999, ϵ = −2.0 to −1.0‰ for core ROV2; α = 0.9987 to 0.9997, ϵ = −1.3 to −0.3‰ for core ROV4). Our modeled results match the measured data well within the analytical error.

4.3 Pore Water Mg Isotopes at Seeps

The Mg concentrations of pore water are typically related to Mg concentration of seawater, carbonate authigenesis, and formation/dissolution of clay minerals (Higgins and Schrag, 2010). Considering that the samples were collected from continental slopes, terrigenous clasts rather than authigenic clay minerals were the main source of silicate minerals in sediment at seeps. The formation of clay minerals was characterized by negative ΔMg/ΔCa (~ −0.95) in pore water profiles and mainly occurs in deeper layers of sediments (Higgins and Schrag, 2010). Likewise, silicate weathering, which may exist at seeps, generally occurs at greater depth (e.g. Torres et al., 2020). Authigenic carbonate precipitation caused by intense SD-AOM tends to occur in the shallow sediments where the decline in Mg is accompanied by a decline in Ca. Since Mg isotope fractionation during formation of clay minerals and carbonate precipitation head in opposite directions (Galy et al., 2002; Higgins and Schrag, 2010), the increase of pore water δ^{26}Mg values with depth helps to eliminate the influence of clay minerals. Therefore, we suggest that the concentration of Mg and change in isotopic composition at a depth of several meters mainly account for the effect of carbonate precipitation rather than the formation of clay minerals. Although carbonate precipitation consumes Ca^{2+} and Mg^{2+} in pore water and preferentially incorporates light Mg isotopes, the δ^{26}Mg value of pore water at the study sites of the South China Sea is still close to that of seawater (**Figure 3**). The invariance of δ^{26}Mg values observed for core ROV1 can be attributed to the minimal decrease in pore water Mg^{2+} concentration (~2 mM). Because aragonite is the dominant carbonate mineral precipitating in sediment at the ROV1 site and aragonite accommodates very little Mg in its crystal lattice (Snyder et al., 2007), the concentration of Mg^{2+} in pore water does not significantly decline with depth. The shallow depth of the SMTZ at this site also facilitates sufficient replenishment of Mg^{2+} ions by downward diffusion of seawater. Although the precipitation of high-Mg calcite consumes much more Mg^{2+} in pore water, the δ^{26}Mg values of pore water only decreased slightly with depth at the ROV2 and ROV4 sites compared to seawater (**Figure 3**). Bubble irrigation at the ROV4 seep site apparently promoted the supply of Mg from seawater to an extent similar to the amount of Mg taken up by high-Mg calcite, although the SMTZ at this site is deeper than at the other two sites. We ascribe the small observed variation of pore water δ^{26}Mg values at the ROV seeps to a low rate of carbonate precipitation and sufficient downward replenishment of Mg from seawater. The concentration of Mg^{2+} in seawater is about five times that of Ca^{2+}, and the precipitation of carbonate minerals at seeps consumes more Ca^{2+} than Mg^{2+} (Himmler et al., 2013; Zwicker et al., 2018). Therefore, carbonate precipitation typically does not cause large variation of δ^{26}Mg compared to δ^{44}Ca values of pore water at seeps (Blättler et al., 2021). At seeps with carbonate authigenesis, the Rayleigh effect in pore water is consequently much weaker for Mg isotopes than for Ca isotopes, and authigenic carbonate derived from SD-AOM can be assumed to form from pore water with a Mg isotopic composition similar to that of seawater. Therefore, the Mg isotopic composition of seep carbonates is probably more affected by fractionation during precipitation than by a variation of pore water Mg isotopic composition caused by a Rayleigh effect. Understanding the behavior of Mg isotopes during carbonate precipitation at seeps may provide the means to use seep carbonate as a proxy of seawater Mg isotope composition and geochemistry in Earth's history.

Laboratory experiments have been conducted to investigate the fractionation of Mg isotopes between calcite and solution ($\Delta^{26}Mg_{cal\text{-}sol}$) during carbonate precipitation (e.g. Immenhauser et al., 2010; Li et al., 2012; Mavromatis et al., 2013; Chen et al., 2020). Immenhauser et al. (2010) and Mavromatis et al. (2013) reported a correlation between $\Delta^{26}Mg_{cal\text{-}sol}$ and precipitation rate of higher $\Delta^{26}Mg_{cal\text{-}sol}$ values at higher precipitation rates. This trend is opposite to the rate-dependent Ca isotope fractionation during calcite precipitation (Tang et al., 2008). It was attributed to the incorporation of partially dehydrated Mg^{2+} ions into the calcite crystal lattice at faster precipitation rates, given that the hydration energy of Mg^{2+} is close to 4 orders of magnitude higher than that of Ca^{2+} (Mavromatis et al., 2013). In contrast, no such correlation was observed in precipitation experiments conducted by Li et al. (2012) and Chen et al. (2020), although the precipitation rates in their experiments varied widely. An equilibrium $\Delta^{26}Mg_{cal\text{-}sol}$ value of −2.47 ± 0.09‰ at 25°C was reported by Chen et al. (2020). Our study now documents higher carbonate precipitation rates than those at ODP Site 1082 and higher $\Delta^{26}Mg_{cal\text{-}sol}$ values, corresponding to a smaller degree of Mg isotope fractionation at the studied seeps. This is consistent with the conclusion drawn from laboratory experiments and travertine calcite precipitation that the extent of Mg isotope fractionation decreases with increasing carbonate growth rate (Immenhauser et al., 2010; Mavromatis et al., 2013; Pogge von Strandmann et al., 2019). However, the carbonate precipitation rates calculated herein, based on pore water geochemistry at seeps, are generally lower than those in laboratory experiments (**Figure 6**). According to Mavromatis et al. (2013), such low carbonate formation rates should lead to equilibrium fractionation of Mg isotopes. The equilibrium $\Delta^{26}Mg_{cal\text{-}sol}$ would be ~ −2.47‰ at 25°C (Chen et al., 2020). However, our modeled results show a smaller fractionation compared to that in calcite equilibrium experiments, indicating kinetically controlled fractionation. This discrepancy may be caused by several factors. Firstly, conversion of the fluxes of Ca and Mg in natural environments to precipitation rates of carbonate per unit reactive surface area requires several assumptions (Blättler et al., 2021). It is currently unrealistic to accurately constrain all the physical and chemical conditions in the natural environment where carbonate formation occurs. Mineralogy, choices of the roughness factor, and the error in the estimation of grain size distribution at seeps may result in large uncertainties in the estimation of carbonate precipitation rates in natural environments (Beckingham et al., 2016). The second factor is the uncertainty in the calculation of the extent of Mg isotope fractionation. Carbonate precipitation was the only process considered in our model outlined above to fit the concentration and isotopic composition of pore water profiles. The real situation is probably more complex due to the precipitation-dissolution equilibrium of carbonate minerals (cf. Karaca et al., 2010) and other processes that influence both concentration and isotopic composition of Mg (e.g. dissolution and desorption of exchangeable Mg from clay minerals;

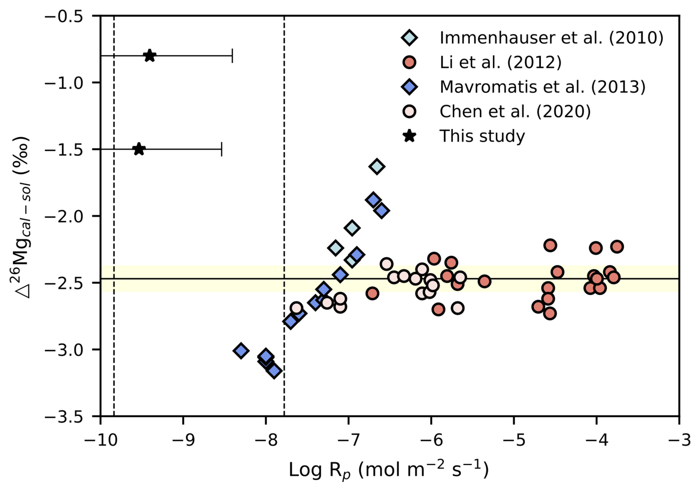

FIGURE 6 | Cross-plot of $\Delta^{26}Mg_{cal\text{-}sol}$ versus calcite precipitation rate (Log R_p). The dashed line represents the range of precipitation rates of seep carbonates (Karaca et al., 2010). A factor of 0.4 was also applied to data from literature to convert Ca fluxes to carbonate precipitation rates (for details see *Rates of Carbonate Precipitation and Mg Isotope Composition*). The estimated equilibrium $\Delta^{26}Mg_{cal\text{-}sol}$ value of −2.47 ± 0.09‰ from literature at 25°C is represented by the solid line and yellow error envelope (Chen et al., 2020). Note that ϵ values in this study are plotted in the figure to describe the fractionation of Mg isotopes and to allow for comparison with $\Delta^{26}Mg_{cal\text{-}sol}$ values obtained from literature.

Mavromatis et al., 2014). In our model, the finite consumption of Mg^{2+}, leading to a limited variation of the Mg isotopic composition in pore waters, resulted in a relatively large error of the estimated isotope fractionation. The third factor is the difference between the experimental conditions in the laboratory and the conditions in the natural environment. Calcite seeds are usually used in experiments, and experimental conditions are generally controlled by a chemostat, free drift, and constant addition of ions (e.g. Li et al., 2012; Mavromatis et al., 2013; Chen et al., 2020). Other possible factors not considered in experiments such as dissolved sulfide in pore water and microbial activity (e.g. methanogens and sulfate-reducing bacteria) may also influence the behavior of Mg isotopes in nature (Lu et al., 2017; Jin et al., 2021). Hence, it is difficult to reproduce carbonate precipitation in the environment during laboratory experiments. More research is needed to better constrain the physical and chemical conditions in natural environments and the array of factors that may influence the behavior of Mg isotopes during carbonate precipitation.

5 CONCLUSIONS

Pore waters from sediments of the Haima methane seeps of the South China Sea were investigated for (1) their cation inventory affecting the mineralogy the seep carbonate precipitating, (2) carbonate precipitation rates, and (3) the relationship between these parameters and Mg isotope fractionation. The different degrees of consumption of Ca, Mg, and Sr with depth suggest that carbonate minerals precipitating are aragonite at the ROV1 site and high-Mg calcite at the ROV2 and ROV4 sites. Precipitation rates between 0.92 and 1.24 μmol cm^{-2} yr^{-1} are similar to rates at seeps from other areas, but significantly lower than rates in laboratory experiments looking at Mg isotope fractionation during carbonate formation. Pore water at all study sites reveals Mg isotope composition close to that of seawater, indicating a weak Rayleigh fractionation effect due to sufficient replenishment of cations from seawater and moderate consumption during carbonate authigenesis in pore water. The modeled low carbonate precipitation rates and small Mg isotope fractionation are in discrepancy to laboratory experiments. The reason for this discrepancy is unknown, but it likely results from uncertainties in the conversion of precipitation rates, the calculation of isotope fractionation, and the complex conditions in natural environments. This study provides first insight into the link between rates of carbonate precipitation in a natural environment at seeps and Mg isotope fractionation. The results help to constrain the multiple controls on Mg isotope fractionation in natural environments.

DATA AVAILABILITY STATEMENT

The original contributions presented in the study are included in the article/**Supplementary Material**. Further inquiries can be directed to the corresponding author.

AUTHOR CONTRIBUTIONS

MJ: conceptualization, methodology, data analysis, and writing–original manuscript. DF: conceptualization, supervision, funding acquisition, and writing–review and editing. KH: writing–review and editing. SG: sample collection and data analysis. ML: numerical simulation. JP: writing–review and editing. XW: data analysis. YH: writing–review and editing. DC: resources, supervision. All authors contributed to manuscript preparation. All authors contributed to the article and approved the submitted version.

FUNDING

This study was partially supported by the National Natural Science Foundation of China (Grants: 42176056, 41773091 and 41973008).

ACKNOWLEDGMENTS

We thank the crew of Haiyang-6 research vessel for sample collection. Comments of Pogge von Strandmann and an anonymous reviewer helped to improve this article.

SUPPLEMENTARY MATERIAL

The Supplementary Material for this article can be found online at: https://www.frontiersin.org/articles/10.3389/fmars.2022.858860/full#supplementary-material

REFERENCES

Aloisi G., Pierre C., Rouchy J. M., Foucher J. P., Woodside J., the MEDINAUT Scientific Party. (2000). Methane-Related Authigenic Carbonates of Eastern Mediterranean Sea Mud Volcanoes and Their Possible Relation to Gas Hydrate Destabilisation. *Earth Planet. Sci. Lett.* 184 (1), 321–338. doi: 10.1016/S0012-821x(00)00322-8

Bao Z., Huang K., Huang T., Shen B., Zong C., Chen K., et al. (2019). Precise Magnesium Isotope Analyses of High-K and Low-Mg Rocks by MC-ICP-MS. *J. Anal. At. Spectrom.* 34 (5), 940–953. doi: 10.1039/c9ja00002j

Bayon G., Pierre C., Etoubleau J., Voisset M., Cauquil E., Marsset T., et al. (2007). Sr/Ca and Mg/Ca Ratios in Niger Delta Sediments: Implications for Authigenic Carbonate Genesis in Cold Seep Environments. *Mar. Geol.* 241 (1-4), 93–109. doi: 10.1016/j.margeo.2007.03.007

Beckingham L. E., Mitnick E. H., Steefel C. I., Zhang S., Voltolini M., Swift A. M., et al. (2016). Evaluation of Mineral Reactive Surface Area Estimates for Prediction of Reactivity of a Multi-Mineral Sediment. *Geochim. Cosmochim. Acta* 188, 310–329. doi: 10.1016/j.gca.2016.05.040

Berner R. A. (1980). *Early Diagenesis – A Theoretical Approach* (Princeton: Princeton University Press).

Blättler C. L., Hong W.-L., Kirsimäe K., Higgins J. A., Lepland A. (2021). Small Calcium Isotope Fractionation at Slow Precipitation Rates in Methane Seep Authigenic Carbonates. *Geochim. Cosmochim. Acta* 298, 227–239. doi: 10.1016/j.gca.2021.01.001

Bradbury H. J., Turchyn A. V. (2019). Reevaluating the Carbon Sink Due to Sedimentary Carbonate Formation in Modern Marine Sediments. *Earth Planet. Sci. Lett.* 519, 40–49. doi: 10.1016/j.epsl.2019.04.044

Chen F., Chen J., Jin H., Li H. (2012). Correlation of $\delta^{13}C_{org}$ in Surface Sediments With Sinking Particulate Matter in South China Sea and Implication for Reconstructing Paleo-Environment. *Acta Sedimentol. Sin.* 30 (2), 340–345. (in Chinese with English abstract).

Chen X.-Y., Teng F.-Z., Sanchez W. R., Romanek C. S., Sanchez-Navas A., Sánchez-Román M. (2020). Experimental Constraints on Magnesium Isotope Fractionation During Abiogenic Calcite Precipitation at Room Temperature. *Geochim. Cosmochim. Acta* 281, 102–117. doi: 10.1016/j.gca.2020.04.033

Chuang P.-C., Dale A. W., Wallmann K., Haeckel M., Yang T. F., Chen N.-C., et al. (2013). Relating Sulfate and Methane Dynamics to Geology: Accretionary Prism Offshore SW Taiwan. *Geochem. Geophys. Geosyst.* 14 (7), 2523–2545. doi: 10.1002/ggge.20168

de Villiers S. (1999). Seawater Strontium and Sr/Ca Variability in the Atlantic and Pacific Oceans. *Earth Planet Sci. Lett.* 171 (4), 623–634. doi: 10.1016/S0012-821x(99)00174-0

DePaolo D. J. (2011). Surface Kinetic Model for Isotopic and Trace Element Fractionation During Precipitation of Calcite From Aqueous Solutions. *Geochim. Cosmochim. Acta* 75 (4), 1039–1056. doi: 10.1016/j.gca.2010.11.020

Fantle M. S., DePaolo D. J. (2007). Ca Isotopes in Carbonate Sediment and Pore Fluid From ODP Site 807a: The Ca^{2+}(aq)–calcite Equilibrium Fractionation Factor and Calcite Recrystallization Rates in Pleistocene Sediments. *Geochim. Cosmochim. Acta* 71 (10), 2524–2546. doi: 10.1016/j.gca.2007.03.006

Fantle M. S., Higgins J. (2014). The Effects of Diagenesis and Dolomitization on Ca and Mg Isotopes in Marine Platform Carbonates: Implications for the Geochemical Cycles of Ca and Mg. *Geochim. Cosmochim. Acta* 142, 458–481. doi: 10.1016/j.gca.2014.07.025

Foster G. L., Pogge von Strandmann P. A. E., Rae J. W. B. (2010). Boron and Magnesium Isotopic Composition of Seawater. *Geochem. Geophys. Geosyst.* 11 (8), Q08015. doi: 10.1029/2010GC003201

Galy A., Bar-Matthews M., Halicz L., O'Nions R. K. (2002). Mg Isotopic Composition of Carbonate: Insight From Speleothem Formation. *Earth Planet. Sci. Lett.* 201 (1), 105–115. doi: 10.1016/S0012-821x(02)00675-1

Gothmann A. M., Stolarski J., Adkins J. F., Higgins J. A. (2017). A Cenozoic Record of Seawater Mg Isotopes in Well-Preserved Fossil Corals. *Geology* 45 (11), 1039–1042. doi: 10.1130/G39418.1

Haeckel M., Boudreau B. P., Wallmann K. (2007). Bubble-Induced Porewater Mixing: A 3-D Model for Deep Porewater Irrigation. *Geochim. Cosmochim. Acta* 71 (21), 5135–5154. doi: 10.1016/j.gca.2007.08.011

Higgins J. A., Schrag D. P. (2010). Constraining Magnesium Cycling in Marine Sediments Using Magnesium Isotopes. *Geochim. Cosmochim. Acta* 74 (17), 5039–5053. doi: 10.1016/j.gca.2010.05.019

Higgins J. A., Schrag D. P. (2015). The Mg Isotopic Composition of Cenozoic Seawater – Evidence for a Link Between Mg-Clays, Seawater Mg/Ca, and Climate. *Earth Planet. Sci. Lett.* 416, 73–81. doi: 10.1016/j.epsl.2015.01.003

Himmler T., Haley B. A., Torres M. E., Klinkhammer G. P., Bohrmann G., Peckmann J. (2013). Rare Earth Element Geochemistry in Cold-Seep Pore Waters of Hydrate Ridge, Northeast Pacific Ocean. *Geo-Marine Lett.* 33 (5), 369–379. doi: 10.1007/s00367-013-0334-2

Huang K.-J., Shen B., Lang X.-G., Tang W.-B., Peng Y., Ke S., et al. (2015). Magnesium Isotopic Compositions of the Mesoproterozoic Dolostones: Implications for Mg Isotopic Systematics of Marine Carbonates. *Geochim. Cosmochim. Acta* 164, 333–351. doi: 10.1016/j.gca.2015.05.002

Huang C. Y., Wu S. F., Zhao M. X., Chen M. T., Wang C. H., Tu X., et al. (1997). Surface Ocean and Monsoon Climate Variability in the South China Sea Since the Last Glaciation. *Mar. Micropaleontol.* 32 (1-2), 71–94. doi: 10.1016/S0377-8398(97)00014-5

Hui G., Li S., Guo L., Zhang G., Gong Y., Somerville I. D., et al. (2016). Source and Accumulation of Gas Hydrate in the Northern Margin of the South China Sea. *Mar. Pet. Geol.* 69, 127–145. doi: 10.1016/j.marpetgeo.2015.10.009

Hu Y., Luo M., Chen L., Liang Q., Feng D., Tao J., et al. (2018). Methane Source Linked to Gas Hydrate System at Hydrate Drilling Areas of the South China Sea: Porewater Geochemistry and Numerical Model Constraints. *J. Asian Earth Sci.* 168, 87–95. doi: 10.1016/j.jseaes.2018.04.028

Hu Y., Luo M., Liang Q., Chen L., Feng D., Yang S., et al. (2019). Pore Fluid Compositions and Inferred Fluid Flow Patterns at the Haima Cold Seeps of the South China Sea. *Mar. Pet. Geol.* 103, 29–40. doi: 10.1016/j.marpetgeo.2019.01.007

Immenhauser A., Buhl D., Richter D., Niedermayr A., Riechelmann D., Dietzel M., et al. (2010). Magnesium-Isotope Fractionation During Low-Mg Calcite Precipitation in a Limestone Cave - Field Study and Experiments. *Geochim. Et Cosmochim. Acta* 74 (15), 4346–4364. doi: 10.1016/j.gca.2010.05.006

Jørgensen B. B., Kasten S. (2006). "Sulfur Cycling and Methane Oxidation," in *Marine Geochemistry*. Eds. D. S. Horst, Z. Matthias (Verlag: Springer), 271–309.

Jin M., Feng D., Huang K., Peckmann J., Li N., Huang H., et al. (2021). Behavior of Mg Isotopes During Precipitation of Methane-Derived Carbonate: Evidence From Tubular Seep Carbonates From the South China Sea. *Chem. Geol.* 567, 120101. doi: 10.1016/j.chemgeo.2021.120101

Karaca D., Hensen C., Wallmann K. (2010). Controls on Authigenic Carbonate Precipitation at Cold Seeps Along the Convergent Margin Off Costa Rica. *Geochem. Geophys. Geosyst.* 11 (8), Q08S27. doi: 10.1029/2010GC003062

Kasemann S. A., Pogge von Strandmann P. A. E., Prave A. R., Fallick A. E., Elliott T., Hoffmann K.-H. (2014). Continental Weathering Following a Cryogenian Glaciation: Evidence From Calcium and Magnesium Isotopes. *Earth Planet. Sci. Lett.* 396, 66–77. doi: 10.1016/j.epsl.2014.03.048

Liang Q. Y., Hu Y., Feng D., Peckmann J., Chen L. Y., Yang S. X., et al. (2017). Authigenic Carbonates From Newly Discovered Active Cold Seeps on the Northwestern Slope of the South China Sea: Constraints on Fluid Sources, Formation Environments, and Seepage Dynamics. *Deep Sea Res. Part I: Oceanogr. Res. Papers* 124, 31–41. doi: 10.1016/j.dsr.2017.04.015

Li W., Beard B. L., Li C., Xu H., Johnson C. M. (2015). Experimental Calibration of Mg Isotope Fractionation Between Dolomite and Aqueous Solution and its Geological Implications. *Geochim. Cosmochim. Acta* 157, 164–181. doi: 10.1016/j.gca.2015.02.024

Li W. Q., Chakraborty S., Beard B. L., Romanek C. S., Johnson C. M. (2012). Magnesium Isotope Fractionation During Precipitation of Inorganic Calcite Under Laboratory Conditions. *Earth Planet. Sci. Lett.* 333, 304–316. doi: 10.1016/j.epsl.2012.04.010

Luff R., Wallmann K. (2003). Fluid Flow, Methane Fluxes, Carbonate Precipitation and Biogeochemical Turnover in Gas Hydrate-Bearing Sediments at Hydrate Ridge, Cascadia Margin: Numerical Modeling and Mass Balances. *Geochim. Cosmochim. Acta* 67 (18), 3403–3421. doi: 10.1016/s0016-7037(03)00127-3

Lu Y., Liu Y., Sun X., Lin Z., Xu L., Lu H., et al. (2017). Intensity of Methane Seepage Reflected by Relative Enrichment of Heavy Magnesium Isotopes in Authigenic Carbonates: A Case Study From the South China Sea. *Deep Sea Res. Part I: Oceanogr. Res. Papers* 129, 10–21. doi: 10.1016/j.dsr.2017.09.005

Mavromatis V., Gautier Q., Bosc O., Schott J. (2013). Kinetics of Mg Partition and Mg Stable Isotope Fractionation During its Incorporation in Calcite. *Geochim. Et Cosmochim. Acta* 114, 188–203. doi: 10.1016/j.gca.2013.03.024

Mavromatis V., Prokushkin A. S., Pokrovsky O. S., Viers J., Korets M. A. (2014). Magnesium Isotopes in Permafrost-Dominated Central Siberian Larch Forest Watersheds. *Geochim. Cosmochim. Acta* 147, 76–89. doi: 10.1016/j.gca.2014.10.009

Moore T. S., Murray R. W., Kurtz A. C., Schrag D. P. (2004). Anaerobic Methane Oxidation and the Formation of Dolomite. *Earth Planet. Sci. Lett.* 229 (1-2), 141–154. doi: 10.1016/j.epsl.2004.10.015

Naehr T. H., Eichhubl P., Orphan V. J., Hovland M., Paull C. K., Ussler W., et al. (2007). Authigenic Carbonate Formation at Hydrocarbon Seeps in Continental Margin Sediments: A Comparative Study. *Deep Sea Res. Part II: Topical Stud. Oceanogr.* 54 (11), 1268–1291. doi: 10.1016/j.dsr2.2007.04.010

Nöthen K., Kasten S. (2011). Reconstructing Changes in Seep Activity by Means of Pore Water and Solid Phase Sr/Ca and Mg/Ca Ratios in Pockmark Sediments of the Northern Congo Fan. *Mar. Geol.* 287 (1-4), 1–13. doi: 10.1016/j.margeo.2011.06.008

Oelkers E. H., Helgeson H. C. (1991). Calculation of Activity Coefficients and Degrees of Formation of Neutral Ion Pairs in Supercritical Electrolyte Solutions. *Geochim. Cosmochim. Acta* 55 (5), 1235–1251. doi: 10.1016/0016-7037(91)90303-M

Pearce C. R., Saldi G. D., Schott J., Oelkers E. H. (2012). Isotopic Fractionation During Congruent Dissolution, Precipitation and at Equilibrium: Evidence From Mg Isotopes. *Geochim. Cosmochim. Acta* 92, 170–183. doi: 10.1016/j.gca.2012.05.045

Pinilla C., Blanchard M., Balan E., Natarajan S. K., Vuilleumier R., Mauri F. (2015). Equilibrium Magnesium Isotope Fractionation Between Aqueous Mg^{2+} and Carbonate Minerals: Insights From Path Integral Molecular Dynamics. *Geochim. Cosmochim. Acta* 163, 126–139. doi: 10.1016/j.gca.2015.04.008

Pogge von Strandmann P. A. E., Forshaw J., Schmidt D. N. (2014). Modern and Cenozoic Records of Seawater Magnesium From Foraminiferal Mg Isotopes. *Biogeosciences* 11 (18), 5155–5168. doi: 10.5194/bg-11-5155-2014

Pogge von Strandmann P. A. E., Olsson J., Luu T.-H., Gislason S. R., Burton K. W. (2019). Using Mg Isotopes to Estimate Natural Calcite Compositions and Precipitation Rates During the 2010 Eyjafjallajökull Eruption. *Front. Earth Sci.* 7. doi: 10.3389/feart.2019.00006

Richter F. M., Mendybaev R. A., Christensen J. N., Hutcheon I. D., Williams R. W., Sturchio N. C., et al. (2006). Kinetic Isotopic Fractionation During Diffusion of Ionic Species in Water. *Geochim. Cosmochim. Acta* 70 (2), 277–289. doi: 10.1016/j.gca.2005.09.016

Saenger C., Wang Z. R. (2014). Magnesium Isotope Fractionation in Biogenic and Abiogenic Carbonates: Implications for Paleoenvironmental Proxies. *Quat. Sci. Rev.* 90, 1–21. doi: 10.1016/j.quascirev.2014.01.014

Schrag D. P., Higgins J. A., Macdonald F. A., Johnston D. T. (2013). Authigenic Carbonate and the History of the Global Carbon Cycle. *Science* 339 (6119), 540–543. doi: 10.1126/science.1229578

Snyder G. T., Hiruta A., Matsumoto R., Dickens G. R., Tomaru H., Takeuchi R., et al. (2007). Pore Water Profiles and Authigenic Mineralization in Shallow Marine Sediments Above the Methane-Charged System on Umitaka Spur, Japan Sea. *Deep Sea Res. Part II: Topical Stud. Oceanogr.* 54 (11-13), 1216–1239. doi: 10.1016/j.dsr2.2007.04.001

Tang J., Dietzel M., Böhm F., Köhler S. J., Eisenhauer A. (2008). Sr^{2+}/Ca^{2+} and $^{44}Ca/^{40}Ca$ Fractionation During Inorganic Calcite Formation: II. Ca Isotopes. *Geochim. Cosmochim. Acta* 72 (15), 3733–3745. doi: 10.1016/j.gca.2008.05.033

Teng F.-Z. (2017). Magnesium Isotope Geochemistry. *Rev. Mineral. Geochem.* 82 (1), 219–287. doi: 10.2138/rmg.2017.82.7

Tipper E., Galy A., Gaillardet J., Bickle M., Elderfield H., Carder E. (2006). The Magnesium Isotope Budget of the Modern Ocean: Constraints From Riverine Magnesium Isotope Ratios. *Earth Planet. Sci. Lett.* 250 (1-2), 241–253. doi: 10.1016/j.epsl.2006.07.037

Torres M. E., Hong W.-L., Solomon E. A., Milliken K., Kim J.-H., Sample J. C., et al. (2020). Silicate Weathering in Anoxic Marine Sediment as a Requirement for Authigenic Carbonate Burial. *Earth-Science Rev.* 200, 102960. doi: 10.1016/j.earscirev.2019.102960

Wallmann K., Aloisi G., Haeckel M., Obzhirov A., Pavlova G., Tishchenko P. (2006). Kinetics of Organic Matter Degradation, Microbial Methane Generation, and Gas Hydrate Formation in Anoxic Marine Sediments. *Geochim. Cosmochim. Acta* 70 (15), 3905–3927. doi: 10.1016/j.gca.2006.06.003

Wang Z. R., Hu P., Gaetani G., Liu C., Saenger C., Cohen A., et al. (2013). Experimental Calibration of Mg Isotope Fractionation Between Aragonite and Seawater. *Geochim. Et Cosmochim. Acta* 102, 113–123. doi: 10.1016/j.gca.2012.10.022

Wang P., Prell W., Blum P. (2000). *Proceeding of the Ocean Drilling Program: Initial Reports 184* (College Station, TX, USA: Texas A&M University).

Wang W., Qin T., Zhou C., Huang S., Wu Z., Huang F. (2017). Concentration Effect on Equilibrium Fractionation of Mg-Ca Isotopes in Carbonate Minerals: Insights From First-Principles Calculations. *Geochim. Cosmochim. Acta* 208, 185–197. doi: 10.1016/j.gca.2017.03.023

Wei J., Li J., Wu T., Zhang W., Li J., Wang J., et al. (2020). Geologically Controlled Intermittent Gas Eruption and its Impact on Bottom Water Temperature and Chemosynthetic Communities—A Case Study in the "HaiMa", Cold Seeps South China Sea. *Geol. J.* 55 (9), 6066–6078. doi: 10.1002/gj.3780

Whiticar M. J. (1999). Carbon and Hydrogen Isotope Systematics of Bacterial Formation and Oxidation of Methane. *Chem. Geol.* 161 (1), 291–314. doi: 10.1016/S0009-2541(99)00092-3

Wombacher F., Eisenhauer A., Bohm F., Gussone N., Regenberg M., Dullo W. C., et al. (2011). Magnesium Stable Isotope Fractionation in Marine Biogenic Calcite and Aragonite. *Geochim. Et Cosmochim. Acta* 75 (19), 5797–5818. doi: 10.1016/j.gca.2011.07.017

Young E. D., Galy A. (2004). The Isotope Geochemistry and Cosmochemistry of Magnesium. *Geochem. Non-Traditional Stable Isotopes* 55, 197–230. doi: 10.2138/gsrmg.55.1.197

Zeebe R. E., Wolf-Gladrow D. A. (2001). *CO_2 in Seawater: Equilibrium, Kinetics and Isotopes* (U. K: Elsevier).

Zwicker J., Smrzka D., Himmler T., Monien P., Gier S., Goedert J. L., et al. (2018). Rare Earth Elements as Tracers for Microbial Activity and Early Diagenesis: A New Perspective From Carbonate Cements of Ancient Methane-Seep Deposits. *Chem. Geol.* 501, 77–85. doi: 10.1016/j.chemgeo.2018.10.010

Conflict of Interest: The authors declare that the research was conducted in the absence of any commercial or financial relationships that could be construed as a potential conflict of interest.

frontiers | Frontiers in Earth Science

ORIGINAL RESEARCH
published: 14 April 2022
doi: 10.3389/feart.2022.862333

Sulfur and Oxygen Isotope Records of Sulfate-Driven Anaerobic Oxidation of Methane in Diffusion-Dominated Marine Sediments

Tingting Chen[1,2], *Harald Strauss*[3], *Yunxin Fang*[4], *Zhiyong Lin*[1,3,5]*, *Xiaoming Sun*[1,2,6]*, *Jiarui Liu*[7], *Yang Lu*[5], *Xin Yang*[1,2], *Haixin Lin*[1,2], *Zhongwei Wu*[1,2] and *Xiao Lin*[1,2]

[1]School of Marine Sciences, Sun Yat-sen University, Guangzhou, China, [2]Guangdong Provincial Key Laboratory of Marine Resources and Coastal Engineering, Guangzhou, China, [3]Institut für Geologie und Paläontologie, Westfälische Wilhelms-Universität Münster, Münster, Germany, [4]Guangzhou Marine Geological Survey, Guangzhou, China, [5]Institut für Geologie, Centrum für Erdsystemforschung und Nachhaltigkeit, Universität Hamburg, Hamburg, Germany, [6]School of Earth Science and Engineering, Sun Yat-sen University, Guangzhou, China, [7]Department of Earth, Planetary and Space Sciences, University of California, Los Angeles, Los Angeles, CA, United States

Edited by:
Dong Feng,
Shanghai Ocean University, China

Reviewed by:
Xiaobin Cao,
Nanjing University, China
Xiting Liu,
Ocean University of China, China

***Correspondence:**
Zhiyong Lin
zhiyong.lin@uni-hamburg.de
Xiaoming Sun
eessxm@mail.sysu.edu.cn

Specialty section:
This article was submitted to Marine Geoscience, a section of the journal Frontiers in Earth Science

Received: *25 January 2022*
Accepted: *30 March 2022*
Published: *14 April 2022*

Citation:
Chen T, Strauss H, Fang Y, Lin Z, Sun X, Liu J, Lu Y, Yang X, Lin H, Wu Z and Lin X (2022) Sulfur and Oxygen Isotope Records of Sulfate-Driven Anaerobic Oxidation of Methane in Diffusion-Dominated Marine Sediments. Front. Earth Sci. 10:862333. doi: 10.3389/feart.2022.862333

Organoclastic sulfate reduction (OSR) and sulfate-driven anaerobic oxidation of methane (SD-AOM) are the two major microbial pathways for sulfate consumption in marine sulfur cycle. The relative changes of sulfur and oxygen isotope ratios in pore water sulfate are affected by the mode of microbial sulfate reduction and have been applied as an indicator for assessing methane excess environments. However, so far, this isotope proxy fails to distinguish sulfate reduction processes fueled by the oxidation of organic matter or by diffusing methane. To better understand the mechanism of sulfur and oxygen isotope partitioning during OSR and SD-AOM, coupled sulfur and oxygen isotopic compositions of pore water sulfate ($\delta^{34}S_{SO4}$ and $\delta^{18}O_{SO4}$) were investigated from four methane diffusing sites (CL56, CL57, CL59, and CL60) of the South China Sea, supplemented by carbon isotopic composition of dissolved inorganic carbon (DIC) and sulfur isotopic composition of pyrite in bulk sediments. Pore water sulfate and DIC concentrations, as well as calculated net sulfate reduction rates suggest that the sulfate reduction at site CL57 was mainly dominated by OSR, whereas sites CL56, CL59, and CL60 were likely impacted by both OSR and SD-AOM. Furthermore, the trend of cross-plotting $\delta^{18}O_{SO4}$ versus $\delta^{34}S_{SO4}$ values from site CL57 was distinguishable from sites CL56, CL59, and CL60, although all study sites show similar patterns to those derived from methane limited environments. This further indicates the trajectory of sulfur and oxygen isotope partitioning was affected by the mode of sulfate reduction (i.e., OSR vs. SD-AOM). At site CL57, the low net sulfate reduction rate would lead to enhanced oxidation of intermediate sulfur species during OSR, thus leading to a higher slope in the $\delta^{18}O_{SO4}$ vs. $\delta^{34}S_{SO4}$ cross-plot (1.26). In contrast, the higher net sulfate reduction rates at sites CL56, CL59, and CL60 due to the impact from SD-AOM would lead to lower slopes in the $\delta^{18}O_{SO4}$ vs. $\delta^{34}S_{SO4}$ cross-plots (0.78 ± 0.11). This study provides new insights into the sulfur and oxygen isotope systematics during microbial sulfate reduction processes in methane diffusing environments.

Keywords: organoclastic sulfate reduction, sulfate-driven anaerobic oxidation of methane, sulfur and oxygen isotopes in sulfate, methane diffusing environments, South China Sea

INTRODUCTION

As a bio-essential element, sulfur predominantly occurs as dissolved sulfate in the modern ocean (Canfield, 2001; Canfield et al., 2005). The formation of sulfide minerals, particularly pyrite (FeS_2), through microbial sulfate reduction processes and their preservation in sediments represent the key pathway for removing sulfate from the seawater in the global sulfur cycle (Jørgensen, 1982; Vairavamurthy et al., 1995). Organoclastic sulfate reduction (OSR) commonly occurs in organic-rich marine sediments, representing the dominant anaerobic metabolic pathway of organic matter remineralization (Jørgensen, 1982; Canfield, 2001). In addition, sulfate-driven anaerobic oxidation of methane (SD-AOM; e.g., Boetius et al., 2000; Orphan et al., 2001) is another key process for sulfate consumption and thus sulfide production, predominantly in methane-rich sediments along continental margins (Lin et al., 2016; Lin et al., 2017; Egger et al., 2018; Lin et al., 2018).

During microbial sulfate reduction (i.e., OSR and SD-AOM), multiple enzyme-catalyzed steps are involved (Rees, 1973; Brunner and Bernasconi, 2005; Eckert et al., 2011), and the mechanisms of the forward and backward enzymatic pathways affects the sulfate reduction rate (SRR; Böttcher et al., 1998; Aharon and Fu, 2000; Brunner et al., 2005). Many studies have documented that the sulfur isotope fractionation is affected by SRR during microbial sulfate reduction, i.e., the lower SRR, the larger sulfur isotope fractionation (Wortmann et al., 2001; Canfield et al., 2006). It was further identified that the combination of sulfur and oxygen isotopic compositions in the residual sulfate pool (i.e., $\delta^{34}S_{SO4}$ and $\delta^{18}O_{SO4}$) can reflect the SRR and decipher the mode of sulfate reduction in marine sediments (Böttcher et al., 1998; Böttcher et al., 1999; Aharon and Fu, 2000; Böttcher and Thamdrup, 2001; Aharon and Fu, 2003; Brunner et al., 2005; Wortmann et al., 2007; Farquhar et al., 2008; Turchyn et al., 2010; Brunner et al., 2012; Antler et al., 2013; Antler et al., 2014; Antler et al., 2015). This is mainly due to differing geochemical behavior of sulfur and oxygen isotope partitioning that occurs in each intracellular step during microbial sulfate reduction (Aharon and Fu, 2000; Brunner et al., 2005; Brunner et al., 2012; Antler et al., 2013).

Since isotopically lighter sulfur (^{32}S) is preferentially utilized during microbial sulfate reduction, the sulfur isotopic composition of residual sulfate ($\delta^{34}S_{SO4}$) increases with progressive sulfate reduction (Canfield, 2001), reflecting a combination of kinetic and equilibrium sulfur isotope fractionation through intracellular pathways (Wing and Halevy, 2014). In contrast, the behavior of oxygen isotopes of sulfate is affected by the exchange of oxygen atoms between the intermediate sulfur species formed during sulfate reduction and ambient water (Mizutani and Rafter, 1973; Fritz et al., 1989). Both, the oxygen and sulfur isotopic compositions of sulfate become gradually higher during microbial sulfate reduction and a constant $\delta^{18}O_{SO4}$ value will ultimately be obtained when an equilibrium of $\delta^{18}O_{SO4}$ with water ($\delta^{18}O_{H2O}$) is reached (Fritz et al., 1989; Brunner and Bernasconi, 2005; Wortmann et al., 2007). Generally, the slope in a cross-plot of $\delta^{18}O_{SO4}$ versus $\delta^{34}S_{SO4}$ (defined as 'SALP', e.g., Antler et al., 2013) prior to oxygen isotopes reaching apparent equilibrium is negatively correlated with the net SRR (Böttcher et al., 1998; Böttcher et al., 1999; Aharon and Fu, 2000; Brunner et al., 2005; Antler et al., 2013, 2015; Turchyn et al., 2016). A higher SALP is attributed to enhanced oxygen isotope exchange where more sulfite is re-oxidized to sulfate (Antler et al., 2013; Turchyn et al., 2016), while a lower SALP commonly results from higher net SRR (Antler et al., 2013).

Most of the reactive organic matter would be utilized via OSR in anoxic environments (e.g., Jørgensen, 1982). If reactive organic matter remains after dissolved sulfate has been depleted, its degradation would lead to methanogenesis (Martens and Berner, 1974; Froelich et al., 1979; Whiticar et al., 1986). Most of the methane generated from methanogenesis or release from methane hydrate deposits along continental margins would be consumed via SD-AOM within the sulfate-methane transition zone (SMTZ) in the sediment (Reeburgh, 1980; Hinrichs et al., 1999; Boetius et al., 2000; Regnier et al., 2011). Depending on the methane diffusing flux, the depths of the SMTZ can vary from several centimeters to tens or hundreds of meters below surface (Borowski et al., 1999; Egger et al., 2018).

Both, OSR and SD-AOM occur in sediments alone continental margins, but their SRR could vary significantly (Aharon and Fu, 2000; Böttcher et al., 2006; Antler et al., 2013; Gong et al., 2021). In methane-in-excess environments (e.g., cold seeps), methane is expelled from the sediment into the water column as gas bubbles (Valentine et al., 2001; Wallmann et al., 2006; Reeburgh, 2007, 2014). In these environments, the SALP values are low due to a typically high net SRR during SD-AOM (e.g., Antler et al., 2014; Antler et al., 2015; Feng et al., 2016; Gong et al., 2021). In contrast, when sulfate reduction is coupled with the oxidation of organic matter or diffusing methane, higher SALP values would be observed (Blake et al., 2006; Aller et al., 2010; Antler et al., 2013; Lin et al., 2017; Hu et al., 2020). However, no obvious differences in sulfur and oxygen partitioning during these two processes were identified. The relatively higher SALP values for both processes are likely caused by relatively slower net SRR in spite of the different electronic donors (Antler and Pellerin, 2018). Recently, the sulfur and oxygen isotopes of pore water sulfate have been explored to recognize the occurrence of SD-AOM in an active seep area (i.e., Haima seeps) of the South China Sea (Gong et al., 2021). The authors have observed small slopes of $\delta^{18}O_{SO4}$ vs. $\delta^{34}S_{SO4}$ (less than 0.5) in both methane-in-excess and diffusing environments and put forwarded that the $\delta^{18}O_{SO4}$ vs. $\delta^{34}S_{SO4}$ patterns in low methane flux environments are governed by variable isotope compositions of pore-water sulfate at greater depth. Since OSR and SD-AOM at depth (in methane diffusing

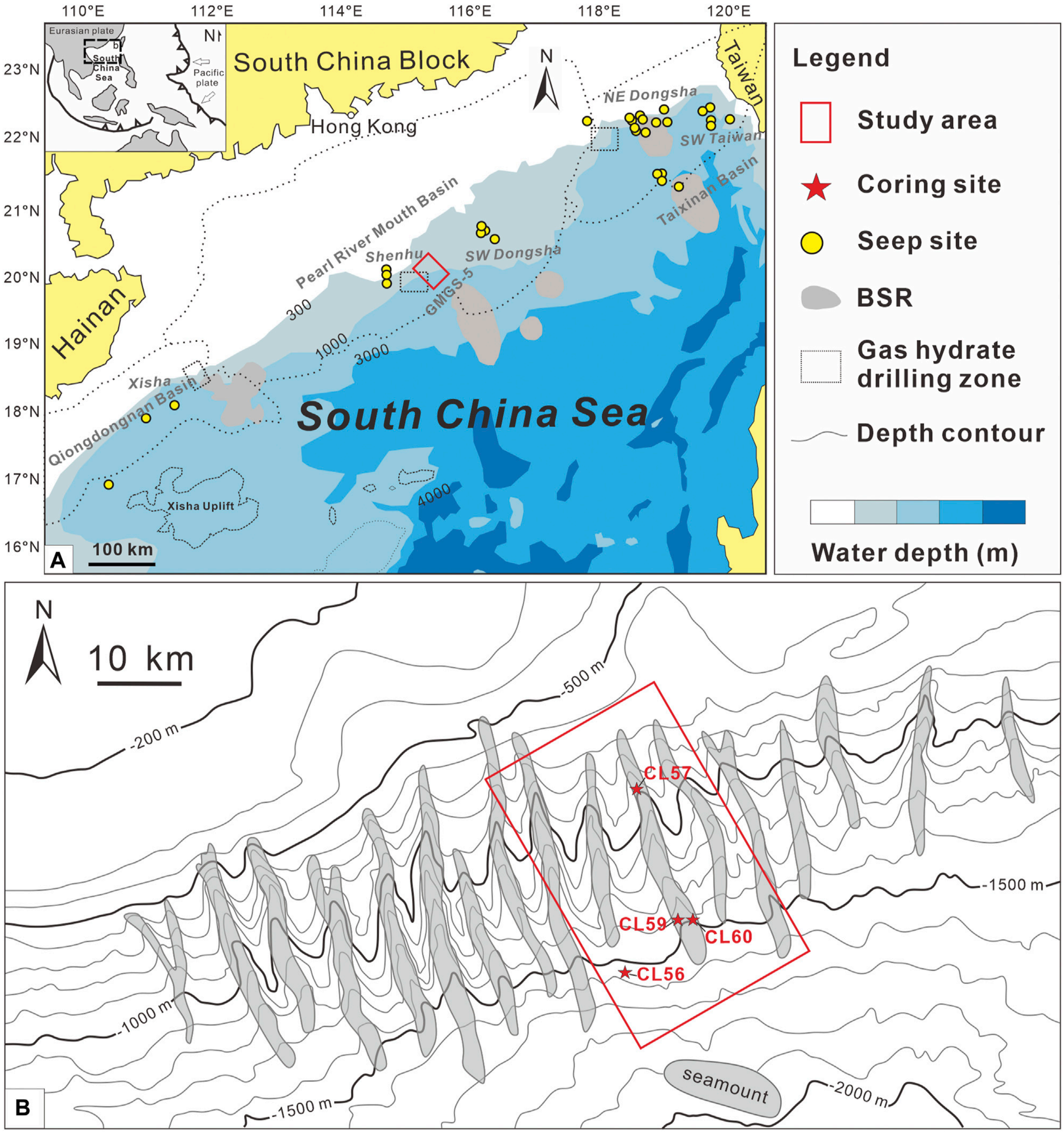

FIGURE 1 | Geological settings and locations of coring sites in the Shenhu area of the northern South China Sea. **(A)** The GMGS-5 gas hydrate drilling area is indicated by a red rectangle, which is located in the Pearl River Mouth Basin. **(B)** Locations of the four coring sites are marked by red stars (after Sun et al., 2012; Lin et al., 2017).

environments) represent the most common processes for sulfate reduction in modern marine sediments, knowledge about the mechanisms and environmental controls on the associated isotope evolution is essential for us to better constrain the oceanic sulfur cycling.

In order to explore the isotope partitioning during OSR and SD-AOM, sulfur and oxygen isotopic compositions of dissolved sulfate were investigated in this study from multiple sites in the Shenhu area, a typical methane diffusing area in the South China Sea (Yang et al., 2010; Wu L. et al., 2013; Wei et al., 2019). Concentrations of pore water sulfate and dissolved inorganic carbon (DIC) and the carbon isotopic composition ($\delta^{13}C_{DIC}$) were supplemented to constrain the principal sulfate reduction process at the study sites.

GEOLOGICAL BACKGROUND

As one of the largest marginal seas in the western Pacific Ocean, the South China Sea is surrounded by the Eurasian Plate, the Pacific Plate and the Indo-Australian Plate (Suess, 2005). The northern slope of the South China Sea is characterized by a typical passive continental margin. Seep carbonates and gas hydrates were widely discovered in this location (Zhang H. Q. et al., 2007; Han et al., 2008; Tong et al., 2013; Feng and Chen, 2015; Liang et al., 2017). The occurrence of gas hydrate was confirmed for several target areas, including the Shenhu area (Zhang H. T. et al., 2007; Yang et al., 2008; Wu D. D. et al., 2013; Wang et al., 2014), the Dongsha area (Han et al., 2008; Feng and Chen, 2015), the Xisha Through (Jiang et al., 2008), as well as the Qiongdongnan Basin (Liang et al., 2017; Wei et al., 2019; Ye et al., 2019). The Shenhu area is located in the middle of the northern slope of the South China Sea. Tectonically, it is located within the Pearl River Mouth Basin (Wu D. et al., 2011), which is characterized by organic-rich sediment ranging in thickness from 1000 to 7000 m (Li et al., 2010; Wu N. et al., 2011). Bottom-simulating reflectors (BSRs), as an indicator for bottom the gas hydrate stabilization zone, are widely identified in the Shenhu area (Yu et al., 2014; Yang et al., 2017; Zhang et al., 2019). Furthermore, high-angle fractures and diapir structures are highly developed in this area, which is essential for methane-bearing fluid migration and gas hydrate formation (Wu et al., 2009).

SAMPLES AND METHODS

Samples

In 2018, GMGS-5 drilling expedition was conducted by the Guangzhou Marine Geological Survey in the northwestern part of the South China Sea (Wei et al., 2019). Studied sediment samples were obtained from four gravity cores collected during the GMGS-5 Cruise in the Shenhu area (**Figure 1**). The water depths of these sites vary from 990 to 1534 m. The sediments show homogeneous lithologies at all sites, mainly consisting of green-gray clay and silt. The pore water samples were extracted at 20 cm intervals using Rhizon samplers with a membrane pore size of 0.2 μm (Seeberg-Elverfeldt et al., 2005). About 10–20 ml pore water sample was extracted from each depth interval and stored at 4°C until further analysis.

Analytical Methods

The concentrations of dissolved sulfate (SO_4^{2-}), calcium (Ca^{2+}), and magnesium (Mg^{2+}) were measured at the Instrumental Analysis and Research Center, Sun Yat-sen University. An Ion Pac AS14-type column and an Ion Pac AS12A-type column were used for anion and cation separation, respectively. Pore water samples were diluted 500-fold with deionized water. A mixed solution with Na_2CO_3 (3.5 mM) and $NaHCO_3$ (1.0 mM) was used as eluent (1.0 ml/min) for sulfate concentration analysis using a Dionex ICS-5000 ion chromatograph. Meanwhile, an 18 mM methanesulfonic acid solution was used as eluent (1.0 ml/min) for Ca^{2+} and Mg^{2+} concentrations using a Dionex ICS-900 ion chromatograph.

For DIC concentration and $\delta^{13}C_{DIC}$ analyses, 0.2 ml of each pore water sample was injected into an evacuated septum tube containing concentrated phosphoric acid. The liberated CO_2 gas was separated by a gas chromatographic column in 75°C and then transferred to a continuous flow isotope ratio mass spectrometer (ThermoFisher MAT253 mass spectrometer interfaced with a Finnigan GasBench) for isotope ratio measurements. Isotope results are reported in the delta notation as per mil difference from the Vienna Peedee Belemnite (V-PDB) standard. The analytical precision was better than ±0.2‰ for $\delta^{13}C_{DIC}$ values. A 50 mM Na_2CO_3 + $NaHCO_3$ standard solution was diluted into concentrations of 0.49, 2.67, 5.83, 9.57, 24.54, and 34.71 mM to determine the calibrations curves. The linear correlation between the intensity of released CO_2 gas and the DIC concentrations of Na_2CO_3 + $NaHCO_3$ standard solution was used for calculating the DIC concentration in the samples. Analyses were conducted at the Third Institute of Oceanography, Ministry of Natural Resources.

For sulfate sulfur and oxygen isotope analyses, pore water samples were filtered (<0.45 μm) and sulfate was precipitated as $BaSO_4$ using an 8.5 wt% $BaCl_2$ solution at pH 2 and sub-boiling conditions. The $BaSO_4$ precipitates were washed with deionized water and filtered through a pre-weighed 0.45 μm cellulose nitrate membrane filter. Precipitates were dried at 40°C and weighed out to calculate the yields. For $\delta^{34}S_{SO4}$ analysis, about 200 μg of $BaSO_4$ precipitate mixed with an equal amount of vanadium pentaoxide (V_2O_5) were combusted to SO_2, and subsequently transferred to a ThermoScientific Delta V Advantage mass spectrometer interfaced to a Flash EA IsoLink CN elemental analyzer (EA-IRMS). The measurements were carried out at the Institut für Geologie und Paläontologie, Westfälische Wilhelms-Universität Münster. The sulfur isotope values are reported in per mil relative to the Vienna Canyon Diablo Troilite (V-CDT) standard and the analytical precision is better than ±0.3‰:

$$\delta^{34}S\ (‰,\ V-CDT) = \left[\left(\frac{(^{34}S/^{32}S)_{sample}}{(^{34}S/^{32}S)_{V-CDT}}\right) - 1\right] \times 1000$$

The analytical performance was calibrated by international reference materials IAEA-S1 ($\delta^{34}S$ = −0.30‰), IAEA-S2 ($\delta^{34}S$ = +21.55‰), IAEA-S3 ($\delta^{34}S$ = −31.4‰) and NBS 127 ($\delta^{34}S$ = +21‰).

Oxygen isotopic compositions of $BaSO_4$ precipitates were determined following combustion at 1450°C in a pyrolysis unit (ThermoFinnigan TC/EA) coupled to a ThermoScientific Delta V Plus mass spectrometer at the Institut für Geologie und Paläontologie, Westfälische Wilhelms-Universität Münster. Results are reported as $\delta^{18}O_{SO4}$ relative to the Vienna Standard Mean Ocean Water (V-SMOW) with an analytical precision better than ±0.5‰:

$$\delta^{18}O\ (‰,\ V-SMOW) = \left[\left(\frac{(^{18}O/^{16}O)_{sample}}{(^{18}O/^{16}O)_{V-SMOW}}\right) - 1\right] \times 1000$$

Measurements of the $\delta^{18}O_{SO4}$ were calibrated with international reference materials NBS 127 ($\delta^{18}O$ = 8.59‰), IAEA-S0-5 ($\delta^{18}O$ = 12.13‰), and IAEA-S0-6 ($\delta^{18}O$ = −11.35‰).

For total organic carbon (TOC) content measurements, about 2 g bulk sediment powder was pre-acidified by 1 M HCl for 6 h to remove inorganic carbon. The residue was washed thoroughly with deionized water for three times and dried at 60°C before analysis. TOC contents were analyzed using an elemental analyzer (Flash 2000 CHNS/O, Thermo Fisher) at the Third Institute of Oceanography, Ministry of Natural Resources. The results were calibrated with reference material BBOT (C = 72.53 wt%) and the analytical reproducibility was better than 3%.

The chromium reduction technique was applied to extract solid-phase sulfur from sediment samples (Canfield et al., 1986; Rice et al., 1993). About 3 g bulk sediment powder was reacted with 20 ml 8 M HCl for 1 h in an O_2-free round bottom flask with continuous N_2 flow for extracting acid volatile sulfide (AVS, mainly iron monosulfides). However, no AVS was observed in all samples. Subsequently, the residue was reacted with 30 ml chromous (II) chloride solution (1 M) at near-boiling temperatures for 2 h to extract chromium reducible sulfur (CRS, mainly pyrite). The liberated hydrogen sulfide gas was trapped as zinc sulfide precipitate in 4% zinc acetate-acetic acid solution. Zinc sulfide was converted into silver sulfide (Ag_2S) by adding 10 ml of 0.1 M silver nitrate solution. The Ag_2S precipitates were collected by membrane filtration (<0.45 μm) and dried at 40°C. The CRS contents were determined gravimetrically based on the dried Ag_2S yields. For sulfur isotope analysis, 200 μg Ag_2S mixed with an equal amount of vanadium pentaoxide (V_2O_5) were combusted to SO_2 using a Thermo Scientific Delta V Advantage mass spectrometer linked to a Flash EA IsoLink CN Elemental Analyzer (EA-IRMS) at the Institut für Geologie und Paläontologie, Westfälische Wilhelms-Universität Münster. The $\delta^{34}S_{CRS}$ values are reported relative to the Vienna Canyon Diablo Troilite (V-CDT) with an analytical precision better than ±0.3‰. The analytical performance was monitored with international reference materials IAEA-S1 ($\delta^{34}S$ = −0.30‰), IAEA-S2 ($\delta^{34}S$ = +21.55‰), IAEA-S3 ($\delta^{34}S$ = −31.4‰), and NBS 127 ($\delta^{34}S$ = +21‰).

Calculation of the Diffusive Sulfate Flux

The linear depth profiles of sulfate concentration at all study sites indicate that sulfate consumption was mainly dominated by SD-AOM (Berner, 1980; Borowski et al., 1996). In this case, the upward flux of methane can be determined via the downward sulfate flux assuming that sulfate flux is stoichiometrically balanced by the methane flux due to SD-AOM (Borowski et al., 1996; Niewöhner et al., 1998) and that sulfate flux consumed by OSR is insignificant.

The vertical sulfate diffusive flux J (nmol cm^{-2} d^{-1}) can be calculated according to Fick's First Law under steady-state conditions (Schulz, 2006):

$$J = -\varphi \cdot D_s \cdot \partial C/\partial z \quad (1)$$

where φ is the sediment porosity, D_s is the diffusion coefficient for bulk sediments, *C* is the concentration of sulfate, z is the depth below the seafloor, and ∂C/∂z is the linear gradient of sulfate concentrations. The porosities of these sites were set at 0.7 for CL56 and CL60, 0.68 for CL59, and 0.66 for CL57, according to the measured porosities from a nearby site (Wu L. et al., 2013). To compensate for tortuosity, the whole sediment diffusion coefficient (D_s) was calculated by the empirical equation (Iversen and Jørgensen, 1993): $D_s = D_0/(1 + 3\ (1 - \varphi))$, using the molecular diffusion coefficient in seawater (D_0) and calculated sediment porosity (φ). Seawater D_0 of sulfate is 4.94 $\times 10^{-1}$ cm^2 d^{-1}at a mean temperature of 5°C (Schulz, 2006).

Modeling of Net Sulfate Reduction Rates

A steady-state scenario at the study sites is supported by the linear relationship of sulfate concentration depth profiles. Therefore, one-dimensional reaction-transport modeling of pore water sulfate concentration profiles can be developed to estimate the net rates of sulfate reduction in subsurface sediments using the software PROFILE (Berg et al., 1998). This numerical procedure assumed that sulfate transport only occurs *via* molecular diffusion. This assumption is largely consistent with the study sites from Shenhu area where subsurface sediments are dominantly affected by sulfate and methane diffusion instead of advection as usually seen at methane seeps (Hu et al., 2020). Since bioirrigation and bioturbation only occur in the uppermost sediments (Van Cappellen and Wang, 1996), data from shallow sediments were not considered in our model. Here, pore water sulfate concentration at the top and sulfate flux at the bottom of the calculation domain were chosen as boundary conditions. The PROFILE model divided the sediment column into several discrete depth intervals (e.g., 3 zones). A constant rate of production or consumption as a function of depth was gained via the best curve fitting of measured concentration profiles (Berg et al., 1998). As these gravity cores only penetrated part of the sulfate zone, the concentration gradients of sulfate used in the modeling were extrapolated *via* the most linear part of the sulfate depth profiles and directed into the SMTZ where sulfate concentrations reach zero. The modeled volumetric rates are in units of nmol cm^{-3} d^{-1}, and the depth-integrated rates are presented in units of nmol cm^{-2} d^{-1}.

RESULTS

Concentrations of Dissolved Sulfate, Calcium, Magnesium, Inorganic Carbon, and $\delta^{13}C_{DIC}$ Values

The concentrations of dissolved SO_4^{2-}, Ca^{2+}, and Mg^{2+} in pore water are presented in **Figures 2A–C**. Overall, sulfate concentrations remain constant at the uppermost 100 cmbsf, followed by a linear decrease to the bottom of the cores. At sites CL56, CL59, and CL60, the sulfate concentrations decline rapidly from near seawater values to ~10 mM with similar gradients. In contrast, the decrease of sulfate concentration at site CL57 is slower, with a value of 24.3 mM at the bottom. Similarly, the Ca^{2+} concentrations display downward decreasing trends at sites CL56, CL59, and CL60, dropping from 8.9 to 5.4 mM, 8.6–5.0 mM, and 8.7–4.6 mM, respectively. The decrease in Ca^{2+} concentration at site CL57 is less pronounced, changing from 9.0 to 7.1 mM. The

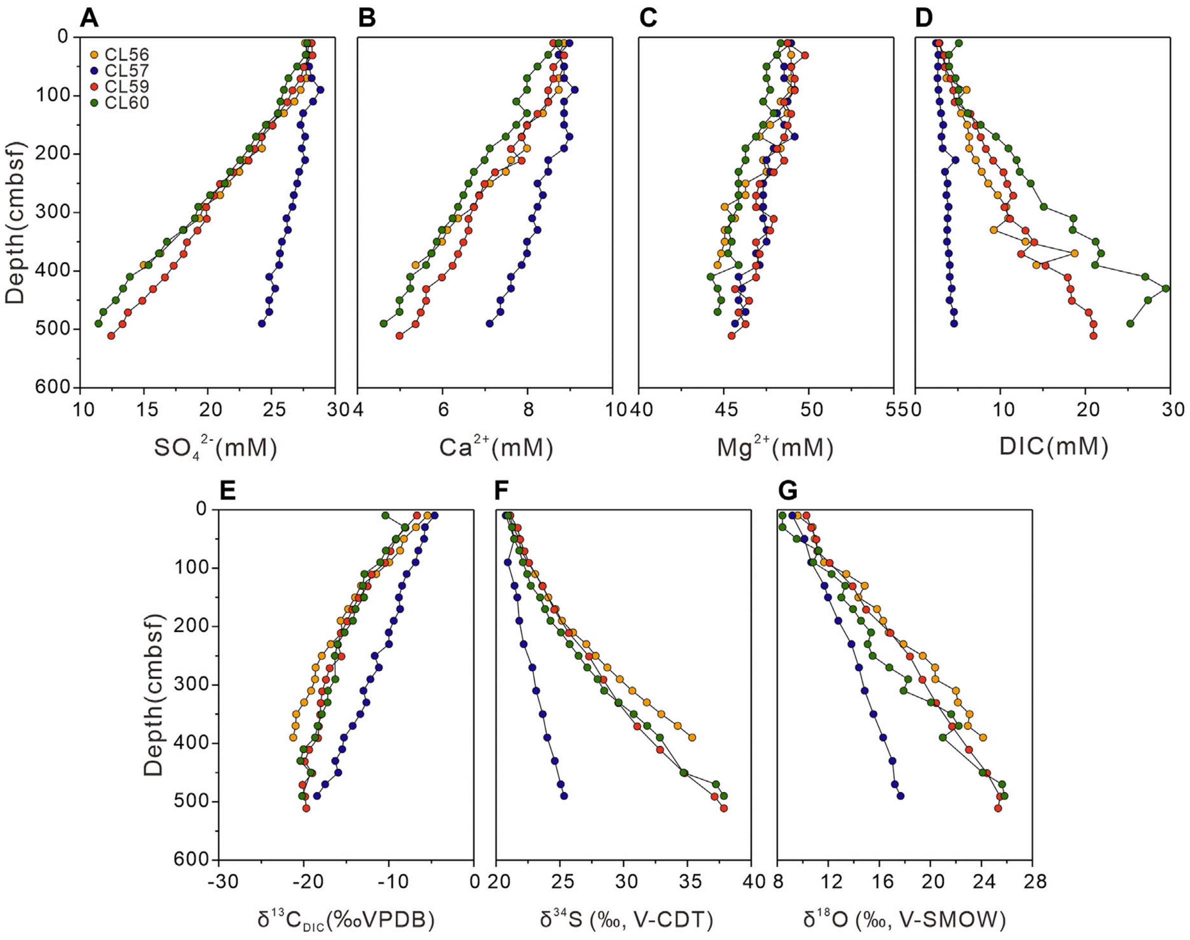

FIGURE 2 | Depth profiles of pore water geochemical data for the study sites. **(A)** sulfate (SO_4^{2-}) concentration; **(B)** calcium (Ca^{2+}) concentration; **(C)** magnesium (Mg^{2+}) concentration; **(D)** dissolved inorganic carbon (DIC) concentration; **(E)** carbon isotopic composition of DIC ($\delta^{13}C_{DIC}$) in per mil (‰) relative to the Vienna Peedee Belemnite Standard (V-PDB); **(F)** sulfur isotopic composition of sulfate ($\delta^{34}S_{SO4}$) in per mil (‰) relative to the Vienna Canyon Diablo Troilite standard (V-CDT); **(G)** oxygen isotopic composition of sulfate ($\delta^{18}O_{SO4}$) in per mil (‰) relative to the Vienna Standard Mean Ocean Water standard (V-SMOW). cmbsf-centimeters below seafloor.

Mg^{2+} concentrations are decreasing slowly from top to depth without any obvious difference at these sites.

The DIC concentrations reveal increasing trends with depth at the study sites with different gradients (**Figure 2D**). In particular, the DIC concentrations of site CL57 show a narrow range from 2.5 to 4.6 mM. For sites CL56, CL59, and CL60, the DIC concentrations vary from 2.8 to 18.7 Mm, 2.8–21.0 mM, 4.0–29.5 mM, respectively. The $\delta^{13}C_{DIC}$ values exhibit decreasing trends with depth (**Figure 2E**), ranging from −5.4 to −21.2‰ at site CL56, −4.6 to −18.4‰ at site CL57, −6.7 to −20.1‰ at site CL59, and −8.1 to −20.4‰ at site CL60, respectively.

Sulfur and Oxygen Isotopic Compositions of Sulfate

The sulfur and oxygen isotopic compositions of pore water sulfate from the study sites are shown in **Figures 2F,G**. Both, $\delta^{34}S_{SO4}$ and $\delta^{18}O_{SO4}$ values increase linearly with depth. For sites CL56, CL59, and CL60, the $\delta^{34}S_{SO4}$ values display relatively rapid increases compared to site CL57, ranging from 21.1 to 35.4‰, 21.1–37.9‰, and 20.9–37.9‰ respectively. In contrast, $\delta^{34}S_{SO4}$ values vary from 20.8 to 25.3‰ at site CL57. Similarly, the $\delta^{18}O_{SO4}$ values at sites CL56, CL59, CL60, and CL57 increase from 9.6 to 24.1‰, 10.3–25.5‰, 8.4–25.8‰, and from 9.2 to 17.7‰, respectively.

Contents of Total Organic Carbon, Total Sulfur, Chromium Reducible Sulfur, and $\delta^{34}S_{CRS}$ Values of Bulk Sediments

TOC contents for bulk sediments and their depth trends (**Figure 3A**) are nearly identical (0.77–1.04 wt%) among study sites for the first 100 cmbsf., the depth trends for sites CL56, CL59, and CL60 are similar, increasing from 0.86 to 1.48 wt%, 0.79 to 1.58 wt%, and 0.86 to 1.57 wt%. For site CL57, however, the TOC contents exhibit an inverse trend, decreasing from 1.21 to 0.54 wt%. Sulfur contents of sediments for sites CL56, CL57, and CL60 are ranging from 0.15 to 0.80 wt%, 0.14 to 0.45 wt%, and 0.15 to 0.78 wt%, respectively.

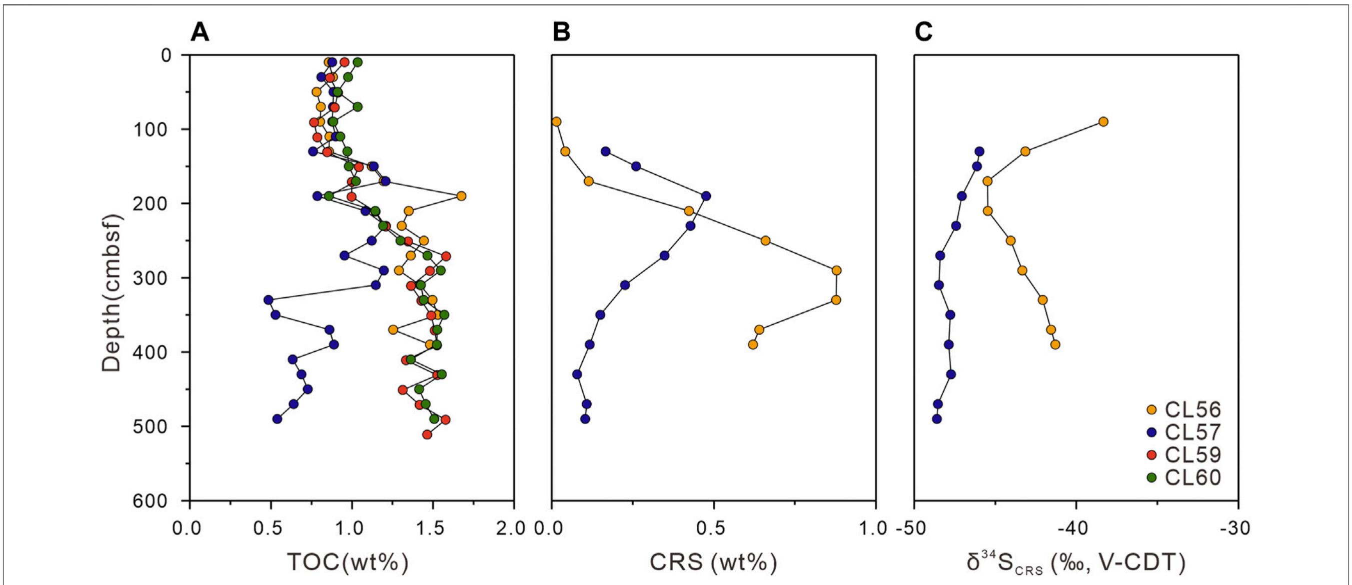

FIGURE 3 | Depth profiles of geochemical data of sediments for the study sites: **(A)** total organic carbon (TOC) contents; **(B)** chromium reducible sulfur (CRS) contents; **(C)** stable sulfur isotopic compositions of CRS ($\delta^{34}S_{CRS}$).

Notably, TOC/TS (C/S ratios) vary from 1.6 to 5.6 for sites CL56, 1.9 to 6.4 for CL57 and 1.9 to 6.2 for CL60, and show disparate patterns among these sites below ~200 cmbsf, with increasing trends for site CL57 and decreasing trends to the bottom cores for sites CL56 and CL60 (**Supplementary Table S2**).

The CRS content for bulk sediments from sites CL56 and CL57 were analyzed (**Figure 3B**). At shallow depths for both sites, the CRS contents are below detection limit. At site CL56, the CRS contents reveal an increase from 0.01 to 0.88 wt% with a peak at 290 cmbsf, followed by a decrease to 0.62 wt% at the bottom of the core. At site CL57, the CRS contents slightly increase from 0.17 to 0.48 wt%, and subsequently decrease from 0.48 to 0.10 wt%, with a peak at 190 cmbsf. The $\delta^{34}S_{CRS}$ values range from −45.5 to −38.3‰ and −48.6 to −46.0‰ at sites CL56 and CL57, respectively (**Figure 3C**). From 90 cmbsf to 170 cmbsf at site CL56, the $\delta^{34}S_{CRS}$ values show a decreasing trend ranging from −38.3 to −45.5‰. Further down, $\delta^{34}S_{CRS}$ values increase from −45.5 to −41.3‰ at the bottom of the core. In contrast, the $\delta^{34}S_{CRS}$ values at site CL57 reveal a slightly decreasing tread with depth from −46.0 to −48.6‰.

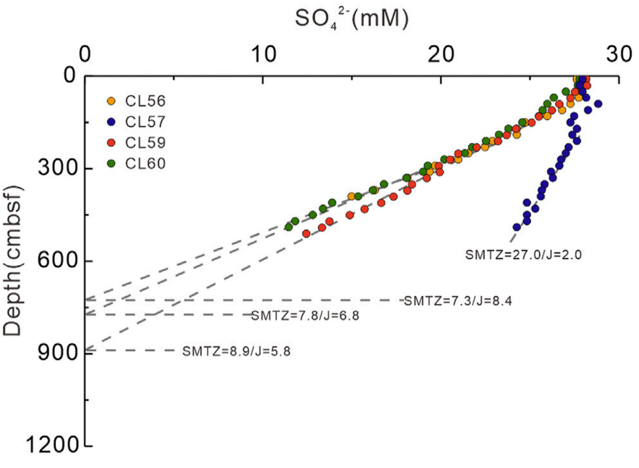

FIGURE 4 | Sulfate diffusive fluxes (J, nmol cm^{-2} d^{-1}) and corresponding depths of SMTZ (m) for the study sites via linear regression fits of sulfate concentration profiles. A higher flux corresponds to a relatively shallower depth of SMTZ. The calculated sulfate flux is roughly equivalent to the methane flux diffusing from below at each site.

Calculated Sulfate Fluxes and Rates of Sulfate Reduction

The estimated fluxes by linear regression of sulfate concentrations for sites CL56, CL57, CL59, and CL60 are 30.8, 7.1, 21.1, and 24.8 mmol m^{-2} a^{-1}, respectively. According to the corresponding sulfate gradients, the depths of the SMTZ where sulfate concentrations decline to zero are shown in **Figure 4**. The estimated SMTZs for sites CL56, CL57, CL59, and CL60 are located at 7.3, 27.0, 8.9, and 7.8 mbsf, respectively.

The net rates of sulfate reduction calculated by the PROFILE model are shown in **Figure 5**. The model divided the sediment column into several zones with different reaction rates, and the depth-integrated rates of sulfate reduction (i.e., the overall rates of sulfate consumption across the whole calculation domains) for sites CL56, CL57, CL59, and CL60 are 8.0, 0.7, 6.3, and 7.5 nmol cm^{-2} d^{-1}. Specifically, for sites CL56, CL59, and CL60, a distinct peak of volumetric sulfate reduction rate (i.e., rate of sulfate consumption for each discrete sediment column) can be seen near the SMTZ, while no net sulfate consumption is found above the SMTZ. However, at site CL57, a relatively lower peak of volumetric sulfate reduction

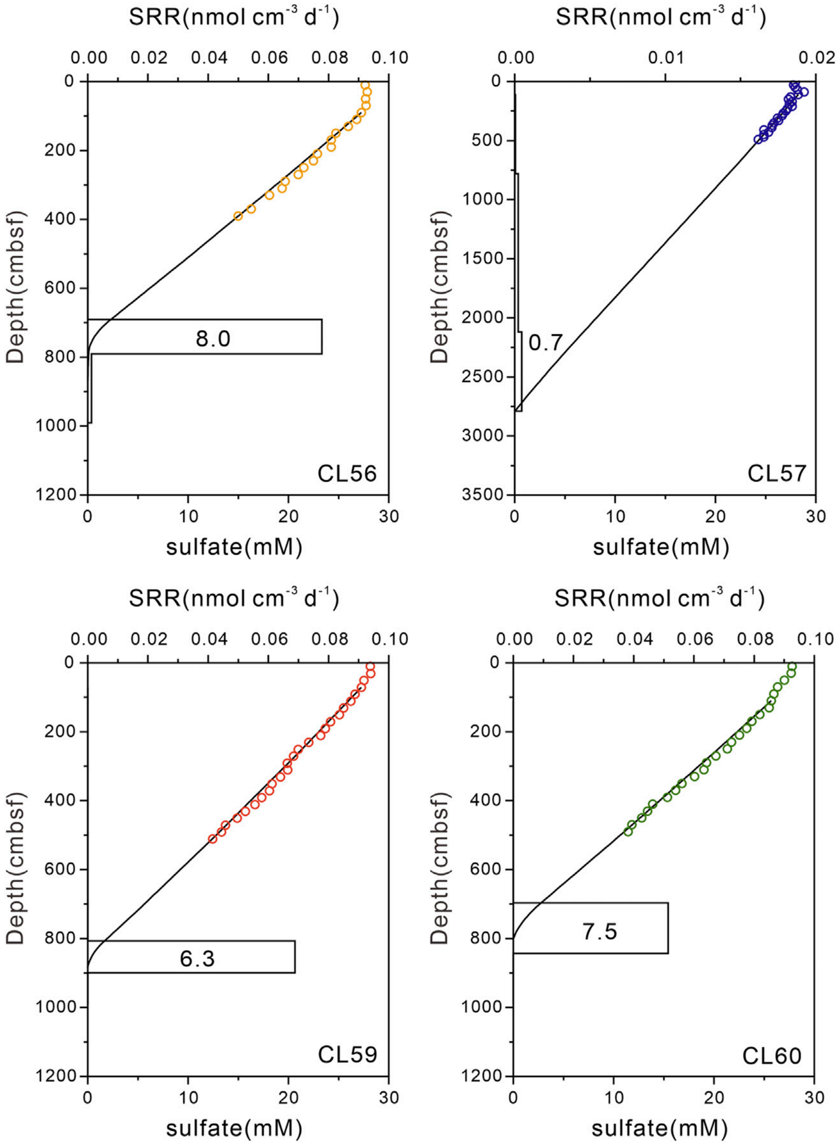

FIGURE 5 | Best fitted sulfate concentration profiles and modeled net sulfate reduction rates (nmol cm^{-3} d^{-1}) for study sites. Sulfate concentrations in the upper tens of centimeters remain more or less invariant due to bioirrigation and thus are not considered in the model. The depth-integrated rate of sulfate reduction for each core are noted in the box.

rate can be identified, and the net sulfate consumption is low throughout the entire core.

DISCUSSION

Sulfate Reduction in the Pore Water and Evidences for Organoclastic Sulfate Reduction and Sulfate-Driven Anaerobic Oxidation of Methane

The sulfate consumption in marine sediments is mainly controlled by **(1)** organoclastic sulfate reduction (OSR, Berner, 1980) and 2) sulfate-driven anaerobic oxidation of methane (SD-AOM, Hinrichs et al., 1999; Boetius et al., 2000). Steep sulfate gradients from seafloor to the SMTZ normally indicate high methane flux in the sediments (Borowski et al., 2000; Hoehler et al., 2000; Dickens, 2001). Sulfate reduction in the sediments affect the shape of pore water sulfate profiles (Niewöhner et al., 1998; Dickens, 2001; Hensen et al., 2003). It was proposed that a linear depletion of sulfate normally reflects co-consumption of sulfate and methane mainly by SD-AOM under steady-state conditions (Jørgensen and Kasten, 2006). In contrast, concave up and down types generally result from OSR-dominated consumption or changes in the methane flux from below under non-steady state conditions (Hensen et al., 2003;

Jørgensen and Kasten, 2006). However, it was found that the co-occurrence of OSR and SD-AOM in the sediment can also lead to a nearly linear sulfate profile (Malinverno and Pohlman, 2011).

In the uppermost sediments at the study sites (above 100 cmbsf), the sulfate concentrations remain nearly constant. Likely, this reflects sufficient replenishment of sulfate from the overlying seawater or sulfide reoxidation caused by near surface bioturbation or bioirrigation (Fossing et al., 2000; Treude et al., 2005; Claypool et al., 2006; Coffin et al., 2008; Minami et al., 2012), which is common in near-surface sediments in the northern slope of the South China Sea (Yang et al., 2010; Ye et al., 2016). Below 100 cmbsf, sulfate concentration profiles of all sites reveal linear depletion. The non-zero sulfate concentrations at the bottom of the cores suggest that the gravity cores have not penetrated the SMTZ. The depths of the SMTZ are obtained by linear regression (**Figure 4**). Previous studies suggested that the depth of the SMTZ is generally related to the upward methane flux, where a shallower depth of the SMTZ is corresponding to a higher methane flux (Borowski et al., 1996; Dickens, 2001). Assuming the methane flux is identical to the sulfate flux, it is apparent that the methane flux at site CL57 (2.0 nmol cm^{-2} d^{-1}) is much lower than for sites CL56, CL59, and CL60 (5.8–8.4 nmol cm^{-2} d^{-1}). Two groups can be divided according to the distinct depths of the SMTZs and the methane fluxes: 1) sites CL56, CL59, and CL60 with shallower depths of the SMTZ as "group A", and 2) site CL57 with a greater depth of the SMTZ as "group B".

The methane fluxes obtained in this study are much lower compared to those seep sites characterized by gas bubble ebullition and remarkably shallower SMTZs (several centimeters; Aharon and Fu, 2000; Luff and Wallmann, 2003). Our results are similar to previous studies in the Shenhu area (Wu L. et al., 2013; Hu et al., 2020), which clearly indicates a typical methane diffusing environment in the study areas. Recently, OSR was identified as a significant microbial pathway responsible for the consumption of pore water sulfate across the SMTZ (Komada et al., 2016; Egger et al., 2018; Jørgensen et al., 2019). In addition, it was argued that it is inappropriate to propose SD-AOM as the dominant sulfate reduction process only based on a linear sulfate gradient (Malinverno and Pohlman, 2011; Jørgensen et al., 2019). Consequently, discriminating the microbial pathways fueling sulfate reduction (i.e., OSR and SD-AOM) in the sediments becomes critical for us to better understand the sedimentary sulfur cycling.

The concentration and the carbon isotopic composition of DIC in sediments have been used to interpret the mode of sulfate reduction (Kastner et al., 2008; Chatterjee et al., 2011; Luo et al., 2013). In alkaline environments, DIC is predominantly composed of bicarbonate (HCO_3^-) (Ussler and Paull, 2008). According to the equations for OSR and SD-AOM, OSR produces two mol of bicarbonate by consuming one mol sulfate ($2CH_2O + SO_4^{2-} \rightarrow 2HCO_3^- + H_2S$), while SD-AOM process produces one mol of bicarbonate by utilizing one mol sulfate ($CH_4 + SO_4^{2-} \rightarrow HCO_3^- + HS^- + H_2O$; Kastner et al., 2008). Thus, the ratios of the production of DIC (ΔDIC) to the consumption of sulfate (ΔSO_4^{2-}) was applied to differentiate the relative contribution of OSR ($\Delta DIC: \Delta SO_4^{2-} = 2:1$) and SD-AOM ($\Delta DIC: \Delta SO_4^{2-} = 1:1$) (Masuzawa et al., 1992). Since the precipitation of carbonate in a high alkalinity environment can lead to the consumption of dissolved Ca^{2+} and Mg^{2+} (Rodriguez et al., 2000), the combination of $\Delta DIC + \Delta Ca^{2+} + \Delta Mg^{2+}$ can be used to reflect the accurate DIC concentrations (**Figure 6**). Here, ΔDIC, ΔCa^{2+}, and ΔSO_4^{2-} are calculated relative to the typical seawater values for DIC (2.1 mM), Ca^{2+} (10.3 mM), and SO_4^{2-} (28.9 mM) (Chen et al., 2010). As the measured Mg^{2+} concentrations at the uppermost depths from all sites are lower than the typical seawater value (53.2 mM, Chen et al., 2010), ΔMg^{2+} is calculated relative to the highest concentration at the top of the study sites (49.0 mM). Data from sites CL56 and CL59 falls into the area between the slopes of 2:1 and 1:1, suggesting the co-occurrence of OSR and SD-AOM at these sites. In contrast, data from site CL57 mainly cluster at or near the slope of 2:1, which indicates that OSR is the predominant process at these sites. Although the data from site CL60 also cluster near the slope of 2:1, we suggest a contribution of SD-AOM cannot be completely ruled out, since the pore water sulfate pattern of site CL60 is similar to sites CL56 and CL59.

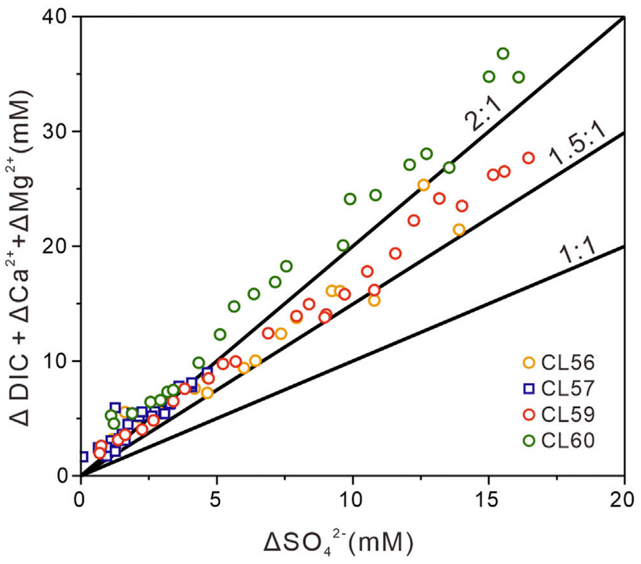

FIGURE 6 | Plots of sulfate removed versus DIC elevated corrected for calcium and magnesium loss due to authigenic carbonate precipitation. The ΔDIC, ΔCa^{2+}, and ΔSO_4^{2-} are the differences between seawater values (2.1 mM for DIC, 10.3 mM for Ca^{2+}, and 28.9 mM for ΔSO_4^{2-}; Chen et al., 2010) and measured results in this study. The ΔMg^{2+} represents the loss of magnesium with depth relative to the uppermost pore water (~49 mM). The diagonal lines indicate 2:1, 1.5:1, and 1:1 ratio. The 2:1 ratio is consistent with sulfate reduction processes dominated by OSR, while the 1:1 ratio is consistent with sulfate reduction fueled by anaerobic oxidation of methane (i.e., SD-AOM).

Pore water DIC is mainly derived from: 1) seawater ($\delta^{13}C_{SW}$: ~ 0‰, Claypool et al., 2006), 2) OSR ($\delta^{13}C_{OM}$: −20‰, Chen et al., 2012), and 3) SD-AOM ($\delta^{13}C_{CH4}$: −35‰ ~ −80‰, Masuzawa et al., 1992). Consequently, the $\delta^{13}C_{DIC}$ values are often applied to indicate the sources of DIC (Borowski et al., 2000; Sivan et al., 2007; Chen et al., 2010; Malinverno and Pohlman, 2011; Hu et al.,

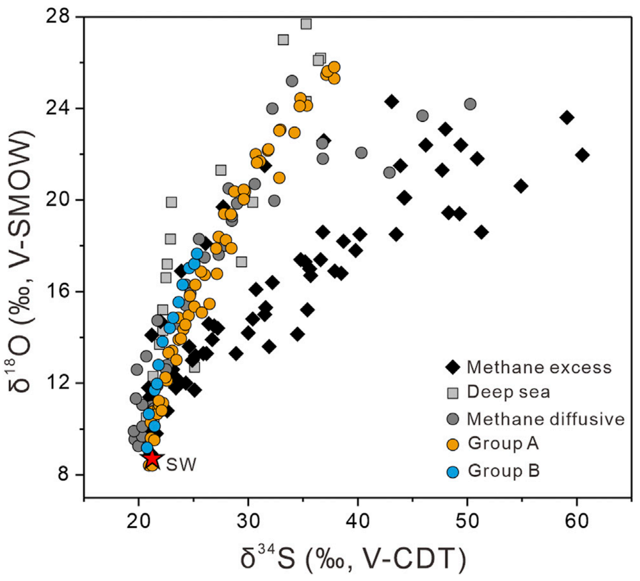

FIGURE 7 | Plots of $\delta^{18}O_{SO4}$ versus $\delta^{34}S_{SO4}$ of study sites (group A: CL56, CL59, and CL60; group B: CL57) departures from the initial sulfate values ($\delta^{34}S$ = +20.24‰, Tostevin et al., 2014; $\delta^{18}O$ = +8.7‰, Johnston et al., 2014), comparing with compiled data from methane excess, methane diffusive, and deep-sea sediments (Aharon and Fu, 2000; Blake et al., 2006; Böttcher et al., 2006; Aller et al., 2010; Strauss et al., 2012; Antler et al., 2014; Antler et al., 2015; Lin et al., 2017; Hu et al., 2020).

2015). The $\delta^{13}C_{DIC}$ values for CL57 are between the seawater value (~0‰) and typical organic matter value (−20‰), suggesting a mixture of DIC derived from diffusing seawater, OSR and potential SD-AOM. This agrees with the 2:1 slope of ($\Delta DIC+\Delta Ca^{2+}+Mg^{2+}$): ΔSO_4^{2-}. The decrease in $\delta^{13}C_{DIC}$ with depth implies an increasing contribution from OSR. In contrast, the $\delta^{13}C_{DIC}$ values at the bottom of the cores for sites CL56, CL59 and CL60 are slightly lower than −20‰, suggesting more contributions from SD-AOM. The lower C/S ratios of bulk sediments corresponding to considerable addition of CRS also indicate more intense SD-AOM at site CL56 relative to that at site CL57 (**Supplementary Table S2**; Liu et al., 2020; Liu et al., 2021; Miao et al., 2021).

Coupled Sulfur and Oxygen Isotopic Compositions of Dissolved Sulfate: Constraints on Sulfate Reduction

Overall, cross-plots of $\delta^{18}O_{SO4}$ versus $\delta^{34}S_{SO4}$ values (**Figure 7**) exhibit a linear increase with depth from seawater values ($\delta^{34}S$ = +21.24‰, Tostevin et al., 2014; $\delta^{18}O$ = +8.7‰, Johnston et al., 2014). Moreover, all the data for this study resemble isotope patterns derived from the methane diffusive environments (**Figure 7**; Antler et al., 2015). Interestingly, the SALP at each site exhibits two different trends (**Figure 8**). For the upper sediment column (~200 cmbsf), $\delta^{18}O_{SO4}$ increases more rapidly than $\delta^{34}S_{SO4}$, resulting in rather higher SALP (1.49–2.82). Such relatively higher SALP values in shallow sediments have also been observed elsewhere (Antler et al., 2013; Antler et al., 2015; Lin et al., 2017). This SALP pattern is consistent with the relatively constant sulfate concentrations (**Figure 2A**) and higher sulfur isotopic compositions (**Figure 3C**) in the upper sediment column, which was explained by the enhanced sulfur disproportionation or reoxidation of sulfide to sulfate (Böttcher et al., 1999; Böttcher and Thamdrup, 2001; Böttcher et al., 2006; Lin et al., 2017). Likely, bioturbation or bioirrigation processes the shallow sediments canfacilitate the penetration of oxygen and thus enhance the oxidative sulfur cycle (Minami et al., 2012).

At greater depth, the SALP value becomes lower at each site, suggesting that the oxidation of intermediate sulfur species is less significant. The range of SALP values (from 0.74 to 1.26) is similar to other environments where methane was undetectable and sulfate reduction is fueled by organic matter oxidation (Antler et al., 2013; Hu et al., 2020). Still, a difference in the SALP can be identified between site CL57 and the others (sites CL56, CL59, and CL60), with the SALP from site CL57 showing a higher value (1.26, see **Figure 9**). This high SALP value indicates a slower net SRR at this site, which could result from a low supply of the electron donor (i.e., organic matter) (**Figure 3A**). In addition, this pattern agrees with the low content and the strongly negative sulfur isotopic composition of CRS at this site (**Figures 3B,C**). In contrast, the sulfate and DIC concentration profiles from sites CL56, CL59 and CL60 indicate that SD-AOM plays a key role in sulfate consumption at depth. Aharon and Fu (2000) proposed that the sulfate reduction rate is a function of the type of organic carbon substrate (e.g., methane and organic matter), which can affect the SALP. It has been suggested that a change in the principal electron donor from organic matter to methane can lead to less reoxidation of the intermediate sulfur species, which may result in a lower SALP (Antler et al., 2014; Yoshinaga et al., 2014). This provides an alternative cause for explaining the lower SALP values at these sites.

To calculate the net sulfate reduction rate for each site, one-dimensional transport-reaction modeling was applied in this study using the PROFILE model (Berg et al., 1998). The depth-integrated rates calculated by the model were considered to represent the net rates of sulfate reduction across each site. The net sulfate reduction rates are much higher for sites CL56, CL59, and CL60, compared to site CL57. For sites CL56, CL59, and CL60, distinct peaks in the net sulfate reduction rate were observed at the depth of the SMTZs. This indicates that most of the sulfate was consumed within the SMTZ, which confirms that SD-AOM is a key process at these sites (**Figure 5**). In contrast, a relatively lower net sulfate reduction rate was observed at the SMTZ at site CL57. This indicates that most of the downwards diffusing sulfate was reduced by the oxidation of organic matter in the sediment. while sulfate consumption fueled by upwards diffusing methane is insignificant supported by very low net SRR at the SMTZ. It was demonstrated that the SALP pattern during sulfate reduction is relatively unaffected during sulfate diffusion or advection (Antler et al., 2013; Fotherby et al., 2021). Thus, it can be inferred that the differences in the SALP patterns (below ~200 cmbsf) between site CL57 and the three other sites reflect a variation of the dominant sulfate reduction mode (i.e., OSR vs. SD-AOM). The higher SALP value from site CL57 indicates a lower net SRR during OSR and very

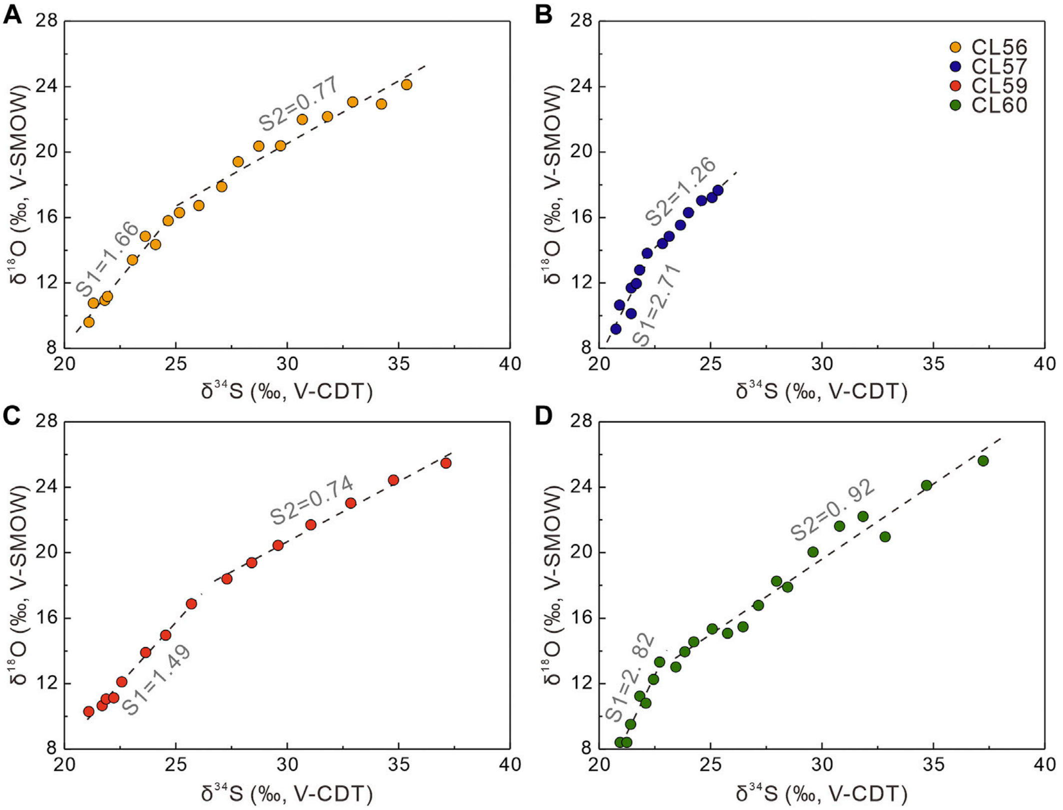

FIGURE 8 | Plots of $\delta^{18}O_{SO4}$ versus $\delta^{34}S_{SO4}$ of **(A)** CL56, **(B)** CL57, **(C)** CL59, and **(D)** CL60. The linear fittings (dash lines) indicate the slope of the apparent linear phase of the $\delta^{18}O_{SO4}$ versus $\delta^{34}S_{SO4}$ cross-plots (SALP), where S1 represents the SALP of shallow part at ~ 200 cmbsf and S2 represents the SALP of deeper part below ~200 cmbsf.

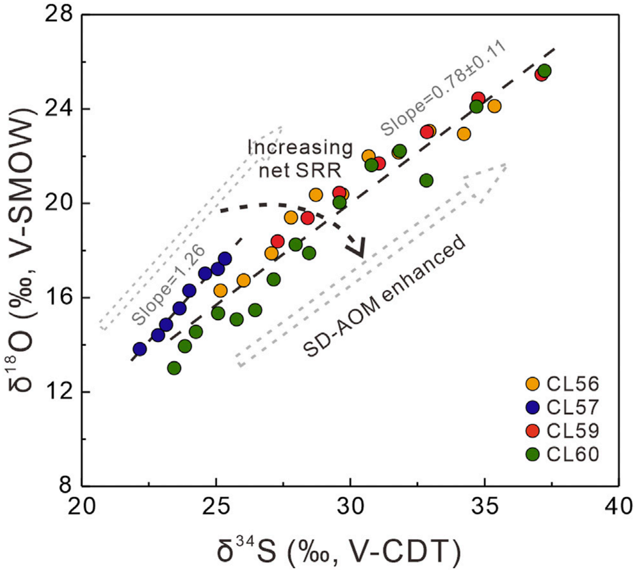

FIGURE 9 | Comparison of the SALP at deeper parts of site CL57 and the others (sites CL56, CL59, and CL60), indicating increasing net sulfate reduction rates dominated by SD-AOM within SMTZ.

limited SD-AOM at this location. In contrast, the lower SALP values for sites CL56, CL59, and CL60 likely reflect more intense SD-AOM at the SMTZs, due to a higher net SRR, although a contribution from OSR cannot be excluded.

CONCLUSION

In this study, pore water and bulk sediment geochemistry was analyzed to decipher how organoclastic sulfate reduction (OSR) and sulfate-driven anaerobic oxidation of methane (SD-AOM) affect the sulfur and oxygen isotopic compositions of dissolved sulfate in methane diffusing environments. Sulfate and DIC profiles as well as the calculated net sulfate reduction rates suggest that OSR is dominant at site CL57, and OSR and SD-AOM likely co-occurred at sites CL56, CL59, and CL60. The patterns of $\delta^{18}O_{SO4}$ versus $\delta^{34}S_{SO4}$ for all study sites are similar to those derived from methane-limited environments. However, different slopes in $\delta^{18}O_{SO4}$ versus $\delta^{34}S_{SO4}$ cross-plot were recognized for site CL57 (a slope of 1.26) and for the other three sites (slopes of 0.78 ± 0.11). It was inferred that the slopes in $\delta^{18}O_{SO4}$ versus $\delta^{34}S_{SO4}$ cross-plot for the study sites are mainly controlled by the dominant sulfate reduction process (i.e., OSR and SD-AOM). Results from this study further improves our understanding for applying a cross-plot of $\delta^{18}O_{SO4}$ versus $\delta^{34}S_{SO4}$ value as a proxy for identifying the dominant mode of sulfate reduction in modern and ancient marine sediments.

DATA AVAILABILITY STATEMENT

The original contributions presented in the study are included in the article/**Supplementary Material**, further inquiries can be directed to the corresponding authors.

AUTHOR CONTRIBUTIONS

TC, XS, and ZL conceived this study; XS and ZL supervise the investigation; TC and ZL wrote the draft of the manuscript; HS revised the manuscript JL, YL, XY, HL, ZW, and XL performed the mineral selection and analysis of those samples.

FUNDING

This research was jointly funded and supported by the National Key Research and Development Program of China (2018YFC0310004), the Natural Science Foundation of China (No. 41806049, 41876038, and 91128101), the Fundamental Research Funds for the Central Universities (No. 18lgpy28), China Postdoctoral Science Foundation (No. 2018M631015), the Guangdong Special Fund for Economic Development (Marine Economy, No. GDME-2018D001), and the China Geological Survey Project for South China Sea Gas Hydrate Resource Exploration (No. DD20160211).

ACKNOWLEDGMENTS

ZL further acknowledges the International Postdoctoral Exchange Fellowship Program provided by China Postdoctoral Council (No. 20180053). A. Fugmann are thanked for his skillful assistance in the stable isotope lab in Münster.

SUPPLEMENTARY MATERIAL

The Supplementary Material for this article can be found online at: https://www.frontiersin.org/articles/10.3389/feart.2022.862333/full#supplementary-material

REFERENCES

Aharon, P., and Fu, B. (2000). Microbial Sulfate Reduction Rates and Sulfur and Oxygen Isotope Fractionations at Oil and Gas Seeps in deepwater Gulf of Mexico. *Geochimica et Cosmochimica Acta* 64, 233–246. doi:10.1016/S0016-7037(99)00292-6

Aharon, P., and Fu, B. (2003). Sulfur and Oxygen Isotopes of Coeval Sulfate-Sulfide in Pore Fluids of Cold Seep Sediments with Sharp Redox Gradients. *Chem. Geology.* 195, 201–218. doi:10.1016/S0009-2541(02)00395-9

Aller, R. C., Madrid, V., Chistoserdov, A., Aller, J. Y., and Heilbrun, C. (2010). Unsteady Diagenetic Processes and Sulfur Biogeochemistry in Tropical Deltaic Muds: Implications for Oceanic Isotope Cycles and the Sedimentary Record. *Geochimica et Cosmochimica Acta* 74, 4671–4692. doi:10.1016/j.gca.2010.05.008

Antler, G., and Pellerin, A. (2018). A Critical Look at the Combined Use of Sulfur and Oxygen Isotopes to Study Microbial Metabolisms in Methane-Rich Environments. *Front. Microbiol.* 9, 519. doi:10.3389/fmicb.2018.00519

Antler, G., Turchyn, A. V., Herut, B., Davies, A., Rennie, V. C. F., and Sivan, O. (2014). Sulfur and Oxygen Isotope Tracing of Sulfate Driven Anaerobic Methane Oxidation in Estuarine Sediments. *Estuarine, Coastal Shelf Sci.* 142, 4–11. doi:10.1016/j.ecss.2014.03.001

Antler, G., Turchyn, A. V., Herut, B., and Sivan, O. (2015). A Unique Isotopic Fingerprint of Sulfate-Driven Anaerobic Oxidation of Methane. *Geology* 43, 619–622. doi:10.1130/G36688.1

Antler, G., Turchyn, A. V., Rennie, V., Herut, B., and Sivan, O. (2013). Coupled Sulfur and Oxygen Isotope Insight into Bacterial Sulfate Reduction in the Natural Environment. *Geochimica et Cosmochimica Acta* 118, 98–117. doi:10.1016/j.gca.2013.05.005

Berg, P., Risgaard-Petersen, N., and Rysgaard, S. (1998). Interpretation of Measured Concentration Profiles in Sediment Pore Water. *Limnol. Oceanogr.* 43, 1500–1510. doi:10.4319/lo.1998.43.7.1500

Berner, R. A. (1980). *Early Diagenesis: A Theoretical Approach*. Princeton, New Jersey: Princeton University Press, 241.

Blake, R. E., Surkov, A. V., Böttcher, M. E., Ferdelman, T. G., Jørgensen, B. B., and Ferdelman, M. (2006). Oxygen Isotope Composition of Dissolved Sulfate in Deep-Sea Sediments: Eastern Equatorial Pacific Ocean. *Proc. Ocean Drill. Progr. Sci. Results* 201, 1–24. doi:10.2973/odp.proc.sr.201.116.2006

Boetius, A., Ravenschlag, K., Schubert, C. J., Rickert, D., Widdel, F., Gieseke, A., et al. (2000). A marine Microbial Consortium Apparently Mediating Anaerobic Oxidation of Methane. *Nature* 407, 623–626. doi:10.1038/35036572

Borowski, W. S., Hoehler, T. M., Alperin, M. J., Rodriguez, N. M., and Paull, C. K. (2000). Significance of Anaerobic Methane Oxidation in Methane-Rich Sediments Overlying the Blake Ridge Gas Hydrates. *Proc. Ocean Drill. Progr. Sci. Results* 164, 87–99. doi:10.2973/odp.proc.sr.164.214.2000

Borowski, W. S., Paull, C. K., and Ussler, W. (1999). Global and Local Variations of Interstitial Sulfate Gradients in Deep-Water, continental Margin Sediments: Sensitivity to Underlying Methane and Gas Hydrates. *Mar. Geology.* 159, 131–154. doi:10.1016/S0025-3227(99)00004-3

Borowski, W. S., Paull, C. K., and Ussler, W. (1996). Marine Pore-Water Sulfate Profiles Indicate *In Situ* Methane Flux from Underlying Gas Hydrate. *Geol* 24, 655–658. doi:10.1130/0091-7613(1996)024<0655:mpwspi>2.3.co;2

Böttcher, M. E., Bernasconi, S. M., and Brumsack, H.-J. (1999). Carbon, Sulfur, and Oxygen Isotope Geochemistry of Interstitial Waters from the Western Mediterranean. *Proc. Ocean Drill. Progr. Sci. Results* 161, 413–421. doi:10.2973/odp.proc.sr.161.229.1999

Böttcher, M. E., Brumsack, H.-J., and De Lange, G. J. (1998). Sulfate Reduction and Related Stable Isotope (34S, 18O) Variations in Interstitial Waters from the Eastern Mediterranean. *Proc. Ocean Drill. Progr. Sci. Results* 160, 365–376. doi:10.2973/odp.proc.sr.160.002.1998

Böttcher, M. E., Ferdelman, T. G., Jørgensen, B. B., Blake, R. E., Surkov, A. V., and Claypool, G. E. (2006). Sulfur Isotope Fractionation by the Deep Biosphere within Sediments of the Eastern Equatorial Pacific and Peru Margin. *Proc. Ocean Drill. Progr. Sci. Results* 201, 1–21. doi:10.2973/odp.proc.sr.201.109.2006

Böttcher, M. E., and Thamdrup, B. (2001). Anaerobic Sulfide Oxidation and Stable Isotope Fractionation Associated with Bacterial Sulfur Disproportionation in the Presence of MnO_2. *Geochim. Cosmochim. Acta* 65, 1573–1581. doi:10.1016/S0016-7037(00)00622-0

Brunner, B., and Bernasconi, S. M. (2005). A Revised Isotope Fractionation Model for Dissimilatory Sulfate Reduction in Sulfate Reducing Bacteria. *Geochimica et Cosmochimica Acta* 69, 4759–4771. doi:10.1016/j.gca.2005.04.015

Brunner, B., Bernasconi, S. M., Kleikemper, J., and Schroth, M. H. (2005). A Model for Oxygen and Sulfur Isotope Fractionation in Sulfate during Bacterial Sulfate Reduction Processes. *Geochimica et Cosmochimica Acta* 69, 4773–4785. doi:10.1016/j.gca.2005.04.017

Brunner, B., Einsiedl, F., Arnold, G. L., Müller, I., Templer, S., and Bernasconi, S. M. (2012). The Reversibility of Dissimilatory Sulphate Reduction and the Cell-Internal Multi-step Reduction of Sulphite to Sulphide: Insights from the Oxygen Isotope Composition of Sulphate. *Isotopes Environ. Health Stud.* 48, 33–54. doi:10.1080/10256016.2011.608128

Canfield, D. E., Kristensen, E., and Thamdrup, B. (2005). Aquatic Geomicrobiology. *Adv. Mar. Biol.* 48, 1–599. doi:10.1016/00253227(93)90147-n10.1016/S0065-2881(05)48017-7

Canfield, D. E. (2001). 12. Biogeochemistry of Sulfur Isotopes. *Rev. Mineral. Geochem.* 43, 607–636. doi:10.2138/gsrmg.43.1.60710.1515/9781501508745-015

Canfield, D. E., Olesen, C. A., and Cox, R. P. (2006). Temperature and its Control of Isotope Fractionation by a Sulfate-Reducing Bacterium. *Geochimica et Cosmochimica Acta* 70, 548–561. doi:10.1016/j.gca.2005.10.028

Canfield, D. E., Raiswell, R., Westrich, J. T., Reaves, C. M., and Berner, R. A. (1986). The Use of Chromium Reduction in the Analysis of Reduced Inorganic Sulfur in Sediments and Shales. *Chem. Geology.* 54, 149–155. doi:10.1016/00092541(86)90078-110.1016/0009-2541(86)90078-1

Chatterjee, S., Dickens, G. R., Bhatnagar, G., Chapman, W. G., Dugan, B., Snyder, G. T., et al. (2011). Pore Water Sulfate, Alkalinity, and Carbon Isotope Profiles in Shallow Sediment above marine Gas Hydrate Systems: A Numerical Modeling Perspective. *J. Geophys. Res.* 116, B09103. doi:10.1029/2011JB008290

Chen, Y., Ussler, W., Haflidason, H., Lepland, A., Rise, L., Hovland, M., et al. (2010). Sources of Methane Inferred from Pore-Water δ13C of Dissolved Inorganic Carbon in Pockmark G11, Offshore Mid-Norway. *Chem. Geology.* 275, 127–138. doi:10.1016/j.chemgeo.2010.04.013

Claypool, G., Milkov, A. V., Lee, Y.-J., Torres, M. E., Borowski, W. S., and Tomaru, H. (2006). Microbial Methane Generation and Gas Transport in Shallow Sediments of an Accretionary Complex, Southern Hydrate Ridge (ODP Leg 204), Offshore Oregon, USA. *Proc. Ocean Drill. Progr. Sci. Results* 204, 1–52. doi:10.2973/odp.proc.sr10.2973/odp.proc.sr.204.113.2006

Coffin, R., Hamdan, L., Hamdan, L., Plummer, R., Smith, J., Gardner, J., et al. (2008). Analysis of Methane and Sulfate Flux in Methane-Charged Sediments from the Mississippi Canyon, Gulf of Mexico. *Mar. Pet. Geology.* 25, 977–987. doi:10.1016/j.marpetgeo.2008.01.014

Dickens, G. R. (2001). Sulfate Profiles and Barium Fronts in Sediment on the Blake Ridge: Present and Past Methane Fluxes through a Large Gas Hydrate Reservoir. *Geochimica et Cosmochimica Acta* 65, 529–543. doi:10.1016/S0016-7037(00)00556-1

Eckert, T., Brunner, B., Edwards, E. A., and Wortmann, U. G. (2011). Microbially Mediated Re-oxidation of Sulfide during Dissimilatory Sulfate Reduction by Desulfobacter Latus. *Geochimica et Cosmochimica Acta* 75, 3469–3485. doi:10.1016/j.gca.2011.03.034

Egger, M., Riedinger, N., Mogollón, J. M., and Jørgensen, B. B. (2018). Global Diffusive Fluxes of Methane in marine Sediments. *Nat. Geosci* 11, 421–425. doi:10.1038/s41561-018-0122-8

Farquhar, J., Canfield, D. E., Masterson, A., Bao, H., and Johnston, D. (2008). Sulfur and Oxygen Isotope Study of Sulfate Reduction in Experiments with Natural Populations from Fællestrand, Denmark. *Geochimica et Cosmochimica Acta* 72, 2805–2821. doi:10.1016/j.gca.2008.03.013

Feng, D., and Chen, D. (2015). Authigenic Carbonates from an Active Cold Seep of the Northern South China Sea: New Insights into Fluid Sources and Past Seepage Activity. *Deep Sea Res. Part Topical Stud. Oceanography* 122, 74–83. doi:10.1016/j.dsr2.2015.02.003

Feng, D., Peng, Y., Bao, H., Peckmann, J., Roberts, H. H., and Chen, D. (2016). A Carbonate-Based Proxy for Sulfate-Driven Anaerobic Oxidation of Methane. *Geology* 44, 999–1002. doi:10.1130/G38233.1

Fossing, H., Ferdelman, T. G., and Berg, P. (2000). Sulfate Reduction and Methane Oxidation in continental Margin Sediments Influenced by Irrigation (South-East Atlantic off Namibia). *Geochimica et Cosmochimica Acta* 64, 897–910. doi:10.1016/S00167037(99)00349-X10.1016/s0016-7037(99)00349-x

Fotherby, A., Bradbury, H. J., Antler, G., Sun, X., Druhan, J. L., and Turchyn, A. V. (2021). Modelling the Effects of Non-steady State Transport Dynamics on the Sulfur and Oxygen Isotope Composition of Sulfate in Sedimentary Pore Fluids. *Front. Earth Sci.* 8, 587085. doi:10.3389/feart.2020.587085

Fritz, P., Basharmal, G. M., Drimmie, R. J., Ibsen, J., and Qureshi, R. M. (1989). Oxygen Isotope Exchange between Sulphate and Water during Bacterial Reduction of Sulphate. *Chem. Geology. Isotope Geosci. section* 79, 99–105. doi:10.1016/0168-9622(89)90012-2

Froelich, P. N., Klinkhammer, G. P., Bender, M. L., Luedtke, N. A., Heath, G. R., Cullen, D., et al. (1979). Early Oxidation of Organic Matter in Pelagic Sediments of the Eastern Equatorial Atlantic: Suboxic Diagenesis. *Geochimica et Cosmochimica Acta* 43, 1075–1090. doi:10.1016/0016-7037(79)90095-4

Gong, S., Feng, D., Peng, Y., Peckmann, J., Wang, X., Hu, Y., et al. (2021). Deciphering the Sulfur and Oxygen Isotope Patterns of Sulfate-Driven Anaerobic Oxidation of Methane. *Chem. Geology.* 581, 120394. doi:10.1016/j.chemgeo.2021.120394

Han, X., Suess, E., Huang, Y., Wu, N., Bohrmann, G., Su, X., et al. (2008). Jiulong Methane Reef: Microbial Mediation of Seep Carbonates in the South China Sea. *Mar. Geology.* 249, 243–256. doi:10.1016/j.margeo.2007.11.012

Hensen, C., Zabel, M., Pfeifer, K., Schwenk, T., Kasten, S., Riedinger, N., et al. (2003). Control of Sulfate Pore-Water Profiles by Sedimentary Events and the Significance of Anaerobic Oxidation of Methane for the Burial of Sulfur in marine Sediments. *Geochimica et Cosmochimica Acta* 67, 2631–2647. doi:10.1016/S0016-7037(03)00199-6

Hinrichs, K.-U., Hayes, J. M., Sylva, S. P., Brewer, P. G., and DeLong, E. F. (1999). Methane-consuming Archaebacteria in marine Sediments. *Nature* 398, 802–805. doi:10.1038/19751

Hoehler, T. M., Borowski, W. S., Alperin, M. J., Rodriguez, N. M., and Paull, C. K. (2000). Model, Stable Isotope, and Radiotracer Characterization of Anaerobic Methane Oxidation in Gas Hydrate-Bearing Sediments of the Blake Ridge. *Proc. Ocean Drill. Progr. Sci. Results* 164, 79–85. doi:10.2973/odp.proc.sr.164.242.2000

Hu, Y., Feng, D., Liang, Q., Xia, Z., Chen, L., and Chen, D. (2015). Impact of Anaerobic Oxidation of Methane on the Geochemical Cycle of Redox-Sensitive Elements at Cold-Seep Sites of the Northern South China Sea. *Deep Sea Res. Part Topical Stud. Oceanography* 122, 84–94. doi:10.1016/j.dsr2.2015.06.012

Hu, Y., Feng, D., Peckmann, J., Gong, S., Liang, Q., Wang, H., et al. (2020). The Impact of Diffusive Transport of Methane on Pore-Water and Sediment Geochemistry Constrained by Authigenic Enrichments of Carbon, Sulfur, and Trace Elements: A Case Study from the Shenhu Area of the South China Sea. *Chem. Geology.* 553, 119805. doi:10.1016/j.chemgeo.2020.119805

Iversen, N., and Jørgensen, B. B. (1993). Diffusion Coefficients of Sulfate and Methane in marine Sediments: Influence of Porosity. *Geochimica et Cosmochimica Acta* 57, 571–578. doi:10.1016/0016-7037(93)90368-7

Jiang, S.-Y., Yang, T., Ge, L., Yang, J.-H., Ling, H.-F., Wu, N.-Y., et al. (2008). Geochemistry of Pore Waters from the Xisha Trough, Northern South China Sea and Their Implications for Gas Hydrates. *J. Oceanogr.* 64, 459–470. doi:10.1007/s10872-008-0039-8

Johnston, D. T., Gill, B. C., Masterson, A., Gill, B. C., Masterson, A., Beirne, E., et al. (2014). Placing an Upper Limit on Cryptic marine sulphur Cycling. *Nature* 513, 530–533. doi:10.1038/nature13698

Jørgensen, B. B., Findlay, A. J., and Pellerin, A. (2019). The Biogeochemical Sulfur Cycle of Marine Sediments. *Front. Microbiol.* 10, 849. doi:10.10.3389/fmicb.2019.00849

Jørgensen, B. B., and Kasten, S. (2006). "Sulfur Cycling and Methane Oxidation," in *Marine Geochemistry*. Editors H. D. Schulz and M. Zabel (Berlin-Heidelberg: Springer), 271–309. doi:10.1007/3-540-32144-6_8

Jørgensen, B. B. (1982). Mineralization of Organic Matter in the Sea Bed-The Role of Sulphate Reduction. *Nature* 296, 643–645. doi:10.1038/296643a0

Kastner, M., Claypool, G., and Robertson, G. (2008). Geochemical Constraints on the Origin of the Pore Fluids and Gas Hydrate Distribution at Atwater Valley and Keathley Canyon, Northern Gulf of Mexico. *Mar. Pet. Geology.* 25, 860–872. doi:10.1016/j.marpetgeo.2008.01.022

Komada, T., Burdige, D. J., Li, H.-L., Magen, C., Chanton, J. P., and Cada, A. K. (2016). Organic Matter Cycling across the Sulfate-Methane Transition Zone of the Santa Barbara Basin, California Borderland. *Geochimica et Cosmochimica Acta* 176, 259–278. doi:10.1016/j.gca.2015.12.022

Li, G., Moridis, G. J., Zhang, K., and Li, X.-S. (2010). Evaluation of Gas Production Potential from marine Gas Hydrate Deposits in Shenhu Area of South China Sea. *Energy Fuels* 24, 6018–6033. doi:10.1021/ef100930m

Liang, Q., Hu, Y., Feng, D., Peckmann, J., Chen, L., Yang, S., et al. (2017). Authigenic Carbonates from Newly Discovered Active Cold Seeps on the Northwestern Slope of the South China Sea: Constraints on Fluid Sources, Formation Environments, and Seepage Dynamics. *Deep Sea Res. Oceanographic Res. Pap.* 124, 31–41. doi:10.1016/j.dsr.2017.04.015

Lin, Z., Sun, X., Peckmann, J., Lu, Y., Xu, L., Strauss, H., et al. (2016). How Sulfate-Driven Anaerobic Oxidation of Methane Affects the Sulfur Isotopic Composition of Pyrite: A SIMS Study from the South China Sea. *Chem. Geology.* 440, 26–41. doi:10.1016/j.chemgeo.2016.07.007

Lin, Z., Sun, X., Strauss, H., Lu, Y., Böttcher, M. E., Teichert, B. M. A., et al. (2018). Multiple Sulfur Isotopic Evidence for the Origin of Elemental Sulfur in an Iron-Dominated Gas Hydrate-Bearing Sedimentary Environment. *Mar. Geology.* 403, 271–284. doi:10.1016/j.margeo.2018.06.010

Lin, Z., Sun, X., Strauss, H., Lu, Y., Gong, J., Xu, L., et al. (2017). Multiple Sulfur Isotope Constraints on Sulfate-Driven Anaerobic Oxidation of Methane: Evidence from Authigenic Pyrite in Seepage Areas of the South China Sea. *Geochimica et Cosmochimica Acta* 211, 153–173. doi:10.1016/j.gca.2017.05.015

Liu, W., Wu, Z., Xu, S., Wei, J., Peng, X., Li, J., et al. (2020). Pore-water Dissolved Inorganic Carbon Sources and Cycling in the Shallow Sediments of the Haima Cold Seeps, South China Sea. *J. Asian Earth Sci.* 201, 104495. doi:10.1016/j.jseaes.2020.104495

Liu, X., Zhang, M., Li, A., Fan, D., Dong, J., Jiao, C., et al. (2021). Depositional Control on Carbon and Sulfur Preservation Onshore and Offshore the Oujiang Estuary: Implications for the C/S Ratio as a Salinity Indicator. *Continental Shelf Res.* 227, 104510. doi:10.1016/j.csr.2021.104510

Luff, R., and Wallmann, K. (2003). Fluid Flow, Methane Fluxes, Carbonate Precipitation and Biogeochemical Turnover in Gas Hydrate-Bearing Sediments at Hydrate Ridge, Cascadia Margin: Numerical Modeling and Mass Balances. *Geochimica et Cosmochimica Acta* 67, 3403–3421. doi:10.1016/S0016-7037(03)00127-3

Luo, M., Chen, L., Wang, S., Yan, W., Wang, H., and Chen, D. (2013). Pockmark Activity Inferred from Pore Water Geochemistry in Shallow Sediments of the Pockmark Field in Southwestern Xisha Uplift, Northwestern South China Sea. *Mar. Pet. Geology.* 48, 247–259. doi:10.1016/j.marpetgeo.2013.08.018

Malinverno, A., and Pohlman, J. W. (2011). Modeling Sulfate Reduction in Methane Hydrate-Bearing continental Margin Sediments: Does a Sulfate-Methane Transition Require Anaerobic Oxidation of Methane? *Geochem. Geophys. Geosyst.* 12, a–n. doi:10.1029/2011GC003501

Martens, C. S., and Berner, R. A. (1974). Methane Production in the Interstitial Waters of Sulfate-Depleted marine Sediments. *Science* 185, 1167–1169. doi:10.1126/science.185.4157.1167

Masuzawa, T., Handa, N., Kitagawa, H., and Kusakabe, M. (1992). Sulfate Reduction Using Methane in Sediments beneath a Bathyal "Cold Seep" Giant Clam Community off Hatsushima Island, Sagami Bay, Japan. *Earth Planet. Sci. Lett.* 110, 39–50. doi:10.1016/0012-821X(92)90037-V

Miao, X., Feng, X., Liu, X., Li, J., and Wei, J. (2021). Effects of Methane Seepage Activity on the Morphology and Geochemistry of Authigenic Pyrite. *Mar. Pet. Geology.* 133, 105231. doi:10.1016/j.marpetgeo.2021.105231

Minami, H., Tatsumi, K., Hachikubo, A., Yamashita, S., Sakagami, H., Takahashi, N., et al. (2012). Possible Variation in Methane Flux Caused by Gas Hydrate Formation on the Northeastern continental Slope off Sakhalin Island, Russia. *Geo-mar. Lett.* 32, 525–534. doi:10.1007/s00367-012-0287-x

Mizutani, Y., and Rafter, T. A. (1973). Isotopic Behaviour of Sulphate Oxygen in the Bacterial Reduction of Sulphate. *Geochem. J.* 6, 183–191. doi:10.2343/geochemj.6.183

Niewöhner, C., Hensen, C., Kasten, S., Zabel, M., and Schulz, H. D. (1998). Deep Sulfate Reduction Completely Mediated by Anaerobic Methane Oxidation in Sediments of the Upwelling Area off Namibia. *Geochim. Cosmochim. Acta* 62, 455–464. doi:10.1016/S0016-7037(98)00055-6

Orphan, V. J., House, C. H., Hinrichs, K.-U., Mckeegan, K. D., and Delong, E. F. (2001). Methane-consuming Archaea Revealed by Directly Coupled Isotopic and Phylogenetic Analysis. *Science* 293, 484–487. doi:10.1126/science.1061338

Reeburgh, W. S. (1980). Anaerobic Methane Oxidation: Rate Depth Distributions in Skan Bay Sediments. *Earth Planet. Sci. Lett.* 47, 345–352. doi:10.1016/0012-821X(80)90021-7

Reeburgh, W. S. (2014). "Global Methane Biogeochemistry," in *Treatise on Geochemistry*. Editors H. D. Holland and K. K. Turekian. Second Edition (Oxford: Elsevier), 71–94. doi:10.1016/B978-0-08-095975-7.00403-4

Reeburgh, W. S. (2007). Oceanic Methane Biogeochemistry. *Chem. Rev.* 107, 486–513. doi:10.1021/cr050362v

Rees, C. E. (1973). A Steady-State Model for sulphur Isotope Fractionation in Bacterial Reduction Processes. *Geochimica et Cosmochimica Acta* 37, 1141–1162. doi:10.1016/0016-7037(73)90052-5

Regnier, P., Dale, A. W., Arndt, S., LaRowe, D. E., Mogollón, J., and Van Cappellen, P. (2011). Quantitative Analysis of Anaerobic Oxidation of Methane (AOM) in marine Sediments: A Modeling Perspective. *Earth-Science Rev.* 106, 105–130. doi:10.1016/j.earscirev.2011.01.002

Rice, C. A., Tuttle, M. L., and Reynolds, R. L. (1993). The Analysis of Forms of Sulfur in Ancient Sediments and Sedimentary Rocks: Comments and Cautions. *Chem. Geology.* 107, 83–95. doi:10.1016/0009-2541(93)90103-P

Rodriguez, N. M., Paull, C. K., and Borowski, W. S. (2000). Zonation of Authigenic Carbonates within Gas Hydrate-Bearing Sedimentary Sections on the Blake Ridge: Offshore Southeastern North America. *Proc. Ocean Drill. Progr. Sci. Results* 164, 301–312. doi:10.2973/odp.proc.sr.164.227.2000

Schulz, H. D. (2006). "Quantification of Early Diagenesis: Dissolved Constituents in Pore Water and Signals in the Solid Phase," in *Marine Geochemistry*. Editors H. D. Schulz and M. Zabel (Berlin-Heidelberg: Springer), 73–124. doi:10.1007/3.540.32144.6_3

Seeberg-Elverfeldt, J., Schlüter, M., Feseker, T., and Kölling, M. (2005). Rhizon Sampling of Porewaters Near the Sediment-Water Interface of Aquatic Systems. *Limnol. Oceanogr. Methods* 3, 361–371. doi:10.4319/lom.2005.3.361

Sivan, O., Schrag, D. P., and Murray, R. W. (2007). Rates of Methanogenesis and Methanotrophy in Deep-Sea Sediments. *Geobiology* 5, 141–151. doi:10.1111/j.1472-4669.2007.00098.x

Strauss, H., Bast, R., Cording, A., Diekrup, D., Fugmann, A., Garbe-Schönberg, D., et al. (2012). Sulphur Diagenesis in the Sediments of the Kiel Bight, SW Baltic Sea, as Reflected by Multiple Stable sulphur Isotopes. *Isotopes Environ. Health Stud.* 48, 166–179. doi:10.1080/10256016.2012.648930

Suess, E. (2005). *RV SONNE Cruise Report SO 177, Sino-German Cooperative Project, South China Sea Continental Margin: Geological Methane Budget and Environmental Effects of Methane Emissions and Gas Hydrates*. IFM-GEOMAR Reports.

Sun, Q., Wu, S., Cartwright, J., and Dong, D. (2012). Shallow Gas and Focused Fluid Flow Systems in the Pearl River Mouth Basin, Northern South China Sea. *Mar. Geology.* 315-318, 1–14. doi:10.1016/j.margeo.2012.05.003

Tong, H., Feng, D., Cheng, H., Yang, S., Wang, H., Min, A. G., et al. (2013). Authigenic Carbonates from Seeps on the Northern continental Slope of the South China Sea: New Insights into Fluid Sources and Geochronology. *Mar. Pet. Geology.* 43, 260–271. doi:10.1016/j.marpetgeo.2013.01.011

Tostevin, R., Turchyn, A. V., Farquhar, J., Johnston, D. T., Eldridge, D. L., Bishop, J. K. B., et al. (2014). Multiple Sulfur Isotope Constraints on the Modern Sulfur Cycle. *Earth Planet. Sci. Lett.* 396, 14–21. doi:10.1016/j.epsl.2014.03.057

Treude, T., Niggemann, J., Kallmeyer, J., Wintersteller, P., Schubert, C. J., Boetius, A., et al. (2005). Anaerobic Oxidation of Methane and Sulfate Reduction along the Chilean continental Margin. *Geochimica et Cosmochimica Acta* 69, 2767–2779. doi:10.1016/j.gca.2005.01.002

Turchyn, A. V., Antler, G., Byrne, D., Miller, M., and Hodell, D. A. (2016). Microbial Sulfur Metabolism Evidenced from Pore Fluid Isotope Geochemistry at Site U1385. *Glob. Planet. Change* 141, 82–90. doi:10.1016/j.gloplacha.2016.03.004

Turchyn, A. V., Brüchert, V., Lyons, T. W., Engel, G. S., Balci, N., Schrag, D. P., et al. (2010). Kinetic Oxygen Isotope Effects during Dissimilatory Sulfate Reduction: A Combined Theoretical and Experimental Approach. *Geochimica et Cosmochimica Acta* 74, 2011–2024. doi:10.1016/j.gca.2010.01.004

Ussler, W., and Paull, C. K. (2008). Rates of Anaerobic Oxidation of Methane and Authigenic Carbonate Mineralization in Methane-Rich Deep-Sea Sediments Inferred from Models and Geochemical Profiles. *Earth Planet. Sci. Lett.* 266, 271–287. doi:10.1016/j.epsl.2007.10.056

Vairavamurthy, M. A., Orr, W. L., and Manowitz, B. (1995). "Geochemical Transformations of Sedimentary Sulfur: an Introduction,". Editors M. A. Vairavamurthy and M. A. A. Schoonen (Washington, D.C: ACS Symposium), 612, 1–14. doi:10.1021/bk-1995-0612.ch001*Geochemical Transformations Sediment. Sulfur*

Valentine, D. L., Blanton, D. C., Reeburgh, W. S., and Kastner, M. (2001). Water Column Methane Oxidation Adjacent to an Area of Active Hydrate Dissociation, Eel River Basin. *Geochimica et Cosmochimica Acta* 65, 2633–2640. doi:10.1016/S0016-7037(01)00625-1

Van Cappellen, P., and Wang, Y. (1996). Cycling of Iron and Manganese in Surface Sediments; a General Theory for the Coupled Transport and Reaction of Carbon, Oxygen, Nitrogen, Sulfur, Iron, and Manganese. *Am. J. Sci.* 296, 197–243. doi:10.2475/ajs.296.3.197

Wallmann, K., Drews, M., Aloisi, G., and Bohrmann, G. (2006). Methane Discharge into the Black Sea and the Global Ocean via Fluid Flow through Submarine Mud Volcanoes. *Earth Planet. Sci. Lett.* 248, 545–560. doi:10.1016/j.epsl.2006.06.026

Wang, X., Collett, T. S., Lee, M. W., Yang, S., Guo, Y., and Wu, S. (2014). Geological Controls on the Occurrence of Gas Hydrate from Core, Downhole Log, and Seismic Data in the Shenhu Area, South China Sea. *Mar. Geology.* 357, 272–292. doi:10.1016/j.margeo.2014.09.040

Wei, J., Liang, J., Lu, J., Zhang, W., and He, Y. (2019). Characteristics and Dynamics of Gas Hydrate Systems in the Northwestern South China Sea - Results of the Fifth Gas Hydrate Drilling Expedition. *Mar. Pet. Geology.* 110, 287–298. doi:10.1016/j.marpetgeo.2019.07.028

Whiticar, M. J., Faber, E., and Schoell, M. (1986). Biogenic Methane Formation in marine and Freshwater Environments: CO2 Reduction vs. Acetate Fermentation-Isotope Evidence. *Geochimica et Cosmochimica Acta* 50, 693–709. doi:10.1016/0016-7037(86)90346-7

Wing, B. A., and Halevy, I. (2014). Intracellular Metabolite Levels Shape Sulfur Isotope Fractionation during Microbial Sulfate Respiration. *Proc. Natl. Acad. Sci. U.S.A.* 111, 18116–18125. doi:10.1073/pnas.1407502111

Wortmann, U. G., Bernasconi, S. M., and Böttcher, M. E. (2001). Hypersulfidic Deep Biosphere Indicates Extreme Sulfur Isotope Fractionation during Single-step Microbial Sulfate Reduction. *Geol* 29, 647–650. doi:10.1130/0091-7613(2001)029<0647:hdbies>2.0.co;2

Wortmann, U. G., Chernyavsky, B., Bernasconi, S. M., Brunner, B., Böttcher, M. E., and Swart, P. K. (2007). Oxygen Isotope Biogeochemistry of Pore Water Sulfate in the Deep Biosphere: Dominance of Isotope Exchange Reactions with Ambient Water during Microbial Sulfate Reduction (ODP Site 1130). *Geochimica et Cosmochimica Acta* 71, 4221–4232. doi:10.1016/j.gca.2007.06.033

Wu, D. D., Wu, N. Y., Zhang, M., Guan, H. X., Fu, S. Y., and Yang, R. (2013a). Relationship of Sulfate-Methane Interface (SMI), Methane Flux and the Underlying Gas Hydrate in Dongsha area,Northern South China Sea. *Earth Sci. J. China Univ. Geosci.* 38, 1309–1320. (in Chinese with English abstract). doi:10.3799/dqkx.2013.128

Wu, D., Wu, N., Ye, Y., Zhang, M., Liu, L., Guan, H., et al. (2011a). Early Diagenesis Records and Pore Water Composition of Methane-Seep Sediments from the Southeast Hainan Basin, South China Sea. *J. Geol. Res.* 2011, 1–10. doi:10.1155/2011/592703

Wu, L., Yang, S., Liang, J., Su, X., Fu, S., Sha, Z., et al. (2013b). Variations of Pore Water Sulfate Gradients in Sediments as Indicator for Underlying Gas Hydrate in Shenhu Area, the South China Sea. *Sci. China Earth Sci.* 56, 530–540. doi:10.1007/s11430-012-4545-6

Wu, N. Y., Yang, S. X., Wang, H. B., Liang, J. Q., Gong, Y. H., Lu, Z. Q., et al. (2009). Gas-bearing Fluid Influx Sub-system for Gas Hydrate Geological System in Shenhu Area, Northern South China Sea. *Chin. J. Geophys.* 52, 1641–1650. (in Chinese with English abstract). doi:10.3969/j.issn.0001-5733.2009.06.027

Wu, N., Zhang, H., Yang, S., Zhang, G., Liang, J., Lu, J. a., et al. (2011b). Gas Hydrate System of Shenhu Area, Northern South China Sea: Geochemical Results. *J. Geol. Res.* 2011, 1–10. doi:10.1155/2011/370298

Yang, S. X., Liang, J. Q., Lu, J. A., Qu, C. W., and Liu, B. (2017). New Understandings on the Characteristics and Controlling Factors of Gas Hydrate Reservoirs in the Shenhu Area on the Northern Slope of the South China Sea. *Earth Sci. Front.* 24, 1–14. doi:10.13745/j.esf.yx.2016-12-43

Yang, T., Jiang, S.-Y., Yang, J.-H., Lu, G., Wu, N.-Y., Liu, J., et al. (2008). Dissolved Inorganic Carbon (DIC) and its Carbon Isotopic Composition in Sediment Pore Waters from the Shenhu Area, Northern South China Sea. *J. Oceanogr.* 64, 303–310. doi:10.1007/s10872-008-0024-2

Yang, T., Jiang, S., Ge, L., Yang, J., Wu, N., Zhang, G., et al. (2010). Geochemical Characteristics of Pore Water in Shallow Sediments from Shenhu Area of South China Sea and Their Significance for Gas Hydrate Occurrence. *Chin. Sci. Bull.* 55, 752–760. doi:10.1007/s11434-009-0312-2

Ye, H., Yang, T., Zhu, G., Jiang, S., and Wu, L. (2016). Pore Water Geochemistry in Shallow Sediments from the Northeastern continental Slope of the South China Sea. *Mar. Pet. Geology.* 75, 68–82. doi:10.1016/j.marpetgeo.2016.03.010

Ye, J., Wei, J., Liang, J., Lu, J., Lu, H., Zhang, W., et al. (2019). Complex Gas Hydrate System in a Gas Chimney, South China Sea. *Mar. Pet. Geology.* 104, 29–39. doi:10.1016/j.marpetgeo.2019.03.023

Yoshinaga, M. Y., Holler, T., Goldhammer, T., Wegener, G., Pohlman, J. W., Brunner, B., et al. (2014). Carbon Isotope Equilibration during Sulphate-Limited Anaerobic Oxidation of Methane. *Nat. Geosci* 7, 190–194. doi:10.1038/NGEO2069

Yu, X., Wang, J., Liang, J., Li, S., Zeng, X., and Li, W. (2014). Depositional Characteristics and Accumulation Model of Gas Hydrates in Northern South China Sea. *Mar. Pet. Geology.* 56, 74–86. doi:10.1016/j.marpetgeo.2014.03.011

Zhang, H. Q., Yang, S. X., Wu, N. Y., Su, X., Holland, M., Schultheiss, P., et al. (2007a). "Successful and Surprising Results for China's First Gas Hydrate Drilling Expedition," in *Fire in the Ice*. National Energy Technology Laboratory, US Department of Energy. (Fall issue 1).

Zhang, H. T., Zhang, H. Q., and Zhu, Y. H. (2007b). Gas Hydrate Investigation and Research in China: Present Status and Progress. *Geol. China* 34, 953–961. (in Chinese with English abstract).

Zhang, W., Liang, J., Wei, J., Su, P., Lin, L., and Huang, W. (2019). Origin of Natural Gases and Associated Gas Hydrates in the Shenhu Area, Northern South China Sea: Results from the China Gas Hydrate Drilling Expeditions. *J. Asian Earth Sci.* 183, 103953. doi:10.1016/J.Jseaes.2019.103953

Conflict of Interest: The authors declare that the research was conducted in the absence of any commercial or financial relationships that could be construed as a potential conflict of interest.

frontiers | Frontiers in Earth Science

REVIEW
published: 02 May 2022
doi: 10.3389/feart.2022.891393

Advance in Numerical Simulation Research of Marine Methane Processes

Sinan Xu[1,2,3]*, Zhilei Sun*[2,3]**, Wei Geng*[2,3]*, Hong Cao*[2,3]*, Xilin Zhang*[2,3]*, Bin Zhai*[2,3] *and Zijun Wu*[1]***

[1]*State Key Laboratory of Marine Geology, School of Ocean and Earth Science, Tongji University, Shanghai, China,* [2]*Laboratory for Marine Geology, Pilot National Laboratory for Marine Science and Technology, Qingdao, China,* [3]*The Key Laboratory of Gas Hydrate, Ministry of Natural Resources, Qingdao Institute of Marine Geology, Qingdao, China*

Edited by:
Dong Feng,
Shanghai Ocean University, China

Reviewed by:
Hongxiang Guan,
Ocean University of China, China
Yin Xijie,
Third Institute of Oceanography State Oceanic Administration, China

***Correspondence:**
Zhilei Sun
wuzj@tongji.edu.cn
Zijun Wu
zhileisun@yeah.net

Specialty section:
This article was submitted to Marine Geoscience, a section of the journal Frontiers in Earth Science

Received: *07 March 2022*
Accepted: *11 April 2022*
Published: *02 May 2022*

Citation:
Xu S, Sun Z, Geng W, Cao H, Zhang X, Zhai B and Wu Z (2022) Advance in Numerical Simulation Research of Marine Methane Processes. Front. Earth Sci. 10:891393. doi: 10.3389/feart.2022.891393

Understanding the modern marine methane processes, which can profoundly affect global climate and have far-reaching impacts on human living environments, is critical for research on the global carbon cycle. Thus, modeling of marine methane processes has attracted increasing attention due to models can accurately simulate and predict the environmental effects of methane on marine and atmospheric ecosystems. In this study, we review the applications of modeling works to marine methane processes, including methanogenesis in sediments, transport and reaction of methane in sediments and seawater, and marine methane emissions to the atmosphere. Compiled a large database of global methanogenesis rates and methane fluxes to the sulfate-methane transition zone, we estimate that the global methanogenesis budget in marine sediments is ~0.87 $\mathrm{Tmol\,yr^{-1}}$ and global sedimentary dissolved inorganic carbon produced by anaerobic oxidation of methane is ~8.9 $\mathrm{Tmol\,yr^{-1}}$. In addition, although anaerobic oxidation of methane in sediments and aerobic oxidation of methane in seawater act as primary filters to prevent methane leakage from sediments to the hydrosphere as well as the atmosphere, large masses of methane in extreme seafloor environments (e.g., mud volcanic eruptions and hydrate leakage) can still escape microbial oxidation and leakage to seawater or the atmosphere. There is still a lack of models that simulate methane in these extreme marine environments. Therefore, more modeling works are needed to assess the efficiency of marine ecosystems, including sediments and hydrosphere, in filtering methane in the event of large-scale methane leakage from the seafloor. This study provides an interdisciplinary view of methane processes in marine systems and helps identify future directions in the modeling of methane processes in marine system.

Keywords: marine methane processes, model application, anaerobic oxidation of methane, aerobic oxidation of methane, carbon cycle

1 INTRODUCTION

Methane (CH_4), the most important greenhouse gas after carbon dioxide (CO_2), plays a key role in the Earth's carbon cycle over geological time and ongoing global warming (Solomon et al., 2009; Etminan et al., 2016; Allen et al., 2018; Nisbet et al., 2019; Akam et al., 2020). Oceans constitute the largest carbon reservoir on Earth and cover about 70% of the world's surface area. Approximately 1,000–5,000 Gt of methane is stored in marine sediments, mainly in the form of methane hydrates (Buffett and Archer, 2004; Burwicz et al., 2011). Even 1% of the methane seeping from sediment can increase the amount of methane in seawater and the atmosphere tenfold (Boetius and Wenzhöfer, 2013). Consequently, numerous modeling studies have been conducted to quantify methane processes in marine sediments and seawater. In this study, we review how models describe methane processes in marine systems, including sediments and seawater.

Compared with CO_2, methane has a relatively short mean lifetime (~9 years) and is very close to a steady state (Dlugokencky et al., 2011). The reduction of methane with hydroxyl radicals (OH^-) in the troposphere and stratosphere is a vital process of removing atmospheric methane (Dlugokencky et al., 2011). As a result, methane emissions are rapidly fed back into the global climate. The concentration and increased rate of methane in the atmosphere have reached their highest level since the preindustrial period (Saunois et al., 2016b). According to the mole fraction of methane in the geologic-atmospheric records, approximately 215 Tg year^{-1} of methane was emitted to the atmosphere in the preindustrial era (Lelieveld et al., 2002). Methane emissions are mainly classified as natural (e.g., those formed in wetlands, termites and oceans) and anthropogenic (e.g., those from rice agriculture, biomass burning, domestic sewage, and coal extraction), with the natural source accounting for most methane emissions. In particular, wetlands (e.g., swamps and tundra) are the largest methane emitting regions (~150 Tg year^{-1}) (Bousquet et al., 2006). Methane emissions from human activities are also not negligible. From the preindustrial era to the current period, anthropogenic methane emissions have increased significantly, reaching ~503–884 Tg year^{-1} (Bousquet et al., 2006; Dlugokencky et al., 2011; Saunois et al., 2016a). Coal extraction, crushing, and processing produce ~120 Tg year^{-1} of methane emissions (Bousquet et al., 2006). Rice agriculture and biomass burning also contribute ~30 and ~50 Tg year^{-1}, respectively (Bousquet et al., 2006). Moreover, human activities can affect natural emissions. For example, human exploitation of marine hydrates might destabilize the methane hydrates in sediments, resulting in substantial methane emissions.

Owing to global warming concerns and the necessity to extract the vast amounts of methane hydrate resources, marine methane processes are drawing growing interest. The scale of leakage from methane hydrate breakdown in marine sediments is large (~20 Tg year^{-1}) due to changes in numerous geological and environmental conditions (Dlugokencky et al., 2011; Ruppel and Kessler, 2017). The transport of methane-rich fluids released by methane hydrate destabilization involves numerous biochemical reactions and complex environmental geological changes that profoundly affect the entire marine ecosystem (Regnier et al., 2011). Thus, the research on marine methane processes is significant for the following reasons: 1) Study of the mechanisms of global warming. Although the total amount of methane released into the atmosphere from the oceans is limited compared to emissions from wetlands and other factors (Dlugokencky et al., 2011; Ruppel and Kessler, 2017), marine sediments are the largest methane reservoir on Earth, most of which is in the form of methane hydrates (Burwicz et al., 2011). Therefore, the stability of methane hydrate reservoirs and their impact on global warming are particularly interesting. 2) The demand for exploration and development of methane hydrate resources. In marine system, the migration of methane fluids is closely related to the accumulation of mineral resources, and is directly involved in the formation of minerals (Schulz and Zabel, 2006). For example, the cold seeping fluids on the seafloor are mainly composed of methane, and cold vents are paramount exploration proxies for methane hydrate resources, especially for shallow-surface hydrate resources. Therefore, the search for cold vents formed by methane hydrate decomposition leakage fluids should be identified for exploring shallow-surface hydrate resources. Further, environmental considerations for the later development of hydrate resources include observation and study of leakage mechanism (Schulz and Zabel, 2006). 3) Research on critical scientific questions in the life and Earth sciences. The transport and reaction of fluids from methane hydrate decomposition involving essential biochemical reactions are a key link in the study of carbon cycle (Ruppel and Kessler, 2017). Moreover, a series of chemical interactions based on methane as the energy base is a prerequisite of life on many celestial bodies, including planets and moons, and a relevant direction for astrobiological research (Miller and Smythe, 1970; Jakosky et al., 1995; Pavlov et al., 2003). Therefore, marine methane processes should be observed and studied to better understand critical scientific questions about the oceanic evolution in geological history and the origin and evolution of life, including those on other planets. In addition, marine methane processes are interesting research issues at the intersection of Earth system sciences and life sciences.

Due to differences in the Gibbs free energy of electron acceptors, the methanogenesis process related to organic matter (OM) degradation occurs in deep sediments with anaerobic environments. The produced methane is transported to upper sediment by molecular diffusion and advection (Schulz and Zabel, 2006; Dale et al., 2008c). Although most seawater is oxygenated (Repeta et al., 2016), the methanogenesis process can occur in the microbial digestive tract and release fresh fecal particles into the ocean. In seawater, methane is mainly produced in the mixed layer, where methane concentration can reach ~5 nM (Bastviken et al., 2004) and the maximum methane concentration leads to the "marine methane paradox" (Lenhart et al., 2015). Owing to the difference in methane chemical potential between the atmosphere and seawater (the net particle flux always flows from the higher chemical energy state system to the lower chemical energy state system), methane in supersaturated surface seawater can leak into the atmosphere

(Holmes et al., 2000; Mrazovac et al., 2012). Modeling works are essential for studying the marine methane processes. 1) Modeling can overcome the spatial and temporal limitations of laboratory conditions. 2) Modeling can quantitatively analyze the variation of methane fluxes during each process. 3) Modeling can reasonably verify the accuracy of experimental data (Boudreau, 1997). In addition, the combination of model and measured data provides a more accurate quantification of methane production and consumption in each marine process. Considerable work has been done by scholars to simulate the abovementioned marine methane processes. Reaction-transport model (RTM) is commonly used to simulate the transport of methane in sediments coupled with methanogenesis and anaerobic oxidation of methane (AOM). The transport of methane-rich fluids in seawater involves the effects of ocean currents, water pressure, and temperature, so more complex mathematical models have been constructed to simulate it (Yamazaki et al., 2006).

In this review, we summarize the modeling research on marine methane processes, including methanogenesis and transport and reaction of methane in sediments, the flux of methane leakage at the sediment-seawater interface (SWI), methane processes in seawater, and methane flux from seawater to the atmosphere.

2 METHANE PROCESSES IN SEDIMENTS

The main processes involved with methane in sediments are methanogenesis, methane phase transition, and methane transport-reaction. In this section, we review the application of models to these processes and the key factors influencing these methane processes.

2.1 Methanogenesis in Deep Sediment

Deep anaerobic marine sediments are the world's largest reservoir of methane (~4.55 × 10^5 Tg C), with 90% of the produced methane stored in the continental margins, which are approximately four to eight times larger than the terrestrial surface biosphere and soils (Reeburgh, 2007; Wadham et al., 2012; Chen et al., 2017). Methanogenesis is the major source of methane in sediments and occurs when porewater sulfate (SO_4^{2-}) is depleted (Jørgensen and Kasten, 2006). There are two main methanogenesis processes (Megonigal et al., 2004; Fenchel et al., 2012; Burdige and Komada, 2015) the autotrophic pathway (using carbon dioxide reduction), and the acetoclastic pathway (using acetate). The latter process usually occurs in fresh inland rivers (Blair, 1998; Conrad, 2005). According to carbon isotopic data combined with model simulations, the main methanogenesis process in marine sediments is carbon dioxide reduction (autotrophic pathway) (Burdige et al., 2016), which is expressed as follows:

$$2CH_2O \xrightarrow{+2H_2O} 2CO_2 + 4H_2 \xrightarrow{-2H_2O} CO_2 + CH_4 \quad (1)$$

The reduction of carbon dioxide can be divided into two steps. First, OM is sequentially broken down into smaller molecules, followed by fermentation, which produces hydrogen gas (H_2). Then, the produced H_2 acts as a driving force for methanogenesis via carbon dioxide reduction (Whiticar, 1999). Modeling has been applied to methanogenesis that relies mainly on OM degradation, which is directly or indirectly involved in almost all biochemical reactions in marine sediments (Arndt et al., 2013). Hence, there are two important factors in methanogenesis modeling: 1) OM degradation rate and 2) switching of OM degradation from sulfate reduction to methanogenesis. Three types of models are commonly used to describe OM degradation (Arndt et al., 2013). 1) Discrete model (*G*-model). This type of model divides OM into a finite number of reactivity fractions, each of which is degraded according to its single degradation constants (Jørgensen, 1978). 2) Reactive continuum model (RCM). This type of model describes OM degradation by assuming a continuous distribution of OM reactivity at the SWI. A commonly used RCM is based on the Gamma distribution function (γ-RCM) (Boudreau and Ruddick, 1991). 3) Power model. This model is an empirical model based on a large dataset of global sedimentary OM data (Middelburg, 1989). According to the OM degradation model, the OM degradation rate can be expressed as follows:

$$R_{OM}(t) = \frac{dG_{OM}(t)}{dt} \quad (2)$$

where R_{OM} denotes the OM degradation rate, t denotes time, and $G_{OM}(t)$ denotes OM content at time t. The sulfate concentration in porewater is an important indicator of the methanogenesis, as it occurs at a lower sulfate concentration (Burdige et al., 2016). A threshold value for a given sulfate concentration (~0.5 mM) is typically used to describe the change in OM degradation switched from sulfate reduction to methanogenesis (Boudreau, 1996; Arndt et al., 2009; Chuang et al., 2019; Dale et al., 2019). The methanogenesis rate (R_{ME}) is expressed as follows:

$$R_{Me} = \frac{1}{2} \cdot f\left(SO_4^{2-}\right) \cdot R_{OM} \quad (3)$$

where 1/2 denotes the ratio between OM consumed and methane produced (**Eq. 1**), and $f(SO_4^{2-})$ is a function representing to the threshold of sulfate concentration, which is expressed as (Boudreau, 1996; Chuang et al., 2019):

$$f\left(SO_4^{2-}\right) = 1 - \frac{\left[SO_4^{2-}\right]}{\left[SO_4^{2-}\right] + K_S} \quad (4)$$

or by the complementary error function (Martens et al., 1998; Dale et al., 2019):

$$f\left(SO_4^{2-}\right) = 0.5 \cdot \mathrm{erfc}\left(\frac{\left[SO_4^{2-}\right] - K_S}{k_{in}}\right) \quad (5)$$

where $[SO_4^{2-}]$ denotes the sulfate concentration, Ks represents the threshold of the sulfate concentration, and k_{in} in **Eq. 5** is a parameter controlling the steepness of $f(SO_4^{2-})$. Typically, sulfate concentration decreases with depth. Hence, **Eq. 4** is a monotonically increasing function with depth. However, the OM degradation rate **Eq. 2** is a monotonically decreasing function with depth. As a result, substituting **Eq. 4** into **Eq. 3** cannot strictly guarantee that the methanogenesis rate **Eq. 3** decreases monotonically with depth, especially in the surface sediments where the change in OM degradation rate is extremely high (Middelburg, 1989). Compared with **Eqs 4**, **5** can solve this problem, as the complementary error function is equal to either 1 or 0 ($f(SO_4^{2-}) = 1$, if $[SO_4^{2-}] < Ks$ or $f(SO_4^{2-}) = 0$, if $[SO_4^{2-}] > Ks$).

From the expression of the methanogenesis rate (**Eqs 2**, **3**), the intensity of methanogenesis in sediments is directly related to the OM degradation rate. Hence, factors affecting OM degradation also influence methanogenesis processes. The content of OM and its reactivity are the main factors that affect OM degradation (Arndt et al., 2013). The higher the OM content at the SWI, the higher is the OM content that can reach in the deep sediments and the higher the methanogenesis rate (Burwicz et al., 2011). Interestingly, the higher the OM reactivity, the lower the methanogenesis rate for the same OM content at the SWI. This is because under higher OM reactivity, more active OM is consumed in the upper sediment, and less OM is transferred to the deep sediment for methanogenesis (Meister et al., 2013). The sedimentation rate is also a paramount factor affecting OM degradation and further methanogenesis (Buffett and Archer, 2004; Burwicz et al., 2011). The sedimentation rate is a critical proxy of depositional environments, as its quantity in shelf regions (~0.05 cm year^{-1}) is usually greater than that in deep sea regions (<0.001 cm year^{-1}) (Tromp et al., 1995; Burwicz et al., 2011). In addition, a higher sedimentation rate is generally coupled with higher OM fluxes and faster burial processes, promoting methanogenesis (Seiter et al., 2004; Meister et al., 2013).

The above shows the main factors affecting methanogenesis in sediments. We collected methanogenesis data from 48 sites around the global ocean and calculated the total methanogenesis rate in sediments by depth integration. We found that the sedimentation rate (*w*) and depth of sulfate-methane transition zone (SMTZ) have a well linear regression result with the depth-integrated methanogenesis rate, where methanogenesis is positively correlated with the sedimentation rate ($R^2 = 0.71$) and negatively correlated with SMTZ depth ($R^2 = 0.79$) (**Table 1** and **Figure 1**). The positive relationship between depth-integrated methanogenesis rate and OM reactivity is weak ($R^2 = 0.53$). The distribution of OM reactivity in global marine sediments is complex, and no model can constrain global OM reactivity well (Arndt et al., 2013). For example, shelf regions are generally considered to have high OM reactivity due to high OM flux from inland and marine biosphere, but there is also a large amount of terrestrial refractory OM (LaRowe et al., 2020). Given the deeper water depth, OM fluxes and OM reactivity are generally lower in abyssal regions. However, high OM reactivity was found in the eastern costal of equatorial Pacific regions. The main reasons are warmer water temperature, which enhances net primary production in surface seawater, and lower water column oxygen concentration, which inhibits OM degradation in seawater and promotes more active OM that can reach sediments (Arndt et al., 2013). Based on the empirical formula we obtained (**Figure 1**) and the mean depth of SMTZ in different regions (Egger et al., 2018), we estimated that approximately 0.87 Tmol year^{-1} methane is produced in global deep marine sediments and 78% in shelf regions (water depth <200 m) (**Table 3**).

2.2 Methane Phase Transition in Sediments

Methane produced in bottom sediments has three phase states: gaseous, liquid (dissolved in porewater), and solid (methane hydrates) (Jørgensen and Kasten, 2006). The phase of methane in sediments varies with environmental factors, typically the ambient temperature, pressure, and salinity (Buffett and Archer, 2004; Regnier et al., 2011). The saturation concentration of methane ($C_{\mathrm{Sa\_Me}}$) in porewater has been extensively studied and can be expressed by a polynomial in temperature, pressure and salinity (**Eq. 6**) (Duan and Weare, 1992).

$$\begin{aligned} C_{Sa\_Me} = {} & 1.437 \times 10^{-7}STP - 4.412 \times 10^{-5}TP - 4.6842 \times 10^{-5}SP \\ & + 4.129 \times 10^{-9}ST + 1.43465 \times 10^{-2}P \\ & - 1.6027 \times 10^{-6}T - 1.2676 \times 10^{-6}S - 4.9581 \times 10^{-4} \end{aligned} \tag{6}$$

where *S*, *T* and *p* denote ambient salinity (–), temperaure (K), and pressure (atm), respectively. This empirical formula is applied to *S* of 1–35, *T* of 273.15–290.15 K, and *p* of 1–30 atm. If the concentration of dissolved methane in porewater is greater than the methane saturation and the ambient pressure and temperature conforms to the conditions for hydrate formation, methane hydrate will form in the sediment. The zone in the sediment where hydrate stability can be preserved is called the gas hydrate stability zone (GHSZ) (Kvenvolden, 1993). The GHSZ depth is mainly determined by the ambient temperature and pressure. The methane phase transitions from liquid + hydrate to liquid + gas below the GHSZ as geothermal temperature increases with depth.

The saturation of free methane in porewater is a key parameter for assessing the state of methane in sediments (Burwicz et al., 2011; Tishchenko et al., 2005). The transition of the methane phase in the GHSZ involves four main processes: methane hydrate formation (gaseous → solid, **Eq. 7**), methane hydrate dissolution (solid → gaseous, **Eq. 8**), free methane gas formation (dissolved → gaseous, **Eq. 9**), and free methane gas dissolution (gaseous → dissolved, **Eq. 10**). The simplest formulation for the above transition is based on a linear dependence (Wallmann et al., 2006a; Burwicz et al., 2011; Regnier et al., 2011), expressed as follows:

$$R_{GH} = k_{GH} \cdot \left(\frac{[CH_4]}{C_S^{diss}} - 1\right),\ if\ [CH_4] \geq C_S^{diss} \tag{7}$$

$$R_{DGH} = k_{DGH} \cdot \left(1 - \frac{[CH_4]}{C_S^{diss}}\right),\ if\ [CH_4] < C_S^{diss} \tag{8}$$

$$R_{FG} = k_{FG} \cdot \left(\frac{[CH_4]}{C_S^{free}} - 1\right),\ if\ [CH_4] \geq C_S^{free} \tag{9}$$

$$R_{DFG} = k_{DFG} \cdot \left(1 - \frac{[CH_4]}{C_S^{free}}\right),\ if\ [CH_4] < C_S^{free} \tag{10}$$

TABLE 1 | Summary of methanogenesis model studies. The table reports data on sedimentation rate (*w*), the depth of SMTZ, OM content at the SWI (G_{OM}), OM apparent reactivity (<*k*>) and depth-integrated methanogenesis rate (R_{ME}) at each site.

Site	Location	Model	w(m yr^{-1})	SMTZ(Mbsf)	G_{OM}(wt%)	<k>(yr^{-1})	R_{ME}(mol m^{-2} yr^{-1})	Preference
summer	Cape	1-G	0.103	0.05	0.71	1	14.6	Martens et al. (1998)
winter	Cape	1-G	0.103	0.14	0.12	0.6	1.45	Martens et al. (1998)
Eckernfoerde	Kiel Bight	1-G	0.006	0.337	0.42	0.019	0.39	Albert et al. (1998)
Eckernfoerde	Kiel Bight	1-G	0.006	0.319	0.42	0.018	0.44	Albert et al. (1998)
Eckernfoerde	Kiel Bight	1-G	0.006	0.324	0.42	0.017	0.45	Albert et al. (1998)
Eckernfoerde	Kiel Bight	1-G	0.006	0.326	0.42	0.015	0.5	Albert et al. (1998)
Eckernfoerde	Kiel Bight	1-G	0.006	0.319	0.42	0.018	0.436	Albert et al. (1998)
Eckernfoerde	Kiel Bight	1-G	0.006	0.307	0.44	0.018	0.471	Albert et al. (1998)
Eckernfoerde	Kiel Bight	1-G	0.006	0.298	0.46	0.018	0.506	Albert et al. (1998)
Eckernfoerde	Kiel Bight	1-G	0.006	0.3	0.18	0.01	0.201	Mogollón et al. (2009)
Opouawe	Opouawe	1-G	0.0016	0.09	1.2	0.0025	0.132	Dale et al. (2010)
M5	Aarhus Bay	1-G	0.002	0.6	1	0.017	0.246	Dale et al. (2008c)
M1	Aarhus Bay	2-G	0.0002	2.1	0.8	0.208	0.001	Dale et al. (2008c)
S3	Canadian	2-G	0.0001	0.08	3.35	0.03	0.0257	Boudreau et al. (1998)
S4	Canadian	2-G	0.0001	0.07	2.3	0.739	0.075	Boudreau et al. (1998)
S5	Canadian	2-G	0.0001	0.1	5	1.5	0.053	Boudreau et al. (1998)
ODP site 1,040	Costa Rica	2-G	0.0001	30	1.2	0.0000002	0.0069	Hensen and Wallmann, (2005)
SL17	Hydrate Ridge	2-G	0.00025	0.06	2.9	0.0275	0.011	Luff et al. (2004)
SO178 3–4 KAL	Okhotsk	2-G	0.0001	500	0.8	0.00001	0.00025	Wallmann et al. (2006a)
LV28 2–4 SL	Okhotsk	2-G	0.0001	400	1.5	0.0001	0.00076	Wallmann et al. (2006a)
SO178 10–6	Okhotsk	2-G	0.00013	10	2	0.0002	0.0025	Wallmann et al. (2006a)
SO178 13–6	Okhotsk	2-G	0.00093	3	2	0.0002	0.0404	Wallmann et al. (2006a)
SO178 29–2	Okhotsk	2-G	0.00115	4	1.8	0.0003	0.0267	Wallmann et al. (2006a)
LV28 20–2	Okhotsk	2-G	0.0009	3	1.8	0.000206	0.013	Wallmann et al. (2006a)
ODP 997	Blake Ridge	2-G	0.00022	22	1	0.000001	0.0108	Wallmann et al. (2006a)
M48-2	Namibian	3-G	0.0034	1.3	1.5	1.08	0.0396	Dale et al. (2009)
ODP 995	Blake Ridge	Power	0.0004	22	2	0.000016	0.0005	Marquardt et al. (2010)
1,041	Costa Rica	Power	0.000131	20	3.5	0.0000043	0.0008	Marquardt et al. (2010)
1,230	Peru	Power	0.001	5	3.1	0.00102	0.0247	Marquardt et al. (2010)
685	Peru	Power	0.000147	8	3	0.0001	0.0164	Marquardt et al. (2010)
1,233	Chile	Power	0.0011	9.2	2.1	0.00042	0.0101	Marquardt et al. (2010)
1,014	California	Power	0.00079	10	5	0.00032	0.00893	Marquardt et al. (2010)
1,084	Namibia	Power	0.00024	2	8	0.0728	0.0563	Marquardt et al. (2010)
1,258	Demerara	RCM	0.000015	400	0.2	0.000002	0.00000281	Arndt et al. (2009)
A3	Arkona Bassin	RCM	0.00074	1.1	4	0.027	0.0431	Mogollón et al. (2011)
A5	Arkona	RCM	0.0022	0.4	6	0.027	0.431	Mogollón et al. (2011)
A7	Arkona	RCM	0.0019	0.6	4.5	0.027	0.152	Mogollón et al. (2011)
U1341	Beringsea	RCM	0.0005	450	1.5	0.0101	0.0000084	Wehrmann et al. (2013)
Pockmark	Eckernf'orde Bay	1-G	0.005	0.2	1.2	0.003	1	Mogollón et al. (2011)
Pockmark	Eckernf'orde Bay	1-G	0.005	0.4	1.2	0.003	0.33	Mogollón et al. (2011)
A-1	Cape	^{14}C	—	—	—	—	17.52	Crill and Martens, (1987)
St B	Eckernf'orde Bay	^{14}C	—	—	—	—	1.28	Treude et al. (2003)
WK	Kiel	^{14}C	—	—	—	—	0.72	Schmaljohann, (1996)
BL	Kiel Harbour	^{14}C	—	—	—	—	0.63	Schmaljohann, (1996)
NS	Skagerrak	^{14}C	—	—	—	—	0.62	Parkes et al. (2007)
S10	Skagerrak	^{14}C	—	—	—	—	0.59	Knab et al. (2008)
S11	Skagerrak	^{14}C	—	—	—	—	0.48	Knab et al. (2008)
A-1	Cape Lookout Bight	^{14}C	—	—	—	—	0.18	Crill and Martens, (1987)

where [CH_4] denotes the methane concentration, $C_S{}^{diss}$ denotes the solubility of dissolved methane, $C_S{}^{free}$ denotes the solubility of gaseous methane, and k_{GH}, k_{DGH}, k_{FG}, and k_{DFG} denote the kinetic constants of gas hydrate formation, free methane gas formation, gas hydrate dissolution, and free methane gas dissolution, respectively.

The thickness of the GHSZ is an essential parameter for assessing hydrate resources (Burwicz et al., 2011). In addition, a sufficient methane source (e.g., deeper hydrate reservoirs and methanogenesis (Burdige et al., 2016)), low temperature, and high pressure are keys to methane hydrate reservoir formation. The minimum content of surface OM content for methane hydrate formation is ~1 wt% (Buffett and Archer, 2004). It is difficult to form methane hydrates in regions within water depth of 600 m because of the high ambient temperature in sediments (Buffett and Archer, 2004), and methane hydrates are commonly found within water depth of 1,000–3,000 m with a bottom water temperature of ~2°C (Kvenvolden, 1993). Methane hydrate formation regions can be divided into passive and active

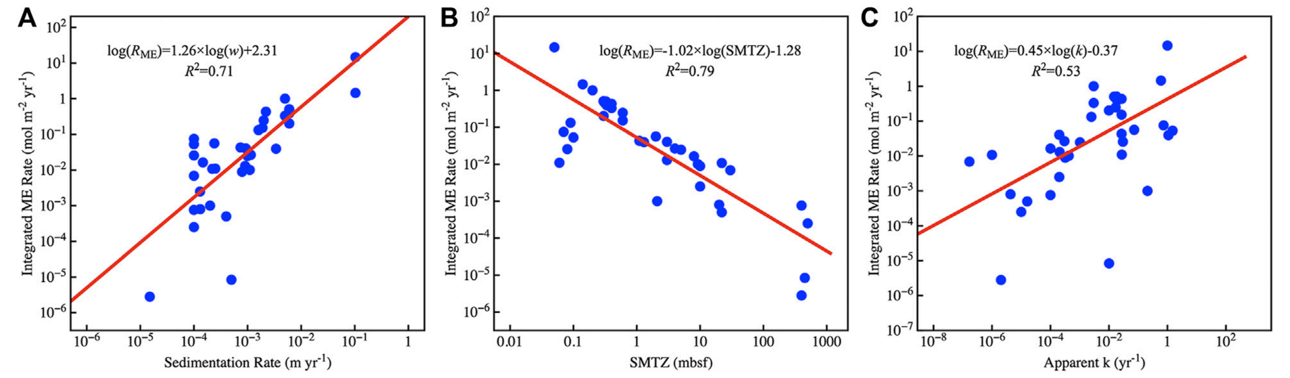

FIGURE 1 | Global empirical relationships. **(A)**. Log–log plots of sedimentation rate and depth-integrated methanogenesis rate. **(B)**. Log–log plots of SMTZ depth and depth-integrated methanogenesis rate. **(C)**. Log–log plots of OM apparent reactivity and depth-integrated methanogenesis rate.

margins (Dale et al., 2008c). Active regions have sufficient overlying methane-rich fluids (methane from deeper hydrate reservoirs), and the abundance of methane hydrates within the GHSZ reaches 30%–50%. By contrast, diffusion dominates the transport of methane in passive margins and hydrate abundances in these regions are smaller (Dale et al., 2008c). The amount of methane stored in marine sediments is within 500–57,000 Gt C (Dickens, 2001; Buffett and Archer, 2004; Milkov, 2004; Klauda and Sandler, 2005; Archer et al., 2009; Burwicz et al., 2011; Pinero et al., 2013; Kretschmer et al., 2015). Buffett and Archer. (2004) first estimated methane hydrate reservoirs in global ocean sediments using the 2-*G* OM degradation model coupled with sulfate reduction, methanogenesis and AOM. They found that the rain rate of particulate OM is key in the global inventory of methane hydrate reservoirs (Archer et al., 2002). In addition, they estimated a total methane hydrate inventory of 3,000 Gt C, but it decreased to 600 Gt C when the methane in the overlying fluid was disregarded (Buffett and Archer, 2004). Klauda and Sandler, (2005) slightly modified Buffett's model and obtained a global methane hydrate inventory of ~57,000 Gt C (Klauda and Sandler, 2005), which was almost two orders of magnitude higher than that of Buffett and Archer. (2004). The main reason for the large error was that the OM degradation model was a 1-*G* model that the entire particulate organic carbon (POC) pool was assumed to be one group with a single degradation rate constant (4.7×10^{-7} year^{-1}). Moreover, biogeochemical reactions associated with the consumption of methane in porewater were ignored (e.g., sulfate reduction and AOM). OM reactivity decreased with sediment depth, whereas this feature cannot be reflected by the *G* model (Middelburg, 1989; Arndt et al., 2013). Burwicz et al. (2011) estimated the global methane hydrate inventory in the range of 4.18–995 Gt C, where the first value refers to present-day conditions (using the relatively low Holocene sedimentation rate) and the second value corresponds to a higher Quaternary sedimentation rate. An RCM (γ-RCM) was used to describe OM degradation in sediments coupled with sulfate reduction and AOM. In addition, an improved power model was used to simulate the OM degradation rate (R_{OM}) (**Eq. 11**) (Wallmann et al., 2006a; Wallmann et al., 2012; Kretschmer et al., 2015).

$$R_{OM}(t) = \frac{K_C}{[DIC] + [CH_4] + K_C} \cdot k_x \cdot G_{OM}(t) \tag{11}$$

where [DIC] and [CH_4] denote the concentration of ambit dissolved inorganic carbon (DIC) and methane, respectively, K_c denotes the Monod inhibition constant (mM), k_x denotes the age-dependent kinetic constant (year^{-1}), and $G_{OM}(t)$ denotes the OM content. These simulations found that the main factors affecting hydrate storage in the GHSZ were the ambient temperature, oxygen content, sedimentation rate, and upward fluid especially in the active margins (Buffett and Archer, 2004; Burwicz et al., 2011). In particular, ambient temperature is a vital factor influencing the stability of methane hydrate reservoirs, as global methane storage may be reduced by 85% if sedimentary temperature increases by even 3°C (Buffett and Archer, 2004).

According to the global exploration of methane hydrate reservoirs, many sites with hydrates have been discovered globally. **Figure 2** shows the main regions in the world where methane hydrates have been found, such as the Gulf of Mexico (Davidson et al., 1986), Caribbean Sea (Reed et al., 1990), the eastern margin of South America (Jahren et al., 2001), western margin of Africa (Ben-Avraham et al., 2002), Bering Sea (Scholl and Hart, 1993), Sea of Okhotsk (Shoji et al., 2005), Okinawa Trough (Sakai et al., 1990), Sea of Japan (Yun et al., 2011), Shikoku Trough (Saito and Suzuki, 2007), South China Sea (Li et al., 2018), eastern Pacific Ocean (Inagaki et al., 2006), California Coast (Dickens and Quinby-Hunt, 1994), Peruvian margin (Kvenvolden and Kastner, 1990), the Gulf of Oman (White, 1979), Ross Sea and Weddell Sea in the Antarctic (Stoll and Bains, 2003; Giustiniani et al., 2018), and Barents Sea (Andreassen et al., 1990). In addition, the methanogenesis

TABLE 2 | Summary of AOM rate studies. The table reports data on the depth of SMTZ, methane flux into SMTZ (J_{CH}) and depth integrated AOM rate (R_{AOM}) at each site. The check marks indicate the presence of methane hydrates in the bottom sediments.

Site	Location	Water depth(m)	SMTZ(mbsf)	J_{CH}(mol m^{-2} yr^{-1})	R_{AOM}(mol m^{-2} y^{-1})	Hydrates	References
MIC-3	Black Sea	2070	0.02	2.7521	17.2	✓	Wallmann et al. (2006c)
Hydrate Ridge	Cascadia Subduction	775	0.035	5.0808	10.92	✓	Luff et al. (2004)
Hydrate Ridge	Cascadia Subduction	790	0.019	3.69745	10.75	✓	Luff et al. (2005)
MIC-4	Black Sea	2085	0.025	3.4018	10.2	✓	Wallmann et al. (2006c)
Hydrate Ridge	Cascadia Subduction	790	0.025	5.59545	9.25	✓	Luff and Wallmann, (2003)
Hydrate Ridge	Cascadia Subduction	790	0.02	2.8762	9.1	✓	Zeebe, (2007)
MIC-5	Black Sea	2089	0.03	3.27405	6.6	✓	Wallmann et al. (2006c)
Hydrate Ridge	Cascadia Subduction	775	0.05	2.7229	6.09	✓	Luff et al. (2004)
Anaximander	Eastern Mediteranean	1720	0.14	0.04015	6	✓	Haese et al. (2003)
America Trench	Costa Rica Forearc	1,000	0.035	1.59505	5.88	✓	Linke et al. (2005)
Beggiatoa 2	Cascadia Subduction	777	0.05	2.09145	5.62	✓	Treude et al. (2003)
BIGO 4	Cascadia Subduction	778	0.03	3.6938	5.51	✓	Sommer et al. (2006a)
Beggiatoa 1	Cascadia Subduction	777	0.03	3.7157	4.85	✓	Treude et al. (2003)
Hydrate Ridge	Cascadia Subduction	790	0.05	2.77765	4.5	×	Luff et al. (2005)
America Trench	Costa Rica Forearc	1,020	1.4	0.13505	3.5	✓	Schmidt et al. (2005)
Pockmark	Kiel Bight	26	0.05	1.4089	3	×	Albert et al. (1998)
Anaximanders	Eastern Mediteranean		0.25	0.2117	3	✓	Aloisi et al. (2004)
Saanich Inlet	West Coast America	225	0.25	0.22265	2.46	×	Murray et al. (1978)
Hikurangi Margin	New Zealand	700	0.05	3.4748	2.2	✓	Dale et al. (2010)
Saanich Inlet	West Coast America	225	0.12	0.1168	1.4	×	Devol et al. (1984)
Hydrate Ridge	Cascadia Subduction	777	0.125	0.29565	1.31	✓	Sommer et al. (2006a)
Pockmark	Kiel Bight	25	0.09	0.4599	1.1	×	Mogollón et al. (2011)
Saanich Inlet	West Coast America	225	0.18	0.2701	0.955	×	Devol et al. (1984)
Congo Fan	Zaire Shelf	4,000	15.5	0.03285	0.8	×	Zabel and Schulz, (2001)
Eckernfoerde Bay	Kiel Bight	26	0.3	0.2628	0.5	×	Albert et al. (1998)
Green Canyon	Gulf of Mexico	647	3	0.02044	0.5	✓	Ussler and Paull, (2008)
Eckernfoerde Bay	Kiel Bight	26	0.3	0.44165	0.426	×	Martens et al. (1998)
Aarhus Bay (M5)	Baltic Sea	15	0.6	0.0584	0.41	×	Dale et al. (2008b)
Eckernfoerde Bay	Kiel Bight	25	0.29	0.15695	0.39	×	Mogollón et al. (2011)
Eckernfoerde Bay	Kiel Bight	25	0.35	0.09125	0.28	×	Mogollón et al. (2009)
Benguela Coastal	Namibian Shelf	110	1.1	0.03869	0.22	×	Dale et al. (2009)
Cariaco Basin	Venezuelan	40	0.5	0.087965	0.142	×	Reeburgh, (1976)
Amazon Fan	Brazilian Shelf	40	0.7	0.04015	0.1	×	Blair and Aller, (1995)
S10	Norwegian Trench	86	1.3	0.0949	0.09	×	Dale et al. (2008b)
M1	Baltic Sea	27	2.1	0.0657	0.088	×	Dale et al. (2008a)
3,703	Namibian Shelf	1,373	3.5	0.09198	0.08	×	Fossing et al. (2000)
SO178 13–6 KL	Sea of Okhotsk	713	2.7	0.0365	0.0785	✓	Wallmann et al. (2006a)
Site 1,040	Costa Rica Forearc	4,312	3.5	0.0584	0.074	×	Haeckel, (2006)
Aarhus Bay	Baltic Sea	16	1.85	0.00803	0.0621	✓	Thomsen et al. (2001)
SO178 29–2 KL	Sea of Okhotsk	771	3.8	0.025915	0.059	×	Wallmann et al. (2006a)
Amazon Fan	Brazilian Shelf	3,510	4	0.01971	0.055	×	Adler et al. (2000)
3,714	Namibian Shelf	2065	5.8	0.05475	0.055	✓	Fossing et al. (2000)
Sakhalin Island	Sea of Okhotsk	1700	2.5	0.0657	0.049	✓	Aloisi et al. (2004)
LV28 20–2 SL	Sea of Okhotsk	685	2.85	0.004818	0.0454	✓	Wallmann et al. (2006a)
st 4	Black Sea	130	1.8	0.0201,115	0.041	×	Jørgensen et al. (2004)
st 5	Black Sea	181	2.1	0.0190,165	0.035	×	Jørgensen et al. (2004)
S13	Norwegian Trench	361	1	0.1898	0.033	×	Dale et al. (2008b)
Benguela Current	West African Margin	400–2,200	50	0.00073	0.03	×	Sivan et al. (2007)
st 6	Black Sea	396	2.5	0.0217,175	0.03	×	Jørgensen et al. (2004)
st 7	Black Sea	1,176	3.5	0.008103	0.018	×	Jørgensen et al. (2004)
SO178 10–6 SL	Sea of Okhotsk	613	9.8	0.0174,105	0.016	✓	Wallmann et al. (2006a)
ODP997	South-Eastern US	2,770	22	0.0045625	0.0105	✓	Borowski et al. (2000)
Blake Ridge	South-Eastern US	2000–3,000	21	0.00219	0.004	✓	Maher et al. (2006)
ODP leg162 site984A	North Atlantic	1,650	125	0.0000365	0.0031	×	Maher et al. (2006)
LV28 2–4 SL	Sea of Okhotsk	1,265		0.00007665	0.000467	✓	Wallmann et al. (2006a)
SO178 3–4 KAL	Sea of Okhotsk	1,602		0.0000511	0.000205	✓	Wallmann et al. (2006a)
site 1,258	Equatorial Atlantic	2,450–3,200	160–400	0.0002774	0.00003	×	Arndt et al. (2009)
site 1,257	Equatorial Atlantic	3,200	150–400	0.0003869	0.00005	×	Arndt et al. (2006)

model and methane phase transition models were employed to predict the global distribution of methane hydrate reservoirs (Burwicz et al., 2011; Kretschmer et al., 2015). Both exploration and modeling works reveal that methane hydrate reservoirs occur in shallow marine sediments, mainly distributed along the coastal regions of continents (**Figure 2**).

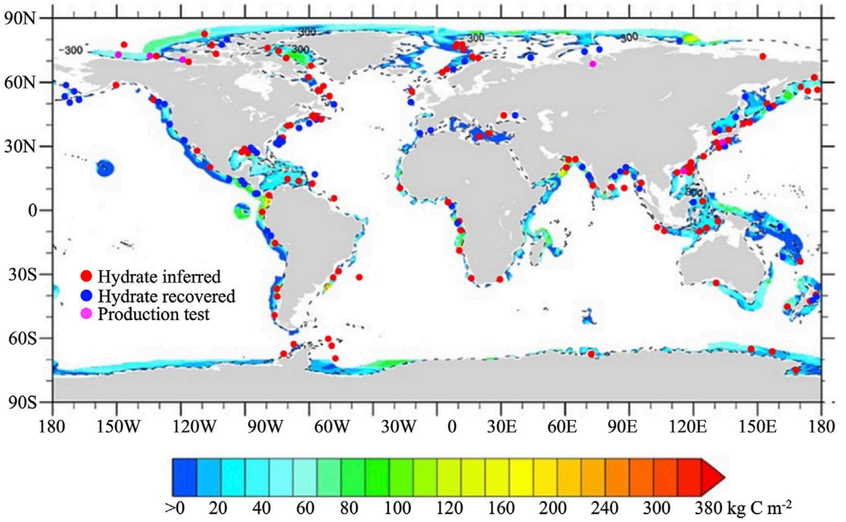

FIGURE 2 | Global distribution of inferred sites, drilling/sampling sites and real production tests for methane hydrate. The underlying map shows global distribution of methane hydrates in marine sediments estimated by model (Kretschmer et al., 2015).

2.3 Transport-Reaction of Methane in Marine Sediments

The methane transported in marine sediments can be divided into dissolved methane (in porewater) and bubbling methane (Regnier et al., 2011). The latter is generated when methane hydrates in the deeper layers break down or when methanogenesis rates are extremely high (Martens and Klump, 1980). Methane transport in the sediment is described by RTM (Meister et al., 2013; Berner, 2020), as follows:

$$\varphi \cdot \frac{\partial [CH_4](x,t)}{\partial t} = \frac{\partial\left(\varphi \cdot \frac{D_m}{\tau^2} \cdot \frac{\partial [CH_4](x,t)}{\partial x}\right)}{\partial x} - \frac{\partial\left(\varphi \cdot w \cdot [CH_4](x,t)\right)}{\partial x} + v \cdot \lambda \cdot \frac{\partial\left([CH_4](x,t) - C_{Sa\_Me}\right)}{\partial x} + \varphi \cdot \sum R(x,t) \qquad (12)$$

where x denotes the depth below the seafloor, t denotes time, φ denotes porosity, D_m denotes the molecular diffusion coefficient of methane, τ denotes tortuosity calculated as $\tau^2 = 1 - \ln(\varphi^2)$ (Boudreau, 1997), w denotes the burial velocity, $[CH_4]$ denotes the methane concentration, and R denotes methane related biogeochemical reactions. The methane-rich upward fluid is expressed by the third term on the right side of **Eq. 11**, v denotes the upward fluid velocity, and C_{Sa_Me} denotes the saturation concentration of methane (**Eq. 6**). The parameter $\lambda = 1$, if $[CH_4] > C_{Sa\_Me}$ and $\lambda = 0$, if $[CH_4] < C_{Sa\_Me}$. Methane transport distinctly differs under passive and active conditions. Under passive conditions, the diffusion process dominates the transport of methane on a long-time scale, and methane cannot reach the SWI. By contrast, the advection process under active conditions rapidly pushes the methane from the deeper to the upper sediments within a short time scale (~12 years), and methane can reach the seawater (Dale et al., 2008c).

The most common reaction involved in methane transport is the AOM (**Eq. 13**), which consumes 90% of the methane in the overlying fluids and is thus the biggest methane sink (Reeburgh, 2007).

$$CH_4 + SO_4^{2-} \rightarrow HCO_3^- + HS^- + H_2O \qquad (13)$$

From **Eq. 13**, the AOM rate is related to the concentration of methane and sulfate. The simplest model describing the AOM rate is follows (Regnier et al., 2011; Van Cappellen and Gaillard, 1996):

$$R_{AOM} = k_{AOM} \cdot [CH_4] \cdot \left[SO_4^{2-}\right] \qquad (14)$$

where k_{AOM} denotes the first-order rate constant for the AOM, $[CH_4]$ denotes the methane concentrations, and $[SO_4{}^{2-}]$ denotes the sulfate concentrations. This model can be easily used to fit measured data and describe the distributions of AOM rates as well as the location and thicknesses of the SMTZs in sediments. In addition, various factors can affect the AOM rate that cannot be reflected by **Eq. 14**, such as temperature, substrate concentration, enzyme reactivity, and bioenergy (Regnier et al., 2005; Dale et al., 2006; Regnier et al., 2011). The concentrations of microorganisms and enzymes involved in the AOM are related to substrate concentration. Specifically, they are limited at low substrate concentrations. In light of this, the AOM rate can be expressed as follows (Regnier et al., 2005):

$$R_{AOM} = v_{max} \cdot \frac{[CH_4]}{[CH_4] + K_m} \cdot \frac{\left[SO_4^{2-}\right]}{\left[SO_4^{2-}\right] + K_s} \qquad (15)$$

where v_{max} denotes the maximum AOM rate, and K_m and K_s represent the half-saturation constants of methane and sulfate, respectively. Furthermore, the minimum energy supply that can facilitate the AOM is ~11 kJ mol^{-1} (Dale et al., 2006), whereas bioenergy available within the SMTZ is limited. Considering the

TABLE 3 | Global budgets of methanogenesis rate and DIC flux related to AOM.

Region (Water Depth (m))	Seafloor Area (km^2)	SMTZ (mbsf)	Me rate ($Tmol\ yr^{-1}$)	J_{CH} ($Tmol\ yr^{-1}$)	DIC Flux ($Tmol\ yr^{-1}$)	Range ($Tmol\ yr^{-1}$)
Inner shelf (0–10)	2.59×10^6	0.5 (±0.7)	0.28	1.2	2.8	0.5–10.5
Inner shelf (10–50)	9.18×10^6	2.0 (±2.0)	0.24	1.2	2.8	0.5–10.5
Outer shelf (50–200)	1.27×10^7	4.0 (±3.1)	0.16	0.7	1.7	0.3–6.4
Slope (200–2000)	3.01×10^7	12.8 (±12.1)	0.11	0.5	1.3	0.2–4.7
Rise (2000–3,500)	6.28×10^7	143.4 (±222.0)	0.02	0.05	0.15	0.02–0.57
Abyss (>3,500)	2.38×10^8	168.9 (±144.5)	0.06	0.07	0.21	0.03–0.77
Total	3.55×10^8	—	0.87	3.8	8.9	1.55–33.4

*The seafloor area data, SMTZ data and methane flux into SMTZ (J_{CH}) data are from Egger et al. (2018). The depth-integrated methanogenesis rate (R_{ME}) were calculated according to the empirical formula in **Figure 1B**, and DIC flux and its range were calculated according to the empirical formula in **Figure 3**.*

limitation of bioenergy, the AOM rate can be expressed as follows:

$$R_{AOM} = v_{max} \cdot F_K \cdot F_T \tag{16}$$

where F_K and F_T denote the kinetic and thermodynamic driving forces for AOM, respectively. The F_K is the abbreviation of the latter two terms of **Eq. 15**, and F_T is expressed as follows:

$$F_T = 1 - \exp\left(\frac{\Delta G_r + \Delta G_{BQ}}{\chi \cdot R \cdot T}\right) \tag{17}$$

where ΔG_r denotes the Gibbs energy of the AOM reaction, ΔG_{BQ} denotes the minimum energy required to sustain the AOM, χ denotes the number of protons translocated across the cell membrane, R denotes the gas constant, and T denotes temperature.

When the methane hydrate in sediments is destabilized or the rate of methanogenesis is high, methane can exist as bubbles in supersaturated porewater (Martens and Klump, 1980). Bubbling methane leakages are widely observed and investigated in coastal sediments (Chanton et al., 1989; Anderson et al., 1998; Veloso-Alarcón et al., 2019). The rate of bubble growth is described by the first-order model (Davie and Buffett, 2001):

$$\Phi = R_b \cdot \left([CH_4] - C_{Sa\_Me}\right) \tag{18}$$

where R_b denotes the rate constant, $[CH_4]$ denotes the methane concentration, and C_{Sa_Me} denotes the saturation concentration of methane in porewater. A continuous three-phase system (solid: hydrate, liquids: porewater, and gas: bubble) has been applied to describe gaseous methane transport in sediments. This approach has been widely applied to soils, aquifers, petroleum and shale gas extraction based on the Darcian flow theory (Schowalter, 1979; Molins and Mayer, 2007; Reagan and Moridis, 2008; Molins et al., 2010). Unlike that of dissolved methane in the porewater, the process of bubble ascent is also influenced by eddy diffusion, which can be described as follows (Haeckel et al., 2007):

$$K_{eddy} \approx 0.928 \cdot \sqrt{g \cdot r_{bubble}^3} \tag{19}$$

where K_{eddy} denotes the first-order eddy diffusivity constant, g denotes the acceleration due to gravity, and r_{bubble} denotes the bubble radius. The velocity of eddy diffusion ($K_{eddy} > 1 \times 10^5$ cm2 $year^{-1}$) is several orders of magnitude greater than that of molecular diffusion, resulting in a sevenfold increase in the maximum AOM rate in the sediments while methane is released into the overlying water column as bubbles (Haeckel et al., 2007). However, the continuous three-phase system assumes that the fluid is transported through a static solid matrix. This limits the application of the system to marine sediments, which are affected by compaction, burial, and particle mixing (Regnier et al., 2011).

Numerous studies have been conducted to simulate AOM reaction in global marine sediments based on **Eqs 12–19** (Regnier et al., 2011). AOM reaction mainly occurs in SMTZ, which is commonly defined as a segment close to the maximum AOM rate. The SMTZ depth varies from 2 cm in the Black Sea (Wallmann et al., 2006b) to 400 m in the equatorial Atlantic (Arndt et al., 2006). Three factors impact the SMTZ depth: 1) methane flux into the SMTZ, 2) upward fluid velocity, and 3) OM content and reactivity (Regnier et al., 2011; Meister et al., 2013; Chuang et al., 2019). Higher methane flux and upward fluid velocity can generate a shallow and narrow SMTZ (Regnier et al., 2011). For example, the SMTZ depth in active margins (~10 m) is much shallower than that in passive margins (~100 m) (Jørgensen and Kasten, 2006; Dale et al., 2008c). Moreover, the higher the content and reactivity of OM in surface sediment, the shallower is the SMTZ, attributable to the consumption of sulfate by OM degradation, which promotes the upward transport of methane-bearing fluids (Meister et al., 2013). The SMTZ is also related to the sedimentation rate. The higher the sedimentation rate, the shallower is the SMTZ (Meister et al., 2013).

The SMTZ acts as the main methane barrier where most electron acceptors are depleted, and OM degradation initiates to dominate methanogenesis (Egger et al., 2018). Approximately ~191 Tmol C $year^{-1}$ of OM is transported to the global seafloor, where 3%–4% of OM is converted into methane (5.7–34.4 Tmol $year^{-1}$) in continental margin sediments (Muller-Karger et al., 2005; Dunne et al., 2007). Egger et al. (2018) compiled methane and sulfate data from 740 sites of global marine sediments and suggested ~3.8 Tmol C annual flux of methane into the SMTZ. According to this methane budget, approximately 3.8 Tmol $year^{-1}$ DIC is produced by the AOM because 1 mol of methane consumed produces 1 mol of DIC (Akam et al., 2020). However, there are some errors in this budget that calculated only by stoichiometric

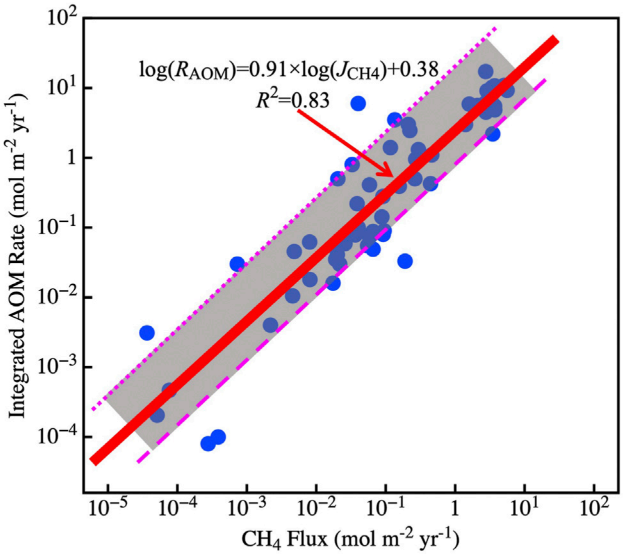

FIGURE 3 | Log–log plots of methane flux into the SMTZ and integrated AOM rate. The gray shaded area indicates the error range of the linear regression, where the upper bound is log(R_{AOM}) = 0.91 × log(J_{CH4}) + 0.95, and the lower bound is log(R_{AOM}) = 0.91 × log(J_{CH4}) −0.40.

relationship of the AOM and methane flux data in Egger et al. (2018). The main reason is that the methane flux calculated by Egger et al. (2018) is based on the gradient of methane at locations where porewater methane and sulfate concentrations are equal. However, the flux calculated by Egger et al. (2018) cannot indicate the methane flux involved in the AOM throughout the sediment, and we found that the ratio between this methane flux and depth integrated AOM rate is not 1:1(**Table 2**). Mathematically, the AOM exists throughout sediments, but the concentrations of methane/sulfate in the surface/bottom sediments are too low to detect. Therefore, it is difficult to quantify the total methane flux in the sediments involved in the AOM. Compiled methane flux into the SMTZ data calculated by Egger et al. (2018) and the depth-integrated AOM rate data in the global marine sediments, we found a good regression in the log-log coordinate between the two (**Figure 3**). According to the methane flux distribution in different marine regions and the empirical formula (**Figure 3**), we estimated that ~8.9 Tmol of AOM-related DIC is produced annually, with ~82% being in the continental shelf sediments (water depth <200 m) (**Table 3**).

3 Methane Transport and Reaction in Seawater

Although sediment AOM consumes nearly all upward methane, particularly in passive margins, methane leakages are commonly observed in active margins (Dale et al., 2008d), such as the northern Barents Sea (Andreassen et al., 2017), East Siberian Arctic Shelf (Shakhova et al., 2010), and Gulf of Mexico (MacDonald et al., 1994). The main pathway of methane leakage from sediments to seawater in active margins (e.g., cold seep and pockmarks) is methane plume (Schulz and Zabel, 2006). The formation of authigenic carbonates promoted by AOM processes is an essential factor in the structure of cold seeps and pockmarks (Bohrmann et al., 1998; Luff and Wallmann, 2003; Aloisi et al., 2004; Nöthen and Kasten, 2011).

Cold seeps are often called the “windows to the deep geosphere” (Boetius and Wenzhöfer, 2013), and they form a central link of material and energy exchange between the lithosphere and hydrosphere together with hydrothermal vents systems. Cold seeps formed by hydrate decomposition leakages have globally been found in the entire bathymetric range of the continental slopes from high to low latitudes. For example, more than 1,200 leakages have been detected in the Hornsund Fault Zone of the Barents Sea (Waage et al., 2019), more than 600 leakages have been discovered in the polar North Atlantic (Bear Island Trough, northern Bjørnøyrenna) (Andreassen et al., 2017), approximately 5,000 leakages have been identified in the northern Gulf of Mexico at water depths of >200 m (Solomon et al., 2009), and 27,000 leakages have been detected in the shallow waters of eastern Siberia (Shakhova et al., 2014). Preliminary estimates suggest that there may be over hundreds of thousands of cold-spring leakage sites globally, erupting simultaneously due to hydrate leakage. Large-scale methane leakages on the seafloor are usually caused by the destabilization of hydrate reservoirs located at shallow water depths or buried at shallow depths and connected to fractures (Freire et al., 2011). The following main factors influence these large leaks. 1) Abnormal overpressure. When hydrocarbons accumulate in the pores of marine sediments and the pressure reaches a high enough level, these hydrocarbons will migrate upward through the GHSZ (Tréhu et al., 2004). The decomposition of methane hydrates at the edge of this stability zone can also form a considerable number of hydraulic fractures in its upper part, which then become an ideal channel for gas migration (Xu and Germanovich, 2006). 2) Regional geological environment fluctuation. These changes are observed in seismic activity (Fischer et al., 2013), tidal cycles (Boles et al., 2001), glacial melting (Andreassen et al., 2017), and bottom water temperature fluctuations (Ferré et al., 2020). 3) Erosion of geological bodies. The erosion of the submarine canyons and destabilization of the canyon sidewall sediments lead to the erosion of the hydrate-bearing caps or reservoirs, resulting in the destabilization and decomposition of the hydrate-bearing layers (Paull et al., 2005). 4) Dramatic changes in the global environment. Dramatic global sea level fluctuations and rapid climate warming during geological history could have triggered the catastrophic release of hydrates by disintegration. For example, the amount of methane hydrates that decomposed and escaped to the atmosphere during the Paleocene/Eocene thermal maximum (PETM) was estimated to be ~2,100 Gt C (Dickens et al., 1997).

In the cold seeps, mud volcanoes, or pockmark regions, methane generally seeps into the hydrosphere in the form of gas flares, also called bubble plumes (Boetius and Wenzhöfer, 2013). Only a few *in situ* measurements approaches can be used to calculate methane flux from sediments to the hydrosphere, and they commonly use remotely operated vehicle (ROV). Combined

TABLE 4 | Synthesis of methane flux into hydrosphere and their detection methods.

Site	Location	Water depth(m)	System	Detection method	CH_4 flux	Reference
A	Mediterranean Sea	6,000	mud volcano	ROV (CALMAR)	3 mmol/m^2/d	Caprais et al. (2010)
B	Mediterranean Sea	6,000	mud volcano	ROV (CALMAR)	0.01 mmol/m^2/d	Caprais et al. (2010)
M7	Congo-Angola	3,171	pockmark	ROV (MARUM)	332 mmol/m^2/d	Decker et al. (2012)
M10	Congo-Angola	3,170	pockmark	ROV (MARUM)	492 mmol/m^2/d	Decker et al. (2012)
central dome	Nile Deep Sea	1,250	mud volcano	ROV (QUEST 4000)	1 mmol/m^2/d	Felden et al. (2013)
central dome	Nile Deep Sea	1,250	mud volcano	ROV (QUEST 4001)	24 mmol/m^2/d	Felden et al. (2013)
central dome	Nile Deep Sea	1,250	mud volcano	ROV (QUEST 4002)	70 mmol/m^2/d	Felden et al. (2013)
bacterial mat	Nile Deep Sea	1,250	mud volcano	ROV (QUEST 4003)	49 mmol/m^2/d	Felden et al. (2013)
bacterial mat	Nile Deep Sea	1,250	mud volcano	ROV (QUEST 4004)	83 mmol/m^2/d	Felden et al. (2013)
bacterial mat	Nile Deep Sea	1,250	mud volcano	ROV (QUEST 4005)	85 mmol/m^2/d	Felden et al. (2013)
warm	Svalbard	370	natural seep	Simrad EK60	67 mol/min	Ferré et al. (2020)
cold	Svalbard	370	natural seep	Simrad EK60	38 mol/min	Ferré et al. (2020)
Arcobacter mat	Nile Deep Sea	1,694	pockmark	ROV Victor 6,000	881 mmol/m^2/d	Grünke et al. (2011)
Beggiatoa	Nile Deep Sea	1,120	mud volcano	ROV QUEST 4000	72 mmol/m^2/d	Grünke et al. (2011)
FWCR	South China Sea	1,150	natural seep	GGA	0.12 mmol/m^2/d	Mau et al. (2020)
SSFR	South China Sea	1,150	natural seep	GGA	79.9 mmol/m^2/d	Mau et al. (2020)
SSFR	South China Sea	1,150	natural seep	GGA	3.4 mmol/m^2/d	Mau et al. (2020)
SSFR	South China Sea	1,150	natural seep	GGA	4.8 mmol/m^2/d	Mau et al. (2020)
Clam	N REGAB	3,147–3,165	pockmark	ROV Victor 6,000	1175 mmol/m^2/d	Pop-Ristova et al. (2012)
Clam S	S REGAB	3,147–3,165	pockmark	ROV Victor 6,000	1 mmol/m^2/d	Pop-Ristova et al. (2012)
Clam S Env	S REGAB	3,147–3,165	pockmark	ROV Victor 6,000	3 mmol/m^2/d	Pop-Ristova et al. (2012)
Mussel S	S REGAB	3,147–3,165	pockmark	ROV Victor 6,000	81 mmol/m^2/d	Pop-Ristova et al. (2012)
Mussel S Env	S REGAB	3,147–3,165	pockmark	ROV Victor 6,000	334 mmol/m^2/d	Pop-Ristova et al. (2012)
Clam	SW REGAB	3,147–3,165	pockmark	ROV Victor 6,000	1170 mmol/m^2/d	Pop-Ristova et al. (2012)
Gas	REGAB	3,160	cold seep	ROV Victor 6,000	81 mmol/m^2/d	Pop-Ristova et al. (2012)
Hydrate ridge	Cascadia margin	832	natural seep	BIGO and FLUFO	11.5 mmol/m^2/d	Sommer et al. (2006b)
BIGO 2	Gulf of Cadiz	1,320	mud volcano	BIGO	0.2 mmol/m^2/d	Sommer et al. (2008)
BIGO 1CO	Gulf of Cadiz	1,317	mud volcano	BIGO and FLUFO	0.45 mmol/m^2/d	Sommer et al. (2009)
BIGO 1EX	Gulf of Cadiz	1,317	mud volcano	BIGO and FLUFO	0.08 mmol/m^2/d	Sommer et al. (2009)
BIGO 2EX	Gulf of Cadiz	1,320	mud volcano	BIGO and FLUFO	0.2 mmol/m^2/d	Sommer et al. (2009)
BIGO 4CO	Gulf of Cadiz	1,318	mud volcano	BIGO and FLUFO	0.4 mmol/m^2/d	Sommer et al. (2009)
FLUFO 4BU	Gulf of Cadiz	1,325	mud volcano	BIGO and FLUFO	0.01 mmol/m^2/d	Sommer et al. (2009)
FLUFO 5BU	Gulf of Cadiz	1,318	mud volcano	BIGO and FLUFO	0.04 mmol/m^2/d	Sommer et al. (2009)
FLUFO 5FLUX	Gulf of Cadiz	1,318	mud volcano	BIGO and FLUFO	0.66 mmol/m^2/d	Sommer et al. (2009)
FLUFO-5FLUX	Hikurangi Margin	660	cold seep	MUC and FLUFO	64.6 mmol/m^2/d	Sommer et al. (2010)
FLUFO-1FLUX	Hikurangi Margin	1,098	cold seep	MUC and FLUFO	5.1 mmol/m^2/d	Sommer et al. (2010)
TVG-18	Cascadia margin	650	cold seep	ROV	23 mmol/m^2/d	Suess et al. (1999)
TVG-18	Cascadia margin	650	cold seep	ROV	375 mmol/m^2/d	Suess et al. (1999)
Hydrate ridge	Cascadia margin	778	natural seep	PVC	100 mmol/m^2/d	Torres et al. (2002)
Beggiatoa field (1)	NE Pacific	777	Cold seep	—	0.6 mmol/m^2/d	Treude et al. (2003)
Beggiatoa field (2)	NE Pacific	777	Cold seep	—	4 mmol/m^2/d	Treude et al. (2003)
DMV	Black Sea	2060	Cold seep	ROV	458 mmol/m^2/d	Lichtschlag et al. (2010)
Dnieper delta	Black Sea	240	natural seep	Benthos-300	5.3 mmol/m^2/d	Artemov et al. (2007)
near shore	Belgian zone	200	natural seep	SRI 8610C	0.13 mmol/m^2/d	Borges et al. (2016)
Eckernförde Bay	Baltic Sea	20	pockmark	—	0.07 mmol/m^2/d	Bussmann and Suess, (1998)
Coal Oil Point	California		pockmark	—	68.3 mmol/m^2/d	Hovland et al. (1993)
UK22/4b	North Sea	120	natural seep	—	125 mmol/m^2/d	Leifer and Judd, (2015)
Lookout Bight	United States	30	natural seep	—	3.9 mmol/m^2/d	Martens and Klump, (1984)
Sorokin trough	Black Sea	1,600	mud volcano	ROV	115 mmol/m^2/d	Sahling et al. (2008)
Tommeliten	North Sea	100	natural seep	ROV Cherokee	34.2 mmol/m^2/d	von Deimling et al. (2011)
East Siberian	Arctic Shelf	70	natural seep		4.5 mmol/m^2/d	Shakhova et al. (2014)
Northern US	Atlantic margin	180–600	natural seep	Okeanos Explorer	0.01 mmol/m^2/d	Skarke et al. (2014)
Eckernförde Bay	Baltic Sea	26	pockmark	MBES	1.9 mmol/m^2/d	Lohrberg et al. (2020)
Eckernförde Bay	Baltic Sea	26	pockmark	MBES	3.3 mmol/m^2/d	Lohrberg et al. (2020)
Eckernförde Bay	Baltic Sea	26	pockmark	MBES	0.98 mmol/m^2/d	Lohrberg et al. (2020)
	Mexico Gulf	1,500	natural seep	ROV	160 × 10^3 Mg/yr	Weber et al. (2014)
Makran	Makran margin	575–2,870	natural seep	ROV (QUEST 4004)	1,152 Mg/yr	Bohrmann et al. (1998)
Kerch seep area	Black Sea	890	natural seep	Seal 5,000	11.9 × 10^3 Mg/yr	Römer et al. (2012)
Central Nile	Mediterranean	1,500–1800	natural seep	ROV (QUEST 4004)	0.6 × 10^3 Mg/yr	Römer et al. (2014)
Dutch Dogger	North Sea	45	natural seep	SBES EK60	593 Mg/yr	Römer et al. (2017)
	Mexico Gulf	3,500	natural seep	ROV	9.9 × 10^3 Mg/yr	Römer et al. (2019)
Kerch Peninsula	Black Sea	1,200	natural seep		55.6 × 10^3 Mg/yr	Römer et al. (2020)
	Cascadia margin	920–1,350	natural seep	ROV Doc Ricketts	88 × 10^3 Mg/yr	Riedel et al. (2018)
	Makran Margin	825–2,865	natural seep	Haiyangdizhi 10	5.9 × 10^3 Mg/yr	Wei et al. (2021)

(Continued on following page)

TABLE 4 | (*Continued*) Synthesis of methane flux into hydrosphere and their detection methods.

Site	Location	Water depth(m)	System	Detection method	CH_4 flux	Reference
Candles	Green Canyon	1,170–1,240	natural seep	ROV	8.2×10^5 mol/yr	Johansen et al. (2020)
Mega Plume	Green Canyon	1,170–1,240	natural seep	ROV	5.2×10^6 mol/yr	Johansen et al. (2020)
Haakon Mosby	Barents Sea	1,280	mudvolcano	ROV Victor 6,000	35×10^6 mol/yr	Niemann et al. (2006)
Haakon Mosby	Barents Sea	1,280	mudvolcano	ROV Victor 6,000	40×10^6 mol/yr	Niemann et al. (2006)

with ROV observation, methane flux (F_{methane}) at the SWI can be estimated as follows (Blomberg et al., 2016; Lohrberg et al., 2020; Mau et al., 2020):

$$F_{methane} = N \cdot n_{methane\_bubble} \cdot M_{methane} \cdot f_{methane} \tag{20}$$

where N denotes the number of seep locations, $n_{\mathrm{methane\_bubble}}$ denotes the amount of methane per gas bubble, M_{methane} denotes the molar mass of methane, and f_{methane} denotes the gas bubble emission frequency, which can be obtained by ROV observation. Another method of estimating methane efflux is the box model that the box is defined by the hydrocasts model (Mau et al., 2020), as follows:

$$F_{methane} = \frac{I \cdot u(z) / l_{path}}{A} \tag{21}$$

where I denotes the estimated methane inventory within the box, $u(z)$ denotes the current velocity, l_{path} denotes the migration of the entire box away from its original position, and A denotes the surface area of the grid. In addition, according to porewater methane profiles, methane flux at the SWI can be calculated by Fick's first law (**Eq. 22**) (Haese et al., 2003; Chen et al., 2017), as follows:

$$F_{methane} = \varphi \cdot D_m \cdot \frac{d[CH_4]}{dz} \tag{22}$$

where φ denotes porosity, D_{m} denotes the molecular diffusion coefficient of methane, and the last term represents the gradient of methane concentration at SWI.

We collected methane flux data in cold seep and pockmarks (**Table 4**). The largest methane flux (1,169–1,175 mmol m^{-2} d^{-1}) is at the center of the giant pockmark REGAB located in the West African margin at a water depth of 3,160 m (Pop-Ristova et al., 2012; Boetius and Wenzhöfer, 2013). The regional methane flux can be obtained on the basis of gas flares observed on the seabed and the estimation of the methane flux at each flare. As shown in **Table 4**, 2.5–169.9 Mg $year^{-1}$ of methane flux is identified in the Gulf of Mexico regions (~6,041.25 km^2), of which more than 90% is occupied by the northern Gulf of Mexico (Weber et al., 2014; Römer et al., 2019; Wei et al., 2021).

The transport of methane in seawater, commonly in the form of gas flares or plumes, is an extremely complex process, where bubble plumes are rapidly dissolved and subsequently diluted by mixing with overlying seawater and then dispersed by ocean currents (Graves et al., 2015). The Navier-Stokes equations are commonly used to describe hydrothermal plumes in the seawater where momentum, mass, heat, methane saturation, and microbially-mediated chemical reactions are considered (Yamazaki et al., 2006; Jiang and Breier, 2014). The radius of methane bubbles (R_{bubble}) typically ranges from 0.001 to 0.015 cm (Shakhova et al., 2014; Higgs et al., 2019). The bubbles less than 10 mm in diameter are expected to dissolve before they reach the surface mixing layer (Gentz et al., 2014). The rate of bubble dissolution depends mainly on the initial bubble size, water temperature, salinity, pressure, and bubble rise rate (Leifer and Patro, 2002; Rehder et al., 2009; Shagapov et al., 2017). The bubble dissolution rate can be written as follows (Fu et al., 2021):

$$\frac{dM}{dz} = \frac{-\left(4\pi R_{bubble}^2\right) \cdot K \cdot (C_S - C_0)}{V_{bubble}} \tag{23}$$

where dM/dz denotes the change in a bubble's methane content over the rise interval dz, V_{bubble} denotes the bubble rise velocity, and K denotes the mass transfer rate.

Based on large ROV observations of methane bubble radius (R_{bubble}) and bubble rising velocity (V_{bubble}), empirical formulae were used to describe bubble rise velocity, as follows (Clift et al., 2005; Leifer et al., 2006):

$$V_{bubble} = 276R_{bubble} - 1648R_{bubble}^2 + 4882R_{bubble}^3 - 7429R_{bubble}^4 + 5618R_{bubble}^5 \tag{24}$$

The well-known theory of Morton, Taylor and Turner (MTT model) has been used to estimate the maximum rising height of a single plume (Morton et al., 1956), and the scaling of the maximum plume rise height (Z_{max}) is given as follows:

$$Z_{max} = C_e \cdot \left(\frac{B_{exit}}{N^3}\right)^{\frac{1}{4}} \tag{25}$$

where B_{exit} denotes the source flux, N denotes the ambient frequency, and C_{e} denotes the scaling coefficient, which was estimated to be 3.76 by analyzing literature data from laboratory plume experiments (Briggs, 1969).

Compared with methane reaction in sediments with sulfate (AOM) in anoxic environments, bottom waters in the continental margin are generally completely oxygenated, with oxygen concentrations ranging from 250 to 350 μM (Boetius and Wenzhöfer, 2013). The consumption of methane in the hydrosphere is related to oxygen, as aerobic oxidation of methane (AeOM):

$$CH_4 + O_2 \rightarrow CO_2 + H_2O \tag{26}$$

The AeOM rate can be calculated as follows (Reeburgh et al., 1991; Valentine et al., 2010; Mau et al., 2020):

$$R_{AeOM} = k \cdot [CH_4] \tag{27}$$

where k denotes the first-order rate constant, and $[CH_4]$ denotes the methane concentration. Many factors that influence AeOM, such as (1) water depth; (2) temporal and spatial distributions of fluid release flux; (3) bubble characteristics (e.g., size, oil film and hydrate coating) (Veloso-Alarcón et al., 2019); (4) ocean euphotic layer; (5) dissolved oxygen concentration, temperature and salinity of seawater (Crespo-Medina et al., 2014); and (6) ocean currents (Steinle et al., 2015). According to the data compiled by Boetius and Wenzhöfer, (2013), the contribution of AeOM to methane consumption in seeps regions can exceed the contribution of AOM, particularly at seeps with low microbial abundance. In regions with low methane fluxes, the AOM consumes 90% of the methane in the overlying fluid (Reeburgh, 2007), whereas most of the methane transported to the seafloor in the seepage regions is consumed by the AeOM (Boetius and Wenzhöfer, 2013).

In cold seep regions, the efficiency of the methane filter (AOM and AeOM) decreases from ~80% for low fluid flow systems (methane flux: ~35 mmol m^{-2} d^{-1}) to ~20% for moderate flow systems (methane flux: ~100 mmol m^{-2} d^{-1}). With microorganisms and bacterial mats absent and with intense gas eruptions, the filter efficiency becomes lower than 10% in high fluid flow systems (e.g., giant pockmark systems) (Pop-Ristova et al., 2012; Boetius and Wenzhöfer, 2013). When such a large amount of methane escapes from microbial oxidation on the seafloor, it will be consumed aerobically in the seawater or transferred to the upper mixed layer and then to the atmosphere (Reeburgh, 2007; Boetius and Wenzhöfer, 2013).

4 METHANE FLUX TO THE ATMOSPHERE

Owing to the human activities, the concentration of greenhouse gases in the atmosphere has been increasing since the 20th century, causing global warming (Sommer et al., 2009; Anderson et al., 2016). The greenhouse effect causes some ecological problems such as glacier retreat, sea-level rise, and the northward shift of the climate zone, which will cause great harm to the natural environment (Larcombe et al., 1995). As the main greenhouse gas, it is significant to calculate the amount of methane transported from seawater to the atmosphere.

The methane flux released from seawater to the atmosphere has been mainly predicted by digital simulation and remote sensing technology (Bovensmann et al., 2010). These methods usually use scientific ship positioning measurements and reverse atmospheric models to estimate methane release. For example, during the 2012 North Sea Elgin blowout accident, such a method was used to assess methane emissions to the atmosphere (Gerilowski et al., 2015). Considering this technology is relatively clumsy and inflexible, passive remote sensing techniques have been developed to collect atmospheric methane concentrations around the study areas, such as wireless remote sensing to collect atmospheric methane concentrations around the study region (Somov et al., 2013; van Kessel et al., 2018). However, when surveying with remote sensing instruments using short-wave infrared radiation, the weak reflectivity of water affects the information (Seelig et al., 2008).

The model calculates the methane flux at the sea-air interface mainly based on the differences in methane chemical potential between seawater and the atmosphere (Seelig et al., 2008). When methane is supersaturated in seawater, the methane in seawater can be emitted to the atmosphere driven by chemical potential. The methane fluxes to the atmosphere are calculated by the diffusive exchange equation (Solomon et al., 2009; Michel et al., 2021):

$$Flux_{Methane} = k_{avg} \cdot \left(C_{plume} - C_{eq}\right) \tag{28}$$

where k_{avg} denotes the gas transfer coefficient at the average wind speed, and C_{eq} denotes the seawater methane concentration in equilibrium with air under ambient conditions (Yamamoto et al., 1976). The gas transfer coefficients are calculated using the empirical formula (Wanninkhof, 1992), as follows:

$$k_{avg} = 0.31 \cdot u_{avg} \cdot \left(\frac{S_C}{600}\right)^{-0.5} \tag{29}$$

where u_{avg} denotes the average wind speed at 10 m above the sea surface, and S_{c} denotes the Schmidt number (a function of salinity and temperature).

The combined cycle model for CO_2 and CH_4 (CMCDMC) was used to assess the role of different environmental parameters in the natural and anthropogenic components of methane leakage and climate change (Krapivin et al., 2017). Given that low-rate methane leaks are nearly completely consumed by the AOM, the climatic impact of methane may be overlooked. However, the high-rate leakage enables methane to enter the seawater and atmosphere directly, thereby causing global warming (Buffett and Archer, 2004). Although there is no conclusive evidence that hydrate-derived methane presently enters the atmosphere, more observational data and improved numerical models will help better describe the climate-hydrate synergy in the future (Ruppel and Kessler, 2017).

5 CHALLENGES AND OUTLOOK

The application of the model to the marine methane processes is summarized as shown in **Figure 4**, including methanogenesis, methane transport and reaction in sediments and seawater, and methane flux from seawater to the atmosphere. The global ocean methane cycle has been increasingly studied, and considerable progress has been made in understanding the marine methane cycle. However, many environmental factors involved in methanogenesis, methane reaction and transport have not been described well by the models. Human understanding of the global methane cycle and the capability to assess the contribution of methane leakage to past and future global changes depend heavily on the accuracy of model construction and calculations. Future progress will rely heavily on additional observational data from different marine environments in the global ocean and on linking models to the observed complexities. Below, we list the remaining problems concerning methane cycle processes to help direct future research.

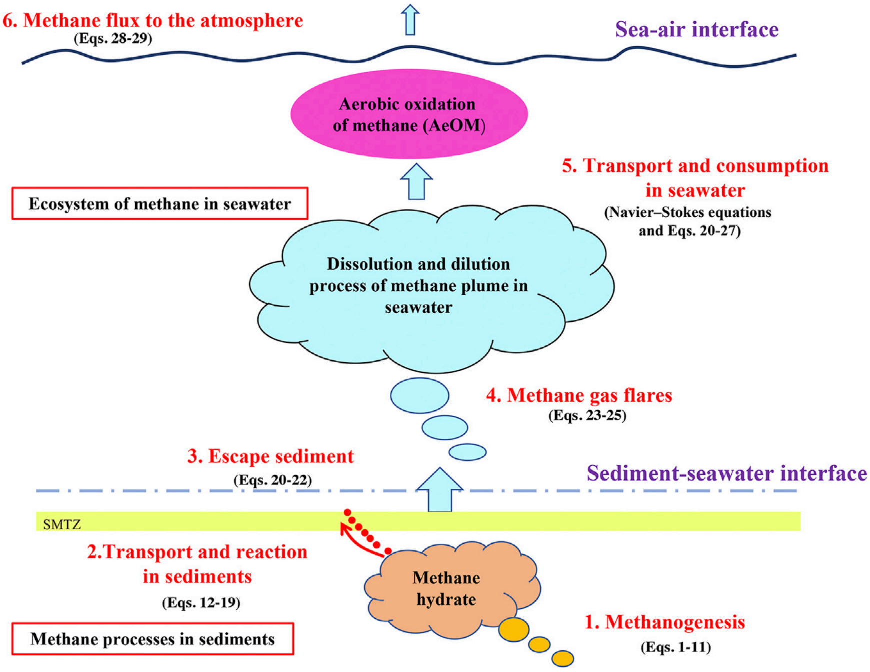

FIGURE 4 | Schematic diagram of the application of model in the marine methane processes.

5.1 Metal-dependent AOM (Metal-AOM)

Sulfate–driven AOM is widely found in global marine sediments, but scholars have found that AOM driven by some active metals (e.g., manganese and iron) is also quite common (Beal et al., 2009). The reduction of the other metal ions with methane is often neglected because the concentration of sulfate in porewater is several orders of magnitude higher than those of other electron acceptors and the almost complete consumption of methane (Reeburgh, 2007). If the manganese flux (~19 Tg year^{-1}) and iron flux (~730 Tg year^{-1}) of the whole world were used to oxidize methane, the result might account for around a fourth of today's AOM consumption. Even if only a small portion of manganese and iron fluxes is used for the AOM, the process can be a massive methane sink, as manganese and iron may be oxidized and reduced by 100–300 times before being buried (Canfield et al., 1993; Beal et al., 2009). Although several experimental studies have been conducted on metal-AOM (Sivan et al., 2011; Egger et al., 2015; Ettwig et al., 2016), there is no single study that assesses metal-AOM via a modelling approach. Thus, more modelling work about metal–AOM needs to be done to help quantify global metal-AOM and enhance the understanding of the changes of δ^{13}C-DIC in porewater.

5.2 Model Construction, Boundary Conditions, and Marine Biological Environments

As methane plumes mainly originate from the decomposition of methane hydrates, transport to the seawater, and eventually reach the atmosphere, a continuum model should be established to describe methane transport in different media (sediment, seawater and atmosphere). At present, the boundary conditions, the initial conditions, and parameters of the mathematical models used for marine geological investigations are ideal (Boudreau, 1997). The transport of porewater species and the initial and boundary conditions are always set as a constant or closed boundary. Further, the pressure and temperature boundary conditions given for simulating the decomposition and release of methane from seabed natural gas hydrates are within a limited predicted range. For complex geological processes, the selection of boundary conditions should be closely combined with field monitoring or laboratory experimental data rather than a simple boundary prediction range or constant. The boundary conditions for methane leakage from sediments and methane migration through different media should be a set of complexes, dynamic boundary conditions that biochemical and geological factors should be considered.

Methane transport in the seabed and seawater is affected by marine and geological organisms (Keppler et al., 2009). Therefore, model accuracy and sensitivity are strongly related to the consideration of biological factors. At present, most mathematical models are lacking in accounting for the effects of marine organisms on methane transport, or the effects of these marine biological factors are treated as a constant (Chuang et al., 2019). By contrast, the activity of marine organisms is influenced by multiple factors. Thus, further work is needed to describe the impact of marine organisms on the methane cycle. The results of field investigation and experimental analyses of recent biochemical reactions of methane should be employed to characterize the models.

5.3 Methane Leakage on the Seafloor

Hydrate can be formed when the seabed temperature and pressure reach certain conditions and if there is a leak that adds alkane fluids to the seabed. Therefore, the stable boundary of hydrates may be at a certain depth in the water body, and the reservoir location may not necessarily be in the sediment. The Gulf of Mexico (Brooks et al., 1994; Boswell, 2009), Joetsu basin in Japan, and the South China Sea have exposed hydrate outcrops or shallow hydrates on the seafloor (Hiruta et al., 2009; Zhang et al., 2017). When methane bubbles ascend on the seafloor in some areas, their surfaces can rapidly form hydrate crusts during upward migration. Therefore, the bubble plumes at the leakage point of cold seeps can be classified as "clean" or "dirty" (Barnes and Goldberg, 1976). There is no numerical simulation for bubble leakage under these conditions. For some anoxic "euxinic basins," such as Cariaco Basin and Black Sea (Reeburgh et al., 1991; Van Rensbergen et al., 2002), research on the processes of methane transport also lacks simulation. Therefore, there is a large room for improvement in accurately simulating modern seabed methane processes, especially methane leaks associated with gas hydrates.

5.4 Predictive Capability of Accidental Large-Scale Methane Leakage

The major advantage of the modeling approach is that it can reasonably predict the trend of methane transport under predetermined conditions (Boudreau, 1997). Owing to the AOM process, methane in sediments hardly seeps into the seawater, or it seeps into the seawater only for a short period (<60 years) and is then quickly re-limited in sediments by the AOM process (Dale et al., 2008c; Regnier et al., 2011). Many ROV observations reveal that strong gas ebullition in the cold seeps or mud volcano regions allows a massive amount of methane to escape microbial oxidation in sediments and be ultimately transported to seawater or even the atmosphere (Boetius and Wenzhöfer, 2013; Andreassen et al., 2017). Nevertheless, there has been no systematic analysis of modeling work combined with ROV observation data to simulate methane processes in cold seeps and mud volcano regions. Considering that diffusion-dominated methane processes in sediments are extremely slow and insignificantly impact on human life (Jørgensen and Kasten, 2006; Regnier et al., 2011), it would be more meaningful to simulate large-scale methane leakage in cold seeps and mud volcano regions. Better modeling work on methane dynamics in extreme environments and under changing environmental conditions can help improve the methane cycle predictive capability.

AUTHOR CONTRIBUTIONS

ZS and SX jointly put forward the research objectives of this task, formulated the research route, wrote and organized this research together with ZW, WG, and HC: Data curation, Formal analysis. XZ and BZ: Review and editing.

FUNDING

This study was supported by the Natural Science Foundation of China (42176057, 41376077, and 41976057), the Shandong Special Fund of Pilot National Laboratory for Marine Science and Technology (Qingdao) (2021QNLM020002), and the Marine Geological Survey Program of China Geological Survey (DD20221707).

REFERENCES

Adler, M., Hensen, C., Kasten, S., and Schulz, H. D. (2000). Computer Simulation of Deep Sulfate Reduction in Sediments of the Amazon Fan. *Int. J. earth Sci.* 88 (4), 641–654. doi:10.1007/s005310050294

Akam, S. A., Coffin, R. B., Abdulla, H. A. N., and Lyons, T. W. (2020). Dissolved Inorganic Carbon Pump in Methane-Charged Shallow Marine Sediments: State of the Art and New Model Perspectives. *Front. Mar. Sci.* 7, 206. doi:10.3389/fmars.2020.00206

Albert, D. B., Martens, C. S., and Alperin, M. J. (1998). Biogeochemical Processes Controlling Methane in Gassy Coastal Sediments—Part 2: Groundwater Flow Control of Acoustic Turbidity in Eckernförde Bay Sediments. *Continental Shelf Res.* 18 (14-15), 1771–1793. doi:10.1016/S0278-4343(98)00057-0

Allen, M. R., Shine, K. P., Fuglestvedt, J. S., Millar, R. J., Cain, M., Frame, D. J., et al. (2018). A Solution to the Misrepresentations of CO_2-equivalent Emissions of Short-Lived Climate Pollutants Under Ambitious Mitigation. *Npj Clim. Atmos. Sci.* 1 (1), 1–8. doi:10.1038/s41612-018-0026-8

Aloisi, G., Wallmann, K., Haese, R. R., and Saliège, J.-F. (2004). Chemical, Biological and Hydrological Controls on the ^{14}C Content of Cold Seep Carbonate Crusts: Numerical Modeling and Implications for Convection at Cold Seeps. *Chem. Geology.* 213 (4), 359–383. doi:10.1016/j.chemgeo.2004.07.008

Anderson, A., Abegg, F., Hawkins, J., Duncan, M., and Lyons, A. (1998). Bubble Populations and Acoustic Interaction with the Gassy Floor of Eckernförde Bay. *Continental Shelf Res.* 18 (14-15), 1807–1838. doi:10.1016/S0278-4343(98)00059-4

Anderson, T. R., Hawkins, E., and Jones, P. D. (2016). CO_2, the Greenhouse Effect and Global Warming: from the Pioneering Work of Arrhenius and Callendar to Today's Earth System Models. *Endeavour.* 40 (3), 178–187. doi:10.1016/j.endeavour.2016.07.002

Andreassen, K., Hogstad, K., and Berteussen, K. A. (1990). Gas Hydrate in the Southern Barents Sea, Indicated by a Shallow Seismic Anomaly. *First Break* 8, 235–245. doi:10.3997/1365-2397.1990012

Andreassen, K., Hubbard, A., Winsborrow, M., Patton, H., Vadakkepuliyambatta, S., Plaza-Faverola, A., et al. (2017). Massive Blow-Out Craters Formed by Hydrate-Controlled Methane Expulsion from the Arctic Seafloor. *Science* 356, 948–953. doi:10.1126/science.aal4500

Archer, D., Buffett, B., and Brovkin, V. (2009). Ocean Methane Hydrates as a Slow Tipping point in the Global Carbon Cycle. *Proc. Natl. Acad. Sci. U.S.A.* 106 (49), 20596–20601. doi:10.1073/pnas.0800885105

Archer, D. E., Morford, J. L., and Emerson, S. R. (2002). A Model of Suboxic Sedimentary Diagenesis Suitable for Automatic Tuning and Gridded Global Domains. *Glob. Biogeochem. Cycles* 16 (1), 17–11721. doi:10.1029/2000GB001288

Arndt, S., Brumsack, H.-J., and Wirtz, K. W. (2006). Cretaceous Black Shales as Active Bioreactors: a Biogeochemical Model for the Deep Biosphere Encountered during ODP Leg 207 (Demerara Rise). *Geochimica et Cosmochimica Acta.* 70 (2), 408–425. doi:10.1016/j.gca.2005.09.010

Arndt, S., Hetzel, A., and Brumsack, H.-J. (2009). Evolution of Organic Matter Degradation in Cretaceous Black Shales Inferred from Authigenic Barite: A

Reaction-Transport Model. *Geochimica et Cosmochimica Acta.* 73 (7), 2000–2022. doi:10.1016/j.gca.2009.01.018

Arndt, S., Jørgensen, B. B., LaRowe, D. E., Middelburg, J. J., Pancost, R. D., and Regnier, P. (2013). Quantifying the Degradation of Organic Matter in marine Sediments: a Review and Synthesis. *Earth-science Rev.* 123, 53–86. doi:10.1016/j.earscirev.2013.02.008

Artemov, Y. G., Egorov, V., Polikarpov, G., and Gulin, S. (2007). Methane Emission to the Hydro-And Atmosphere by Gas Bubble Streams in the Dnieper Paleo-Delta, the Black Sea. *Mar. Ecol. J.* 6 (3), 5–26.

Barnes, R. O., and Goldberg, E. D. (1976). Methane Production and Consumption in Anoxic marine Sediments. *Geology* 4 (5), 297–300. doi:10.1130/0091-7613(1976)4<297:mpacia>2.0.co;2

Bastviken, D., Cole, J., Pace, M., and Tranvik, L. (2004). Methane Emissions From Lakes: Dependence of Lake Characteristics, Two Regional Assessments, and a Global Estimate. *Glob. Biogeochem. Cycles* 18 (4), a–n. doi:10.1029/2004GB002238

Beal, E. J., House, C. H., and Orphan, V. J. (2009). Manganese- and Iron-Dependent Marine Methane Oxidation. *Science* 325, 184–187. doi:10.1126/science.1169984

Ben-Avraham, Z., Smith, G., Reshef, M., and Jungslager, E. (2002). Gas Hydrate and Mud Volcanoes on the Southwest African Continental Margin off South Africa. *Geology* 30 (10), 927–930. doi:10.1130/0091-7613(2002)030<0927:ghamvo>2.0.co;2

Berner, R. A. (2020). *Early Diagenesis: A Theoretical Approach*. Princeton, NJ: Princeton University Press.

Blair, N. E., and Aller, R. C. (1995). Anaerobic Methane Oxidation on the Amazon Shelf. *Geochimica et Cosmochimica Acta.* 59 (18), 3707–3715. doi:10.1016/0016-7037(95)00277-7

Blair, N. (1998). The δ^{13}C of Biogenic Methane in marine Sediments: the Influence of Corg Deposition Rate. *Chem. Geology.* 152 (1-2), 139–150. doi:10.1016/S0009-2541(98)00102-8

Blomberg, A. E. A., Saebo, T. O., Hansen, R. E., Pedersen, R. B., and Austeng, A. (2017). Automatic Detection of marine Gas Seeps Using an Interferometric Sidescan Sonar. *IEEE J. Oceanic Eng.* 42 (3), 590–602. doi:10.1109/JOE.2016.2592559

Boetius, A., and Wenzhöfer, F. (2013). Seafloor Oxygen Consumption Fuelled by Methane From Cold Seeps. *Nat. Geosci.* 6 (9), 725–734. doi:10.1038/ngeo1926

Bohrmann, G., Greinert, J., Suess, E., and Torres, M. (1998). Authigenic Carbonates from the Cascadia Subduction Zone and Their Relation to Gas Hydrate Stability. *Geology* 26 (7), 6472–6650. doi:10.1130/0091-7613(1998)026<0647:acftcs>2.3.co;2

Boles, J. R., Clark, J. F., Leifer, I., and Washburn, L. (2001). Temporal Variation in Natural Methane Seep Rate Due to Tides, Coal Oil Point Area, California. *J. Geophys. Res.* 106 (C11), 27077–27086. doi:10.1029/2000JC000774

Borges, A. V., Champenois, W., Gypens, N., Delille, B., and Harlay, J. (2016). Massive marine Methane Emissions from Near-Shore Shallow Coastal Areas. *Sci. Rep.* 6 (1), 1–8. doi:10.1038/srep27908

Borowski, W. S., Hoehler, T. M., Alperin, M. J., Rodriguez, N. M., and Paull, C. K. (2000). Significance of Anaerobic Methane Oxidation in Methane-Rich Sediments Overlying the Blake Ridge Gas Hydrates. *Dillon, Proceedings ODP, Scientific Results*. Editors C. K. Paull, R. Matsumoto, P. J. Wallace, and W. P. Dillon (College Station, TX: Ocean Drilling Program) 164, 87–99.

Boswell, R. (2009). Gulf of Mexico Gas Hydrate Drilling and Logging Expedition Underway. *Nat. Gas Oil.* 304, 285–4541.

Boudreau, B. P. (1996). A Method-Of-Lines Code for Carbon and Nutrient Diagenesis in Aquatic Sediments. *Comput. Geosciences.* 22 (5), 479–496. doi:10.1016/0098-3004(95)00115-8

Boudreau, B. P. (1997). *Diagenetic Models and Their Implementation*. Berlin: Springer.

Boudreau, B. P., Mucci, A., Sundby, B., Luther, G. W., and Silverberg, N. (1998). Comparative Diagenesis at Three Sites on the Canadian continental Margin. *J. Mar. Res.* 56 (6), 1259–1284. doi:10.1357/002224098765093634

Boudreau, B. P., and Ruddick, B. R. (1991). On a Reactive Continuum Representation of Organic Matter Diagenesis. *Am. J. Sci.* 291 (5), 507–538. doi:10.2475/ajs.291.5.507

Bousquet, P., Ciais, P., Miller, J. B., Dlugokencky, E. J., Hauglustaine, D. A., Prigent, C., et al. (2006). Contribution of Anthropogenic and Natural Sources to Atmospheric Methane Variability. *Nature* 443 (7110), 439–443. doi:10.1038/nature05132

Bovensmann, H., Buchwitz, M., Burrows, J. P., Reuter, M., Krings, T., Gerilowski, K., et al. (2010). A Remote Sensing Technique for Global Monitoring of Power Plant CO_2 Emissions From Space and Related Applications. *Atmos. Meas. Tech.* 3 (4), 781–811. doi:10.5194/amt-3-781-2010

Briggs, G. (1969). Optimum Formulas for Buoyant Plume Rise. *Philosophical Trans. R. Soc. Lond. Ser. A, Math. Phys. Sci.* 265 (1161), 197–203.

Brooks, J. M., Anderson, A. L., Sassen, R., Kennicutt, M. C., and Guinasso, N. L., JR (1994). Hydrate Occurrences in Shallow Subsurface Cores from continental Slope Sediments. *Ann. New York Acad. Sci.* 715 (1), 381–391. doi:10.1111/j.1749-6632.1994.tb38851.x

Buffett, B., and Archer, D. (2004). Global Inventory of Methane Clathrate: Sensitivity to Changes in the Deep Ocean. *Earth Planet. Sci. Lett.* 227 (3-4), 185–199. doi:10.1016/j.epsl.2004.09.005

Burdige, D. J., Komada, T., Magen, C., and Chanton, J. P. (2016). Methane Dynamics in Santa Barbara Basin (USA) Sediments as Examined With a Reaction-Transport Model. *J Mar. Res.* 74 (6), 277–313. doi:10.1357/002224016821744151

Burdige, D. J., and Komada, T. (2015). "Sediment Pore Waters," in *Biogeochemistry of marine Dissolved Organic Matter* (Elsevier), 535–577. doi:10.1016/b978-0-12-405940-5.00012-1

Burwicz, E. B., Rüpke, L. H., and Wallmann, K. (2011). Estimation of the Global Amount of Submarine Gas Hydrates Formed via Microbial Methane Formation Based on Numerical Reaction-Transport Modeling and a Novel Parameterization of Holocene Sedimentation. *Geochimica et Cosmochimica Acta.* 75 (16), 4562–4576. doi:10.1016/j.gca.2011.05.029

Bussmann, I., and Suess, E. (1998). Groundwater Seepage in Eckernförde Bay (Western Baltic Sea): Effect on Methane and Salinity Distribution of the Water Column. *Continental shelf Res.* 18 (14-15), 1795–1806. doi:10.1016/S0278-4343(98)00058-2

Canfield, D. E., Thamdrup, B., and Hansen, J. W. (1993). The Anaerobic Degradation of Organic Matter in Danish Coastal Sediments: Iron Reduction, Manganese Reduction, and Sulfate Reduction. *Geochimica et Cosmochimica Acta.* 57 (16), 3867–3883. doi:10.1016/0016-7037(93)90340-3

Caprais, J.-C., Lanteri, N., Crassous, P., Noel, P., Bignon, L., Rousseaux, P., et al. (2010). A New CALMAR Benthic Chamber Operating by Submersible: First Application in the Cold-Seep Environment of Napoli Mud Volcano (Mediterranean Sea). *Limnol. Oceanogr. Methods.* 8 (6), 304–312. doi:10.4319/lom.2010.8.304

Chanton, J. P., Martens, C. S., and Kelley, C. A. (1989). Gas Transport From Methane-Saturated, Tidal Freshwater and Wetland Sediments. *Limnol. Oceanogr.* 34 (5), 807–819. doi:10.4319/lo.1989.34.5.0807

Chen, N. C., Yang, T. F., Hong, W. L., Chen, H. W., Chen, H. C., Hu, C. Y., et al. (2017). Production, Consumption, and Migration of Methane in Accretionary Prism of Southwestern Taiwan. *Geochem. Geophys. Geosyst.* 18, 2970–2989. doi:10.1002/2017GC006798

Chuang, P.-C., Yang, T. F., Wallmann, K., Matsumoto, R., Hu, C.-Y., Chen, H.-W., et al. (2019). Carbon Isotope Exchange during Anaerobic Oxidation of Methane (AOM) in Sediments of the Northeastern South China Sea. *Geochimica et Cosmochimica Acta.* 246, 138–155. doi:10.1016/j.gca.2018.11.003

Clift, R., Grace, J. R., and Weber, M. E. (2005). *Bubbles, Drops, and Particles*. Courier Corporation.

Conrad, R. (2005). Quantification of Methanogenic Pathways Using Stable Carbon Isotopic Signatures: a Review and a Proposal. *Org. Geochem.* 36 (5), 739–752. doi:10.1016/j.orggeochem.2004.09.006

Crespo-Medina, M., Meile, C. D., Hunter, K. S., Diercks, A.-R., Asper, V. L., Orphan, V. J., et al. (2014). The Rise and Fall of Methanotrophy Following a Deepwater Oil-Well Blowout. *Nat. Geosci.* 7 (6), 423–427. doi:10.1038/ngeo2156

Crill, P. M., and Martens, C. S. (1987). Biogeochemical Cycling in an Organic-Rich Coastal marine basin. 6. Temporal and Spatial Variations in Sulfate Reduction Rates. *Geochimica et Cosmochimica Acta.* 51 (5), 1175–1186. doi:10.1016/0016-7037(87)90210-9

Dale, A. W., Aguilera, D. R., Regnier, P., Fossing, H., Knab, N. J., and Jørgensen, B. B. (2008a). Seasonal Dynamics of the Depth and Rate of Anaerobic Oxidation of Methane in Aarhus Bay (Denmark) Sediments. *J. Mar. Res.* 66 (1), 127–155. doi:10.1357/002224008784815775

Dale, A. W., Regnier, P., Knab, N. J., Jørgensen, B. B., and Van Cappellen, P. (2008b). Anaerobic Oxidation of Methane (AOM) in marine Sediments from the Skagerrak (Denmark): II. Reaction-Transport Modeling. *Geochimica et Cosmochimica Acta* 72 (12), 2880–2894. doi:10.1016/j.gca.2007.11.039

Dale, A. W., Van Cappellen, P., Aguilera, D. R., and Regnier, P. (2008c). Methane Efflux From Marine Sediments in Passive and Active Margins: Estimations From Bioenergetic Reaction–Transport Simulations. *Earth Planet. Sci. Lett.* 265 (3-4), 329–344. doi:10.1016/j.epsl.2007.09.026

Dale, A. W., Brüchert, V., Alperin, M., and Regnier, P. (2009). An Integrated Sulfur Isotope Model for Namibian Shelf Sediments. *Geochimica et Cosmochimica Acta.* 73 (7), 1924–1944. doi:10.1016/j.gca.2008.12.015

Dale, A. W., Flury, S., Fossing, H., Regnier, P., Røy, H., Scholze, C., et al. (2019). Kinetics of Organic Carbon Mineralization and Methane Formation in marine Sediments (Aarhus Bay, Denmark). *Geochimica et Cosmochimica Acta.* 252, 159–178. doi:10.1016/j.gca.2019.02.033

Dale, A. W., Regnier, P., and Van Cappellen, P. (2006). Bioenergetic Controls on Anaerobic Oxidation of Methane (AOM) in Coastal Marine Sediments: a Theoretical Analysis. *Am. J. Sci.* 306 (4), 246–294. doi:10.2475/ajs.306.4.246

Dale, A. W., Sommer, S., Haeckel, M., Wallmann, K., Linke, P., Wegener, G., et al. (2010). Pathways and Regulation of Carbon, Sulfur and Energy Transfer in marine Sediments Overlying Methane Gas Hydrates on the Opouawe Bank (New Zealand). *Geochimica et Cosmochimica Acta.* 74 (20), 5763–5784. doi:10.1016/j.gca.2010.06.038

Davidson, D. W., Garg, S. K., Gough, S. R., Handa, Y. P., Ratcliffe, C. I., Ripmeester, J. A., et al. (1986). Laboratory Analysis of a Naturally Occurring Gas Hydrate from Sediment of the Gulf of Mexico. *Geochimica et Cosmochimica Acta.* 50 (4), 619–623. doi:10.1016/0016-7037(86)90110-9

Davie, M. K., and Buffett, B. A. (2001). A Numerical Model for the Formation of Gas Hydrate below the Seafloor. *J. Geophys. Res.* 106 (B1), 497–514. doi:10.1029/2000JB900363

Decker, C., Caprais, J.-C., Khripounoff, A., and Olu, K. (2012). First Respiration Estimates of Cold-Seep Vesicomyid Bivalves From *In Situ* Total Oxygen Uptake Measurements. *Comptes rendus biologies.* 335 (4), 261–270. doi:10.1016/j.crvi.2012.03.002

Devol, A. H., Anderson, J. J., Kuivila, K., and Murray, J. W. (1984). A Model for Coupled Sulfate Reduction and Methane Oxidation in the Sediments of Saanich Inlet. *Geochimica et cosmochimica acta.* 48 (5), 993–1004. doi:10.1016/0016-7037(84)90191-1

Dickens, G. R., Castillo, M. M., and Walker, J. C. G. (1997). A Blast of Gas in the Latest Paleocene: Simulating First-Order Effects of Massive Dissociation of Oceanic Methane Hydrate. *Geology.* 25 (3), 259–262. doi:10.1130/0091-7613(1997)025<0259:abogit>2.3.co;2

Dickens, G. R., and Quinby-Hunt, M. S. (1994). Methane Hydrate Stability in Seawater. *Geophys. Res. Lett.* 21 (19), 2115–2118. doi:10.1029/94GL01858

Dickens, G. R. (2001). The Potential Volume of Oceanic Methane Hydrates With Variable External Conditions. *Org. Geochem.* 32 (10), 1179–1193. doi:10.1016/S0146-6380(01)00086-9

Dlugokencky, E. J., Nisbet, E. G., Fisher, R., and Lowry, D. (2011). Global Atmospheric Methane: Budget, Changes and Dangers. *Phil. Trans. R. Soc. A.* 369 (1943), 2058–2072. doi:10.1098/rsta.2010.0341

Duan, Z., and Weare, J. H. (1992). Reply to Comment by J. J. Carroll on "The Prediction of Methane Solubility in Natural Waters to High Ionic Strength from 0 to 250°C and from 0 to 1600 Bar". *Geochimica et Cosmochimica Acta* 56, 4303. doi:10.1016/0016-7037(92)90215-510.1016/0016-7037(92)90271-j

Dunne, J. P., Sarmiento, J. L., and Gnanadesikan, A. (2007). A Synthesis of Global Particle Export From the Surface Ocean and Cycling Through the Ocean Interior and on the Seafloor. *Glob. Biogeochem. Cycles.* 21 (4), a–n. doi:10.1029/2006GB002907

Egger, M., Rasigraf, O., Sapart, C. J., Jilbert, T., Jetten, M. S. M., Röckmann, T., et al. (2015). Iron-Mediated Anaerobic Oxidation of Methane in Brackish Coastal Sediments. *Environ. Sci. Technol.* 49 (1), 277–283. doi:10.1021/es503663z

Egger, M., Riedinger, N., Mogollón, J. M., and Jørgensen, B. B. (2018). Global Diffusive Fluxes of Methane in marine Sediments. *Nat. Geosci.* 11 (6), 421–425. doi:10.1038/s41561-018-0122-8

Etminan, M., Myhre, G., Highwood, E. J., and Shine, K. P. (2016). Radiative Forcing of Carbon Dioxide, Methane, and Nitrous Oxide: A Significant Revision of the Methane Radiative Forcing. *Geophys. Res. Lett.* 43 (2412), 614623–615612. doi:10.1002/2016GL071930

Ettwig, K. F., Zhu, B., Speth, D., Keltjens, J. T., Jetten, M. S. M., and Kartal, B. (2016). Archaea Catalyze Iron-Dependent Anaerobic Oxidation of Methane. *Proc. Natl. Acad. Sci. U.S.A.* 113 (45), 12792–12796. doi:10.1073/pnas.1609534113

Felden, J., Lichtschlag, A., Wenzhöfer, F., de Beer, D., Feseker, T., Pop Ristova, P., et al. (2013). Limitations of Microbial Hydrocarbon Degradation at the Amon Mud Volcano (Nile Deep-Sea Fan). *Biogeosciences.* 10 (5), 3269–3283. doi:10.5194/bg-10-3269-2013

Fenchel, T., Blackburn, H., King, G. M., and Blackburn, T. H. (2012). *Bacterial Biogeochemistry: The Ecophysiology of mineral Cycling.* Cambridge, MA: Academic Press.

Ferré, B., Jansson, P. G., Moser, M., Serov, P., Portnov, A., Graves, C. A., et al. (2020). Reduced Methane Seepage From Arctic Sediments During Cold Bottom-Water Conditions. *Nat. Geosci.* 13 (2), 144–148. doi:10.1038/s41561-019-0515-3

Fischer, D., Mogollón, J. M., Strasser, M., Pape, T., Bohrmann, G., Fekete, N., et al. (2013). Subduction Zone Earthquake as Potential Trigger of Submarine Hydrocarbon Seepage. *Nat. Geosci.* 6 (8), 647–651. doi:10.1038/ngeo1886

Fossing, H., Ferdelman, T. G., and Berg, P. (2000). Sulfate Reduction and Methane Oxidation in Continental Margin Sediments Influenced by Irrigation (South-East Atlantic off Namibia). *Geochimica et Cosmochimica Acta.* 64 (5), 897–910. doi:10.1016/S0016-7037(99)00349-X

Freire, A. F. M., Matsumoto, R., and Santos, L. A. (2011). Structural-stratigraphic Control on the Umitaka Spur Gas Hydrates of Joetsu Basin in the Eastern Margin of Japan Sea. *Mar. Pet. Geology.* 28, 1967–1978. doi:10.1016/j.marpetgeo.2010.10.004

Fu, X., Waite, W. F., and Ruppel, C. D. (2021). Hydrate Formation on Marine Seep Bubbles and the Implications for Water Column Methane Dissolution. *J. Geophys. Res. Oceans.* 126 (9), e2021JC017363. doi:10.1029/2021JC017363

Gentz, T., Damm, E., Schneider von Deimling, J., Mau, S., McGinnis, D. F., and Schlüter, M. (2014). A Water Column Study of Methane Around Gas Flares Located at the West Spitsbergen continental Margin. *Continental Shelf Res.* 72, 107–118. doi:10.1016/j.csr.2013.07.013

Gerilowski, K., Krings, T., Hartmann, J., Buchwitz, M., Sachs, T., Erzinger, J., et al. (2015). Atmospheric Remote Sensing Constraints on Direct Sea-Air Methane Flux from the 22/4b North Sea Massive Blowout Bubble Plume. *Mar. Pet. Geology.* 68, 824–835. doi:10.1016/j.marpetgeo.2015.07.011

Giustiniani, M., Tinivella, U., Sauli, C., and Della Vedova, B. (2018). Distribution of the Gas Hydrate Stability Zone in the Ross Sea, Antarctica. *Andean Geology.* 45 (1), 78–86. doi:10.5027/andgeoV45n1-2989

Graves, C. A., Steinle, L., Rehder, G., Niemann, H., Connelly, D. P., Lowry, D., et al. (2015). Fluxes and Fate of Dissolved Methane Released at the Seafloor at the Landward Limit of the Gas Hydrate Stability Zone Offshore Western Svalbard. *J. Geophys. Res. Oceans.* 120, 6185–6201. doi:10.1002/2015JC011084

Grünke, S., Felden, J., Lichtschlag, A., Girnth, A.-C., de Beer, D., Wenzhöfer, F., et al. (2011). Niche Differentiation Among Mat-Forming, Sulfide-Oxidizing Bacteria at Cold Seeps of the Nile Deep Sea Fan (Eastern Mediterranean Sea). *Geobiology* 9 (4), 330–348. doi:10.1111/j.1472-4669.2011.00281.x

Haeckel, M. (2006). "A Transport-Reaction Model of the Hydrological Systems of the Costa Rica Subduction Zone," in Proceedings of the Ocean Drilling Program, Scientific Results, Leg), 1–26.

Haeckel, M., Boudreau, B. P., and Wallmann, K. (2007). Bubble-Induced Porewater Mixing: A 3-D Model for Deep Porewater Irrigation. *Geochimica et Cosmochimica Acta.* 71 (21), 5135–5154. doi:10.1016/j.gca.2007.08.011

Haese, R. R., Meile, C., Van Cappellen, P., and De Lange, G. J. (2003). Carbon Geochemistry of Cold Seeps: Methane Fluxes and Transformation in Sediments from Kazan Mud Volcano, Eastern Mediterranean Sea. *Earth Planet. Sci. Lett.* 212, 361–375. doi:10.1016/S0012-821X(03)00226-7

Hensen, C., and Wallmann, K. (2005). Methane Formation at Costa Rica Continental Margin-Constraints for Gas Hydrate Inventories and Cross-Décollement Fluid Flow. *Earth Planet. Sci. Lett.* 236 (1-2), 41–60. doi:10.1016/j.epsl.2005.06.007

Higgs, B., Mountjoy, J. J., Crutchley, G. J., Townend, J., Ladroit, Y., Greinert, J., et al. (2019). Seep-bubble Characteristics and Gas Flow Rates from a Shallow-Water, High-Density Seep Field on the Shelf-To-Slope Transition of the Hikurangi Subduction Margin. *Mar. Geology.* 417, 105985. doi:10.1016/j.margeo.2019.105985

Hiruta, A., Snyder, G. T., Tomaru, H., and Matsumoto, R. (2009). Geochemical Constraints for the Formation and Dissociation of Gas Hydrate in an Area of High Methane Flux, Eastern Margin of the Japan Sea. *Earth Planet. Sci. Lett.* 279 (3-4), 326–339. doi:10.1016/j.epsl.2009.01.015

Holmes, M. E., Sansone, F. J., Rust, T. M., and Popp, B. N. (2000). Methane Production, Consumption, and Air-Sea Exchange in the Open Ocean: An Evaluation Based on Carbon Isotopic Ratios. *Glob. Biogeochem. Cycles.* 14 (1), 1–10. doi:10.1029/1999GB001209

Hovland, M., Judd, A. G., and Burke, R., Jr (1993). The Global Flux of Methane from Shallow Submarine Sediments. *Chemosphere.* 26 (1-4), 559–578. doi:10.1016/0045-6535(93)90442-8

Inagaki, F., Nunoura, T., Nakagawa, S., Teske, A., Lever, M., Lauer, A., et al. (2006). Biogeographical Distribution and Diversity of Microbes in Methane Hydrate-Bearing Deep Marine Sediments on the Pacific Ocean Margin. *Proc. Natl. Acad. Sci. U.S.A.* 103 (8), 2815–2820. doi:10.1073/pnas.0511033103

Jørgensen, B. B. (1978). A Comparison of Methods for the Quantification of Bacterial Sulfate Reduction in Coastal marine Sediments. *Geomicrobiology J.* 1 (1), 11–27. doi:10.1080/01490457809377721

Jahren, A. H., Arens, N. C., Sarmiento, G., Guerrero, J., and Amundson, R. (2001). Terrestrial Record of Methane Hydrate Dissociation in the Early Cretaceous. *Geology* 29 (2), 159–162. doi:10.1130/0091-7613(2001)029<0159:tromhd>2.0.co;2

Jakosky, B. M., Henderson, B. G., and Mellon, M. T. (1995). Chaotic Obliquity and the Nature of the Martian Climate. *J. Geophys. Res.* 100 (E1), 1579–1584. doi:10.1029/94JE02801

Jiang, H., and Breier, J. A. (2014). Physical Controls on Mixing and Transport within Rising Submarine Hydrothermal Plumes: A Numerical Simulation Study. *Deep Sea Res. Oceanographic Res. Pap.* 92, 41–55. doi:10.1016/j.dsr.2014.06.006

Johansen, C., Macelloni, L., Natter, M., Silva, M., Woosley, M., Woolsey, A., et al. (2020). Hydrocarbon Migration Pathway and Methane Budget for a Gulf of Mexico Natural Seep Site: Green Canyon 600. *Earth Planet. Sci. Lett.* 545, 116411. doi:10.1016/j.epsl.2020.116411

Jørgensen, B. B., Böttcher, M. E., Lüschen, H., Neretin, L. N., and Volkov, I. I. (2004). Anaerobic Methane Oxidation and a Deep H2S Sink Generate Isotopically Heavy Sulfides in Black Sea Sediments. *Geochimica et Cosmochimica Acta* 68 (9), 2095–2118. doi:10.1016/j.gca.2003.07.017

Jørgensen, S. E., and Kasten, S. (2006). Sulfur Cycling and Methane Oxidation. *Ecol. Model.* 196, 271–309. doi:10.1016/j.ecolmodel.2006.03.010

Keppler, F., Boros, M., Frankenberg, C., Lelieveld, J., McLeod, A., Pirttilä, A. M., et al. (2009). Methane Formation in Aerobic Environments. *Environ. Chem.* 6 (6), 459–465. doi:10.1071/EN09137

Klauda, J. B., and Sandler, S. I. (2005). Global Distribution of Methane Hydrate in Ocean Sediment. *Energy Fuels.* 19, 459–470. doi:10.1021/ef049798o

Knab, N. J., Cragg, B. A., Borowski, C., Parkes, R. J., Pancost, R., and Jørgensen, B. B. (2008). Anaerobic Oxidation of Methane (AOM) in marine Sediments from the Skagerrak (Denmark): I. Geochemical and Microbiological Analyses. *Geochimica et Cosmochimica Acta.* 72 (12), 2868–2879. doi:10.1016/j.gca.2008.03.016

Krapivin, V. F., Varotsos, C. A., and Soldatov, V. Y. (2017). Simulation Results from a Coupled Model of Carbon Dioxide and Methane Global Cycles. *Ecol. Model.* 359, 69–79. doi:10.1016/j.ecolmodel.2017.05.023

Kretschmer, K., Biastoch, A., Rüpke, L., and Burwicz, E. (2015). Modeling the Fate of Methane Hydrates under Global Warming. *Glob. Biogeochem. Cycles.* 29 (5), 610–625. doi:10.1002/2014GB005011

Kvenvolden, K. A. (1993). Gas Hydrates-Geological Perspective and Global Change. *Rev. Geophys.* 31 (2), 173–187. doi:10.1029/93RG00268

Kvenvolden, K. A., and Kastner, M. (1990). "32. Gas Hydrates of the Peruvian Outer continental Margin1," in Proceedings of the Ocean Drilling Program, Scientific Results: Citeseer), 517–526.

Larcombe, P., Carter, R., Dye, J., Gagan, M., and Johnson, D. (1995). New Evidence for Episodic post-glacial Sea-Level Rise, central Great Barrier Reef, Australia. *Mar. Geology.* 127 (1-4), 1–44. doi:10.1016/0025-3227(95)00059-8

LaRowe, D. E., Arndt, S., Bradley, J. A., Estes, E. R., Hoarfrost, A., Lang, S. Q., et al. (2020). The Fate of Organic Carbon in marine Sediments - New Insights from Recent Data and Analysis. *Earth-Science Rev.* 204, 103146. doi:10.1016/j.earscirev.2020.103146

Leifer, I., and Judd, A. (2015). The UK22/4b Blowout 20 Years on: Investigations of Continuing Methane Emissions from Sub-seabed to the Atmosphere in a North Sea Context. *Mar. Pet. Geology.* 68, 706–717. doi:10.1016/j.marpetgeo.2015.11.012

Leifer, I., Luyendyk, B. P., Boles, J., and Clark, J. F. (2006). Natural Marine Seepage Blowout: Contribution to Atmospheric Methane. *Glob. Biogeochem. Cycles.* 20, a–n. doi:10.1029/2005GB002668

Leifer, I., and Patro, R. K. (2002). The Bubble Mechanism for Methane Transport from the Shallow Sea Bed to the Surface: A Review and Sensitivity Study. *Continental Shelf Res.* 22 (16), 2409–2428. doi:10.1016/S0278-4343(02)00065-1

Lelieveld, J., Peters, W., Dentener, F. J., and Krol, M. C. (2002). Stability of Tropospheric Hydroxyl Chemistry. *J.-Geophys.-Res.* 107 (D23), 17–21. doi:10.1029/2002JD002272

Lenhart, K., Klintzsch, T., Langer, G., Nehrke, G., Bunge, M., Schnell, S., et al. (2015). Evidence for Methane Production by marine Algae (Emiliana Huxleyi) and its Implication for the Methane Paradox in Oxic Waters. *Biogeosciences Discuss.* 12, 20323–20360. doi:10.5194/bgd-12-20323-201

Li, J.-f., Ye, J.-l., Ye, J.-l., Qin, X.-w., Qiu, H.-j., Wu, N.-y., et al. (2018). The First Offshore Natural Gas Hydrate Production Test in South China Sea. *China Geology.* 1 (1), 5–16. doi:10.31035/cg2018003

Lichtschlag, A., Felden, J., Wenzhöfer, F., Schubotz, F., Ertefai, T. F., Boetius, A., et al. (2010). Methane and Sulfide Fluxes in Permanent Anoxia: *In Situ* Studies at the Dvurechenskii Mud Volcano (Sorokin Trough, Black Sea). *Geochimica et Cosmochimica Acta.* 74 (17), 5002–5018. doi:10.1016/j.gca.2010.05.031

Linke, P., Wallmann, K., Suess, E., Hensen, C., and Rehder, G. (2005). *In Situ* benthic Fluxes from an Intermittently Active Mud Volcano at the Costa Rica Convergent Margin. *Earth Planet. Sci. Lett.* 235, 79–95. doi:10.1016/j.epsl.2005.03.009

Lohrberg, A., Schmale, O., Ostrovsky, I., Niemann, H., Held, P., and Schneider von Deimling, J. (2020). Discovery and Quantification of a Widespread Methane Ebullition Event in a Coastal Inlet (Baltic Sea) Using a Novel Sonar Strategy. *Sci. Rep.* 10 (1), 1–13. doi:10.1038/s41598-020-60283-0

Luff, R., Greinert, J., Wallmann, K., Klaucke, I., and Suess, E. (2005). Simulation of Long-Term Feedbacks from Authigenic Carbonate Crust Formation at Cold Vent Sites. *Chem. Geology.* 216 (1-2), 157–174. doi:10.1016/j.chemgeo.2004.11.002

Luff, R., Wallmann, K., and Aloisi, G. (2004). Numerical Modeling of Carbonate Crust Formation at Cold Vent Sites: Significance for Fluid and Methane Budgets and Chemosynthetic Biological Communities. *Earth Planet. Sci. Lett.* 221, 337–353. doi:10.1016/S0012-821X(04)00107-4

Luff, R., and Wallmann, K. (2003). Fluid Flow, Methane Fluxes, Carbonate Precipitation and Biogeochemical Turnover in Gas Hydrate-Bearing Sediments at Hydrate Ridge, Cascadia Margin: Numerical Modeling and Mass Balances. *Geochimica et Cosmochimica Acta.* 67, 3403–3421. doi:10.1016/S0016-7037(03)00127-3

MacDonald, I. R., Guinasso, N. L., Jr, Sassen, R., Brooks, J. M., Lee, L., and Scott, K. T. (1994). Gas Hydrate that Breaches the Sea Floor on the continental Slope of the Gulf of Mexico. *Geology.* 22 (8), 699–702. doi:10.1130/0091-7613(1994)022<0699:ghtbts>2.3.co;2

Maher, K., Steefel, C. I., DePaolo, D. J., and Viani, B. E. (2006). The Mineral Dissolution Rate Conundrum: Insights from Reactive Transport Modeling of U Isotopes and Pore Fluid Chemistry in marine Sediments. *Geochimica et Cosmochimica Acta.* 70 (2), 337–363. doi:10.1016/j.gca.2005.09.001

Marquardt, M., Hensen, C., Piñero, E., Wallmann, K., and Haeckel, M. (2010). A Transfer Function for the Prediction of Gas Hydrate Inventories in marine Sediments. *Biogeosciences.* 7 (9), 2925–2941. doi:10.5194/bg-7-2925-2010

Martens, C. S., Albert, D. B., and Alperin, M. J. (1998). Biogeochemical Processes Controlling Methane in Gassy Coastal Sediments—Part 1. A Model Coupling Organic Matter Flux to Gas Production, Oxidation and Transport. *Continental Shelf Res.* 18 (14-15), 1741–1770. doi:10.1016/S0278-4343(98)00056-9

Martens, C. S., and Val Klump, J. (1984). Biogeochemical Cycling in an Organic-Rich Coastal Marine basin 4. An Organic Carbon Budget for Sediments Dominated by Sulfate Reduction and Methanogenesis. *Geochimica et Cosmochimica Acta.* 48 (10), 1987–2004. doi:10.1016/0016-7037(84)90380-6

Martens, C. S., and Val Klump, J. (1980). Biogeochemical Cycling in an Organic-Rich Coastal marine basin—I. Methane Sediment-Water Exchange Processes. *Geochimica et Cosmochimica Acta.* 44 (3), 471–490. doi:10.1016/0016-7037(80)90045-9

Mau, S., Tu, T.-H., Becker, M., dos Santos Ferreira, C., Chen, J.-N., Lin, L.-H., et al. (2020). Methane Seeps and Independent Methane Plumes in the South China Sea Offshore Taiwan. *Front. Mar. Sci.* 7, 543. doi:10.3389/fmars.2020.00543

Megonigal, J. P., Hines, M. E., and Visscher, P. T. (2004). Anaerobic Metabolism: Linkages to Trace Gases and Aerobic Processes. *Biogeochemistry*. Editor W. H. Schlesinger (Oxford, UK: Elsevier-Pergamon), 317–424.

Meister, P., Liu, B., Ferdelman, T. G., Jørgensen, B. B., and Khalili, A. (2013). Control of Sulphate and Methane Distributions in Marine Sediments by Organic Matter Reactivity. *Geochimica et Cosmochimica Acta.* 104, 183–193. doi:10.1016/j.gca.2012.11.011

Michel, A. P. M., Preston, V. L., Fauria, K. E., and Nicholson, D. P. (2021). Observations of Shallow Methane Bubble Emissions from Cascadia Margin. *Front. Earth Sci.* 9, 285. doi:10.3389/feart.2021.613234

Middelburg, J. J. (1989). A Simple Rate Model for Organic Matter Decomposition in marine Sediments. *Geochimica et Cosmochimica acta.* 53 (7), 1577–1581. doi:10.1016/0016-7037(89)90239-1

Milkov, A. V. (2004). Global Estimates of Hydrate-Bound Gas in Marine Sediments: How Much Is Really Out There? *Earth-science Rev.* 66 (3-4), 183–197. doi:10.1016/j.earscirev.2003.11.002

Miller, S. L., and Smythe, W. D. (1970). Carbon Dioxide Clathrate in the Martian Ice Cap. *Science* 170 (3957), 531–533. doi:10.1126/science.170.3957.531

Mogollón, J. M., Dale, A. W., L'Heureux, I., and Regnier, P. (2011). Impact of Seasonal Temperature and Pressure Changes on Methane Gas Production, Dissolution, and Transport in Unfractured Sediments. *J. Geophys. Res.* 116 (G3). doi:10.1029/2010JG001592

Mogollón, J. M., L'Heureux, I., Dale, A. W., and Regnier, P. (2009). Methane Gas-phase Dynamics in marine Sediments: A Model Study. *Am. J. Sci.* 309 (3), 189–220. doi:10.2475/03.2009.01

Molins, S., Mayer, K. U., Amos, R. T., and Bekins, B. A. (2010). Vadose Zone Attenuation of Organic Compounds at a Crude Oil Spill Site - Interactions between Biogeochemical Reactions and Multicomponent Gas Transport. *J. Contaminant Hydrol.* 112 (1-4), 15–29. doi:10.1016/j.jconhyd.2009.09.002

Molins, S., and Mayer, K. U. (2007). Coupling Between Geochemical Reactions and Multicomponent Gas and Solute Transport in Unsaturated media: A Reactive Transport Modeling Study. *Water Resour. Res.* 43 (5), n/a. doi:10.1029/2006WR005206

Morton, B., Taylor, G. I., and Turner, J. S. (1956). Turbulent Gravitational Convection from Maintained and Instantaneous Sources. *Proc. R. Soc. Lond. A.* 234 (1196), 1–23. doi:10.1098/rspa.1956.0011

Mrazovac, S. M., Milan, P. R., Vojinovic-Miloradov, M. B., and Tosic, B. S. (2012). Dynamic Model of Methane-Water Diffusion. *Appl. Math. Model.* 36 (9), 3985–3991. doi:10.1016/j.apm.2011.11.009

Muller-Karger, F. E., Varela, R., Thunell, R., Luerssen, R., Hu, C., and Walsh, J. J. (2005). The Importance of continental Margins in the Global Carbon Cycle. *Geophys. Res. Lett.* 32 (1), L01602. doi:10.1029/2004GL021346

Murray, J. W., Grundmanis, V., and Smethie, W. M., Jr (1978). Interstitial Water Chemistry in the Sediments of Saanich Inlet. *Geochimica et Cosmochimica Acta.* 42 (7), 1011–1026. doi:10.1016/0016-7037(78)90290-9

Niemann, H., Lösekann, T., De Beer, D., Elvert, M., Nadalig, T., Knittel, K., et al. (2006). Novel Microbial Communities of the Haakon Mosby Mud Volcano and Their Role as a Methane Sink. *Nature.* 443 (7113), 854–858. doi:10.1038/nature05227

Nisbet, E. G., Manning, M. R., Dlugokencky, E. J., Fisher, R. E., Lowry, D., Michel, S. E., et al. (2019). Very Strong Atmospheric Methane Growth in the 4Years 2014–2017: Implications for the Paris Agreement. *Glob. Biogeochem. Cycles.* 33 (3), 318–342. doi:10.1029/2018GB006009

Nöthen, K., and Kasten, S. (2011). Reconstructing Changes in Seep Activity by Means of Pore Water and Solid Phase Sr/Ca and Mg/Ca Ratios in Pockmark Sediments of the Northern Congo Fan. *Mar. Geology.* 287 (1-4), 1–13. doi:10.1016/j.margeo.2011.06.008

Parkes, R. J., Wellsbury, P., Mather, I. D., Cobb, S. J., Cragg, B. A., Hornibrook, E. R. C., et al. (2007). Temperature Activation of Organic Matter and Minerals during Burial Has the Potential to Sustain the Deep Biosphere over Geological Timescales. *Org. Geochem.* 38 (6), 845–852. doi:10.1016/j.orggeochem.2006.12.011

Paull, C. K., Schlining, B., Ussler, W., III, Paduan, J. B., Caress, D., and Greene, H. G. (2005). Distribution of Chemosynthetic Biological Communities in Monterey Bay, California. *Geology* 33 (2), 85–88. doi:10.1130/G20927.1

Pavlov, A. A., Hurtgen, M. T., Kasting, J. F., and Arthur, M. A. (2003). Methane-Rich Proterozoic Atmosphere? *Geology* 31 (1), 87–90. doi:10.1130/0091-7613(2003)031<0087:mrpa>2.0.co;2

Piñero, E., Marquardt, M., Hensen, C., Haeckel, M., and Wallmann, K. (2013). Estimation of the Global Inventory of Methane Hydrates in marine Sediments Using Transfer Functions. *Biogeosciences* 10 (2), 959–975. doi:10.5194/bg-10-959-2013

Pop Ristova, P., Wenzhöfer, F., Ramette, A., Zabel, M., Fischer, D., Kasten, S., et al. (2012). Bacterial Diversity and Biogeochemistry of Different Chemosynthetic Habitats of the REGAB Cold Seep (West African Margin, 3160 M Water Depth). *Biogeosciences* 9 (12), 5031–5048. doi:10.5194/bg-9-5031-2012

Reagan, M. T., and Moridis, G. J. (2008). Dynamic Response of Oceanic Hydrate Deposits to Ocean Temperature Change. *J. Geophys. Res.* 113 (C12), C12023. doi:10.1029/2008JC004938

Reeburgh, W. S. (1976). Methane Consumption in Cariaco Trench Waters and Sediments. *Earth Planet. Sci. Lett.* 28 (3), 337–344. doi:10.1016/0012-821X(76)90195-3

Reeburgh, W. S. (2007). Oceanic Methane Biogeochemistry. *Chem. Rev.* 107, 486–513. doi:10.1021/cr050362v

Reeburgh, W. S., Ward, B. B., Whalen, S. C., Sandbeck, K. A., Kilpatrickt, K. A., and Kerkhof, L. J. (1991). Black Sea Methane Geochemistry. *Deep Sea Res. A. Oceanographic Res. Pap.* 38, S1189–S1210. doi:10.1016/S0198-0149(10)80030-5

Reed, D. L., Silver, E. A., Tagudin, J. E., Shipley, T. H., and Vrolijk, P. (1990). Relations between Mud Volcanoes, Thrust Deformation, Slope Sedimentation, and Gas Hydrate, Offshore north Panama. *Mar. Pet. Geology.* 7 (1), 44–54. doi:10.1016/0264-8172(90)90055-L

Regnier, P., Dale, A., Pallud, C., Van Lith, Y., Bonneville, S., Hyacinthe, C., et al. (2005). Incorporating Geomicrobial Processes in Subsurface Reactive Transport Models. *Reactive Transport Soil groundwater: Process. models*. Editors G. Nuetzmann, P. Viotti, and P. Agaard (Berlin: Springer-Verlag), 107–126.

Regnier, P., Dale, A. W., Arndt, S., LaRowe, D. E., Mogollón, J., and Van Cappellen, P. (2011). Quantitative Analysis of Anaerobic Oxidation of Methane (AOM) in Marine Sediments: A Modeling Perspective. *Earth-Science Rev.* 106 (1-2), 105–130. doi:10.1016/j.earscirev.2011.01.002

Rehder, G., Leifer, I., Brewer, P. G., Friederich, G., and Peltzer, E. T. (2009). Controls on Methane Bubble Dissolution Inside and outside the Hydrate Stability Field From Open Ocean Field Experiments and Numerical Modeling. *Mar. Chem.* 114 (1-2), 19–30. doi:10.1016/j.marchem.2009.03.004

Repeta, D. J., Ferrón, S., Sosa, O. A., Johnson, C. G., Repeta, L. D., Acker, M., et al. (2016). Marine Methane Paradox Explained by Bacterial Degradation of Dissolved Organic Matter. *Nat. Geosci.* 9 (12), 884–887. doi:10.1038/ngeo2837

Riedel, M., Scherwath, M., Römer, M., Veloso, M., Heesemann, M., and Spence, G. D. (2018). Distributed Natural Gas Venting Offshore along the Cascadia Margin. *Nat. Commun.* 9 (1), 3264–3314. doi:10.1038/s41467-018-05736-x

Römer, M., Hsu, C.-W., Loher, M., MacDonald, I. R., dos Santos Ferreira, C., Pape, T., et al. (2019). Amount and Fate of Gas and Oil Discharged at 3400 M Water Depth from a Natural Seep Site in the Southern Gulf of Mexico. *Front. Mar. Sci.* 6, 700. doi:10.3389/fmars.2019.00700

Römer, M., Sahling, H., dos Santos Ferreira, C., and Bohrmann, G. (2020). Methane Gas Emissions of the Black Sea-Mapping from the Crimean continental Margin to the Kerch Peninsula Slope. *Geo-mar Lett.* 40 (4), 467–480. doi:10.1007/s00367-019-00611-0

Römer, M., Sahling, H., Pape, T., Bahr, A., Feseker, T., Wintersteller, P., et al. (2012). Geological Control and Magnitude of Methane Ebullition from a High-Flux Seep Area in the Black Sea-The Kerch Seep Area. *Mar. Geology.* 319-322, 57–74. doi:10.1016/j.margeo.2012.07.005

Römer, M., Sahling, H., Pape, T., dos Santos Ferreira, C., Wenzhöfer, F., Boetius, A., et al. (2014). Methane Fluxes and Carbonate Deposits at a Cold Seep Area of the Central Nile Deep Sea Fan, Eastern Mediterranean Sea. *Mar. Geology.* 347, 27–42. doi:10.1016/j.margeo.2013.10.011

Römer, M., Wenau, S., Mau, S., Veloso, M., Greinert, J., Schlüter, M., et al. (2017). Assessing marine Gas Emission Activity and Contribution to the Atmospheric Methane Inventory: A Multidisciplinary Approach from the Dutch Dogger

Bank Seep Area (North Sea). *Geochem. Geophys. Geosyst.* 18 (7), 2617–2633. doi:10.1002/2017GC006995

Ruppel, C. D., and Kessler, J. D. (2017). The Interaction of Climate Change and Methane Hydrates. *Rev. Geophys.* 55 (1), 126–168. doi:10.1002/2016RG000534

Sahling, H., Bohrmann, G., Spiess, V., Bialas, J., Breitzke, M., Ivanov, M., et al. (2008). Pockmarks in the Northern Congo Fan Area, SW Africa: Complex Seafloor Features Shaped by Fluid Flow. *Mar. Geology.* 249 (3-4), 206–225. doi:10.1016/j.margeo.2007.11.010

Saito, H., and Suzuki, N. (2007). Terrestrial Organic Matter Controlling Gas Hydrate Formation in the Nankai Trough Accretionary Prism, Offshore Shikoku, Japan. *J. Geochemical Exploration.* 95 (1-3), 88–100. doi:10.1016/j.gexplo.2007.05.007

Sakai, H., Gamo, T., Kim, E.-S., Tsutsumi, M., Tanaka, T., Ishibashi, J., et al. (1990). Venting of Carbon Dioxide-Rich Fluid and Hydrate Formation in Mid-Okinawa Trough Backarc Basin. *Science* 248 (4959), 1093–1096. doi:10.1126/science.248.4959.1093

Saunois, M., Bousquet, P., Poulter, B., Peregon, A., Ciais, P., Canadell, J. G., et al. (2016a). The Global Methane Budget 2000–2012. *Earth Syst. Sci. Data.* 8 (2), 697–751. doi:10.5194/essd-8-697-2016

Saunois, M., Jackson, R. B., Bousquet, P., Poulter, B., and Canadell, J. G. (2016b). The Growing Role of Methane in Anthropogenic Climate Change. *Environ. Res. Lett.* 11, 120207. doi:10.1088/1748-9326/11/12/120207

Schmaljohann, R. (1996). Methane Dynamics in the Sediment and Water Column of Kiel Harbour (Baltic Sea). *Mar. Ecol. Prog. Ser.* 131, 263–273. doi:10.3354/meps131263

Schmidt, M., Hensen, C., Mörz, T., Müller, C., Grevemeyer, I., Wallmann, K., et al. (2005). Methane Hydrate Accumulation in "Mound 11" Mud Volcano, Costa Rica Forearc. *Mar. Geology.* 216 (1-2), 83–100. doi:10.1016/j.margeo.2005.01.001

Scholl, D., and Hart, P. (1993). Velocity and Amplitude Structures on Seismic-Reflection Profiles-Possibly Massive Gas-Hydrate Deposits and Underlying Gas Accumulations in the Bering Sea Basin. *The future of energy gases: U. S. Geological Survey Professional Paper*. Editors D. G. Howell 1570, 331–352.

Schulz, H. D., and Zabel, M. (2006). *Marine Geochemistry*. Berlin: Springer.

Schowalter, T. T. (1979). Mechanics of Secondary Hydrocarbon Migration and Entrapment. *Bulletin.* 63 (5), 723–760. doi:10.1306/2F9182CA-16CE-11D7-8645000102C1865D

Seelig, H. D., Hoehn, A., Stodieck, L. S., Klaus, D. M., Adams, W. W., Iii, and Emery, W. J. (2008). The Assessment of Leaf Water Content Using Leaf Reflectance Ratios in the Visible, Near-, and Short-wave-infrared. *Int. J. Remote Sensing* 29 (13), 3701–3713. doi:10.1080/01431160701772500

Seiter, K., Hensen, C., Schröter, J., and Zabel, M. (2004). Organic Carbon Content in Surface Sediments-Defining Regional Provinces. *Deep Sea Res. Part Oceanographic Res. Pap.* 51 (12), 2001–2026. doi:10.1016/j.dsr.2004.06.014

Shagapov, V. S., Chiglintseva, A. S., Rusinov, A. A., and Tazetdinov, B. I. (2017). Migration of a Single Gas Bubble in Water during the Formation of Stable Gas-Hydrate Crust on its Surface. *Theor. Found. Chem. Eng.* 51 (2), 216–223. doi:10.1134/s0040579517020075

Shakhova, N., Semiletov, I., Leifer, I., Sergienko, V., Salyuk, A., Kosmach, D., et al. (2014). Ebullition and Storm-Induced Methane Release from the East Siberian Arctic Shelf. *Nat. Geosci* 7, 64–70. doi:10.1038/ngeo2007

Shakhova, N., Semiletov, I., Salyuk, A., Yusupov, V., Kosmach, D., and Gustafsson, Ö. (2010). Extensive Methane Venting to the Atmosphere from Sediments of the East Siberian Arctic Shelf. *Science* 327 (5970), 1246–1250. doi:10.1126/science.1182221

Shoji, H., Minami, H., Hachikubo, A., Sakagami, H., Hyakutake, K., Soloviev, V., et al. (2005). Hydrate-Bearing Structures in the Sea of Okhotsk. *Eos Trans. AGU* 86 (2), 13–18. doi:10.1029/2005EO020001

Sivan, O., Adler, M., Pearson, A., Gelman, F., Bar-Or, I., John, S. G., et al. (2011). Geochemical Evidence for Iron-Mediated Anaerobic Oxidation of Methane. *Limnol. Oceanogr.* 56 (4), 1536–1544. doi:10.4319/lo.2011.56.4.1536

Sivan, O., Schrag, D. P., and Murray, R. W. (2007). Rates of Methanogenesis and Methanotrophy in Deep-Sea Sediments. *Geobiology* 5 (2), 141–151. doi:10.1111/j.1472-4669.2007.00098.x

Skarke, A., Ruppel, C., Kodis, M., Brothers, D., and Lobecker, E. (2014). Widespread Methane Leakage from the Sea Floor on the Northern US Atlantic Margin. *Nat. Geosci.* 7 (9), 657–661. doi:10.1038/ngeo2232

Solomon, E. A., Kastner, M., MacDonald, I. R., and Leifer, I. (2009). Considerable Methane Fluxes to the Atmosphere from Hydrocarbon Seeps in the Gulf of Mexico. *Nat. Geosci.* 2, 561–565. doi:10.1038/ngeo574

Sommer, S., Linke, P., Pfannkuche, O., Niemann, H., and Treude, T. (2010). Benthic Respiration in a Seep Habitat Dominated by Dense Beds of Ampharetid Polychaetes at the Hikurangi Margin (New Zealand). *Mar. Geology.* 272 (1-4), 223–232. doi:10.1016/j.margeo.2009.06.003

Sommer, S., Linke, P., Pfannkuche, O., Schleicher, T., Schneider, D., Reitz, A., et al. (2009). Seabed Methane Emissions and the Habitat of Frenulate Tubeworms on the Captain Arutyunov Mud Volcano (Gulf of Cadiz). *Mar. Ecol. Prog. Ser.* 382, 69–86. doi:10.3354/meps07956

Sommer, S., Pfannkuche, O., Linke, P., Luff, R., Greinert, J., Drews, M., et al. (2006a). Efficiency of the Benthic Filter: Biological Control of the Emission of Dissolved Methane from Sediments Containing Shallow Gas Hydrates at Hydrate Ridge. *Glob. Biogeochem. Cycles* 20, a–n. doi:10.1029/2004GB002389

Sommer, S., Pfannkuche, O., Linke, P., Luff, R., Greinert, J., Drews, M., et al. (2006b). Efficiency of the Benthic Filter: Biological Control of the Emission of Dissolved Methane from Sediments Containing Shallow Gas Hydrates at Hydrate Ridge. *Glob. Biogeochem. Cycles.* 20 (2), GB2019. doi:10.1029/2004gb002389

Sommer, S., Türk, M., Kriwanek, S., and Pfannkuche, O. (2008). Gas Exchange System for Extended *In Situ* Benthic Chamber Flux Measurements Under Controlled Oxygen Conditions: First Application-Sea Bed Methane Emission Measurements at Captain Arutyunov Mud Volcano. *Limnol. Oceanogr. Methods.* 6 (1), 23–33. doi:10.4319/lom.2008.6.23

Somov, A., Baranov, A., Spirjakin, D., Spirjakin, A., Sleptsov, V., and Passerone, R. (2013). Deployment and Evaluation of a Wireless Sensor Network for Methane Leak Detection. *Sensors Actuators A: Phys.* 202, 217–225. doi:10.1016/j.sna.2012.11.047

Steinle, L., Graves, C. A., Treude, T., Ferré, B., Biastoch, A., Bussmann, I., et al. (2015). Water Column Methanotrophy Controlled by a Rapid Oceanographic Switch. *Nat. Geosci.* 8 (5), 378–382. doi:10.1038/ngeo2420

Stoll, H. M., and Bains, S. (2003). Coccolith Sr/Ca Records of Productivity during the Paleocene-Eocene thermal Maximum from the Weddell Sea. *Paleoceanography* 18 (2), a–n. doi:10.1029/2002PA000875

Suess, E., Torres, M., Bohrmann, G., Collier, R., Greinert, J., Linke, P., et al. (1999). Gas Hydrate Destabilization: Enhanced Dewatering, Benthic Material Turnover and Large Methane Plumes at the Cascadia Convergent Margin. *Earth Planet. Sci. Lett.* 170 (1-2), 1–15. doi:10.1016/S0012-821X(99)00092-8

Thomsen, T. R., Finster, K., and Ramsing, N. B. (2001). Biogeochemical and Molecular Signatures of Anaerobic Methane Oxidation in a marine Sediment. *Appl. Environ. Microbiol.* 67 (4), 1646–1656. doi:10.1128/AEM.67.4.1646-1656.2001

Torres, M. E., McManus, J., Hammond, D., De Angelis, M., Heeschen, K., Colbert, S., et al. (2002). Fluid and Chemical Fluxes in and Out of Sediments Hosting Methane Hydrate Deposits on Hydrate Ridge, OR, I: Hydrological Provinces. *Earth Planet. Sci. Lett.* 201 (3-4), 525–540. doi:10.1016/S0012-821X(02)00733-1

Tréhu, A. M., Flemings, P. B., Bangs, N. L., Chevallier, J., Gràcia, E., Johnson, J. E., et al. (2004). Feeding Methane Vents and Gas Hydrate Deposits at South Hydrate Ridge. *Geophys. Res. Lett.* 31 (23). doi:10.1029/2004GL021286

Treude, T., Boetius, A., Knittel, K., Wallmann, K., and Barker Jørgensen, B. (2003). Anaerobic Oxidation of Methane above Gas Hydrates at Hydrate Ridge, NE Pacific Ocean. *Mar. Ecol. Prog. Ser.* 264, 1–14. doi:10.3354/meps264001

Tromp, T. K., Van Cappellen, P., and Key, R. M. (1995). A Global Model for the Early Diagenesis of Organic Carbon and Organic Phosphorus in Marine Sediments. *Geochimica et Cosmochimica Acta.* 59 (7), 1259–1284. doi:10.1016/0016-7037(95)00042-X

Ussler, W., III, and Paull, C. K. (2008). Rates of Anaerobic Oxidation of Methane and Authigenic Carbonate Mineralization in Methane-Rich Deep-Sea Sediments Inferred from Models and Geochemical Profiles. *Earth Planet. Sci. Lett.* 266 (3-4), 271–287. doi:10.1016/j.epsl.2007.10.056

Valentine, D. L., Kessler, J. D., Redmond, M. C., Mendes, S. D., Heintz, M. B., Farwell, C., et al. (2010). Propane Respiration Jump-Starts Microbial Response to a Deep Oil Spill. *Science* 330 (6001), 208–211. doi:10.1126/science.1196830

Van Cappellen, P., and Gaillard, J.-F. (1996). Biogeochemical Dynamics in Aquatic Sediments. *Biogeochem. Dyn. Aquat. sediments. Reactive transport porous media.*, 335–376. doi:10.1515/9781501509797-011

Van Rensbergen, P., De Batist, M., Klerkx, J., Hus, R., Poort, J., Vanneste, M., et al. (2002). Sublacustrine Mud Volcanoes and Methane Seeps Caused by Dissociation of Gas Hydrates in Lake Baikal. *Geology* 30 (7), 631–634. doi:10.1130/0091-7613(2002)030<0631:smvams>2.0.co;2

van Kessel, T. G., Ramachandran, M., Klein, L. J., Nair, D., Hinds, N., Hamann, H., et al. (2018). Methane Leak Detection and Localization Using Wireless Sensor Networks for Remote Oil and Gas Operations. *IEEE SENSORS*, 1–4. doi:10.1109/icsens.2018.8589585

Veloso-Alarcón, M. E., Jansson, P., De Batist, M., Minshull, T. A., Westbrook, G. K., Pälike, H., et al. (2019). Variability of Acoustically Evidenced Methane Bubble Emissions Offshore Western Svalbard. *Geophys. Res. Lett.* 46 (15), 9072–9081. doi:10.1029/2019GL082750

von Deimling, J. S., Rehder, G., Greinert, J., McGinnnis, D. F., Boetius, A., and Linke, P. (2011). Quantification of Seep-Related Methane Gas Emissions at Tommeliten, North Sea. *Continental Shelf Res.* 31 (7-8), 867–878. doi:10.1016/j.csr.2011.02.012

Waage, M., Portnov, A., Serov, P., Bünz, S., Waghorn, K. A., Vadakkepuliyambatta, S., et al. (2019). Geological Controls on Fluid Flow and Gas Hydrate Pingo Development on the Barents Sea Margin. *Geochem. Geophys. Geosyst.* 20 (2), 630–650. doi:10.1029/2018GC007930

Wadham, J. L., Arndt, S., Tulaczyk, S., Stibal, M., Tranter, M., Telling, J., et al. (2012). Potential Methane Reservoirs beneath Antarctica. *Nature* 488, 633–637. doi:10.1038/nature11374

Wallmann, K., Aloisi, G., Haeckel, M., Obzhirov, A., Pavlova, G., and Tishchenko, P. (2006a). Kinetics of Organic Matter Degradation, Microbial Methane Generation, and Gas Hydrate Formation in Anoxic Marine Sediments. *Geochimica et Cosmochimica Acta* 70, 3905–3927. doi:10.1016/j.gca.2006.06.003

Wallmann, K., Drews, M., Aloisi, G., and Bohrmann, G. (2006b). Methane Discharge Into the Black Sea and the Global Ocean via Fluid Flow through Submarine Mud Volcanoes. *Earth Planet. Sci. Lett.* 248 (1-2), 545–560. doi:10.1016/j.epsl.2006.06.026

Wallmann, K., Drews, M., Aloisi, G., and Bohrmann, G. (2006c). Methane Discharge into the Black Sea and the Global Ocean via Fluid Flow Through Submarine Mud Volcanoes. *Earth Planet. Sci. Lett.* 248, 545–560. doi:10.1016/j.epsl.2006.06.026

Wallmann, K., Pinero, E., Burwicz, E., Haeckel, M., Hensen, C., Dale, A., et al. (2012). The Global Inventory of Methane Hydrate in Marine Sediments: A Theoretical Approach. *Energies* 5 (7), 2449–2498. doi:10.3390/en5072449

Wanninkhof, R. (1992). Relationship between Wind Speed and Gas Exchange Over the Ocean. *J. Geophys. Res.* 97 (C5), 7373–7382. doi:10.1029/92JC00188

Weber, T. C., Mayer, L., Jerram, K., Beaudoin, J., Rzhanov, Y., and Lovalvo, D. (2014). Acoustic Estimates of Methane Gas Flux from the Seabed in a 6000 Km^2 region in the Northern Gulf of Mexico. *Geochem. Geophys. Geosyst.* 15 (5), 1911–1925. doi:10.1002/2014GC005271

Wehrmann, L. M., Arndt, S., März, C., Ferdelman, T. G., and Brunner, B. (2013). The Evolution of Early Diagenetic Signals in Bering Sea Subseafloor Sediments in Response to Varying Organic Carbon Deposition over the Last 4.3Ma. *Geochimica et Cosmochimica Acta.* 109, 175–196. doi:10.1016/j.gca.2013.01.025

Wei, J., Wu, T., Deng, X., Haider, S. W., Kahkashan, S., and Yang, S. (2021). Seafloor Methane Emission on the Makran continental Margin. *Sci. Total Environ.* 801, 149772. doi:10.1016/j.scitotenv.2021.149772

White, R. S. (1979). Gas Hydrate Layers Trapping Free Gas in the Gulf of Oman. *Earth Planet. Sci. Lett.* 42 (1), 114–120. doi:10.1016/0012-821X(79)90196-1

Whiticar, M. J. (1999). Carbon and Hydrogen Isotope Systematics of Bacterial Formation and Oxidation of Methane. *Chem. Geology.* 161 (1-3), 291–314. doi:10.1016/S0009-2541(99)00092-3

Xu, W., and Germanovich, L. N. (2006). Excess Pore Pressure Resulting from Methane Hydrate Dissociation in marine Sediments: A Theoretical Approach. *J. Geophys. Res.* 111 (B1), 111. doi:10.1029/2004JB003600

Yamamoto, S., Alcauskas, J. B., and Crozier, T. E. (1976). Solubility of Methane in Distilled Water and Seawater. *J. Chem. Eng. Data.* 21 (1), 78–80. doi:10.1021/je60068a029

Yamazaki, T., Nakano, Y., Monoe, D., Oomi, T., Nakata, K., and Fukushima, T. (2006). "A Model Analysis of Methane Plume Behavior in an Ocean Water Column," in The Sixteenth International Offshore and Polar Engineering Conference: OnePetro).

Yun, T. S., Lee, C., Lee, J.-S., Bahk, J. J., and Santamarina, J. C. (2011). A Pressure Core Based Characterization of Hydrate-Bearing Sediments in the Ulleung Basin, Sea of Japan (East Sea). *J. Geophys. Res.* 116 (B2), B02204. doi:10.1029/2010JB007468

Zabel, M., and Schulz, H. D. (2001). Importance of Submarine Landslides for Non-steady State Conditions in Pore Water Systems—Lower Zaire (Congo) Deep-Sea Fan. *Mar. Geology.* 176 (1-4), 87–99. doi:10.1016/S0025-3227(01)00164-5

Zeebe, R. E. (2007). Modeling CO_2 Chemistry, $\delta^{13}C$, and Oxidation of Organic Carbon and Methane in Sediment Porewater: Implications for Paleo-Proxies in Benthic Foraminifera. *Geochimica et Cosmochimica Acta.* 71 (13), 3238–3256. doi:10.1016/j.gca.2007.05.004

Zhang, X., Du, Z., Luan, Z., Wang, X., Xi, S., Wang, B., et al. (2017). *In Situ* Raman Detection of Gas Hydrates Exposed on the Seafloor of the South China Sea. *Geochem. Geophys. Geosyst.* 18 (10), 3700–3713. doi:10.1002/2017GC006987

Conflict of Interest: The authors declare that the research was conducted in the absence of any commercial or financial relationships that could be construed as a potential conflict of interest.

frontiers | Frontiers in Marine Science

ORIGINAL RESEARCH
published: 13 July 2022
doi: 10.3389/fmars.2022.944841

Impact of High Methane Flux on the Properties of Pore Fluid and Methane-Derived Authigenic Carbonate in the ARAON Mounds, Chukchi Sea

Ji-Hoon Kim[1*], Myong-Ho Park[2], Dong-Hun Lee[3], Hirotsugu Minami[4], Young-Keun Jin[5], Akihiro Hachikubo[4], Jin Hur[6], Jong-Sik Ryu[7], Moo-Hee Kang[1], Kwangchul Jang[8], Masato Kida[4], Yongwon Seo[9], Meilian Chen[10], Jong Kuk Hong[5], Yungoo Song[11] and Sanghee Park[12]

[1] Marine Geology and Energy Division, Korea Institute of Geoscience and Mineral Resources, Daejeon, South Korea, [2] CCS Research Center, Kongju National University, Gongju, South Korea, [3] Marine Environment Research Division, National Institute of Fisheries Science, Busan, South Korea, [4] Environmental and Energy Resources Research Center, Kitami Institute of Technology, Kitami, Japan, [5] Division of Earth Sciences, Korea Polar Research Institute, Incheon, South Korea, [6] Department of Environment and Energy, Sejong University, Seoul, South Korea, [7] Department of Earth and Environmental Sciences, Pukyong National University, Busan, South Korea, [8] Division of Glacier Environment Research, Korea Polar Research Institute, Incheon, South Korea, [9] Department of Urban and Environmental Engineering, Ulsan National Institute of Science and Technology, Ulsan, South Korea, [10] Environmental Program, Guangdong Technion - Israel Institute of Technology, Shantou, China, [11] Department of Earth System Sciences, Yonsei University, Seoul, South Korea, [12] Division of Earth and Environment Sciences, Korea Basic Science Institute, Cheonju, South Korea

OPEN ACCESS

Edited by:
*Jörn Peckmann,
University of Hamburg,
Germany*

Reviewed by:
*Niu Li,
South China Sea Institute of
Oceanology (CAS), China
Claudio Argentino,
UiT The Arctic University
of Norway, Norway*

***Correspondence:**
*Ji-Hoon Kim
save@kigam.re.kr*

Specialty section:
*This article was submitted to
Marine Biogeochemistry,
a section of the journal
Frontiers in Marine Science*

Received: *15 May 2022*
Accepted: *07 June 2022*
Published: *13 July 2022*

Citation:
*Kim J-H, Park M-H, Lee D-H,
Minami H, Jin Y-K, Hachikubo A,
Hur J, Ryu J-S, Kang M-H, Jang K,
Kida M, Seo Y, Chen M, Hong JK,
Song Y and Park S (2022) Impact of
High Methane Flux on the Properties
of Pore Fluid and Methane-Derived
Authigenic Carbonate in the ARAON
Mounds, Chukchi Sea.
Front. Mar. Sci. 9:944841.
doi: 10.3389/fmars.2022.944841*

We investigated the pore fluid and methane-derived authigenic carbonate (MDAC) chemistry from the ARAON Mounds in the Chukchi Sea to reveal how methane (CH_4) seepage impacts their compositional and isotopic properties. During the ARA07C and ARA09C Expeditions, many *in situ* gas hydrates (GHs) and MDACs were found near the seafloor. The fluid chemistry has been considerably modified in association with the high CH_4 flux and its related byproducts (GHs and MDACs). Compared to Site ARA09C-St 08 (reference site), which displays a linear SO_4^{2-} downcore profile, the other sites (e.g., ARA07C-St 13, ARA07C-St 14, ARA09C-St 04, ARA09C-St 07, and ARA09C-St 12) that are found byproducts exhibit concave-up and/or kink type SO_4^{2-} profiles. The physical properties and fluid pathways in sediment columns have been altered by these byproducts, which prevents the steady state condition of the dissolved species through them. Consequently, chemical zones are separated between bearing and non-bearing byproducts intervals under non-steady state condition from the seafloor to the sulfate-methane transition (SMT). GH dissociation also significantly impacts pore fluid properties (e.g., low Cl^-, enriched δD and $\delta^{18}O$). The upward CH_4 with depleted $\delta^{13}C$ from the thermogenic origin affects the chemical signatures of MDACs. The enriched $\delta^{18}O$ fluid from GH dissociation also influences the properties of MDACs. Thus, in the ARAON Mounds, the chemistry of the fluid and MDAC has significantly changed, most likely responding to the CH_4 flux and GH dissociation through geological time. Overall, our findings will improve the understanding and prediction of the pore fluid and MDAC chemistry in the Arctic Ocean related to CH_4 seepage by global climate change.

Keywords: pore fluid, methane flux, gas hydrate, MDAC, ARAON Mounds

INTRODUCTION

Methane (CH_4) seepages (cold seeps) migrating from deep sediment to the seafloor have widely occurred along continental margins (Campbell, 2006; Judd and Hovland, 2007; Suess, 2014 and references therein). However, most of the CH_4 released by this mechanism is consumed in the sediments and/or in the water column before reaching the atmosphere (Boetius et al., 2000; Boetius and Wenzhöfer, 2013). Nevertheless, it has been reported that an annual approximately 0.4-12.2 Tg CH_4 is discharged into the water column by the methane seepage (Judd et al., 2002), which can provide enough CH_4 to form gas hydrates (GHs) and carbonates on the seafloor and to change seafloor morphology. As a result, methane seepages contribute to the global carbon cycles as well as marine geology and (bio)geochemistry.

Recently, the cryosphere extent (e.g., ice sheet, permafrost, and glaciers) in Arctic regions has been continuously reduced due to rapid temperature increases compared to those in other regions. Therefore, numerous methane releases related to submarine permafrost and GH degradation have been reported in the Arctic regions, e.g., the Eastern Siberian Arctic Shelf, offshore Svalbard, and the Chukchi Sea (Shakhova et al., 2005; Westbrook et al., 2009; Shakhova et al., 2010; Hong et al., 2017). The shrinkage of the cryosphere extent is expected to accelerate continuously in the future, releasing a large amount of CH_4. This CH_4 released from the sediment column will play a critical positive feedback role in global warming, marine geology, (bio)geochemistry, and microbial activities, linked to the ebullition of gas transport (Schuur et al., 2015; Argentino et al., 2021; Kim et al., 2021a; Lee et al., 2021; Sauer et al., 2021).

Elevated bathymetric features from a few meters to kilometers in diameter, simply called mounds, have been observed on the seafloor (e.g., Chapman et al., 2004; Bahr et al., 2007; Buerk et al., 2010; Römer et al., 2014; Koch et al., 2015). These structures are prominent conduits for the transport of deep hydrocarbons to the seafloor, where many seafloor gas vents and GHs are observed (Paull et al., 2008; Römer et al., 2014; Hong et al., 2017; Waage et al., 2019). During the ARA07C Expedition, many GHs were found on the seafloor of the ARAON Mounds (water depth of ~600 m) located in the Chukchi Sea (Kim et al., 2020; Choi et al., 2021). Kim et al. (2020) revealed that the CH_4 in GHs primarily originates from deep thermogenic gas, which is upwardly transported to the seafloor through fractures and/or faults in this mound and influences the compositional and isotopic properties of the gases differently between GH-bearing and non-GH bearing sediments. The CH_4 that migrates to the seafloor can be oxidized by microbes, either aerobically near the sediment-water interface, or anaerobically in the subsurface (Barnes and Goldberg, 1976; Reeburgh, 1976), which can alter the (geo/bio) chemical properties of pore fluid and microbial activities. In particular, the anaerobic oxidation of methane (AOM) in the sulfate-methane transition (SMT) increases dissolved sulfide and alkalinity in pore fluid, which in turn provides energy for chemosynthetic symbionts (Paull et al., 1984; Sibuet and Olu, 1998; Sahling et al., 2002) and precipitates methane-derived authigenic carbonates (MDACs), respectively (Aloisi et al., 2000; Luff et al., 2004; Bayon et al., 2009; Himmler et al., 2011; Himmler et al., 2015). Indeed, many *in situ* MDACs have been observed in the ARAON Mounds during the ARA07C Expedition (Jin and Shipboard Scientific Party, 2017; Kim et al., 2020). Consequently, gas seepage and its associated byproducts (i.e., GH and MDAC) can remarkably alter the pore fluid chemistry in the ARAON Mounds. However, to date, the fluid chemistry associated with these mounds has not been investigated. As a result, it is not clear how gas seepage and its associated byproducts impact regional hydrology, alter the chemical properties of pore fluids, and interact with pore fluids under current and past global climate changes.

Here, we investigate two questions to decipher the pore fluid chemistry in the ARAON Mounds: 1) how methane seepage from deep-seated sediment impacts the fluid properties and 2) how GHs and MDACs interact with pore fluid. In addition, no data exist on the chemical and biomarker signatures of MDACs found at the ARAON Mounds. To unravel these questions, we first investigate the compositional and isotopic properties of pore fluid and MDAC from three sampling site groups in the ARAON Mounds: 1) a reference site (ARA09C-St 08) without methane seepage, 2) GH bearing sites (ARA07C-St 13, ARA09C-St 06, ARA09C-St 16), and 3) non-GH bearing sites (ARA07C-St 14, ARA09C-St 04, ARA09C-St 07, and ARA09C-St 12) with methane seepage (**Figure 1**). Our findings will improve the understanding and prediction of fluid and MDAC chemistry linked with methane seepage from deep-seated sediments to the seafloor in the Arctic Ocean.

REGIONAL SETTINGS

The Chukchi Sea extends from 66°N in the south to the edge of the Arctic Basin in the north, covering an area of 620,000 km² (Jakobsson, 2002). In this sea, the Chukchi Shelf encompasses a shallow continental margin north of Chukotka and Alaska is less than 50 m depth in the south, to 450-750 m depth at the shelf break around the northward extension known as the Chukchi Rise. The Chukchi Borderland is an adjacent fragment of continental crust extending north into the Canada Basin of the Arctic Ocean (Grantz et al., 1998), which incorporates the Northwind Ridge and the Chukchi Plateau (**Figure 1**).

The study area, the ARAON Mounds, has a relatively gentle slope (approximately 2°) with a > 3 km wide terrace, as shown in the multibeam data, and eight mound structures have been observed along the edge of the terrace between water depths of 568 m to 704 m by the sub-bottom profiler (SBP) image (**Figure 1**) Jin and Shipboard Scientific Party, 2017; Jin and Shipboard Scientific Party, 2019). These mounds are named ARAON Mound 01 to 08 (AM01 to AM08) from northwest to southeast, and they are approximately 10 m higher than the surrounding seafloor with 200-700 m in diameter (**Figure 1**). In addition, the SBP image shows that the acoustic facies,

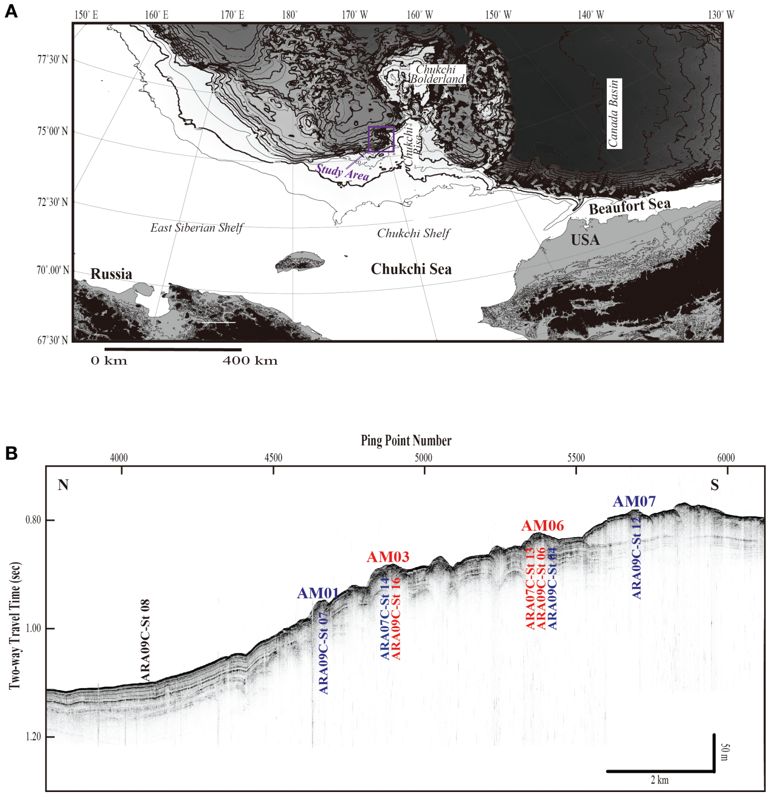

FIGURE 1 | (A) Major physiographic features and locations of the study area during the ARA07C and ARA09C Expeditions. **(B)** Sub-bottom profile (SBP) images of the ARAON Mounds (AMs) surveyed during the ARA09C Expedition. Black color site: reference site without GHs and MDACs, blue color sites: observation of MDACs, and red color sites: observation of GHs and MDACs.

stratigraphy, and structure of the subsurface are different at each mound (**Figure 1**) because of the different behavior of thick transparent facies interbedded in the stratified facies (Jin and Shipboard Scientific Party, 2017; Jin and Shipboard Scientific Party, 2019; Kim et al., 2021b). In terms of acoustic characteristics and tectonic views, the ARAON Mounds seem to form in association with basin bounding-faults by prolonged seepage and to be active at this stage (Kim et al., 2021b).

MATERIALS AND METHODS

Fluid and MDAC Sampling

Two gravity cores (GCs; ARA07C-St 13 and ARA07C-St 14) and five GCs (ARA09C-St 04, ARA09C-St 06, ARA09C-St 07, ARA09C-St 12, and ARA09C-St 16) were collected from the ARAON Mounds during the ARA07C Expedition in 2016 and the ARA09C Expedition in 2018 onboard Ice-Breaking Research Vessel (*IBRV*) ARAON, respectively. In addition, one GC was sampled at Site ARA09C-St 08 as a reference site. The retrieved core length of all GCs is less than 6 m (**Figure 1**; **Table 1**).

Pore fluid was extracted by Rhizons in whole round cores or split cores in ~10-60 cm intervals at room temperature on the *IBRV* ARAON. Extracted pore fluid was collected in acid-prewashed syringes equipped with an in-line 0.20 μm disposable polytetrafluoroethylene filter. The bottom seawater was also collected from Site ARA09C-St 04 (**Table 1**) using a CTD/rosette system that holds 12-5L Niskin bottles (Seabird 911 Plus). Fluid subsamples for shipboard and anion analyses were collected in acid-prewashed high-density polyethylene (HDPE) bottles. Fluid aliquots for cation and $^{87}Sr/^{86}Sr$ isotope ratios analyses were transferred into acid-prewashed HDPE bottles (~2-4 ml) and acidified with 20 μl ultrapure grade HNO_3. Subsamples for stable isotopic properties of water (δD and $\delta^{18}O$) and dissolved inorganic carbon ($\delta^{13}C_{DIC}$) were collected in 2 ml septum screw-lid glass vials. Fluid samples for $\delta^{13}C_{DIC}$ analysis were preserved with 30 μl $HgCl_2$. Pore fluid and seawater samples were stored at approximately 4°C in the refrigerator until the analyses.

Gas hydrates from Sites ARA07C-St 13, ARA09C-St 06, and ARA09C-St 16 were carefully scraped to minimize any contamination that may have occurred during the earlier handling and were dissociated in clean 20 ml glass beakers at room temperature on the *IBRV* ARAON. The aliquots of these fluids (hydrate-bound waters) for the analyses of compositional and isotopic properties were collected using the same techniques as described above for pore fluid

TABLE 1 | Summaries of location, water depth, core length, and SMT depth in each site from the ARA07C and ARA09C Expeditions.

Sample Type	ARAON Mound No	Site	Latitude (°N)	Longitude (°W)	Water Depth (m)	Core Length (m)	SMT Depth (mbsf)	Remark
Pore Fluid	Background	ARA09C-St 08	75.7397	169.8545	813	5.29	not reach	Not find GHs and MDACs
	AM01	ARA09C-St 07	75.7120	169.7947	699	4.51	~3.3	Find MDACs
	AM03	ARA07C-St 14	75.7034	169.7592	653	1.67	~0.9	Find MDACs
		ARA09C-St 16	75.7034	169.7608	662	2.60	< 0.5	Find GHs/MDACs
	AM06	ARA07C-St 13	75.6800	169.7365	610	2.35	~1.3	Find GHs/MDACs
		ARA09C-St 04	75.6799	169.7368	605	2.64	1.2	Find MDACs
		ARA09C-St 06	75.6807	169.7366	609	2.57	< 0.5	Find GHs/MDACs
	AM07	ARA09C-St 12	75.6637	169.7410	582	2.64	~2.1	Find MDACs
Seawater	AM06	ARA09C-St 04	75.6799	169.7367	605	–	–	Bottom water depth: 600 m

-, no data.
MDAC, methane-derived authigenic carbonate; GH, gas hydrate.

and seawater, and then stored at approximately 4°C in the refrigerator until the analyses.

Methane-derived authigenic carbonates were distributed from ~0.2 to ~2.2 meters below the seafloor (mbsf) in the cores during the ARA07C and ARA09C Expeditions (**Table 2**). Some MDACs were observed with several cm-thickness in the split cores (Jin and Shipboard Scientific Party, 2017; Jin and Shipboard Scientific Party, 2019). MDACs were hand-picked in the split cores and collected in plastic bags during these expeditions (**Figure 2**). These samples were stored at approximately 4°C in the refrigerator until the analyses.

Fluid Analyses

The chlorinity (Cl^-) and alkalinity of the pore fluid, hydrate-bound water, and seawater were measured onboard during the ARA07C and ARA09C Expeditions. The Cl^- concentration was measured *via* titration with 0.1 M silver nitrate ($AgNO_3$) and the alkalinity was determined immediately by titration with 0.02 M HCl. The reproducibilities of Cl^- and alkalinity by repeated analyses of the International Association of Physical Sciences of the Oceans (IAPSO) standard seawater were < 2% and < 0.5%, respectively. Sulfate (SO_4^{2-}) in pore fluid and hydrate-bound water from the ARA07C Expedition and the bottom seawater from Site ARA09C-St 04 was analyzed by ion chromatography (IC) at the Korea Basic Science Institute (KBSI; Dionex ICS-1100, Thermo Scientific). IAPSO standard seawater was repeatedly used to verify the analytical quality of the instruments, and the analytical reproducibility was better than 3%. In addition, SO_4^{2-} in pore fluid and hydrate-bound water collected from the ARA09C Expedition was analyzed using the IC at the Kitami Institute of Technology (KIT; 2707 plus Autosampler, 1525 Binary HPLC Pump, and 432 Conductivity Detector, Nihon Waters K.K., Japan). The reproducibility, estimated from repeated analyses of IAPSO standard seawater, was < 3%.

TABLE 2 | Carbon and oxygen isotopic values of MDACs collected during the ARA07C Expedition.

Site	Depth (mbsf)	$\delta^{13}C$ (‰ V-PDB)	$\delta^{18}O$ (‰ V-PDB)
ARA07C-St 13	0.38	-32.7	5.6
	0.44	-31.9	5.2
	0.72	-32.2	5.5
	1.12	-34.4	6.2
	1.16	-25.6	4.6
	1.71	-28.1	5.4
ARA07C-ST 14	0.73	-32.1	5.9
	1.10	-25.6	6.8

Major and minor cations (Na^+, K^+, Mg^{2+}, Ca^{2+}, Sr^{2+}, and H_4SiO_4) were analyzed by inductively coupled plasma-optical emission spectroscopy (Perkin Elmer Optima 8300) at the KBSI. The reproducibility, estimated from repeated analyses of certified reference materials (SLRS-5 and TMDW), was < 5%.

Stable water isotopes (δD and $\delta^{18}O$) of pore fluid, hydrate-bound water, and seawater from the ARA07C and ARA09C Expeditions were determined with a VG Prism stable isotope ratio mass spectrometer (SIRMS) at the KBSI and an off-axis integrated cavity output spectroscopy laser absorption spectrometer (Los Gatos Research (LGR) Liquid Water Isotope Analyzer [LWIA-24d]) at the KIT, respectively. The analytical reproducibilities by the SIRMS and LWIA were ±0.1‰ for $\delta^{18}O$ and ±1‰ for δD, and ±0.2‰ for $\delta^{18}O$ and ±0.6‰ for δD, respectively.

The carbon isotopic composition ($\delta^{13}C_{DIC}$) in the fluid was analyzed with a Finnigan DELTA-Plus mass spectrometer using a Gas-Bench II automated sampler at Oregon State University. The reproducibility was better than 0.07‰, based on the multiple standard measurements. Isotopic values are reported in the conventional δ-notation relative to Vienna Standard Mean Ocean Water (V-SMOW) for hydrogen and oxygen, and Vienna Pee Dee Belemnite (V-PDB) for carbon.

Dissolved strontium in the fluid was separated for isotopic analysis using Sr-Spec columns (Eichrom-Sr resin). Strontium isotopic ratios ($^{87}Sr/^{86}Sr$) were measured using a Neptune multi-collector inductively coupled plasma mass spectrometer (Thermo Finnigan, Bremen, Germany) upgraded with a large dry interface pump at the KBSI. The measured $^{87}Sr/^{86}Sr$ ratios were normalized to $^{86}Sr/^{88}Sr = 0.1194$, and repeated NBS 987 measurements yielded 0.71025 ± 0.00002 ($2\sigma_{mean}$, $n = 24$).

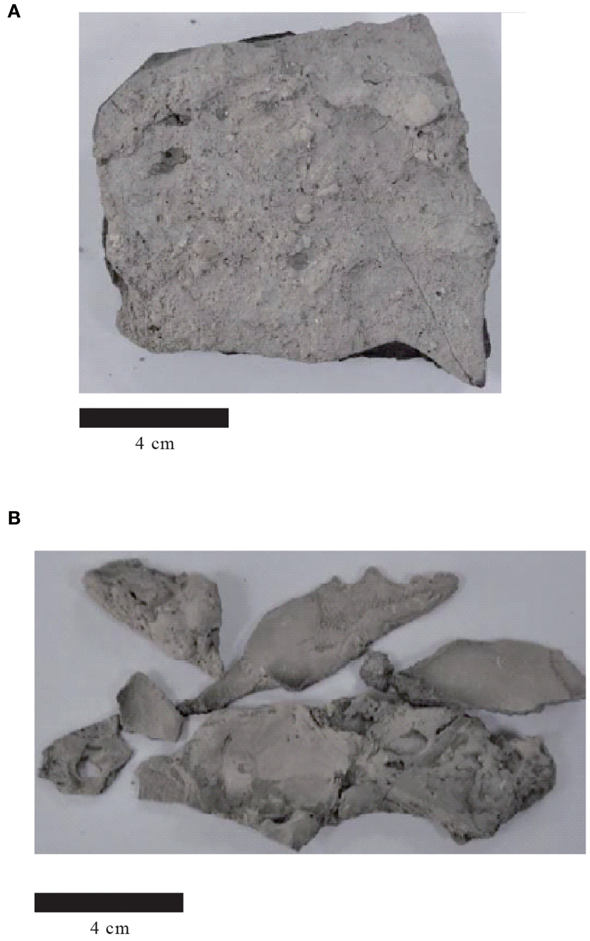

FIGURE 2 | Photographs of methane-derived authigenic carbonate (MDAC) from **(A)** 1.16 mbsf at Site ARA07C-St 13 and **(B)** 1.10 mbsf at Site ARA07C-St 14.

MDAC Analyses

The pretreatment of MDACs from the ARA07C Expedition was performed at the Korea Institute of Geoscience and Mineral Resources (KIGAM). The sample was washed several times using ultrapure distilled water and sonicated for a few minutes to eliminate adhered materials. Then, it was rinsed again with ultrapure distilled water and dried at 60 °C in an oven for 12 h. For $\delta^{13}C$ and $\delta^{18}O$ analyses in MDACs, approximately 5 mg of sample was reacted with 100% H_3PO_4 at 90°C for 5 min, and the evolved CO_2 gas was automatically injected into a VG Prism SIRMS at the KBSI. The analytical reproducibility was better than ±0.1‰ for both $\delta^{13}C$ and $\delta^{18}O$. Isotopic values are reported in the conventional δ-notation relative to V-PDB for carbon and oxygen.

Lipid Biomarkers

The MDAC sample was ultrasonically extracted three times with solvent mixtures (dichloromethane (DCM):methanol (MeOH) (2:1 v/v)). Detailed procedures for lipid biomarker analyses have been previously described by Lee et al. (2018). In short, one-half of the total lipid extract (TLE) was dried over anhydrous Na_2SO_4 and treated with tetrabutylammonium sulfite reagent to remove elemental sulfur. The TLE was chromatographically separated into apolar and polar fractions over an Al_2O_3 column (activated for 2 h at 150°C). The apolar fraction was eluted using hexane:DCM (9:1 v/v), and 40 µL of 5α-androstane (10 µg/ml) was added as an internal standard. The polar fraction was recovered with DCM:MeOH (1:1 v/v) as an eluent and 40 µl of C_{22} 7,16-diol (10 µg/ml) was added as an internal standard. This aliquot was derivatized through silylation, prior to quantification by gas chromatography (GC) and identification with gas chromatography-mass spectrometry (GC-MS). Molecular compounds were determined by comparing their mass spectral fragmentation patterns and retention times with previously published data (Stadnitskaia et al., 2008; Lee et al., 2018). The $\delta^{13}C$ values of lipid compounds are expressed *via* conventional δ-notation relative to V-PDB and the analytical reproducibility is less than ±0.4‰ for all lipid compounds.

RESULTS

Compositional and Isotopic Properties of Fluids

The compositional and isotopic properties of the seawater and pore fluids are represented in **Figure 3** and **Supplementary Table 1**. The Cl^-, Na^+, K^+, $\delta^{18}O$, δD, and $^{87}Sr/^{86}Sr$ values of pore fluids from Sites ARA07C-St 13, ARA07C-St 14, ARA09C-St 04, ARA09C-St 07, ARA09C-St 08, and ARA09C-St 12 are relatively uniform throughout the sampling depth, and these values are generally similar to those of the bottom seawater from Site ARA09C-St 04 (**Figure 3**; **Supplementary Table 1**). However, the downcore profile of SO_4^{2-} from these sites can be classified into two groups. The first group, Site ARA09C-St 08 (reference site), shows a linear decrease from the seawater value (~30 mM) at the top of the sediment to ~24 mM at 5.20 mbsf. In addition, the $\delta^{13}C_{DIC}$ values from this site continuously decrease, ranging from -20.1‰ to -1.3‰ (**Figure 3**; **Supplementary Table 1**). These results imply that Site ARA09C-St 08 does not reach the SMT. In contrast, the downcore profile of SO_4^{2-} in the second group, including Sites ARA07C-St 13, ARA07C-St 14, ARA09C-St 04, ARA09C-St 07, and ARA09C-St 12, exhibits three distinct variations with depth. This profile shows a relatively constant or gradual decrease at shallow depths from the seafloor and then abruptly decreases to the SMT. Below the SMT, it has a relatively constant or a slight decrease (**Figure 3**; **Supplementary Table 1**). The SMT depths of Sites ARA07C-St 13, ARA07C-St 14, ARA09C-St 04, ARA09C-St 07, and ARA09C-St 12 are estimated to be ~1.3 mbsf, ~0.9 mbsf, ~1.2 mbsf, ~3.3 mbsf, and ~2.1 mbsf, respectively (**Figure 3**; **Table 1**). The minimum $\delta^{13}C_{DIC}$ value occurs around the SMT at each site (**Figure 3**; **Supplementary Table 1**).

The downcore profiles of Ca^{2+}, Mg^{2+}, and Sr^{2+} at Sites ARA07C-St 13, ARA07C-St 14, ARA09C-St 04, ARA09C-St 07,

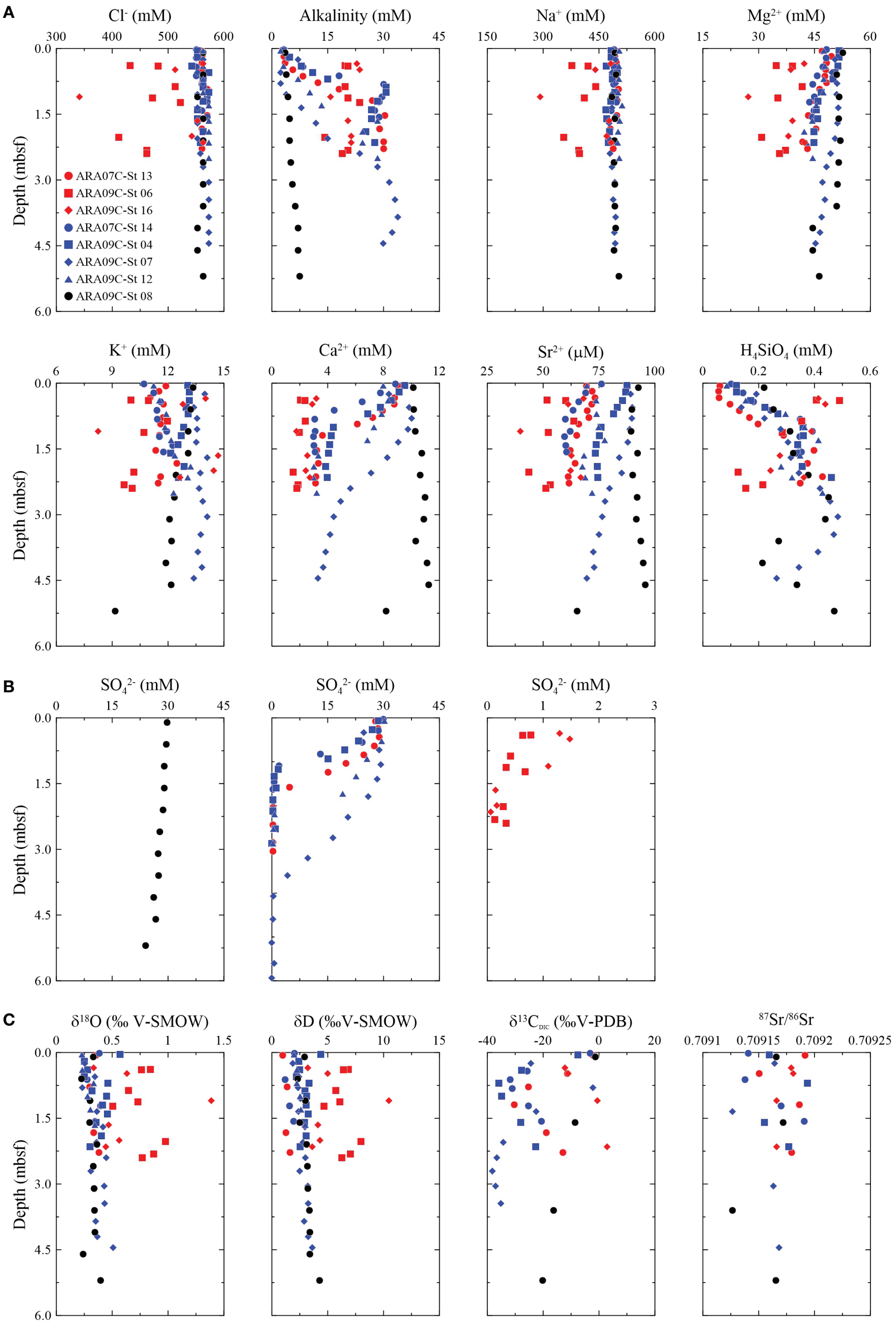

FIGURE 3 | (A) Downcore profiles of Cl-, alkalinity, Na^+, Mg^{2+}, K^+, Ca^{2+}, Sr^{2+}, and H_4SiO_4 in pore fluids from the ARAON Mounds. **(B)** Downcore profile of SO_4^{2-} in pore fluids from the reference site, non-GH bearing sites, and GH bearing sites in the ARAON Mounds. **(C)** Downcore profiles of $\delta^{18}O$, δD, $\delta^{13}C_{DIC}$, and $^{87}Sr/^{86}Sr$ in pore fluids from the ARAON Mounds. Black color site: reference site without GHs and MDCAs, blue color sites: observation of MDACs, and red color sites: observation of GHs and MDACs.

and ARA09C-St 12 display trends similar to those of SO_4^{2-}. In contrast, the downcore profile of alkalinity oppositely overlaps with that of SO_4^{2-} (**Figure 3**; **Supplementary Table 1**). The H_4SiO_4 concentrations (0.29 ± 0.12 mM, n=64) in all samples from Sites ARA07C-St 13, ARA07C-St 14, ARA09C-St 04, ARA09C-St 07, ARA09C-St 08, and ARA09C-St 12 are higher than that of bottom seawater from Site ARA09C-St 04 (~0.04 mM; **Figure 3**; **Supplementary Table 1**).

Compared to other sites in the ARAON Mounds, chemical compositions (e.g., Cl^-, Na^+, Mg^{2+}, K^+, Ca^{2+}, and Sr^{2+}) have depleted values while stable water isotopes ($\delta^{18}O$ and δD) have enriched values at several intervals of pore fluids from Sites ARA09C-St 06 and ARA09C-St 16 (**Figures 3, 4**; **Supplementary Table 1**). The SO_4^{2-} concentrations at these sites are very low with a maximum value of ~2.0 mM and do not exhibit any distinct trend along the entire core length (**Figure 3**; **Supplementary Table 1**). Alkalinity also shows no trend, and its concentration is greater than ~14 mM at these sites (**Figure 3**; **Supplementary Table 1**). The $\delta^{13}C_{DIC}$ values increase from -12.2‰ at ~0.35 mbsf to 2.9‰ at ~2.15 mbsf of Site ARA09C-St 16 (**Figure 3**; **Supplementary Table 1**), which is a higher value than those of other sites that reach the SMT in the ARAON Mounds. The $^{87}Sr/^{86}Sr$ ratios from Site ARA09C-St 16 are relatively constant (0.70917 ± 0.00001, n=4; **Figure 3**; **Supplementary Table 1**) and are similar to the open seawater (~0.70917; Paytan et al., 1993) and the bottom seawater from Site ARA09C-St 04 (0.70919; **Supplementary Table 1**).

Hydrate-Bound Water

The compositional and isotopic properties of the hydrate-bound waters are represented in **Supplementary Table 1**. Most dissolved chemical compositions in the hydrate-bound waters have lower concentrations than those in pore fluids at the same site. Although the values of $\delta^{18}O$ and δD are limited as we have analyzed one sample from the bottom of Site ARA07C-St 13, they are 2.6‰ and 16.5‰, respectively, which are much higher than those of pore fluids at this site, ranging from 0.3‰ to 0.4‰ and from 0.9‰ and 1.6‰, respectively. However, the $^{87}Sr/^{86}Sr$ ratio in the hydrate-bound water from Site ARA09C-St 16 is 0.70923, which is similar to pore fluids from this site (0.70917 ± 0.00001, n=4; **Figure 3**; **Supplementary Table 1**).

MDACs

The MDACs were observed at Sites ARA07C-St 13 and ARA07C-St 14 during the ARA07C Expedition (**Figure 2**; **Table 2**) and at Sites ARA09C-St 04, ARA09C-St 06, ARA09C-St 07, ARA09C-St 12, and ARA09C-St 16 during the ARA09C Expedition (Jin and Shipboard Scientific Party, 2017; Jin and Shipboard Scientific Party, 2019; Kim et al., 2020). We analyze the $\delta^{13}C$ and $\delta^{18}O$ of MDACs from the ARA07C Expedition. $\delta^{13}C_{MDAC}$ and $\delta^{18}O_{MDAC}$ values vary from -34.4‰ to -25.2‰, and from 4.6‰ to 6.2‰, respectively (**Figure 5**; **Table 2**).

Lipid Biomarker Inventory of MDAC

The MDAC sample includes various lipid components of anaerobic methanotrophs, but there is a lack of biomarkers derived from aerobic methanotrophs. Among the apolar components, the irregular, tail-to-tail linked isoprenoid acyclic C_{20} (2, 6, 11, 15-tetramethylhexadecane or crocetane) and C_{25} (2, 6, 10, 15, 19-pentame-thylicosane, PM) hydrocarbons are present in the MDAC sample. The $\delta^{13}C$ values of the isoprenoid hydrocarbons (i.e., crocetane, PMI) are -119.1‰ and -105.5‰, respectively (**Figure 6**). Similarly, the isoprenoid glycerol diethers archaeol and *sn*-2-hydroxyarchaeol are detected in the polar fractions of MDAC samples with $\delta^{13}C$ values of -104.5‰ to -101.2‰. Another distinct group of detected compounds is non-isoprenoid glycerol diethers (DGDs), tentatively inferred previously as a marker of uncharacterized sulfate reducing bacteria (Werne et al., 2002; Pancost et al., 2011). These compounds (e.g., DGD (If), DGD (IIa), and DGD (IId)) have low $\delta^{13}C$ values in the range of -78.2‰ to -66.1‰ (**Figure 6**).

DISCUSSION

Pore Fluid Source

The dissolved chemical species concentrations and water isotopes ($\delta^{18}O$, δD, and $^{87}Sr/^{86}Sr$) values in pore fluids from Sites ARA07C-St 13, ARA07C-St 14, ARA09C-St 04, ARA09C-St 07, ARA09C-St 08, and ARA09C-St 12 are quite similar to those in the bottom seawater from Site ARA09C-St 04 (**Figure 3**; **Supplementary Table 1**). Moreover, the measured $\delta^{18}O$ and δD values in pore fluids do not have a distinct relationship with each other or with Cl^- concentrations (**Figure 4**). Consequently, the pore fluids at these sites predominantly originate from the overlying ambient seawater in the ARAON Mounds. As H_4SiO_4 and Ca^{2+} concentrations in pore fluid samples from these sites have enriched and depleted values, respectively, compared to the bottom seawater (**Figure 3**; **Supplementary Table 1**), pore fluid properties are likely to be altered within the sediment column by water-rock interactions and by mineral precipitation (Kim et al., 2016; Kim et al., 2022).

In contrast, the downcore profiles of dissolved chemical species and stable water isotopes from Sites ARA09C-St 06 and ARA09C-St 16 show distinctly depleted and enriched excursions at several intervals, respectively, relative to those in pore fluids and seawater from other sites in the ARAON Mounds (**Figures 3 , 4**; **Supplementary Table 1**). In addition, the measured $\delta^{18}O$ and δD values in pore fluids from these sites have a good positive correlation ($R^2 > 0.98$) whereas they show a good negative correlation with Cl^- concentrations ($R^2 > 0.83$) (**Figure 4**). These characteristics are typical when the fluid derived from GH dissociation affects the pore fluid. Indeed, many GHs found *in situ* at Sites ARA09C-St 06 and ARA09C-St 16 during the ARA09C Expedition (Jin and Shipboard Scientific Party, 2019). As the pressure decreases and temperature increases when the cores are retrieved from the sediment column to the deck, GHs in the sediment of

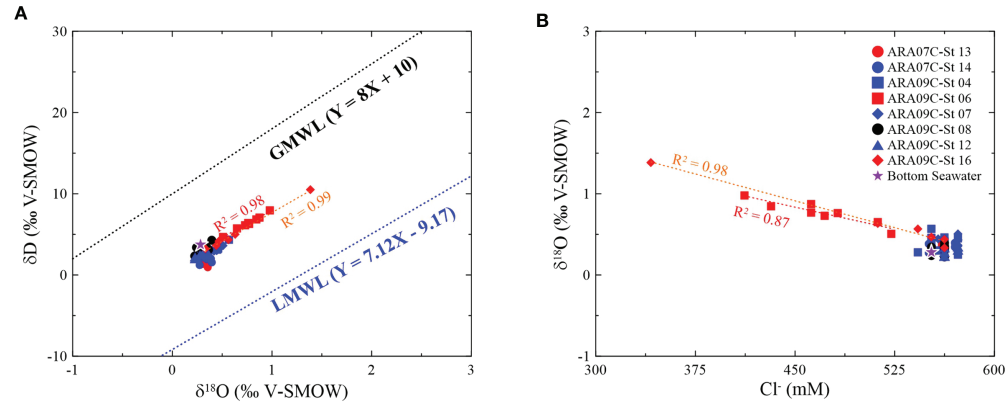

FIGURE 4 | Scatter plots of **(A)** δD versus $\delta^{18}O$ and **(B)** $\delta^{18}O$ versus Cl^- in bottom seawater (violet star; Site ARA09C-St 04) and pore fluids from the ARAON Mounds. The GMWL is the global meteoric water line (**Craig, 1961**), and the LMWL is the local meteoric water line at Inuvik, Canada, by the Global Network of Isotopes in Precipitation (http://www-naweb.iaea.org/napc/ih/IHS_resources_gnip.html). Black color site: reference site without GHs and MDACs, blue color sites: observation of MDACs, and red color sites: observation of GHs and MDACs.

Sites ARA09C-St 06 and ARA09C-St 16 are dissociated and release freshwater into the sediment (e.g., Hesse and Harrison, 1981; Matsumoto and Borowski, 2000; Ussler and Paull, 2001; Hesse, 2003; Torres et al., 2008; Torres et al., 2011). Therefore, the fluid from GH dissociation results in pore fluid freshening with enriched δD and $\delta^{18}O$ values. In addition, because GH dissociation causes the sediment expansion in the core liner during the core retrieving (Kim et al., 2020), ambient seawater can flow sediment in Sites ARA09C-St 06 and ARA09C-St 16. As a result, pore fluid chemistry can be contaminated by the ambient seawater, which interrupts the estimation of the SMT depth of these sites based on the only SO_4^{2-} profile of pore fluids. Overall, the compositional and isotopic properties of pore fluids from Sites ARA09C-St 06 and ARA09C-St 16 have been severely altered by the GH decomposition. We also found an *in situ* GH at the bottom of Site ARA07C-St 13 (core catcher; > 2.35 mbsf), however, the fluid from the GH dissociation cannot significantly influence the pore fluid properties at several intervals of this site, as it does at Sites ARA09C-St 06 and ARA09C-St 16.

Hydrate Saturation

Based on low Cl^- values that are affected by GH dissociation and background Cl^- value in pore fluid that is not affected by GH dissociation, GH saturation (S_h, % of pore space) can be estimated using the following equation (Matsumoto and Borowski, 2000; Ussler and Paull, 2001; Hesse, 2003; Torres et al., 2008; Torres et al., 2011):

$$S_h = \left[\beta\left(C_b - C_s\right)\right] / \left[C_s + \beta\left(C_b - C_s\right)\right] \times 100 \text{ (Eq. 1)}$$

where C_b represents the *in situ* background dissolved Cl^- of the water, which in this study is the pore fluid value at 0.35 mbsf from Site ARA09C-St 16 (~563 mM). C_s is the Cl^- measured in the sample after GH dissociation and β is a dimensionless constant that accounts for the density change due to GH dissociation and equals 1.257 (Ussler and Paull, 2001; Malinverno et al., 2008; Torres et al., 2011; Kim et al., 2013).

The estimated S_h values at Sites ARA09C-St 06 and ARA09C-St 16 have ranges of approximately 9-32% (*n*=8; average=20%) and 2-46% (*n*=4; average=16%), respectively, which vary widely within < 2.5 m-length core at each site (**Table 3**). These results indicate that the GH is likely to be heterogeneous within the sediment of Sites ARA09C-St 06 and ARA09C-St 16.

Linkage Between SO_4^{2-} Concentration and Methane Flux

The downcore profile of SO_4^{2-} concentration in pore fluids from Site ARA09C-St 08 indicates that this site does not reach the SMT under steady state condition (**Figure 3**). In contrast, these profiles at Sites ARA07C-St 13, ARA07C-St 14, ARA09C-St 04, ARA09C-St 07, and ARA09C-St 12 are concave-up and/or kink type with a minimum SO_4^{2-} concentration of ~0 mM. Since this downcore profile of SO_4^{2-} usually suggests the non-steady state of pore fluid chemistry (Hensen et al., 2003; Henkel et al., 2011), the observed SO_4^{2-} profiles imply that Sites ARA07C-St 13,

TABLE 3 | Gas hydrate saturation (***S_h***) from Sites ARA09C-St 06 and ARA09C-St 16.

Site	Depth (mbsf)	Cl^- (mM)	S_h (%)
ARA09C-St 06	0.39	432.0	27.6
	0.40	482.3	17.4
	0.87	512.4	11.0
	1.13	472.2	19.5
	1.23	522.5	8.9
	2.03	411.9	31.6
	2.32	462.2	21.5
	2.40	462.2	21.5
ARA09C-St 16	0.48	512.4	11.0
	1.10	341.6	44.9
	1.65	552.6	2.3
	2.00	542.6	4.5

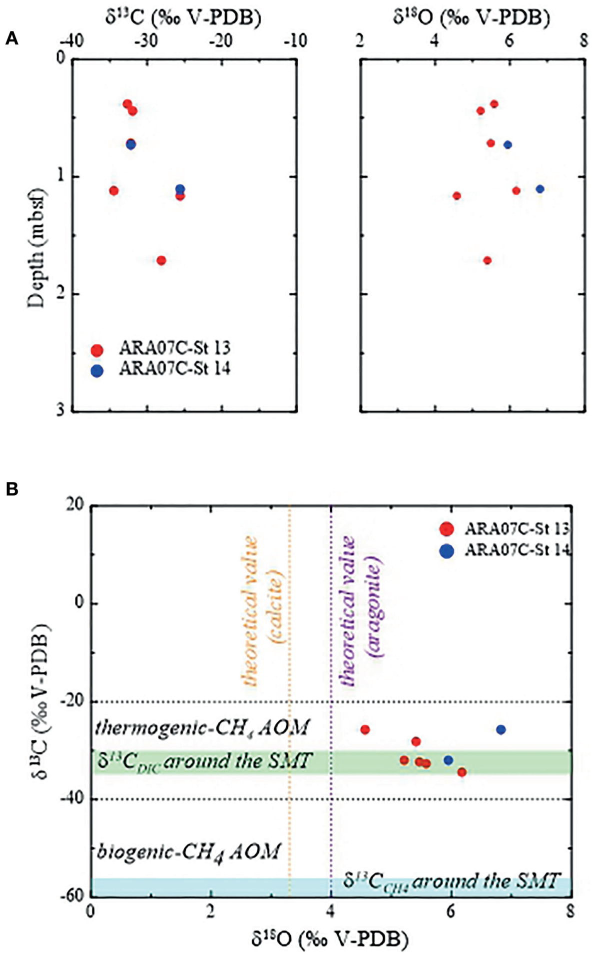

FIGURE 5 | **(A)** Downcore profiles of $\delta^{13}C$ and $\delta^{18}O$ in MDACs from the ARAON Mounds. **(B)** Scatter plots of $\delta^{13}C$ versus $\delta^{18}O$ in MDACs from the ARAON Mounds. The violet and light orange line are the theoretical $\delta^{18}O_{argonite}$ and $\delta^{18}O_{calcite}$ estimated by the equation of Kim et al. (2007) and Kim and O'Neil (1997), respectively. The upper and lower black lines are boundaries for MDACs incorporated with thermogenic CH_4 and microbial CH_4, respectively (Naehr et al., 2007; Crémière et al., 2016; Crémière et al., 2018). The cyan area and light green area are the ranges of $\delta^{13}C_{CH4}$ (Kim et al., 2020) and $\delta^{13}C_{DIC}$ (this study) around the SMT, respectively. Red closed circles: MDACs from Site ARA07C-St 13 and blue closed circles: MDACs from Site ARA07C-St 14.

ARA07C-St 14, ARA09C-St 04, ARA09C-St 07, and ARA09C-St 12 penetrate the SMT under the non-steady state condition. The non-steady state downcore profiles of SO_4^{2-} have already been documented in many regions such as the Argentine Basin, South China Sea, offshore Namibia, and offshore Svalbard (Niewöhner et al., 1998; Fossing et al., 2000; Hong et al., 2017; Hu et al., 2019), which is attributed to either bioirrigation of macrofauna, seawater intrusion during methane ebullition, mass-transport deposits, or increasing upward methane and fluid flux. Because the bioirrigation of macrofauna has rarely been observed in split sediment cores from Sites ARA07C-St 13, ARA07C-St 14, ARA09C-St 06, and ARA09C-St 16, and methane flares have not been observed at all of ARAON Mounds sites (Jin and Shipboard Scientific Party, 2017; Jin and Shipboard Scientific Party, 2019), bioirrigation of macrofauna and the seawater intrusion associated with methane ebullition have not likely occurred at these mounds. In addition, sediment structures related to mass transport deposits have not been found in the sediment facies and SBP images of ARAON Mounds (Jin and Shipboard Scientific Party, 2017; Jin and Shipboard Scientific Party, 2019; Kim et al., 2021b), implying that large-scale sediment reworking cannot account for the non-steady state of SO_4^{2-}. In contrast, during the ARA07C and ARA09C Expeditions, we found many *in situ* GHs at shallow depths at Sites ARA07C-St 13, ARA09C-St 06, and ARA09C-St 16 (core length < 3 m) (Jin and Shipboard Scientific Party, 2017; Jin and Shipboard Scientific Party, 2019; Kim et al., 2020; Choi et al., 2021). To form the GH near the seafloor in the marine environment, the CH_4 flux from deep-seated sediment to the seafloor through the conduit should be high. Thus, we postulate that the non-steady state shown in the downcore profile of SO_4^{2-} of the ARAON Mounds is linked to the variation in upward CH_4 flux from the deep sediment column. This result is partly consistent with the gas chemistry in the ARAON Mounds (Kim et al., 2020).

Kim et al. (2020) revealed that the CH_4 source originates from thermogenic and microbial, which remarkably changes around the SMT on the basis of gas chemistry in the ARAON Mounds. The thermogenic CH_4 that migrated from deep-seated sediments (> 1 km) toward the seafloor through the faults/fractures alters the shallow gas compositional and isotopic properties below/around the SMT in this mound while the microbial CH_4 mainly impacts the area above/around the SMT (Kim et al., 2020). Since the SO_4^{2-} gradient of pore fluid can be mainly controlled by the upward gas flux in the marine sediment (Borowski et al., 1996; Borowski et al., 1997), its sharp decreasing gradient above the SMT at Sites ARA07C-St 13, ARA07C-St 14, ARA09C-St 04, ARA09C-St 07, and ARA09C-St 12 (**Figure 3**) can be directly attributed to the upward thermogenic CH_4 flux around the SMT. However, this mechanism does not explain a gradually decreasing or non-observed SO_4^{2-} gradient in the shallow sediments of these sites (**Figure 3**). It is likely another process that modifies the fluid chemistry associated with GHs and MDACs within the sediment column.

Impact of MDAC and GH Formation on Fluid Chemistry

The downcore profiles of Ca^{2+}, Mg^{2+}, and Sr^{2+} at Sites ARA07C-St 13, ARA07C-St 14, ARA09C-St 04, ARA09C-St 07, and ARA09C-St 12 generally follow the trend of SO_4^{2-}, with rapidly lower concentrations in the zone showing a linear decrease (**Figure 3**; see *Compositional and Isotopic Properties of Fluids*). These results suggest that intense carbonate precipitation occurs in this zone at each site, as evidenced by the many MDACs found during the ARA07C and ARA09C Expeditions (Jin and Shipboard Scientific Party, 2017; Jin and Shipboard Scientific Party, 2019; Kim et al., 2020). In contrast, an MDAC does not occur above the SMT. Therefore,

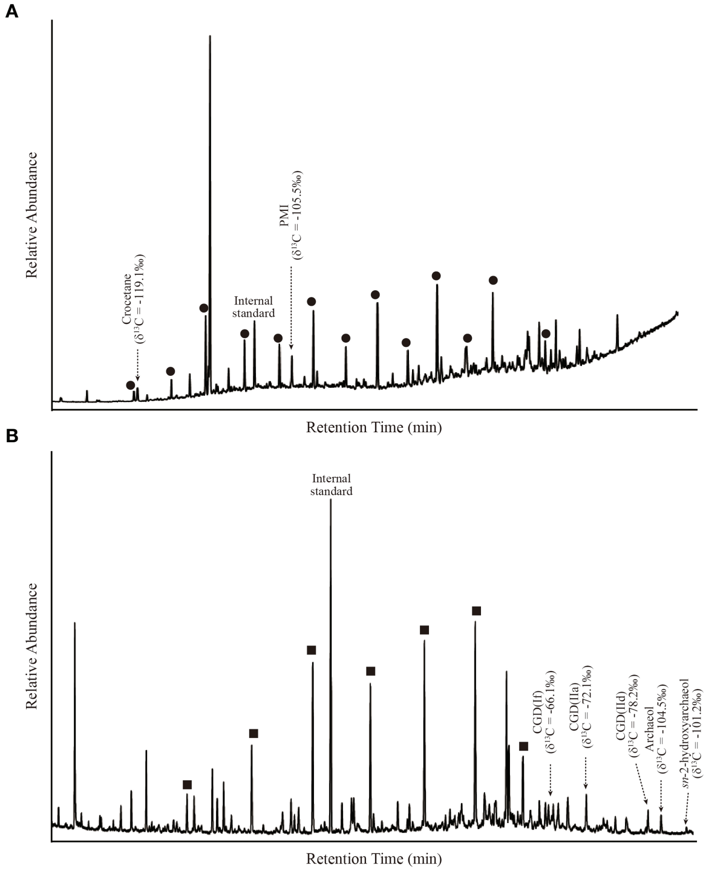

FIGURE 6 | Gas chromatograms of the total lipid extracts from MDAC (1.16 mbsf at Site ARA07C-St 13); **(A)** *n*-alkanes, and **(B)** straight-chain alcohols.

the precipitation of carbonates is likely to be triggered by the increase in alkalinity associated with the AOM.

The carbon isotopes ($\delta^{13}C_{MDAC}$) of MDACs reflect the CH_4 source involved in the AOM reaction. In general, the $\delta^{13}C_{MDAC}$ in association with the thermogenic CH_4 usually ranges from ~-40‰ to -20‰ while it is less than -40‰ by the AOM using microbial CH_4 (Naehr et al., 2007; Crémière et al., 2016; Crémière et al., 2018). The measured $\delta^{13}C_{MDAC}$ values at the ARAON Mounds range from -36.4‰ to -21.9‰ (**Figure 5**), indicating thermogenic CH_4 as a predominant source of MDACs in the ARAON Mounds. This result is consistent with the CH_4 source around/below the present SMT in these mounds (Kim et al., 2020). Under such conditions, specific lipid molecules (e.g., archaeol and *sn*-2-hydroxyarchaeol) preserved within MDAC, can identify the predominance of anaerobic methanotrophs (ANMEs), as well as paleoenvironmental conditions (e.g., methane sources and fluctuation) in association with the AOM reaction during the formation of MDAC (Blumenberg et al., 2004; Elvert and Niemann, 2008; Niemann and Elvert, 2008; Himmler et al., 2015). Typically, microbial communities dominated by ANME-2 at the cold seeps of the northwestern Black Sea contain higher amounts of *sn*-2-hydroxyarchaeol relative to archaeol, whereas the reverse is observed in microbial mats dominated by ANME-1 (Blumenberg et al., 2004). Indeed, the ratio of isotopically depleted *sn-2*-hydroxyarchaeol relative to archaeol can be used to distinguish ANME-1 (0–0.8) from ANME-2 (1.1–5.5), with ANME-3 (2.4) falling within the range of ANME-2 (Niemann et al., 2005; Niemann and Elvert, 2008). The compound ratios (i.e., *sn*-2-hydroxyarchaeol/ archaeol) in MDAC from the ARAON Mounds are ~1 (**Figure 6**), implying that ANME-1 is predominantly involved in the AOM reaction to form MDACs using the deep CH_4 sources. The diagnostic archaeal (crocetane, PMI, archaeol, and, *sn*-2-hydroxyarchaeol) and bacterial lipids (DGDs) with strongly depleted ^{13}C in MDAC (**Figure 6**) also support this interpretation.

The formation of MDACs in the ARAON Mounds can drastically alter the physical properties of sediment and flow pathway because it reduces the permeability of sediments and potentially prevents direct flow or retards gas and fluid migration within the sediments (Hovland, 2002; Bahr et al., 2007; Bayon et al., 2009). Similarly, the formation and growth of GHs in the sediment by a high CH_4 flux can modify physical properties and flow pathways (Sassen et al., 1999; Römer et al., 2012; Sultan et al., 2014). Therefore, we postulate that MDACs and GHs observed widespread in the ARAON Mounds are likely to prevent

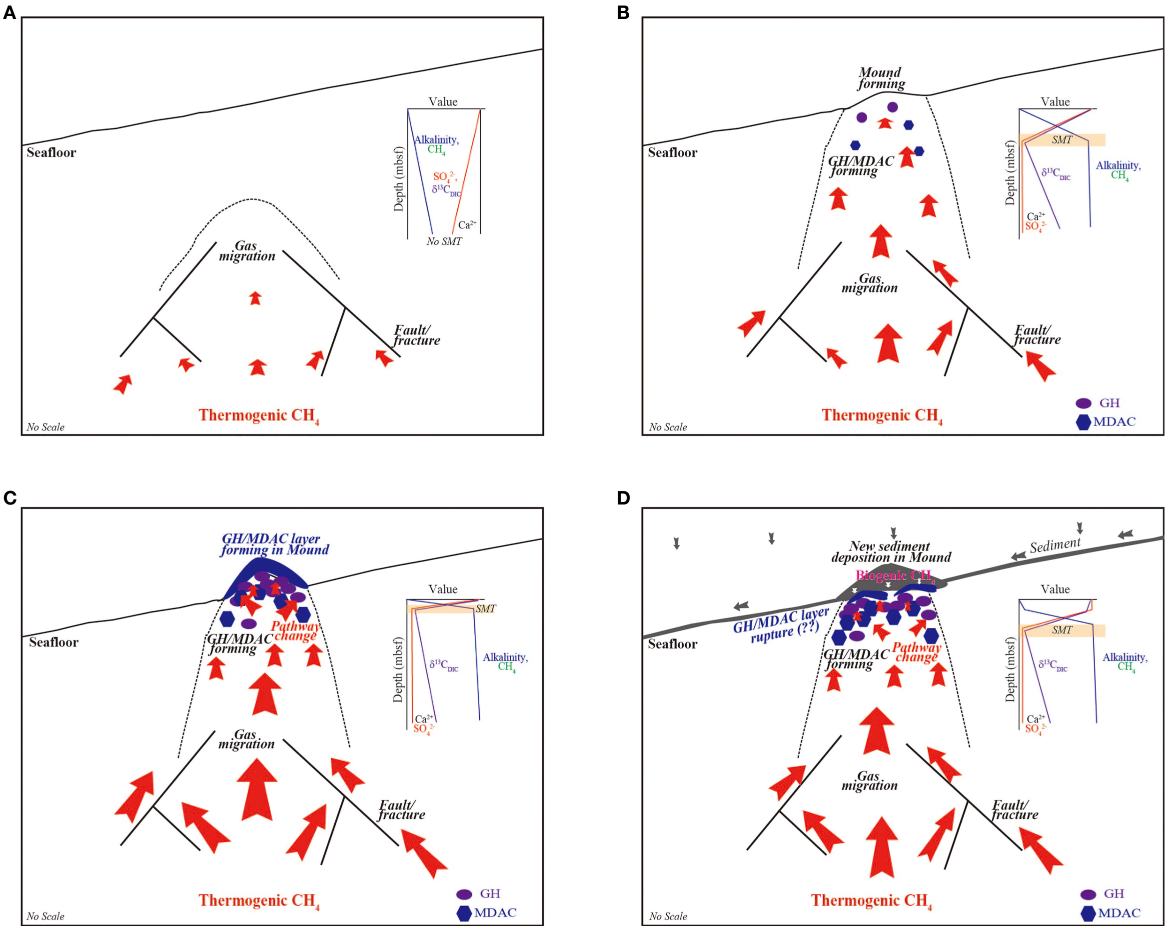

FIGURE 7 | Schematic diagram illustrating the change of seafloor morphology, fluid and gas migration, fluid chemistry (SO_4^{2-}, alkalinity, Ca^{2+}, CH_4, and $\delta^{13}C_{DIC}$), and MDACs and GHs production in the ARAON Mounds in association with the CH_4 flux; **(A)** beginning of the upward CH_4 flux from the deep sediment, **(B)** mound formation on the seafloor and beginning of GH and MDAC production in the sediment column under high upward CH_4 flux, **(C)** GH and MDAC production in the seafloor and flow pathway change under a high upward CH_4 flux, and **(D)** new sediment deposition at the mound and/or GH and MDAC production under a high upward CH_4 flux.

or interrupt the upward migration of gas and fluid in the sediment column (**Figure 7**). Given that the fluid coupled with gas continuously migrates through the sediment column, the downcore profile of SO_4^{2-} reaches steady state condition and the CH_4 source should be steadily changed from the seafloor to deep-seated sediment with the CH_4 flux (**Figures 7A–C**). Otherwise, the upward gas and fluid are blocked or redirected by MDACs and GHs within the sediment column, and then sediment is continuously deposited over them within a short time scale. The gas and pore fluid chemistry above these deposits are mainly controlled by ambient seawater and by (bio)geochemical reactions (e.g., organic matter degradation by sulfate reduction, microbial methanogenesis) associated with the microbial activity to degrade the organic matter rather than by the upward CH_4 flux (**Figure 7D**). As a result, the chemical zone is entirely separated between the below and above deposition of the MDACs and GHs (**Figure 7D**).

Influence of Methane Flux and GH Dissociation on MDAC Chemistry

The $\delta^{18}O$ signature of carbonates can inform the oxygen isotopic composition of the fluid when the carbonate precipitates (e.g., Greinert et al., 2001; Naehr et al., 2007). Assuming that aragonite and carbonated formed in isotopic equilibrium with ambient bottom seawater at the temperature and $\delta^{18}O$ value of the ARAON Mounds, respectively, the theoretical $\delta^{18}O_{aragonite}$ and $\delta^{18}O_{carbonate}$ values can be estimated by these equations (Kim and O'Neil, 1997; Kim et al., 2007);

$$1000\ln\alpha_{aragonite\text{-}seawater} = 17.88 \times \frac{10^3}{T}(\text{Kelvin}) - 31.14 \quad \text{(Eq. 2)}$$

$$1000\ln\alpha_{calcite\text{-}seawater} = 18.03 \times \frac{10^3}{T}(\text{Kelvin}) - 32.42 \quad \text{(Eq. 3)}$$

The temperature and $\delta^{18}O$ value of the present bottom seawater from Site ARA09C-St 04, as measured during the ARA09C Expedition, are 0.8°C (Jin and Shipboard Scientific Party, 2019) and 0.3‰ (V-SMOW; **Supplementary Table 1**), respectively. Thus, the theoretical $\delta^{18}O$ of aragonite and carbonate is ~4.0‰ (V-PDB) and ~3.3‰ (V-PDB), respectively. All analyzed $\delta^{18}O_{MDAC}$ values from Sites ARA07C-St 13 and ARA07C-St 14 are higher than these calculated equilibrium values (**Figure 5**; **Table 2**), suggesting the incorporation of enriched ^{18}O fluid during MDAC precipitation. The enriched ^{18}O fluid may originate from either clay mineral dehydration, opal diagenesis, or GH dissociation (Hesse and Harrison, 1981; Kastner et al., 1991; Ussler and Paull, 1995; Hesse, 2003; Kim et al., 2013; Kim et al., 2021a). In general, the $^{87}Sr/^{86}Sr$ ratio tends to be lower than that of the ambient present seawater by clay dehydration, and the $\delta^{18}O$ value increases with a relatively constant δD value by opal diagenesis (Kastner et al., 1991; Kim et al., 2013; Kim et al., 2021a). Since most $^{87}Sr/^{86}Sr$ ratios in pore fluids are similar to the present bottom seawater of ARA09C-St 04 and the values of $\delta^{18}O$ and δD are relatively constant in the non-GH-bearing intervals, irrespective of sampling depth **(Figures 3, 4; Supplementary Table 1**), we excluded clay mineral dehydration and opal diagenesis as the primary sources for enriched ^{18}O fluid in the ARAON Mounds. Instead, it is reasonable that the ^{18}O-enrichment of MDACs can be attributed to fluids derived from GH dissociation in relation to climate change through geological time (Greinert et al., 2001; Naehr et al., 2007), as indicated by the occurrences of shallow GHs around MDACs at Sites ARA07-St 13, ARA09C-St 06, and ARA09C-St 16 (**Figures 1**, **2**; **Tables 1**, **2**; **Supplementary Table 1**).

SUMMARY AND IMPLICATIONS

The compositional and isotopic properties (e.g., Cl^-, Na^+, δD, $\delta^{18}O$, and $^{87}Sr/^{86}Sr$) of pore fluids from Sites ARA07C-St 13, ARA07C-St 14, ARA09C-St 04, ARA09C-St 07, ARA09C-St 08, and ARA09C-St 12 are similar to those of bottom seawater from Site ARA09C-St 04, indicating that the source of pore fluid is mainly derived from the ambient seawater in the ARAON Mounds. In contrast, pore fluids from Sites ARA09C-St 06 and ARA09C-St 16, where many *in situ* GHs are found, have low Cl^- concentrations with high δD and $\delta^{18}O$ values, which are typical features of fluids affected by GH dissociation. At these sites, the SO_4^{2-} downcore profiles have no distinct trend with higher $\delta^{13}C_{DIC}$ values (-12.2‰ to 2.9‰ at Site ARA09C-St 16) compared to other sites and prevent the estimation of the SMT, which also supports the impact of GH dissociation. Interestingly pore fluids from Site ARA07C-St 13 do not have typical characteristics that are affected by GH dissociation while they show similar properties to those of the bottom seawater from Site ARA09C-St 04, even though GHs were found at the end of the sediment core.

The SO_4^{2-} downcore profile from Site ARA09C-St 08 does not reach the SMT (minimum SO_4^{2-} concentration = ~25 mM) under a steady-state condition with a linearly decreasing trend. In contrast, these profiles from Sites ARA07C-St 13, ARA07C-St 14, ARA09C-St 04, ARA09C-St 07, and ARA09C-St 12 are concave-up and/or kink type, with a minimum SO_4^{2-} concentration of ~0 mM, indicating the penetration of the SMT under the non-steady state condition. Many *in situ* MDACs and GHs have been widely found in the sediment, thus, the observed trend of the SO_4^{2-} downcore profile is strongly associated with them. When the gas and fluid continuously flow upward, these byproducts prevent and/or at least severely retard as well as redirect their flow pathways through the sediments because the physical properties of the sediment and fluid pathways are remarkably changed by them. As a result, the exchange of dissolved species does not take place smoothly within the sediment column between the bearing and non-bearing GH and MDAC intervals, which leads to the separation of chemical zones between them. Hence, the downcore profiles of SO_4^{2-} and other dissolved ions (e.g., Ca^{2+}, Mg^{2+}, and alkalinity) have concave-up and/or kink type under the non-steady state condition. Overall, the pore fluid chemistry in the ARAON Mounds exhibits spatiotemporal variations in response to the CH_4 flux as well as the existence of GH and MDACs.

The $\delta^{13}C_{MDAC}$ values of all MDACs from Sites ARA07C-St 13 and ARA07C-St 14 are higher than -40‰, and $\delta^{18}O_{MDAC}$ values are also higher than the theoretical equilibrium values (~4.0‰ for aragonite and ~3.3‰ for calcite, respectively) on the basis of the temperature and $\delta^{18}O$ value of the bottom seawater from Site ARA09C-St 04. These results imply that thermogenic CH_4 migrates from the deeper sediment and that the ^{18}O-enriched fluid derived from GH dissociation incorporates to precipitate carbonate.

It is expected that rapid global warming will continuously amplify in the future (Schuur et al., 2015; Kim et al., 2021a). We can also predict that the seafloor morphology and regional hydrology including the formation of GHs and MDACs of the ARAON Mounds as well as other regions of the Arctic Ocean, will rapidly change in association with future climate change. The present information of fluids and MDACs observed in the ARAON Mounds can provide some clues to predict these changes at these mounds and in the Arctic Ocean in response to future climate change. To precisely understand and predict these changes due to future climate change, more studies targeting methane seepage and its role in the Arctic Ocean are needed.

DATA AVAILABILITY STATEMENT

The original contributions presented in the study are included in the article/**Supplementary Material**. Further inquiries can be directed to the corresponding author.

AUTHOR CONTRIBUTIONS

J-HK designed and coordinated the study, analyzed the samples, interpreted the data, and led the writing of the manuscript. M-HP, D-HL, HM, AH, J-SR, YS and SP analyzed the samples, wrote, and reviewed the manuscript. Y-KJ, M-HK, MK, and J-HK conducted the survey, wrote, and reviewed the draft. JH, KJ, YS, and MC interpreted the data, wrote, and reviewed the manuscript. All authors assisted with interpretation and contributed to the writing of the manuscript.

FUNDING

This study was funded by Korea Ministry of Science and ICT (GP2020-006 and GP2021-009), by the Korea Ministry of Oceans and Fisheries (20210632), and by Korea Ministry of Trade, Industry and Energy (Project No. 20212010200010).

ACKNOWLEDGMENTS

We would like to thank the captain and crew of the *IBRV* ARAON for their help at sea. We also gratefully acknowledge the comments from Jörn Peckmann and reviewers, which improved this manuscript.

SUPPLEMENTARY MATERIAL

The Supplementary Material for this article can be found online at: https://www.frontiersin.org/articles/10.3389/fmars.2022.944841/full#supplementary-material

REFERENCES

Aloisi, G., Pierre, C., Rouchy, J.-M., Foucher, J.-P. and Woodside, J. (2000). Methane-Related Authigenic Carbonates of Eastern Mediterranean Sea Mud Volcanoes and Their Possible Relation to Gas Hydrate Destabilisation. *Earth Planet. Sci. Lett.* 184, 321–338. doi: 10.1016/S0012-821X(00)00322-8

Argentino, C., Waghorn, K. A., Vadakkepuliyambatta, S., Polteau, S., Bünz, S. and Panieri, G. (2021). Dynamic and History of Methane Seepage in the SW Barents Sea: New Insights From Leirdjupet Fault Complex. *Sci. Rep.* 11, 4373. doi: 10.1038/s41598-021-83542-0

Bahr, A., Pape, T., Bohrmann, G., Mazzini, A., Haeckel, M., Reitz, A., et al. (2007). Authigenic Carbonate Precipitates From the NE Black Sea: A Mineralogical, Geochemical, and Lipid Biomarker Study. *Int. J. Earth Sci.* 98, 677–695. doi: 10.1007/s00531-007-0264-1

Barnes, R. O. and Goldberg, E. D. (1976). Methane Production and Consumption in Anoxic Marine Sediments. *Geology* 4, 297–300. doi: 10.1130/0091-7613(1976)4<297:MPACIA>2.0.CO;2

Bayon, G., Henderson, G. M. and Bohn, M. (2009). U-Th Stratigraphy of a Cold Seep Carbonate Crust. *Chem. Geol.* 260, 47–56. doi: 10.1016/j.chemgeo.2008.11.020

Blumenberg, M., Seifert, R., Reitner, J., Pape, T. and Michaelis, W. (2004). Membrane Lipid Patterns Typify Distinct Anaerobic Methanotrophic Consortia. *PNAS* 101, 11111–11116. doi: 10.1073/pnas.0401188101

Boetius, A., Ravenschlag, K., Schubert, C. J., Rickert, D., Widdel, F., Gieseke, A., et al. (2000). A Marine Microbial Consortium Apparently Mediating Anaerobic Oxidation of Methane. *Nature* 407, 623–626. doi: 10.1038/35036572

Boetius, A. and Wenzhöfer, F. (2013). Seafloor Oxygen Consumption Fuelled by Methane From Cold Seeps. *Nat. Geosci.* 6, 725–734. doi: 10.1038/ngeo1926

Borowski, W. S., Paull, C. K. and Ussler, W.III. (1996). Marine Pore-Water Sulfate Profiles Indicate *in Situ* Methane Flux From Underlying Gas Hydrate. *Geology* 24, 655–658. doi: 10.1130/0091-7613(1996)024<0655:MPWSPI>2.3.CO;2

Borowski, W. S., Paull, C. K. and Ussler, W.III. (1997). Carbon Cycling Within the Upper Methanogenic Zone of Continental Rise Sediments: An Example From the Methane-Rich Sediments Overlying the Blake Ridge Gas Hydrate Deposits. *Mar. Chem.* 57, 299–311. doi: 10.1016/S0304-4203(97)00019-4

Buerk, D., Klaucke, I., Sahling, H. and Weinrebe, W. (2010). Morpho-Acoustic Variability of Cold Seeps on the Continental Slope Offshore Nicaragua: Results of Fluid Flow Interaction With Sedimentary Processes. *Mar. Geol.* 275, 53–65. doi: 10.1016/j.margeo.2010.04.007

Campbell, K. A. (2006). Hydrocarbon Seep and Hydrothermal Vent Paleoenvironments and Paleontology: Past Developments and Future Research Directions. *Palaeogeogr. Palaeoclimatol. Palaeoecol.* 232, 362–407. doi: 10.1016/j.palaeo.2005.06.018

Chapman, R., Pohlman, J., Coffin, R., Chanton, J. and Lapham, L. (2004). Thermogenic Gas Hydrates in the Northern Cascadia Margin. *EOS (Transactions. Am. Geophysical. Union).* 85, 361–368. doi: 10.1029/2004EO380001

Choi, W., Lee, J., Kim, Y.-G., Kim, H., Rhee, T. S., Jin, Y. K., et al. (2021). The Impact of the Abnormal Salinity Enrichment in Pore Water on the Thermodynamic Stability of Marine Natural Gas Hydrates in the Arctic Region. *Sci. Total. Environ.* 799, 149357. doi: 10.1016/j.scitotenv.2021.149357

Craig, H. (1961). Isotopic Variation in Meteoric Waters. *Science* 133, 1702–1703. doi: 10.1126/science.133.3465.1702

Crémière, A., Chand, S., Sahy, D., Thorsnes, T., Martma, T., Noble, S. R., et al. (2018). Structural Controls on Seepage of Thermogenic and Microbial Methane Since the Last Glacial Maximum in the Harstad Basin, Southwest Barents Sea. *Mar. Petrol. Geol.* 98, 569–581. doi: 10.1016/j.marpetgeo.2018.07.010

Crémière, A., Lepland, A., Chand, S., Sahy, D., Kirsimäe, K., Bau, M., et al. (2016). Fluid Source and Methane-Related Diagenetic Processes Recorded in Cold Seep Carbonates From the Alvheim Channel, Central North Sea. *Chem. Geol.* 432, 16–33. doi: 10.1016/j.chemgeo.2016.03.019

Elvert, M. and Niemann, H. (2008). Occurrence of Unusual Steroids and Hopanoids Derived From Aerobic Methanotrophs at an Active Marine Mud Volcano. *Org. Geochem.* 39, 167–177. doi: 10.1016/j.orggeochem.2007.11.006

Fossing, H., Ferdelman, T. G. and Berg, P. (2000). Sulfate Reduction and Methane Oxidation in Continental Margin Sediments Influenced by Irrigation (South-East Atlantic Off Namibia). *Geochim. Cosmochim. Acta* 64, 897–910. doi: 10.1016/S0016-7037(99)00349-X

Grantz, A., Clark, D. L., Phillips, R. L., Srivastava, S. P., Blome, C. D., Gray, L. B., et al. (1998). Phanerozoic Stratigraphy of Northwind Ridge, Magnetic Anomalies in the Canada Basin, and the Geometry and Timing of Rifting in the Amerasia Basin, Arctic Ocean. *Geol. Soc Am. Bull.* 110, 801–820. doi: 10.1130/0016-7606(1998)110<0801:PSONRM>2.3.CO;2

Greinert, J., Bohrmann, G. and Suess, E. (2001). "Gas Hydrate-Associated Carbonates and Methane-Venting at Hydrate Ridge: Classification, Distribution, and Origin of Authigenic Lithologies," in *Natural Gas Hydrates: Occurrence, Distribution, and Detection*. Eds. Paull, C. K. and Dillon, W. P. (Washington, D.C: American Geophysical Union), 99–113.

Henkel, S., Schwenk, T., Hanebuth, T. J. J., Strasser, M., Riedinger, N., Formolo, M., et al. (2011). "Pore Water Geochemistry as a Tool for Identifying and Dating Recent Mass-Transport Deposits," in *Submarine Mass Movements and Their Consequences*. Eds. Yamada, Y., Kawamura, K., Ikehara, K., Ogawa, Y., Urgeles, R., Mosher, D., Chaytor, J. and Strasser, M. (Dordrecht, Heidelberg, London, New York: Springer), 87–97.

Hensen, C., Zabel, M., Pfeifer, K., Schwenk, T., Kasten, S., Riedinger, N., et al. (2003). Control of Sulfate Pore-Water Profiles by Sedimentary Events and the Significance of Anaerobic Oxidation of Methane for the Burial of Sulfur in Marine Sediments. *Geochim. Cosmochim. Acta* 67, 2631–2647. doi: 10.1016/S0016-7037(03)00199-6

Hesse, R. (2003). Pore Water Anomalies of Submarine Gas-Hydrate Zones as Tool to Assess Hydrate Abundance and Distribution in the Subsurface: What Have We Learned in the Past Decade? *Earth-Sci. Rev.* 61, 149–179. doi: 10.1016/S0012-8252(02)00117-4

Hesse, R. and Harrison, W. E. (1981). Gas Hydrates (Clathrates) Causing Pore-Water Freshening and Oxygen Isotope Fractionation in Deep-Water Sedimentary Sections of Terrigenous Continental Margins. *Earth Planet. Sci. Lett.* 55, 453–462. doi: 10.1016/0012-821X(81)90172-2

Himmler, T., Birgel, D., Bayon, G., Pape, T., Ge, L., Bohrmann, G., et al. (2015). Formation of Seep Carbonates Along the Makran Convergent Margin, Northern Arabian Sea and a Molecular and Isotopic Approach to Constrain the Carbon Isotopic Composition of Parent Methane. *Chem. Geol.* 415, 102–117. doi: 10.1016/j.chemgeo.2015.09.016

Himmler, T., Brinkmann, F., Bohrmann, G. and Peckmann, J. (2011). Corrosion Patterns of Seep-Carbonates From the Eastern Mediterranean Sea. *Terra. Nova.* 23, 206–212. doi: 10.1111/j.1365-3121.2011.01000.x

Hong, W. L., Torres, M. E., Carroll, J., Cremiere, A., Panieri, G., Yao, H., et al. (2017). Seepage From an Arctic Shallow Marine Gas Hydrate Reservoir is Insensitive to Momentary Ocean Warming. *Nat. Commun.* 8, 5745. doi: 10.1038/ncomms15745

Hovland, M. (2002). On the Self-Sealing Nature of Marine Seeps. *Cont. Shelf. Res.* 22, 2387–2394. doi: 10.1016/S0278-4343(02)00063-8

Hu, Y., Luo, M., Liang, Q., Chen, L., Feng, D., Yang, S., et al. (2019). Pore Fluid Compositions and Inferred Fluid Flow Patterns at the Haima Cold Seeps of the South China Sea. *Mar. Petrol. Geol.* 103, 29–40. doi: 10.1016/j.marpetgeo.2019.01.007

Jakobsson, M. (2002). Hypsometry and Volume of the Arctic Ocean and its Constituent Seas. *Geochem. Geophys. Geosyst.* 3, 1–18. doi: 10.1029/2001GC000302

Jin, Y. K.Shipboard Scientific Party (2017). *ARA07C Cruise Report: 2016 Korea-Russia-Germany East Siberian Sea Research Program* (Incheon: Korea Polar Research Institute).

Jin, Y. K.Shipboard Scientific Party (2019). *ARA09C Cruise Report: 2018 Korea-Russia-Japan East Siberian/Chukchi Sea Research Program* (Incheon: Korea Polar Research Institute).

Judd, A. G. and Hovland, M. (2007). *Seabed Fluid Flow* (New York: Cambridge University Press).

Judd, A. G., Hovland, M., Dimitrov, L. I., Garcia, G. S. and Jukes, V. (2002). The Geological Methane Budget at Continental Margins and its Influence on Climate Change. *Geofluids* 2, 109–126. doi: 10.1046/j.1468-8123.2002.00027.x

Kastner, M., Elderfield, H. and Martin, J. B. (1991). Fluids in Convergent Margins - What Do We Know About Their Composition, Origin, Role in Diagenesis and Importance for Oceanic Chemical Fluxes. *Philos. Trans. R. Soc A.* 335, 243-259. doi: 10.1098/rsta.1991.0045.

Kim, J.-H., Hachikubo, A., Kida, M., Minami, H., Lee, D.-H., Jin, Y. K., et al. (2020). Upwarding Gas Source and Postgenetic Processes in the Shallow Sediments From the ARAON Mounds, Chukchi Sea. *J. Nat. Gas. Sci. Eng.* 76, 103223. doi: 10.1016/j.jngse.2020.103223

Kim, J.-H., Hong, W.-L., Torres, M. E., Ryu, J.-S., Kang, M.-H., Han, D., et al. (2021a). A Pulse of Meteoric Subsurface Fluid Discharging Into the Chukchi Sea During the Early Holocene Thermal Maximum (EHTM). *Geochem. Geophys. Geosyst.* 22, e2021GC009750. doi: 10.1029/2021GC009750

Kim, J.-H., Ryu, J. S., Hong, W.-L., Jang, K., Joo, Y. J., Lemarchand, D., et al. (2022). Assessing the Impact of Freshwater Discharge on the Fluid Chemistry in the Svalbard Fjords. *Sci. Total. Environ.* 835, 155516. doi: 10.1016/j.scitotenv.2022.155516

Kim, J.-H., Torres, M. E., Haley, B. A., Ryu, J. S., Park, M. H., Hong, W.-L., et al. (2016). Marine Silicate Weathering in the Anoxic Sediment of the Ulleung Basin: Evidence and Consequences. *Geochem. Geophys. Geosyst.* 17, 3437–3453. doi: 10.1002/2016GC006356

Kim, J.-H., Torres, M. E., Hong, W.-L., Choi, J., Riedel, M., Bahk, J.-J., et al. (2013). Pore Fluid Chemistry From the Second Gas Hydrate Drilling Expedition in the Ulleung Basin (UBGH2): Source, Mechanisms and Consequences of Fluid Freshening in the Central Part of the Ulleung Basin, *East Sea. Mar. Petrol. Geol.* 47, 99–112. doi: 10.1016/j.marpetgeo.2012.12.011

Kim, S., Polyak, L., Joe, Y. J., Nissem, F., Kim, H. J., Cho, Y., et al. (2021b). Seismostratigraphic and Geomorphic Evidence for the Glacial History of the Northwestern Chukchi Margin, Arctic Ocean. *J. Geophys. Res. Earth Surf.* 126, e2020JF006030. doi: 10.1029/2020JF006030

Kim, S. T. and O'Neil, J. R. (1997). Equilibrium and Nonequilibrium Oxygen Isotope Effects in Synthetic Carbonates. *Geochim. Cosmochim. Acta* 61, 3461–3475. doi: 10.1016/S0016-7037(97)00169-5

Kim, S.-T., O'Neil, J. R., Hillaire-Marcel, C. and Mucci, A. (2007). Oxygen Isotope Fractionation Between Synthetic Aragonite and Water: Influence of Temperature and Mg^{2+} Concentration. *Geochem. Cosmochim. Acta* 71, 4704–4715. doi: 10.1016/j.gca.2007.04.019

Koch, S., Berndt, C., Bialas, J., Haeckel, M., Crutchley, G., Papenberg, C., et al. (2015). Gas-Controlled Seafloor Doming. *Geology* 43, 571–574. doi: 10.1130/G36596.1

Lee, D.-H., Kim, J.-H., Lee, Y. M., Kim, J.-H., Jin, Y. K., Paull, C., et al. (2021). Geochemical and Microbial Signatures of Siboglinid Tubeworm Habitats at an Active Mud Volcano in the Canadian Beaufort Sea. *Front. Mar. Sci.* 8. doi: 10.3389/fmars.2021.656171

Lee, D. H., Kim, J.-H., Lee, Y. M., Stadnitskaia, A., Jin, Y. K., Niemann, H., et al. (2018). Biogeochemical Evidence of Anaerobic Methane Oxidation on Active Submarine Mud Volcanoes on the Continental Slope of the Canadian Beaufort Sea. *Biogeosciences* 15, 7419–7433. doi: 10.5194/bg-15-7419-2018

Luff, R., Wallmann, K., and Aloisi, G. (2004). Numerical modeling of carbonate crust formation at cold vent sites: significance for fluid and methane budgets and chemosynthetic biological communities. *Earth Planet. Sci. Lett.* 221, 337-353. doi: 10.1016/S0012-821X(04)00107-4

Malinverno, A., Kastner, M., Torres, M. E. and Wortmann, U. G. (2008). Gas Hydrate Occurrence in a Transect Across the Cascadia Margin From Pore Water Chlorinity and Downhill Geophysical Logs (IODP 311). *J. Geophys. Res.* 113, B08103. doi: 10.1029/2008JB005702

Matsumoto, R. and Borowski, W. S. (2000). "Gas Hydrate Estimates From Newly Determined Oxygen Isotopic Fractionation (α_{GH-IW}) and $\delta^{18}O$ Anomalies of the Interstitial Waters: Leg 164, Blake Ridge," in *Proceedings of the Ocean Drilling Program Scientific Results*, vol. 164 . Eds. Paull, C. K., Matsumoto, R., Wallace, P. J. and Dillon, W. P. (College Station, TX: Ocean Drilling Program), 59–66.

Naehr, T. H., Eichhubl, P., Orphan, V. J., Hovland, M., Paull, C. K., Ussler, W., III, et al. (2007). Authigenic Carbonate Formation at Hydrocarbon Seeps in Continental Margin Sediments: A Comparative Study. *Deep-Sea. Res. II.: Top. Stud. Oceanogr.* 54, 1268–1291. doi: 10.1016/j.dsr2.2007.04.010.

Niemann, H. and Elvert, M. (2008). Diagnostic Lipid Biomarker and Stable Carbon Isotope Signatures of Microbial Communities Mediating the Anaerobic Oxidation of Methane With Sulphate. *Org. Geochem.* 39, 1668–1677. doi: 10.1016/j.orggeochem.2007.11.003

Niemann, H., Elvert, M., Hovland, M., Orcutt, B., Judd, A., Suck, I., et al. (2005). Methane Emission and Consumption at a North Sea Gas Seep (Tommeliten Area). *Biogeosciences* 2, 335–351. doi: 10.5194/bg-2-335-2005

Niewöhner, C., Hensen, C., Kasten, S., Zabel, M. and Schulz, H. D. (1998). Deep Sulfate Reduction Completely Mediated by Anaerobic Methane Oxidation in Sediments of the Upwelling Area Off Namibia. *Geochim. Cosmochim. Acta* 62, 455–464. doi: 10.1016/S0016-7037(98)00055-6

Pancost, R. D., McClymont, E. L., Bingham, E. M., Roberts, Z., Charman, D. J., Hornibrook, E. R. C., et al. (2011). Archaeol as a Methanogen Biomarker in Ombrotrophic Bogs. *Org. Geochem.* 42, 1279–1287. doi: 10.1016/j.orggeochem.2011.07.003

Paull, C. K., Hecker, B., Commeau, R., Freeman-Lynde, R. P., Neumann, C., Corso, W. P., et al. (1984). Biological Communities at the Florida Escarpment Resemble Hydrothermal Vent Taxa. *Science* 226, 965–967. doi: 10.1126/science.226.4677.965

Paull, C. K., Normark, W. R., Ussler, W., III., Caress, D. W. and Keaten, R. (2008). Association Among Active Seafloor Deformation, Mound Formation, and Gas Hydrate Growth and Accumulation Within the Seafloor of the Santa Monica Basin, Offshore California. *Mar. Geol.* 250, 258–275. doi: 10.1016/j.margeo.2008.01.011

Paytan, A., Kastner, M., Martin, E. E., Macdougall, J. D. and Herbert, T. (1993). Marine Barite as a Monitor of Seawater Strontium Isotope Composition. *Nature* 366, 445–449. doi: 10.1038/366445a0

Reeburgh, W. S. (1976). Methane Consumption in Cariaco Trench Waters and Sediments. *Earth Planet. Sci. Lett.* 28, 337–344. doi: 10.1016/0012-821X(76)90195-3

Römer, M., Sahling, H., Pape, T., Bahr, A., Feseker, T., Wintersteller, P., et al. (2012). Geological Control and Quantity of Methane Ebullition From a High-Flux Seep Area in the Black Sea-The Kerch Seep Area. *Mar. Geol.* 319-322, 57–74. doi: 10.1016/j.margeo.2012.07.005

Römer, M., Sahling, H., Pape, T., Ferreira, C. D., Wenzhofer, F., Boetius, A., et al. (2014). Methane Fluxes and Carbonate Deposits at a Cold Seep Area of the Central Nile Deep Sea Fan, Eastern Mediterranean Sea. *Mar. Geol.* 347, 27–42. doi: 10.1016/j.margeo.2013.10.011

Sahling, H., Rickert, D., Lee, R. W., Linke, P. and Suess, E. (2002). Macrofaunal Community Structure and Sulfide Flux at Gas Hydrate Deposits From the

Cascadia Convergent Margin, NE Pacific. *Mar. Ecol. Prog. Ser.* 231, 121–138. doi: 10.3354/meps231121

Sassen, R., Joye, S., Sweet, S. T., DeFreitas, D. A., Milkov, A. V. and MacDonald, I. R. (1999). Thermogenic Gas Hydrates and Hydrocarbon Gases in Complex Chemosynthetic Communities, Gulf of Mexico Continental Slope. *Org. Geochem.* 30, 485–497. doi: 10.1016/S0146-6380(99)00050-9

Sauer, S., Hong, W.-L., Yao, H., Lepland, A., Klug, M., Eichinger, F., et al. (2021). Methane Transport and Sources in an Arctic Deep-Water Cold Seep Offshore NW Svalbard (Vestnesa Ridge, 79ºN). *Deep-Sea. Res. I.: Oceanogr. Res. Pap.* 167, 103430. doi: 10.1016/j.dsr.2020.103430

Schuur, E. A. G., McGuire, A. D., Schädel, C., Grosse, G., Harden, J. W., Hayes, D. J., et al. (2015). Climate Change and the Permafrost Carbon Feedback. *Nature* 520, 171–179. doi: 10.1038/nature14338

Shakhova, N., Semiletov, I. and Panteleev, G. (2005). The Distribution of Methane on the East Siberian Arctic Shelves: Implications for the Marine Methane Cycle. *Geophys. Res. Lett.* 32, L09601. doi: 10.1029/.2005GL02275

Shakhova, N., Semiletov, I., Salyuk, A., Yusupov, V., Kosmach, D. and Gustafsson, O. (2010). Extensive Methane Venting to the Atmosphere From Sediments of the East Siberian Arctic Shelf. *Science* 327, 1246–1250. doi: 10.1126/science.1182221

Sibuet, M. and Olu, K. (1998). Biogeography, Biodiversity and Fluid Dependence of Deep-Sea Cold-Seep Communities at Active and Passive Margins. *Deep-Sea. Res. II.: Top. Stud. Oceanogr.* 45, 517–567. doi: 10.1016/S0967-0645(97)00074-X

Stadnitskaia, A., Ivanov, M. K. and Sinninghe Damsté, J. S. (2008). Application of Lipid Biomarkers to Detect Sources of Organic Matter in Mud Volcano Deposits and Post-Eruptional Methanotrophic Processes in the Gulf of Cadiz, NE Atlantic. *Mar. Geol.* 255, 1–14. doi: 10.1016/j.margeo.2007.11.006

Suess, E. (2014). Marine Cold Seeps and Their Manifestations: Geological Control, Biogeochemical Criteria and Environmental Conditions. *Int. J. Earth Sci.* 103, 1889–1916. doi: 10.1007/s00531-014-1010-0

Sultan, N., Bohrmann, G., Ruffine, L., Pape, T., Riboulot, V., Colliat, J. L., et al. (2014). Pockmark Formation and Evolution in Deep Water Nigeria: Rapid Hydrate Growth Versus Slow Hydrate Dissolution. *J. Geophys. Res. Solid. Earth.* 119, 2679–2694. doi: 10.1002/2013JB010546

Torres, M. E., Collett, T. S., Rose, K. K., Sample, J. C., Agena, W. F. and Rosenbaum, E. J. (2011). Pore Fluid Geochemistry From the Mount Elbert Gas Hydrate Stratigraphic Test Well, Alaska North Slope. *Mar. Petrol. Geol.* 28, 311–331. doi: 10.1016/j.marpetgeo.2009.10.001

Torres, M. E., Tréhu, A. M., Cespedes, N., Kastner, M., Wortmann, U. G., Kim, J. H., et al. (2008). Methane Hydrate Formation in Turbidite Sediments of Northern Cascadia, IODP Expedition 311. *Earth Planet. Sci. Lett.* 27, 170–180. doi: 10.1016/j.epsl.2008.03.061

Ussler, W.III. and Paull, C. K. (1995). Effects of Ion-Exclusion and Isotopic Fractionation on Pore-Water Geochemistry During Gas Hydrate Formation and Decomposition. *Geo-Mar. Lett.* 15, 37–44. doi: 10.1007/BF01204496

Ussler, W.III. and Paull, C. K. (2001). "Ion Exclusion Associated With Marine Gas Hydrate Deposits," in *Natural Gas Hydrates: Occurrence, Distribution, and Detection*. Eds. Paull, C. K. and Dillon, W. P. (Washington, D.C: American Geophysical Union), 41–51.

Waage, M., Portnov, A., Serov, P., Bünz, S., Waghorn, K. A., Vadakkepuliyambatta, S., et al. (2019). Geological Controls on Fluid Flow and Gas Hydrate Pingos Development on the Barents Sea Margin. *Geochem. Geophys. Geosyst.* 20, 630–650. doi: 10.1029/2018GC007930

Werne, J. P., Baas, M. and Sinninghe Damsté, J. S. (2002). Molecular Isotopic Tracing of Carbon Flow and Trophic Relationships in a Methane-Supported Benthic Microbial Community. *Limnol. Oceanogr.* 47, 1694–1701. doi: 10.4319/lo.2002.47.6.1694

Westbrook, G. K., Thatcher, K. E., Rohling, E. J., Piotrowski, A. M., Pälike, H., Osborne, A. H., et al. (2009). Escape of Methane Gas From the Seabed Along the West Spitsbergen Continental Margin. *Geophys. Res. Lett.* 36, L15608. doi: 10.1029/2009GL039191

Conflict of Interest: The authors declare that the research was conducted in the absence of any commercial or financial relationships that could be construed as a potential conflict of interest.

frontiers | Frontiers in Marine Science

TYPE Review
PUBLISHED 12 September 2022
DOI 10.3389/fmars.2022.968647

OPEN ACCESS

EDITED BY
Dong Feng,
Shanghai Ocean University, China

REVIEWED BY
Zhilei Sun,
Qingdao Institute of Marine Geology (QIMG), China
Junxi Feng,
Guangzhou Marine Geological Survey, China

*CORRESPONDENCE
Hailong Lu
hlu@pku.edu.cn

SPECIALTY SECTION
This article was submitted to Marine Biogeochemistry, a section of the journal Frontiers in Marine Science

RECEIVED 14 June 2022
ACCEPTED 24 August 2022
PUBLISHED 12 September 2022

CITATION
Li Y, Chang J and Lu H (2022) Geochemical characteristics of gases associated with natural gas hydrate. *Front. Mar. Sci.* 9:968647. doi: 10.3389/fmars.2022.968647

Geochemical characteristics of gases associated with natural gas hydrate

Yuanyuan Li[1,2], Jingyi Chang[1,2] and Hailong Lu[2,*]

[1]College of Engineering, Peking University, Beijing, China, [2]Beijing International Center for Gas Hydrate, School of Earth and Space Sciences, Peking University, Beijing, China

With more natural gas hydrate samples recovered and more research approaches applied to hydrate-associated gas studies, data concerning the geochemical characteristics of hydrate-associated gases have been increased significantly in the past decades. Although systematic reviews of hydrocarbons are available, fewer studies have focused on the systematic classification of gas hydrates, yet. In this study, the primary origins and secondary processes that affect the geochemical characteristics of the gases are discussed. The primary origins are affected mainly by the type and /or maturity of the organic matter, which determine the main signature of the gas is microbial gas or thermogenic gas in a broad scheme. Apart from primary origins, secondary processes after gas generation such as migration, mixing, biodegradation and oxidation occur during the migration and/or storage of gases can significantly alter their primary features. Traditional methods such as stable isotope and molecular ratios are basic proxies, which have been widely adopted to identify these primary origins and secondary processes. Isotopic compositions of C_{2+} gases have been employed to identify the precursor of the gases or source rocks in recent years. Data from novel techniques such as methane clumped isotope and noble gases bring additional insights into the gas origins and sources by providing information about the formation temperature of methane or proxies of mantle contribution. A combination of these multiple geochemical approaches can help to elucidate an accurate delineation of the generation and accumulation processes of gases in a gas hydrate reservoir.

KEYWORDS

gas hydrate, thermogenic gas, microbial gas, clumped isotope, noble gas

1 Introduction

Natural gas hydrates are crystalline compounds composed of water and gases formed under high pressure and low temperature, mainly occurring in permafrost and continental slope sediment (Kvenvolden, 1988; Dickens et al, 1995; Sloan and Sloan, 1998; Buffett and Archer, 2004). As a potential energy resource and an important part of the global carbon cycle, natural gas hydrate has been investigated intensively in recent years [e.g., (Collett et al., 2019; Ye et al., 2019; Li et al., 2021; Zhang et al., 2021b)].

As the gigantic reserve of natural gas hydrate makes it a key part of the carbon cycle with a huge potential environmental effect, understanding the origins of gases can help to constrain the global methane fluxes and potential global climate effects (Nisbet et al., 2014; Schaefer et al., 2016; Schwietzke et al., 2016). Moreover, as an unconventional energy resource, detailed composition information about gas associated with natural gas hydrate can benefit resource evaluation and optimized site selection for production test and prospective commercial exploitation (Li et al., 2018; Ye et al., 2018; Jin et al., 2020; Liang et al., 2022). Furthermore, previous studies indicate that different gas components influence the temperature-pressure phase equilibrium curve of gas hydrate and further affect the thickness of gas hydrate stability zone (GHSZ) (Tréhu AM et al., 2006; Sloan et al., 2010). Hydrates containing heavy hydrocarbon gas may be more thermodynamically stable, so that molecular composition may provide extra clues for hydrate distribution (Xiao et al., 2019).

Compare to the oil and gas which containing long-chain hydrocarbons and biomarkers , the gases associated with hydrate are with relatively simple composition (Kvenvolden, 1988; Dickens et al., 1995; Kvenvolden, 1995; Sloan and Sloan, 1998; Buffett and Archer, 2004). Therefore, the techniques can be used to infer the generation and evolution of the gases are quite limited in the earlier stage of hydrate-associated research, mainly relying on the stable isotope and molecular ratios, thus provide limited information for delineating the definite origins and sources (Bernard et al., 1977; Schoell, 1980; Whiticar, 1999; Milkov and Etiope, 2018). Fortunately, with the increase of energy demand and the need for energy transformation, more attention has been paid to the gas hydrate attribute to its clean signature with huge reserves. More hydrate samples have been obtained in recent years [e.g. (Rodrigues et al., 2019; Ye et al., 2019; Zhang et al., 2019; Lai et al., 2021a)], and several test mining of hydrate area has been implemented [e.g. (Lorenson et al., 2011; Stern et al., 2011; Kida et al., 2015; Ye et al., 2018; Liang et al., 2022)]. Furthermore, thanks to the improvement of mass spectrometry resolution and the deeper understanding of the mechanism of isotope fractionation (Eiler, 2013; Ono et al., 2014; Young et al., 2017; Dong et al, 2020), new techniques such as clumped isotope have been gradually applied to the gas geochemistry research of hydrate (Figure 1), providing valuable information for the formation temperature and

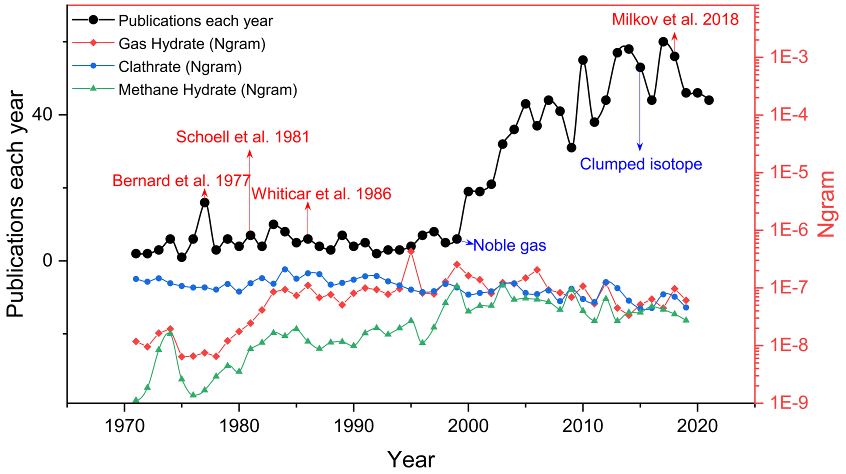

FIGURE 1
The line of black solid dot represents the number of research articles about gas geochemistry (molecular and/or isotopic composition data) of natural gas hydrate published each year from 1970 to 2021 (data from web of science), modified from Milkov and Etiope (2018). Note that data for about 87% of all samples were published after the genetic diagrams of Bernard et al. (1977); Schoell (1983); Whiticar et al. (1986) and Milkov and Etiope (2018)were proposed. Three line of colored dot represents how those phrases (gas hydrate, clathrate and methane hydrate) have occurred in a corpus of books over the selected years (1970-2019) (data from Google N-gram viewer, (Michel et al., 2011)). We can see that use of "gas hydrate" and "methane hydrate" started to rise in 1980s, match to the publication of the genetic diagrams, while the frequency of the term "clathrate" declined steadily from the 1970s.

kinetic secondary processes of methane (Wang et al, 2015a; Ijiri et al, 2018; Giunta et al., 2021; Zhang et al., 2021a; Lalk et al., 2022). Noble gases, which require higher quality testing methods, have also been used in recent years to study the contribution of deep mantle sources to hydrate reservoirs (Figure 1) (Ruffine et al., 2018; Moore et al., 2020; Snyder et al., 2020). Abundant samples combined with the multi-approaches make it possible to accumulate systematic and valuable data about geochemical characteristics of hydrate-associated gases for a specific area (Figure 1). However, these case studies are required further systematic discussion and summary to excavate more profound insights and provide more uniform criterions and references for future study.

In this study, the geochemical data of gases associated with hydrate (including hydrate-bound gas, void gas, headspace gas and venting gas, etc.) published in recent years are compiled, and the effect of processes from the primary generation to the later accumulation of hydrate-associated gas are summarized, the methods of gas source and origin identification in recent years are discussed, to provide profound insights into the understanding of the formation mechanism and accumulation history of gas hydrate system.

2 Geochemical characteristics of natural gas hydrate

The existence of natural gas hydrate requires suitable temperature and pressure conditions, which make them mainly occurring in certain interval (GHSZ) of permafrost and marine sediment. Many factors such as gas composition, pressure gradient, geothermal gradient, and salinity affect gas hydrate stability conditions in nature. The GHSZ profiles for marine setting and permafrost environment are different (Figures 2A, B). The top and bottom of the GHSZ in these two conditions are defined by the intersection of the geothermal gradient (and/or hydrothermal gradient) with the hydrate phase boundary curve.

The dataset of this study came from about 72 studies with more than 1,300 gas samples around the world (Figure 3). Of these, 133 are derived from terrestrial permafrost regions, 114 from terrestrial freshwater lakes (Lake Baikal), and the rest from marine sediments of continental margin. Most of the samples are hydrate-bound gas, void gas, headspace gas or venting gas which associated with natural gas hydrate. Almost all published isotope data of hydrate-associated gases have been compiled in Figure 4. The heaviest $\delta^{13}C-C_1$ is found at -22.5‰ in Mountain Qilian (Wang et al., 2015b) and the lightest at -102.2‰ in Amazon Fan from the distribution plot (Rodrigues et al., 2019), with an average of -61.67‰ (Figure 4A). A total of 1193 $\delta^{13}C-C_1$ data from 46 area were counted to estimate the $\delta^{13}C-C_1$ range of gases associated with natural gas hydrate. The highest frequency range of $\delta^{13}C-C_1$ appears in -70~-60‰, especially -70~ -65‰ in the frequency histogram of the $\delta^{13}C-C_1$ (Figure 4B), which may indicate that the microbial gas is quantitatively dominant in the current dataset. Samples from permafrost are with higher $\delta^{13}C-C_1$ (-55~ -30‰) compared to those from freshwater setting (-70~ 55‰), while samples from marine sediments are with widest distribution of $\delta^{13}C-C_1$ range from -102‰ to -30‰. $\delta D-C_1$ ranges from most enriched at -115‰ in the Gulf of Mexico (Sassen et al., 2001) to most depleted at -326.3‰ in Lake Baikal (Hachikubo et al., 2010), with an average value of -209.75‰ (Figure 4C). A total of 744 $\delta D-C_1$ data from same area

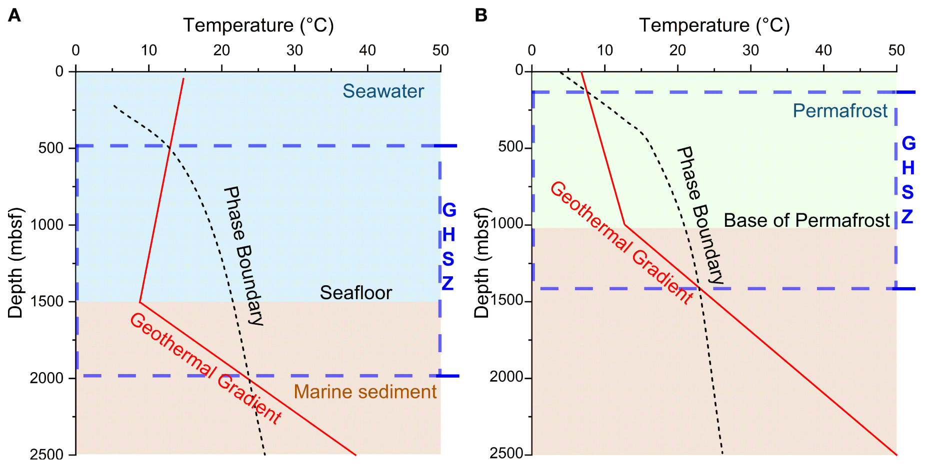

FIGURE 2
Gas hydrate stability zone (GHSZ) for gas hydrates in **(A)** marine environment and **(B)** permafrost environment, modified from (Chen and Merey, 2021).

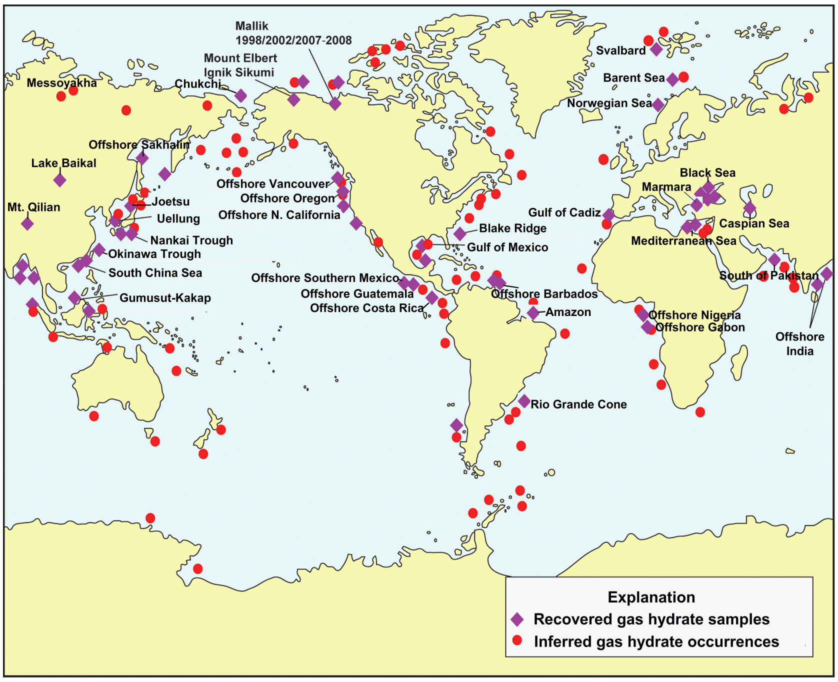

FIGURE 3
Location of sampled and inferred methane hydrate occurrences in marine sediment of outer continental margins and permafrost regions, modified from (Collett et al., 2009). Data of samples adopted in this study are highlighted with site name on this map.

with $\delta^{13}C$-C_1 data were counted to estimate the δD-C_1 range of gases associated with natural gas hydrate, the high-frequency range is distributed in -200 to -175‰ (Figure 4D). There is also a small high frequency band of δD-C_1 around -300‰, which represent the hydrogen isotope signature of methane generated from acetate fermentation in freshwater setting. Similar to the $\delta^{13}C$-C_1, the distribution of samples from different environment are with distinct dominated frequency interval in the frequency histogram, which manifest as samples from freshwater are with lowest δD-C_1, followed by permafrost regions, and finally marine sediment, which can be ascribed to the different sources of hydrogen in methane.

2.1 Permafrost vs. marine sediment

Continental gas hydrate, has been identified in Messoyakha field of western Siberia, Alaska, Mackenzie delta and Qinghai-Tibet plateau [e.g., (Lorenson et al., 2011; Wang et al., 2018)], which are considered to be a major environmental concern on a number of levels since there are no methane-barrier from marine sediment and seawater compared to marine gas hydrate. As knowledge of permafrost-associated gas hydrates has grown, it has become clear that many permafrost-associated gas hydrates are inextricably linked to an associated conventional petroleum system, and that their formation history (trapping of migrated gas *in situ* during Pleistocene cooling) is consistent with having been sourced at least partially in nearby thermogenic gas deposits. It can also be found that methane from continental gas hydrate is more enriched in ^{13}C and more depleted in D compared to that from marine settings (Figures 4A, C), which may ascribe to the mixing of microbial methane generated *via* acetate fermentation (Wang et al., 2018).

2.2 Microbial vs. thermogenic gas

The brief description of published geochemical characteristics of hydrate-associated gases around the world are summarized in Table S1. It can be found that hydrate with microbial origin formed by the typical acetate fermentation pathway has been identified in Lake Baikal (Figures 5A, C) (Kida et al., 2006; Hachikubo et al., 2010). The hydrates formed by the typical CO_2 reduction pathway occur in India, Blake Ridge, Black Sea, offshore northern California, Nankai Trough, offshore Oregon, Okhotsk Sea, and Ulleung Basin, etc. (Figures 5A–C) (Brooks et al., 1991; Ginsburg and Soloviev, 1997; Waseda and Uchida, 2004; Collett et al., 2008; Choi et al., 2013; Collett et al., 2019). It had been considered that most of the

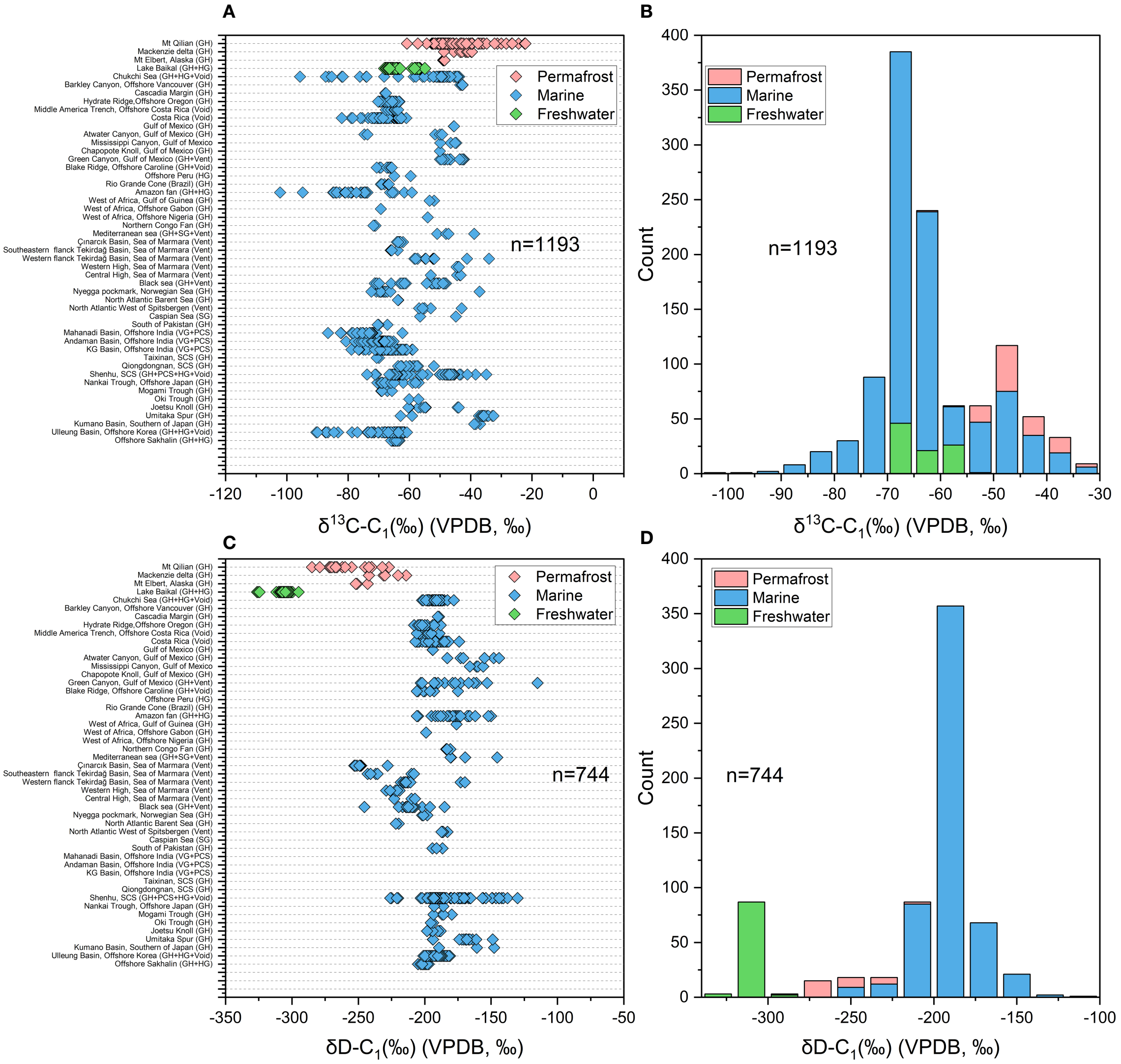

FIGURE 4
(A) The distribution of $\delta^{13}C-C_1$ of hydrate-associated gas from different area around the world. **(B)** The frequency histogram of $\delta^{13}C-C_1$ of hydrate-associated gas counted from 1193 data. **(C)** The distribution of $\delta D-C_1$ of hydrate-associated gas from different area. **(D)** The frequency histogram of $\delta D-C_1$ of hydrate-associated gas counted from 744 data. GH, Gas Hydrate dissociated gases; Vent, Venting Gases; Void, Void gases; HG, Headspace gases; PCS, gas from Pressure coring systems (PCS).

gases contained in natural gas hydrates mainly derived from microbial sources in the early stage of hydrate investigation, and most of the previous gas-hydrate assessments had been carried out based on that natural hydrate was formed from microbial gas. However, more and more thermogenic gas hydrates have also been recovered in later studies, for example from Caspian Sea (Lüdmann and Wong, 2003), Cascadia Margin (Pohlman et al., 2005), Gulf of Mexico (Sassena et al., 1999; Sassena et al., 2001a; Sassena et al., 2001b), Svalbard (Smith et al., 2014), west African province (De Prunel et al., 2017), NW Borneo region of the South China Sea (SCS) (Paganoni et al., 2016; Paganoni et al., 2018), Qiongdongnan of SCS (Ye et al., 2019), Shenhu of SCS (Zhang et al., 2019) and sea of Marmara (Ruffine et al., 2018), etc (Figures 5A–C).

It can also be seen that with the increase of samples obtained and the diversification of research methods (such as the isotopic composition of C_{2+}, clumped isotopes and noble gases), the understanding of the origin of hydrate-associated gases in a certain region has gradually deepened. For example, the Shenhu area of the SCS, of which the hydrate-associated gas was originally thought to be pure microbial gas (Fu and Lu, 2010; Wu et al., 2011; Liu et al., 2015; Dai et al., 2017), has been gradually realized that it is with structurally controlled mixed gas sources with considerable thermogenic contribution in recent

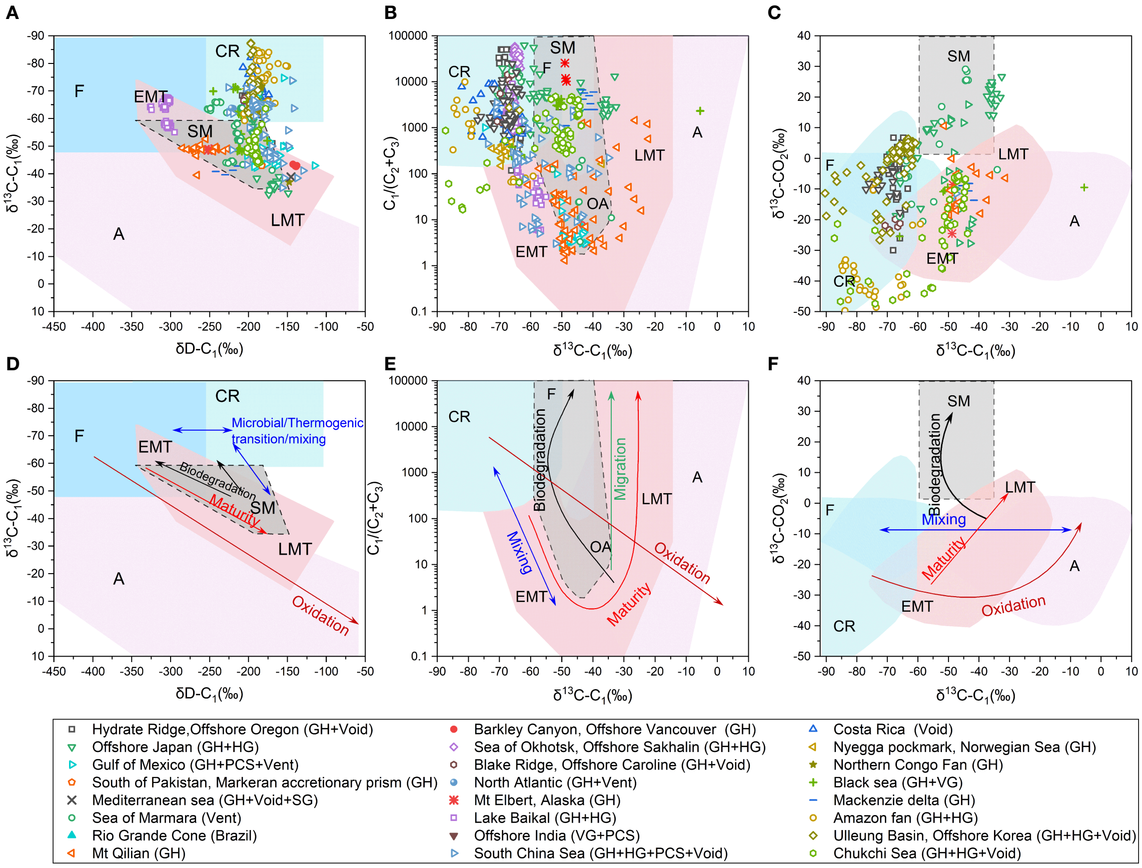

FIGURE 5
Genetic diagram of δ^{13}C-C$_1$ versus δD-C$_1$ **(A)**; δ^{13}C-C$_1$ vs. C$_1$/(C$_2$ +C$_3$) **(B)**; δ^{13}C-C$_1$ vs. δ^{13}C-CO$_2$ **(C)** with dataset plotted in. Genetic diagram of δ^{13}C-C$_1$ versus δD-C$_1$ **(D)**; δ^{13}C-C$_1$ vs. C$_1$/(C$_2$ +C$_3$) **(E)**; δ^{13}C-C$_1$ vs. δ^{13}C-CO$_2$ **(F)** with secondary alteration processes (migration, mixing, biodegradation, oxidation and maturity) plotted, modified from (Milkov and Etiope, 2018). EMT-early mature thermogenic; OA-oil associated; LMT-late mature thermogenic; SM-secondary microbial; A-abiotic; F-fermentation; CR-CO$_2$ reduction.

years, and there is a paragenetic relationship between the hydrate-associated gas and surrounding conventional oil and gas reservoirs (Zhang et al., 2019; Lai et al., 2022; Liang et al., 2022). New subtype of gases, such as secondary microbial gases generated by hydrocarbon biodegradation, has been widely recognized in more areas with the deepening of the understanding of the gas generation (Figures 5A–C) [e.g., (Milkov, 2018; Ruffine et al., 2018; Lai et al., 2022; Li et al., 2022)].

3 Primary origins of hydrate-associated gases

Gases bound in hydrate usually formed by biodegradation of organic matter, which includes bacterial gas (or called microbial gas) produced by bacterial processes and thermogenic gas formed through thermochemical reactions (Schoell, 1983). The characteristics of biogenic gas are controlled by the type and thermal maturity of organic matter, i.e. kerogen type, burial history and geothermal gradient (Tissot et al., 1974; Tissot and Welte, 1984; Whiticar, 1994).

The origin material of natural gas is divided into sapropelic type, which are mainly type I/II kerogen and dominated by marine source organic matter, and humic type which are mainly type III kerogen and dominated by terrestrial organic matter (Van Krevelen, 1961). The natural gas generated by sapropelic organic matter is named oil-type gas, and that by humic organic matter is named as coal-type gas. Study of organic matter in hydrate-bearing sediment of Okinawa trough suggested that terrestrial organic matter is more prone to the formation of microbial gases as compared with marine organic matter (Saito and Suzuki, 2007). However, Dai et al. (2017) proposed that most of the gas-forming hydrates are oil-type gas from marine organic matter, and coal-type gas has only been reported in Qilian Mountain and offshore Vancouver island (Wang, 2010; Cao et al., 2012).

The thermal maturation stages of organic matter are labelled (1) Immature (diagenesis), the initial thermal mature stage where microbial gas is dominated; (2) Mature (catagenesis), the intermediate stage where oil and methane are generated from kerogen decomposition; (3) Post-mature (metagenesis), the final stage where almost pure methane (dry gas) formed mainly from thermal cracking of oil and bitumen (Tissot and Welte, 1984; Wiese and Kvenvolden, 1993). Therefore, the natural gas component changes from microbial dry gas to thermogenic wet gas and then to thermogenic dry gas in the immature, mature and over-mature stage of organic matter evolution (Tissot and Welte, 1984; Wiese and Kvenvolden, 1993).

4 Secondary processes after gas generation

After being generated in source rocks, natural gases may experience a series of secondary processes, such as mixing, migration, oxidation and biodegradation, etc., before the formation of reservoir. The primary geochemical characteristics of the gases can be obscured by these secondary processes, resulting in isotopic and molecular compositional fractionation. As a result, it is necessary to identify these secondary processes and their effects, to properly interpret the origins and sources of the gases.

4.1 Migration

Microbial methane produced in the GHSZ alone is not sufficient for the accumulation of concentrated gas hydrate in most cases. Most of the allochthonous gas in the GHSZ might have been migrated from the deeper sediments, mainly involving three kinds of processes: (1) diffusion; (2) migration of water-dissolved gas; (3) buoyancy of free gas. Diffusion is quite slow, unlikely to bring up sufficient gas to form highly saturated hydrate reservoirs in most cases (Xu and Ruppel, 1999). However, the latter two are relatively efficient processes.

Diffusion-associated fractionations of isotope and molecular composition of hydrocarbons are expected to occur as a function of mass and are thought to behave "chromatographically", by which lighter isotopes and hydrocarbons move more quickly than their heavier counterparts (Thompson, 1979; Leythaeuser et al., 1982; Choi et al., 2013). It is also found that ^{12}C-^{12}C bond is more prone to breakage than ^{12}C-^{13}C bond and the compounds with heavy carbon isotope ^{13}C is more easily absorbed by rocks, minerals and organic matters (Chanton, 2005). As a result, $^{13}C_{-CH4}$ and D_{-CH4} for a diffused gas are depleted relative to its source, while $C_1/(C_2+C_3)$ is relatively increased (Coleman et al., 1977; Prinzhofer and Pernaton, 1997; Zhang and Krooss, 2001; Schloemer and Krooss, 2004). Coleman et al. (1977) validated the effect of diffusion on the molecular composition of gases and proposed that C_{2+} hydrocarbons can be entirely stripped off from the migrated gases. It is proposed that the migration *via* diffusion can cause measurable carbon isotope fractionation of more than 5‰ (Chen, 1994; Prinzhofer and Pernaton, 1997). Both simulation and experimental results reveal that the fractionation by diffusion is affected by TOC content and porosity and permeability of rock, the migration pathway and the type of migrating gas, etc. (Galimov, 1967; Craig, 1968; Gunter and Gleason, 1971; Stahl, 1977; Chen, 1994; Zhang and Krooss, 2001; Li et al., 2003).

There are still debates on whether isotopic fractionation occurs or not in the process of natural gas migration other than diffusion, although most studies suggest that there is no isotope fractionation during migration (Stahl and Carey, 1975; Coleman et al., 1977; Fuex, 1980; Faber and Stahl, 1984; Zhang and Krooss, 2001). The isotopic compositions of natural gases, recovered from different depths of the same well shows no obvious difference (Stahl and Carey, 1975; Coleman et al., 1977; Faber and Stahl, 1984). Schoell proposed that the migration of natural gas would not cause the change in $\delta^{13}C_{-CH4}$, insteadly the isotopic compositions of natural gases are controlled by the type and thermal evolution of original organic matter (Schoell, 1983; Schoell, 1984). Experiment and numerical simulation conducted by Fuex (1980) showed that migration fractionation of methane was almost negligible, and the most likely cause of this insignificant fractionation was the difference in water solubility between $^{12}CH_4$ and $^{13}CH_4$, and in most cases such fractionation would not exceed 1-permil. It is also suggested that depletion in methane carbon isotope is caused by bacterial activities rather than by migration (Fuex, 1980; Faber and Stahl, 1984). Based on the discussions above, migration is expected to cause thermogenic gas zone to shift upward in the $C_1/(C_2+C_3)$ versus $\delta^{13}C_{-CH4}$ diagram, corresponding to an increase in $C_1/(C_2+C_3)$ ratio but no significant change in $\delta^{13}C_{-CH4}$ (Figure 5E) (Bernard et al., 1977).

4.2 Mixing

Mixing of natural gases, which can be from the identical source rock at varying maturity stages or different source rocks, and biogenic and abiogenic origins, is a common phenomenon (Whiticar, 1994). The mixing of microbial and thermogenic gas has been well recognized in gas hydrates in Shenhu area of South China Sea (SCS) (Zhang et al., 2019), Norwegian Sea (Vaular et al., 2010) and Japan Sea (Waseda and Iwano, 2008). In recent years, the mixing of thermogenic gas with secondary biodegraded gas has also been identified in areas such as Western High of Sea of Marmara (Ruffine et al., 2018).

The molecular and isotopic composition of natural gas are adopted to identify mixing and to determine the composition and contribution of each gas-endmember (Schoell, 1983; Chung et al., 1988; Whiticar, 1994; Prinzhofer and Huc, 1995). As shown in Figure 3A, mixing of microbial and thermogenic gas can be identified by the carbon isotope of methane ($\delta^{13}C$-C_1) and the dry coefficient of the gas ($C_1/(C_2+C_3)$) (Figure 5E) (Bernard et al., 1977), and a linear relationship between the two endmembers has been recognized, changing strictly with the mixing ratio in the $\delta^{13}C$-C_1 versus δD-C_1 diagram (Figure 5D). Prinzhofer and Pernaton (1997) proposed that the mixing of two gas endmembers result in a straight line in the plot of C_2/C_1 versus $\delta^{13}C$ and an exponential line in the plot of log (C_2/C_1) versus $\delta^{13}C$. Prinzhofer et al. (2000) indicated that in any plot where the ratio of two numerators with a common denominator (for example, $\delta^{13}C$-C_1, $\delta^{13}C$-C_2 and $\delta^{13}C$-C_3) is drawn, the mixing between the two end-members is on a straight line, and the linear relationship becomes more pronounced when isotope of C_{2+} gases is applied. Chung et al. (1988) proposed "natural gas plot" based on the semi-linear relationships of the carbon isotopic compositions of n-alkanes in pure thermogenic gases, which can help to estimate the relative contribution of microbial gas or thermogenic gas in a two end-member mixing model, after the $\delta^{13}C$ of thermogenic methane is obtained by extrapolating the line of isotopic values of C_{2+} gases. This method has been widely used in hydrate gas studies [e.g., (Hachikubo et al., 2015; Lai et al., 2021a)].

4.3 Hydrate formation and dissociation

The gas hydrate system has always been in a dynamic equilibrium state and is extremely sensitive to environmental conditions, especially temperature and pressure conditions change, driving forces leading to its dissociation have been primarily ascribed to event such as pressure reduction (e.g., (Teichert et al., 2003, Watanabe et al., 2008), temperature rise [e.g. (Cremiere et al., 2016, Kennett et al., 2000, Phrampus and Hornbach, 2012)], salinity changes (Riboulot et al., 2018) and glacial-interglacial transition (Chen et al., 2019, Deng et al. 2021). Isotopic and molecular fractionation may occur during the hydrate formation, dissolution and dissociation, so it is necessary to clarify whether the isotope fractionation is caused by hydrate crystallization itself. Laboratory studies by Hachikubo et al (2008) found that the δD of hydrate-bound gases is several permil depleted than that of residual gas, while there was no significant difference in $\delta^{13}C$. Nevertheless, the difference in δD is not so significant that affects the determination of gas origin. The effect of temperature on isotopic fractionation was also studied, and it was found that the fractionation was more evident with temperature decreasing (Hachikubo et al (2008), which was confirmed by Kimura et al. (2021). Experimental study from Luzi et al (2011a) has shown that hydrate formation has no significant effect on the carbon isotope ratios for CH_4 hydrate, whereas a noticeable $\delta^{13}C$ depletion was observed with CO_2 hydrates compared to the gas phase. Similar isotope depletion in hydrate phase was observed by Kimura et al. (2021). However, contrary experimental results from Chen et al. (2018) indicates that heavy isotopes tend to preferentially enter the hydrate phase during the formation of CO_2 hydrate and the carbon isotope fractionation is less intensive than that of oxygen and hydrogen. A comparison of stable isotope ratios of hydrate-bound and sediment gases, which were collected at the same depth of the same core from Lake Baikal, was performed, revealing that the $\delta^{13}C_{\text{-CH4}}$ and $\delta D_{\text{-CH4}}$ of the hydrate-bound gas were 1-2‰ and 5‰ smaller than the sediment gas, respectively (Kimura et al., 2020). The hydrogen isotope fractionation was in good agreement with the prediction from the experimental results of synthetic methane hydrate (Hachikubo et al., 2008), while the reason for the isotopic fractionation in ^{13}C was still unknown. Lin and Zeng (2010) discovered that the molecular compositions are differentiated during hydrate formation, methane content decreases in hydrate phase as compared with wet gases (C_{2+}) due to the difference in combination ability with water.

Lapham et al. (2012) experimentally studied the possible fractionation during hydrate dissolution or decomposition (two different physical processes), and it was confirmed that there is no isotope fractionation during both processes. Lai et al. (2021b) conducted a step-wise depressurization experiment with hydrate-bearing sediment to study the possible changes in the molecular and isotopic composition of gases released in depressurization process, indicating that no significant change in carbon isotopic composition while heavy hydrocarbons released mainly in the later stage of hydrate dissociation.

4.4 Biodegradation

When migrating upward into the shallow sediments, thermogenic gases containing certain amount of C_{2+} components might experience biodegradation with the involvement of microorganisms, and their original characteristics would be changed while yielding secondary methane (Head et al., 2003; Jones et al., 2008; Knittel and Boetius, 2009; Jones et al., 2010; Gao et al., 2013; Mesle et al., 2013; Schlegel et al., 2013). As microorganisms preferentially consume C_{2+} gases and produce secondary microbial C_1 as the terminal product, C_1 will be gradually accumulated and the ratio of $C_1/(C_2+C_3)$ will be increased (Figure 5D) (Zeikus, 1977; Larter et al., 2005; Boreham and Edwards, 2008). Generally, methane generated from hydrocarbon biodegradation is relatively enriched in ^{13}C compared to methane from primary methanogenesis (Valentine et al., 2004; Milkov and Dzou, 2007). It is also found that, biodegradation preferentially consumes ^{12}C of propane and results in the enrichment of ^{13}C in residual propane while the isotopic composition of ethane is not changed (James and Burns, 1984). As a result, the carbon isotopic compositions of hydrocarbon components in original thermogenic gases generally display a smooth progressive distribution pattern from C_1 to C_5, while those of biodegraded gases exhibit a serrated configuration, especially with unique ^{13}C enrichment of propane (James and Burns, 1984). Moreover, as CO_2 with ^{12}C derived from biodegraded hydrocarbons is preferentially converted into secondary microbial methane, the residual CO_2 becomes more enriched in ^{13}C (> +2‰) (Figures 5C, F) (Lillis and Magoon, 2007). Such significant enrichment in ^{13}C of CO_2 is unique, and it can be a proxy of biodegradation degree. Typical gas hydrates, which contain biodegraded-gases with enriched ^{13}C isotope composition of CO_2 (+25‰), have been reported in the Western high of Sea of Marmara (Ruffine et al., 2018).

4.5 Oxidation

Hydrate-associated gases will be oxidized by anaerobic or aerobic process while upward escaping, and the dominant process depends on the surrounding redox conditions. For aerobic oxidation, both enriched cultures with methane-oxidizing bacteria and analytical results of natural gas samples have suggested that oxidation can lead to the decrease in C_1 content and enrichment in ^{13}C and D of residual C_1 (Figures 5D–F), because the C_1 with lighter isotope is preferentially oxidized during this process (Coleman et al., 1981; Etiope et al., 2011; Daskalopoulou et al., 2018). Coleman et al. (1981) proposed that the extent of isotope fractionation is associated with temperature, and the change in δD value of methane is 8~14 times greater than that of $\delta^{13}C$ value. Kinnaman et al. (2007) suggested that the isotope fractionation becomes less intensive with the increment of carbon number (i.e., $C_1>C_2>C_3>C_4$), and the degree of isotope fractionation appears insignificant with substrate decreasing.

For anoxic sediments, the anaerobic oxidation of methane (AOM) predominates with the involvement of microorganism (Barnes and Goldberg, 1976; Reeburgh, 1976). Variation in methane isotopic composition has been observed in active AOM marine sediments, and it has been attributed to the difference in sulfate availability (Borowski et al., 1997; Pohlman et al., 2008; Yoshinaga et al., 2014). Batch enrichment cultures revealed that at seawater sulfate concentrations (28 mM), AOM will induce kinetic isotope fractionations, resulting in the enrichment of ^{13}C and D in the residual methane (Holler et al., 2009; Ono et al., 2021). In contrast, at low sulfate concentrations AOM results in ^{13}C-depletion in the remained methane and were explained as isotopic equilibration between methane and inorganic carbon mediated by AOM (Yoshinaga et al., 2014).

5 Discussion

Accurate depict of the formation and accumulation process of the hydrate-associated gas requires information obtained from various aspects. Development of both conventional and novel techniques make it possible to deepen our understanding of the gas geochemistry study. Here, we discuss the hydrate-associated gas geochemistry from three aspects *via* a complete overview of the state of the art, recent research breakthroughs, and areas of continued controversy.

5.1 Stable isotope & Gas composition

5.1.1 Developments

Stable isotope and molecular composition have always been basic properties of the gases that reflect their origins and sources. The most commonly used method to interpret the origin of gases is the plot of $C_1/(C_2+C_3)$ versus $\delta^{13}C_{-CH4,}$ known as “Bernard plot” because it was originally proposed by Bernard et al. (1976). Based on the analytical results of natural gases, Bernard et al. (1976) noticed that the microbial gas always is with a higher dry coefficient ($C_1/(C_2+C_3)$ > 1000) and lighter $\delta^{13}C_{-CH4}$ ($\delta^{13}C_{-CH4}$<-60‰), while thermogenic gas usually is with lower dry coefficient (0< $C_1/(C_2+C_3)$< 50) and heavier $\delta^{13}C_{-CH4}$ ($\delta^{13}C_{-CH4}$ >-50‰). Schoell first proposed of using the carbon and hydrogen isotopes of methane to recognize the origin of hydrocarbon gases (Schoell, 1980; Schoell, 1983). The genetic diagram includes microbial gases from marine ($\delta^{13}C$< -60‰, δD -200‰ ~ -150‰) and terrestrial environment ($\delta^{13}C$< -60‰, δD -250‰ ~ -200‰), oil-associated thermogenic gases ($\delta^{13}C$ -60‰~ -25‰, δD -300‰~ -150‰) and non-oil-associated gases (δD >-150‰). Whiticar further modified the diagram by merging all thermogenic gases into one area, and specified microbial gases into CO_2 reduction and acetate fermentation (Whiticar et al., 1986; Whiticar, 1999). Gutsalo and Plotnikov (1981) proposed the first genetic diagram based on the carbon isotopic compositions of methane and carbon dioxide ($\delta^{13}C_{-CO2}$ vs. $\delta^{13}C_{-CH4}$), which grouped the gases into abiogenic gas, microbial gas and thermogenic gas. Milkov 2011 added to the diagram the genetic region of secondary microbial gases from oil biodegradation, and Etiope et al added new region of abiogenic CH_4 to this genetic diagram (Etiope and Lollar, 2013; Etiope and Schoell, 2014; Etiope, 2017).

Milkov and Etiope (2018) revised the three plots based on the data from more than 20,000 natural gas samples published in recent decades, updating a more detailed classification of gas origins (Figure 5). In addition to the above classification diagram, other information from geological geochemical or even experimental studies can benefit to figure out the gas origin. The primary microbial gases are characterized by the composition with C_1-C_3 hydrocarbons only, which is supported by the results from laboratory experiments that microbes can merely generate these three hydrocarbons (Oremland et al., 1988; Hinrichs et al., 2006). The geological setting can provide boundary condition to identify the microbial gas, such as the absence of oil in the sediment or reservoir. Similarly, thermogenic gases are usually associated with conventional oil reservoir and characterized by the presence of all the methane homologues (i.e., C_1-C_5).

5.1.2 Recent advances

Most studies of hydrate-related gases stop at distinguishing whether the gas is thermogenic derived from deep sources or microbial from shallow methanogenesis. For gases from deep sources, there are few ways to identify the specific source rocks, which constrain the understanding of the generation and accumulation processes of gas hydrate deposits for a specific area.

Rooney et al. (1995) proposed that the relationship between methane and ethane in the early stages of thermogenic gas generation can be described with the following equation **Eq (1)**:

$$\delta C_2 = -0.5\left(\delta C_{org} - \delta C_1\right) + \delta C_{org} \tag{1}$$

where δC_{org} is referred to $\delta^{13}C$ of the organic matter; generally -27‰ taken for terrestrial sources, and -20‰ for marine sources (Rooney et al., 1995; Lorenson and Collett, 2018). Lorenson and Collett (2018) studied δC_1 and δC_2 of hydrate gas offshore India and found that gas from KG basin is mainly microbial, while those from the deep Mahanadi Basin are mainly derived from the gas-prone terrestrial organic matter (Figure 6A). Liang et al. (2022) proposed that microbial and thermogenic gases associated with gas hydrate from the Shenhu area were derived from marine and terrigenous organic matter, respectively, based on the isotopic composition of C_1 and C_2 (Figure 6A). The integrated isotopic values of C_1, C_2 and C_3 can better identify the gas origins and the types of their precursor organic matter (Figure 6B). Liang et al. (2022) pointed out that most of the hydrate containing gases in Shenhu area fell into the sapropelic gas area (Figure 6B), which is close to conventional gas reservoirs in the plot (area IV in Figure 4), indicating for the first time that the thermogenic gas in hydrate is cogenetic with conventional oil and gas reservoirs in Panyu low uplift of Baiyun Sag. Above studies emphasize the importance of high-precision isotope measurement of C_{2+} components in hydrate-associated gases, which can provide clues for the identification of the source rocks of the gases.

In addition, detailed organic geochemistry, microbial and geological investigation have been proved to be robust tools to provide extra clues for gas origins and sources in recent years (Lai et al., 2022; Li et al., 2022; Lin et al., 2022). Presence of biomarkers of deeply buried thermogenic hydrocarbons and microbial communities associated with hydrocarbon degradation are remarkable signatures to identify the secondary biodegraded gas. This kind of integrated study should be widely used in the future research of hydrate-associated gases (Lai et al., 2022).

5.1.3 Unresolved questions

Although several methods have been proposed for the identification of the origins of hydrate-associated gas, sometimes it is still difficult for a specific case because there are unclear boundaries and overlaps between different classifications (Figure 5) (Martini et al., 1996; Prinzhofer and Pernaton, 1997; Martini et al., 1998; Valentine et al., 2004; Etiope and Schoell, 2014; Smith et al., 2014). The molecular and isotopic fractionation caused by post-generation processes makes the identification of gas origins more challenging

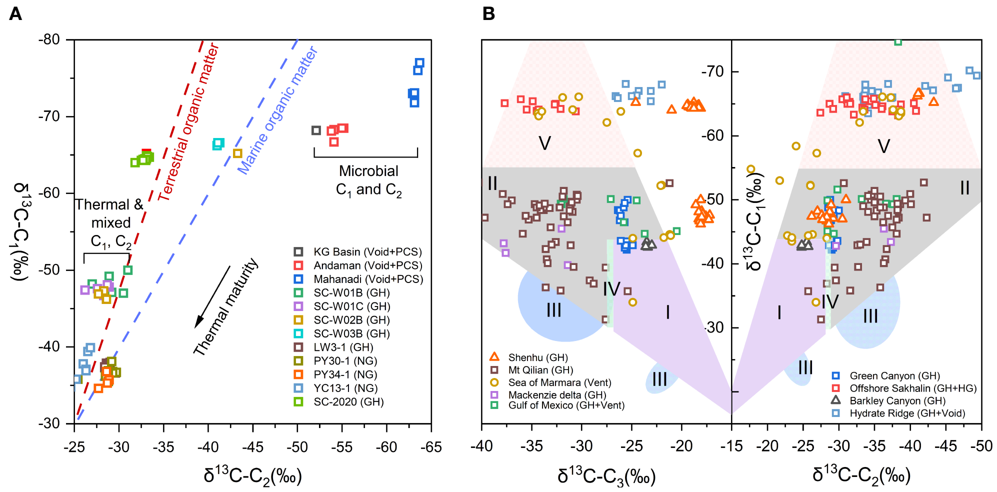

FIGURE 6

(A) Relationship of different types of organic matter in the source rocks and hydrate-associated gas. The diagonal lines are adapted from (Lorenson and Collett, 2018). VG-Void Gas, PCS-pressure core gas; GH-Gas Hydrate dissociated gases; NG-Natural gas. **(B)** Plot of the $\delta^{13}C_1$, $\delta^{13}C_2$, and $\delta^{13}C_3$ values of the hydrate-bound gas samples. The genetic diagram is adapted from (Dai, 1992).(I-Humic type gas; II-Sapropel type gas; III-Gas mixture with the reversal of carbon isotope; IV-Humic type gas and sapropel type gas; V-Biogenic gas). .

(Prinzhofer and Pernaton, 1997; Martini et al., 1998; Whiticar, 1999). In addition, empirical diagrams are often proposed through a large amount of statistical data, which may not applicable to hydrate samples from all geological settings. Empirical formulas often ignore the effects from secondary process like mixing, migration and biodegradation. However, these processes often obscure the original signal of the gases, so it is better to interpret the data with other aspects of evidence, such as organic geochemistry of hydrate-bearing sediment, geophysics data, etc.

It is also an unsolved problem to quantitatively identify the contributions of different gas sources. Especially for the mixed-origins gas hydrate, the contribution proportion of shallow *in-situ* microbial gas and allochthonous thermogenic gas is still a difficult problem. Sun et al. (2020) reconstructed a geological model combining seismic, well and geological interpretation to predict hydrocarbon generation, migration and formation of gas hydrate in Shenhu area. The modeling shows that about 80% of the methane-forming hydrate is with thermogenic source and the total organic carbon (TOC) content is considered to be important factor related to biogenically-sourced gas hydrate distribution. However, TOC and hydrocarbon-generation index (HI) are important parameters that considered in this study, more relevant parameters about source rocks especially biogenic source rocks should be evaluated in the future studies.

5.2 Clumped isotope

5.2.1 Developments

Additional proxies are required to help distinguish between different sources and post-generation processes. As a novel technique established in the past 10 years, methane clumped isotopes are with potential to improve our understanding of gas origins. Clumped isotopes are referred to multiply substituted isotopologues with two or more rare isotopes e.g. $^{13}CH_3D$ and $^{12}CH_2D_2$ for methane (Eiler, 2007; Eiler, 2013). The first study of methane clumped isotopes was conducted at Caltech on ultra-high resolution isotope mass spectrometry (Thermo fisher, Ultra), but upon that time only a total Δ18 signal could be available, unable to distinguish $^{13}CH_3D$ from $^{12}CH_2D_2$ (Stolper et al., 2014b). Later, measurement of $^{13}CH_3D$ was also achieved using Tunable Infrared Laser Direct Absorption Spectroscopy (TILDAS) at MIT (Ono et al., 2014). The recognition of both $^{12}CH_3D$ and $^{13}CH_3D$ signals on a single measurement was succeeded for the first time with a higher resolution mass spectrometry (Nu, Panorama) in 2016 at UCLA (Young et al., 2016; Young et al., 2017), although Ultra and TILDAS also achieved this function in the following years (Eldridge et al., 2019; Gonzalez et al., 2019; Dong et al., 2020; Dong et al., 2021). Recently, a commercial instrument (Ultra), which is developed by Thermo-Fisher , has been successful in clumped isotope measurement in Tokyo Institute of Technology, indicative of the maturity of this technology (Zhang et al., 2021a). Methane clumped isotope analysis quantify the abundances of isotopologues of methane relative to the ideal gas state of random distributions of isotopes over methane molecules (Young et al., 2016; Douglas et al., 2017; Young et al., 2017). Clumped isotopes of methane may primarily record its formation or equilibration temperature if the isotopologues are thought thermally equilibrated when both the $\Delta^{13}CH_3D$ and $\Delta^{12}CH_2D_2$ values are on the thermodynamic equilibrium curve in Figure 7 (Stolper et al., 2014a; Webb and Miller, 2014; Wang

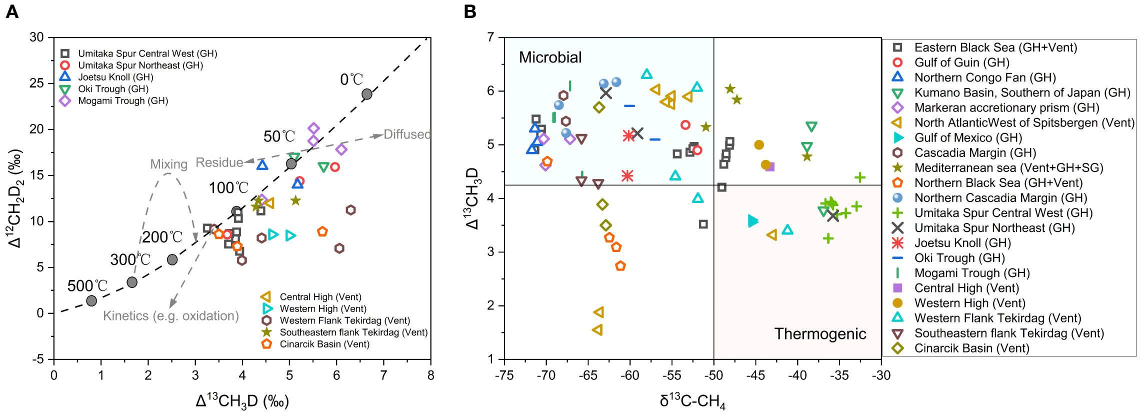

FIGURE 7
(A) Compile of the published clumped isotope of hydrate associated gases plotted in thermodynamic equilibrium curve in $\Delta^{12}CH_2D_2$ vs. $\Delta^{13}CH_3D$ space (both axes are in per mil). Mixing and diffusion trend are adopted from (Douglas et al., 2016), oxidation trend from (Douglas et al., 2017). **(B)** Cross-plot of the published clumped isotope ($\Delta^{13}CH_3D$) and conventional stable isotope ($\delta^{13}C-C_1$) of hydrate associated gases (both axes are in per mil), modified from (Lalk et al., 2022). SG-Sedimentary Gases.

et al., 2015a). This method is established based on the theory of isotopologue exchange reaction [Eq (2)], of which the equilibrium is controlled by temperature.

$$^{13}CH_4 + {}^{12}CH_3D \rightarrow {}^{13}CH_3D + {}^{12}CH_4 \qquad (2)$$

The formation temperature of methane obtained by this method provides crucial clues for its origin. Microbial gas is formed at low temperature (usually<75°C) *via* biogeochemical processes in subsurface sediments, while thermogenic gases generated from pyrolysis of organic matter usually occur at high temperatures (usually>150°C). Abiotic gases involve a variety of reactions, which can be classified as reaction in mantle, magmatic system (~>600°C) or water-rock interaction (~50-500°C).

5.2.2 Recent advances

Clumped isotopologue analyses have been applied to studying hydrate-associated methane from Hydrate Ridge on Cascadia Margin (Wang et al., 2015a), Kumano Basin mud volcano in Nankai accretionary complex (Ijiri et al., 2018), Japan Sea (Zhang et al., 2021a), Sea of Marmara (Giunta et al., 2021), as well as 46 samples from the other 11 regions in the world (Lalk et al., 2022) (Figure 7A, B).

The $\Delta^{13}CH_3D$ of microbial methane from both porewaters and gas hydrates recovered from sediments in the northern Cascadia margin yielded methane formation temperature ranging from 12°C to 42°C (Figure 7B) (Wang et al., 2015a), which is in accordance with the surrounding environment. Similarly, clumped methane isotopologues of the gases from Kumano forearc basin in Nankai accretionary complex indicate that ~90% of methane is produced microbially at an estimated temperature between 16° and 30°C (Figure 7B), consistent with a relatively shallow microbial source in the sediments of 300-900mbsf (Ijiri et al., 2018). However, from clumped isotopes the formation temperatures of methane are calculated to be 15 to 170°C for the methane gases from the Sea of Japan (Figures 7A, B). By combining clumped isotope results with other traditional approaches, the microbial methane is quantified to be 20-80% compared to the thermogenic (Zhang et al., 2021a). Giunta et al. (2021) measured $^{13}CH_3D$ and $^{12}CH_2D_2$ of methane from cold seeps emanating at the seafloor of Sea of Marmara (SoM) (Figures 7A, B), and it is found that the isotopic characteristics of methane in SoM cannot be simply explained by mixing of multiple reservoirs but appears to be affected to varying degrees by bond re-equilibration with clay minerals (Ruffine et al., 2018). This might imply that the temperature obtained from clumped isotope represents the re-equilibration condition of post-generation rather than the actual formation temperature of methane. Lalk et al. (2022) analyzed 46 gas hydrates and associated gases from seepages of different types (cold seeps, oil seeps, pockmarks, and mud volcanoes) in 11 regions around the world (Figure 7B), discovering that the formation temperatures of methane associated with cold seeps and pockmarks locate in the microbial range between 15°C and 70°C. However, the temperature of methane gases from oil-associated gas hydrates are estimated to be 50°C to 120°C, corresponding to secondary methane generated by oil biodegradation. The methane gases associated with mud volcanoes are with a wide range of $\Delta^{13}CH_3D$ values, and the correspondent temperatures of methane formation are not consistent with the conditions indicated by conventional proxies, suggesting their diverse origins which could be attributed to the tectonic settings (Lalk et al., 2022).

5.2.3 Unresolved questions

Clumped isotopes with equilibrium signals can provide important information for temperature and can be used as thermometers (Stolper et al., 2014a). However, not all data measured in reality are ideally in equilibrium. Most of the temperature results calculated with clumped isotopes of thermogenic gases are consistent with those of their surrounding environment (Douglas et al., 2017; Young et al., 2017; Stolper et al., 2018; Giunta et al., 2019; Giunta et al., 2021), indicating that clumped isotope can reflect the formation temperature of methane. However, in laboratory based thermal experiments, such as pyrolysis of shale, coal, or hydrocarbons, significant non-equilibriums in clumped isotopes have been observed (Shuai et al., 2018; Dong et al., 2021), which is considered to be a statistical combinational effect or kinetic isotope effects (KIE) during pyrolysis. Simulating experiments also reveal that hydrocarbons may approach equilibrium in clumped isotope with maturity increasing (Xia and Gao, 2019; Dong et al., 2021).

Compared to thermogenic gas, the values of clumped isotopes of microbial methane are in a wide range. The temperature, deduced from clumped isotopic composition of microbial methane generated in laboratory culture experiments, is much lower than its actual culture condition (Stolper et al., 2015; Wang et al., 2015a; Young et al., 2017; Gruen et al., 2018; Giunta et al., 2019; Douglas et al., 2020). The extremely depletion in $^{12}CH_2D_2$ is mainly ascribed to quantum tunneling effect or combinatorial effects of 4 hydrogen atoms of methane from different reservoirs or experiencing different fractionations (Young et al., 2017; Cao et al., 2019; Young, 2019; Taenzer et al., 2020), while the moderate $^{13}CH_3D$ depletion is mainly attributed to quantum tunneling or kinetic isotope effect of methanogenesis (Wang et al., 2015a; Cao et al., 2019; Young, 2019; Douglas et al., 2020). In surface environments such as cattle rumen and freshwater ecosystems, disequilibrium clumped isotope characteristics of biogenic methane were widely reported, exhibiting obvious kinetic signals, and corresponding temperatures were much higher than the actual ambient condition (Stolper et al., 2015; Wang et al., 2015a; Douglas et al., 2016; Young et al., 2017; Ash et al., 2019; Giunta et al., 2019; Douglas et al., 2020). However, methane gases taken from marine sediments usually show a relatively consistent temperature compared to the ambient condition (Figures 7A, B) (Inagaki et al., 2015; Wang et al., 2015a; Young et al., 2017; Ijiri et al., 2018). The mechanisms for the equilibration of methane clumped isotopes in marine sediments can involve the processes of methanogenesis or oxidation of methane. For methanogenesis, the rates of methane formation and enzyme reversibility are recognized as the two main factors affecting the kinetics of clumped isotope equilibration based on the culturing experiments and observations on natural samples (Stolper et al., 2015; Wang et al., 2015a; Douglas et al., 2016; Douglas et al., 2020). For oxidation of methane, reversible bond reordering in the AOM process was identified as the key process controlling the equilibration of clumped isotopes (Ash et al., 2019; Ono et al., 2021).

In addition to the above disequilibrium condition, secondary post-generation processes such as oxidation, migration and mixing of methane can also alter the original clumped isotope signal (Stolper et al., 2015; Wang et al., 2015a; Yeung et al., 2015; Young et al., 2017; Giunta et al., 2019; Labidi et al., 2020; Giunta et al., 2021; Warr et al., 2021). Mixing may lead to a non-linearity trajectory in the $\Delta^{13}CH_3D$-$\Delta^{12}CH_2D_2$ diagram (Figure 7A) (Douglas et al., 2016; Young et al., 2016), with a curvature depending on bulk isotopic compositions ($\delta^{13}C$ and δD) of end-members. The curvature of the mixing line is negligible when the values of end-member δD and $\delta^{13}C$ are close, but it becomes progressively significant when the values of end-member δD and $\delta^{13}C$ become more different (Stolper et al., 2015; Douglas et al., 2016). Diffusion of methane, either in the condition of vacuum or interaction with particles, is predicted to favor the light isotopologues to be enriched in diffused gas as compared with the residual gas (Figure 7A). Two variants of $\Delta^{13}CH_3D$ and $\Delta^{12}CH_2D_2$ should be with an integer mass ratio of 18/16, so any fractionation caused by molecular mass, like diffusion, should display a 1:1 slope in this space (Douglas et al., 2017). Douglas et al. (2017) proposed that atmospheric chemical reactions of methane with $OH^{.-}$, $Cl^{.-}$ would increase the abundance of $^{12}CH_2D_2$ and $^{13}CH_3D$ (Figure 7A), but their enrichment degrees are different. Microbial methanotrophy, including aerobic and anaerobic oxidation of methane, can change initial clumped isotope signatures of methane as well (Wang et al. 2015a; Ash et al., 2019; Young, 2019; Ono et al., 2021). For aerobic oxidation of methane, Wang et al. (2016) found a decrease in $\Delta^{13}CH_3D$ and a significant increase in δD and $\delta^{13}C$ values of CH_4 in bio-simulation experiments under aerobic condition. While for anaerobic oxidation of methane (AOM), reversible bond re-ordering is proposed to be the key process leading to near-equilibrium values based on observations in natural samples (Ash et al., 2019). Laboratory culture experiments (Young, 2019; Ono et al., 2021) qualitatively confirm the role of AOM in modifying methane clumped isotope signatures, but some of these experimental results do not quantitatively agree with the observations in natural samples. Ono et al. (2021) reported that $\Delta^{13}CH_3D$ values of residual CH_4 were 3.1‰ higher than the expected equilibrium values, which might be associated with KIE resulted from rapid AOM rates during incubation, while Young (2019) observed distinct bond re-ordering trends in $\Delta^{13}CH_3D$ vs. $\Delta^{12}CHD_2$ plot under changing sulfate concentrations. The specific mechanism of how AOM catalyzes bond re-ordering requires further investigation.

5.3 Noble gases

5.3.1 Developments

Noble gases are chemically inert, so their elemental ratios can be changed only by physical processes but not by microbial activities and chemical reactions. Based on these specific properties, methods are established to decipher complex geochemical processes (Winckler et al., 2000). Noble gases are well constrained in different units of the earth surface system, coming from three-endmember sources: (i) atmosphere, or air-saturated water (ASW): e.g., ^{20}Ne, ^{36}Ar, ^{38}Ar, ^{84}Kr, ^{132}Xe; (ii) ^{3}He-rich mantle; and (iii) crustal, rich in radiogenic noble gases accumulated by radioactive decay, e.g. U + Th → $^{4}He^{*}$, $^{21}Ne^{*}$, $^{136}Xe^{*}$; $^{40}K \rightarrow {}^{40}Ar^{*}$ (Ballentine and Burnard, 2002).

The elemental and isotopic compositions of noble gases facilitate additional constraints on the genetic origins of and semiquantitative estimation of the biogenic and thermogenic contributions of natural gas. Noble gases are also employed to study the dynamics of fluid migration, estimate the residence time of hydrocarbon gases in reservoir, and specify post-genetic processes that might have modified hydrocarbon composition (Zhou et al., 2005; Zhou and Ballentine, 2006; Schlegel et al., 2011; Hunt et al., 2012; Darrah et al., 2014; Darrah et al., 2015; Wen et al., 2015; Barry et al., 2016; Harkness et al., 2017).

Previous experimental and theoretical studies have demonstrated that formation of hydrate will result in fractionation to certain degree between noble gases, as reflected by the enrichment of heavier noble gases in gas hydrate (Nikitin, 1937; Barrer and Stuart, 1957; Hunt et al., 2013). Noble gases studies of gas hydrates from Blake Ridge show that the formation of hydrate is characterized by the Xe enrichment in hydrate phase due to noble gas fractionation (Dickens and Kennedy, 2000). Natural gas hydrates from Hydrate Ridge are almost with no He and Ne, but contain high Ar and Kr and Xe, suggesting that the heavier noble gases were preferentially entered gas hydrate structure compared with the lighter noble gases, which could be ascribed to the thermodynamic effect or solubility difference (Winckler et al., 2002). The experimental results of synthesizing hydrate of mixed methane and noble gases (He, Ne, Ar, Kr and Xe) reveal that Kr and Xe are enriched relative to Ar but without detectable He and Ne in hydrate, also indicative of the effect of mass fractionation of noble gases in hydrate formation process (Hunt et al., 2011; Hunt et al., 2013).

5.3.2 Recent advances

As discussed in previous sections, traditional methods are with limitations to delineate gas origins, noble gases can provide additional clues about the thermal maturity of natural gases and the migration of allothogenic fluids. Crustal noble gases like ^{4}He, ^{21}Ne and ^{40}Ar are present in high concentrations in thermogenic gases, whereas recently formed microbial gases are nearly devoid of radiogenic noble gases (Hunt et al., 2012; Darrah et al., 2015; Wen et al., 2015; Harkness et al., 2017). On the contrary, the increase of atmospherically derived gases like ^{20}Ne and ^{36}Ar seems to correspond to an elevated proportion of microbial gas (Ballentine et al., 2002; Ballentine and Burnard, 2002). Furthermore, the ^{3}He/^{4}He (shown as R/Ra, where R is the ^{3}He/^{4}He in a gas sample and Ra is the ^{3}He/^{4}He of air, 1.39×10^{-6}), provides proxies to identify the participation of abiotic gases from the mantle or continental crust after eliminating the contribution of the atmosphere by referring to ^{4}He/^{20}Ne ratio (Figure 8) (Graham, 2002). High R/Ra and high ^{4}He/^{20}Ne ratios are the indication of the input of mantle-derived gases (Figure 8) (Oxburgh et al., 1986; Poreda et al., 1986).

The content and isotope ratios of noble gases in hydrate-bearing sediments from the Haskon Mosby Mud Volcano reveal that all the samples are with non-atmospheric He, which is considered to be crustal/radiogenic origin, and transported to hydrate stability zone through mud volcano (Figure 8) (Prasolov et al., 1999). One of these sites is with higher isotopic ^{3}He/^{4}He ratio, which probably contains the contribution from mantle. The ^{3}He/^{4}He ratio of hydrate-associated venting gas in Sea of Marmara is as high as 5.25 Ra (Figure 8) (Ruffine et al., 2018), and similar high ^{3}He/^{4}He ratio was also found in the southern part of the Ganos fault in the same area (Burnard et al., 2012), indicating a possible mantle contribution through large-scale fault systems (Gautheron and Moreira, 2002). Snyder et al. (2020) reported noble gas results from gas hydrate in the Japan sea and found that hydrate gas is mainly of a mixture of thermogenic/crustal source, biogenic gases and mantle source. The existence of hydrate with mantle ^{3}He/^{4}He characteristics indicates that fluids enriched in mantle gases are the main cause of the mobilization of thermogenic gas in the active chimney structures of the Japan Sea (Figure 8).

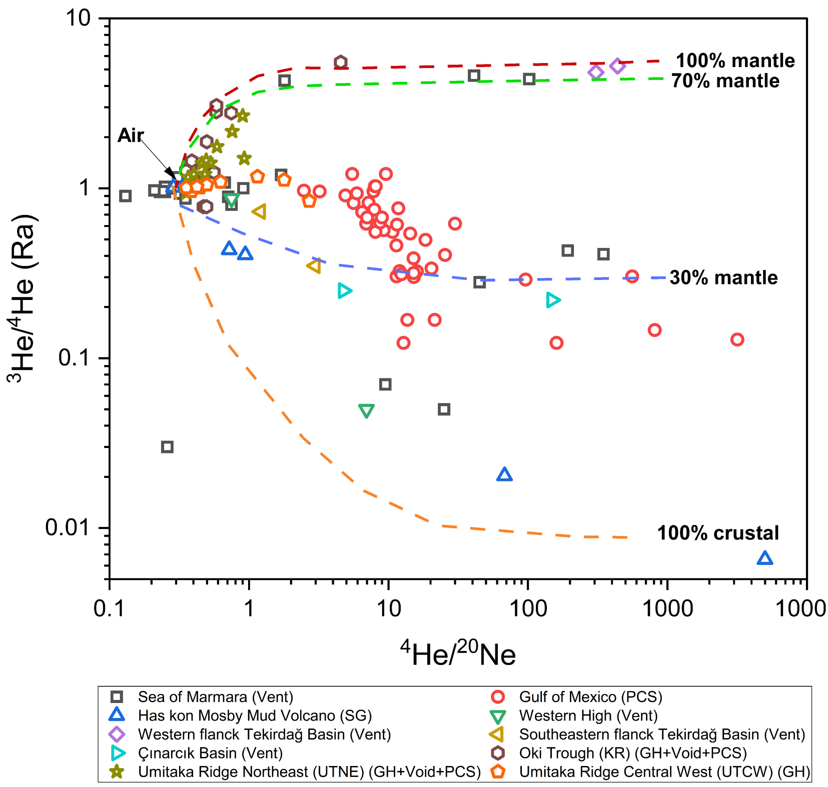

FIGURE 8
Compiled of published noble gases geochemical data of hydrate associated gases plotted in He isotope versus ^{4}He/^{20}Ne ratio.

5.3.3 Unresolved questions

Fractionation of noble gases during the hydrate formation, combined with the episodic cycle of hydrate melting and refreezing, complicated the scenarios for noble gases studies associated with gas hydrate. For example, high $^3He/^4He$ ratios, which are generally related to mantle source gas, are found in hydrate-associated gases which were determined as biogenic origin by $\delta^{13}C_{\text{-CH4}}$ in samples from Sea of Japan. However, low $^3He/^4He$ ratios are observed in hydrate-associated gases with thermogenic carbon isotope signature (Snyder et al., 2020). The authors proposed that hydrates which were formed from thermogenic gas in chimney experienced decomposition and reformation, and helium was lost in this process because it is difficult to be encaged in hydrate by its small molecular size (Snyder et al., 2020). Therefore, the melting and reprecipitation effect of gas hydrate may prevent the identification of the magmatic or radiogenic contribution.

Air contamination and gas-water interactions in the pretreatment process prevent accurate measurement of noble gases degassing from hydrate-bearing pressurized core, Moore et al. (2020) proposed the modified quantitative degassing method which can minimize these effects and applied this technique to samples from the Gulf of Mexico (Figure 8), which may be important for future hydrate-associated noble gases study. Although this modified method reduces the impact of air pollution, it still requires complex procedures and large sample quantity, so it is still in need of a better pre-treatment scheme for noble gas detection.

6 Conclusion

Many natural gas hydrate samples have been collected and studied through multiple approaches during the past decades. Based on the data published, the factors affecting the geochemical characteristics of hydrate-associated gases have been summarized, and the methods for identifying gas origins and delineating the post-generation processes have been reviewed.

1. Apart from the gas of abiotic origin, most of the hydrate-associated gases are derived from the degradation of organic matter. Different types of organic matter are with distinct hydrocarbon-generation profile in the course of thermal evolution, as indicated by the molecular and isotopic compositions of their products. Oil-type gas and coal-type gas are the products of different types of organic matter, while microbial gases and thermogenic gases are the product in different evolution stages of organic matter in the burial history of sediments.

2. The characteristics of hydrate-associated gases are affected not only by the primary properties of organic materials such as organic type and thermal maturity but also associated with the secondary processes in gas accumulation processes after generation. Among the secondary processes, migration, mixing and biodegradation are common in hydrate-bearing area.

3. Clumped isotopes with equilibrium signals can be a robust proxy to estimate the formation temperature of methane, whereas the data without equilibrium signals can reflect the secondary processes that lead to the deviation from the equilibrium state. Most published methane clumped isotopes from marine sediments are found locating in a reasonable temperature zone which are generally consistent to their surroundings.

4. Noble gases can play an important role in recognizing the dynamics of thermogenic hydrocarbon generation generated by interactions between hydrothermal fluids and deeply buried organic matter. As such, noble gas helium isotopic signatures provide an indicator of large-scale deep migration pathways.

Author contributions

Conceptualization, HL; writing—original draft preparation, YL; writing—review and editing, CJ and HL; supervision, HL; funding acquisition, HL. All authors have read and agreed to the published version of the manuscript.

Funding

This work was supported by China Geological Survey (No. DD20221703).

Acknowledgments

We would like to express our gratitude to researchers who focus on the gas geochemical characteristics of natural gas hydrate, their previous work laid the foundation of this review. We also appreciate the efforts of the editors and reviewers, who gave constructive comments and suggestions which greatly improved this manuscript and inspired in-depth discussion.

Conflict of interest

The authors declare that the research was conducted in the absence of any commercial or financial relationships that could be construed as a potential conflict of interest.

Publisher's note

Supplementary material

The Supplementary Material for this article can be found online at: https://www.frontiersin.org/articles/10.3389/fmars.2022.968647/full#supplementary-material

References

Ash, J. L., Egger, M., Treude, T., Kohl, I., Cragg, B., Parkes, R. J., et al. (2019). Exchange catalysis during anaerobic methanotrophy revealed by 12CH2D2 and 13CH3D in methane. *Geochemi. Perspect. Lett.* 10, 26–30. doi: 10.7185/geochemlet.1910

Ballentine, C. J., Burgess, R., and Marty, B. (2002). Tracing fluid origin, transport and interaction in the crust. *Rev. Mineral. Geochem.* 47 (1), 539–614. doi: 10.2138/rmg.2002.47.13

Ballentine, C. J., and Burnard, P. G. (2002). Production, release and transport of noble gases in the continental crust. *Rev. Mineral. Geochem.* 47 (1), 481–538. doi: 10.2138/rmg.2002.47.12

Barnes, R. O., and Goldberg, E. D. (1976). Methane production and consumption in anoxic marine sediments. *Geology* 4, 297–300. doi: 10.1130/0091-7613(1976)4<297:MPACIA>2.0.CO;2

Barrer, R. M., and Stuart, W. I. (1957). Non-stoicheiometric clathrate compounds of water. *Proc. R. Soc. London. Ser. A Math. Phys. Sci.* 243, 172–189. doi: 10.1098/rspa.1957.0213

Barry, P. H., Lawson, M., Meurer, W. P., Warr, O., Mabry, J. C., Byrne, D. J., et al. (2016). Noble gases solubility models of hydrocarbon charge mechanism in the sleipner vest gas field. *Geochim. Cosmochim. Acta* 194, 291–309. doi: 10.1016/j.gca.2016.08.021

Bernard, B. B., Brooks, J. M., and Sackett, W. M. (1976). Natural gas seepage in the gulf of Mexico. *Earth Planet. Sci. Lett.* 31, 48–54. doi: 10.1016/0012-821X(76)90095-9

Bernard, B., Brooks, J. M., and Sackett, W. M. (1977). A geochemical model for characterization of hydrocarbon gas sources in marine sediments. *Offshore Technol. Conf.* 435–438. doi: 10.4043/2934-MS

Boreham, C. J., and Edwards, D. S. (2008). Abundance and carbon isotopic composition of neo-pentane in Australian natural gases. *Org. Geochem.* 39 (5), 550–566. doi: 10.1016/j.orggeochem.2007.11.004

Borowski, W. S., Paull, C. K., and Ussle, W. (1997). Carbon cycling within the upper methanogenic zone of continental rise sediments: An example from the methane-rich sediments overlying the Blake ridge gas hydrate deposits. *Mar. Chem.* 57, 299–311. doi: 10.1016/S0304-4203(97)00019-4

Brooks, J. M., Michael, E. F., and XXXM.C., K. I. (1991). Observations of gas hydrates in marine sediments, offshore northern California. *Mar. Geol.* 96, 103–109. doi: 10.1016/0025-3227(91)90204-H

Buffett, B., and Archer, D. (2004). Global inventory of methane clathrate: sensitivity to changes in the deep ocean. *Earth Planet. Sci. Lett.* 227 (3-4), 185–199. doi: 10.1016/j.epsl.2004.09.005

Burnard, P., Bourlange, S., Henry, P., Geli, L., Tryon, M. D., Natal'in, B., et al. (2012). Constraints on fluid origins and migration velocities along the marmara main fault (Sea of marmara, Turkey) using helium isotopes. *Earth Planet. Sci. Lett.* 341-344, 68–78. doi: 10.1016/j.epsl.2012.05.042

Cao, X., Bao, H., and Peng, Y. (2019). A kinetic model for isotopologue signatures of methane generated by biotic and abiotic CO2 methanation. *Geochim. Cosmochim. Acta* 249, 59–75. doi: 10.1016/j.gca.2019.01.021

Cao, D. Y., Wang, D., LI, J., and Dou, X. Q. (2012). Gas source analysis of natural gas hydrate of muli coalfield in qilian mountain permafrost, qinghai province, China. *J. China Coal Soc.* 37, 1364–1368. doi: CNKI:SUN:MTXB.0.2012-08-020

Chanton, J. P. (2005). The effect of gas transport on the isotope signature of methane in wetlands. *Org. Geochem.* 36 (5), 753–768. doi: 10.1016/j.orggeochem.2004.10.007

Chen, A. D. (1994). Origin and migration of natual gas in Ordovician reservoir in shang ganning basin central gas field. *Acta Petrolei Sin.* 15, 1–10. doi: 10.1007/BF02943584

Chen, F., Wang, X., Li, N., Cao, J., Bayon, G., Peckmann, J., et al (2019). Gas Hydrate Dissociation During Sea-Level Highstand Inferred From U/Th Dating of Seep Carbonate From the South China. *Sea. Geophys. Res. Lett.* 46 (23), 13928–13938. doi: 10.1029/2019gl085643

Chen, M., Deng, X. B., Liu, C. L., Ren, H. B., Yin, X. J., and Zhang, A. M. (2018). Experimental study on carbon isotopic composition changes during the formation of gas hydrates. *Geoscience* 32, 205–212.

Chen, L., and Merey, S. (2021). *Oceanic methane hydrates: fundamentals, technological innovations, and sustainability*. (Cambridge, MA, Gulf Professional) 1–37.

Choi, J., Kim, J.-H., Torres, M. E., Hong, W.-L., Lee, J.-W., Yi, B. Y., et al. (2013). Gas origin and migration in the ulleung basin, East Sea: Results from the second ulleung basin gas hydrate drilling expedition (UBGH2). *Mar. Petroleum Geol.* 47, 113–124. doi: 10.1016/j.marpetgeo.2013.05.022

Chung, H. M., Gormly, J. R., and Squires, R. M. (1988). Origin of gaseous hydrocarbons in subsurface environments: theoretical considerations of carbon isotope distribution. *Chem. Geol.* 71, 97–104. doi: 10.1016/0009-2541(88)90108-8

Coleman, D. D., Meents, W. F., Liu, C. L., and Keogh, R. A. (1977). Isotopic identification of leakage gas from underground storage reservoirs. progress report. *Ill., State Geol. Surv., Ill. Pet.* 111, 1–10. doi: 10.2118/6491-MS

Coleman, D. D., Risatti, J. B., and Schoell, M. (1981). Fractionation of carbon and hydrogen isotopes by methane-oxidizing bacteria. *Geochim. Cosmochim. Acta* 45, 1033–1037. doi: 10.1016/0016-7037(81)90129-0

Collett, T. S., Boswell, R., Waite, W. F., Kumar, P., Roy, S. K., Chopra, K., et al. (2019). India National gas hydrate program expedition 02 summary of scientific results: Gas hydrate systems along the eastern continental margin of India. *Mar. Pet. Geol.* 108, 39–142. doi: 10.1016/j.marpetgeo.2019.05.023

Collett, T. S., Johnson, A. H., Knapp, C. C., and Boswell, R. (2009). Natural gas hydrates: A review. *AAPG Memoir* 89, 149–219. doi: 10.1306/13201142M891602

Collett, T. S., Riedel, M., Cochran, J. R., Boswell, R., Kumar, P., and Sathe, A. V. (2008). “India Continental margin gas hydrate prospects: results of the Indian national gas hydrate program (NGHP) expedition 01,” in *Proceedings of the 6th International Conference on Gas Hydrates (ICGH 2008).*

Craig, H. (1968). Isotope separation by carrier diffusion. *Science* 159, 93–96. doi: 10.1126/science.159.3810.93

Cremiere, A., Lepland, A., Chand, S., Sahy, D., Condon, D. J., Noble, S. R., et al (2016). Timescales of methane seepage on the Norwegian margin following collapse of the Scandinavian Ice Sheet. *Nat Commun.* 7, 11509. doi: 10.1038/ncomms11509

Dai, J. X. (1992). The discrimination of various of alkane gases. *Sci. Sin.* 22, 185–193. doi: 10.1360/zb1992-22-2-185

Dai, J. X., Ni, Y. Y., Huang, S. P., Peng, W. L., Han, W. X., Gong, D. Y., et al. (2017). Genetic types of gas hydrates in China. *Pet. Explor. Dev.* 44, 837–848. doi: 10.11698/PED.2017.06.01

Darrah, T. H., Jackson, R. B., Vengosh, A., Warner, N. R., Whyte, C. J., Walsh, T. B., et al. (2015). The evolution of Devonian hydrocarbon gases in shallow aquifers of the northern Appalachian basin: Insights from integrating noble gas and hydrocarbon geochemistry. *Geochim. Cosmochim. Acta* 170, 321–355. doi: 10.1016/j.gca.2015.09.006

Darrah, T. H., Vengosh, A., Jackson, R. B., Warner, N. R., and Poreda, R. J. (2014). Noble gases identify the mechanisms of fugitive gas contamination in drinking-water wells overlying the Marcellus and Barnett shales. *Proc. Natl. Acad. Sci.* 111 (39), 14076–14081. doi: 10.1073/pnas.1322107111

Daskalopoulou, K., Calabrese, S., Grassa, F., Kyriakopoulos, K., Parello, F., Tassi, F., et al. (2018). Origin of methane and light hydrocarbons in natural fluid emissions: A key study from Greece. *Chem. Geol.* 479, 286–301. doi: 10.1016/j.chemgeo.2018.01.027

De Prunel, A., Ruffine, L., Riboulot, V., Peters, C. A., Croguennec, C., Guyader, V., et al. (2017). Focused hydrocarbon-migration in shallow sediments of a pockmark cluster in the Niger delta (Off Nigeria). *Geochem., Geophys., Geosyst.* 18, 93–112. doi: 10.1002/2016GC006554

Deng, Y., Chen, F., Guo, Q., Hu, Y., Chen, D., Yang, S., et al. (2021). Possible Links Between Methane Seepages and Glacial-Interglacial Transitions in the South China Sea. *Geophys. Res. Lett.* 48 (8), e2020GL091429. doi: 10.1029/2020gl091429

Dickens, G. R., and Kennedy, B. M. (2000). “"Noble gases in methane hydrate from the Blake ridge",” in *Proceedings of the ocean drilling program. scientific results. ocean drilling program.* 164 (1), 187–192. doi: 10.2973/odp.proc.sr.164.211.2000

Dickens, G. R., O'Neil, J. R., Rea, D. K., and Owen, R. M. (1995). Dissociation of oceanic methane hydrate as a cause of the carbon isotope excursion at the end of the Paleocene. *Paleoceanography* 10, 965–971. doi: 10.1029/95PA02087

Dong, G., Xie, H., Eiler, J., Zhang, N., Mayuko, N., Yoshida, N., et al. (2020). “Clumped isotope analysis of methane using HR-IRMS: New insights into origin and formation mechanisms of natural gases and a potential geothermometer,” in *Thermo scientific white paper WP30767.*

Dong, G., Xie, H., Formolo, M., Lawson, M., Sessions, A., and Eiler, J. (2021). Clumped isotope effects of thermogenic methane formation: Insights from pyrolysis of hydrocarbons. *Geochim. Cosmochim. Acta* 303, 159–183. doi: 10.1016/j.gca.2021.03.009

Douglas, P. M. J., Gonzalez Moguel, R., Walter Anthony, K. M., Wik, M., Crill, P. M., Dawson, K. S., et al. (2020). Clumped isotopes link older carbon substrates with slower rates of methanogenesis in northern lakes. *Geophy. Res. Lett.* 47 (6), 1–10. doi: 10.1029/2019gl086756

Douglas, P. M. J., Stolper, D. A., Eiler, J. M., Sessions, A. L., Lawson, M., Shuai, Y., et al. (2017). Methane clumped isotopes: Progress and potential for a new isotopic tracer. *Org. Geochem.* 113, 262–282. doi: 10.1016/j.orggeochem.2017.07.016

Douglas, P. M. J., Stolper, D. A., Smith, D. A., Walter Anthony, K. M., Paull, C. K., Dallimore, S., et al. (2016). Diverse origins of Arctic and subarctic methane point source emissions identified with multiply-substituted isotopologues. *Geochim. Cosmochim. Acta* 188, 163–188. doi: 10.1016/j.gca.2016.05.031

Eiler, J. M. (2007). "Clumped-isotope" geochemistry–the study of naturally-occurring, multiply-substituted isotopologues. *Earth Planet. Sci. Lett.* 262 (3-4), 309–327. doi: 10.1016/j.epsl.2007.08.020

Eiler, J. M. (2013). The isotopic anatomies of molecules and minerals. *Annu. Rev. Earth Planet. Sci.* 41 (1), 411–441. doi: 10.1146/annurev-earth-042711-105348

Eldridge, D. L., Korol, R., Lloyd, M. K., Turner, A. C., Webb, M. A., Miller, T. F., et al. (2019). Comparison of experimental vs theoretical abundances of 13CH3D and 12CH2D2 for isotopically equilibrated systems from 1 to 500 °C. *ACS Earth Space Chem.* 3 (12), 2747–2764. doi: 10.1021/acsearthspacechem.9b00244

Etiope, G. (2017). Abiotic methane in continental serpentinization sites: An overview. *Proc. Earth Planet. Sci.* 17, 9–12. doi: 10.1016/j.proeps.2016.12.006

Etiope, G., Baciu, C. L., and Schoell, M. (2011). Extreme methane deuterium, nitrogen and helium enrichment in natural gas from the homorod seep (Romania). *Chem. Geol.* 280 (1-2), 89–96. doi: 10.1016/j.chemgeo.2010.10.019

Etiope, G., and Lollar, B. S. (2013). Abiotic methane on earth. *Rev. Geophysics* 51 (2), 276–299. doi: 10.1002/rog.20011

Etiope, G., and Schoell, M. (2014). Abiotic gas: Atypical, but not rare. *Elements* 10 (4), 291–296. doi: 10.2113/gselements.10.4.291

Faber, E., and Stahl, W. J. (1984). Geochemical surface exploration for hydrocarbons in north Sea. *AAPG Bull.* 68, 363–386. doi: 10.1306/AD460A26-16F7-11D7-8645000102C1865D

Fuex, A. N. (1980). Experimental evidence against an appreciable isotopic fractionation of methane during migration. *Org. Geochem.* 12, 725–732. doi: 10.1016/0079-1946(79)90153-8

Fu, S. Y., and Lu, J. A. (2010). The characteristics and origin of gas hydrate in shenhu area, south China Sea. *Mar. Geol. Lett.* 26, 6–10. doi: 10.16028/j.1009

Galimov, E. M. (1967). 13C enrichment of methane during passage through rocks. *Geochem. Int.* 4, 1180–1181.

Gao, L., Brassell, S. C., Mastalerz, M., and Schimmelmann, A. (2013). Microbial degradation of sedimentary organic matter associated with shale gas and coalbed methane in eastern Illinois basin (Indiana), USA. *Int. J. Coal Geol.* 107, 152–164. doi: 10.1016/j.coal.2012.09.002

Gautheron, C., and Moreira, M. (2002). Helium signature of the subcontinental lithospheric mantle. *Earth Planet. Sci. Lett.* 199, 39–47. doi: 10.1016/S0012-821X(02)00563-0

Ginsburg, G. D., and Soloviev, V. A. (1997). Methane migration within the submarine gas-hydrate stability zone under deep-water conditions. *Mar. Geol.* 137, 49–57. doi: 10.1016/S0025-3227(96)00078-3

Giunta, T., Labidi, J., Kohl, I. E., Ruffine, L., Donval, J. P., Géli, L., et al. (2021). Evidence for methane isotopic bond re-ordering in gas reservoirs sourcing cold seeps from the Sea of marmara. *Earth Planet. Sci. Lett.* 553, 116619. doi: 10.1016/j.epsl.2020.116619

Giunta, T., Young, E. D., Warr, O., Kohl, I., Ash, J. L., Martini, A., et al. (2019). Methane sources and sinks in continental sedimentary systems: New insights from paired clumped isotopologues 13CH3D and 12CH2D2. *Geochim. Cosmochim. Acta* 245, 327–351. doi: 10.1016/j.gca.2018.10.030

Gonzalez, Y., Nelson, D. D., Shorter, J. H., McManus, J. B., Dyroff, C., Formolo, M., et al. (2019). Precise measurements of (12)CH2D2 by tunable infrared laser direct absorption spectroscopy. *Anal. Chem.* 91 (23), 14967–14974. doi: 10.1021/acs.analchem.9b03412

Graham, D. W. (2002). Noble gas isotope geochemistry of mid-ocean ridge and ocean island basalts: Characterization of mantle source reservoirs. *Rev. Mineral. Geochem.* 47 (1), 247–317. doi: 10.2138/rmg.2002.47.8

Gruen, D. S., Wang, D. T., Könneke, M., Topçuoğlu, B. D., Stewart, L. C., Goldhammer, T., et al. (2018). Experimental investigation on the controls of clumped isotopologue and hydrogen isotope ratios in microbial methane. *Geochim. Cosmochim. Acta* 237, 339–356. doi: 10.1016/j.gca.2018.06.029

Gunter, B. D., and Gleason, J. D. (1971). Isotope fractionation during gas chromatographic separations. *J. Chromatographic Sci.* 9, 191–192. doi: 10.1093/chromsci/9.3.191

Gutsalo, L. K., and Plotnikov, A. M. (1981). Carbon isotopic composition in the CH4-CO2 system as a criterion for the origin of methane and carbon dioxide in earth natural gases (in Russian). *Doklady Akademii Nauk SSSR* 259, 470–473.

Hachikubo, A., Khlystov, O., Krylov, A., Sakagami, H., Minami, H., Nunokawa, Y., et al. (2010). Molecular and isotopic characteristics of gas hydrate-bound hydrocarbons in southern and central lake baikal. *Geo-Marine Lett.* 30 (3-4), 321–329. doi: 10.1007/s00367-010-0203-1

Hachikubo, A., Ozeki, T., Kosaka, T., and Sakagami, H. (2008a). "Isotopic fractionation of guest gas at the formation of methane and ethane hydrates," in *Proceedings of the 6th International Conference on Gas Hydrates (ICGH 2008).*

Hachikubo, A., Yanagawa, K., Tomaru, H., Lu, H. L., and Matsumoto, R. (2015). Molecular and isotopic composition of volatiles in gas hydrates and in sediment from the joetsu basin, Eastern margin of the Japan Sea. *Energies* 8 (6), 4647–4666. doi: 10.3390/en8064647

Harkness, J. S., Darrah, T. H., Warner, N. R., Whyte, C. J., Moore, M. T., Millot, R., et al. (2017). The geochemistry of naturally occurring methane and saline groundwater in an area of unconventional shale gas development. *Geochim. Cosmochim. Acta* 208, 302–334. doi: 10.1016/j.gca.2017.03.039

Head, I.M., Jones, D. M., and Larter, S. R. (2003). Biological activity in the deep subsurface and the origin of heavy oil. *Nature* 426, 344–352. doi: 10.1038/nature02134

Hinrichs, K.-U., Hayes, J. M., Bach, W., Spivack, A. J., Hmelo, L. R., Holm, N. G., et al. (2006). Biological formation of ethane and propane in the deep marine subsurface. *Proc. Natl. Acad. Sci.* 103, 14684–14689. doi: 10.1073/pnas.0606535103

Holler, T., Wegener, G., Knittel, K., Boetius, A., Brunner, B., Kuypers, M. M., et al. (2009). Substantial (13) C/(12) c and D/H fractionation during anaerobic oxidation of methane by marine consortia enriched *in vitro*. *Environ. Microbiol. Rep.* 1 (5), 370–376. doi: 10.1111/j.1758-2229.2009.00074.x

Hunt, A. G., Darrah, T. H., and Poreda, R. J. (2012). Determining the source and genetic fingerprint of natural gases using noble gas geochemistry: A northern Appalachian basin case study. *AAPG Bull.* 96 (10), 1785–1811. doi: 10.1306/03161211093

Hunt, A. G., Pohlman, J., Stern, L., Ruppel, C., Moscati, R. J., Landis, G. P., et al. (2011). "Observations of mass fractionation of noble gases in synthetic methane hydrate," in *Proceedings of the 7th International Conference on Gas Hydrates (ICGH 2011)*, Edinburgh, Scotland, United Kingdom.

Hunt, A. G., Stern, L., Pohlman, J. W., Ruppel, C., Moscati, R. J., and Landis, G. P. (2013). Mass fractionation of noble gases in synthetic methane hydrate: Implications for naturally occurring gas hydrate dissociation. *Chem. Geol.* 339, 242–250. doi: 10.1016/j.chemgeo.2012.09.033

Ijiri, A., Inagaki, F., Kubo, Y., Adhikari, R. R., Hattori, S., Hoshino, T., et al. (2018). Deep-biosphere methane production stimulated by geofluids in the nankai accretionary complex. *Sci. Adv.* 4, eaao4631. doi: 10.1126/sciadv.aao4631

Inagaki, F., Hinrichs, K. U., Kubo, Y., Bowles, M. W., Heuer, V. B., Hong, W. L., et al. (2015). Exploring deep microbial life in coal-bearing sediment down to similar to 2.5 km below the ocean floor. *Science* 349, 420–424. doi: 10.1126/science.aaa6882

James, A. T., and Burns, B. J. (1984). Microbial alteration of subsurface natural gas accumulations. *AAPG Bull.* 68, 957–960. doi: 10.1306/AD46169C-16F7-11D7-8645000102C1865D

Jin, J., Wang, X., Guo, Y., Li, J., Li, Y., Zhang, X., et al. (2020). Geological controls on the occurrence of recently formed highly concentrated gas hydrate accumulations in the shenhu area, south China Sea. *Mar. Pet. Geol.* 116, 104294. doi: 10.1016/j.marpetgeo.2020.104294

Jones, D. M., Head, I. M., Gray, N. D., Adams, J. J., Rowan, A. K., Aitken, C. M., et al. (2008). Crude-oil biodegradation *via* methanogenesis in subsurface petroleum reservoirs. *Nature* 451 (7175), 176–180. doi: 10.1038/nature06484

Jones, E. J., Voytek, M. A., Corum, M. D., and Orem, W. H. (2010). Stimulation of methane generation from nonproductive coal by addition of nutrients or a microbial consortium. *Appl. Environ. Microbiol.* 76 (21), 7013–7022. doi: 10.1128/AEM.00728-10

Kennett, J. P., Cannariato, K. G. H., , I. L., and Behl, R. J.. (2000). Carbon Isotopic Evidence for Methane Hydrate Instability During Quaternary Interstadials. *Science* 288, 128–133. doi: 10.1126/science.288.5463.12

Kida, M., Jin, Y., Watanabe, M., Konno, Y., Yoneda, J., Egawa, K., et al. (2015). Chemical and crystallographic characterizations of natural gas hydrates recovered from a production test site in the eastern nankai trough. *Mar. Pet. Geol.* 66, 396–403. doi: 10.1016/j.marpetgeo.2015.02.019

Kida, M., Khlystov, O., Zemskaya, T., Takahashi, N., Minami, H., Sakagami, H., et al. (2006). Coexistence of structure I and II gas hydrates in lake baikal suggesting gas sources from microbial and thermogenic origin. *Geophy. Res. Lett.* 33 (24), L24603. doi: 10.1029/2006gl028296

Kimura, H., Fuseya, G., Takeya, S., and Hachikubo, A. (2021). Carbon isotope fractionation during the formation of CO2 hydrate and equilibrium pressures of (12)CO2 and (13)CO2 hydrates. *Molecules* 26 (14), 4215. doi: 10.3390/molecules26144215

Kimura, H., Hachikubo, A., Sakagami, H., Minami, H., Yamashita, S., Khlystov, O., et al. (2020). Isotopic difference between hydrate-bound and sediment gases retrieved at lake baikal. *Limnol. Freshw. Biol.* 4), 924–925. doi: 10.31951/2658-3518-2020-a-4-924

Kinnaman, F. S., Valentine, D. L., and Tyler, S. C. (2007). Carbon and hydrogen isotope fractionation associated with the aerobic microbial oxidation of methane, ethane, propane and butane. *Geochim. Cosmochim. Acta* 71 (2), 271–283. doi: 10.1016/j.gca.2006.09.007

Knittel, K., and Boetius, A. (2009). Anaerobic oxidation of methane: progress with an unknown process. *Annu. Rev. Microbiol.* 63, 311–334. doi: 10.1146/annurev.micro.61.080706.093130

Kvenvolden, K. A. (1988). Methane hydrate — a major reservoir of carbon in the shallow geosphere? *Chem. Geol.* 71, 41–51. doi: 10.1016/0009-2541(88)90104-0

Kvenvolden, K. A. (1995). A review of the geochemistry of methane in natural gas hydrate. *Org. Geochem.* 23, 997–1008. doi: 10.1016/0146-6380(96)00002-2

Labidi, J., Young, E. D., Giunta, T., Kohl, I. E., Seewald, J., Tang, H., et al. (2020). Methane thermometry in deep-sea hydrothermal systems: Evidence for re-ordering of doubly-substituted isotopologues during fluid cooling. *Geochim. Cosmochim. Acta* 288, 248–261. doi: 10.1016/j.gca.2020.08.013

Lai, H., Fang, Y., Kuang, Z., Ren, J., Liang, J., Lu, J.a., et al. (2021a). Geochemistry, origin and accumulation of natural gas hydrates in the qiongdongnan basin, south China Sea: Implications from site GMGS5-W08. *Mar. Pet. Geol.* 123 (2021), 104774. doi: 10.1016/j.marpetgeo.2020.104774

Lai, H., Fang, Y., Kuang, Z., Xing, D., Li, X., Kang, D., et al. (2021b). Molecular and carbon isotopic characteristics during natural gas hydrate decomposition: Insights from a stepwise depressurization experiment on a pressure core. *Energy Fuels* 35 (19), 15579–88. doi: 10.1021/acs.energyfuels.1c01978

Lai, H., Qiu, H., Kuang, Z., Ren, J., Fang, Y., Liang, J., et al. (2022). Integrated signatures of secondary microbial gas within gas hydrate reservoirs: A case study in the shenhu area, northern south China Sea. *Mar. Pet. Geol.* 136 (2022), 105486. doi: 10.1016/j.marpetgeo.2021.105486

Lalk, E., Pape, T., Gruen, D. S., Kaul, N., Karolewski, J. S., Bohrmann, G., et al. (2022). Clumped methane isotopologue-based temperature estimates for sources of methane in marine gas hydrates and associated vent gases. *Geochim. Cosmochim. Acta*. doi: 10.1016/j.gca.2022.04.013

Lapham, L. L., Wilson, R. M., and Chanton, J. P. (2012). Pressurized laboratory experiments show no stable carbon isotope fractionation of methane during gas hydrate dissolution and dissociation. *Rapid Commun. Mass Spectrom* 26 (1), 32–36. doi: 10.1002/rcm.5290

Larter, S. R., Head, I. M., Huang, H., Bennett, B., Jones, M., Aplin, A. C., et al. (2005). "Biodegradation, gas destruction and methane generation in deep subsurface petroleum reservoirs: an overview," in *Pet. geology: Northwest Europe and global perspectives*. Eds. A. G. Dore and B. Vining (London: Geological Society). Proceedings of the 6th Petroleum Geology Conference.

Leythaeuser, D., Schaefer, R. G., and Yukler, A. (1982). Role of diffusion in primary migration of hydrocarbons. *AAPG Bull.* 66, 408–429. doi: 10.1306/03B59B2A-16D1-11D7-8645000102C1865D

Liang, Q., Xiao, X., Zhao, J., Zhang, W., Li, Y., Wu, X., et al. (2022). Geochemistry and sources of hydrate-bound gas in the shenhu area, northern south China sea: Insights from drilling and gas hydrate production tests. *J. Pet. Sci. Eng.* 208 (2022), 109459. doi: 10.1016/j.petrol.2021.109459

Li, J., Liu, Z. L., Li, Z. S., Hu, G. Y., Yan, Q. T., Shan, X. Q., et al. (2003). Experiment investigation on the carbon isotope and composition fractionation of methane during gas migration by diffusion. *Natural Gas Geosci.* 14, 463–468. doi: 10.3969/j.issn.1672-1926.2003.06.008

Li, A., Li, Q., Xu, C., Cai, F., Wang, H., and Zhang, W. (2021). Review of methane seepages in the Okinawa trough: Progress and outlook. *Geofluids* 2021, 1–13. doi: 10.1155/2021/5539893

Lillis, P. G., Warden,A., Claypool,G. E., and Magoon, L. B. (2007). "Petroleum systems ofthe San Joaquin basin province – geochemical characteristics of gas types. In:*Hosford Scheirer A (ed) Petroleum systems and geologic assessment of oil and gas in the San Joaquin Basin Province, California*. (Energy Resources Program, U.S. Geological Survey, Reston: US Geological Survey professional paper) vol 1713.

Lin, G., Lu, J., Luo, K., Fang, Y., Liu, J., Ji, X., et al. (2022). Characterization of bacterial and archaeal community structure in deep subsurface sediments in the shenhu area, northern south China Sea. *Mar. Pet. Geol.* 136 (2022), 105468. doi: 10.1016/j.marpetgeo.2021.105468

Lin, X. Y., and Zeng, J. H. (2010). Gas composition differentiation during natural gas hydrate formation and its geological significance. *Geoscience* 24, 1157–1163. doi: 10.3969/j.issn.1000-8527.2010.06.018

Li, Y., Pang, L., Wang, Z., Meng, Q., Guan, P., Xu, X., et al. (2022). Geochemical characteristics and significance of organic matter in hydrate-bearing sediments from shenhu area, south China Sea. *Molecules* 27 (8), 2533. doi: 10.3390/molecules27082533

Liu, C., Meng, Q., He, X., Li, C., Ye, Y., Zhang, G., et al. (2015). Characterization of natural gas hydrate recovered from pearl river mouth basin in south China Sea. *Mar. Pet. Geol.* 61, 14–21. doi: 10.1016/j.marpetgeo.2014.11.006

Li, J.-f., Ye, J.-l., Qin, X.-w., Qiu, H.-j., Wu, N.-y., Lu, H.-l., et al. (2018). The first offshore natural gas hydrate production test in south China Sea. *China Geol.* 1 (1), 5–16. doi: 10.31035/cg2018003

Lorenson, T. D., and Collett, T. S. (2018). National gas hydrate program expedition 01 offshore india; gas hydrate systems as revealed by hydrocarbon gas geochemistry. *Mar. Pet. Geol.* 92, 477–492. doi: 10.1016/j.marpetgeo.2017.11.011

Lorenson, T. D., Collett, T. S., and Hunter, R. B. (2011). Gas geochemistry of the mount Elbert gas hydrate stratigraphic test well, Alaska north slope: Implications for gas hydrate exploration in the Arctic. *Mar. Pet. Geol.* 28 (2), 343–360. doi: 10.1016/j.marpetgeo.2010.02.007

Lüdmann, T., and Wong, H. K. (2003). Characteristics of gas hydrate occurrences associated with mud diapirism and gas escape structures in the northwestern Sea of Okhotsk. *Mar. Geol.* 201 (4), 269–286. doi: 10.1016/s0025-3227(03)00224-x

Luzi, M., Schicks, J. M., and Erzinger, J. (2011a). “"Carbon isotopic fractionation of synthetic methane and carbon dioxide hydrates"," in *Proceedings of the 7th International Conference on Gas Hydrates (ICGH 2011)*.

Martini, A. M., Budai, J. M., Walter, L. M., and Schoell, M. (1996). Microbial generation of economic accumulations of methane within a shallow organic-rich shale. *Nature* 383, 155–158. doi: 10.1038/383155a0

Martini, A., Walter, L., Budai, J., Ku, T., Kaiser, C., and Schoell, M. (1998). Genetic and temporal relations between formation waters and biogenic methane: Upper Devonian Antrim shale, Michigan basin, USA. *Geochim. Cosmochim. Acta* 62, 1699–1720. doi: 10.1016/S0016-7037(98)00090-8

Mesle, M., Dromart, G., and Oger, P. (2013). Microbial methanogenesis in subsurface oil and coal. *Res. Microbiol.* 164 (9), 959–972. doi: 10.1016/j.resmic.2013.07.004

Michel, J. B., Shen, Y. K., Aiden, A. P., Veres, A., Gray, M. K., Team, G. B., et al. (2011). Quantitative analysis of culture using millions of digitized books. *Science* 331, 176–182. doi: 10.1126/science.1199644

Milkov, A. V. (2011). Worldwide distribution and significance of secondary microbial methane formed during petroleum biodegradation in conventional reservoirs. *Org. Geochem.* 42 (2), 184–207. doi: 10.1016/j.orggeochem.2010.12.003

Milkov, A. V. (2018). Secondary microbial gas In: H. Wilkes (Ed.), *Hydrocarbons, Oils and Lipids: Diversity, Origin, Chemistry and Fate*. Springer, Cham. 1–10. doi: 10.1007/978-3-319-54529-5_22-1

Milkov, A. V., and Dzou, L. (2007). Geochemical evidence of secondary microbial methane from very slight biodegradation of undersaturated oils in a deep hot reservoir. *Geology* 35 (5), 455. doi: 10.1130/g23557a.1

Milkov, A. V., and Etiope, G. (2018). Revised genetic diagrams for natural gases based on a global dataset of > 20,000 samples. *Org. Geochem.* 125, 109–120. doi: 10.1016/j.orggeochem.2018.09.002

Moore, M. T., Phillips, S. C., Cook, A. E., and Darrah, T. H. (2020). Improved sampling technique to collect natural gas from hydrate-bearing pressure cores. *Appl. Geochem.* 122 (2020), 104773. doi: 10.1016/j.apgeochem.2020.104773

Nikitin, B. A. (1937). Chemical properties of the rare gases. *Nature* 140, 643. doi: 10.1038/140643a0

Nisbet, E. G., Dlugokencky, E. J., and Bousquet, P. (2014). Methane on the rise-again. *Science* 343, 493–494. doi: 10.1126/science.1247828

Ono, S., Rhim, J. H., Gruen, D. S., Taubner, H., Kölling, M., and Wegener, G. (2021). Clumped isotopologue fractionation by microbial cultures performing the anaerobic oxidation of methane. *Geochim. Cosmochim. Acta* 293, 70–85. doi: 10.1016/j.gca.2020.10.015

Ono, S., Wang, D. T., Gruen, D. S., Sherwood Lollar, B., Zahniser, M. S., McManus, B. J., et al. (2014). Measurement of a doubly substituted methane isotopologue, (1)(3)CH(3)D, by tunable infrared laser direct absorption spectroscopy. *Anal. Chem.* 86 (13), 6487–6494. doi: 10.1021/ac5010579

Oremland, R. S., Whiticar, M. J., Strohmaier, F. E., and Kiene, R. P. (1988). Bacterial ethane formation from reduced, ethylated sulphur compounds in anoxic sediments. *Geochim. Cosmochim. Acta* 52, 1895–1904. doi: 10.1016/0016-7037(88)90013-0

Oxburgh, E. R., O'nions, R. K., and Hill, R. I. (1986). Helium isotopes in sedimentary basins. *Nature* 324, 632–635. doi: 10.1038/324632a0

Paganoni, M., Cartwright, J. A., Foschi, M., Shipp, R. C., and Van Rensbergen, P. (2016). Structure II gas hydrates found below the bottom-simulating reflector. *Geophy. Res. Lett.* 43 (11), 5696–5706. doi: 10.1002/2016gl069452

Paganoni, M., Cartwright, J. A., Foschi, M., Shipp, C. R., and Van Rensbergen, P. (2018). Relationship between fluid-escape pipes and hydrate distribution in offshore sabah (NW Borneo). *Mar. Geol.* 395, 82–103. doi: 10.1016/j.margeo.2017.09.010

Phrampus, B. J., and Hornbach, M. J. (2012). Recent changes to the Gulf Stream causing widespread gas hydrate destabilization. *Nature* 490 (7421), 527–530. doi: 10.1038/nature11528

Pohlman, J. W., Canuel, E. A., Chapman, N. R., Spence, G. D., Whiticar, M. J., and Coffin, R. B. (2005). The origin of thermogenic gas hydrates on the northern cascadia margin as inferred from isotopic (13C/12C and D/H) and molecular composition of hydrate and vent gas. *Org. Geochem.* 36 (5), 703–716. doi: 10.1016/j.orggeochem.2005.01.011

Pohlman, J. W., Ruppel, C., Hutchinson, D. R., Downer, R., and Coffin, R. B. (2008). Assessing sulfate reduction and methane cycling in a high salinity pore water system in the northern gulf of Mexico. *Mar. Pet. Geol.* 25 (9), 942–951. doi: 10.1016/j.marpetgeo.2008.01.016

Poreda, R. J., Jenden, P. D., Kaplan, I. R., and Craig, H. (1986). Mantle helium in Sacramento basin naturalgas wells. *Geochim. Cosmochim. Acta* 50, 2847–2853. doi: 10.1016/0016-7037(86)90231-0

Prasolov, E. M., Tokarev, I. V., Ginsburg, G. D., Soloviev, V. A., and Eltsova, G. M. (1999). Helium and other noble gases in gas-hydrate sediments of the has kon mosby mud volcano. *Geo-Marine Lett.* 19, 84–88. doi: 10.1007/s003670050096

Prinzhofer, A. A., and Huc, A. Y. (1995). Genetic and post-genetic molecular and isotopic fractionations in natural gases. *Chem. Geol.* 126, 281–290. doi: 10.1016/0009-2541(95)00123-9

Prinzhofer, A., Mello, M. R., Freitas, L., and Takaki, T. (2000). New geochemical characterization of natural gas and its use in oil and gas evaluation. *AAPG Bull.* 73, 107–19. doi: 10.1016/s0304-3959(02)00346-9.

Prinzhofer, A., and Pernaton, E. (1997). Isotopically light methane in natural gas: bacterial imprint or diffusive fractionation? *Chem. Geol.* 142, 193–200. doi: 10.1016/S0009-2541(97)00082-X

Reeburgh, W. S. (1976). Methane consumption in cariaco trench waters and sediments. *Earth Planet. Sci. Lett.* 28, 337–344. doi: 10.1016/0012-821X(76)90195-3

Riboulot, V., Ker, S., Sultan, N., Thomas, Y., Marsset, B., Scalabrin, C., et al (2018). Freshwater lake to salt-water sea causing widespread hydrate dissociation in the Black Sea. *Nat Commun* 9 (1), 117. doi: 10.1038/s41467-017-02271-z

Rodrigues, L., Ketzer, J., Oliveira, R., dos Santos, V., Augustin, A., Cupertino, J., et al. (2019). Molecular and isotopic composition of hydrate-bound, dissolved and free gases in the Amazon deep-Sea fan and slope sediments, Brazil. *Geosciences* 9 (2), 73. doi: 10.3390/geosciences9020073

Rooney, M. A., Claypool, G. E., and Chung, H. M. (1995). Modeling thermogenic gas generation using carbon isotope ratios of natural gas hydrocarbons. *Chem. Geol.* 126, 219–232. doi: 10.1016/0009-2541(95)00119-0

Ruffine, L., Donval, J.-P., Croguennec, C., Burnard, P., Lu, H., Germain, Y., et al. (2018). Multiple gas reservoirs are responsible for the gas emissions along the marmara fault network. *Deep Sea Res. Part II: Topical Stud. Oceanog.* 153, 48–60. doi: 10.1016/j.dsr2.2017.11.011

Saito, H., and Suzuki, N. (2007). Terrestrial organic matter controlling gas hydrate formation in the nankai trough accretionary prism, offshore Shikoku, Japan. *J. Geochem. Explor.* 95 (1-3), 88–100. doi: 10.1016/j.gexplo.2007.05.007

Sassena, R., Joye, S., Sweeta, S. T., DeFreitasa, D. A., Milkov, A. V., and MacDonald, I. R. (1999). Thermogenic gas hydrates and hydrocarbon gases in complex chemosynthetic communities, gulf of Mexico continental slope. *Org. Geochem.* 30, 485–497. doi: 10.1016/S0146-6380(99)00050-9

Sassena, R., Losh, S. L., Iii, L. C., Roberts, H. H., Whelan, J. K., Milkov, A. V., et al. (2001a). Massive vein-filling gas hydrate: relation to ongoing gas migration from the deep subsurface in the gulf of mexico. *Mar. Pet. Geol.* 18, 551–560. doi: 10.1016/S0264-8172(01)00014-9

Sassena, R., Sweet, S. T., DeFreitas, D. A., Morelosb, J. A., and Milkov, A. V. (2001b). Gas hydrate and crude oil from the mississippi fan foldbelt, downdip gulf of mexico salt basin: significance to petroleum system. *Org. Geochem.* 32, 999–1008. doi: 10.1016/S0146-6380(01)00064-X

Sassen, R., Sweet, S. T., Milkov, A. V., DeFreitas, D. A., and Kennicutt, II, M.C. (2001). Thermogenic vent gas and gas hydrate in the gulf of Mexico. *Geology* 29, 107–110. doi: 10.1130/0091-7613(2001)029<0107:TVGAGH>2.0.CO;2

Schaefer, R. G., Fletcher, S. E. M., Veidt, C., Lassey, K. R., and Brailsford, (2016). A 21st-century shift from fossil-fuel to biogenic methane emissions indicated by 13CH4. *Science* 352, 80–84. doi: 10.1126/science.aad2705

Schlegel, M. E., McIntosh, J. C., Petsch, S. T., Orem, W. H., Jones, E. J. P., and Martini, A. M. (2013). Extent and limits of biodegradation by *in situ* methanogenic consortia in shale and formation fluids. *Appl. Geochem.* 28, 172–184. doi: 10.1016/j.apgeochem.2012.10.008

Schlegel, M. E., Zhou, Z., McIntosh, J. C., Ballentine, C. J., and Person, M. A. (2011). Constraining the timing of microbial methane generation in an organic-rich shale using noble gases, Illinois basin, USA. *Chem. Geol.* 287 (1-2), 27–40. doi: 10.1016/j.chemgeo.2011.04.019

Schloemer, S., and Krooss, B. M. (2004). Molecular transport of methane, ethane and nitrogen and the influence of diffusion on the chemical and isotopic composition of natural gas accumulations. *Geofluids* 4, 81–108. doi: 10.1111/j.1468-8123.2004.00076.x

Schoell, M. (1980). The hydrogen and carbon isotopic composition of methane from natural gases of various origins. *Geochim. Cosmochim. Acta* 44, 649–661. doi: 10.1016/0016-7037(80)90155-6

Schoell, M. (1983). Genetic characterization of natural gases. *AAPG Bull.* 22, 229–230. doi: 10.1306/AD46094A-16F7-11D7-8645000102C1865D

Schoell, M. (1984). Recent advances in petroleum isotope geochemistry. *Org. Geochem.* 6, 645–663. doi: 10.1016/0146-6380(84)90086-X

Schwietzke, S., Sherwood, O. A., Bruhwiler, L. M., Miller, J. B., Etiope, G., Dlugokencky, E. J., et al. (2016). Upward revision of global fossil fuel methane emissions based on isotope database. *Nature* 538 (7623), 88–91. doi: 10.1038/nature19797

Shuai, Y., Douglas, P. M. J., Zhang, S., Stolper, D. A., Ellis, G. S., Lawson, M., et al. (2018). Equilibrium and non-equilibrium controls on the abundances of clumped isotopologues of methane during thermogenic formation in laboratory experiments: Implications for the chemistry of pyrolysis and the origins of natural gases. *Geochim. Cosmochim. Acta* 223, 159–174. doi: 10.1016/j.gca.2017.11.024

Sloan, E. D., Koh, C. A., and Sum, A. K. (2010). Gas hydrate stability and sampling: The future as related to the phase diagram. *Energies* 3 (12), 1991–2000. doi: 10.3390/en3121991

Sloan, E. D. (1998). *Clathrate hydrates of natural gas, second ed.* (New York: Marcel Dekker Inc,), 726.

Smith, A. J., Mienert, J., Bünz, S., and Greinert, J. (2014). Thermogenic methane injection *via* bubble transport into the upper Arctic ocean from the hydrate-charged vestnesa ridge, Svalbard. *Geochem. Geophysics Geosyst.* 15, 1945–1959. doi: 10.1002/2013GC005179

Snyder, G. T., Sano, Y., Takahata, N., Matsumoto, R., Kakizaki, Y., and Tomaru, H. (2020). Magmatic fluids play a role in the development of active gas chimneys and massive gas hydrates in the Japan Sea. *Chem. Geol.* 535 (2020), 119462. doi: 10.1016/j.chemgeo.2020.119462

Stahl, W. J. (1977). Carbon and nitrogen isotopes in hydrocarbon research and exploration. *Chem. Geol.* 20, 121–149. doi: 10.1016/0009-2541(77)90041-9

Stahl, W. J., and Carey, B. D. (1975). Source-rock identification by isotope analyses of natural gases from fields in the val verde and delaware basins, west texas. *Chem. Geol.* 16, 257–267. doi: 10.1016/0009-2541(75)90065-0

Stern, L. A., Lorenson, T. D., and Pinkston, J. C. (2011). Gas hydrate characterization and grain-scale imaging of recovered cores from the mount Elbert gas hydrate stratigraphic test well, Alaska north slope. *Mar. Pet. Geol.* 28 (2), 394–403. doi: 10.1016/j.marpetgeo.2009.08.003

Stolper, D. A., Lawson, M., Davis, C. L., Ferreira, A. A., Santos Neto, E. V., Ellis, G. S., et al. (2014a). Gas formation. formation temperatures of thermogenic and biogenic methane. *Science* 344 (6191), 1500–1503. doi: 10.1126/science.1254509

Stolper, D. A., Lawson, M., Formolo, M. J., Davis, C. L., Douglas, P. M. J., and Eiler, J. M. (2018). The utility of methane clumped isotopes to constrain the origins of methane in natural gas accumulations. *Geological Society London Special Publications* 468 (1), 23–52. doi: 10.1144/sp468.3

Stolper, D. A., Martini, A. M., Clog, M., Douglas, P. M., Shusta, S. S., Valentine, D. L., et al. (2015). Distinguishing and understanding thermogenic and biogenic sources of methane using multiply substituted isotopologues. *Geochim. Cosmochim. Acta* 161, 219–247. doi: 10.1016/j.gca.2015.04.015

Stolper, D. A., Sessions, A. L., Ferreira, A. A., Santos Neto, E. V., Schimmelmann, A., Shusta, S. S., et al. (2014b). Combined 13C–d and d–d clumping in methane: Methods and preliminary results. *Geochim. Cosmochim. Acta* 126, 169–191. doi: 10.1016/j.gca.2013.10.045

Sun, L., Wang, X., He, M., Jin, J., Li, J., Yuanping, L., et al. (2020). Thermogenic gas controls high saturation gas hydrate distribution in the pearl river mouth basin: Evidence from numerical modeling and seismic anomalies. *Ore Geol. Rev.* 127 (2020), 103846. doi: 10.1016/j.oregeorev.2020.103846

Taenzer, L., Labidi, J., Masterson, A. L., Feng, X., Rumble, D., Young, E. D., et al. (2020). Low Δ12CH2D2 values in microbialgenic methane result from combinatorial isotope effects. *Geochim. Cosmochim. Acta* 285, 225–236. doi: 10.1016/j.gca.2020.06.026

Teichert, B. M. A., Eisenhauer, A., Bohrmann, G., Haase-Schramm, A., Bock, B., and Linke, P., et al (2003). U/Th systematics and ages of authigenic carbonates from Hydrate Ridge, Cascadia Margin: Recorders of fluid flow variations. *Geochim. Cosmochim. Acta* 67 (20), 3845–3857. doi: 10.1016/s0016-7037(03)00128-5

Thompson, K. F. M. (1979). Light hydrocarbons in subsurface sediments. *Geochim. Cosmochim. Acta* 43, 657–672. doi: 10.1016/0016-7037(79)90251-5

Tissot, B., Durand, B., Espitalie, J., and Combaz, A. (1974). Influence of nature and diagenesis of organic matter in formation of petroleum. *AAPG Bull.* 58 (3), 499–506. doi: 10.1306/83D91425-16C7-11D7-8645000102C1865D

Tissot, B. P., and Welte, D. H. (1984). *Petroleum Formation and Occurrence. A New Approach to Oil and Gas Exploration* (Berlin: Springer-Verlag), 538. doi.org/10.1007/978-3-642-87813-8

Tréhu, A. M., Ruppel, C., Holland, M., Dickens, G. R., Torres, M. E., Collett, T. S., et al. (2006). Gas hydrates in marine sediments: lessons from scientific ocean drilling. *Oceanography* 19, 124–142. doi: 10.5670/oceanog.2006.11

Valentine, D. L., Chidthaisong, A., Rice, A., Reeburgh, W. S., and Tyler, S. C. (2004). Carbon and hydrogen isotope fractionation by moderately thermophilic methanogens 1 1Associate editor: N. e. ostrom. *Geochim. Cosmochim. Acta* 68 (7), 1571–1590. doi: 10.1016/j.gca.2003.10.012

Van Krevelen, D. W. (1961). Graphical-statistical method for the study of structure and reaction processes of coal. *Fuel* 29, 269–283.

Vaular, E. N., Barth, T., and Haflidason, H. (2010). The geochemical characteristics of the hydrate-bound gases from the nyegga pockmark field, Norwegian Sea. *Org. Geochem.* 41 (5), 437–444. doi: 10.1016/j.orggeochem.2010.02.005

Wang, T. (2010). Gas hydrate resource potential and its exploration and development prospect of the muli coalfield in the northeast Tibetan plateau. *Energy Explor. Exploit.* 28, 147–158. doi: 10.1260/0144-5987.28.3.147

Wang, D. T., Gruen, D. S., Sherwood, L. B., Hinrichs, K.-U., Stewart, L. C., Holden, J. F., et al (2015a). Nonequilibrium clumped isotope signals in microbial methane. *Science* 348, 428–431. doi: 10.1126/science.aaa43

Wang, P., Huang, X., Pang, S., Zhu, Y., Lu, Z., Zhang, S., et al (2015b). Geochemical dynamics of the gas hydrate system in the qilian mountain permafrost, qinghai, Northwest China. *Mar. Pet. Geol.* 59, 72–90. doi: 10.1016/j.marpetgeo.2014.07.009

Wang, D. T., Welander, P. V., and Ono, S. (2016). Fractionation of the methane isotopologues 13CH4, 12CH3D, and 13CH3D during aerobic oxidation of methane by methylococcus capsulatus (Bath). *Geochim. Cosmochim. Acta* 192, 186–202. doi: 10.1016/j.gca.2016.07.031

Wang, P., Zhu, Y., Lu, Z., Bai, M., Huang, X., Pang, S., et al. (2018). Research progress of gas hydrates in the qilian mountain permafrost, qinghai, Northwest China: Review. *SCIENTIA Sin. Physica Mechanica Astronomica* 49 (3), 034606. doi: 10.1360/sspma2018-00133

Warr, O., Young, E. D., Giunta, T., Kohl, I. E., Ash, J. L., and Sherwood Lollar, B. (2021). High-resolution, long-term isotopic and isotopologue variation identifies the sources and sinks of methane in a deep subsurface carbon cycle. *Geochim. Cosmochim. Acta* 294, 315–334. doi: 10.1016/j.gca.2020.12.002

Waseda, A., and Iwano, H. (2008). Characterization of natural gases in Japan based on molecular and carbon isotope compositions. *Geofluids* 8 (4), 286–292. doi: 10.1111/j.1468-8123.2008.00222.x

Waseda, A., and Uchida, T. (2004). The geochemical context of gas hydrate in the Eastern nankai trough. *Resource Geol.* 54, 69–78. doi: 10.1111/j.1751-3928.2004.tb00188.x

Watanabe, Y., Nakai, S. i., Hiruta, A., Matsumoto, R., and Yoshida, K. (2008). U–Th dating of carbonate nodules from methane seeps off Joetsu, Eastern Margin of Japan Sea. Earth Planet. *Sci. Lett.* 272 (1–2), 89–96. doi: 10.1016/j.epsl.2008.04.012

Webb, M. A., and Miller, T. F. (2014). Position-specific and clumped stable isotope studies: Comparison of the urey and path-integral approaches for carbon dioxide, nitrous oxide, methane, and propane. *J. Phys. Chem. A* 118 (2), 467–474. doi: 10.1021/jp411134v

Wen, T., Castro, M. C., Ellis, B. R., Hall, C. M., and Lohmann, K. C. (2015). Assessing compositional variability and migration of natural gas in the Antrim shale in the Michigan basin using noble gas geochemistry. *Chem. Geol.* 417, 356–370. doi: 10.1016/j.chemgeo.2015.10.029

Whiticar, M. J. (1994). Correlation of natural gases with their sources. *AAPG Memoir* 60, 261–283. doi: 10.1306/M60585C16

Whiticar, M. J. (1999). Carbon and hydrogen isotope systematics of bacterial formation and oxidation of methane. *Chem. Geol.* 161, 291–314. doi: 10.1016/S0009-2541(99)00092-3

Whiticar, M. J., Faber, E., and Schoell, M. (1986). Biogenic methane formation in marine and freshwater environments: CO2 reduction vs. acetate fermentation–isotope evidence. *Geochim. Cosmochim. Acta* 50, 693–709. doi: 10.1016/0016-7037(86)90346-7

Wiese, K., and Kvenvolden, K. A. (1993). Introduction to microbial and thermal methane. *United States Geological Survey Prof. Paper* 1570, 13–20.

Winckler, G., Aeschbach-Hertig, W., Holocher, J., Kipfer, R., Levin, I., Poss, C., et al. (2002). Noble gases and radiocarbon in natural gas hydrates. *Geophy. Res. Lett.* 29 (10), 63–61-63-64. doi: 10.1029/2001gl014013

Winckler, G., Kipfer, R., Aeschbach–Hertig, W., Botz, R., Schmidt, M., Schuler, S., et al. (2000). Sub Sea floor boiling of red sea brines: new indication from noble gas data. *Geochim. Cosmochim. Acta* 64, 1567–1575. doi: 10.1016/S0016-7037(99)00441-X

Wu, N. Y., Zhang, H. Q., Yang, S. X., Zhang, G. X., Liang, J. Q., Lu, J. A., et al. (2011). Gas hydrate system of shenhu area, northern south China Sea: Geochemical results. *J. Geological Res.* 2011, 1–10. doi: 10.1155/2011/370298

Xia, X., and Gao, Y. (2019). Kinetic clumped isotope fractionation during the thermal generation and hydrogen exchange of methane. *Geochim. Cosmochim. Acta* 248, 252–273. doi: 10.1016/j.gca.2019.01.004

Xiao, K., Zou, C., Yang, Y., Zhang, H., Li, H., and Qin, Z. (2019). A preliminary study of the gas hydrate stability zone in a gas hydrate potential region of China. *Energy Sci. Eng.* 8 (4), 1080–1091. doi: 10.1002/ese3.569

Xu, W., and Ruppel, C. (1999). Predicting the occurrence, distribution, and evolution of methane gas hydrate in porous marine sediments. *J. Geophy. Res.: Solid Earth* 104 (B3), 5081–5095. doi: 10.1029/1998jb900092

Ye, J., Qin, X., Qiu, H., Xie, W., Lu, H., Lu, C., et al. (2018). Data report: Molecular and isotopic compositions of the extracted gas from china's first offshore natural gas hydrate production test in south China Sea. *Energies* 11 (10), 2793. doi: 10.3390/en11102793

Yeung, L. Y., Ash, J. L., and Young, E. D. (2015). Biological signatures in clumped isotopes of O2. *Science* 348, 431–434. doi: 10.1126/science.aaa6284

Ye, J., Wei, J., Liang, J., Lu, J., Lu, H., and Zhang, W. (2019). Complex gas hydrate system in a gas chimney, south China Sea. *Mar. Pet. Geol.* 104, 29–39. doi: 10.1016/j.marpetgeo.2019.03.023

Yoshinaga, M. Y., Holler, T., Goldhammer, T., Wegener, G., Pohlman, J. W., Brunner, B., et al. (2014). Carbon isotope equilibration during sulphate-limited anaerobic oxidation of methane. *Nat. Geosci.* 7 (3), 190–194. doi: 10.1038/ngeo2069

Young, E. D. (2019). A two-dimensional perspective on CH4 isotope clumping. *Deep Carbon* 1029, 388–414. doi: 10.1017/9781108677950

Young, E. D., Kohl, I. E., Lollar, B. S., Etiope, G., Rumble, D., Li, S., et al. (2017). The relative abundances of resolved 12CH2D2 and 13CH3D and mechanisms controlling isotopic bond ordering in abiotic and biotic methane gases. *Geochim. Cosmochim. Acta* 203, 235–264. doi: 10.1016/j.gca.2016.12.041

Young, E. D., Rumble, D., Freedman, P., and Mills, M. (2016). A large-radius high-mass-resolution multiple-collector isotope ratio mass spectrometer for analysis of rare isotopologues of O2, N2, CH4 and other gases. *Int. J. Mass Spectrometry* 401, 1–10. doi: 10.1016/j.ijms.2016.01.006

Zeikus, J. G. (1977). The biology of methanogenic bacteria. *Bacteriol. Rev.* 41, 514–541. doi: 10.1128/br.41.2.514-541.1977

Zhang, T., and Krooss, B. M. (2001). Experimental investigation on the carbon isotope fractionation of methane during gas migration by diffusion through sedimentary rocks at elevated temperature and pressure. *Geochim. Cosmochim. Acta* 65, 2723–2742. doi: 10.1016/S0016-7037(01)00601-9

Zhang, W., Liang, J., Liang, Q., Wei, J., Wan, Z., Feng, J., et al. (2021b). Gas hydrate accumulation and occurrence associated with cold seep systems in the northern south China Sea: An overview. *Geofluids* 2021, 1–24. doi: 10.1155/2021/5571150

Zhang, W., Liang, J. Q., Wei, J. G., Su, P. B., Lin, L., and Huang, W. (2019). Origin of natural gases and associated gas hydrates in the shenhu area, northern south China Sea: Results from the China gas hydrate drilling expeditions. *J. Asian Earth Sci.* 183, 1–16. doi: 10.1016/j.jseaes.2019.103953

Zhang, N., Snyder, G. T., Lin, M., Nakagawa, M., Gilbert, A., Yoshida, N., et al. (2021a). Doubly substituted isotopologues of methane hydrate (13CH3D and 12CH2D2): Implications for methane clumped isotope effects, source apportionments and global hydrate reservoirs. *Geochim. Cosmochim. Acta* 315, 127–151. doi: 10.1016/j.gca.2021.08.027

Zhou, Z., and Ballentine, C. J. (2006). 4He dating of groundwater associated with hydrocarbon reservoirs. *Chem. Geol.* 226 (3-4), 309–327. doi: 10.1016/j.chemgeo.2005.09.030

Zhou, Z., Ballentine, C. J., Kipfer, R., Schoell, M., and Thibodeaux, S. (2005). Noble gas tracing of groundwater/coalbed methane interaction in the San Juan basin, USA. *Geochim. Cosmochim. Acta* 69 (23), 5413–5428. doi: 10.1016/j.gca.2005.06.027

frontiers | Frontiers in Earth Science

TYPE Original Research
PUBLISHED 23 September 2022
DOI 10.3389/feart.2022.1003510

Geochemical implications for gas hydrate occurrence and seepage at Sites GMGS5-W07 and W09 in Qiongdongnan Basin, South China Sea

Yinghan Lu[1,2], Hailin Yang[1,2]*, Hailong Lu[1,2]*, Yunxin Fang[3,4]* and Zenggui Kuang[3,4]

[1]School of Earth and Space Sciences, Peking University, Beijing, China, [2]Beijing International Center for Gas Hydrate, Beijing, China, [3]Guangzhou Marine Geology Survey, Guangzhou, China, [4]Southern Marine Science and Engineering Guangdong Laboratory, Guangzhou, China

The compositions and morphological characteristics of minerals and the cycle of trace elements in sedimentary environments are considered to be powerful indicators for the occurrence and evolution of gas hydrates. In this article, total organic carbon (TOC) content, particle size distribution, mineral composition, element distribution, and iron speciation of sediments from sites GMGS5-W07 and GMGS5-W09 of the South China Sea are studied. The high content of TOC and the occurrence of authigenic mineral assemblages suggest the accumulation potential of gas hydrate at the two sites. In the methane-rich layers, redox-sensitive trace elements, such as Co, Ni, Cu, Zn, As, Sb, Fe, and Mn, are enriched while reducing conditions lead to the accumulation of Fe and the increase of Fe(II) species proportion in sediments. Enrichment factors and Pearson correlation analysis of trace elements show that the circulation of trace elements at site W07 is more strongly affected by methane-rich fluids than at site W09. Fe-oxyhydroxides play a critical role in the development of As and Sb enrichments, and in particular, seep fluids may be a pivotal extra input of Mo, As, and Sb at site W07. Therefore, more intense methane seepage might have happened at site W07, and this conjecture has been further confirmed by higher Sr/Ca in sediments. Based on these results, the change in seepage intensity is not associated with the occurrence of gas hydrate.

KEYWORDS

gas hydrate, seepage, South China Sea, Fe species, trace elements, authigenic minerals, particle size

OPEN ACCESS

EDITED BY
Dong Feng,
Shanghai Ocean University, China

REVIEWED BY
Zhiyong Lin,
University of Hamburg, Germany
Niu Li,
South China Sea Institute of Oceanology (CAS), China

*CORRESPONDENCE
Hailin Yang,
hyang@pku.edu.cn
Yunxin Fang,
419487092@qq.com
Hailong Lu,
hlu@pku.edu.cn

SPECIALTY SECTION
This article was submitted to Marine Geoscience, a section of the journal Frontiers in Earth Science

RECEIVED 26 July 2022
ACCEPTED 17 August 2022
PUBLISHED 23 September 2022

CITATION
Lu Y, Yang H, Lu H, Fang Y and Kuang Z (2022), Geochemical implications for gas hydrate occurrence and seepage at Sites GMGS5-W07 and W09 in Qiongdongnan Basin, South China Sea. *Front. Earth Sci.* 10:1003510.
doi: 10.3389/feart.2022.1003510

1 Introduction

The geochemical conditions of gas hydrate-bearing sediments have been recognized, which have also been known to affect the formation of authigenic mineral and the behaviors of elements. In recent years, a scientific geochemical method of identifying gas hydrate-bearing environments has been established through a series of proxies, including but not limited to organic carbon content, authigenic minerals, and element composition (Chen et al., 2016; Feng and Chen, 2015; Himmler et al., 2013; Li N et al., 2016; Liu et al., 2020; Smrzka et al., 2020; Tong et al., 2013; Wang et al., 2018).

Sediment granularity is an important factor influencing gas hydrate saturation, and the suitable reservoir is in favor of gas hydrate storage (Ginsburg et al., 2000; Lu et al., 2011). It is generally stored in coarse-grained sediments, such as sand deposits with high porosity and methane seepage (Collett et al., 1988; Uchida and Tsuji, 2004; Boswell, 2007). However, numerous submarine gas hydrate may be stored in the clay (<4 μm) and silt (4–63 μm) of fine-grained sediments, and gas hydrate has the characteristics of small thickness and low saturation with disseminated structure (Shaohua et al., 2015). Some studies showed that there may be a good corresponding relationship between the microbiological shell and a relatively large layer of fine-grained sediments with gas hydrate, such as Blake Ridge in the western Atlantic Ocean (Kraemer et al., 2000) and the South China Sea (Zhang et al., 2007; Li C et al., 2016).

A special mineral assemblage has been confirmed in the gas hydrate- or seepage-impact environment. In general, minerals commonly found in gas hydrate-bearing environments include authigenic carbonate minerals (e.g., calcite, dolomite, aragonite, and high-Mg calcite), sulfate minerals (e.g., gypsum and barite), and pyrite (Ritger et al., 1987; Peckmann et al., 2001; Luff and Wallmann, 2003; Egawa et al., 2015; Feng and Chen, 2015; Zhou et al., 2020). These minerals are thought to be the products of sulfate-dependent anaerobic oxidation of methane (AOM, Eq. 1, Boetius et al., 2000; Devol and Ahmed, 1981; Murray et al., 1978), and this process increases the alkalinity of the environment and provides anions for the formation of authigenic minerals. AOM is the most typical reaction that occurs at the sulfate-methane transition zone (SMTZ) (Knittel and Boetius, 2009) or might proceed in the gas hydrate zone (Cui et al., 2019) and is also strongly affected by the seepage strength (Joye et al., 2004; Boetius and Wenzhöfer, 2013). For the abovementioned reasons, authigenic minerals are critical geochemical proxies closely related to the hydrate deposition environments and can indicate the presence of gas hydrate and methane upwelling to a certain extent (Feng and Chen, 2015; Zhang et al., 2018; Zhou et al., 2020).

$$CH_4 + SO_4^{2-} \rightarrow HCO_3^- + HS^- + H_2O \qquad (1)$$

Deposition area where gas hydrates exist and methane seepage have occurred will affect the circulation of elements in sediments, especially redox-sensitive trace elements (Tribovillard et al., 2006; Tribovillard et al., 2013; Hu et al., 2015b; Chen et al., 2016; Smrzka et al., 2020). Past research has shown that redox-sensitive elements such as Mo, U, and V are strongly enriched under anoxic conditions, and to a lesser extent, certain other trace metals like Cr and Co are also classified to judge the oxidation and reduction environments (Tribovillard et al., 2006; Algeo and Tribovillard, 2009; Tribovillard et al., 2012). Ni, Cu, Zn, and Cd are mainly associated with organic matter, and may be reserved to the sediment in association with pyrite after the reduction processes decompose organic matter (Tribovillard et al., 2006). Under normal circumstances, Ba and P in the ocean environment can evaluate the level of paleoproductivity, while sedimentary environments with gas hydrate are often accompanied by high organic matter fluxes (Dymond et al., 1992; Tribovillard et al., 2006).

Otherwise, the geochemical cycling of Fe is redox-active in near-surface marine sediments and methane-rich layers (Froelich et al., 1979; Raiswell and Canfield, 2012; Riedinger et al., 2014; Hu et al., 2015a; Nevin and Lovley, 2002). Under normal reducing conditions, Fe exists mainly in divalent cationic form and forms sulfide or sometimes siderite. Under oxidizing conditions, Fe^{2+} will be oxidized to Fe^{3+} and mainly deposited as hydroxides or oxides, such as hematite and goethite, respectively (Nevin and Lovley, 2002; Hedrich et al., 2011). In sediments affected by sulfidic conditions, the precipitation of Fe sulfides is favorable, which leads to authigenic Fe accumulation (Scholz et al., 2014a, b), namely, Fe-oxyhydroxides and ferrous Fe, which will experience the circulation of reprecipitation and redissolution and release into the pore water among oxic zone, suboxic zone, and sulfidic zone. Methane seepages could represent a source of dissolved Fe to the deep ocean with the amount of Fe released into seawater from methane fluids (Lemaitre et al., 2014). In such environments, the release of hydrogen sulfide and bicarbonate through AOM leads to the reduction of Fe-oxyhydroxides and the precipitation of Fe sulfides (Hensen et al., 2003; März et al., 2008; Yang et al., 2018). Based on this, Fe speciation could be regarded as a tool to assess variable redox conditions during seepage history (Hu et al., 2015a). In addition, Fe speciation also contributes to the interpretation of fluctuations of redox-sensitive elements in the seepage-impact environment under various redox conditions. The mobilization of Fe (oxyhydr)oxide-bound P has been reported around the SMTZ (März et al., 2008), and the enrichment of some redox-sensitive elements, such as, Sb, and Mo, has a link with the adsorption of Fe-oxyhydroxides (Dymond et al., 1992; Tribovillard et al., 2013; Hu et al., 2014).

Geochemical methods such as elemental content, mineral composition, and TOC content in seafloor sediments have long been a critical scientific tool for revealing gas hydrate accumulation and methane seepage in the study area. In this article, we compared the sediment's total organic carbon contents, particle size compositions, authigenic minerals, and trace elements contents of two adjacent sites with different hydrate accumulation circumstances (gas hydrate content and seepage activity) on the north slope of the South China Sea during the fifth "China Gas Hydrate Drilling Expedition" (GMGS5) in 2018. Different from previous research, our work provides an opportunity to distinguish the geochemical conditions under different scenarios of gas hydrate occurrence and seepage evolution.

2 Geological setting and gas hydrate occurrence in the Qiongdongnan Basin

2.1 Geological setting

Benefitting from the widely distributed sedimentary basins, various faults or diapir structures and adequate organic matter supply, the northern continental slope of the South China Sea (SCS) is not only rich in oil and gas but also a hotspot for the exploration and exploitation of gas hydrates (Zhang et al., 2002; Wu et al., 2005; Wang et al., 2006). From now on, China has considerable reserves of gas hydrate in the SCS, including Xisha Sea Area (XSA), Shenhu Sea Area (SSA), Dongsha Sea Area (DSA), Pearl River Mouth Basin (PRMB), and Qiongdongnan Basin (QDNB) (Zhang et al., 2002; Jiang et al., 2008; Wu et al., 2008; Li et al., 2013; Liu et al., 2014; Zhang et al., 2015; Xu et al., 2016; Fang et al., 2019; Wei et al., 2019).

The Qiongdongnan Basin (QDNB), which is located at the northeast continental shelf of the SCS, covers an area of approximately 65,000 km^2. The water depth varies considerably, and the sedimentation rate is high (Ye et al., 1985; Zhao et al., 1999). The pre-Cenozoic basement of the QDNB is composed of Paleozoic metamorphic rocks, dolomites, cretaceous intermediate-acid granites, diorites, and volcanic clastic rocks (Huang et al., 2016). The sedimentary sequences include Paleogene, Neogene, and Quaternary strata (Zhu et al., 2009). Through petroleum explorations, benefitting from the extensive surface sea deposits and continental shelf slope deposits, the QDNB has good gas hydrate generation and storage capacity, especially the Eocene and Oligocene Yacheng formations are the main source rocks (Zhu et al., 2009; Su et al., 2012; Huang et al., 2016).

2.2 Gas hydrate expedition in the Qiongdongnan Basin

Since 2007, the Guangzhou Marine Geological Survey (GMGS) has carried out five gas-hydrate drilling expeditions in the SCS, the survey area includes eastern PRMB, XSA, SSA, and QDNB (Sha et al., 2015; Zhang et al., 2015; Wei et al., 2018; Wei et al., 2019). Through comprehensive survey methods of geology, geophysics, geochemistry, and biological characteristics, multilevel and multi-information abnormal signs related to gas hydrate were discovered. Research of the bottom simulating reflection (BSR) (Liang et al., 2019), the abnormal chemical composition of pore water (Sun et al., 2007), active cold seeps (Liang et al., 2017; Fang et al., 2019), authigenic carbonate minerals (Chen et al., 2016; Liang et al., 2017), and mud diapirs and gas chimneys (Zhang et al., 2019) have confirmed that the QDNB is rich in gas hydrate resources. In addition, sediments in which gas hydrates-recovered in the QDNB were dominated by clay and fine silt (Liang et al., 2019; Wei et al., 2019; Ye et al., 2019), and mainly exist in various fractures (Wei et al., 2021).

In 2018, the fifth gas hydrate drilling expedition (GMGS5) in the northwestern continental slope of the SCS was conducted by GMGS (Figure 1A). Four sites (W01, W07, W08, and W09) were selected to drill six boreholes (W01B, W07B, W08B, W08C, W09B, and W09C) in this investigation. In particular, vast quantities of gas hydrates were discovered and collected at site W08, which was the most typical and representative gas hydrate site drilled during this investigation (Wei et al., 2019; Lai et al., 2021). The samples in this article come from site W07 and W09 (Table 1), all of which are at the depth of 1,600–1,800 m in the deep water of the eastern part of the QDNB (Figure 1B). The seabed terrain is relatively flat (1.3–2.8 of W-E slope), which is conducive to the accumulation of gas hydrates (Wei et al., 2019). The seismic profile shows that, influenced by the position of the Songnan Low Uplift, site W07 and W09 were both drilled through the seepage pathways on the two chimneys (Liang et al., 2019; Wei et al., 2021).

Near site W09, active clams and a mound-like structure were observed, while life activity was limited (Wei et al., 2021). Confirmed by the coring and sampling results and pilot hole logging while drilling (LWD) anomalies, gas hydrates existed at the depth of 7–158 mbsf (Liang et al., 2019). The gas hydrate content increased with depth and showed a bump in the middle layer (from 60 mbsf to 100 mbsf, Figure 1C), multiple layers exhibited very high gas hydrate content (up to >80%) (Wei et al., 2019), which were dominated by fracture-filling hydrate (Wei et al., 2021).

There were many pockmarks near site W07, but no obvious traces of life activity were found (Wei et al., 2021). The core data from site W07 showed that gas hydrate was present at 6–8% of pore volume at depths with elevated LWD resistivities (Wei et al., 2021). Low saturation hydrates were present at site W07 and gas hydrate saturation increased with depth from the seafloor to the end of the hole (Wei et al., 2019; Wei et al., 2021) (Figure 1C).

Estimated gas hydrate contents at site W09 were higher than W07, whether it was based on the chloride concentration or degassing (Wei et al., 2019). Both site W07 and W09 have kick-type sulfate profiles, positive chloride anomalies in the shallow sediment (Figure 1D), and authigenic carbonates at multiple layers, which may indicate that dynamic changes in fluid flux and

TABLE 1 Information of samples from site GMGS5-W07 and GMGS5-W09.

Site	Samples	Depth/mbsf	Water depth/mbsf	[a]SMI depth/mbsf	[a]TGHOZ depth/mbsf	[a]AGHS/m^3	[b]BSR depth/mbsf
W07	W07B-1	0.00	~1775	20.05	22.5	13.70 and 3.03	142
	W07B-2	9.75					
	W07B-3	44.23					
	W07B-4	70.95					
	W07B-5	118.00					
	W07B-6	122.85					
W09	W09B-1	0.00	~1722	9.19	12.5	22.24 and 16.25	148
	W09B-2	5.50					
	W09B-3	11.90					
	W09B-4	13.75					
	W09B-5	16.70					
	W09B-6	58.00					
	W09B-7	60.75					
	W09B-8	75.75					

[a] As reported by Wei et al., (2019). TGHOZ, the top of the gas hydrate occurrence zone; AGHS, the average gas hydrate saturation, estimated using chloride concentration and degassing, respectively.

[b] As reported by Wei et al. (2021).

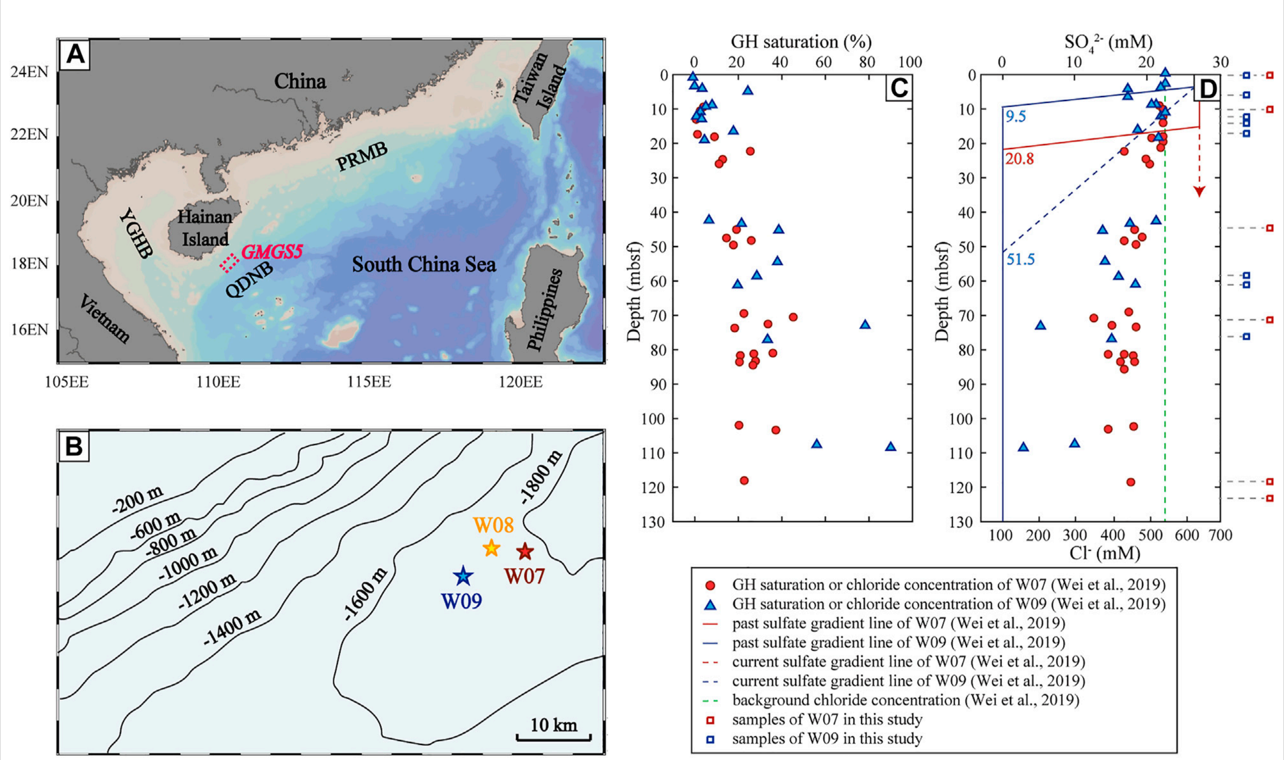

FIGURE 1
Gap of sampling locations and gas hydrate saturation of research sites in this study. **(A)** Geological settings and location of GMGS5 drilling area (red dotted frame). QDNB: Qiongdongnan Basin, YGHB: Yinggehai Basin, PRMB: Pearl River Mouth Basin. **(B)** Submarine topography of study area and locations of sites during GMGS5 (pointed stars, after Liang et al., 2019). **(C)** Gas hydrate saturation calculated based on chloride concentration of site W07 and W09 from Wei et al. (2019). **(D)** Chloride concentration and sulfate profiles of site W07 and W09 from Wei et al. (2019), and the depth of experimental samples in this study.

multistage gas hydrate evolution occurred on a time scale from months to thousands of years (Borowski et al., 1996; Torres et al., 1996; Fischer et al., 2013; Wei et al., 2019). Due to the increased fluid flux, gas hydrates were expected to be formed in the shallow sediment at site W07 and W09 (Wei et al., 2019). Methane seepage at the two sites accumulated the release of H_2S, causing the SMTZ to be shallow and the sedimentary environment to be reducible (Wei et al., 2019). Moreover, the seepage in site W07 was younger than W09, indicating that there may exist more free gas in W07 (Wei et al., 2021).

3 Methodology

3.1 Particle size analysis

The particle size distribution was determined *via* dynamic image analysis (CAMSIZER X2, Retsch Technology GmbH, 42,781 Haan, Retsch-Allee 1-5, Germany) at the School of Ocean Sciences, China University of Geosciences (Beijing) (CUGB). The sample preparation process sequence is as follows: 0.2000 ± 0.0010 g of the sample was accurately weighed into a 50 ml beaker, and a small amount of ultrapure water was added to immerse the sample. 10 ml of 30% H_2O_2 was added to each beaker and soaked for about 24 h to remove organic carbon. To remove the remaining H_2O_2, the sample was heated and boiled for 5min; 2 ml of 30% HCl was added to remove $CaCO_3$ after cooling. After standing for 24 h, 2 g of NaOH was added to remove biogenic opal. The sediment composition and mean particle size were obtained, and the classification and naming of the sediments adopt the Folk classification method (Folk et al., 1970).

3.2 Total organic carbon analysis

The total organic carbon (TOC) content of each sediment sample was determined using Elementar Vario TOC (Germany) at the School of Ocean Sciences, CUGB, following the procedure described by: 0.0200 ± 0.0005 g powdered sample was weighed into the tin foil cup, excess of 10% HCl was added to the tin foil cup to remove $CaCO_3$, was allowed to stand for 24 h; the cup was washed with distilled water and placed it in an oven for drying; and the tin foil cup was folded into a small square and text by the total organic carbon analyzer. Parallel samples, blank samples, and standard samples (GBW07312) were also analyzed for quality control, with the relative errors of all samples being within 2%.

3.3 Mineral analysis

X-ray diffraction (XRD) analysis of the samples was carried out using an X-ray diffractometer (Bruker D2 phaser, Germany) at the School of Ocean Sciences, CUGB. The scanning parameters: Cu-Kα radiation (λ = 0.154 nm), 2θ scan range 5°–70°, accelerating voltage 30 kV, current 10 mA, scan speed 2°/min, sampling step 0.02°.

The morphological properties of sediment samples were observed by field emission scanning electron microscope (FESEM) analysis using a Hitachi SU8220 FESEM at State Key Laboratory of Tribology, Tsinghua University. The images were taken using a 10 kV accelerating voltage with ~180 K × magnification.

3.4 Major and trace element analysis

Major and trace elements in sediments were determined by inductively coupled plasma optical emission spectroscopy (ICP-OES, IRIS Intrepid II, Thermo Scientific) at the School of Earth and Space Sciences, Peking University. Accuracy of the major and trace elements results within 5%–10%. Among them, the different chemical species of Fe in sediments were extracted in the sequential extraction method as described by Poulton and Canfield (2005) and Yang et al. (2018), each step is shown in Table 2. To ensure the reliability of the experimental results, the results were acceptable when the yield was between 80 and 120% (Poulton and Canfield, 2005; Larner et al., 2006; Claff et al., 2010).

4 Results

4.1 Particle size distribution

The average size of site W07 particles was measured to be 16.75–181.63 μm, with a wide range of particle size distribution. The silt was the dominant particle size overall, with an average between 48.67% and 86.93%, while sand was the second component, with a content of 2.75%–47.63%. The particle size distribution of site W09 was in the range of 14.27–28.85 μm, with a narrow range distribution. The first component was dominated by silt, with content of 83.90–90.00%, while the second component was dominated by clay, with content of 7.95–13.73%.

Overall, the sediment particles at site W07 were coarser than at W09, and the range of particle size distribution with depth changed more widely (Figures 2A,B). The surface sediments at site W07 were the most special among all layers, with the highest sand content (47.63%), maximum particle size (181.63 μm), widest particle size distribution, and highly non-uniformity (Figure 2A). Below the surface, sediments were dominated by silt, and the clay particle content increased and remained at about 10–13%. The phenomenon of coarse particles appeared again at 70.95 mbsf, different from the surface sediments, the particle size was more uniform. The particle size of the sediments at site W09 was relatively uniform, and the deep layers were better than

TABLE 2 Sequential extraction processes for studying the speciation of Fe in sediments.

Step	Extraction	Fe species	Fraction
1	1 mol L^{-1} Na-acetate brought to pH 4.5 with acetic acid for 24 h	Siderite ($FeCO_3$) and ankerite ($Ca(Mg, Fe) (CO_3)_2$)	Carbonate-associated
2	1 mol L^{-1} hydroxylamine-HCl for 48 h	Serrihydrite ($Fe_5HO_8 \cdot 4H_2O$) and lepidocrocite (γ-FeOOH)	Easily reducible (amorphous) oxides
3	Na-dithionite buffer brought to pH 4.8 with 0.30 mol L^{-1} acetic acid and 0.2 mol L^{-1} sodium citrate for 2 h	Goethite (α-FeOOH), hematite (α-Fe_2O_3), and akageneite (β-FeOOH)	Reducible (crystalline) oxides
4	0.2 mol L^{-1} ammonium oxalate and 0.17 mol L^{-1} oxalic acid solution for 6 h	Magnetite (Fe_3O_4)	Recalcitrant oxides
5	HNO_3, HCl, HF, and $HClO_4$	Mainly silicates	Residual

Summed by Poulton and Canfield (2005); Yang et al. (2018).

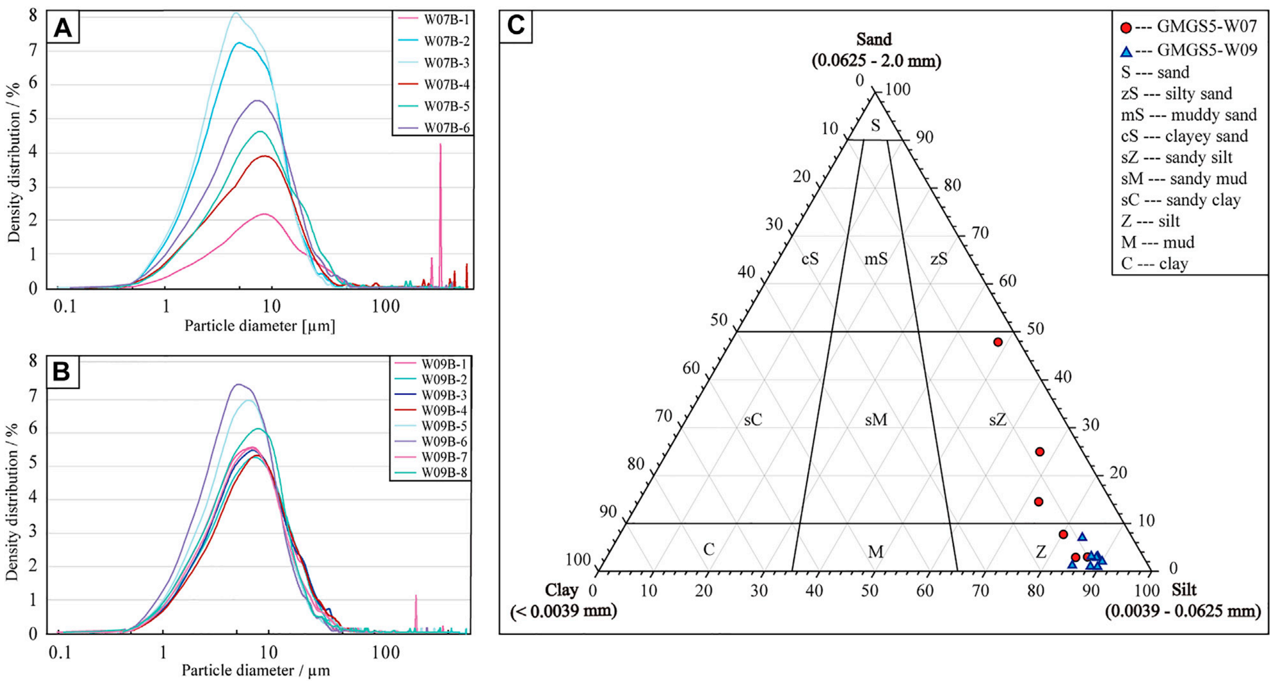

FIGURE 2
Sediment particle size analysis results of site W07 and W09. **(A,B)** show the particle size distribution, density distribution based on volume, and particle diameter calculated by the particle projection. **(C)** shows the textural classification of the samples based on Folk et al. (1970).

that of the shallow (Figure 2B). The silt content of site W09 was higher than 80%, and the sand content was always lower than that of silt and higher than that of clay at all sampling layers, but the sand content was significantly lower than that at site W07.

For ease of interpretation, the particle size of the sediments is generally separated into three fractions (Udden, 1914; He et al., 2009): clay (<4 μm), silt (4–63 μm), and sand (>63 μm), representing fine sediments, medium-sized sediments, and coarse sediments, respectively. Here, the sediment particle size triangle map projection was obtained using the method of Folk (Folk et al., 1970). As shown in Figure 2C, the particle size of site W07 was concentrated in silt and sandy silt, and the cast points were relatively dispersed and roughly distributed in a linear shape. While sediment samples from site W09 had finer particles, all of which were silt, with concentrated cast points and better sorting.

4.2 Total organic carbon content

Sediment total organic carbon (TOC) contents of site W07 varied between 0.54% and 0.74%, with an average of 0.60%. The surface sediments on the seafloor had the highest TOC content

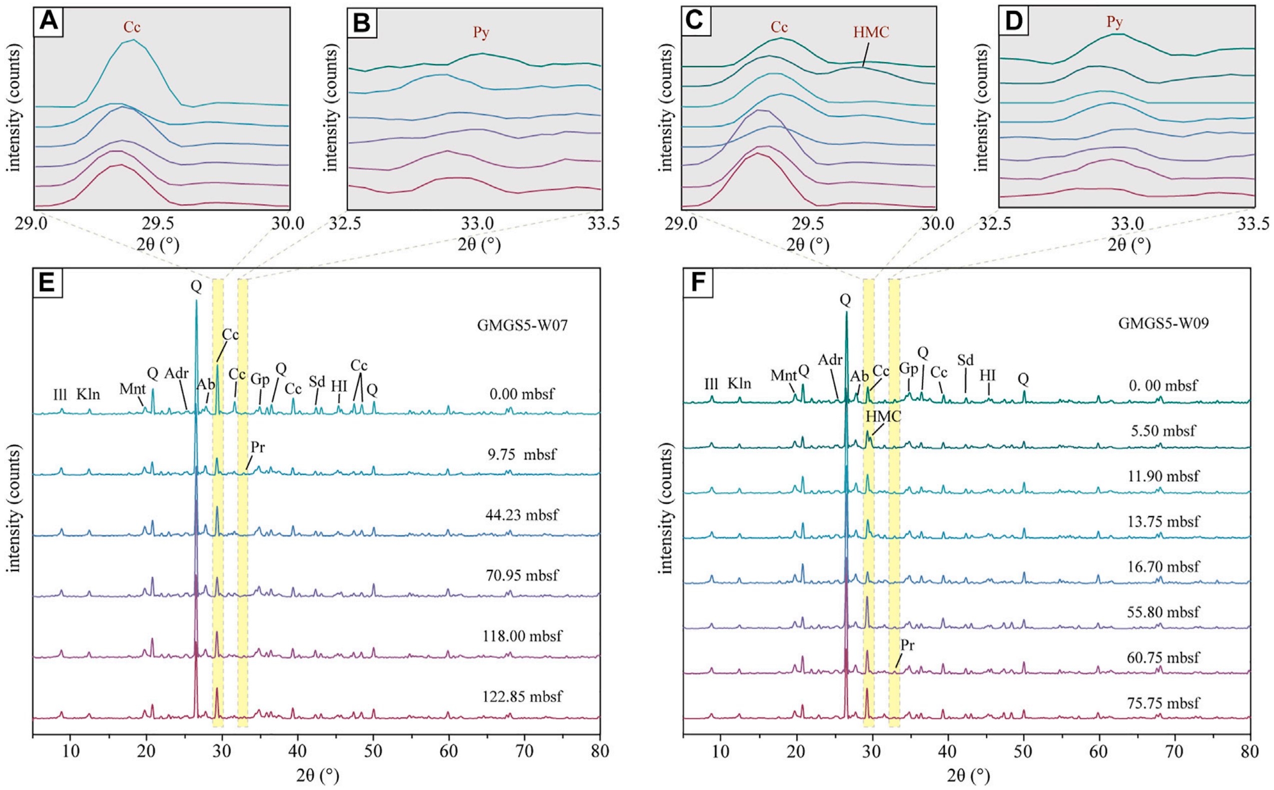

FIGURE 3
X-ray diffraction results at site W07 **(E)** and W09 **(F)**. **(A,C)** and **(B,D)** were zoomed by 29.0°<2θ < 30.0° and 22.5°<2θ < 33.5°, respectively. Ill: Illite; Kln: Kaolinite; Mnt: Montmorillonite; Q: Quartz; Ab: Albite; Cc: Calcite; Sd: siderite; HMC: high-Mg calcite; Adr: Anhydrite; Gp: Gypsum; and Hl: Halite.

of 0.74%, while the TOC contents of the remaining layers were less than 0.60%. Sediment TOC contents of site W09 varied between 0.50% and 0.58%, with an average of 0.54%. The peak of TOC appeared at 5.50 mbsf and 75.75 mbsf, respectively. On the whole, TOC contents of the sediments at the two sites were similar and varied little with depth.

4.3 Mineral composition and microscopic characteristics

The XRD patterns were quite similar at the two sites (Figure 3). There was a special assemblage of minerals at the two sites, which was characterized by clay minerals (illite and kaolinite), clastic rock minerals (quartz and albite), carbonate minerals (calcite and siderite), sulfate minerals (gypsum and anhydrite), and pyrite (Figures 3E,F). The characteristic peaks of quartz and calcite were strong in all layers, representing the main mineral phase in the sediments. The difference was that the clastic minerals of site W07 were higher, while site W09 had more clay minerals. To facilitate any comparisons in characteristic mineral content, we chose calcite as a representative of carbonate and pyrite as a representative of sulfide, and the characteristic peaks of calcite (2θ = 29.30° ± 0.10°) and pyrite (2θ = 33.00° ± 0.10°) were zoomed in Figure 3. Zoomed-up insets showed the difference, and there was a clear peak of calcite in surface sediments and not varied significantly with depth at site W07, but the signal suddenly increased below 58.00 mbsf at site W09 (Figures 3A,C). Especially, an obvious characteristic peak can be observed at 2θ of 29.72° in the layer of 5.50 mbsf at site W09, which was identified as high-Mg calcite (Figure 3C). Looking back to pyrite, it seems to be more obvious in the surface layer than the deep, more obvious in site W09 than W07, with even no obvious characteristic peaks appearing in individual layers of site W07 (Figures 3B,D).

Under the scanning electron microscope, mineral crystals such as faces, corners, and edges were well-preserved (Figure 4), representing that those minerals were precipitated spontaneously and had not experienced transportation and abrasion. Among the observed authigenic carbonate minerals, calcite showed a relatively high content with mostly granulate, and aragonite had a needle-like shape (Figure 4). Moreover, some microalgae shells were also observed under the FESEM, like coccolithophores (Figure 4).

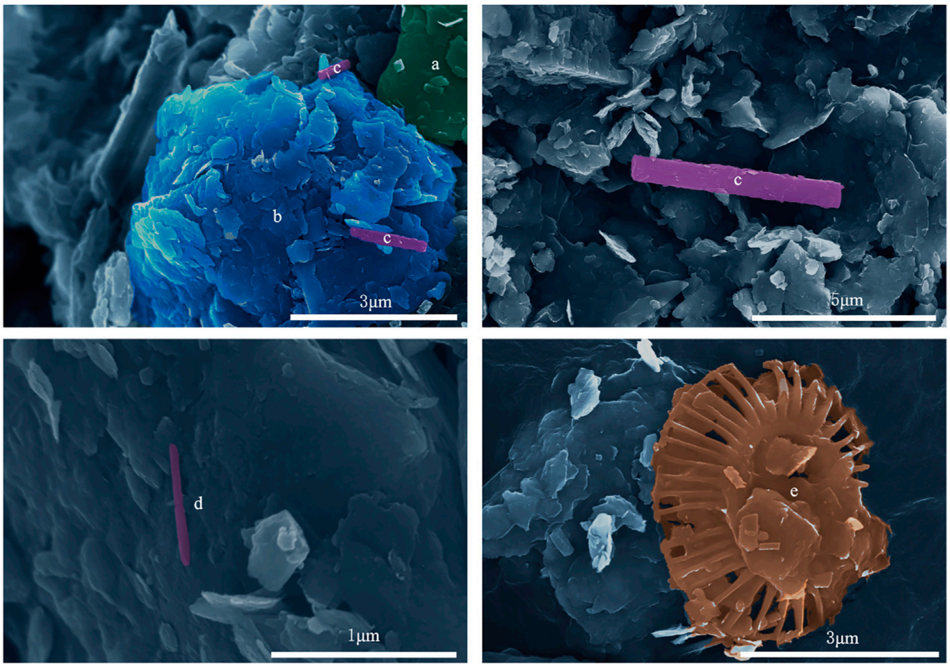

FIGURE 4
Typical samples under FESEM. **(A)** granular calcite; **(B)** flaky clay mineral; **(C)** columnar aragonite; **(D)** acicular aragonite; and **(E)** shell of coccolithophore.

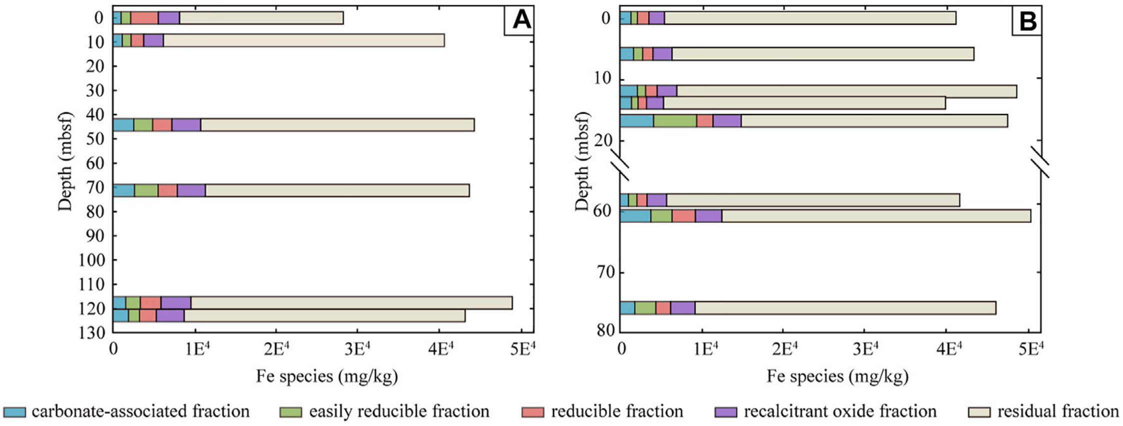

FIGURE 5
Mass accumulation of Fe species in sediments of site W07 **(A)** and W09 **(B)**.

4.4 Iron content and its chemical species

Through step-by-step extraction, the total amount of Fe (Fe_T) in the samples of the two sites and the proportions of Fe species were obtained. After calculating the recovery rate (the ratio of Fe_T proportions of different Fe species to the Fe_T), the results were all between 80 and 120%, which were judged to be the valid data (Poulton and Canfield, 2005; Larner et al., 2006; Claff et al., 2010).

4.4.1 Total iron content

Fe_T of the sediment samples at site W07 varied between 2.8 and 4.1 wt%, with the surface content being the lowest and showing an increasing trend with depth. There was a peak at 44.23 mbsf, and then the second peak appears at 118.00 mbsf (Figure 5). The Fe_T of sediment samples from site W09 varied more complicatedly with depth, fluctuating between 3.8 and 4.5 wt%, with a relatively higher content occurring in 5.50, 16.70, and 60.75 mbsf (Figure 5). Overall, the Fe_T at site W09 was characterized by a high overall content and concentrated distribution compared to site W07.

4.4.2 Chemical species of iron

As can be seen from Figure 5, the concentrations of different forms of iron at site W07 were 1,009–2,651 mg/kg (equivalent to 3.1%–7.2% of total iron content) in the carbonate-associated fraction (siderite and ankerite), 1,085–2,870 mg/kg (3.0%–7.8%) in the easily reducible fraction (amorphous oxides: ferrihydrite and lepidocrocite), 1,553–3,353 mg/kg (4.3%–12.2%) in the reducible fraction (crystalline oxides: goethite, hematite, and akageneite), 2,378–3,649 mg/kg (6.6%–9.5%) in the recalcitrant oxide fraction (magnetite), and 19,970–39,206 mg/kg (72.6%–94.6%) in the residual fraction (mainly silicates).

The concentrations of different forms of iron at site W09 were 1,046–4,123 mg/kg (2.7%–9.2%) in the carbonate-associated fraction (siderite and ankerite), 798–5,284 mg/kg (2.0%–11.8%) in the easily reducible fraction (amorphous oxides: ferrihydrite and lepidocrocite), 1,044–2,871 mg/kg (2.8%–6.6%) in the reducible fraction (crystalline oxides: goethite, hematite, and akageneite), 1,902–3,482 mg/kg (4%–7.8%) in the recalcitrant oxide fraction (magnetite), and 32,658–41,684 mg/kg (72.9%–99.0%) in the residual fraction (mainly silicates).

Among the deposit forms of iron in the sediments at the two sites, there was no obvious advantage in the proportion of iron in different forms (except residual fraction). Specifically, the proportions of reducible fraction and recalcitrant oxide at site W07 were higher, while iron in site W09 was dominated by a carbonate-associated fraction and easily reducible fraction (Figure 5).

5 Discussion

5.1 Geochemical conditions for gas hydrate accumulation

5.1.1 Reservoir sediment matrix

Sediment particle size is a vital controlling factor for gas hydrates to store in reservoirs. It is undeniable that particle size generally decreases with the pore size, and the sediment permeability decreases with decreasing pore size (Vargas-Cordero et al., 2020). Consequently, the enrichment of gas hydrates in previous studies often showed the relationship corresponding to the layers with coarse-grained sediments and high sand content (Lu et al., 2011; Jinhua et al., 2018).

Different from the previous understanding, the results in this article show that gas hydrates are stored in fine-grained sediments, mainly silts, at site W07 and W09 (Figure 2C), indicating that the deposition environment is low-energy and relatively stable. The phenomenon of high-content gas hydrate exists in primarily fine-grained sediments also present in the SCS, specifically, sand content of the sediment hydrate accumulated in SSA is less than 10%, while the hydrate saturation is as high as 10–45% (Wang et al., 2010). In addition, recent studies have pointed out that agglomerates consisting of clay and silt particle may increase the apparent particle size and pore throat size of the sediments, preventing the relative permeability drop, and ultimately promoting gas hydrate growth in silt-rich sediments (Vargas-Cordero et al., 2020). The fine-grained particle restricts the pore spaces for gas hydrate growth, and at the same time, under the connection of structural fractures, massive gas hydrates with a vein-like or the disseminated structure have been formed in the boreholes in the study area (Liang et al., 2019). In addition, relatively coarse-grained particles are contained in the sediments at site W07 (Figures 2A,C), which may be the result of gas escape.

It is noteworthy that many coccolithophore shells can be observed under FESEM in the sediments (Figure 4) of the study sites. Layers with gas hydrate exhibit a positive feedback relationship with foraminifera and coccolithophore shells are common in SCS, such as the GMGS3 drilling area (Zhang et al., 2017) and site SH7B in SSA (Chen et al., 2013). In our study area, the appearance of coccolithophore shells increases the content of coarse-grained particles and the porosity of the sediments, which will provide more space for the formation and occurrence of gas hydrates.

5.1.2 Mineral compositions of reservoir sediments

The main mineral composition is expectedly similar in two different settings, and the change of mineral facies is not obvious with depth (Figures 3E,F). Influenced by gas hydrate environment, these minerals are largely authigenic with intact crystal forms (Figure 4).

As the direct product of AOM, authigenic carbonates deposit since a high concentration of HCO_3^- (Moore et al., 2004; Feng and Chen, 2015). Gas hydrate concentration at site W09 continued to increase with depth (Figure 1C), alkalinity driven by strong AOM promoted the process of combining Ca^{2+} and CO_3^{2-} to generate authigenic carbonate. Consequently, the content of calcite increased in the bottom layers (Figure 3C). Site W07 has a low and stable gas hydrate concentration, so it does not cause a significant variation of carbonate content in depth (Figure 3A). Yet, there is no obvious reason for a strong calcite signal in surface sediments at site W07, so it is speculated that calcite may not be self-generating. Otherwise, needle-like aragonites are often found in gas hydrate environments (Tong et al., 2013), which provides vital evidence for microbial activities associated with gas hydrates in the study area.

Pyrite is produced by combining with hydrogen sulfide generated in the geochemical process of gas hydrates environment (Schulz and Zabel, 2006). Compared with siderite, pyrite is a product of sulfate reduction, and consequently, related to a more reducing and acidic environment to some extent (Yang et al., 2018). The XRD analysis shows that the response of pyrite in all sediment samples is very weak, but the emergence of more pyrite under XRD in site W09 may correspond to its richer gas hydrate and more reducing sedimentary environment (Figures 3B,D). Apart from that, the presence of sulfate minerals, such as gypsum, in the study area indicates depositional environments with high sulfate contents.

5.1.3 Redox conditions of reservoir sediments

Natural gas hydrates that exist under seafloor are most commonly formed from microbial methane, so methanogenesis from sedimentary organic carbon plays a critical role in gas hydrate formation (Kvenvolden, 1993; Kvenvolden, 1995). Studies have shown that gas is generated if the average sediment organic carbon content is greater than 0.5% (Waseda, 1998), and probably 75% of the gas hydrates accumulate within the area with sediments containing >0.5% TOC content (Harvey and Huang, 1995). In contrast, sediments at site W07 have higher TOC contents (TOC_{W07} = 0.60%, TOC_{W09} = 0.54%), suggesting better gas production capacity and may lead to more free gas in sediments.

5.2 Geochemical behaviors of elements

5.2.1 Migration and transformation of iron

Dissolution, precipitation, and transformation of Fe-minerals are dynamic in response to alternating redox conditions in marine sediments, which is one of the key active elements in the ocean (Froelich et al., 1979; Klinkhammer et al., 1982; Nevin and Lovley, 2002; Lyons and Severmann, 2006). Dynamic changes in methane fluid and multistage gas hydrate evolution change the geochemistry conditions, thereby causing the migration and transformation of Fe in the study area. Sequential extraction experiments show important differences in Fe_T and different forms of Fe-minerals among the methane-rich layer and its adjacent layer, indicating that significant Fe migration and transformation have occurred (Figure 6).

For better explanation, here, we think that Fe (II)-containing minerals are concentrated in the first step extracts, and Fe in other extractions is defined as Fe (III)-containing minerals. It is noteworthy that an obvious increase in Fe (II)-containing minerals have occurred in 11.90, 16.70, and 60.75 mbsf at site W09, where enormous gas hydrates (nodular, vein-like, and fracture-filling hydrate) or hydrate dismission appeared (Figure 6). In addition, in site W07, the phenomenon of the Fe (II)-containing minerals increased at 44.23 and 70.95 mbsf, where vein-like hydrate and enormous hydrate occurred (Figure 6). Interestingly, enrichment of Fe occurred in these methane-rich layers, which is similar to the proportion of Fe (II). In sum, the abovementioned results can be summarized as two important phenomena: 1) The Fe_T in methane-rich layers increased, conversely, decreased in the adjacent layers; 2) Suddenly an increase of Fe(II)-containing minerals appeared in methane-rich layers. The explanation of these two phenomena can be divided into two parts: dissolution and precipitation during Fe migration, which is discussed, respectively, in the following two paragraphs.

The residual fraction (mainly silicates) did not seem to be the main source of dissolved Fe, although it occupies the main ingredient of Fe in all sediment samples. There is a phenomenon that the Fe_T of the methane-rich layer is higher, but the residual fraction content is lower than that of the adjacent layers, such as 16.70 mbsf at site W09. In addition, the dissolved amount is not enough to provide so much Fe to participate in migration, like 60.75 mbsf at site W09. In this way, the remaining species should be the main contributor to migration, and while the dissolved components may not be specific, but all does contribute.

The concentrated precipitation of Fe-minerals in the gas hydrate-bearing environment is related to the oxidation of methane that promotes environmental reducibility. The presence of methane, carbon dioxide, and hydrogen sulfide are characteristics of the gas hydrate-bearing environment, especially when seepage have occurred (Dando et al., 1999; Pape et al., 2008). Geochemical conditions near the methane-rich layers are biased toward reducing along with the process of AOM, causing the Fe-minerals to dissolve into the pore water and gradually migrate to the methane-rich layer (e.g., Hensen et al., 2003; März et al., 2008; Yang et al., 2018). In the methane-rich layer, Fe^{3+} is reduced and the surrounding Fe^{2+} (original and reduced from Fe^{3+}) is "attracted" and "captured" at the same time (Figure 6). Ultimately, the migration and transformation process will be initiated with these aggregated Fe ions precipitating in the form of minerals. Although Fe (III)-containing minerals are more stable, the reducibility of the environment and the increase of Fe^{2+} promote the increase of Fe(II)-containing minerals precipitation. Therefore, the increase of Fe(II)-containing minerals, rather than Fe (III)-containing minerals, are more evident in all deposited Fe-minerals.

5.2.2 Enrichment of redox-sensitive trace elements

The proportion of trace elements in marine sediments may be affected by various factors, and untreated content-change of trace elements would obscure important geological information (Tribovillard et al., 2006). Compared with other elements, Al in sediments has stable and conservative physical and chemical properties, which is always used as a normalization element (Brumsack, 1989; Morford and Emerson, 1999). Usually, after Al

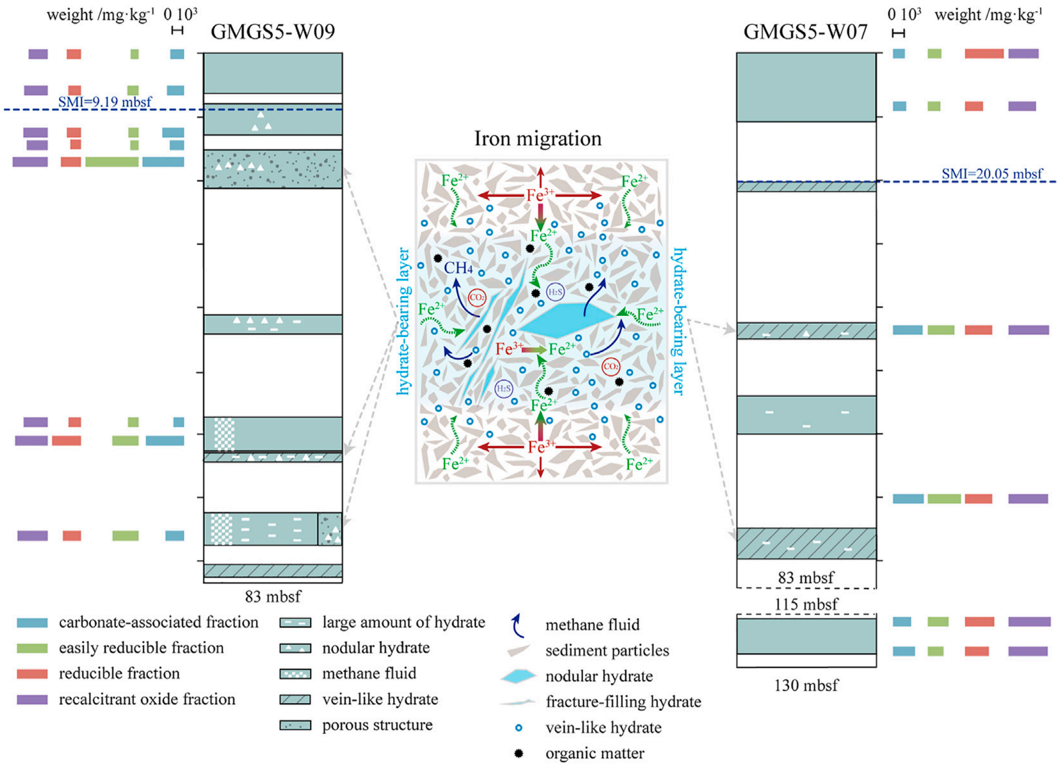

FIGURE 6
Gas hydrate accumulation at site W09 and W07 under X-CT image and drilling results (after Liang et al., 2019; Wei et al., 2019; Wei et al., 2021), different species of Fe from sequential extraction experiments results, and migration mechanism of Fe.

standardization, the influence of terrestrial inputs and biogenic diluents (calcium carbonate and opal) in marine sediments could be eliminated. Moreover, to better interpret the standardization results, it is customary to use enrichment factors (EF): $EF_{element}$ $X = X/Al_{sample}/X/Al_{average}$ (Tribovillard et al., 2006). Element X is enriched relative to the average upper curst when $EF_X > 1$, and it is depleted when $EF_X < 1$. If $EF_X > 10$, it represents very rich X (Tribovillard et al., 2006; Algeo and Tribovillard, 2009). The Earth's upper crust compositions (McLennan, 2001) were used to calculate $X/Al_{average}$ in this article, and the enrichment factor analysis of the elements in the sediment samples of site W07 and W09 were presented in Table 3.

To correlate intercorrelations between trace elements and TOC, Pearson correlation analysis was performed. Correlation coefficients with absolute values greater than 0.6 were considered strongly correlated, which were highlighted in bold fonts in Table 4 and Table 5.

The results demonstrate that EFs of Co, Ni, Cu, Zn, Fe, Mn, and Ba are slightly higher than the Earth's upper crust, which suggests null to minor enrichment (Figure 7). In previous studies, no obvious enrichment of these trace elements in gas hydrate-bearing sediments of SCS were also found (Deng et al., 2017; Lin et al., 2022). Redox-sensitive elements like Co, Ni, Cu, and Zn are sensitive to hypoxic environment and organic matter (Morford and Emerson, 1999; Tribovillard et al., 2006), and these elements show that the degree of enrichment slightly increases in methane-rich layers of the two sites (Figure 7). The results of Pearson correlation analysis show that Co, Ni, Cu, and Zn are not proportional to TOC, but have a strong and significant correlation with Fe and Mn (Table 4, 5). This result illustrates that Fe- and Mn-dependent oxidation (of methane) may dominate the enrichment of trace elements in these two sites. Ba_{EF} in marine sediments can be used as an effective indicator for marine paleoproductivity (Dymond et al., 1992). Since the positive correlation between Ba and TOC content is not very strong (Table 4, 5), it is still possible that a part of Ba is carried by the upwelling of methane fluxes from gas hydrate decomposition. The relationship between Fe, Mn, and TOC contents shows a weak–moderate negative correlation (Table 4, 5), which means that organic matter is not a source of Fe and Mn. The difference is that the correlations of Fe and Mn with Ba of the two sites are diametrically opposite. Therefore, the positive correlations of Fe and Mn with Ba at site W07 is the result of the influence of methane seepage to a large extent. Conversely, the negative correlations of Fe and Mn with Ba at site W09 suggests that elements are likely to be from other sources, such as the direct precipitation of seawater.

TABLE 3 Enrichment factors for trace elements and TOC% of sediments.

Samples	Mo_{EF}	V_{EF}	Co_{EF}	Ni_{EF}	Cu_{EF}	Zn_{EF}	Cr_{EF}	As_{EF}	Sb_{EF}	Fe_{EF}	Mn_{EF}	Ba_{EF}	TOC %
W07B-1	6.22	0.94	1.17	1.39	1.38	2.42	1.47	67.20	233.08	0.93	4.76	1.62	0.74
W07B-2	3.78	0.86	0.92	0.81	0.75	1.52	1.23	53.79	178.83	0.89	0.99	0.76	0.58
W07B-3	2.02	1.07	1.20	1.12	1.21	1.93	1.51	51.60	127.55	1.10	1.28	0.94	0.6
W07B-4	4.36	0.75	0.87	0.68	1.13	1.36	1.07	56.45	199.64	0.73	0.95	0.67	0.58
W07B-5	5.02	1.10	1.16	1.23	1.04	2.23	1.41	56.84	190.16	1.07	1.19	0.72	0.54
W07B-6	2.48	1.17	1.15	1.07	1.40	2.22	1.47	61.73	195.43	1.09	1.11	0.81	0.58
W09B-1	3.70	1.26	1.44	1.27	1.15	2.22	1.84	60.26	149.73	1.32	1.39	0.89	0.55
W09B-2	19.51	1.23	1.39	1.33	1.36	2.10	1.61	60.58	130.91	1.29	1.42	0.98	0.52
W09B-3	1.11	1.26	1.50	1.28	1.24	2.23	1.70	61.53	121.58	1.35	1.53	0.93	0.57
W09B-4	1.69	1.02	1.16	1.01	0.95	1.91	1.47	57.77	121.62	1.09	1.17	0.80	0.54
W09B-5	0.38	1.37	1.62	1.33	1.31	2.35	1.89	58.92	101.32	1.51	1.90	1.01	0.52
W09B-6	3.01	1.72	1.86	1.74	1.90	2.81	2.31	73.77	229.58	1.71	1.87	0.98	0.52
W09B-7	1.58	1.35	1.57	1.34	1.21	2.70	1.88	62.90	154.29	1.47	1.70	1.06	0.51
W09B-8	1.96	1.05	1.24	1.39	1.33	2.13	1.41	58.18	122.58	1.17	1.12	3.47	0.58

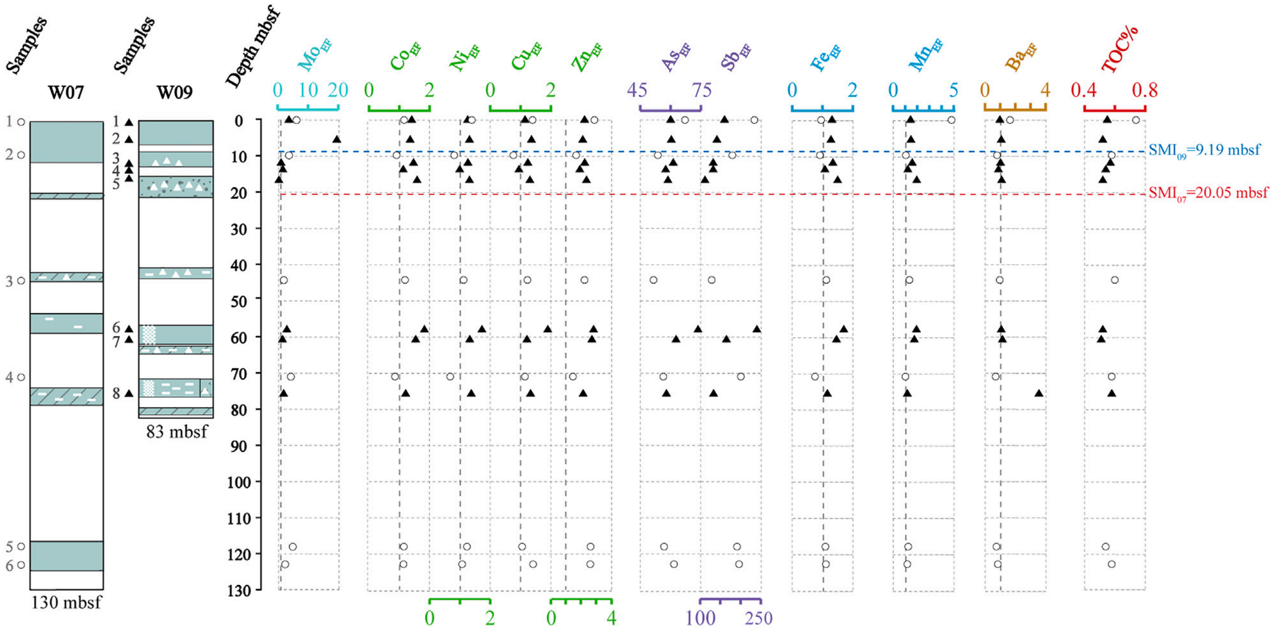

FIGURE 7

TOC% and enrichment factors of Mo (Mo_{EF}), Co (Co_{EF}), Ni (Ni_{EF}), Cu (Cu_{EF}), Zn (Zn_{EF}), As (As_{EF}), Sb (Sb_{EF}), Fe (Fe_{EF}), Mn (Mn_{EF}), and Ba (Ba_{EF}) in the sediment profile at site W07 and site W09. The enrichment factor (EF) was calculated as $X_{EF} = [(X/Al)_{sample}/(X/Al)_{average}]$, and the samples were normalized using Earth's upper crust compositions (McLennan, 2001).

Mo shows a minor to moderate enrichment in sediments (Figure 7). The anomalously enriched Mo in many studies is interpreted as H_2S generated by the AOM during the seepage, which accumulates on the top of the sediment profile, and even seeps out into the seawater (Hu et al., 2014; Chen et al., 2016; Li C. et al., 2016; Liu et al., 2020). Since Mo is easily migrated and enriched in the deposition environment containing hydrogen sulfide, which often occurs in environments with intense methane seepage and strong AOM near SMTZ (Peketi et al., 2012; Hu et al., 2015b; Deng et al., 2017), this may have interfered

TABLE 4 Results of Pearson correlation analysis of site GMGS5-W07.

	Mo_{EF}	**V_{EF}**	**Co_{EF}**	**Ni_{EF}**	**Cu_{EF}**	**Zn_{EF}**	**Cr_{EF}**	**As_{EF}**	**Sb_{EF}**	**Fe_{EF}**	**Mn_{EF}**	**Ba_{EF}**	**TOC %**
Mo_{EF}	1	−0.44	−0.46	−0.19	−0.53	−0.22	−0.58	0.09	**0.64**	−0.46	−0.44	**−0.88**	**−0.81**
V_{EF}		1	**0.95**	**0.91**	0.56	**0.97**	**0.95**	0.35	−0.24	**0.97**	**0.79**	0.56	−0.16
Co_{EF}			1	**0.95**	0.54	**0.91**	**0.97**	0.093	−0.47	**0.97**	**0.94**	**0.68**	−0.066
Ni_{EF}				1	0.34	**0.94**	**0.90**	0.096	−0.34	**0.94**	**0.89**	0.49	−0.36
Cu_{EF}					1	0.52	0.48	0.53	−0.031	0.41	0.41	0.34	0.23
Zn_{EF}						1	**0.87**	0.43	−0.064	**0.92**	**0.74**	0.37	−0.38
Cr_{EF}							1	0.06	−0.53	**0.99**	**0.90**	**0.77**	0.036
As_{EF}								1	**0.76**	0.11	−0.23	-0.39	−0.36
Sb_{EF}									1	−0.43	**−0.69**	**-0.89**	−0.58
Fe_{EF}										1	**0.87**	**0.68**	−0.11
Mn_{EF}											1	**0.75**	0.0078
Ba_{EF}												1	**0.62**
TOC %													1

Bold fonts represent strong correlation (the absolute value of Pearson coefficient is greater than 0.6).

TABLE 5 Results of Pearson correlation analysis of site GMGS5-W09.

	Mo_{EF}	**V_{EF}**	**Co_{EF}**	**Ni_{EF}**	**Cu_{EF}**	**Zn_{EF}**	**Cr_{EF}**	**As_{EF}**	**Sb_{EF}**	**Fe_{EF}**	**Mn_{EF}**	**Ba_{EF}**	**TOC %**
Mo_{EF}	1	−0.068	−0.14	0.034	0.12	−0.24	−0.17	−0.025	0.0041	−0.14	−0.17	−0.14	−0.28
V_{EF}		1	**0.98**	**0.83**	**0.84**	**0.89**	**0.99**	**0.90**	**0.78**	**0.98**	**0.88**	−0.39	−0.55
Co_{EF}			1	**0.79**	**0.78**	**0.90**	**0.98**	**0.82**	**0.67**	**1.00**	**0.93**	−0.38	−0.52
Ni_{EF}				1	**0.98**	**0.78**	**0.77**	**0.84**	**0.78**	**0.79**	0.56	0.14	−0.20
Cu_{EF}					1	**0.69**	**0.77**	**0.87**	**0.80**	**0.77**	0.54	0.0046	−0.22
Zn_{EF}						1	**0.9**	**0.81**	**0.75**	**0.92**	**0.79**	−0.20	−0.51
Cr_{EF}							1	**0.88**	**0.76**	**0.98**	**0.90**	−0.44	−0.59
As_{EF}								1	**0.96**	**0.81**	**0.60**	−0.27	−0.37
Sb_{EF}									1	**0.67**	0.41	−0.16	−0.36
Fe_{EF}										1	**0.94**	−0.37	−0.56
Mn_{EF}											1	−0.53	**−0.65**
Ba_{EF}												1	**0.65**
TOC %													1

Bold fonts represent strong correlation (the absolute value of Pearson coefficient is greater than 0.6).

with the relationship between Mo and other trace elements in the study area (Table 4, 5). Recently, mild to extreme enrichment of Mo were recognized in gas hydrate- or seepage-impact anoxic sediments of the SCS (Chen et al., 2016; Deng et al., 2017; Lin et al., 2022). In our study, it can be seen that Mo_{EF} is only moderately enriched in sample W09B-2 (Mo_{EF} = 19.51), indicating the SMI below it (Figure 7). It is also understandable that the enrichment of Mo is not evident in deep sediments, where the AOM process is not as strong as near SMTZ. A convincing mechanism to explain the distribution of Mo, As, and Sb is the so-called particulate shuttle process, which illustrates that these elements will be scavenged by Fe- and Mn-oxyhydroxides in the water column (Tribovillard et al., 2006; Scott and Lyons, 2012; Tribovillard et al., 2013). Except derived from the seawater, seep fluid is a plausible additional source of Fe, Mo, As, and Sb (Nath et al., 2008; Cangemi et al., 2010). It seems that the particulate shuttle process is unfeasible because there is no favorable relationship between Mo_{EF} and Fe/Al (Figure 8), but additional input of seep fluids may play a critical role.

As and Sb are of special interest as they are extremely enriched in sediments (Figure 7). In fact, the phenomenon of anomalous enrichment of As and Sb in gas hydrate accumulation area is relatively recent, and the most likely reason may be affected by authigenic Fe fraction (Nath et al., 2008; Hu et al., 2014). The enrichment factor of As exceeds 60, while the content of Sb is even higher in our study, which is around 200-fold higher than the average value. Significant enrichments of As and Sb also appeared in the hydrocarbon seeps of the Niger Delta margin, but

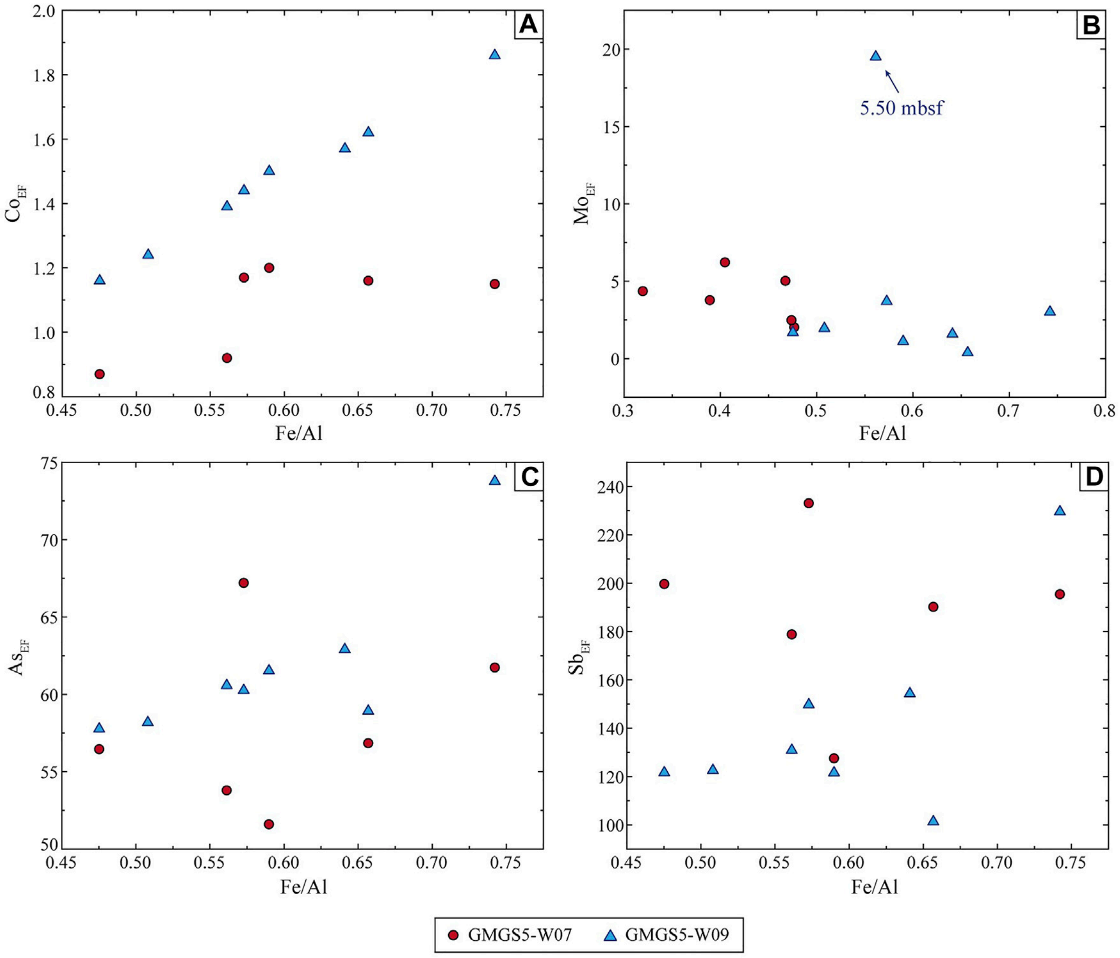

FIGURE 8
Trace elements patterns. **(A)** Co$_{EF}$ vs. Fe/Al, **(B)** Mo$_{EF}$ vs. Fe/Al, **(C)** As$_{EF}$ vs. Fe/Al, and **(D)** Sb$_{EF}$ vs. Fe/Al ratios for sediment samples. The enrichment factor (EF) was calculated as $X_{EF} = [(X/Al)_{sample}/(X/Al)_{average}]$, and the samples were normalized using Earth's upper crust compositions (McLennan, 2001).

moderate enrichments were more common in the seep areas of the SCS (Hu et al., 2014; Lin et al., 2022). As mentioned in chapter 5.2.1, Fe(III)–Fe(II) transition undergoes in the gas hydrate-bearing layers under hypoxic conditions. This process will release trace elements (e.g., As and Sb) and eventually lead to an increase in the EFs. In particular, positively and highly correlations between As, Sb, and Fe/Al are found in site W09 (Figure 8), confirming that the cycle of Fe-oxyhydroxides should be involved in the adsorption and release of As and Sb. Also, high contents of As and Sb in study sediments suggest the availability of abundant dissolved As and Sb during Fe-oxyhydroxides formation. However, the relationship between As, Sb, and Fe/Al in site W07 is not obvious (Figure 8), which is presumed to have received additional ascending fluids input.

5.2.3 Evidence of seepages from Sr/Ca and Mg/Ca

The formation of gas hydrates may lead to a higher concentration of Mg^{2+} in the surrounding pore water, thereby inhibiting the crystallization of calcite and promoting the formation of aragonite (Berner, 1975). As a result, the formation of aragonite and high-Mg calcite can reflect methane seepage to a certain extent. Aragonite is formed in the period of high seepage or high methane flux, while high-Mg calcite is formed in the period of methane diffusion with low or no seepage (Bayon et al., 2007). In addition, the ratios of Sr/Ca and Mg/Ca can be used to identify aragonite (Sr-rich) and high-Mg calcite (Mg-rich) in methane seepage sediments (Bayon et al., 2007; Yang et al., 2014; Chen et al., 2016).

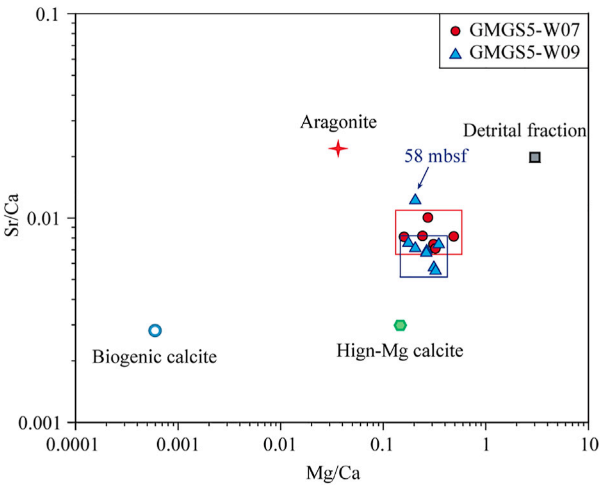

FIGURE 9
Sr/Ca ratios vs. Ma/Ca ratios of the sediment samples. The end-member ratios of aragonite, high-Mg calcite, biogenic calcite, and the detrital fraction from Yang et al. (2014) were used.

Figure 9 shows that the ratios of Sr/Ca and Mg/Ca in all sediments are more inclined to distribute along the direction of precipitation of the high-Mg calcite, suggesting that Sr/Ca and Mg/Ca in the sediments may mainly in the form of high-Mg calcite. Overall, it can be considered that methane seepage in site W07 and W09, at least at the shallow layers, are relatively weak (Figure 9). But it is worth noting that sediments at site W07 have higher Sr/Ca ratios, which may represent more active gas activity during the multistage gas hydrate evolution. Meanwhile, the characteristic peak of high-Mg calcite is only found in the sediments of site W09 (Figure 3C), which further confirms the seepage of site W09 is much weaker than site W07. But there is an exception in the layer of 58.00 mbsf at site W09, where seepage happened related to the present nearby high-concentration gas hydrates decomposition and lead to the Sr/Ca and Mg/Ca values of sediments being more inclined to aragonite (Figure 9).

6 Conclusion

In this study, the geochemical characteristics of sediments from sites GMGS5-W07 and GMGS5-W09 are investigated, and the following conclusions can be reached:

(1) Based on the physical and chemical characteristics of sediments, fine-grained sediments dominated by silt suggest a low-energy and relatively stable sedimentary environment, and the appearance of coccolithophore shells can provide more pore space for gas hydrate to form. TOC contents of sediments in both the sites are greater than 0.5%, suggesting sufficient gas availability for gas hydrate formation. Moreover, the appearances of authigenic carbonate minerals, sulfate minerals, and pyrite might be associated with the occurrence of gas hydrates in the sediments of the two sites.

(2) The reducing condition of gas hydrate-bearing sediments might be a significant factor of chemical species of Fe. The migration and chemical state transformation of Fe in sediments might be associated with gas hydrate occurrence. The methane-rich layer can convert Fe^{3+} to Fe^{2+} and capture authigenic iron carbonates in association with methane oxidation in an anoxic environment.

(3) Redox-sensitive elements in the sediments are mainly hosted by Fe- and Mn-oxyhydroxides, and the enrichment of Co, Ni, Cu, Zn, As, and Sb might be associated with the occurrence of massive gas hydrate. Mo, As, and Sb in the sediments of site W07 are likely to be additionally affected by deep methane fluids, while they are not observed at site W09. This finding suggests that geochemical behaviors of redox-sensitive elements are more affective to seep fluids than gas hydrate saturation in sediments.

Data availability statement

The raw data supporting the conclusion of this article will be made available by the authors, without undue reservation.

Author contributions

YL, HY, and HL conceived this study; YF and ZK supervised the investigation; YL and HY wrote the draft of the manuscript; and HL and YF revised the manuscript.

Funding

This study was funded by the Instrumental Analysis Fund of Peking University, the College Student Innovation Entrepreneurship Training Program of CUGB (Grant Number 201911415084), the Project of China Geological Survey (Grant Number DD20221705), and the Guangdong Major Project of Basic and Applied Basic Research (Grant Number 2020B0301030003).

Acknowledgments

The authors are grateful to all participants of GMGS5 and for equipment support from the School of Ocean Sciences (CUGB), the State Key Laboratory of Tribology (Tsinghua University), the Beijing International Centre for Gas Hydrate (Peking University), and the School of Earth and Space Sciences (Peking University) during the preparation of this article. Many thanks would go to Dr. Dong Feng, the editor for this special issue, and reviewers for helping in refining the manuscript.

Conflict of interest

The authors declare that the research was conducted in the absence of any commercial or financial relationships that could be construed as a potential conflict of interest.

Publisher's note

References

Algeo, T. J., and Tribovillard, N. (2009). Environmental Analysis of Paleoceanographic Systems Based on Molybdenum–Uranium Covariation. *Chem. Geol.* 268, 211–225. doi:10.1016/j.chemgeo.2009.09.001

Bayon, G., Pierre, C., Etoubleau, J., Voisset, M., Cauquil, E., Marsset, T., et al. (2007). Sr/Ca and Mg/Ca Ratios in Niger Delta Sediments: Implications for Authigenic Carbonate Genesis in Cold Seep Environments. *Mar. Geol.* 241, 93–109. doi:10.1016/j.margeo.2007.03.007

Berner, R. A. (1975). The Role of Magnesium in the Crystal Growth of Calcite and Aragonite from Sea Water. *Geochimica Cosmochimica Acta* 39, 489–504. doi:10.1016/0016-7037(75)90102-7

Boetius, A., Ravenschlag, K., Schubert, C. J., Rickert, D., Widdel, F., Gieseke, A., et al. (2000). A Marine Microbial Consortium Apparently Mediating Anaerobic Oxidation of Methane. *Nature* 407, 623–626. doi:10.1038/35036572

Boetius, A., and Wenzhöfer, F. (2013). Seafloor Oxygen Consumption Fuelled by Methane from Cold Seeps. *Nat. Geosci.* 6, 725–734. doi:10.1038/ngeo1926

Borowski, W. S., Paull, C. K., and Ussler, I. (1996). Marine Pore-Water Sulfate Profiles Indicate *In Situ* Methane Flux from Underlying Gas Hydrate. *Geol.* 24, 655–658. doi:10.1130/0091-7613(1996)024<0655:mpwspi>2.3.co;2

Boswell, R. (2007). Exploration Priorities for Marine Gas Hydrate Resources. *Fire Ice 2007 Spring/Summer*, 11–13.

Brumsack, H. (1989). Geochemistry of Recent TOC-Rich Sediments from the Gulf of California and the Black Sea. *Geol. Rundsch.* 78, 851–882. doi:10.1007/bf01829327

Cangemi, M., Di Leonardo, R., Bellanca, A., Cundy, A., Neri, R., and Angelone, M. (2010). Geochemistry and Mineralogy of Sediments and Authigenic Carbonates from the Malta Plateau, Strait of Sicily (Central Mediterranean): Relationships with Mud/fluid Release from a Mud Volcano System. *Chem. Geol.* 276, 294–308. doi:10.1016/j.chemgeo.2010.06.014

Chen, F., Hu, Y., Feng, D., Zhang, X., Cheng, S., Cao, J., et al. (2016). Evidence of Intense Methane Seepages from Molybdenum Enrichments in Gas Hydrate-Bearing Sediments of the Northern South China Sea. *Chem. Geol.* 443, 173–181. doi:10.1016/j.chemgeo.2016.09.029

Chen, F., Su, X., Lu, H. F., Zhou, Y., and Zhuang, C. (2013). Relations between Biogenic Component (Foraminifera) and Highly Saturated Gas Hydrates Distribution from Shenhu Area, Northern South China Sea. *Earth Science–Journal China Univ. Geosciences* 38, 907–915.

Claff, S. R. S. C., Sullivan, L. A., Burton, E. D., and Bush, R. T. (2010). A Sequential Extraction Procedure for Acid Sulfate Soils: Partitioning of Iron. *Geoderma* 155, 224–230. doi:10.1016/j.geoderma.2009.12.002

Collett, T. S., Bird, K. J., Kvenvolden, K. A., and Magoon, L. B. (1988). Geologic Interrelations Relative to Gas Hydrates within the North Slope of Alaska. *U. S. Geol. Surv. Open-File Rep.* 88, 150.

Cui, H., Su, X., Chen, F., Holland, M., Yang, S., Liang, J., et al. (2019). Microbial Diversity of Two Cold Seep Systems in Gas Hydrate-Bearing Sediments in the South China Sea. *Mar. Environ. Res.* 144, 230–239. doi:10.1016/j.marenvres.2019.01.009

Dando, P. R., Stüben, D., and Varnavas, S. P. (1999). Hydrothermalism in the Mediterranean Sea. *Prog. Oceanogr.* 44, 333–367. doi:10.1016/s0079-6611(99)00032-4

Deng, Y., Fang, Y., Zhang, X., Chen, F., Wang, H., Ren, J., et al. (2017). Trace Element Geochemistry of Sediments in Qiongdongnan Area, the South China Sea, and its Implications for Gas Hydrates. *Mar. Geol. Quat. Geol.* 37, 70–81.

Devol, A. H., and Ahmed, S. I. (1981). Are High Rates of Sulphate Reduction Associated with Anaerobic Oxidation of Methane? *Nature* 291, 407–408. doi:10.1038/291407a0

Dymond, J., Suess, E., and Lyle, M. (1992). Barium in Deep-Sea Sediment: A Geochemical Proxy for Paleoproductivity. *Paleoceanography* 7, 163–181. doi:10.1029/92pa00181

Egawa, K. K. E. I., Nishimura, O., Izumi, S., Fukami, E., Jin, Y., Kida, M., et al. (2015). Bulk Sediment Mineralogy of Gas Hydrate Reservoir at the East Nankai Offshore Production Test Site. *Mar. Pet. Geol.* 66, 379–387. doi:10.1016/j.marpetgeo.2015.02.039

Fang, Y., Wei, J., Lu, H., Liang, J., Lu, J., Fu, J., et al. (2019). Chemical and Structural Characteristics of Gas Hydrates from the Haima Cold Seeps in the Qiongdongnan Basin of the South China Sea. *J. Asian Earth Sci.* 182, 103924. doi:10.1016/j.jseaes.2019.103924

Feng, D., and Chen, D. (2015). Authigenic Carbonates from an Active Cold Seep of the Northern South China Sea: New Insights into Fluid Sources and Past Seepage Activity. *Deep Sea Res. Part II Top. Stud. Oceanogr.* 122, 74–83. doi:10.1016/j.dsr2.2015.02.003

Fischer, D., Mogollón, J. M., Strasser, M., Pape, T., Bohrmann, G., Fekete, N., et al. (2013). Subduction Zone Earthquake as Potential Trigger of Submarine Hydrocarbon Seepage. *Nat. Geosci.* 6, 647–651. doi:10.1038/ngeo1886

Folk, R. L., Andrews, P. B., and Lewis, D. W. (1970). Detrital Sedimentary Rock Classification and Nomenclature for Use in New Zealand. *N. Z. J. Geol. Geophys.* 13, 937–968. doi:10.1080/00288306.1970.10418211

Froelich, P. N., Klinkhammer, G. P., Bender, M. L., Luedtke, N. A., Heath, G. R., Cullen, D., et al. (1979). Early Oxidation of Organic Matter in Pelagic Sediments of the Eastern Equatorial Atlantic: Suboxic Diagenesis. *Geochimica Cosmochimica Acta* 43, 1075–1090. doi:10.1016/0016-7037(79)90095-4

Ginsburg, G., Soloviev, V., Matveeva, T., and Andreeva, I. (2000). 24. Sediment Grain-Size Control on Gas Hydrate Presence. *Sites* 994 (995), 997.Proc. of the Ocean Drilling Program, Scientific Results. 237-245.

Harvey, L. D., and Huang, Z. (1995). Evaluation of the Potential Impact of Methane Clathrate Destabilization on Future Global Warming. *J. Geophys. Res.* 100, 2905–2926. doi:10.1029/94jd02829

He, H., Chen, H., Yao, Q., Qin, Y., Mi, T., and Yu, Z. (2009). Behavior of Different Phosphorus Species in Suspended Particulate Matter in the Changjiang Estuary. *Chin. J. Ocean. Limnol.* 27, 859–868. doi:10.1007/s00343-009-9021-6

Hedrich, S., Schlömann, M., and Johnson, D. B. (2011). The Iron-Oxidizing Proteobacteria. *Microbiology* 157, 1551–1564. doi:10.1099/mic.0.045344-0

Hensen, C., Zabel, M., Pfeifer, K., Schwenk, T., Kasten, S., Riedinger, N., et al. (2003). Control of Sulfate Pore-Water Profiles by Sedimentary Events and the Significance of Anaerobic Oxidation of Methane for the Burial of Sulfur in Marine Sediments. *Geochimica Cosmochimica Acta* 67, 2631–2647. doi:10.1016/s0016-7037(03)00199-6

Himmler, T., Haley, B. A., Torres, M. E., Klinkhammer, G. P., Bohrmann, G., Peckmann, J., et al. (2013). Rare Earth element geochemistry in cold-seep pore waters of Hydrate Ridge, northeast Pacific Ocean. *Geo-Marine Letters.* 33, 369–379. doi:10.1007/s00367-013-0334-2

Hu, Y., Feng, D., Chen, L., Zheng, G., Peckmann, J., and Chen, D. (2015a). Using Iron Speciation in Authigenic Carbonates from Hydrocarbon Seeps to Trace Variable Redox Conditions. *Mar. Petroleum Geol.* 67, 111–119. doi:10.1016/j.marpetgeo.2015.05.001

Hu, Y., Feng, D., Liang, Q., Xia, Z., Chen, L., and Chen, D. (2015b). Impact of Anaerobic Oxidation of Methane on the Geochemical Cycle of Redox-Sensitive Elements at Cold-Seep Sites of the Northern South China Sea. *Deep Sea Res. Part II Top. Stud. Oceanogr.* 122, 84–94. doi:10.1016/j.dsr2.2015.06.012

Hu, Y., Feng, D., Peckmann, J., Roberts, H. H., and Chen, D. (2014). New Insights into Cerium Anomalies and Mechanisms of Trace Metal Enrichment in Authigenic

Carbonate from Hydrocarbon Seeps. *Chem. Geol.* 381, 55–66. doi:10.1016/j.chemgeo.2014.05.014

Huang, B., Tian, H., Li, X., Wang, Z., and Xiao, X. (2016). Geochemistry, Origin and Accumulation of Natural Gases in the Deepwater Area of the Qiongdongnan Basin, South China Sea. *Mar. Petroleum Geol.* 72, 254–267. doi:10.1016/j.marpetgeo.2016.02.007

Jiang, S., Yang, T., Ge, L., Yang, J., Ling, H., Wu, N., et al. (2008). Geochemistry of Pore Waters from the Xisha Trough, Northern South China Sea and Their Implications for Gas Hydrates. *J. Oceanogr.* 64, 459–470. doi:10.1007/s10872-008-0039-8

Jinhua, Z., Nianqiao, F., Wei, W., Ming, S., Hongping, X., Yong, P., et al. (2018). Accumulation Conditions and Enrichment Controlling Factors of Natural Gas Hydrate Reservoirs. *China Pet. Explor.* 23, 35.

Joye, S. B., Boetius, A., Orcutt, B. N., Montoya, J. P., Schulz, H. N., Erickson, M. J., et al. (2004). The Anaerobic Oxidation of Methane and Sulfate Reduction in Sediments from Gulf of Mexico Cold Seeps. *Chem. Geol.* 205, 219–238. doi:10.1016/j.chemgeo.2003.12.019

Klinkhammer, G., Heggie, D. T., and Graham, D. W. (1982). Metal Diagenesis in Oxic Marine Sediments. *Earth Planet. Sci. Lett.* 61, 211–219. doi:10.1016/0012-821x(82)90054-1

Knittel, K., and Boetius, A. (2009). Anaerobic Oxidation of Methane: Progress with an Unknown Process. *Annu. Rev. Microbiol.* 63, 311–334. doi:10.1146/annurev.micro.61.080706.093130

Kraemer, L. M., Owen, R. M., and Dickens, G. R. (2000). Lithology of the Upper Gas Hydrate Zone, Blake Outer Ridge: A Link between Diatoms, Porosity, and Gas Hydrate, Proceedings of the Ocean Drilling Program. *Sci. Results Tex. A&M Univ.* 144, 229–236.

Kvenvolden, K. A. (1995). A Review of the Geochemistry of Methane in Natural Gas Hydrate. *Org. Geochem.* 23, 997–1008. doi:10.1016/0146-6380(96)00002-2

Kvenvolden, K. A. (1993). Gas Hydrates Geological Perspective and Global Change. *Rev. Geophys.* 31, 173–187. doi:10.1029/93rg00268

Lai, H., Fang, Y., Kuang, Z., Ren, J., Liang, J., Lu, J., et al. (2021). Geochemistry, Origin and Accumulation of Natural Gas Hydrates in the Qiongdongnan Basin, South China Sea: Implications from Site GMGS5-W08. *Mar. Petroleum Geol.* 123, 104774. doi:10.1016/j.marpetgeo.2020.104774

Larner, B. L., Seen, A. J., and Townsend, A. T. (2006). Comparative Study of Optimised BCR Sequential Extraction Scheme and Acid Leaching of Elements in the Certified Reference Material NIST 2711. *Anal. Chim. Acta* 556, 444–449. doi:10.1016/j.aca.2005.09.058

Lemaitre, N., Bayon, G., Ondréas, H., Caprais, J., Freslon, N., Bollinger, C., et al. (2014). Trace Element Behaviour at Cold Seeps and the Potential Export of Dissolved Iron to the Ocean. *Earth Planet. Sci. Lett.* 404, 376–388. doi:10.1016/j.epsl.2014.08.014

Li, C., Hu, G., Zhang, W., Ye, Y., Liu, C., Li, Q., et al. (2016). Influence of Foraminifera on Formation and Occurrence Characteristics of Natural Gas Hydrates in Fine-Grained Sediments from Shenhu Area, South China Sea. *Sci. China Earth Sci.* 59, 2223–2230. doi:10.1007/s11430-016-5005-3

Li, L., Lei, X., Zhang, X., and Sha, Z. (2013). Gas Hydrate and Associated Free Gas in the Dongsha Area of Northern South China Sea. *Mar. Petroleum Geol.* 39, 92–101. doi:10.1016/j.marpetgeo.2012.09.007

Li, N., Feng, D., Chen, L., Wang, H., and Chen, D. (2016). Using Sediment Geochemistry to Infer Temporal Variation of Methane Flux at a Cold Seep in the South China Sea. *Mar. Petroleum Geol.* 77, 835–845. doi:10.1016/j.marpetgeo.2016.07.026

Liang, J., Zhang, W., Lu, J. A., Wei, J., Kuang, Z., and He, Y. (2019). Geological Occurrence and Accumulation Mechanism of Natural Gas Hydrates in the Eastern Qiongdongnan Basin of the South China Sea: Insights from Site GMGS5-W9-2018. *Mar. Geol.* 418, 106042. doi:10.1016/j.margeo.2019.106042

Liang, Q., Hu, Y., Feng, D., Peckmann, J., Chen, L., Yang, S., et al. (2017). Authigenic Carbonates from Newly Discovered Active Cold Seeps on the Northwestern Slope of the South China Sea: Constraints on Fluid Sources, Formation Environments, and Seepage Dynamics. *Deep Sea Res. Part I Oceanogr. Res. Pap.* 124, 31–41. doi:10.1016/j.dsr.2017.04.015

Lin, Z., Sun, X., Chen, K., Strauss, H., Klemd, R., Smrzka, D., et al. (2022). Effects of sulfate reduction processes on the trace element geochemistry of sedimentary pyrite in modern seep environments. *Geochimica et Cosmochimica Acta.* 333, 75–94. doi:10.1016/j.gca.2022.06.026

Liu, S., Feng, X., Feng, Z., Xiao, X., and Feng, L. (2020). Geochemical Evidence of Methane Seepage in the Sediments of the Qiongdongnan Basin, South China Sea. *Chem. Geol.* 543, 119588. doi:10.1016/j.chemgeo.2020.119588

Liu, W., Shi, Y., Zhang., X., Zeng, N., Y, J., and He, H., 2014. Geotechnical Features of the Seabed Soils in the East of Xisha Trough and the Mechanical Properties of Gas Hydrate-Bearing Fine Deposits. *Mar. Geol. Quat. Geol.* 34, 39–47.

Lu, H., Kawasaki, T., Ukita, T., Moudrakovski, I., Fujii, T., Noguchi, S., et al. (2011). Particle Size Effect on the Saturation of Methane Hydrate in Sediments-Constrained from Experimental Results. *Mar. Petroleum Geol.* 28, 1801–1805. doi:10.1016/j.marpetgeo.2010.11.007

Luff, R., and Wallmann, K. (2003). Fluid Flow, Methane Fluxes, Carbonate Precipitation and Biogeochemical Turnover in Gas Hydrate-Bearing Sediments at Hydrate Ridge, Cascadia Margin: Numerical Modeling and Mass Balances. *Geochimica Cosmochimica Acta* 67, 3403–3421. doi:10.1016/s0016-7037(03)00127-3

Lyons, T. W., and Severmann, S. (2006). A Critical Look at Iron Paleoredox Proxies: New Insights from Modern Euxinic Marine Basins. *Geochimica Cosmochimica Acta* 70, 5698–5722. doi:10.1016/j.gca.2006.08.021

März, C., Hoffmann, J., Bleil, U., de Lange, G. J., and Kasten, S. (2008). Diagenetic Changes of Magnetic and Geochemical Signals by Anaerobic Methane Oxidation in Sediments of the Zambezi Deep-Sea Fan (SW Indian Ocean). *Mar. Geol.* 255, 118–130. doi:10.1016/j.margeo.2008.05.013

McLennan, S. M. (2001). Relationships between the Trace Element Composition of Sedimentary Rocks and Upper Continental Crust. *Geochem. Geophys. Geosyst.* doi:10.1029/2000gc000109

Moore, T. S., Murray, R. W., Kurtz, A. C., and Schrag, D. P. (2004). Anaerobic Methane Oxidation and the Formation of Dolomite. *Earth Planet. Sci. Lett.* 229, 141–154. doi:10.1016/j.epsl.2004.10.015

Morford, J. L., and Emerson, S. (1999). The Geochemistry of Redox Sensitive Trace Metals in Sediments. *Geochimica cosmochimica acta* 63, 1735–1750. doi:10.1016/s0016-7037(99)00126-x

Murray, J. W., Grundmanis, V., and Smethie, W. M., Jr (1978). Interstitial Water Chemistry in the Sediments of Saanich Inlet. *Geochimica Cosmochimica Acta* 42, 1011–1026. doi:10.1016/0016-7037(78)90290-9

Nath, B., Jean, J., Lee, M., Yang, H., and Liu, C. (2008). Geochemistry of High Arsenic Groundwater in Chia-Nan Plain, Southwestern Taiwan: Possible Sources and Reactive Transport of Arsenic. *J. Contam. Hydrology* 99, 85–96. doi:10.1016/j.jconhyd.2008.04.005

Nevin, K. P., and Lovley, D. R. (2002). Mechanisms for Fe (III) oxide reduction in sedimentary environments. *Geomicrobiol. J.* 19, 141–159. doi:10.1128/AEM.68.5.2294-2299.2002

Pape, T., Blumenberg, M., Seifert, R., Bohrmann, G., and Michaelis, W. (2008). Marine Methane Biogeochemistry of the Black Sea: a Review. *Links Between Geol. Process. Microb. Activities Evol. Life*, 281–311.

Peckmann, J., Reimer, A., Luth, U., Luth, C., Hansen, B. T., Heinicke, C., et al. (2001). Methane-derived Carbonates and Authigenic Pyrite from the Northwestern Black Sea. *Mar. Geol.* 177, 129–150. doi:10.1016/s0025-3227(01)00128-1

Peketi, A., Mazumdar, A., Joshi, R. K., Patil, D. J., Srinivas, P. L., and Dayal, A. M. (2012). Tracing the Paleo Sulfate-Methane Transition Zones and H_2S Seepage Events in Marine Sediments: An Application of C-S-Mo Systematics. *Geochem. Geophys. Geosystems* 13.

Poulton, S. W. S. P., and Canfield, D. E. D. B. (2005). Development of a Sequential Extraction Procedure for Iron: Implications for Iron Partitioning in Continentally Derived Particulates. *Chem. Geol.* 214, 209–221. doi:10.1016/j.chemgeo.2004.09.003

Raiswell, R., and Canfield, D. E. (2012). The Iron Biogeochemical Cycle Past and Present. *Geochem. Perspect.* 1, 1–220. doi:10.7185/geochempersp.1.1

Riedinger, N., Formolo, M. J., Lyons, T. W., Henkel, S., Beck, A., and Kasten, S. (2014). An Inorganic Geochemical Argument for Coupled Anaerobic Oxidation of Methane and Iron Reduction in Marine Sediments. *Geobiology* 12, 172–181. doi:10.1111/gbi.12077

Ritger, S., Carson, B., and Suess, E. (1987). Methane-derived Authigenic Carbonates Formed by Subduction-Induced Pore-Water Expulsion along the Oregon/Washington Margin. *Geol. Soc. Am. Bull.* 98, 147–156. doi:10.1130/0016-7606(1987)98<147:macfbs>2.0.co;2

Scholz, F., McManus, J., Mix, A. C., Hensen, C., and Schneider, R. R. (2014a). The Impact of Ocean Deoxygenation on Iron Release from Continental Margin Sediments. *Nat. Geosci.* 7, 433–437. doi:10.1038/ngeo2162

Scholz, F., Severmann, S., McManus, J., and Hensen, C. (2014b). Beyond the Black Sea Paradigm: The Sedimentary Fingerprint of an Open-Marine Iron Shuttle. *Geochimica Cosmochimica Acta* 127, 368–380. doi:10.1016/j.gca.2013.11.041

Schulz, H. D., and Zabel, M. (2006). *Marine Geochemistry*. Netherland: Springer.

Scott, C., and Lyons, T. W. (2012). Contrasting Molybdenum Cycling and Isotopic Properties in Euxinic versus Non-euxinic Sediments and Sedimentary Rocks: Refining the Paleoproxies. *Chem. Geol.* 324, 19–27. doi:10.1016/j.chemgeo.2012.05.012

Sha, Z., Liang, J., Zhang, G., Yang, S., Lu, J., Zhang, Z., et al. (2015). A Seepage Gas Hydrate System in Northern South China Sea: Seismic and Well Log Interpretations. *Mar. Geol.* 366, 69–78. doi:10.1016/j.margeo.2015.04.006

Shaohua, Q., Ming, S., Rui, Y., Zenggui, K., Jinqiang, L., and Nengyou, W. (2015). The Progress and Revelations of Marine Gas Hydrate Explorations: Reservoir Characteristics. *Adv. New Renew. Energy* 3, 357–366.

Smrzka, D., Feng, D., Himmler, T., Zwicker, J., Hu, Y., Monien, P., et al. (2020). Trace Elements in Methane-Seep Carbonates: Potentials, Limitations, and Perspectives. *Earth-Science Rev.* 208, 103263. doi:10.1016/j.earscirev.2020.103263

Su, L., Zheng, J., Chen, G., Zhang, G., Guo, J., and Xu, Y. (2012). The Upper Limit of Maturity of Natural Gas Generation and its Implication for the Yacheng Formation in the Qiongdongnan Basin, China. *J. Asian Earth Sci.* 54, 203–213. doi:10.1016/j.jseaes.2012.04.016

Sun, C., Wu, N., Niu, B., and Sun, Y. (2007). Geochemical Characteristics of Gaseous Hydrocarbons and Hydrate Resource Prediction in the Qiong-Dongnan Basin of the South China Sea. *Geoscience* 21, 95.

Tong, H., Feng, D., Cheng, H., Yang, S., Wang, H., Min, A. G., et al. (2013). Authigenic Carbonates from Seeps on the Northern Continental Slope of the South China Sea: New Insights into Fluid Sources and Geochronology. *Mar. petroleum Geol.* 43, 260–271. doi:10.1016/j.marpetgeo.2013.01.011

Torres, M. E., Brumsack, H. J., Bohrmann, G., and Emeis, K. C. (1996). Barite Fronts in Continental Margin Sediments: a New Look at Barium Remobilization in the Zone of Sulfate Reduction and Formation of Heavy Barites in Diagenetic Fronts. *Chem. Geol.* 127, 125–139. doi:10.1016/0009-2541(95)00090-9

Tribovillard, N., Algeo, T. J., Baudin, F., and Riboulleau, A. (2012). Analysis of Marine Environmental Conditions Based on Molybdenum-Uranium Covariation-Applications to Mesozoic Paleoceanography. *Chem. Geol.* 324-325, 46–58. doi:10.1016/j.chemgeo.2011.09.009

Tribovillard, N., Algeo, T. J., Lyons, T., and Riboulleau, A. (2006). Trace Metals as Paleoredox and Paleoproductivity Proxies: An Update. *Chem. Geol.* 232, 12–32. doi:10.1016/j.chemgeo.2006.02.012

Tribovillard, N., Du Châtelet, E. A., Gay, A., Barbecot, F., Sansjofre, P., and Potdevin, J. (2013). Geochemistry of Cold Seepage-Impacted Sediments: Per-Ascensum or Per-Descensum Trace Metal Enrichment? *Chem. Geol.* 340, 1–12. doi:10.1016/j.chemgeo.2012.12.012

Uchida, T., and Tsuji, T. (2004). Petrophysical Properties of Natural Gas Hydrates-Bearing Sands and Their Sedimentology in the Nankai Trough. *Resour. Geol.* 54, 79–87. doi:10.1111/j.1751-3928.2004.tb00189.x

Udden, J. A. (1914). Mechanical Composition of Clastic Sediments. *Geol. Soc. Am. Bull.* 25, 655–744. doi:10.1130/gsab-25-655

Vargas-Cordero, I., Tinivella, U., Villar-Muñoz, L., Bento, J. P., Cárcamo, C., López-Acevedo, D., et al. (2020). Gas Hydrate versus Seabed Morphology Offshore Lebu (Chilean Margin). *Sci. Rep.*, 21928. doi:10.1038/s41598-020-78958-z10

Wang, S., Wen, Y., and Song, H. (2006). Mapping the Thickness of the Gas Hydrate Stability Zone in the South China Sea. TAO: Terrestrial. *Atmos. Ocean. Sci.* 17, 815.

Wang, X. J., Wu, S. G., Wang, D. W., Ma, Y., Yao, G., and Gong, Y. (2010). The Role of Polygonal Faults in Fluid Migration and Gas Hydrate Reservoir Forming in Southeast Hainan Basin. Oil Geophys. *Prospect* 45, 122–128.

Wang, X., Li, N., Feng, D., Hu, Y., Bayon, G., and Liang, Q. (2018). Using chemical compositions of sediments to constrain methane seepage dynamics: A case study from Haima cold seeps of the South China Sea. *J. Asian Earth Sci.* 168, 137–144. doi:10.1016/j.jseaes.2018.11.011

Waseda, A. (1998). Organic Carbon Content, Bacterial Methanogenesis, and Accumulation Processes of Gas Hydrates in Marine Sediments. *Geochem. J.* 32, 143–157. doi:10.2343/geochemj.32.143

Wei, D., Jinqiang, L., Wei, Z., Zenggui, K., Tong, Z., and Yulin, H. (2021). Typical Characteristics of Fracture-Filling Hydrate-Charged Reservoirs Caused by Heterogeneous Fluid Flow in the Qiongdongnan Basin, Northern South China Sea. *Mar. Petroleum Geol.* 124, 104810. doi:10.1016/j.marpetgeo.2020.104810

Wei, J., Fang, Y., Lu, H., Lu, H., Lu, J., Liang, J., et al. (2018). Distribution and Characteristics of Natural Gas Hydrates in the Shenhu Sea Area, South China Sea. *Mar. Petroleum Geol.* 98, 622–628. doi:10.1016/j.marpetgeo.2018.07.028

Wei, J., Liang, J., Lu, J., Zhang, W., and He, Y. (2019). Characteristics and Dynamics of Gas Hydrate Systems in the Northwestern South China Sea - Results of the Fifth Gas Hydrate Drilling Expedition. *Mar. Petroleum Geol.* 110, 287–298. doi:10.1016/j.marpetgeo.2019.07.028

Wu, N., Yang, S., Zhang, H., Liang, J., Wang, H., Su, X., et al. (2008). "Preliminary Discussion on Gas Hydrate Reservoir System of Shenhu Area, North Slope of South China Sea," in Proceedings of the 6th International Conference on Gas Hydrates (ICGH 2008), Vancouver. British Columbia, Canada, July 6-10, 2008.

Wu, S., Zhang, G., Huang, Y., Liang, J., and Wong, H. K. (2005). Gas Hydrate Occurrence on the Continental Slope of the Northern South China Sea. *Mar. Petroleum Geol.* 22, 403–412. doi:10.1016/j.marpetgeo.2004.11.006

Xu, X. D., Zhang, Y. Z., Liang, G., Xiong, X., Xing, L., Guo, X., et al. (2016). Hydrocarbon Source Condition and Accumulation Mechanism of Natural Gas in Deepwater Area of Qiongdongnan Basin, Northern South China Sea. *Nat. Gas. Geosci.* 27, 1985–1992.

Yang, H., Lu, H., and Ruffine, L. (2018). Geochemical Characteristics of Iron in Sediments from the Sea of Marmara. *Deep Sea Res. Part II Top. Stud. Oceanogr.* 153, 121–130. doi:10.1016/j.dsr2.2018.01.010

Yang, K., Chu, F., and Zhu, J. (2014). Mg/Ca and Sr/Ca Ratios of Authigenic Carbonate Minerals and Calcareous Biogenic Shells in the Cold-Seep Acrbonates, North of the South China Sea and Their Environmental Implication. *Haiyang Xuebao (in Chin.* 36, 39–48.

Ye, J., Wei, J., Liang, J., Lu, J., Lu, H., and Zhang, W. (2019). Complex Gas Hydrate System in a Gas Chimney, South China Sea. *Mar. Petroleum Geol.* 104, 29–39. doi:10.1016/j.marpetgeo.2019.03.023

Ye, Z. Z., He, Q. X., and Zhang, M. S. (1985). Sedimentary Structure and Facies Pattern of Bioarenaceous Limestone in Late Pleistocene of Xisha Shidao. Acta Sedimentol. *Sin* 3, 1–15.

Zhang, G., Huang, Y., Zhu, Y., and Wu, B. (2002). Prospect of Gas Hydrate Resources in the South China Sea. *Mar. Geol. Quat. Geol.* 22, 75–82.

Zhang, G., Liang, J., Yang, S., Zhang, M., Holland, M., Schultheiss, P., et al. (2015). Geological Features, Controlling Factors and Potential Prospects of the Gas Hydrate Occurrence in the East Part of the Pearl River Mouth Basin, South China Sea. *Mar. Petroleum Geol.* 67, 356–367. doi:10.1016/j.marpetgeo.2015.05.021

Zhang, H. Q., Yang, S. X., Wu, N. Y., Su, X., Holland, M., Schultheiss, P., et al. (2007). Successful and Surprising Results for China's First Gas Hydrate Drilling Expedition. *Fire Ice* 7, 6–9.

Zhang, M. Z. M., Lu, H. L. H., Guan, H. G. H., Liu, L. L. L., Wu, D. W. D., and Wu, N. W. N. (2018). Methane Seepage Intensities Traced by Sulfur Isotopes of Pyrite and Gypsum in Sediment from the Shenhu Area, South China Sea. *Acta Oceanol. Sin.* 37, 20–27. doi:10.1007/s13131-018-1241-1

Zhang, W., Liang, J., Lu, J., Wei, J., Su, P., Fang, Y., et al. (2017). Accumulation Features and Mechanisms of High Saturation Natural Gas Hydrate in Shenhu Area, Northern South China Sea. *Petroleum Explor. Dev.* 44, 708–719. doi:10.1016/s1876-3804(17)30082-4

Zhang, W., Liang, J., Su, P., Wei, J., Gong, Y., Lin, L., et al. (2019). Distribution and Characteristics of Mud Diapirs, Gas Chimneys, and Bottom Simulating Reflectors Associated with Hydrocarbon Migration and Gas Hydrate Accumulation in the Qiongdongnan Basin, Northern Slope of the South China Sea. *Geol. J.* 54, 3556–3573. doi:10.1002/gj.3351

Zhao, Q., Jian, Z., Li, B., Cheng, X., and Wang, P. (1999). Microtektites in the Middle Pleistocene Deep-Sea Sediments of the South China Sea*. *Sci. China Ser. D-Earth. Sci.* 42, 531–535. doi:10.1007/bf02875247

Zhou, Y. A., Di, P. B. C. D., Li, N. B. C. D., Chen, F. A., Su, X. F., and Zhang, J. A. (2020). Unique Authigenic Mineral Assemblages and Planktonic Foraminifera Reveal Dynamic Cold Seepage in the Southern South China Sea. *Minerals* 10, 275–287. doi:10.3390/min10030275

Zhu, W., Huang, B., Mi, L., Wilkins, R. W., Fu, N., and Xiao, X. (2009). Geochemistry, Origin, and Deep-Water Exploration Potential of Natural Gases in the Pearl River Mouth and Qiongdongnan Basins, South China Sea. *Am. Assoc. Pet. Geol. Bull.* 93, 741–761. doi:10.1306/02170908099

frontiers | Frontiers in Marine Science

TYPE Original Research
PUBLISHED 21 October 2022
DOI 10.3389/fmars.2022.982814

OPEN ACCESS

EDITED BY
Davide Oppo,
University of Louisiana at Lafayette,
United States

REVIEWED BY
Zenggui Kuang,
Guangzhou Marine Geological Survey,
China
Ferdinando Cilenti,
University of Louisiana at Lafayette,
United States

*CORRESPONDENCE
Yuhong Lei
leiyh@mail.iggcas.ac.cn

SPECIALTY SECTION
This article was submitted to
Marine Biogeochemistry,
a section of the journal
Frontiers in Marine Science

RECEIVED 30 June 2022
ACCEPTED 27 September 2022
PUBLISHED 21 October 2022

CITATION
Song Y, Lei Y, Zhang L, Cheng M, Miao L, Li C and Liu N (2022) Spatial-temporal variations of the gas hydrate stability zone and hydrate accumulation models in the Dongsha region, China.
Front. Mar. Sci. 9:982814.
doi: 10.3389/fmars.2022.982814

Spatial-temporal variations of the gas hydrate stability zone and hydrate accumulation models in the Dongsha region, China

Yingrui Song[1,2,3], Yuhong Lei[1,2]*, Likuan Zhang[1,2],
Ming Cheng[1,2], Laicheng Miao[2], Chao Li[1,2] and Naigui Liu[1,2]

[1]Key Laboratory of Petroleum Resources Research, Institute of Geology and Geophysics, Chinese Academy of Sciences, Beijing, China, [2]Innovation Academy for Earth Science, Chinese Academy of Sciences, Beijing, China, [3]University of Chinese Academy of Sciences, Beijing, China

It is of great significance to study the spatial-temporal variations of the thickness of the gas hydrate stability zone (GHSZ) to understand the decomposition, migration, accumulation and dissipation of gas hydrate, the corresponding relationship between bottom-simulating reflectors (BSRs) and gas hydrate, and the distribution of heterogeneous gas hydrate. We selected the Dongsha region in the South China Sea (SCS) as the research object to calculate the spatial-temporal variation of the GHSZ since 10 Ma, analyzed the main factors affecting the thickness of the GHSZ, discussed the dynamic accumulation processes of gas hydrate, and proposed an accumulation model of gas hydrate in the Dongsha region. The results show that the thicknesses of the GHSZ in the study area were between 0 m and 100 m from 10 to 5.11 Ma, and the relatively higher bottom water temperature (BWT) was the key factor leading to the thinner thickness of the GHSZ during this period. From 5.11-0 Ma, the thickness of the GHSZ gradually increased but showed several fluctuations in thickness due to changes in the geothermal gradient, seawater depth, BWT, and other factors. The decrease in the BWT was the main factor leading to GHSZ thickening from 5.11 to 0 Ma. The thicknesses of the GHSZ are between 110 m and 415 m at present. The present spatial distribution features show the following characteristics. The GHSZ in the deep canyon area is relatively thick, with thicknesses generally between 225 m and 415 m, while the GHSZ in other areas is relatively thin, with thicknesses between 110 m and 225 m. Based on the characteristics of the GHSZ, two hydrate accumulation models are proposed: a double-BSRs model due to thinning of the GHSZ and a multilayer hydrate model due to thickness changes of the GHSZ, with single or multiple BSRs.

KEYWORDS

the South China Sea, the Dongsha region, gas hydrate, gas hydrate stability zone, accumulation model

1 Introduction

The gas hydrate stable zone (GHSZ), as a necessary condition for hydrate accumulation, is of great significance for gas hydrate exploration and exploitation (Kvenvolden, 1993; Sloan and Koh, 2008; Collett, 2009; Lei et al., 2021). The GHSZ is the range of thermodynamic equilibrium of three- phases of compounds composed of natural gas hydrate (NGH), water and gas (Rempel and Buffett, 1997), and its distribution characteristics are mainly affected by temperature, pressure, gas composition and pore water salinity. Changes in these parameters lead to changes in the thickness and spatial-temporal distribution characteristics of the GHSZ (Foucher et al., 2002; Haacke et al., 2007; Zander et al., 2017).

Researchers have shown that the spatial-temporal variations of the GHSZ are closely related to the origin and mechanism of multiple bottom-simulating reflectors (BSRs), the BSR and the dynamic accumulation process of gas hydrate. Therefore, studying the spatial-temporal variation of the GHSZ can help us understand the dynamic decomposition, migration, accumulation and dissipation of gas hydrate, and the spatial distribution characteristics of gas hydrate (Bangs et al., 2005; Haacke et al., 2007; Pecher et al., 2017; Lei et al., 2021; Song et al., 2022; Zhang et al., 2022).

Previous studies have shown that the formation mechanism of some multiple BSRs is the thinning of the GHSZ due to the rise in the formation temperature, decrease in pressure, shallow seawater depth, tectonic uplift and other reasons. The hydrate formed in the early stage migrates out of the GHSZ, decomposes the gas hydrate and leaves the lower paleo-BSR. The decomposed gas and the newly migrated gas migrate upward to the new GHSZ and form hydrate accumulation and new BSR in the upper layer (Foucher et al., 2002; Bangs et al., 2005; Haacke et al., 2007; Pecher et al., 2017; Zander et al., 2017; Song et al., 2022). In the multiple BSRs that have this origin, no gas hydrates are present above the lower BSR, while there are gas hydrates above the upper BSR in the present GHSZ (Foucher et al., 2002; Bangs et al., 2005; Haacke et al., 2007; Pecher et al., 2017; Zander et al., 2017). In addition, the development of vertical multilayer gas hydrate and its relationship with BSR in the GHSZ may be closely related to the variation of the GHSZ and the multistage accumulation and damage of hydrates (Majumdar et al., 2016; Lei et al., 2021; Song et al., 2022). Therefore, the study of the spatial-temporal evolution of the GHSZ plays an important role in understanding the formation mechanism of the double\multiple BSRs.

At present, previous studies on the dynamic accumulation process of BSR and current hydrate mainly explain the correlation between BSR and current hydrate accumulation based on the fine anatomy of high-resolution seismic data and the characteristics of current hydrate accumulation (Horozal et al., 2017; Zhang et al., 2020; Zhang et al., 2022). However, these studies did not consider that the area of stable hydrate accumulation, the GHSZ, may change as the change of external environment. Due to the uncertainty of the GHSZ, the relationship between BSR and dynamic hydrate accumulation will also change. In recent years, the spatial-temporal evolution of the GHSZ and the dynamic accumulation relationship between BSR and hydrates was began to explore (Piñero et al., 2014; Burwicz et al., 2017; Wang et al., 2017a; Kroeger et al., 2019; Song et al., 2022). Piñero (2014), Burwicz (2017), Wang (2017a) and Kroeger (2019) specially considered the characteristics of the GHSZ with times in their model about dynamic hydrate accumulation. Song (2022) studied the spatial-temporal variation of the GHSZ and the relationship between double BSRs in the Shenhu area of the South China Sea (SCS), and elaborated the possible relationship between the evolution of the GHSZ and the GHSZ (Song et al., 2022). Recent studies have shown that the spatial-temporal variation of GHSZ plays an important role in understanding the dynamic accumulation process of BSR and gas hydrate.

Therefore, it is of great significance to study the spatial-temporal variation of the thickness of the GHSZ, and to understand the origin of BSR; the corresponding relationship between BSR and gas hydrate; the dynamic decomposition, migration, accumulation and dissipation of gas hydrate; and the hydrate accumulation models and to improve the exploration effect of gas hydrate.

Based on this information, this paper chose the Taixinan Basin of the northern South China Sea (SCS) as the research object, selected the appropriate methods and parameters; simulated the spatial-temporal variations of the GHSZ and distribution characteristics in the study area; discussed the dynamic decomposition, migration, accumulation and dissipation of gas hydrates related to the change in the GHSZ; and proposed a model of gas hydrate accumulation in the Dongsha region. This study provides a reference and inspiration for understanding the distribution pattern of gas hydrate and reducing the multiple solution of BSRs in the Dongsha region.

2 Geological background

The area of gas hydrate development in the Dongsha region is located in the continental margin of the Taixinan Basin in the northeast SCS (Figure 1A). The Taixinan Basin experienced three tectonic variation stages: the late Paleocene–early Oligocene continental margin rifting stage, late Oligocene–middle Miocene continental margin depression stage and late Miocene–Holocene passive continental margin rifting stage (Yi et al., 2007). Therefore, a tectonic pattern of north–south zones and east–west blocks was formed in the study area (Zhang, 2016).

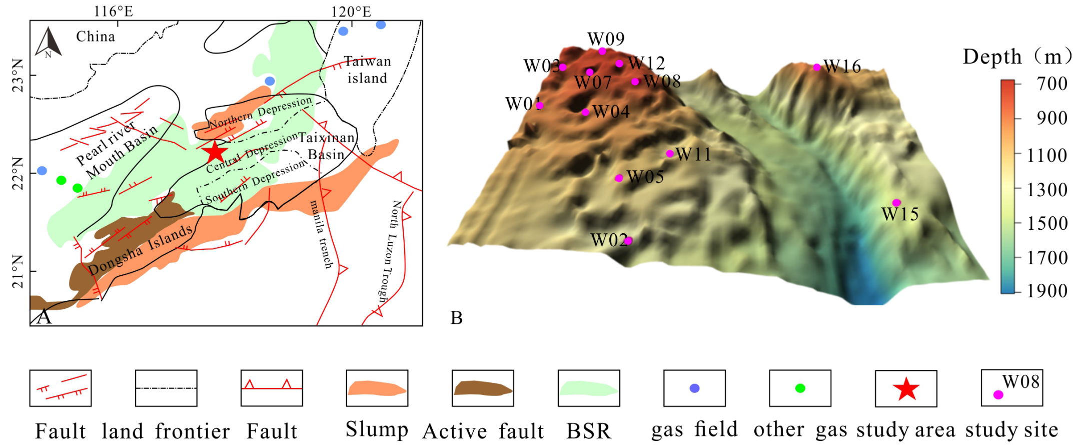

FIGURE 1
Geographic location and coring site characteristics of the Dongsha region. **(A)** Tectonic units of the southwest Taiwan Basin (data resource: Li et al., 2020). **(B)** Seawater depth and location characteristics of coring sites in the Dongsha region.

Multiple sets of source rocks of Jurassic, Cretaceous, Paleogene and Neogene ages are present in the Taixinan Basin (Zhang, 2016). The total organic carbon (TOC) contents of Jurassic and Cretaceous offshore terrestrial shale ranges from 0.7% to 2.4%, and the organic matter maturities range from 0.5% to 1.39% (Wang, 2016). The TOC contents of coal measure strata from upper Oligocene to lower Miocene deposits range from 0.5% to 2.0%, and organic matter maturities range from 0.56% to 1.03% (Wang, 2016; Zhang, 2016). These three sets of strata are important source rocks of thermogenic hydrocarbons in the Taixinan Basin. The marine mudstone strata of the upper Miocene and Quaternary are good biogenic source rocks (Gong et al., 2017; Li et al., 2021) with TOC contents ranging from 0.42% to 1.13% and organic maturities ranging from 0.2% to 0.6% (He et al., 2013).

Migration channels such as faults and mud diapirs are present in the Dongsha region (He and Liu, 2008). NW–NWW and NNE–NEE faults are the main faults in the study area (Yi et al., 2007) (Figure 1A). NW–NWW faults were formed during the continental margin rifting period from 56 to 17 Ma (Gong et al., 2008; Wang, 2016), and NNE–NEE faults were formed during the Dongsha movement which began at 10.2 Ma (Zhao et al., 2012; Li et al., 2015). In addition, a large number of cone-shaped, dome-shaped and even elongated gas chimneys are present near the fault active zone in the Dongsha region (Zhang, 2016; Sha et al., 2019). These faults and mud diapirs communicate with gas source stoves and the GHSZ, which are important channels for upward gas migration to the GHSZ in the Dongsha region (Zhang, 2016).

The present seawater depths in the Dongsha region are between 700 m and 1900 m (Zhang et al., 2014a). The pressures at the drilling sites range from 7.4 MPa to 17.7 MPa (Wang, 2016). The geothermal gradients range from 40°C/km to 90°C/km (Li et al., 2015). The heat flow values range from 60 Mw/m^2 to 90 Mw/m^2 (Sha et al., 2015a). The bottom water temperatures (BWTs) range from 2°C to 5°C. The sedimentation rates in the Dongsha region have been between 3.1 cm/ka and 7.4 cm/ka since the middle Pleistocene (Sha et al., 2019). Consequently, the Dongsha region has the temperature and pressure conditions conductive to the formation and preservation of gas hydrate. In 2013, the Guangzhou Marine Geological Survey (GMGS), Ministry of Land and Resources and China Geological Survey (CGS) drilled 13 stations in the research area, and hydrate was found in the cores from 5 stations (Zhang et al., 2014a; Zhang et al., 2014b; Sha et al., 2015b). NGHs occur in silty clays in massive, nodular, nodular, vein-like and dispersed forms (Zhang et al., 2014b). The thicknesses of the hydrate layer in this region are between 6 m and 37 m, the porosities of the sediments are between 55% and 65%, and the saturation values of the hydrate are approximately 45% to 100% (Zhang et al., 2014b). Sufficient gas sources, widely distributed migration channels, appropriate temperature and pressure conditions and drilling results indicate that the research area is a favorable gas hydrate exploration area.

3 Methodology and parameters

3.1 Methodology

The GHSZ is the range where the three phases of NGH, water and gas reach thermodynamic equilibrium, which is mainly limited by temperature, pressure and salinity (Figure 2) (Kvenvolden, 1993; Rempel and Buffett, 1997). The intersection of the geothermal gradient and temperature–pressure phase equilibrium boundary below the seafloor is the bottom

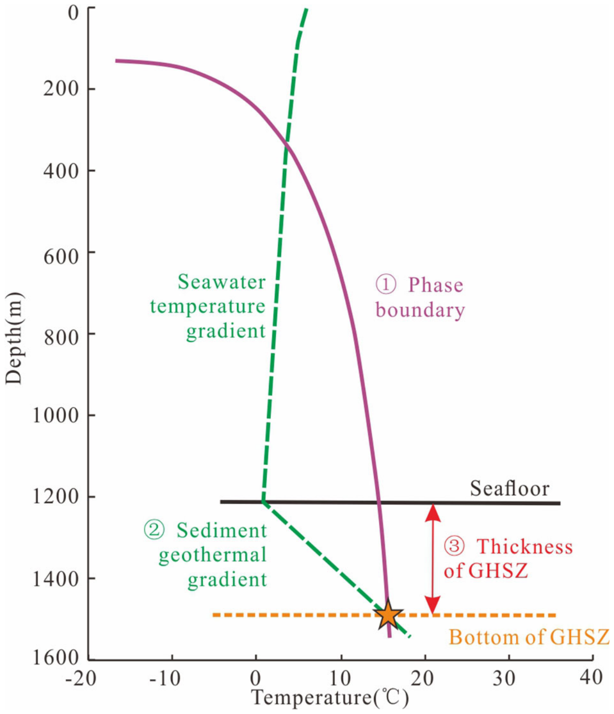

FIGURE 2
Calculation diagram of the GHSZ thickness controlled by ocean temperature (T) and pressure (P).

boundary of the GHSZ, the bottom is the top boundary of the GHSZ, and the vertical distance between the top and bottom boundary is the thickness of the GHSZ. Therefore, the thickness of the GHSZ can be calculated by using the temperature and pressure phase balance formula of gas hydrate combined with the geothermal gradient curve (Dickens and Quinby-Hunt, 1994; Bishnoi and Dholabhai, 1999; Sloan and Koh, 2008).

When calculating the thickness of the GHSZ, it is assumed that the gas consists entirely of methane. The boundary of the methane hydrate phase under temperature–depth control can be derived from the equilibrium formula of the hydrate phase (Formula 1) and the transformation equation of pressure and depth (Formula 2) to obtain the relationship between the temperature and depth of the hydrate phase boundary. The methane GHSZ is a function of depth (pressure) and temperature (Max, 1990; Miles, 1995). Here, the hydrate phase equilibrium formula fitted by Miles (1995) based on laboratory data of methane hydrate was used to calculate the thickness of the GHSZ (Equation. 1):

$$P = 2.8074023 + 0.1559474T + 0.048275T^2 - 0.00278083T^3 + 0.00015922T^4 \tag{1}$$

where P is the pressure, in MPa, and T is the temperature, in °C.

According to the liquid pressure equation, the conversion relationship between pressure and depth can be obtained as follows (Equation 2):

$$P = P_{\text{atm}} + \rho g(h + D) \times 10^{-6} \tag{2}$$

where P_{atm} is atmospheric pressure, with a value of 0.101325 MPa; D is the present seawater depth, in m; ? is seawater density, with a value of 1035 kg/m^3; g is gravity, with a value of 9.81 m/s^2, and h is the thickness of the GHSZ, in m.

The calculation formula of the geothermal gradient is Equation 3:

$$G = \frac{T - T_i}{h - h_i} \tag{3}$$

where T is the BWT, in °C; T_i is the sediment temperature at point i, in °C; h_i is the vertical distance to the seafloor at point i, in m; and G is the geothermal gradient, in °C/m.

According to the above formula, the hydrate phase boundary formula related to temperature and depth is obtained by using hydrate phase equilibrium formula and liquid pressure formula. The distance from the intersection point of the geothermal gradient to the seafloor sediment is the thickness of the GHSZ. At present, the Colorado School of Mines Hydrate program (CSMHYD) is a mainstream software to calculate the thickness of the GHSZ. However, this program cannot be used for batch calculation, and can not meet the needs of large-scale area research.

In this study, a program for calculation the thickness of GHSZ was written according to the above theoretical formulas. This procedure chose C language as the programming language, which can realize the fast mass calculation. The 100 rows (W-E direction) * 68 columns (N-S direction) nodes, totaling 6400 total nodes, will be set on the plane for the characteristics of the 3D plane GHSZ in the study area. The areas without control points are interpolated using the Kriging interpolation technique in the Surfer software. The characteristic of 1D and 2D GHSZ is obtained by intercepting the 3D plane, which is convenient for comparison and analysis with the actual profile.

3.2 Parameters

3.2.1 Present parameters

Present parameters include the present formation water pressure, present BWT, and present geothermal gradient and density. The present measured drilling pressure in the study area shows that the shallow formation is under hydrostatic pressure (Wang, 2016). Therefore, the present seawater depth (D) can be used to calculate the present formation water pressure. The present seawater depths in the study area are approximately 700 ~1900 m (Figure 1B) (Zhang et al., 2014a). The seawater depths west of Sites W15-W16 and to the east of Sites W08-W11 are large, ranging from 1350 m to 1900 m. The seawater depths in other areas are relatively shallow, mainly varying from 700 m to 1350 m (Figure 1B). The present BWT data are derived from the fitting formula (Equation 4) of the BWT (T_s) and seawater depth (D) established by Zhu (2007) (Figure 3). The results show that the BWTs are is between 2.83°C and 5.66°C in the study area. The present geothermal gradient refers to the plane distribution map of the present geothermal gradient in the Dongsha region according to the measured geothermal gradient in the Dongsha region drawn by Li et al. (2015). In addition, it is assumed that the seawater density (ρ) in the study area is always constant, and the value is 1.035g/m^3 (Wang et al., 2013).

$$\begin{cases} T_s = -8.7946 \ \ \ln D + 62.958 \ \ \ 100 \ m < D \le 800 \ \ m \\ lnT_s = -0.7485 \times (lnD - 2.0339) \ \ \ 800 \ \ m < D \le 2800 \ \ m \\ \qquad\qquad T_s = 2.2 \end{cases} \tag{4}$$

where T_s is the BWT, in °C.

3.2.2 Paleo-parameters

On the premise that atmospheric pressure and seawater density do not change, the paleo-calculated parameters include the paleo-seawater depth, paleo-BWT and paleo-geothermal gradient. The relative trend of the adopted paleo-parameters is shown in Figure 4.

The depth of paleo-seawater is an important parameter to calculate the thickness of the paleo-GHSZ. Paleo-seawater depth (D_p) is a function of the present seawater depth (D), relative sea level variation (ρH_1) and seafloor subsidence (ρH_2) (Formula 5). Changes in the relative sea level over time (ρH_1) reference the research results of Pang et al. (2007) on the history of changes in

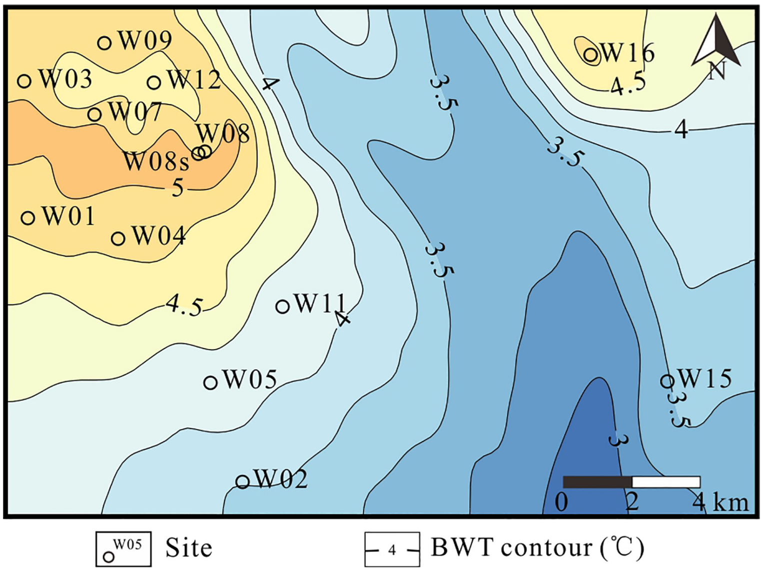

FIGURE 3
BWT characteristics in the Dongsha region, northern SCS.

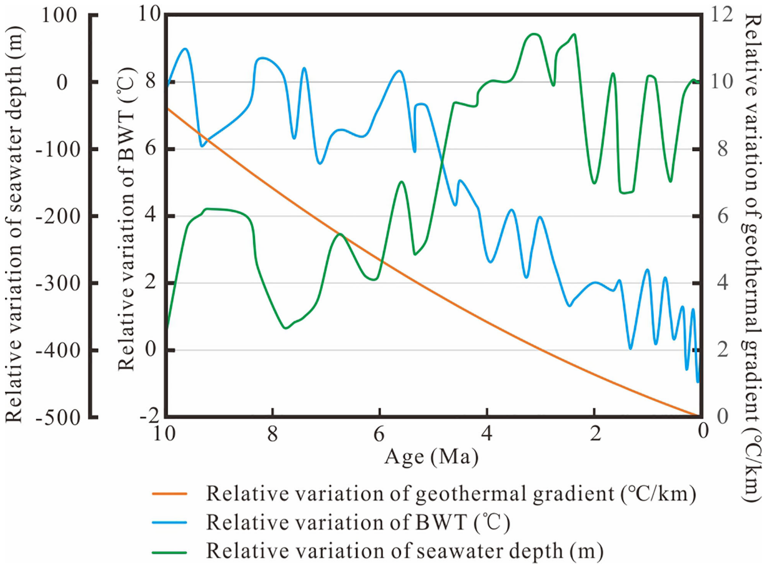

FIGURE 4
Relative trend of the paleo-parameters used to simulate the historical variation in the GHSZ.

relative sea level in the Pearl River Mouth Basin; the changes in submarine subsidence over time (ρH_2) and the changes in depositional thickness over time (ρH_3) reference the research results of Hu et al. (2019) on the history of seabed burial subsidence in the northern SCS. The changes in relative sea level over time (ρH_1), seafloor subsidence over time (ρH_2) and changes in depositional thickness over time (ρH_3) are the changes in paleo-seawater depth, and the values are shown in Figure 4.

$$D_p = D + \Delta H_1 + \Delta H_2 - \Delta H_3 \tag{5}$$

where D_p is the paleo-seawater depth, in m; ρH_1 is the history of relative sea level fluctuation, in m; ρH_2 is the history of seafloor subsidence, in m; and ρH_3 is the history of the depositional thickness, in m.

Lear et al. (2015) used δ^{18}O and Mg/Ca values of benthic forams to estimate the variation in the paleo-BWTs since 17 Ma at ODP Site 806 in the adjacent study area. The relative characteristics of the parameters are shown in Figure 4. The change in the geothermal gradient refers to the variation in the geothermal gradient of Liu et al. (2018), and the characteristics of the relative change are shown in Figure 4.

4 Results

Using the above methods and parameters, the variation processes of the thickness of the GHSZ since 10 Ma in the Dongsha area were calculated, and the results are shown in Figures 5–7.

The thickness characteristics of gas hydrate in the GHSZ at a single site since 10 Ma show the following characteristics. From 10 to 5.11 Ma, the thicknesses of the GHSZ on the east and west sides of the study area were very thin, generally less than 25 m. From 5.11 to 0 Ma, the thicknesses of the GHSZ gradually thickened, but there were several fluctuations in thickness processes due to temperature, pressure, seawater depth and other factors (Figure 5).

The thickness characteristics of the GHSZ in the 2D section at Sites W09, W07, W08, W05 and W16 are shown in Figure 6. The thicknesses of the GHSZ from 10 to 5.11 Ma were generally less than 10 m. At 5.11 Ma, the thicknesses of the GHSZ in the deep canyon area between W05 and W16 were relatively large, with values ranging from 70 m to 80 m. The thicknesses of the GHSZ in other areas were generally less than 10 m (Figure 6A). At 3.28 Ma, the thicknesses of the GHSZ increased significantly. The GHSZ in the deep canyon area between Sites W05 and W16 was approximately 230 m, and the thicknesses of the GHSZ in other areas were between 90 m and 180 m (Figure 6B). At 3 Ma, compared with 3.28 Ma, the thickness of the GHSZ was reduced. The thickness of the GHSZ in the deep canyon was approximately 200 m, and the thicknesses of the GHSZ on both sides of the canyon were between 50 m and 140 m (Figure 6C). Compared to 3 Ma, the GHSZ thickened significantly at 1.64 Ma. The thickness of the GHSZ in the deep canyon area between Sites W05 and W16 increased to approximately about 240 m, while the thicknesses of the GHSZ

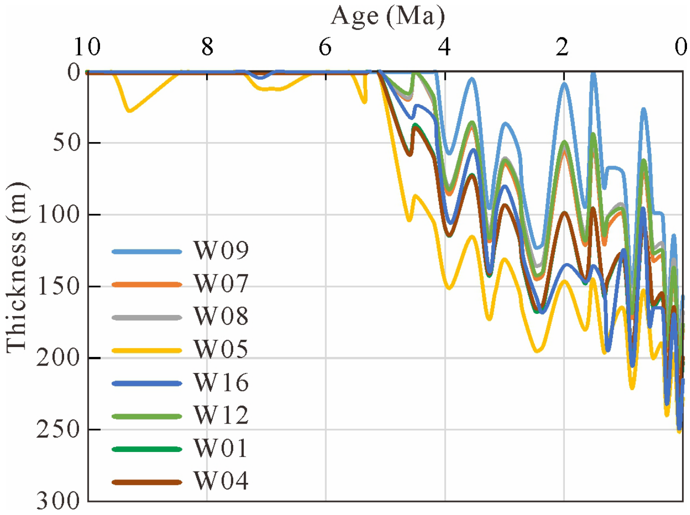

FIGURE 5
Characteristics of the GHSZ at different sites since 10 Ma.

in other areas varied between 100 m and 220 m (Figure 6D). At 0.85 Ma, the thickness of the GHSZ in the deep canyon zone increased to 300 m, and the thicknesses of the GHSZ in other areas ranged from 120 m to 230 m (Figure 6E). At 0.68 Ma, the thickness of the GHSZ obviously decreased. The thickness of the GHSZ between Sites W05 and W16 in the deep canyon zone decreased to 220 m, and the thicknesses of the GHSZ in other areas were approximately 40 m to 210 m. The thickness of GHSZ between Sites W08 and W09 decreased the most, mainly between 40 m and 70 m (Figure 6F). At 0.07 Ma, the

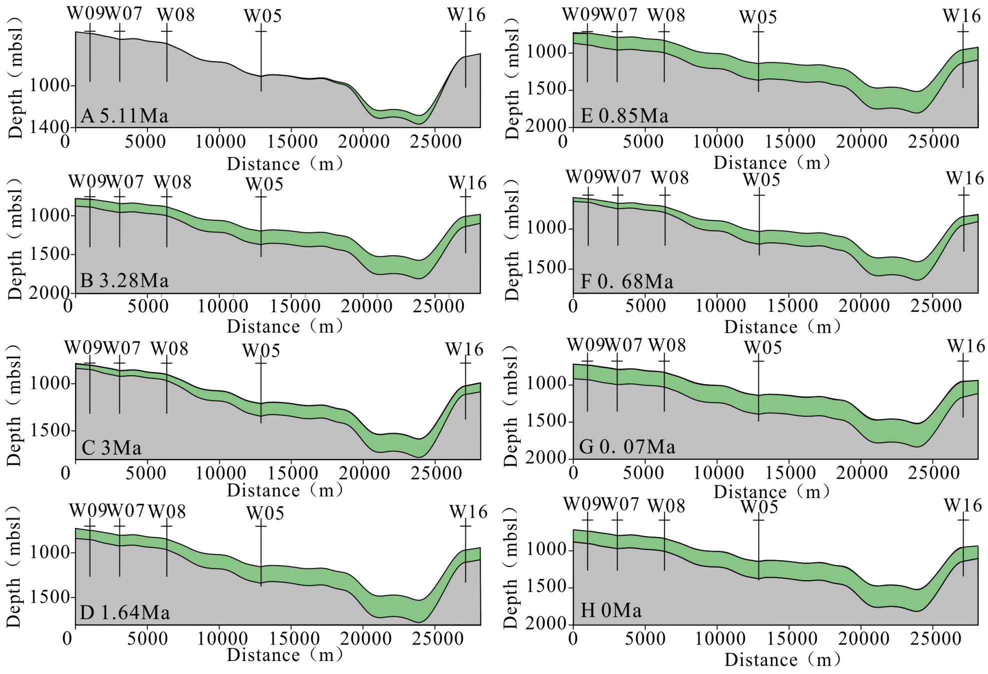

FIGURE 6
Characteristics of the GHSZ in the 2D profile. **(A)** 5.11 Ma, **(B)** 3.28 Ma, **(C)** 3 Ma, **(D)** 1.64 Ma, **(E)** 0.85 Ma, **(F)** 0.68 Ma, **(G)** 0.07 Ma, **(H)** 0 Ma.

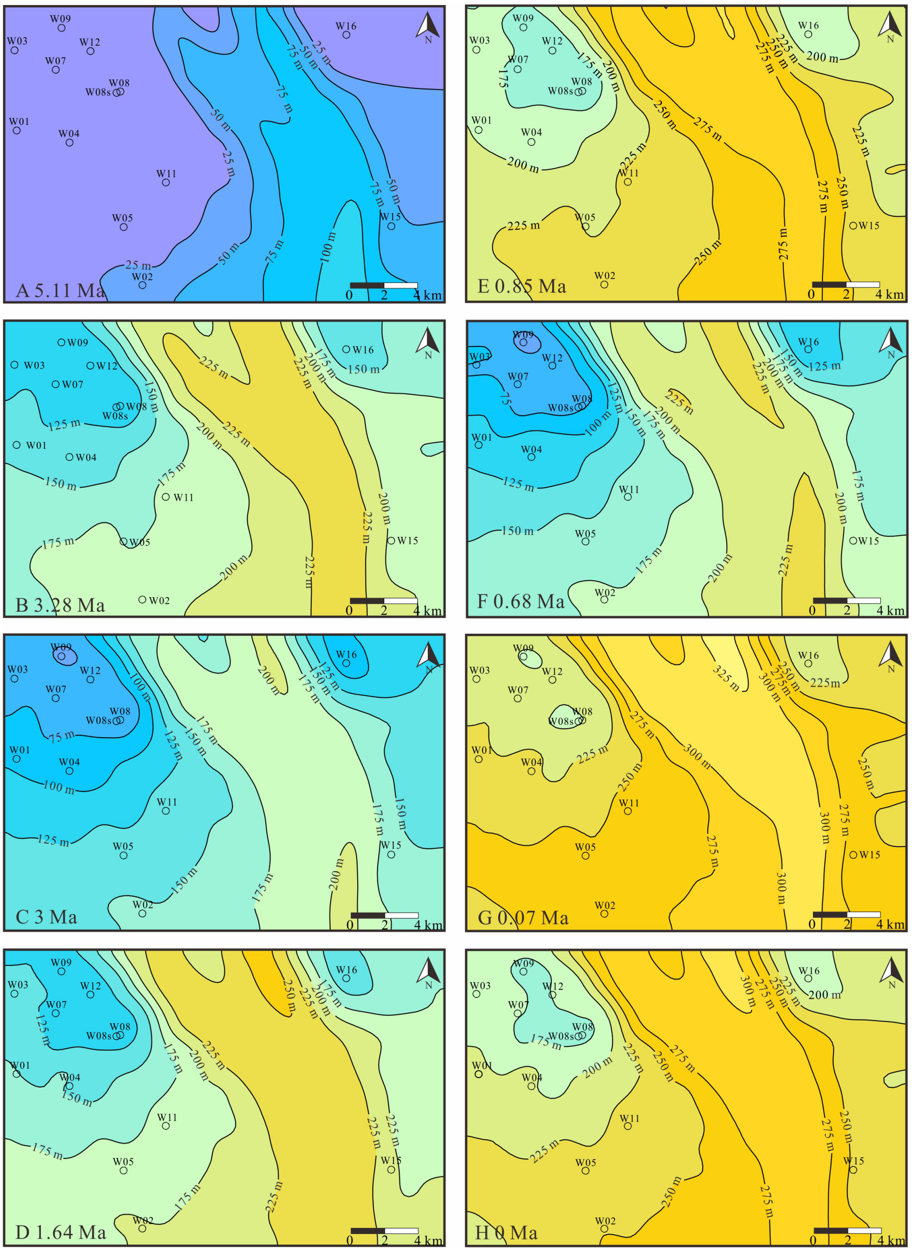

FIGURE 7
Characteristics of the GHSZ in the Dongsha region. **(A)** 5.11 Ma, **(B)** 3.28 Ma, **(C)** 3 Ma, **(D)** 1.64 Ma, **(E)** 0.85 Ma, **(F)** 0.68 Ma, **(G)** 0.07 Ma, **(H)** 0 Ma.

thicknesses of the GHSZ increased significantly. The thickness of the GHSZ in the deep canyon zone increased to 320 m, and the thicknesses of the GHSZ in other areas also increased, ranging from 180 m to 260 m (Figure 6G). Compared to 0.07 Ma, the thickness of the GHSZ at 0 Ma was slightly reduced. The thickness of the GHSZ in the canyon area with deep water was approximately 300 m, and the thicknesses of the GHSZ in other areas were approximately 170 m to 260 m (Figure 6H).

The plane distribution maps showing the thickness of the GHSZ in the Dongsha region in different geological periods is given (Figure 7). Since 5.11 Ma, several thinning processes of gas hydrate in the GHSZ have occurred in the study area with the trend of increasing overall thickness. At 5.11 Ma, the thicknesses of the GHSZ in the study area were relatively thin, ranging from 0 m to 100 m. The thicknesses of the GHSZ at Site W16 in the western, northwestern and northeastern parts of the study area were generally less than 10 m, and the thicknesses of the GHSZ in the southeastern parts of the study area were relatively thick (Figure 7A). Compared to 5.11 Ma, the thickness distribution of the GHSZ at 3.28 Ma was significantly thicker, and the thicknesses ranged from 90 m to 310 m (Figure 7B). At 3 Ma, the thickness of the GHSZ became thinner overall, and the thicknesses ranged from 0 m to 258 m (Figure 6C). At 1.64 Ma, the GHSZ thickened obviously, with thicknesses between 90 m and 330 m (Figure 7D). The thickness of the GHSZ at 0.85 Ma continued to increase, and the thickness values were between 110 m and 390 m (Figure 7E). The thicknesses of the GHSZ at 0.68 Ma were thinner, ranging from 0 m to 306 m (Figure 7F), and the thicknesses of the GHSZ at 0.07 Ma were thicker, ranging from 125 m to 470 m (Figure 7G). At 0 Ma, the GHSZ became thinner, and the thicknesses ranged from 110 m to 415 m (Figure 7H). The present spatial distribution characteristics of the thickness of the GHSZ in the Dongsha region are as follows: the thickness of the GHSZ in the northeastern and northwestern regions is the thinnest. The thicknesses of the deep canyon between W11, W12, W16 and W15 are thicker, generally between 225 m and 415 m, while the thicknesses of the GHSZ in other areas are thinner, between 110 m and 225 m. The thickness distribution of the GHSZ at different ages is consistent with that at the present, but the thickness of the GHSZ is different at different times.

5 Discussion

5.1 Main factors affecting the thickness changes of the GHSZ

Previous studies have shown that the seawater depth, geothermal gradient, and BWT are all important factors influencing the GHSZ (Collett, 2009). In these previous studies, the relationship between the parameters and the thickness of the GHSZ was determined by ansatze method (Paull et al., 1991; Milkov and Sassen, 2003; Wang and Lau, 2020) or linear correlation coefficient analysis (Wang et al., 2017b; Xiao et al., 2020). Then the influence of the parameters changes on the dynamic accumulation of hydrate was obtained. However, due to the lack of consideration of the time variation process of each parameter, the discussion results usually cannot accurately match the previous variation of the thickness of GHSZ. Therefore, these methods cannot get an accurate conclusion of how much the parameter changes affect the dynamic accumulation process of hydrate.

The single-factor sensitivity analysis method can provide a more accurate analysis of the impact of the change of a single uncertain factor on the results. Apply the true changing values of these paraments. The actual variation value of the thickness of GHSZ is calculated. Taking Site W16 as an example, the single-factor sensitivity analysis method is used to analyze the factors affecting the thickness of the GHSZ. Under the condition in which all other factors remain unchanged, the influence of the change in one factor on the thickness of the GHSZ is discussed.

Figure 5 shows the thickness characteristics of the GHSZ at Site W16. The thickness of the GHSZ is less than 10 m from 10 to 5.11 Ma. When other conditions remain unchanged, the geothermal gradient decreases from 44.05 °C/km at 10 Ma to 38.53 °C/km at 5.11 Ma, and the GHSZ thickens by 28.78 m. Similarly, the depth of seawater decreases from 464.20 m at 10 Ma to 885.00 m at 5.11 Ma, and the GHSZ thickens by 207.49 m. When other conditions remain unchanged, the temperature of the BWT decreases from 12.80 °C at 10 Ma to 12.58°C at 5.11 Ma, and the thickness of the GHSZ remains unchanged at 0.57 m. In conclusion, only when the BWT changes does the thickness of the GHSZ always change less than 10 m, which is the most consistent with the actual situation, in which the thickness of the GHSZ is less than 10 m. The higher BWT is the main reason for the thickness of the GHSZ being less than 10 m, which occurred from10 to 5.11 Ma.

According to the thickness characteristics of the GHSZ at Site W16 (Figure 4), from 5.11 to 0 Ma, the GHSZ thickens from 0.52 m to 214.70 m. As shown in Figure 8, when other conditions remain unchanged, the geothermal gradient decreases from 38.53°C/km at 5.11 Ma to 34.70°C/km at 10 Ma, and the GHSZ thickens by 26.56 m. When other conditions remain unchanged, the depth of seawater decreases from 464.20 m at 5.11 Ma to 885.00 m at 0 Ma, and the thickness of the GHSZ decreases by 3.75 m. When other conditions remain constant, the BWT increases from 12.58 °C at 5.11 Ma to 5.34°C at 0 Ma, and the GHSZ thickens from 0.58 m to 214.70 m. In conclusion, only when the BWT changes is the thickness change of the GHSZ (214.12 m) close to that of the actual GHSZ (214.18 m). The higher BWT is the main reason for the GHSZ thickening to 214.70 m from 5.11 to 0 Ma.

5.2 Hydrate accumulation models related to GHSZ variation

NGHs revealed by seismic data and drilling in the Dongsha region have complex spatial distribution rules and strong heterogeneity. Double BSRs, different correspondences between NGHs and BSRs, and vertical multilayer NGHs are developed at some sites (Figure 9) (Zhang et al., 2014a; Zhang et al., 2014b; Li et al., 2015; Zhang et al., 2015). The heterogeneity of the spatial distribution of gas hydrates and the complexity of the relationship between gas hydrates and BSRs are closely related to the dynamic decomposition, migration, accumulation and dissipation of gas hydrates caused by the change in the thickness of the GHSZ and the coupling relationship between the GHSZ, gas source and migration channels. According to Zhang et al. (2017), the gas hydrates in the Dongsha region experienced at least three hydrate

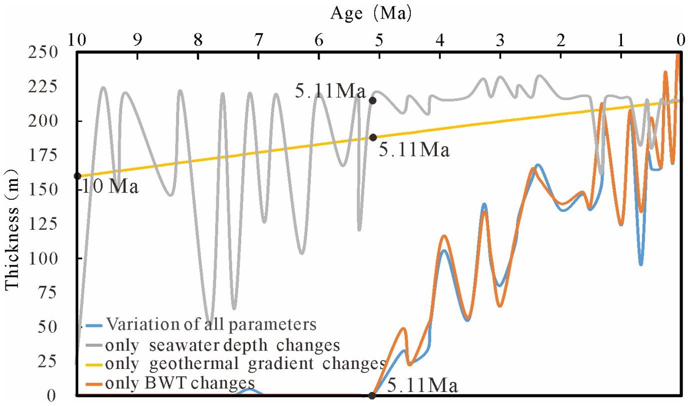

FIGURE 8
Effects of the geothermal gradient, BWT and seawater depth on the thickness of the GHSZ since 10 Ma.

accumulation stages (0.78-0.357 Ma, 0.357-0.107 Ma and 0.107-0.063 Ma) and two hydrate destruction stages (0.33-0.107 Ma and 0.063-0.0466 Ma). Based on the analysis of the thickness characteristics of the GHSZ mentioned above, this section analyzes the dynamic accumulation processes and model of gas hydrate in the Dongsha region in combination with the seismic data and the geological age of gas hydrates formation revealed by drilling.

Point A near Site W08 in the Dongsha region shows obvious double BSRs (Figure 10A) (Li et al., 2015). The seawater depth at this point is 1118 m, and the upper BSR (BSR-1) is located1327 meters below sea level (mbsl) (209 meters below the seafloor (mbsf)), while the lower BSR (BSR-2) is located at 1419 mbsl (301 mbsf) (Li et al., 2015). According to the present BWT (4.22°C), geothermal gradient (50 °C/km), seawater depth (1118 m) and formation pore water salinity (3.5% NaCl), the thickness of the present GHSZ at point A is 203 m, that is, the bottom boundary of the GHSZ at point A is basically consistent with the position of BSR-1. BSR-2 is located 92 m below BSR-1, and its possible formation mechanisms are as follows: one mechanism is the formation of gas hydrate above BSR-2 from deep thermogenic gas or a mixture of thermogenic gas and biogenic gas. The other mechanism may be due to the thinning of the GHSZ and the migration of NGH from the early stage to the bottom of the GHSZ,

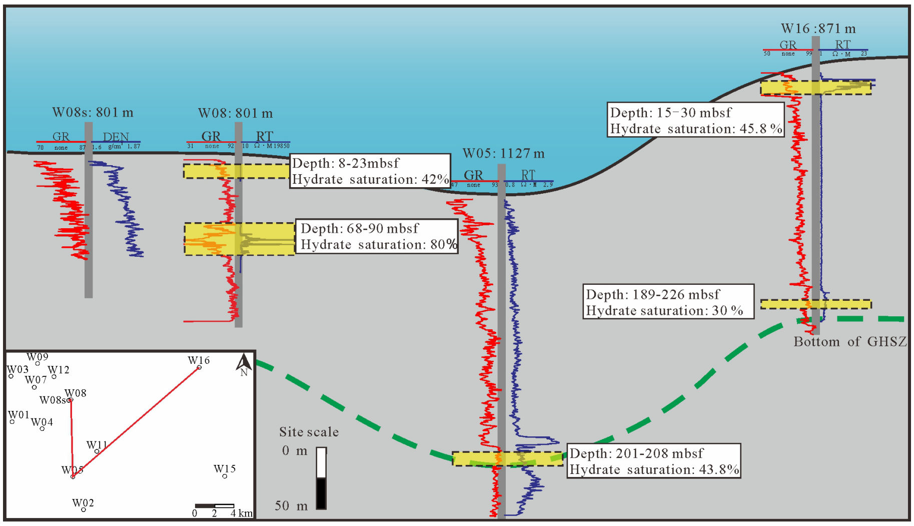

FIGURE 9
Distribution characteristics of single site hydrate in the Dongsha region (data resource: Zhang et al., 2014b; Wang, 2016).

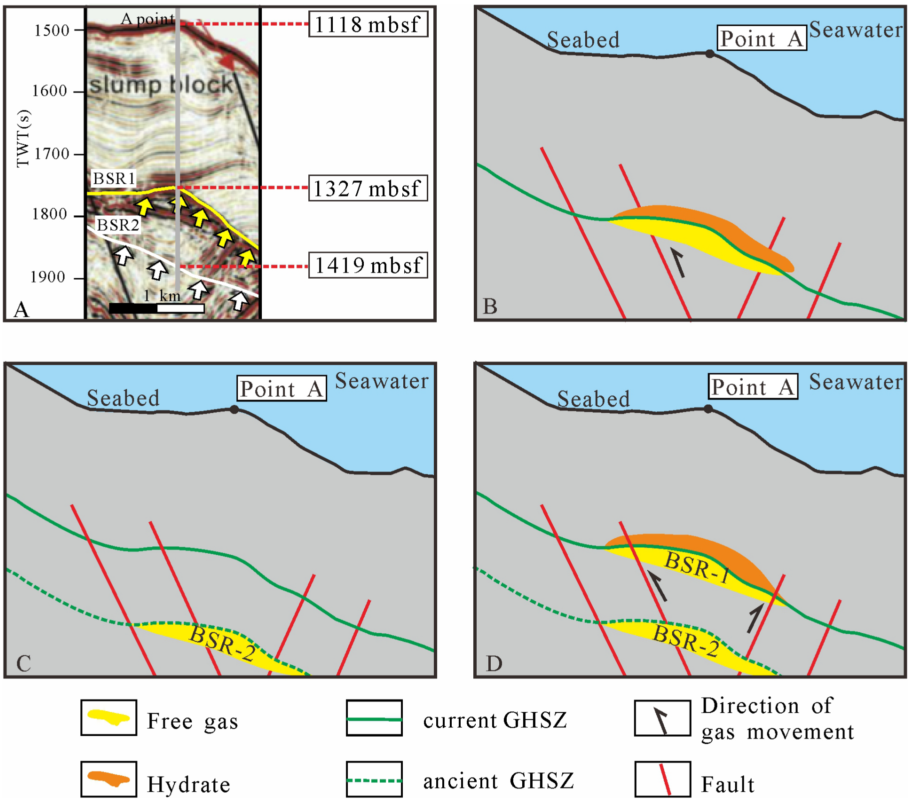

FIGURE 10
(A) Seismic refection characteristics of double BSRs across point A at Site W08 (modified from: Li et al., 2015). **(B–D)** Hydrate accumulation model of a double BSRs model due to thinning of the GHSZ at point A at Site W08.

resulting in the resolution and escape of the hydrate and the residual paleo-BSR. The organic geochemical analysis results of the gas hydrate analytical gas at Site W08 show that the proportions of CH_4 in the total hydrocarbon gas range from 99.94% to 99.96%, and the proportions of C_2H_6 in the total hydrocarbon gas range from 0.03% to 0.06%, $\delta^{13}C_1$ values range from -68.4 ‰ to -71.2 ‰, and δD_1 values range from -182 ‰ to -184 ‰. These results indicate that it is a typical biogenic gas (Sha et al., 2019). The schematic diagram of the hydrate phase equilibrium curve of different gas components (Figure 11) shows that if BSR-2 is a BSR formed by thermogenic gas components, namely, only 98% CH_4+2% C_3H_8, or 80% CH_4 and 20% C_2H_6, then the thickness of the bottom boundary of the GHSZ is consistent with that of BSR-2, and the thickness of the GHSZ is approximately 203 m, as calculated from the gas hydrate gas composition at Site W08, which is consistent with that of BSR-1. Therefore, BSR-2 near point A was not formed due to the existence of thermal gas but was more likely to be the residual paleo-BSR caused by the destruction of the NGH that was formed due to the thinning of the GHSZ.

According to the factors of BSR-1 and BSR-2 at point A near Site W08, combined with the natural gas source, the variation of the GHSZ and the stages of hydrate accumulation and dissipation, the hydrate accumulation model of a double BSRs model due to thinning of the GHSZ at point A is proposed (Figure 10). Before 0.357 Ma, biogenic gas migrated to the GHSZ through faults, mud volcanoes and other channels to form gas hydrate and formed the early BSR (BSR-1) (Figure 10B). During 0.33-0.107 Ma, the thickness of the GHSZ at point A was reduced due to changes in the geothermal gradient and BWT. The formed hydrate and BSR (BSR-2) moved below the bottom boundary of the GHSZ, and the hydrate was destroyed (Figure 10C). If the permeability of the formation surrounding the early NGH was very low or there was little convection, and a large amount of free gas still existed in the original hydrate reservoir, the early BSR-2 did not disappear. During 0.107-0 Ma, biogenic gas generated in the late period of the hydrocarbon source range migrated to the GHSZ along faults and mud volcanoes, forming new hydrates and new BSR (BSR-1) (Figure 10D). The abovementioned characteristics of gas hydrate decomposition, migration, accumulation and dissipation due to the thickness change of the GHSZ and multistage biogas migration along the channel led to the formation of no gas hydrate above the deep BSR-2 at point A and the development of gas hydrate at the upper part of shallow BSR-1.

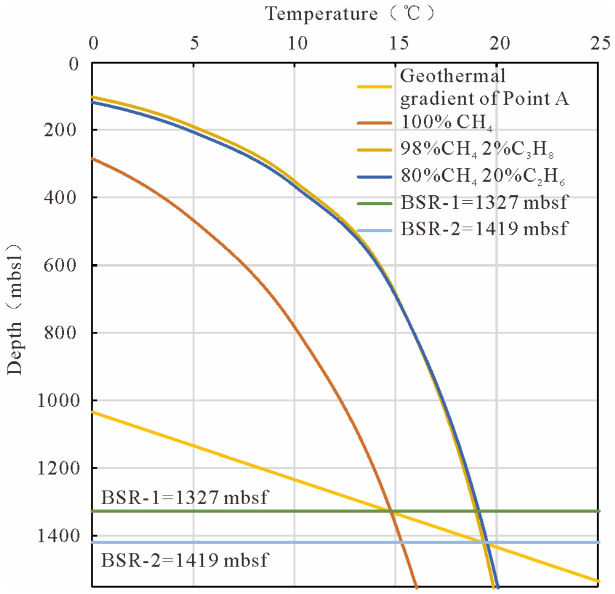

FIGURE 11
Calculation of the GHSZ with different hydrate gas compositions at point A at Site W08.

Sites W07, W08, W09 and W16 in the Dongsha region all contain multilayer hydrate development, as shown by drilling (Zhang et al., 2014b), and the formation of multilayer gas hydrate at some sites is also related to the variation of the GHSZ. For example, two hydrate layers were drilled at Site W16, the shallow hydrate layers were distributed 15 m to 30 m below the seafloor, and no obvious BSR was found below the hydrate. Hydrate existed in argillaceous siltstones and sandstones as nodules, and the saturation value were between 32% and 65%. Hydrate is distributed in the deeper layer 189 m to 226 m below the seafloor. Hydrate occurs in mud in dispersive and vein-like forms, and the saturation values are 24% to 36% (Zhang et al., 2014b; Wang, 2016; Zhang et al., 2017). A geochronological analysis of gas hydrate in this area shows that the shallow gas hydrate at Site W16 formed between 0.063 and 0.107 Ma, and the lower gas hydrate formed between 0.78 and 0.357 Ma (Zhang et al., 2017).

Combined with the historical variations of the GHSZ at Site W16, the hydrate accumulation model of a multilayer hydrate model due to the thickness change of the GHSZ at Site W16 is proposed (Figure 12). From 0.78 to 0.357 Ma, biogenic gas migrated to the GHSZ along faults, mud volcanoes and other channels and formed NGHs and BSRs (Figure 12A). After hydrate formation, the thickness of the GHSZ became thicker due to the decrease in the geothermal gradient, deeper seawater depth and lower BWT. Meanwhile, due to formation subsidence and deposition of new strata, the relative relationship between the GHSZ and formation changed, and the depth of hydrate occurrence became deeper (Figure 12B). During the period from 0.357 to 0.107 Ma, the thickness of the GHSZ first thickened, then became thinner, and then thickened due to the decrease, increase, and decrease in the BWT. However, the gas hydrate formed in the early stage was still located in the GHSZ (Figure 12C). Due to the decrease in the geothermal gradient and BWT, the thickness of the GHSZ became thinner, reaching to 214.70 m. At this time, the biogas generated by hydrocarbon source stokes migrated to the GHSZ along faults, mud volcanoes and other channels to generate new gas hydrates. If the free gas content in the lower part of the hydrate is high and the properties of the hydrate reservoir and underlying layer are different, a new BSR may also be formed. Otherwise, there may be no obvious BSR in the lower part of the hydrate (Figure 12D).

The above analysis shows that the thickening, thinning and thickening process of the GHSZ is closely related to the dynamic accumulation processes of gas hydrate decomposition, migration, accumulation and dissipation due to changes in external conditions, such as the geothermal gradient and seawater depth. By understanding the processes of the GHSZ, the combination of hydrate formation time and geologic time, the gas source, the migration channel coupling relationship of the GHSZ, etc., which help in clarifying the dynamic accumulation processes of gas hydrate and to further understanding the hydrate and free gas, the spatial distribution pattern of BSRs, hydrates and corresponding relationship with the BSR is of great significance.

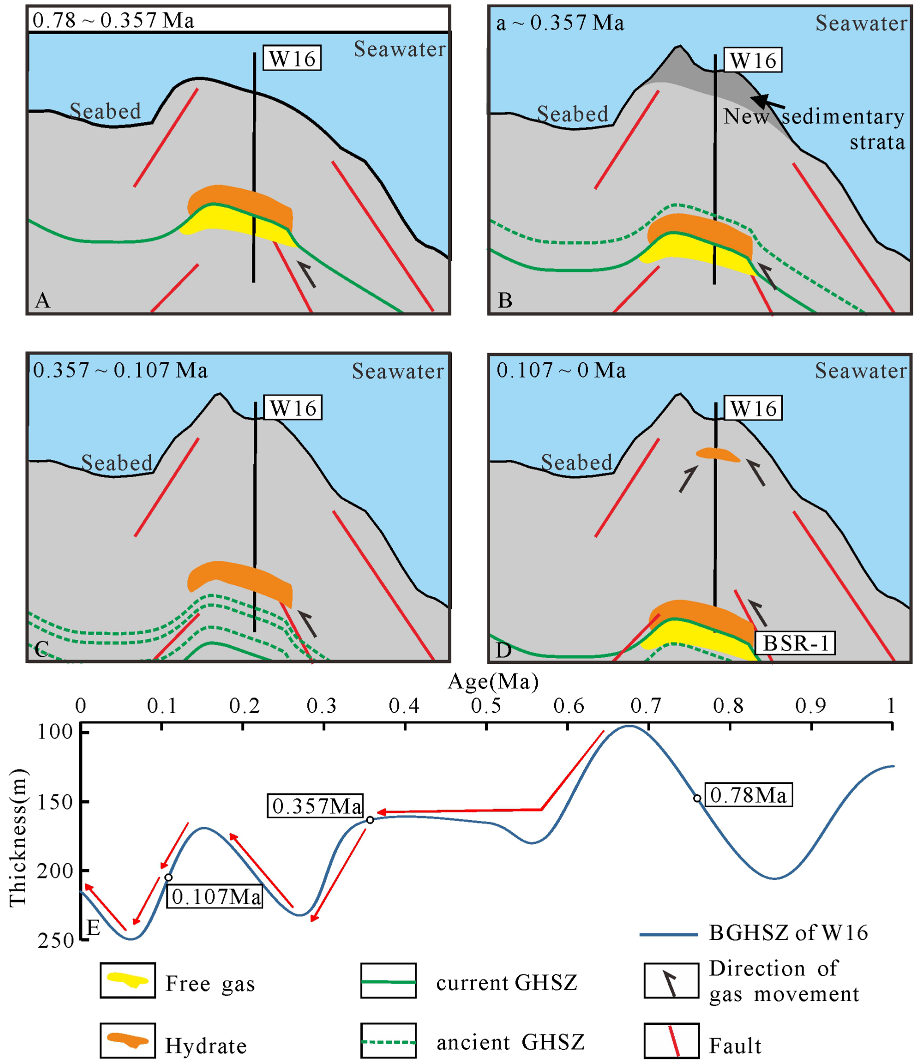

FIGURE 12
(A–D) Hydrate accumulation in a multilayer hydrate model due to thickness change in the GHSZ at Site W16. **(E)** Thickness variation in the GHSZ at W16 since 1 Ma.

6 Conclusions

Based on the variations in seawater depth, BWT, geothermal gradient and other parameters in the Dongsha region, Taixinan Basin, South China Sea, the thickness variations of the GHSZ in the Dongsha region are studied, and two hydrate accumulation models of gas hydrate related to the thickness changes of the GHSZ are discussed.

1. During the period of 10 to 5.11 Ma, the thickness of the GHSZ in the study area was thin, with values ranging from 0 m to 100 m. The higher BWT was the key factor leading to the thinner thickness of the 10-5.11 Ma GHSZ. From 5.11 to 0 Ma, the GHSZ generally showed a trend of gradually thickening. However, due to the changes in the seawater depth, BWT, geothermal gradient and other factors, several fluctuations in thickness occurred. The decrease in the BWT was the key factor leading to GHSZ thickening during the period of 5.11 to 0 Ma. The thickness of the GHSZ reached a maximum at approximately 0.07 Ma, with values ranging from 125 m to 470 m. The thicknesses of the GHSZ are between 110 m and 415 m in the Dongsha region at present. The thickness of the GHSZ

in the northeastern and northwestern regions is the thinnest. The present spatial distribution features of the GHSZ in the deep canyon area are thicker, with thicknesses generally between 225 m and 415 m, while the GHSZ in other areas is thinner, with thicknesses between 110 m and 225 m.

2. Two hydrate dynamic accumulation models related to the variation in the GHSZ in the Dongsha region, northern SCS. The first hydrate accumulation model is a double BSRs model that shows the formation as due to the thickness change in the GHSZ. The thinning of the GHSZ leads to the migration of the early hydrate and BSR out of the GHSZ to form the residual BSR in the lower part, and there is no hydrate development above the BSR. The gas in the late migration to the new GHSZ reaccumulates hydrate and forms a new BSR. The second hydrate accumulation model is a multilayer hydrate model, with single or multiple BSRs due to the general change in the thickness of the GHSZ.

Data availability statement

The original contributions presented in the study are included in the article material, further inquiries can be directed to the corresponding author.

Author contributions

YS: Writing—review and editing, Visualization. YL: Make important revisions to the paper, Investigation, Supervision. LZ: Investigation, Supervision. MC: Conceptualization, Visualization, Investigation. LM: Make important revisions to the paper, Investigation. CL: Methodology, Investigation. NL: Formal analysis, Resources. All authors contributed to the article and approved the submitted version.

Acknowledgments

This study was supported by the Key Research Program of the Institute of Geology and Geophysics, CAS (IGGCAS-201903), National Natural Science Foundation of China (42030808), Strategic priority Research Program of the Chinese Academy of Sciences (XDA14010202). The authors would like to thank Professor D. Oppo and two reviewer for their constructive comments and suggestions.

Conflict of interest

The authors declare that the research was conducted in the absence of any commercial or financial relationships that could be construed as a potential conflict of interest.

Publisher's note

References

Bangs, N. L. B., Musgrave, R. J., and Tréhu, A. M. (2005). Upward shifts in the southern hydrate ridge gas hydrate stability zone following postglacial warming, offshore Oregon. *J. Geophys. Res.* 110 (3), 1–13. doi: 10.1029/2004JB003293

Bishnoi, P. R., and Dholabhai, P. D. (1999). Equilibrium comditions for hydrate formation for a ternary mixture of methane, propane and carbon dioxide, and a natural gas mixture in the presence of electrolytes and methanol. *Fluid Phase Equilibria* 158-160 (5), 821–827. doi: 10.1016/S0378-3812(99)00103-X

Burwicz, E., Reichel, T., Wallmann, K., Rottke, W., Haeckel, M., and Hensen, C.. (2017). 3-d basin-scale reconstruction of natural gas hydrate system of the green canyon, gulf of Mexico. *Geochemistry Geophysics Geosystems* 18 (5), 1959–1985. doi: 10.1002/2017GC006876

Collett, T. S. (2009). "Gas hydrate petroleum systems in marine and Arctic permafrost environments," in *Unconventional energy resources: Making the unconventional conventional: 29th annual GCSSEPM proceedings* (Houston, Texas: Gulf Coast Section of the Society of Economic Paleontologists and Mineralogists Foundation), 6–30. doi: 10.5724/gcs.09.29.0006

Dickens, G. R., and Quinby-Hunt, M. S. (1994). Methane hydrate stability in sea water. *Geophysical Res. Lett.* 21 (19), 2115–2118. doi: 10.1029/94GL01858

Foucher, J. P., Nouzé, H., and Henry, P. (2002). Observation and tentative interpretation of a double BSR on the nankai slope. *Mar. Geology* 187, 161–175. doi: 10.1016/S0025-3227(02)00264-5

Gong, J. L., Sun, X. M., Lin, Z. Y., Lu, H. F., and Lu, Y. J. (2017). Geochemical and microbial characters of sediment from the gas hydrate area in the taixinan basin, south China Sea. *Acta Oceanol. Sin.* 36 (9), 52–64. doi: 10.1007/s13131-017-1111-2

Gong, Y. H., Wu, S. G., Zhang, G. X., Wang, H. B., Liang, J. Q., Guo, Y. Q., et al. (2008). Relation between gas hydrate and geologic structures in dongsha islands sea area of south China Sea. *Mar. Geology& Quaternary Geology* 28 (1), 99–104. doi: 10.16562/j.cnki.0256-1492.2008.01.013

Haacke, R. R., Westbrook, G. K., and Hyndman, R. D. (2007). Gas hydrate, fluid flow and free gas: Formation of the bottom-simulating reflector. *Earth Planetary Sci. Letters.* 261, 407–420. doi: 10.1016/j.epsl.2007.07.008

He, J. X., and Liu, H. L. (2008). *Petroleum geology and prospecting area of NSCS. 1st ed.* (Beijing: Petropub), 34–67.

He, J. X., Yan, W., Zhu, Y. H., Zhang, W., Gong, F. X., Liu, S. L., et al. (2013). Bio-genetic and sub-biogenetic gas resource potential and genetic types of natural gas hydrates in the northern marginal basins of south China Sea. *Natural Gas industry.* 33 (6), 121–134. doi: 10.3787/j.issn.1000-0976.2013.06.023

Horozal, S., Bahk, J. J., Urgeles, R., Kim, G. Y., Cukur, D., Kim, S. P., et al. (2017). Mapping gas hydrate and fluid flow indicators and modeling gas hydrate stability zone (GHSZ) in the ulleung basin, East (Japan) Sea: Potential linkage between the occurrence of mass failures and gas hydrate dissociation. *Mar. Petroleum Geology* 80, 171–191. doi: 10.1016/j.marpetgeo.2016.12.001

Hu, S. B., Long, Z. L., Zhu, J. Z., Hu, D., Huang, Y. P., Shi, Y. L., et al. (2019). Characteristics of geothermal field and the tectonic-thermal evolution in pearl river mouth basin. *Acta Petrol. Sin.* 40 (S1), 178–187. doi: 10.7623/syxb2019S1015

Kroeger, K. F., Crutchley, G. J., Kellett, R., and Barnes, P.M. (2019). A 3-d model of gas generation, migration, and gas hydrate formation at a young convergent margin (Hikurangi margin, new Zealand). *Geochemistry Geophysics Geosystems* 20 (11), 5126–5147. doi: 10.1029/2019GC008275

Kvenvolden, K. A. (1993). Gas hydrates–geological perspective and global change. *Rev. Geophysics* 31 (2), 173–187. doi: 10.1029/93RG00268

Lear, C. H., Coxall, H. K., Foster, G. L., Lunt, D. J., Mawbey, E. M., Rosenthal, Y., et al. (2015). Neogene ice volume and ocean temperatures: Insights from infaunal foraminiferal Mg/Ca paleothermometry. *Paleoceanography.* 30, 1437–1454. doi: 10.1002/2015PA002833

Lei, Y. H., Song, Y. R., Zhang, L. K., Miao, L. C., Cheng, M., and Liu, N. G. (2021). Research progress and development direction of reservoir-forming system of marine gas hydrates. *Acta Petrolei Sin.* 42 (06), 801–820. doi: 10.7623/syxb202106009

Li, Y., Fang, Y. X., Zhou, Q. Z., Xu, X. P., Liu, J. Z., Zhou, Y. G., et al. (2021). Geochemical insights into contribution of petroleum hydrocarbons to the formation of hydrates in the taixinan basin, the south China Sea. *Geosci. Frontiers* 12, 100974. doi: 10.1016/j.gsf.2020.03.006

Li, L., Liu, H. J., Zhang, X., Lei, X. H., and Sha, Z. B. (2015). BSRs, estimated heat flow, hydrate-related gas volume and their implications for methane seepage and gas hydrate in the dongsha region, northern south China Sea. *Mar. Petroleum Geology.* 67, 785–794. doi: 10.1016/j.marpetgeo.2015.07.008

Liu, P., Zhang, X. T., Du, J. Y., Cheng, W., Tao, W. F., and Tao, Y. (2018). Tectonic-thermal evolution process and the petroleum geological significance of relatively low geothermal gradient in a rift basin: An example from xijiang main sag in pearl river mouth basin. *Geological Sci. Technol. Information.* 37 (2), 146–156. doi: 10.19509/j.cnki.dzkq.2018.0221

Li, Y., Zhou, Q. Z., Xu, X. P., Liu, J. Z., Zhou, G. Y., Fang, Y. X., et al. (2020). Porewater geochemical and lipid biomarker signatures for anaerobic methane oxidation in the hydrate-bearing system from the taixinan basin, the south China Sea. *J. Asian Earth Sci.* 203, 104559. doi: 10.1016/j.jseaes.2020.104559

Majumdar, U., Cook, A. E., Shedd, W., and Frye, M. (2016). The connection between natural gas hydrate and bottom- simulating reflectors. *Geophysical Res. Lett.* 43 (13), 7044–7051. doi: 10.1002/2016GL069443

Max, M. D. (1990). Gas hydrates and acoustically laminated sediments: potential environmental cause of nomalously low acoustic bottom loss in deep ocean sediments. *U.S. Naval Res. Lab. Rep.* 9235, 68. Available at: https://apps.dtic.mil/sti/pdfs/ADA218418.pdf.

Miles, P. R. (1995). Potential distribution of methane hydrate beneath the European continental margins. *Geophysical Res. Letters.* 20 (23), 3179–3182. doi: 10.1029/95GL03013

Milkov, A. V., and Sassen, R. (2003). Two-dimensional modeling of gas hydrate decomposition in the northwestern gulf of Mexico: significance to global change assessment. *Global Planetary Change.* 36, 31–46. doi: 10.1016/S0921-8181(02)00162-5

Pang, X., Chen, C. M., Peng, D. J., Zhu, M., Shu, Y., He, M., et al. (2007). Sequence stratigraphy of deep-water fan system of pearl river, south China Sea. *Earth Sci. Frontiers.* 14 (1), 220–229. doi: 10.1016/S1872-5791(07)60010-4

Paull, C. K., Ussler, W.III, and Dillon, W. P. (1991). Is the extent of glaciation limited by marine gas-hydrates? *Geophysical Res. Lett.* 18, 432–434. doi: 10.1029/91GL00351

Pecher, I. A., Villinger, H., Kaul, N., Crutchley, G. J., Mountjoy, J. J., Huhn, K., et al. (2017). A fluid pulse on the hikurangi subduction margin: Evidence from a heat flux transect across the upper limit of gas hydrate stability. *Geophysical Res. Lett.* 44 (12), 385–395. doi: 10.1002/2017GL076368

Piñero, E., Hensen, C., Haeckel, M., Wallmann, K., Rottke, W., Fuchs, T., et al. (2014). "Gas hydrate accumulations at the Alaska north sloge: total assessment based on 3D petroleum system modeling," in *Proceedings of the 8th international conference on gas hydrate (ICGH8-2014)* (Beijing, China: China Geological Survey and Chinese Academy of Sciences).

Rempel, A. W., and Buffett, B. A. (1997). Formation and accumulation of gas hydrate in porous media. *J. Geophysical Res.* 102, 151–164. doi: 10.1029/97JB00392

Sha, Z. B., Liang, J. Q., Su, P. B., Zhang, G. X., Lu, J. A., and Wang, J. L. (2015a). Natural gas hydrate accumulation elements and drilling results analysis in the eastern part of the pearl river mouth basin. *Earth Sci. Front.* 22 (06), 125–135. doi: 10.13745/j.esf.2015.06.009

Sha, Z. B., Liang, J., Zhang, G. X., Yang, S. X., Lu, J. A., Zhang, Z. J., et al. (2015b). A seepage gas hydrate system in northern south China Sea: seismic and well log interpretations. *Mar. Geology* 366, 69–78. doi: 10.1016/j.margeo.2015.04.006

Sha, Z. B., Xu, Z. Q., Fu, S. Y., Liang, J. Q., Zhang, W., Su, P. B., et al. (2019). Gas sources and its implications for hydrate accumulation in the eastern pearl river mouth basin. *Mar. Geology& Quaternary Geology* 39 (4), 116–125. doi: 10.16562/j.cnki.0256-1492.2019010902

Sloan, E. D., and Koh, C. A. (2008). *Clathrate hydrates of the natural gases. 3rd ed* (Boca Raton, FL: CRC Press).

Song, Y. R., Lei, Y. H., Zhang, L. K., Cheng, M., Li, C., and Liu, N. G. (2022). Spatial-temporal evolution of the gas hydrate stability zone and accumulation patterns of double BSRs formation in the shenhu area. *Front. Earth Sci.* 10. doi: 10.3389/feart.2022.880933

Wang, Y. L. (2016). *Accumulation conditions and distribution controlling factors of natural gas hydrate in dongsha prospect* (Beijing: China University of Petroleum). doi: 10.3969/j.issn.1006-7175.2013.11.001

Wang, H., Crutchley, G. J., and Stern, T. (2017a). Gas hydrate formation in compressional, extensional and un-faulted structural settings-examples from new zealand's hikurangi margin. *Mar. Petroleum Geology* 88, 69–80. doi: 10.1016/j.marpetgeo.2017.08.001

Wang, J. J., and Lau, H. C. (2020). Thickness of gas hydrate stability zone in permafrost and marine gas hydrate deposits: Analysis and implications. *Fuel.* 282, 118784. doi: 10.1016/j.fuel.2020.118784

Wang, Y. M., Liu, S. W., Hao, F. F., Zhao, Y. L., and Hao, C. Y. (2017b). Geothermal investigation of the thickness of gas hydrate stability zone in the north continental margin of the south China Sea. *Acta Oceanol. Sin.* 36 (4), 72–79. doi: 10.1007/s13131-017-1014-2

Wang, C., Lu, J. H., Zhu, R., and Yu, W. T. (2013). *Validation on the applicability of TEOS-10 equation in the SCS based on WOA09 thermohaline data* Vol. 19 (Water Conservancy Science and Technology and Economy), 9 (11), 1–6.

Xiao, K., Zou, C. C., Yang, Y. X., Zhang, H., Li, H. X., and Qin, Z. (2020). A preliminary study of the gas hydrate stability zone in a gas hydrate potential region of China. *Energy Sci. &Engineering.* 8 (4), 1080–1091. doi: 10.1002/ese3.569

Yi, H., Zhong, G. J., and Ma, J. F. (2007). Fracture characteristics and basin evolution of the taixinan basin in Cenozoic. *Petroleum Geology Experiment* 29 (6), 560–564. doi: 10.3969/j.issn.1001-6112.2007.06.006

Zander, T., Haeckel, M., Berndt, C., Chi, W., Klaucke, I., Bialas, J., et al. (2017). On the origin of multiple BSRs in the Danube deep-sea fan, black Sea. *Earth Planetary Sci. Lett.* 462, 15–25. doi: 10.1016/j.epsl.2017.01.006

Zhang, W. (2016). *Research on the development and evolution of mud Diapir/Mud volcano and their relationship with migration and accumulation of petroleum and natural gas-hydrate in major basins, northern south China Sea* (Guangzhou: University of Chinese Academy). doi: 10.3799/dqkx.2010.008

Zhang, G. X., Chen, F., Sha, Z. B., Liang, J. Q., Su, X., and Lu, H. F. (2017). The geological evolution process of natural gas hydrate reservoirs in the northeastern south China Sea. *Earth Sci. Front.* 24 (4), 015–023. doi: 10.13745/j.esf.yx.2016-12-27

Zhang, G. X., Liang, J. Q., Lu, J. A., Yang, S. X., Zhang, M., Holland, M., et al. (2015). Geological features, controlling factors and potential prospects of the gas hydrate occurrence in the east part of the pearl river mouth basin, south China Sea. *Mar. Petroleum Geology.* 67, 356–367. doi: 10.1016/j.marpetgeo.2015.05.021

Zhang, G. X., Liang, J. Q., Lu, J. A., Yang, S. X., Zhang, M., Su, X., et al. (2014b). Characteristics of natural gas hydrate reservoirs on the northeastern slop of the south China Sea. *Natural Gas Industry* 11 (34), 1–10. doi: 10.3787/j.issn.1000-0976.2014.11.001

Zhang, W., Liang, J. Q., Qiu, H. J., Deng, W., Meng, M. M., He, Y. L., et al. (2022). Double bottom simulating reflectors and tentative interpretation with implications for the dynamic accumulation of gas hydrates in the northern slope of the qiongdongnan basin, south China Sea. *J. Asian Earth Sci.* 229, 105151. doi: 10.1016/j.jseaes.2022.105151

Zhang, W., Liang, J. Q., Wan, Z. F., Su, P. B., Huang, W., Wang, L. F., et al. (2020). Dynamic accumulation of gas hydrates associated with the channel-levee system in the shenhu area, northern south China Sea. *Mar. Petroleum Geology.* 117, 104354. doi: 10.1016/j.marpetgeo.2020.104354

Zhang, G. X., Yang, S. X., Zhang, M., Liang, J. Q., Lu, J. A., Holland, M., et al. (2014a). *GMGS2 expedition investigates rich and complex gas hydrate environment in the south China Sea* Vol. 14 (NETL), 1–5. Available at: https://www.netl.doe.gov/oil-gas/natural-gas-resources. Fire in the Ice (Methane Hydrate Newsletter).

Zhao, S. J., Wu, S. G., Shi, H. S., Dong, D. D., Chen, D. X., and Wang, Y. (2012). Structures and dynamic mechanism related to the dongsha movement at the northern margin of south China Sea. *Prog. Geophysics* 27 (03), 1008–1019. doi: 10.6038/j.issn.1004-2903.2012.03.022

Zhu, W. L. (2007). *Natural gas geology in the continental margin basin of the northern south China Sea* (Beijing: Petroleum Industry Press), 3–22. doi: 10.1021/bk-2007-0967.ap001

frontiers | Frontiers in Earth Science

TYPE Original Research
PUBLISHED 25 October 2022
DOI 10.3389/feart.2022.1029471

OPEN ACCESS

EDITED BY
Marzia Rovere,
Institute of Marine Sciences, Italy

REVIEWED BY
Dong Feng,
Shanghai Ocean University, China
Vitor Hugo Magalhaes,
Portuguese Institute for Sea and
Atmosphere (IPMA), Portugal

*CORRESPONDENCE
Claudio Argentino,
claudio.argentino@uit.no

SPECIALTY SECTION
This article was submitted to Marine Geoscience,
a section of the journal
Frontiers in Earth Science

RECEIVED 27 August 2022
ACCEPTED 07 October 2022
PUBLISHED 25 October 2022

CITATION
Argentino C, Lee A, Fallati L, Sahy D, Birgel D, Peckmann J, Bünz S and Panieri G (2022), Biogeochemistry and timing of methane-derived carbonate formation at Leirdjupet fault complex, SW Barents sea.
Front. Earth Sci. 10:1029471.
doi: 10.3389/feart.2022.1029471

Biogeochemistry and timing of methane-derived carbonate formation at Leirdjupet fault complex, SW Barents sea

Claudio Argentino[1]*, Amicia Lee[2], Luca Fallati[3], Diana Sahy[4], Daniel Birgel[5], Jörn Peckmann[5], Stefan Bünz[1] and Giuliana Panieri[1]

[1]CAGE—Centre for Arctic Gas Hydrate, Environment and Climate, Department of Geosciences, UiT The Arctic University of Norway, Tromsø, Norway, [2]Department of Geosciences, UiT The Arctic University of Norway, Tromsø, Norway, [3]Department of Earth and Environmental Sciences, University of Milano-Bicocca, Milano, Italy, [4]British Geological Survey, Nottingham, United Kingdom, [5]Center for Earth System Research and Sustainability, Institute for Geology, Universität Hamburg, Hamburg, Germany

The origin of modern seafloor methane emissions in the Barents Sea is tightly connected to the glacio-tectonic and oceanographic transformations following the last ice age. Those regional events induced geological structure re-activation and destabilization of gas hydrate reservoirs over large areas of the European continental margins, sustaining widespread fluid plumbing systems. Despite the increasing number of new active seep discoveries, their accurate geochronology and paleo-dynamic is still poorly resolved, thus hindering precise identification of triggering factors and mechanisms controlling past and future seafloor emissions. Here, we report the distribution, petrographic (thin section, electron backscatter diffraction), isotopic ($\delta^{13}C$, $\delta^{18}O$) and lipid biomarker composition of methane-derived carbonates collected from Leirdjupet Fault Complex, SW Barents Sea, at 300 m depth during an ROV survey in 2021. Carbonates are located inside a 120 x 220 m elongated pockmark and form <10 m^2 bodies protruding for about 2 m above the adjacent seafloor. Microstructural analyses of vein-filling cements showed the occurrence of three–five generations of isopachous aragonitic cement separated by dissolution surfaces indicative of intermittent oxidizing conditions. The integration of phase-specific isotopic analysis and U/Th dating showed $\delta^{13}C$ values between −28.6‰ to −10.1‰ and $\delta^{18}O$ between 4.6‰ and 5.3‰, enabling us to track carbonate mineral precipitation over the last ~8 ka. Lipid biomarkers and their compound-specific $\delta^{13}C$ analysis in the bulk carbonate revealed the presence of anaerobic methanotrophic archaea of the ANME-2 clade associated with sulfate-reducing bacteria of the Seep-SRB1 clade, as well as traces of petroleum. Our results indicate that methane and petroleum seepage in this area followed a similar evolution as in other southernmost Barents Sea sites controlled by the asynchronous deglaciation of the Barents Sea shelf, and that methane-derived carbonate precipitation is still an active process at many Arctic locations.

KEYWORDS

Aom (anaerobic oxidation of methane), authigenic carbonate, cold seep, lipid biomarkers, U/Th, Leirdjupet fault complex, Barents Sea

Introduction

Natural seafloor methane emissions, known as cold seeps, are common features along continental margins (Phrampus et al., 2020), where vast amounts of methane, trapped in deep subsurface hydrocarbon reservoirs or shallower gas hydrates, migrate through faults or sediments with low permeability pathways toward the surface (Judd and Hovland, 2007; Suess, 2014). Cold seeps are inhabited by peculiar chemosynthetic communities (Sahling et al., 2002; Foucher et al., 2007; Fischer et al., 2012; Levin et al., 2016), including bacterial mats, tubeworms, and bivalves, which are gaining their energy by oxidation of reduced compounds (HS^-, CH_4) at an otherwise nutrient-poor seafloor (Levin et al., 2016). Despite the fact that cold seeps are widespread along continental margins, they only provide a minor contribution of the global methane emissions, especially when compared to natural land sources (Weber et al., 2019). In fact, ca. 90% of the methane seeping from marine sediments (Hinrichs and Boetius, 2002; Reeburgh, 2007; Knittel and Boetius, 2009) is microbially consumed close to the seafloor by the anaerobic oxidation of methane (AOM) consortium (Boetius et al., 2000). The remaining small fraction of methane escaping the sedimentary bio-filter is almost entirely oxidized by aerobic methane-oxidizing bacteria in the water-column before reaching the sea surface (McGinnis et al., 2006; Sparrow et al., 2018; Jansson et al., 2019). Methane-derived carbon is sequestered into authigenic carbonates precipitating within the sediment due to an alkalinity increase produced by the AOM consortium ($CH_4 + SO_4^{2-} \rightarrow HCO_3^- + HS^- + H_2O$). These carbonates, also known as methane-derived authigenic carbonates (MDAC), are invaluable tools in cold-seep research as they record the fluid composition in which they form and have been extensively used as benchmarks in the development of new geochemical proxies for AOM (Feng et al., 2016; Smrzka et al., 2016; Crémière et al., 2020; Yao et al., 2020) and redox conditions (Himmler et al., 2010; Zwicker et al., 2018; Bayon et al., 2020; Smrzka et al., 2020). These studies allow to provide more accurate reconstructions of sediment biogeochemistry and seepage activity. The $\delta^{13}C$ composition of seep carbonates typically ranges from −60‰ to −30‰ (Judd and Hovland, 2007), mainly reflecting the incorporation of dissolved inorganic carbon (DIC) released by AOM ($\delta^{13}C_{DIC} < -30$‰) and organic matter mineralization ($\delta^{13}C_{DIC} > -30$‰) (Meyers, 1994; Swart, 2015) superimposed by the background seawater DIC signal (~0‰). The $\delta^{13}C$ value of the carbonate tends to be more negative (close to CH_4 composition, generally << −30‰), the higher the methane flux and AOM rate. However, oxidation of deeper, thermogenic gas or hydrocarbons have been shown to result in the precipitation of carbonates with heavier $\delta^{13}C$ signatures (Roberts and Feng, 2013). Generally, the $\delta^{18}O$ values of methane-derived carbonates depend on the temperature of precipitation and carbonate mineralogy, but gas hydrate derived water is ^{18}O-enriched (Davidson et al., 1983) and can lead to anomalously heavy carbonate $\delta^{18}O$ signatures, which are not in isotopic equilibrium with seawater (Bohrmann et al., 1998; Teichert et al., 2005; Bohrmann and Torres, 2006). Such conditions have been reported from many modern cold seeps from gas hydrate bearing areas, e.g. Cascadia Margin (Bohrmann et al., 1998, 2002; Greinert et al., 2013), Gulf of Cadiz (Magalhães et al., 2012), Gulf of Mexico (Roberts and Feng, 2013), Congo Fan (Feng et al., 2010a), Barents Sea (Crémière et al., 2016; Argentino et al., 2021; Yao et al., 2021); the $\delta^{18}O$ proxy has been applied to fossil seep carbonates as well (Pierre and Rouchy, 2004; Campbell, 2006; Campbell et al., 2008; Argentino et al., 2019; Bojanowski et al., 2021). Owing to their microbial origin, seep carbonates incorporate and harbor typical communities of methane-oxidizing archaea and sulfate-reducing bacteria (Marlow et al., 2014). Eventually, the prokaryotes involved in AOM leave behind detectable organic traces in the lipid biomarker inventory of the rock that can be preserved for hundreds of millions of years in the sedimentary record (Peckmann and Thiel, 2004; Birgel and Peckmann, 2008) providing insights into AOM dynamics and microbial ecology (Peckmann et al., 2009; Kim and Zhang, 2022). Finally, the timing of carbonate formation at modern seeps (<500 ka BP) can be determined with a precision in the order of $\pm 10^2$–10^3 y *via* Uranium/Thorium (U/Th) dating (Teichert et al., 2003; Feng et al., 2010b; Himmler et al., 2019). The absolute dating of seep carbonates is essential to reconstruct the high-resolution history of seepage, enabling geoscientists to determine the evolution of seepage over critical climatic phases of Earth history, which can help predict future global warming scenarios.

Cold seep research conducted over the years in the Barents Sea (Crémière et al., 2016; Andreassen et al., 2017; Serov et al., 2017; Yao et al., 2020) and other Arctic paleo-glaciated margins (Portnov et al., 2016; Schneider et al., 2018; Himmler et al., 2019; Kravchishina et al., 2021) revealed episodes of massive seafloor gas seepage following deglaciations. These events are highlighting the role of grounded ice sheets as "capacitors" facilitating the storage of methane into sub-glacial gas hydrates and inducing large-scale release upon ice retreat. Arctic paleo-systems are considered good analogs to modern western Antarctica and Greenland settings (Elverhøi et al., 2002; Esteves et al., 2017), where ongoing and projected ice-sheet retreat might lead to the development of widespread methane seeps sourced by underlying hydrocarbon reservoirs and gas hydrates. Consequently, understanding the timing and dynamics of

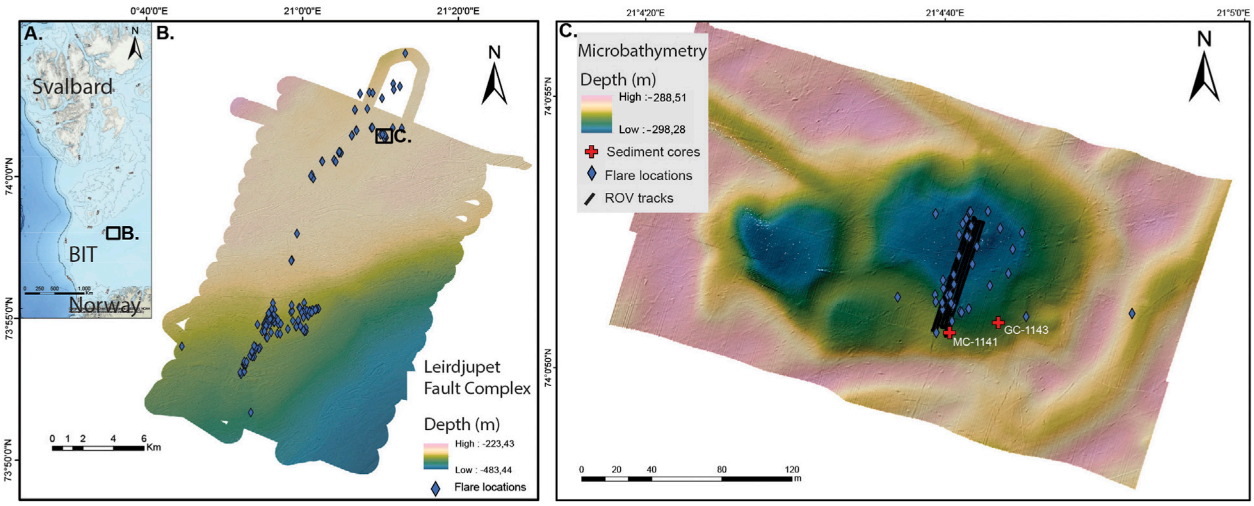

FIGURE 1
(A) Bathymetric map of the Western Barents Sea showing the location of the study area (box). **(B)** Distribution of gas flares (polygons) at Leirdjupet Fault Complex and location of the pockmark site (box). **(C)** Microbathymetry of the pockmark site showing ROV tracks used for the photogrammetry survey in the methane-derived carbonate area, location of flares and two sediment cores previously reported in Argentino et al. (2021). BIT = Bear Island Trough. This color scale is accessible for people with color-vision deficiencies (Crameri et al., 2020).

seepage throughout deglaciations in paleo-glaciated margins is essential to better predict future scenarios and greenhouse fluxes into the hydrosphere and atmosphere at modern glaciated margins. Extensive research conducted in the last decade was undertaken to map the distribution of seeps in the western Barents Sea, leading to the discovery of widespread methane emissions mostly occurring in its southern sector, but especially associated with major hydrocarbon fields of economic relevance (Chand et al., 2012; Crémière et al., 2016, 2018). Subsurface seismic features consisting of fluid/gas chimneys, pipes, faults, buried pockmarks and gas-hydrate-related bottom-simulating reflectors (BSR) provided evidence for a well-developed fluid-flow system fed by microbial and thermogenic gas leakage from Mesozoic reservoirs (Vadakkepuliyambatta et al., 2013, 2017). Methane seepage-derived carbonates collected from the seafloor at some active locations (Crémière et al., 2016, 2018) were essential to resolve the geochronology of seepage in the SW Barents Sea and correlate episodes of major gas emissions with deglacial history of the Barents Sea Ice Sheet. Methane seeps have been recently discovered and reported from other sectors of the SW Barents Sea (Andreassen et al., 2017; Waage et al., 2020; Argentino et al., 2021). Their temporal constraints on when the major seepage activity was remains poorly resolved, thus hindering a more precise identification of the triggering factors and mechanisms controlling the evolution of seafloor emissions throughout deglaciation. Filling this gap would allow us to establish a comprehensive reconstruction of the spatial and temporal relationships between ice-sheet retreat and seafloor methane emissions along the whole western Barents Sea, connecting the southernmost sites close to the Norwegian mainland (Sauer et al., 2015; Crémière et al., 2016, 2018) to the seeps located in the NW Barents Sea (Hong et al., 2017) and W Svalbard (Panieri et al., 2017; Himmler et al., 2019), providing the means to interpret the evolution of modern glaciated counterparts affected by global warming.

We investigated carbonate crusts collected during a survey with a remotely operated underwater vehicle (ROV) in 2021 at Leirdjupet Fault Complex, SW Barents Sea (Figure 1A). Carbonates are exposed at the seafloor inside a pockmark feature, located on an active ~30 km long fluid seepage system (Argentino et al., 2021) (Figure 1B). ROV multibeam echosounder surveys enabled us to obtain micro-bathymetry of the seafloor of the pockmark area (Figure 1C), and the ROV photogrammetry allowed us to generate high-resolution orthomosaic and 3D models of carbonate outcrops. We conducted petrographic and microstructural (Electron Backscatter Diffraction) investigations of rock samples and then selected pure aragonite cements for phase-specific isotopic analysis $\delta^{13}C$, $\delta^{18}O$ and U/Th dating. Lipid biomarkers and their compound-specific $\delta^{13}C$ values were used to characterize microbial communities preserved in authigenic carbonates for the first time in this area to provide deeper insights into AOM dynamics. This study provides the first absolute temporal constraints on the inception and evolution of seepage at Leirdjupet Fault Complex, which may be used as key site to extrapolate the relative magnitude and timing of past methane emissions along the whole western Barents Sea margin by correlation.

Study area

The Leirdjupet Fault Complex (LFC) is located on a transverse shelf trough named Bear Island Trough, in the SW Barents Sea (Figure 1A). The fault complex was first visited by CAGE in 2017 for hydroacoustic exploration and at that time methane seepage was detected along a ~35 km transect striking NE-SW making LFC one of the most active areas in the SW Barents Sea (Figure 1A). Water depths within the explored area range from 220 m to 400 m and the seafloor morphology is marked by ploughmarks and moraines related to the glacial dynamics of the Late Weichselian Barents Sea Ice Sheet, which covered the Bear Island Trough until ~15 ka BP (Winsborrow et al., 2010; Patton et al., 2017). In 2018, seafloor observations using a tow-camera-multicorer system allowed to describe and map the habitat distributions and their relationships with subsurface methane fluxes (Argentino et al., 2022). Active seeps are characterized by white patches of bacterial mats surrounded by frenulate siboglinids thriving on methane and AOM-related hydrogen. The analysis of fluids emitted at the seafloor indicated a mix of thermogenic and microbial gas derived from Mesozoic reservoirs and shallower Tertiary deposits, sustaining the formation of shallow gas hydrate reservoirs during ice ages and eventually destabilized by late deglaciation (Argentino et al., 2021). Recently, the AKMA-CAGE21-1 expedition visited the LFC area on R/V Kronprins Haakon in 2021 with the ROV Ægir6000 for high-resolution seafloor imaging and targeted samplings of seabed features, i.e. sediments, rocks. The carbonate samples investigated for this study were collected from an elongated 120 x 220 m seafloor depression at 300 m depth previously interpreted as a pockmark (Argentino et al., 2021) and located in the northern sector of LFC (Figure 1B). The pockmark is composed of three smaller seafloor depressions, the largest of which is located to the north-eastern corner and is currently the most active in terms of the number of methane flares (Figure 1C), and for that reason it was selected for ROV photogrammetry and samplings.

Methods

Seafloor imagery acquisition and processing

ROV Ægir6000, equipped with a dedicated photogrammetry sledge, explored the most active part of the pockmark. This setting allowed to acquire high-definition videos parallel to the seafloor. The ROV, moving at a constant speed of 0.5 knots, followed four predefined 70 m long transects with an altitude of 2 m to guarantee optimal lateral overlap between adjacent tracks. A photogram every 2 s was automatically extracted from the nadiral camera's videos. Then, the images were processed in Agisoft Metashape®, following a well-established photogrammetry workflow (Fallati et al., 2020; Montalbetti et al., 2022). As final outputs a 3D mesh, orthomosaics and Digital Terrain Models (DTMs) at high-resolution were obtained, allowing us to get detailed morphometric parameters of the carbonate outcrops at a cm-scale resolution.

Carbonate sampling

Methane-derived carbonate CAGE21-1-KH-05_Dive19-CarC-05, hereafter named CarC-05, was collected from a carbonate slab exposed at the seafloor using the ROV manipulating arm. On deck, the sample was subsampled for macrofauna, washed with freshwater to remove salt residues and stored at 4°C. The carbonate rock was sawed onshore at UiT-The Arctic University of Norway and split into rock chips for thin section preparation. Thin sections CarC-05-A and CarC-05-C were analyzed *via* optical microscopy for carbonate microfacies description and CarC-05-C was selected for mineralogical characterization *via* scanning electron microscopy—Electron Backscatter Diffraction (EBSD). A total of three generations of cavity-filling cements were sampled from CarC-05-1C using a hand-held microdrill and subjected to U/Th dating and $\delta^{13}C$ and $\delta^{18}O$ analyses. The subsamples are named CarC-05-C-*1*, CarC-05-C-*2* and CarC-05-C-*3*. Lipid biomarker analysis were conducted on bulk rock material of CarC-05. In this study we also report the isotopic composition of cm-sized carbonate concretions found in gravity core CAGE18-4-HH-GC-1143 at 4 cm below the seafloor (bsf) and multicore CAGE18-4-HH-MC-1141 at 18 cm and 26 cm bsf, collected in 2018 from the same pockmark (Argentino et al., 2021), and hereafter named GC-1143, MC-1141a and MC-1141b.

Scanning electron microscopy—Electron backscatter diffraction (EBSD)

Crystallographic orientation data was collected *via* electron backscatter diffraction (EBSD) with an Oxford Instruments Nordlys S detector on a Zeiss Merlin SEM at The Arctic University of Norway in Tromsø. Crystallographic data were collected using 20 kV accelerating voltage, 70° specimen tilt angle and 22–26 mm working distance. Detailed maps were measured with a step size of 8–15 µm and seven bands detected. Oxford Instruments Aztec software was used for data acquisition and initial data processing, MTEX v.5.7.0 open source software toolbox (Bachmann et al., 2010) for MATLAB was used for enhanced data processing and pole figure plotting. Individual crystal orientations with median absolute deviation (MAD) values >1.0 were removed.

Stable isotope geochemistry ($\delta^{13}C$, $\delta^{18}O$) and U/Th geochronology

The stable isotope composition ($\delta^{13}C$, $\delta^{18}O$) of carbonate samples was measured on a Thermo Scientific Gasbench II coupled to a Finnigan MAT 253 triple collector isotope ratio mass spectrometer at the Stable Isotope Lab-SIL of UiT, after reaction with anhydrous phosphoric acid for 3 h at 50°C. Data are reported in ‰ notation relative to Vienna Pee Dee belemnite (V-PDB). Analytical error was better than 0.1‰ (1SD) for both carbon and oxygen.

U/Th dating was conducted at the British Geological Survey's Geochronology and Tracers Facility, following the protocol outlined by Crémière et al. (2016). U and Th were measured on a Thermo Neptune Plus multicollector ICP-MS using a ^{236}U-^{229}Th isotopic tracer. Instrument parameters were monitored using CRM112a and IRMM3636 uranium and an in-house ^{229}Th-^{230}Th-^{232}Th reference solution as bracketing standards. A correction was applied to account for the presence of intial deterital/hydrogenous ^{230}Th based on values reported by Crémière et al. (2016) from MDAC-free background sediment samples from a similar water depth range as covered in this study. U/Th activity ratios are reported in Supplementary Table S1.

Lipid biomarkers and compound-specific isotope analysis ($\delta^{13}C$)

125 g of bulk material from CarC-01 was crushed, then decalcified by slowly pouring 10% HCl onto the sample, until 80 wt% of the sample was dissolved. The material collected after decalcification was saponified with 6% KOH in methanol to release bound fatty acids and extracted by using dichloromethane/methanol (3:1 volume). Prior to saponification and extraction, 200 µL of five α (H)-cholestane, 1-nonadecanol, and 2-methyl-octadecanoic acid were added as internal standards. The combined total lipid extracts (TLE) were then separated into maltenes (*n*-hexane soluble) and asphaltenes (dichloromethane). The maltenes were further separated with a NH_2-modified silica gel column into four fractions with of increasing polarity: hydrocarbons (fraction 1), ketones/esters (fraction 2), alcohols (fraction 3) and carboxylic acids (fraction 4). Fractions three and four were derivatized using N,N-*bis* trimethylsilyltriflour(o)acetamide(s) (BSTFA) and boron trifluoride (BF3)/MeOH, respectively and analyzed *via* gas chromatography-mass spectrometry (GC-MS) using an Agilent 7890 A GC system coupled to an Agilent 5975C inert MSD mass spectrometer at the University of Hamburg. Compound-specific stable carbon isotope analyses were determined using a Trace GC Ultra linked *via* a Thermo Finnigan Combustion interface with a Finnigan MAT 252 isotope mass spectrometer (GC-IRMS) at MARUM, University of Bremen. The GC-MS was equipped with a Thermo Fisher TG-5 MS fused silica column (length: 30 m; inner diameter: 0.25 mm, 0.25 µm film thickness). The GC temperature program used for GC-MS runs was: injection at 50°C, 3 min isothermal; from 50°C to 325°C at a ramp of 6°C min^{-1}; 25 min isothermal. The carrier gas was helium. The GC-IRMS was equipped with an Agilent HP-5MS capillary column (length: 30 m; inner diameter: 0.25 mm, 0.25 µm film thickness), the temperature program was: injection at 120 °C, 3 min isothermal, from 120 °C to 320 °C at 5 °C/min^{-1}, then held for 15 min $\delta^{13}C$ values are reported in per mil notation relative to Vienna Pee Dee belemnite (V-PDB) standard. Accuracy and precision were determined by analyses of an external *n*-alkane standard calibrated against the A4 mix isotope standard (Arndt Schimmelmann, Indiana University).

Results

Seafloor observations in the carbonate area

High-resolution seafloor observations from the ROV survey conducted in the pockmark during AKMA-CAGE21-1 expedition enabled us to obtain information regarding the modality of formation of methane-derived carbonates in relation to methane seepage and the implications for seafloor ecosystems. Thanks to the ROV photogrammetry, georeferenced digital models of 560 m^2 of the pockmark seafloor were obtained. The high-resolution photographs of the orthomosaic (Figure 2A) and the DTM (4 mm/pix) (Figure 2B) allowed to describe the carbonate outcrops and the surrounding environments accurately. Carbonate outcrops on the seafloor display a recurring stratiform morphology (Figures 2B–D), consisting of plane-parallel strata with average thickness of 20–30 cm piled up locally to form small (<10 m^2 wide) bodies protruding up to 2 m above the adjacent seafloor. Boulder-size blocks are commonly found at the base of these features (Figure 2E). The carbonate deposits are colonized by filter feeders, i.e. anemones and sponges, and offer shelter to higher organisms, i.e. fishes, within large cavities and under carbonate slabs protruding above the seabed (Figure 2E, F, G). Bacterial mats form small white patches (<1 m^2 wide) distributed along the outer rims of carbonate deposits and around the bubbling spots on the carbonates (Figures 2E, F). The transition from the carbonate outcrops to the flat background seafloor is sharp and marked by an evident decrease in macrofauna abundance.

Petrography and EBSD microanalysis

LFC carbonate sample CarC-05 is composed of a dark brown microcrystalline carbonate enclosing fine grained

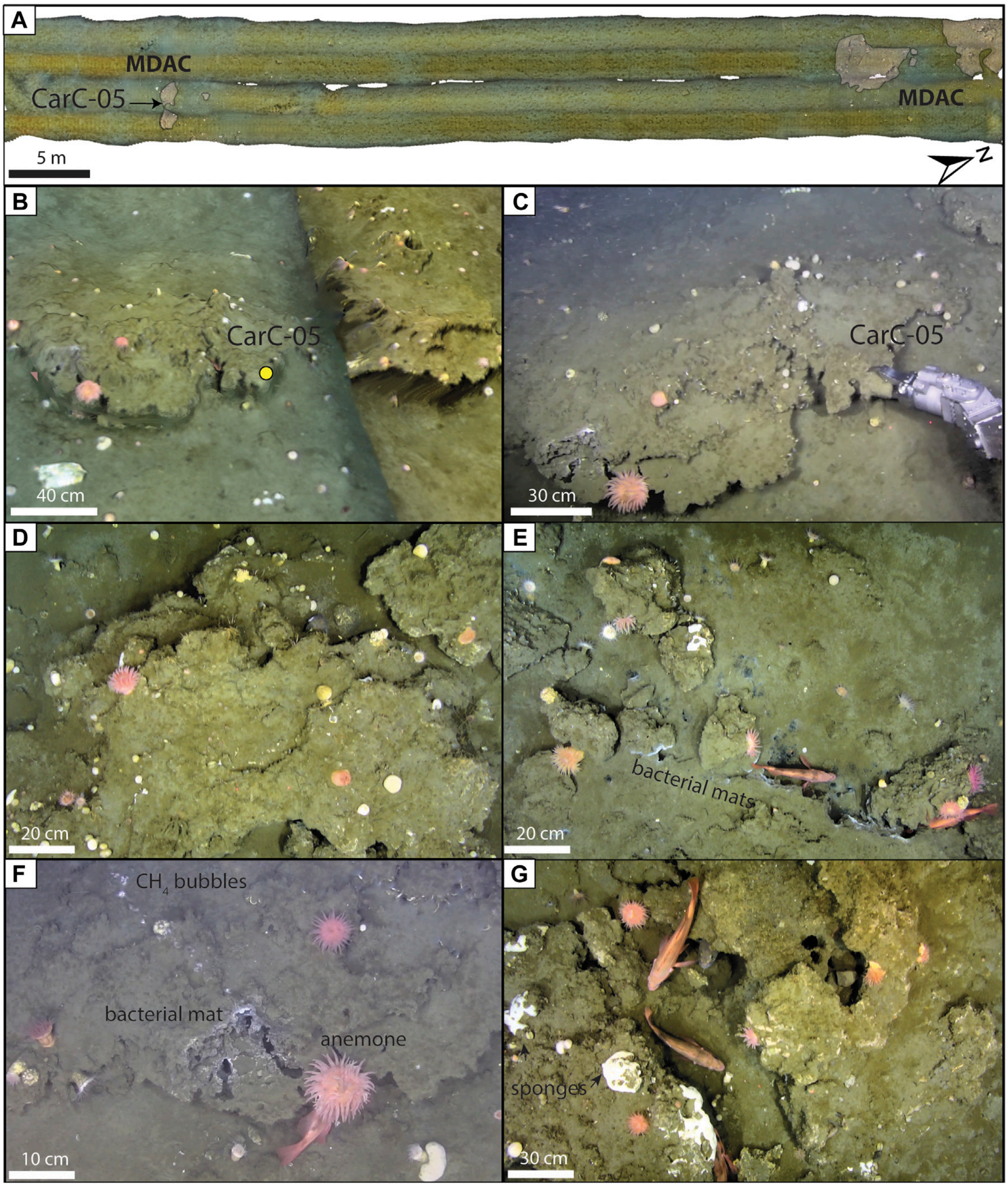

FIGURE 2
Seafloor observations of the carbonate outcrops acquired during AKMA-CAGE21-1 expedition. **(A)** Orthomosaic of the ROV transect across the carbonate outcrops. Carbonate bodies are highlighted with pale color. **(B)** 3D mesh of the carbonate outcrops from which the CarC-05 was collected. **(C)** Sampling of carbonate sample CarC-05 from a stratified carbonate body using the ROV manipulator arm (front camera). **(D)** Stratified carbonate deposits; three layers can be recognized (ortho camera). **(E)** Bacterial mats colonized the outer rim of the carbonate. Some boulders are found at the base of the carbonate structure (ortho camera). **(F)** Bacterial mat around a bubbling spot through the carbonate. Methane bubbles are visible in the photograph. Large anemones are distributed on top and on the rim of the carbonate layers (front camera). **(G)** Anemones and sponges on a carbonate; fishes hiding in cavities within the carbonate body (ortho camera).

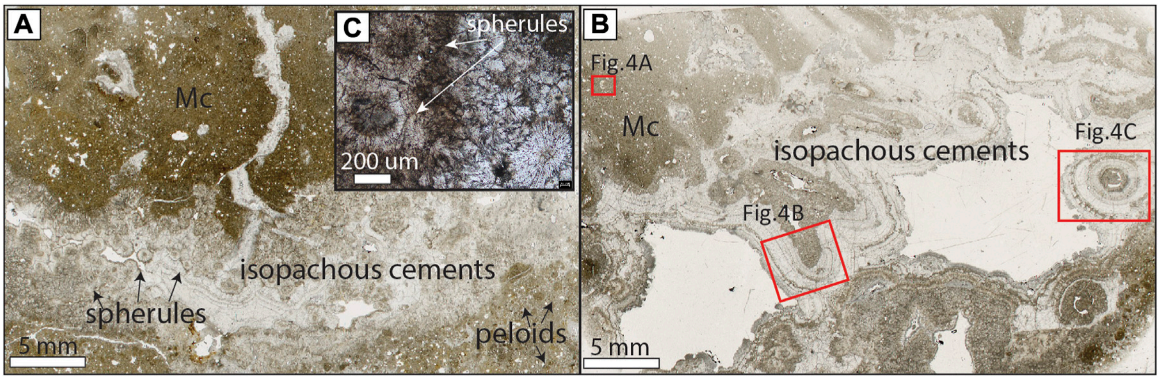

FIGURE 3
Thin section scans from sample CarC-05 collected from the top of a carbonate body. **(A)** Thin section CarC-05-*A* displaying a dark-brown microcrystalline carbonate (Mc) locally displaying peloidal features and crosscut by veins filled by isopachous cements. **(B)** Thin section CarC-05-*C* showing the areas analyzed *via* EBSD, targeting microcrystalline carbonate and isopachous cements **(C)** Close-up view of microcrystalline spherules.

siliciclastic particles of quartz and feldspars. Within the micrite, we identified a peloidal fabric (Figure 3A). Individual peloids are 200–300 μm in diameter and show a microcrystalline composition and regular circular section. The microcrystalline facies is crosscut by veins filled by three–five generations of isopachous cement separated by surfaces showing an irregular outline and locally coated by a thin layer of opaque material, here interpreted as dissolution surfaces (Figure 3B). Early cement phases often engulf microcrystalline spherules with diameters ~100 μm (Figure 3C), generating a mottled microfabric, whereas later stage phases are generally clean. Spherules are pale white colored and display an irregular shape compared to peloids. EBSD investigations indicated that all authigenic carbonate phases in CarC-05 are composed of aragonite (Figure 4). The phase map in Figure 4A shows a dominant aragonitic mineralogy of the microcrystalline carbonate of the matrix engulfing a low magnesium calcite foraminiferal test. EBSD analysis also revealed a secondary high magnesium carbonate phase (calcite or dolomite) overgrowth on the test. Crystal orientation data are represented through an orientation map located to the right side of Figure 4A. The orientation map of the microcrystalline matrix shows randomly oriented microcrystals, similarly to what was typically found in altered biogenic materials (Cusack et al., 2008; Casella et al., 2018). The orientation map of the isopachous cements and the pole figures highlight a strong crystallographic relationship between neighboring grains (orientation axis) (Figures 4B,C). Dissolution surfaces between cement phases are associated with some empty spaces in the orientation map due to absence of diffraction. Misorientation maps have been prepared to highlight areas where the crystal orientations deviate from the grain average (Supplementary Figure S1). To the best of our knowledge this is the first application of EBSD analysis to methane-derived carbonates.

Isotope composition ($\delta^{13}C$, $\delta^{18}O$) and U/Th ages

The carbon isotope composition of fibrous aragonite cements CarC-05-C-*1*, CarC-05-C-*2* and CarC-05-C-*3* shows, in spite of only three sample points being used, a trend toward higher $\delta^{13}C$ values passing from earlier phases to later cements (Table 1). Sample CarC-05-C-*1* has the lowest $\delta^{13}C$ values of −28.6‰ and is associated with $\delta^{18}O$ = 5.3‰. The U/Th age of this phase is 8.223 ± 0.229 ka BP, indicating carbonate precipitation during the Early Holocene. Sample CarC-05-C-*2* has a $\delta^{13}C$ = −27.0‰ and $\delta^{18}O$ = 4.6‰; U/Th analysis yielded an age of 7.976 ± 0.248 ka BP. Sample CarC-05-C-*3* shows a $\delta^{13}C$ = −10.1‰ and $\delta^{18}O$ = 5.0‰ and is associated with a U/Th age of 4.087 ± 1.547 ka BP. The contact between this phase and CarC-05-C-*2* is marked by a major dissolution surface making this U/Th age not suitable for extrapolating average growth rates due to unconstrained hiatus. Assuming a linear distance of 0.8–1 mm between the microdrilling spots of CarC-05-C-*1* and CarC-05-C-*2* (center of the cement), and putatively short episode of carbonate dissolution occurred (Figure 4C), the average growth rate ranges were between 3.24 mm/ka and 4.05 mm/ka. The overall $\delta^{13}C$ composition of vein cements is heavier than microcrystalline carbonate concretions from nearby sediment cores GC-1143 and MC-1141, which range from −31.5‰ to −30.0‰; the oxygen signatures of the latter show a narrow range from 5.0‰ to

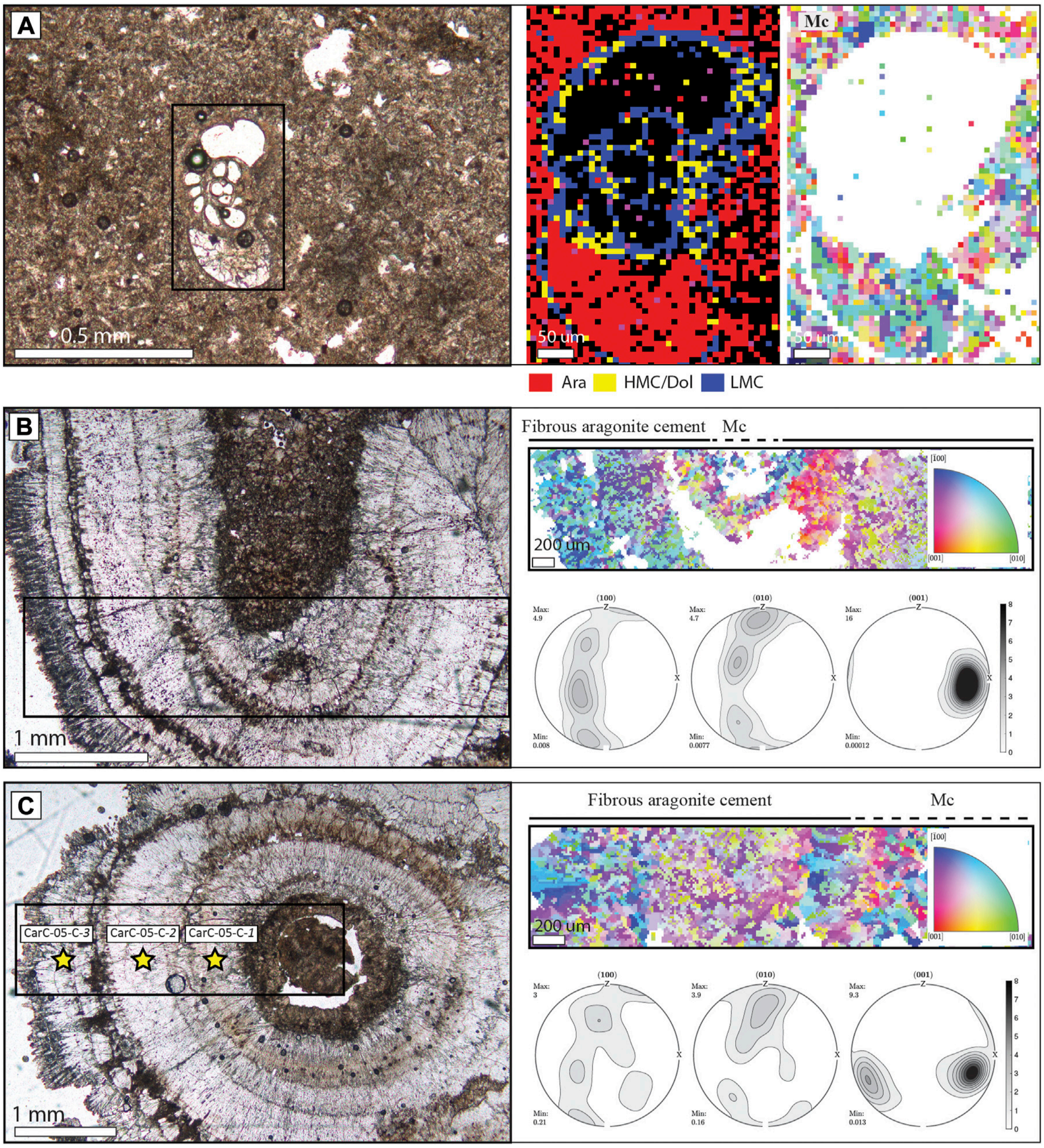

FIGURE 4
Thin section micrographs and EBSD phase and crystal orientation maps of areas marked in Figure 3B. Orientation maps help visualize crystal directions normal to the plane of observation using the color key in the insets. Orientations are also plotted as stereographic projections in the pole figures. **(A)** Micrite microfacies engulfing a foraminiferal test. The EBSD phase map clearly shows a dominant aragonitic mineralogy for the microcrystalline carbonate, with low magnesium calcite corresponding to the test. Some low magnesium calcite/dolomite is found on the test. Microcrystalline carbonate shows randomly-oriented microcrystals in the orientation map. **(B)** Fibrous aragonite cements showing variable orientation of the individual crystals passing from a preferred [–100] crystal direction on the left side of the section to [001] on the right. Cement phases are separated by dissolution surfaces. **(C)** Isopachous cements showing a rather constant crystal orientation close to [–100] direction. The micro-drilled subsample locations are showed with starts. Mc= microcrystalline carbonate.

TABLE 1 Isotopic composition of methane-derived carbonates from Leirdjupet Fault Complex and U/Th ages.

Sample	Texture	Phase	$\delta^{13}C$ (‰)	$\delta^{18}O$ (‰)	U/Th age (ka BP)
CarC-05-C-*1*	Fibrous cement	Ara	−28.6	5.3	8.223 ± 0.229
CarC-05-C-*2*	Fibrous cement	Ara	−27.0	4.6	7.976 ± 0.248
CarC-05-C-*3*	Fibrous cement	Ara	−10.1	5.0	4.087 ± 1.547
GC-1143*	Mc	Ara	−30.0	5.0	n.d
MC-1141a*	Mc	Ara/HMC	−31.0	5.3	n.d
MC-1141b*	Mc	Ara/HMC	−31.5	5.0	n.d

Mc=microcrystalline carbonate; Ara = aragonite; HMC, high-Mg calcite; n. d. = not determined; *after Argentino et al., 2021.

TABLE 2 Results from lipid biomarker analysis of methane-derived carbonate CarC-05.

Compound	$\delta^{13}C$ (‰)	Concentration ng/g rock	Source
Hydrocarbons			
crocetane/phytane	−111	292	ANME
PMI	−107	137	ANME
n-alkanes	−29.3	628	—
Σ hydrocarbons	—	1096	—
Alcohols			
archaeol	−122	1432	ANME
sn2-hydroxy-archaeol	−121	2896	ANME
Σ alcohols	—	5386	—
Fatty acids			
iso-C_{15}	−102	82	SRB
anteiso-C_{15}	−102	143	SRB
Σ fatty acids	—	1235	—
Proxies		Information	
OH-Ar/Ar	2.0	ANME-2	—
ai/*i* C_{15}-FA	1.7	Seep-SRB1	—
$CPI_{23\text{-}33}$	0.95	oil-derived alkanes	—

Concentration (ng/g rock) of the most representative lipid biomarkers of AOM-related archaea (ANME) and sulfate-reducing bacteria (SRB) in carbonate sample CarC-05, and their compound-specific isotopic composition; PMI, pentamethylicosane; DAGE, dialkyl glycerol diether. Full datasets are reported in the Supplementary Table S2.

5.3‰, similar to the values obtained from aragonite cements CarC-05-C-*1* and CarC-05-C-*3*.

Lipid biomarkers

The total lipid biomarker content of the carbonate sample was 7.7 μg/g rock lipids, where the majority of compounds was found in the alcohol fraction (70 wt%), followed by fatty acids (16 wt%), and hydrocarbons, which comprised 14 wt%. Table 2 reports representative AOM-related biomarkers, whereas the complete datasets are reported in Supplementary Table S2. The hydrocarbon fraction was dominated by *n*-alkanes ranging from *n*-C_{15} to *n*-C_{33}, and comprising ca. 60% of all compounds in the hydrocarbon fraction (Table 2). The tail-to-tail linked isoprenoid crocetane is co-eluting with the minor head-to-tail linked isoprenoid phytane (<10% of all hydrocarbons); together with the tail-to-tail linked isoprenoid pentamethlyicosane (PMI) they make up 39.2% of the hydrocarbon fraction (Table 2). The $\delta^{13}C$ value of the mixed crocetane/phytane is −111‰, the value of PMI is −107‰. The head-to-tail linked isoprenoid pristane is a only minor component (38.4 ng/g) and carries an isotopic composition of −30‰ (Supplementary Table S2). *n*-Alkanes (*n*-C_{15}-*n*-C_{33}) had $\delta^{13}C$ values varying between −34.5‰ and −27.4‰ (average $\delta^{13}C = -29.3 \pm 1.5$‰; N = 19) (Table 2), with *n*-C_{23} showing the most depleted value (Supplementary Table S2). The alkane distribution shows no odd-to-even carbon number preference, resulting in a $CPI_{23\text{-}33}$ (Marzi et al., 1993) value of 0.95. The compounds in the alcohol fraction are dominated by the two archaeal isoprenoid alcohols archaeol (Ar) and *sn*2-hydroxyarchaeol (OH-Ar), comprising 80% of all compounds in the alcohol fraction. Both compounds show low $\delta^{13}C$ values of −122‰ (Ar) and −121‰ (OH-Ar) (Table 2). Putative degradation products of the two archaeols are the *sn*2-and *sn*3-phytanyl-monoether isoprenoids, found with very minor contents of 17.6 ng/g and 22.3 ng/g and $\delta^{13}C$ values of −122‰ and −120‰, respectively. Further compounds in the alcohol fraction were bacterial, non-isoprenoid dialkyl glycerol diether lipids (DAGEs), which comprised ca. 15% of all alcohols and $\delta^{13}C$ values ranging from −121‰ to −98‰. The fatty acid fraction contained fatty acids with chain lengths from C_{12} to C_{18} and a total content of 1,234.6 ng/g. Fatty acids are composed of saturated and unsaturated *n*- and branched fatty acids of bacterial origin. Among the most abundant fatty acids were *iso*- and *anteiso*-C_{15} fatty acids with contents of 82.3 ng/g and 143.2 ng/g, respectively; both are ^{13}C-depleted with $\delta^{13}C$ values of −102‰. Most ^{13}C-depleted fatty acids were *n*-$C_{14:1}$ and *iso*-C_{16}, revealing contents of 11.6 ng/g and 46.9 ng/g and $\delta^{13}C$ values of −117‰ and −110‰, respectively (Table 2). Phytanoic acid has also been detected with a $\delta^{13}C$ value of −107‰.

Discussion

Carbonates reveal diffuse fluid flow

The seafloor observation of methane-derived carbonates from decades of seep research at continental margins indicated a few recurring morphologies mainly controlled by subsurface fluid distributions (diffuse vs. focused flow) and interactions between carbonates and fauna (Campbell, 2006; Judd and Hovland, 2007; Suess, 2014, 2018). Chemoherms are carbonate build-ups growing into the water column due to the accumulation and cementation of biogenic material, i.e. shells of chemosymbiotic bivalves, layers of microbial mats. These structures can reach remarkable lengths of up to 200 m and heights of tens of meters, reflecting spatially-localized activity protracting for several thousands of years. Examples of seep deposits projecting into the bottom water have been reported from Hydrate Ridge (Greinert et al., 2001; Teichert et al., 2005) and the Black Sea (Michaelis et al., 2002), while fossil analogs have been discovered in ancient accretionary prisms and fore arc settings such as the northern Apennine chain in Italy (Aharon, 1994; Conti and Fontana, 1999; Cau et al., 2015) and the East Coast Basin, New Zealand (Campbell et al., 2008). Another more common type of deposit are the so called “carbonate pavements”, a term referring to stratiform carbonate deposits forming hardgrounds on the seafloor (Suess, 2014). These deposits form at or close to the sediment-seawater interface and testify for a more diffuse seepage inducing the precipitation of authigenic carbonates over wide areas marked by shallow sulfate-methane transitions (Pierre and Fouquet, 2007; Panieri et al., 2017). Differently from chemoherms representing spatially-localized fluid escape features with high topographic relief and limited lateral extent, e.g., Hydrate Ridge (Teichert et al., 2005), carbonate pavements can reach several thousands of m^2 in extent and generally show rather flat or mound-like morphologies (Judd et al., 2020). At the seafloor, vertically-stacked carbonate slabs can form mound-like buildups of a few meters in height locally (Roberts and Feng, 2013; Pierre et al., 2017). These carbonate deposits form an efficient seal to upward migrating fluids and record various episodes of fracturing and cementation caused by gas accumulations beneath the deposits (Loher et al., 2018). Based on the seafloor observations we ascribe the Leirdjupet Fault Complex carbonates to the latter type of deposits. ROV surveys in the pockmark area highlighted the presence of carbonate hardgrounds exploited as substrate by sessile fauna (Figure 3). Bacterial mats and active methane bubbling only occur associated with cm-sized orifices within the carbonates and around the outer rim of the slabs, pointing toward and effective sealing behavior of the deposits at this site. At LFC, methane-rich fluids coming from underlying faulted successions (Argentino et al., 2021) encounter a carbonate cap in the shallow sedimentary column (meters), channeling the fluids into small conduits within the MDAC or deviating them laterally toward their boarder. Bacterial mats colonize the areas on the seafloor where sulfate-driven anaerobic oxidation of methane generates sulfidic conditions and are therefore a reliable proxy for high methane fluxes (Argentino et al., 2022). Based on the geometries and spatial distribution of carbonate outcrops and chemosynthetic communities at the seafloor observed during the ROV dive at this site (Figure 1B), we believe that the carbonate deposits cropping out of the seafloor represents only a minor portion of the whole deposits, mostly buried beneath the sediment-water interface and possibly extending beyond the 560 m^2 of data coverage.

Biogeochemistry of methane-derived carbonates at LFC

Petrographic and microstructural analysis of carbonate sample CarC-05 collected from a stratiform deposit at the seafloor (Figure 3A) revealed a dynamic history of mineral precipitation and dissolution. The sample is composed of microcrystalline aragonite crosscut by veins filled by isopachous cements consisting of fibrous aragonite (Figure 4). The contact between the veins and the enclosing matrix is smooth and regular indicating fluid intrusion through the micrite during an early semi-lithified stage. The aragonite mineralogy of CarC-05 reflects precipitation close to the seafloor, due to the kinetic inhibition of sulfate on calcite precipitation (Mayorga et al., 2019) or, more likely, the lack of sulfide catalysis favoring Mg calcite and dolomite formation (Lu et al., 2018), and therefore is an indicator of a shallow sulfate-methane transition zone and intense AOM. The presence of high magnesium calcite in cm-sized concretions in sediment core MC-1141 at 18 cm bsf and 26 cm (Argentino et al., 2021), on the other hand, reflects a deeper zone of formation characterized by lower sulfate and higher sulfide pore water concentration gradients at the periphery of the pockmark (Figure 1C). High AOM rates during the precipitation of sample CarC-05 are also testified by its biomarker inventory, especially by the high abundance of the ^{13}C-depleted isoprenoid crocetane ($\delta^{13}C= -111$‰) and an OH-Ar/Ar ratio >1.1. Both indicators are typical of methanotrophic *Methanosarcinales* of the subgroup ANME-2 (Hinrichs et al., 2000; Niemann and Elvert, 2008) (Table 2). ANME-2 are commonly found in cold seep environments with a shallow SMTZ associated with aragonite MDACs, whereas ANME-1 are found at greater depths typically associated with high-Mg calcite mineralogies (Peckmann et al., 2009; Guan et al., 2016; Yao et al., 2021; Iasakov et al., 2022). The syntrophic sulfate-reducing partner of ANME-2 belongs to the *Desulfosarcina/ Desulfococcus* Seep-SRB1 cluster based on the *ai*-$C_{15:0}$/*i*-$C_{15:0}$ value <2 (Niemann and Elvert, 2008; Yao et al., 2021). The significant ^{13}C-depletion in fatty acids derived from sulfate-reducing bacteria, i.e. *iso*- and *anteiso*-C_{15} fatty acids (Table 2), is consistent with assimilation of methane-derived carbon. Intense microbial activity left typical petrographic features in the carbonate such as peloidal microfacies (Figure 3A) similar to other modern (Feng et al., 2008) and fossil methane-derived carbonates (Conti et al., 2010) and spherules possibly representing fossil sulfate-driven AOM aggregates (Himmler et al., 2022). In sample CarC-05, the vein filling displays three to five generations of cements separated by dissolution surfaces. Local corrosive conditions at methane seeps are commonly associated with aerobic methane oxidation (MoX) (Birgel et al., 2011; Himmler et al., 2011): $CH_4 + 2O_2 \rightarrow CO_2 + H_2O$. The carbon dioxide generated by MoX transforms into carbonic acid (H_2CO_3), and readily dissociates into bicarbonate (HCO_3^-) and/or carbonate (CO_3^{2-}) ions, releasing hydrogen ions. The consequent decrease in pH affects carbonate stability and favors its dissolution. The dissolution patterns are consistent with variations in seepage intensity and episodic establishment of oxygenated conditions favoring MoX. However, specific sterols of MoX bacteria, like 4,4-dimethyl and 4α-methyl sterols (Cordova-Gonzalez et al., 2020; Whiticar, 2020; Yao et al., 2021) were not identified, therefore the corrosion features may have been caused by other processes than MoX. Bacterial sulfide oxidation to sulfate ($H_2S + 2O_2 \rightarrow SO_4^{2-} + 2H^+$) is an alternative process that might have contributed to the generation of the corrosion surfaces and would explain the absence of pyrite in the sample (Figure 3) (Himmler et al., 2011; Leprich et al., 2021). Unfortunately, sulfur-oxidizing bacteria do not produce characteristic biomarkers (Peckmann et al., 2004); however, the high contents of *n*-C_{16} and *n*-$C_{16:1}$ fatty acids and their rather high $\delta^{13}C$ values compared to biomarkers of sulfate reducers (Elvert et al., 2003) may be explained by mixed sources of these fatty acids, possibly including sulfur-oxidizing bacteria (Arning et al., 2008). The vein-filling cements CarC-05-C-*1*, CarC-05-C-*2*, CarC-05-C-*3* show varying, but low $\delta^{13}C$ values compared to non-seep marine carbonates which generally range from −7‰ to +8‰ (Judd and Hovland, 2007). These results indicate persistent methane oxidation in the pore waters, but a variable proportion of methane-derived carbon incorporated into the aragonite cements during growth due to dynamic seepage conditions (Roberts and Feng, 2013). These findings are consistent with a number of studies demonstrating that seepage activity can vary both spatially and temporally (Judd and Hovland, 2007; Suess, 2014; Ferré et al., 2020; Dølven et al., 2022), influencing subsurface biogeochemical processes (e.g. AOM, carbonate precipitation) (Rooze et al., 2020), the composition and distribution of seafloor chemosynthetic communities (Levin, 2005; Fischer et al., 2012) as well as local water-column biogeochemistry (Sert et al., 2020; Zhang et al., 2020; Gründger et al., 2021). We conducted thermodynamic modelling of the oxygen isotopic composition of aragonite cements forming in equilibrium with coeval bottom waters (8 ka BP and 4 ka BP) to check whether samples recorded some influence from gas hydrates. Assuming average bottom water temperatures of 4.3°C and 3°C (El bani Altuna et al., 2021), and seawater $\delta^{18}O$ SMOW of 0‰ (Fairbanks, 1989) we obtained aragonite $\delta^{18}O$ values of 3.9‰ and 4.2‰ (Kim et al., 2007). The obtained range of values of 4.6‰–5.3‰ is above the theoretical values and would correspond to temperatures below 1.2°C. Gas hydrates are not stable at this site at present-day pressure and temperature conditions and have not been stable since ~15 ka BP (Argentino et al., 2021). Fluids released by shallow gas hydrates take hundreds to few thousands of years to reach the seafloor in an advective system (Crémière et al., 2016; Serov et al., 2017), therefore an influence of gas hydrates for the examined aragonite cements is rather unlikely. A contribution of heavy, ^{18}O-enriched water released by deep-related processes such as clay dehydration (Kastner et al., 1991) is not considered here, as there is no seismic evidence for deep warm fluid advection or opal-A to opal-CT transition in the upper sedimentary section of this area (cage.no). Stable isotope analyses of foraminiferal samples from the SW Barents Sea (Risebrobakken et al., 2010) indicated frequent temperature deviations of ±2°C–3°C from the mean bottom water temperatures throughout the Holocene, which might explain the variability of the obtained values, similarly to what was observed in late aragonitic phases from the Harstad Basin (Crémière et al., 2018). The $\delta^{13}C$ values measured in CarC-05-C-*1* and CarC-05-C-*2* are lower (−28.6‰ and −27.0‰, respectively) than the average isotopic composition of sedimentary organic matter in this area i.e. ca. −25‰ to −24‰ (Argentino et al., 2021), which is pointing to an incorporation of methane-derived carbon during precipitation. Evidence for the seepage of microbial methane stems from the

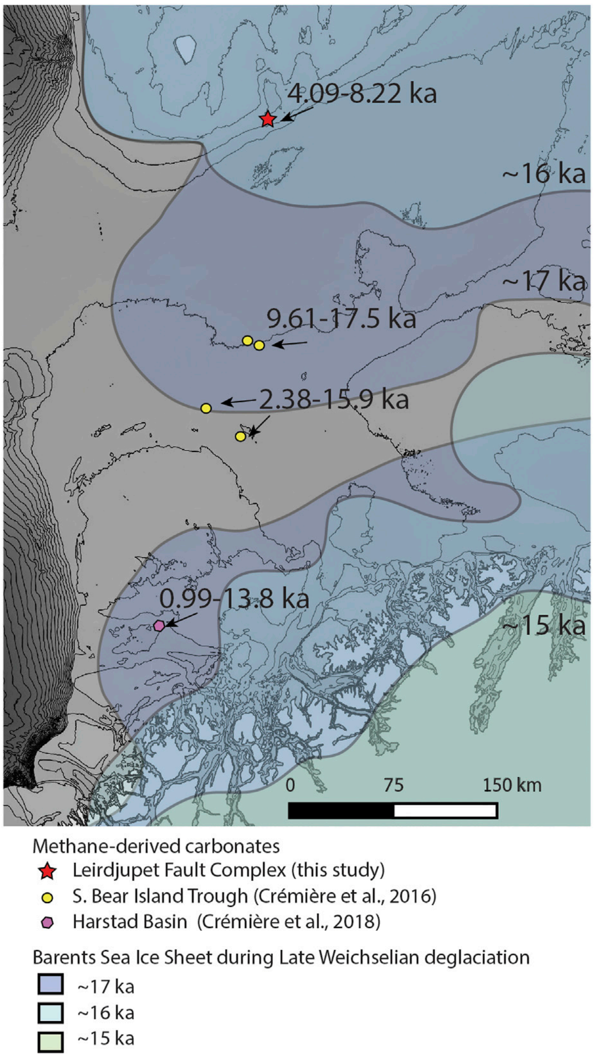

FIGURE 5
Location of methane-derived carbonate outcrops with available U/Th ages from the SW Barents Sea and approximated positions of the retreating ice-front at different stages of deglaciation of the Barents Sea Ice Sheet after Winsborrow et al., 2010.

carbon isotopic values of archaeol and *sn*2-hydroxy-archaeol with average $\delta^{13}C$ values of −122‰ (Table 2). These archaeal isoprenoids usually display a 50–70‰ offset for ANME-2 from the methane source (Niemann and Elvert, 2008), which is in agreement with biogenic methane, while the reported range of $\delta^{13}C_{methane}$ varies from −64.4‰ to −22.1‰ in this area (Argentino et al., 2021). Although the archaeal lipid biomarkers are not carrying a signature of thermogenic methane, the *n*-alkane distribution with a CPI_{23-33} of 0.95 indicates the presence of traces of petroleum (*cf.* Marzi et al., 1993), which may contribute to the local presence of isotopically heavy methane. Mid- and long-chain *n*-alkanes carry a more or less uniform $\delta^{13}C$ values signature from −30‰ to −28‰, which is in the range of petroleum derived hydrocarbons (Supplementary Table S2). Overall, carbonate cements recorded a localized progressive decrease in AOM rates with the most negative $\delta^{13}C$ value associated with the early cements and the highest values in the last cement phase. This trend can be caused by the progressive clogging of fluid migration pathways through the formation of MDACs (Hovland, 2002) and lower methane inputs into the zone of carbonate precipitation, or to an overall decrease in upward migrating fluids from the deeper reservoirs. The latter scenario wassuggested by Argentino et al. (2021) based on the correlation of geochemical anomalies related to paleo-SMTZ (low $\delta^{13}C_{foraminifera}$, sulfur enrichments, barite fronts) in sediment cores at LFC. Our new isotopic data and U/Th ages from the carbonate samples support that interpretation and add additional time-constraints to the dynamics of methane seepage at the northern LFC in the pockmark site.

Timing of carbonate formation and regional correlations

The SW Barents Sea hosts widespread sub-surface fluid plumbing systems consisting of shallow faults and fractures splaying from major deep-seated faults in hydrocarbon reservoirs or source rocks (Vadakkepuliyambatta et al., 2013). Surface expressions of fluid seepage such as pockmarks have been mapped over much of the Bear Island Trough, counting several hundred millions (Rise et al., 2014). The main phase of pockmark formation in the SW Barents Sea is hypothesized to have occurred during short-lived events (a few thousands of years) following the Late Weichselian ice-sheet retreat due to destabilization of gas hydrates. Although most of these features are no longer active (Chand et al., 2012; Mazzini et al., 2016), some are associated with active water-column gas flares indicating protracted seepage activity (Crémière et al., 2016, 2018). Detailed investigations of carbonate crusts associated with pockmarks in the SW Barents Sea have only been conducted for a few locations in the eastern Harstad Basin (Crémière et al., 2018) and SW Bear Island Trough (Crémière et al., 2016) and provided age ranges of 0.99–13.8 ka and 2.38–17.5 ka, respectively (Figure 5). Leirdjupet Fault Complex is located on the northern Bear Island Trough, 160–226 km north of the sites studied by Crémière et al. (2016). Paleo-hydrate destabilization in the pockmark area was suggested based on the combination of gas hydrate stability models and high $\delta^{18}O$ values in carbonate concretions from sediment cores and carbonate precipitation was constrained temporally to <14.5 ka BP by radiocarbon pinpoint and lithostratigraphy. Pore fluid datasets place the modern sulfate-methane transition along LFC between ~40 cm and ~110 cm below the seafloor whereas paleo-SMTZs have been identified by sediment proxies at shallower depths indicating an overall decrease in methane fluxes (Argentino et al., 2021). The new U-Th dates provided here are indicating a protracted MDAC formation during the period from ~8 to ~4 ka, but also evidence active present-day seepage (ROV observation of methane bubbles and microbial mats). We suggest that AOM and resultant carbonate precipitation continued from ~14.5 ka until today, with only a few interruptions marked by local carbonate dissolution reflecting the occurrence of episodic oxidizing conditions. In particular, a major dissolution event occurred between the precipitation of phases CarC-05-C-2 and CarC-05-C-3 (Figures 4B, C), producing a hiatus of a few thousand years possibly related to deep processes acting on the migration of methane-rich fluids, e.g. fault-reactivation (Crémière et al., 2018). Since the carbonate sample was collected from the top of a carbonate outcrop, we are unable to extrapolate our interpretations to the entire carbonate deposits. We are also unable to trace the evolution of LFC deposits buried in the sediment. However, we know from glacial morphology reconstructions (Winsborrow et al., 2010) and thermomechanical ice-sheet models (Patton et al., 2017), that this area was covered by a grounded ice sheet until ca. 16 ka BP and the edge of gas hydrate stability crossed northern LFC at around 15 ka (Argentino et al., 2021). Therefore, the inception of seepage at LFC was tightly linked to the timing of grounded ice sheet retreat, and caused by the consequent gas hydrate destabilization and glacially-induced changes in stress fields (Argentino et al., 2021). The methane seepage history recorded in the methane-derived carbonates at LFC followed a similar evolution as in vicinal sites in the south (Crémière et al., 2016, 2018), chiefly controlled by the asynchronous deglaciation of the Barents Sea shelf areas, demonstrating that despite the overall decrease in seafloor gas expulsion recorded since last deglaciation, methane-derived carbonate precipitation is still an active process at many Arctic locations.

Conclusion

Fault-controlled methane seepage at the Leirdjupet Fault complex has been detected along a ~35 km transect during CAGE expeditions in 2018 and 2021, representing one of the most active seepage areas in the SW Barents Sea. Seafloor imagery acquired using a remotely operated underwater vehicle enabled us to characterize the seabed features and chemosynthetic communities in a 120 x 220 m elongated pockmark, and to collect methane-derived carbonate samples to study biogeochemical processes associated with methane oxidation. Carbonates form <10 m^2 bodies composed of vertically stacked slabs with a thickness of 20–30 cm, projecting as high as 2 m above the seafloor. White patches (<1 m^2 wide) of bacterial mats only occur around the outer rim of carbonate crusts and around cm-sized cavities and cracks within the carbonates and not in surrounding sediments, pointing toward an effective sealing behavior of the carbonate deposits at this site. Microstructural analyses of vein-filling cements from a rock sample collected from the top of a carbonate body showed the occurrence of three to five generations of isopachous aragonitic cements separated by dissolution surfaces indicative of intermitted oxygenated conditions. Phase-specific stable isotope analysis and U/Th dating of aragonite cement revealed trend of decreasing $\delta^{13}C$ values with time, ranging from $\delta^{13}C$ = −28.6‰ (early phase) to $\delta^{13}C$ = −10.1‰ (late phase), which enabled us to trace anaerobic oxidation of methane from 8.223 ka to 4.087 ka. Molecular and compound-specific isotopic analysis of lipid biomarkers allowed the identification of ANME-2 archaea and Seep-SRB1 sulfate-reducing bacteria and the detection of traces of petroleum. This study provides new biogeochemical and temporal constraints on the inception and evolution of seepage at LFC, which can be used to correlate past methane emissions along the western Barents Sea margin.

Data availability statement

The original contributions presented in the study are included in the article/Supplementary Material, further inquiries can be directed to the corresponding author.

Author contributions

CA and GP conceived the study. CA and AL conducted microstructural analyses, LF conducted seafloor image aquisitions and processing. DS performed U/Th analyses. CA, DB and JP conducted sample preparation and analysis of biomarkers. All the authors contributed to the discussion and improvement of the manuscript and approved the article for submission.

Funding

The research was supported by AKMA project (Research Council of Norway grant No. 287869) within the frame of the Centre for Arctic Gas Hydrate, Environment and Climate (CAGE) (Research Council of Norway grant No. 223259). Biomarker analyses were conducted during a research stay funded by Erasmus+ staff mobility 2021 granted to CA.

Acknowledgments

We would like to acknowledge the captain and crew onboard R/V *Helmer Hanssen* and *Kronsprins Haakon* for the assistance during the expeditions CAGE18-4, CAGE21-1-AKMA. We are grateful to Matteus Lindgren (UiT) for technical support in stable isotope analysis and Sabine Beckmann (Universität Hamburg) for support in the organic geochemistry laboratory. We acknowledge GC-IRMS measurements by Enno Schefuß and Ralph Kreutz (MARUM, Universität Bremen). We thank the two reviewers for their comments and suggestions that greatly improved the manuscript.

Conflict of interest

The authors declare that the research was conducted in the absence of any commercial or financial relationships that could be construed as a potential conflict of interest.

Publisher's note

Supplementary material

The Supplementary Material for this article can be found online at: https://www.frontiersin.org/articles/10.3389/feart.2022.1029471/full#supplementary-material

References

Aharon, P. (1994). Geology and biology of modern and ancient submarine hydrocarbon seeps and vents: An introduction. *Geo-Marine Lett.* 14, 69–73. doi:10.1007/BF01203716

Andreassen, K., Hubbard, A., Winsborrow, M., Patton, H., Vadakkepuliyambatta, S., Plaza-Faverola, A., et al. (2017). Massive blow-out craters formed by hydrate-controlled methane expulsion from the Arctic seafloor. *Science* 356 (80), 948–953. doi:10.1126/science.aal4500

Argentino, C., Conti, S., Fioroni, C., Fontana, D., Sciences, G., and Emilia, R. (2019). Evidences for paleo-gas hydrate occurrence: What we can infer for the miocene of the northern apennines (Italy). *Geosciences* 9, 134. doi:10.3390/geosciences9030134

Argentino, C., Savini, A., and Panieri, G. (2022). "Integrating fine-scale habitat mapping and pore water analysis in cold seep research: A case study from the SW Barents Sea," in *World atlas of submarine gas hydrates in continental margins* (Cham: Springer International Publishing), 505–514. doi:10.1007/978-3-030-81186-0_43

Argentino, C., Waghorn, K. A., Vadakkepuliyambatta, S., Polteau, S., Bünz, S., and Panieri, G. (2021). Dynamic and history of methane seepage in the SW Barents Sea: New insights from Leirdjupet Fault complex. *Sci. Rep.* 11, 4373. doi:10.1038/s41598-021-83542-0

Arning, E. T., Birgel, D., Schulz-Vogt, H. N., Holmkvist, L., Jørgensen, B. B., Larson, A., et al. (2008). Lipid biomarker patterns of phosphogenic sediments from upwelling regions. *Geomicrobiol. J.* 25, 69–82. doi:10.1080/01490450801934854

Birgel, D., and Peckmann, J. (2008). Aerobic methanotrophy at ancient marine methane seeps: A synthesis. *Org. Geochem.* 39, 1659–1667. doi:10.1016/j.orggeochem.2008.01.023

Bachmann, F., Hielscher, R., and Schaeben, H. (2010). Texture analysis with MTEX – free and open source software toolbox. *Solid State Phenom.* 160, 63–68. doi:10.4028/www.scientific.net/ssp.160.63

Bayon, G., Lemaitre, N., Barrat, J.-A., Wang, X., Feng, D., and Duperron, S. (2020). Microbial utilization of rare Earth elements at cold seeps related to aerobic methane oxidation. *Chem. Geol.* 555, 119832. doi:10.1016/j.chemgeo.2020.119832

Birgel, D., Feng, D., Roberts, H. H., and Peckmann, J. (2011). Changing redox conditions at cold seeps as revealed by authigenic carbonates from Alaminos Canyon, northern Gulf of Mexico. *Chem. Geol.* 285, 82–96. doi:10.1016/j.chemgeo.2011.03.004

Boetius, A., Ravenschlag, K., Schubert, C. J., Rickert, D., Widdel, F., Gieseke, A., et al. (2000). A marine microbial consortium apparently mediating anaerobic oxidation of methane. *Nature* 407, 623–626. doi:10.1038/35036572

Bohrmann, G., Greinert, J., Suess, E., and Torres, M. (1998). Authigenic carbonates from the Cascadia subduction zone and their relation to gas hydrate stability. *Geol.* 26, 647–650. doi:10.1130/0091-7613(1998)026<0647:acftcs>2.3.co;2

Bohrmann, G., Suess, E., Greinert, J., Teichert, B., and Naehr, T. (2002). Gas hydrate carbonates from Hydrate Ridge. cascadia convergent margin : Indicators of near-seafloor clathrate deposits gas hydrate carbonates from Hydrate Ridge. cascadia convergent margin : Indicators of near-seafloor clathrate deposits.

Bohrmann, G., and Torres, M. E. (2006). Gas hydrates in marine sediments. *Mar. Geochem.*, 481–512. doi:10.1007/3-540-32144-6_14

Bojanowski, M. J., Oszczypko-Clowes, M., Barski, M., Oszczypko, N., Radzikowska, M., and Ciesielska, Z. (2021). Slope destabilization provoked by dissociation of gas hydrates in the Outer Carpathian basin during the Oligocene: Sedimentological, petrographic, isotopic and biostratigraphic record. *Mar. Pet. Geol.* 123, 104585. doi:10.1016/j.marpetgeo.2020.104585

Campbell, K. A., Francis, D. A., Collins, M., Gregory, M. R., Nelson, C. S., Greinert, J., et al. (2008). Hydrocarbon seep-carbonates of a miocene forearc (East Coast basin), north Island, New Zealand. *Sediment. Geol.* 204, 83–105. doi:10.1016/j.sedgeo.2008.01.002

Campbell, K. a. (2006). Hydrocarbon seep and hydrothermal vent paleoenvironments and paleontology: Past developments and future research directions. *Palaeogeogr. Palaeoclimatol. Palaeoecol.* 232, 362–407. doi:10.1016/j.palaeo.2005.06.018

Casella, L. A., Griesshaber, E., Roda, M. S., Ziegler, A., Mavromatis, V., Henkel, D., et al. (2018). Micro- and nanostructures re fl ect the degree of diagenetic alteration in modern and fossil brachiopod shell calcite : A multi-analytical screening approach (cl , FE-SEM , afm , EBSD). *Palaeogeogr. Palaeoclimatol. Palaeoecol.* 502, 13–30. doi:10.1016/j.palaeo.2018.03.011

Cau, S., Franchi, F., Roveri, M., and Taviani, M. (2015). The Pliocene-age Stirone river hydrocarbon chemoherm complex (northern Apennines, Italy). *Mar. Pet. Geol.* 66, 582–595. doi:10.1016/j.marpetgeo.2015.05.027

Chand, S., Thorsnes, T., Rise, L., Brunstad, H., Stoddart, D., Bøe, R., et al. (2012). Multiple episodes of fluid flow in the SW Barents Sea (Loppa High) evidenced by gas flares, pockmarks and gas hydrate accumulation. *Earth Planet. Sci. Lett.* 332, 305–314. doi:10.1016/j.epsl.2012.03.021

Conti, S., Fontana, D., and Mecozzi, S. (2010). A contribution to the reconstruction of Miocene seepage from authigenic carbonates of the northern Apennines (Italy). *Geo-Mar. Lett.* 30, 449–460. doi:10.1007/s00367-010-0196-9

Conti, S., and Fontana, D. (1999). Miocene chemoherms of the northern Apennines, Italy. *Geology* 27, 927–930. doi:10.1130/0091-7613(1999)027<0927:MCOTNA>2.3.CO;2

Cordova-Gonzalez, A., Birgel, D., Kappler, A., and Peckmann, J. (2020). Carbon stable isotope patterns of cyclic terpenoids: A comparison of cultured alkaliphilic aerobic methanotrophic bacteria and methane-seep environments. *Org. Geochem.* 139, 103940. doi:10.1016/j.orggeochem.2019.103940

Crameri, F., Shephard, G. E., and Heron, P. J. (2020). The misuse of colour in science communication. *Nat. Commun.* 11, 5444–5510. doi:10.1038/s41467-020-19160-7

Crémière, A., Chand, S., Sahy, D., Thorsnes, T., Martma, T., Noble, S. R., et al. (2018). Structural controls on seepage of thermogenic and microbial methane since the last glacial maximum in the Harstad Basin, southwest Barents Sea. *Mar. Pet. Geol.* 98, 569–581. doi:10.1016/j.marpetgeo.2018.07.010

Crémière, A., Lepland, A., Chand, S., Sahy, D., Condon, D. J., Noble, S. R., et al. (2016). Timescales of methane seepage on the Norwegian margin following collapse of the Scandinavian Ice Sheet. *Nat. Commun.* 7, 11509–11510. doi:10.1038/ncomms11509

Crémière, A., Pellerin, A., Wing, B. A., and Lepland, A. (2020). Multiple sulfur isotopes in methane seep carbonates track unsteady sulfur cycling during anaerobic methane oxidation. *Earth Planet. Sci. Lett.* 532, 115994–115998. doi:10.1016/j.epsl.2019.115994

Cusack, M., England, J., Dalbeck, P., Tudhope, A. W., Fallick, A. E., and Allison, N. (2008). Electron backscatter diffraction (EBSD) as a tool for detection of coral diagenesis. *Coral Reefs* 27, 905–911. doi:10.1007/s00338-008-0414-3

Davidson, D. W., Leaist, D. G., and Hesse, R. (1983). Oxygen-18 enrichment in the water of a clathrate hydrate. *Geochim. Cosmochim. Acta* 47, 2293–2295. doi:10.1016/0016-7037(83)90053-4

Dølven, K. O., Ferré, B., Silyakova, A., Jansson, P., Linke, P., and Moser, M. (2022). Autonomous methane seep site monitoring offshore Western svalbard: Hourly to seasonal variability and associated oceanographic parameters. *Ocean. Sci.* 18, 233–254. doi:10.5194/os-18-233-2022

El bani Altuna, N., Rasmussen, T. L., Ezat, M. M., Vadakkepuliyambatta, S., Groeneveld, J., and Greaves, M. (2021). Deglacial bottom water warming intensified Arctic methane seepage in the NW Barents Sea. *Commun. Earth Environ.* 2, 188–189. doi:10.1038/s43247-021-00264-x

Elverhøi, A., Siegert, M., Dowdeswell, J., and Svendsen, J.-I. (2002). The eurasian arctic during the last ice age. *Am. Sci.* 90, 32. doi:10.1511/2002.13.753

Elvert, M., Boetius, A., Knittel, K., and Jørgensen, B. B. (2003). Characterization of specific membrane fatty acids as chemotaxonomic markers for sulfate-reducing bacteria involved in anaerobic oxidation of methane. *Geomicrobiol. J.* 20, 403–419. doi:10.1080/01490450303894

Esteves, M., Bjarnadóttir, L. R., Winsborrow, M. C. M., Shackleton, C. S., and Andreassen, K. (2017). Retreat patterns and dynamics of the Sentralbankrenna glacial system, central Barents Sea. *Quat. Sci. Rev.* 169, 131–147. doi:10.1016/j.quascirev.2017.06.004

Fairbanks, R. G. (1989). A 17, 000-year glacio-eustatic sea level record: Influence of glacial melting rates on the younger dryas event and deep-ocean circulation. *Nature* 342, 637–642. doi:10.1038/342637a0

Fallati, L., Saponari, L., Savini, A., Marchese, F., Corselli, C., and Galli, P. (2020). Multi-temporal UAV data and object-based image analysis (OBIA) for estimation of substrate changes in a post-bleaching scenario on a Maldivian reef. *Remote Sens. (Basel).* 12, 2093. doi:10.3390/rs12132093

Feng, D., Chen, D. F., Qi, L., and Roberts, H. H. (2008). Petrographic and geochemical characterization of seep carbonate from Alaminos Canyon, Gulf of Mexico. *Sci. Bull. (Beijing).* 53, 1716–1724. doi:10.1007/s11434-008-0157-0

Feng, D., Chen, D., Peckmann, J., and Bohrmann, G. (2010a). Authigenic carbonates from methane seeps of the northern Congo fan: Microbial formation mechanism. *Mar. Pet. Geol.* 27, 748–756. doi:10.1016/j.marpetgeo.2009.08.006

Feng, D., Peng, Y., Bao, H., Peckmann, J., Roberts, H. H., and Chen, D. (2016). A carbonate-based proxy for sulfate-driven anaerobic oxidation of methane. *Geology* 44, 999–1002. doi:10.1130/G38233.1

Feng, D., Roberts, H. H., Cheng, H., Peckmann, J., Bohrmann, G., Lawrence Edwards, R., et al. (2010b). U/Th dating of cold-seep carbonates: An initial comparison. *Deep Sea Res. Part II Top. Stud. Oceanogr.* 57, 2055–2060. doi:10.1016/j.dsr2.2010.09.004

Ferré, B., Jansson, P. G., Moser, M., Serov, P., Portnov, A., Graves, C. A., et al. (2020). Reduced methane seepage from Arctic sediments during cold bottom-water conditions. *Nat. Geosci.* 13, 144–148. doi:10.1038/s41561-019-0515-3

Fischer, D., Sahling, H., Nöthen, K., Bohrmann, G., Zabel, M., and Kasten, S. (2012). Interaction between hydrocarbon seepage, chemosynthetic communities, and bottom water redox at cold seeps of the Makran accretionary prism: Insights from habitat-specific pore water sampling and modeling. *Biogeosciences* 9, 2013–2031. doi:10.5194/bg-9-2013-2012

Foucher, J. P., Westbrook, G. K., Boetius, A., Ceramicola, S., Dupré, S., Mascle, J., et al. (2007). Structure and drivers of cold seep ecosystems. *Oceanogr. Wash. D. C).* 22, 92–109. doi:10.5670/oceanog.2009.11

Greinert, J., Bohrmann, G., and Suess, E. (2001). Gas hydrate-associated carbonates and methane-venting at Hydrate Ridge: Classification, distribution, and origin of authigenic lithologies. *Geophys. Monogr. Ser.* 124, 99–113. doi:10.1029/GM124p0099

Greinert, J., Bohrmann, G., and Suess, E. (2013). Gas hydrate-associated carbonates and methane-venting at Hydrate Ridge: Classification, distribution, and origin of authigenic lithologies. *Geophys. Monogr. Ser.* 124, 99–113. doi:10.1029/GM124p0099

Gründger, F., Probandt, D., Knittel, K., Carrier, V., Kalenitchenko, D., Silyakova, A., et al. (2021). Seasonal shifts of microbial methane oxidation in Arctic shelf waters above gas seeps. *Limnol. Oceanogr.* 66, 1896–1914. doi:10.1002/lno.11731

Guan, H., Feng, D., Wu, N., and Chen, D. (2016). Methane seepage intensities traced by biomarker patterns in authigenic carbonates from the South China Sea. *Org. Geochem.* 91, 109–119. doi:10.1016/j.orggeochem.2015.11.007

Himmler, T., Bach, W., Bohrmann, G., and Peckmann, J. (2010). Rare Earth elements in authigenic methane-seep carbonates as tracers for fluid composition during early diagenesis. *Chem. Geol.* 277, 126–136. doi:10.1016/j.chemgeo.2010.07.015

Himmler, T., Brinkmann, F., Bohrmann, G., and Peckmann, J. (2011). Corrosion patterns of seep-carbonates from the eastern Mediterranean Sea. *Terra Nov.* 23, 206–212. doi:10.1111/j.1365-3121.2011.01000.x

Himmler, T., Crémière, A., Birgel, D., Wirth, R., Orphan, V. J., Kirsimäe, K., et al. (2022). Putative fossils of chemotrophic microbes preserved in seep carbonates from Vestnesa Ridge, off northwest Svalbard, Norway. *Geology* 50, 169–173. doi:10.1130/G49620.1

Himmler, T., Sahy, D., Martma, T., Bohrmann, G., Plaza-Faverola, A., Bünz, S., et al. (2019). A 160, 000-year-old history of tectonically controlled methane seepage in the Arctic. *Sci. Adv.* 5, eaaw1450. doi:10.1126/sciadv.aaw1450

Hinrichs, K.-U., and Boetius, A. (2002). "The anaerobic oxidation of methane: New insights in microbial ecology and biogeochemistry," in *Ocean margin systems* (Berlin, Heidelberg: Springer Berlin Heidelberg), 457–477. doi:10.1007/978-3-662-05127-6_28

Hinrichs, K.-U., Summons, R. E., Orphan, V., Sylva, S. P., and Hayes, J. M. (2000). Molecular and isotopic analysis of anaerobic methane-oxidizing communities in marine sediments. *Org. Geochem.* 31, 1685–1701. doi:10.1016/S0146-6380(00)00106-6

Hong, W. L., Torres, M. E., Carroll, J. L., Crémière, A., Panieri, G., Yao, H., et al. (2017). Erratum: Seepage from an arctic shallow marine gas hydrate reservoir is insensitive to momentary ocean warming. *Nat. Commun.* 8, 16126. doi:10.1038/ncomms16126

Hovland, M. (2002). On the self-sealing nature of marine seeps. *Cont. Shelf Res.* 22, 2387–2394. doi:10.1016/S0278-4343(02)00063-8

Iasakov, T. R., Kanapatskiy, T. A., Toshchakov, S. V., Korzhenkov, A. A., Ulyanova, M. O., and Pimenov, N. V. (2022). The Baltic Sea methane pockmark microbiome: The new insights into the patterns of relative abundance and ANME niche separation. *Mar. Environ. Res.* 173, 105533. doi:10.1016/j.marenvres.2021.105533

Jansson, P., Triest, J., Grilli, R., Ferré, B., Silyakova, A., Mienert, J., et al. (2019). High-resolution underwater laser spectrometer sensing provides new insights into methane distribution at an Arctic seepage site. *Ocean. Sci.* 15, 1055–1069. doi:10.5194/os-15-1055-2019

Judd, A. G., and Hovland, M. (2007). Seabed fluid flow: The impact of geology, biology and the marine environment. doi:10.1007/s00254-004-1086-0

Judd, A., Noble-James, T., Golding, N., Eggett, A., Diesing, M., Clare, D., et al. (2020). The croker carbonate slabs: Extensive methane-derived authigenic carbonate in the Irish sea—nature, origin, longevity and environmental significance. *Geo-Mar. Lett.* 40, 423–438. doi:10.1007/s00367-019-00584-0

Kastner, M., Elderfield, H., and Martin, J. B. (1991). Fluids in convergent margins: What do we know about their composition, origin, role in diagenesis and importance for oceanic chemical fluxes? *Philos. Trans. - R. Soc. Lond. A* 335, 243–259. doi:10.1098/rsta.1991.0045

Kim, B., and Zhang, Y. G. (2022). Methane hydrate dissociation across the Oligocene–Miocene boundary. *Nat. Geosci.* 15, 203–209. doi:10.1038/s41561-022-00895-5

Kim, S., Neil, J. R. O., Hillaire-marcel, C., and Mucci, A. (2007). Oxygen isotope fractionation between synthetic aragonite and water : Influence of temperature and Mg2 + concentration Oxygen isotope fractionation between synthetic aragonite and water : Influence of temperature and Mg 2 + concentration. doi:10.1016/j.gca.2007.04.019

Knittel, K., and Boetius, A. (2009). Anaerobic oxidation of methane: Progress with an unknown process. *Annu. Rev. Microbiol.* 63, 311–334. doi:10.1146/annurev.micro.61.080706.093130

Kravchishina, M. D., Lein, A. Y., Flint, M. V., Baranov, B. V., Miroshnikov, A. Y., Dubinina, E. O., et al. (2021). Methane-derived authigenic carbonates on the seafloor of the laptev Sea shelf. *Front. Mar. Sci.* 8. doi:10.3389/fmars.2021.690304

Leprich, D. J., Flood, B. E., Schroedl, P. R., Ricci, E., Marlow, J. J., Girguis, P. R., et al. (2021). Sulfur bacteria promote dissolution of authigenic carbonates at marine methane seeps. *ISME J.* 15, 2043–2056. doi:10.1038/s41396-021-00903-3

Levin, L. a. (2005). Ecology of cold seep sediments : Interactions of fauna with flow , chemistry and microbes. *Oceanogr. Mar. Biol. Annu. Rev.* 43, 1–46. doi:10.1201/9781420037449.ch1

Levin, L. A., Baco, A. R., Bowden, D. A., Colaco, A., Cordes, E. E., Cunha, M. R., et al. (2016). Hydrothermal vents and methane seeps: Rethinking the sphere of influence. *Front. Mar. Sci.* 3, 1–23. doi:10.3389/fmars.2016.00072

Loher, M., Marcon, Y., Pape, T., Römer, M., Wintersteller, P., dos Santos Ferreira, C., et al. (2018). Seafloor sealing, doming, and collapse associated with gas seeps and authigenic carbonate structures at Venere mud volcano, Central Mediterranean. *Deep Sea Res. Part I Oceanogr. Res. Pap.* 137, 76–96. doi:10.1016/j.dsr.2018.04.006

Lu, Y., Sun, X., Xu, H., Konishi, H., Lin, Z., Xu, L., et al. (2018). Formation of dolomite catalyzed by sulfate-driven anaerobic oxidation of methane: Mineralogical and geochemical evidence from the northern South China Sea. *Am. Mineral.* 103, 720–734. doi:10.2138/am-2018-6226

Magalhães, V. H., Pinheiro, L. M., Ivanov, M. K., Kozlova, E., Blinova, V., Kolganova, J., et al. (2012). Formation processes of methane-derived authigenic carbonates from the Gulf of Cadiz. *Sediment. Geol.* 243–244, 155–168. doi:10.1016/j.sedgeo.2011.10.013

Marlow, J. J., Steele, J. A., Ziebis, W., Thurber, A. R., Levin, L. A., and Orphan, V. J. (2014). Carbonate-hosted methanotrophy represents an unrecognized methane sink in the deep sea. *Nat. Commun.* 5, 5094. doi:10.1038/ncomms6094

Marzi, R., Torkelson, B. E., and Olson, R. K. (1993). A revised carbon preference index. *Org. Geochem.* 20, 1303–1306. doi:10.1016/0146-6380(93)90016-5

Mayorga, I. C., Astilleros, J. M., and Fernández-Díaz, L. (2019). Precipitation of caco 3 polymorphs from aqueous solutions: The role of ph and sulphate groups. *Minerals* 9, 178–216. doi:10.3390/min9030178

Mazzini, A., Svensen, H. H., Planke, S., Forsberg, C. F., and Tjelta, T. I. (2016). Pockmarks and methanogenic carbonates above the giant Troll gas field in the Norwegian North Sea. *Mar. Geol.* 373, 26–38. doi:10.1016/j.margeo.2015.12.012

McGinnis, D. F., Greinert, J., Artemov, Y., Beaubien, S. E., and Wüest, A. (2006). Fate of rising methane bubbles in stratified waters: How much methane reaches the atmosphere? *J. Geophys. Res.* 111, C09007. doi:10.1029/2005JC003183

Meyers, P. A. (1994). Preservation of elemental and isotopic source identification of sedimentary organic matter. *Chem. Geol.* 114, 289–302. doi:10.1016/0009-2541(94)90059-0

Michaelis, W., Seifert, R., Nauhaus, K., Treude, T., Thiel, V., Blumenberg, M., et al. (2002). Microbial reefs in the Black Sea fueled by anaerobic oxidation of methane. *Science* 297, 1013–1015. doi:10.1126/science.1072502

Montalbetti, E., Fallati, L., Casartelli, M., Maggioni, D., Montano, S., Galli, P., et al. (2022). Reef complexity influences distribution and habitat choice of the corallivorous seastar Culcita schmideliana in the Maldives. *Coral Reefs* 41, 253–264. doi:10.1007/s00338-022-02230-1

Niemann, H., and Elvert, M. (2008). Diagnostic lipid biomarker and stable carbon isotope signatures of microbial communities mediating the anaerobic oxidation of methane with sulphate. *Org. Geochem.* 39, 1668–1677. doi:10.1016/j.orggeochem.2007.11.003

Panieri, G., Bünz, S., Fornari, D. J., Escartin, J., Serov, P., Jansson, P., et al. (2017). An integrated view of the methane system in the pockmarks at Vestnesa Ridge, 79°N. *Mar. Geol.* 390, 282–300. doi:10.1016/j.margeo.2017.06.006

Patton, H., Hubbard, A., Andreassen, K., Auriac, A., Whitehouse, P. L., Stroeven, A. P., et al. (2017). Deglaciation of the Eurasian ice sheet complex. *Quat. Sci. Rev.* 169, 148–172. doi:10.1016/j.quascirev.2017.05.019

Peckmann, J., Birgel, D., and Kiel, S. (2009). Molecular fossils reveal fluid composition and flow intensity at a Cretaceous seep. *Geology* 37, 847–850. doi:10.1130/G25658A.1

Peckmann, J., and Thiel, V. (2004). Carbon cycling at ancient methane-seeps. *Chem. Geol.* 205, 443–467. doi:10.1016/j.chemgeo.2003.12.025

Peckmann, J., Thiel, V., Reitner, J., Taviani, M., Aharon, P., and Michaelis, W. (2004). A microbial mat of a large sulfur bacterium preserved in a miocene methane-seep limestone. *Geomicrobiol. J.* 21, 247–255. doi:10.1080/01490450490438757

Phrampus, B. J., Lee, T. R., and Wood, W. T. (2020). A global probabilistic prediction of cold seeps and associated SEAfloor FLuid expulsion anomalies (SEAFLEAs). *Geochem. Geophys. Geosyst.* 21. doi:10.1029/2019GC008747

Pierre, C., Demange, J., Blanc-Valleron, M. M., and Dupré, S. (2017). Authigenic carbonate mounds from active methane seeps on the southern Aquitaine Shelf (Bay of Biscay, France): Evidence for anaerobic oxidation of biogenic methane and submarine groundwater discharge during formation. *Cont. Shelf Res.* 133, 13–25. doi:10.1016/j.csr.2016.12.003

Pierre, C., and Fouquet, Y. (2007). Authigenic carbonates from methane seeps of the Congo deep-sea fan. *Geo-Mar. Lett.* 27, 249–257. doi:10.1007/s00367-007-0081-3

Pierre, C., and Rouchy, J. M. (2004). Isotopic compositions of diagenetic dolomites in the Tortonian marls of the Western Mediterranean margins: Evidence of past gas hydrate formation and dissociation. *Chem. Geol.* 205, 469–484. doi:10.1016/j.chemgeo.2003.12.026

Portnov, A., Vadakkepuliyambatta, S., Mienert, J., and Hubbard, A. (2016). Ice-sheet-driven methane storage and release in the Arctic. *Nat. Commun.* 7, 10314. doi:10.1038/ncomms10314

Reeburgh, W. S. (2007). Oceanic methane biogeochemistry. *Chem. Rev.* 107, 486–513. doi:10.1021/cr050362v

Rise, L., Bellec, V. K., Ch, S., and Bøe, R. (2014). Pockmarks in the southwestern Barents Sea and finnmark fjords. *Nor. Geol. Tidsskr.* 94, 263–282. doi:10.17850/njg94-4-02

Risebrobakken, B., Moros, M., Ivanova, E. V., Chistyakova, N., and Rosenberg, R. (2010). Climate and oceanographic variability in the SW Barents Sea during the Holocene. *Holocene* 20, 609–621. doi:10.1177/0959683609356586

Roberts, H. H., and Feng, D. (2013). 3. Carbonate precipitation at Gulf of Mexico hydrocarbon seeps: An overview. *Hydrocarb. Seepage*, 43–61. doi:10.1190/1.9781560803119.ch3

Rooze, J., Peterson, L., Peterson, R. N., and Meile, C. (2020). Porewater flow patterns in surficial cold seep sediments inferred from conservative tracer profiles and early diagenetic modeling. *Chem. Geol.* 536, 119468. doi:10.1016/j.chemgeo.2020.119468

Sahling, H., Rickert, D., Lee, R. W., Linke, P., and Suess, E. (2002). Macrofaunal community structure and sulfide flux at gas hydrate deposits from the Cascadia convergent margin, NE Pacific. *Mar. Ecol. Prog. Ser.* 231, 121–138. doi:10.3354/meps231121

Sauer, S., Knies, J., Lepland, A., Chand, S., Eichinger, F., and Schubert, C. J. (2015). Hydrocarbon sources of cold seeps off the Vesterålen coast, northern Norway. *Chem. Geol.* 417, 371–382. doi:10.1016/j.chemgeo.2015.10.025

Schneider, A., Panieri, G., Lepland, A., Consolaro, C., Forwick, M., Johnson, J. E., et al. (2018). Methane seepage at vestnesa ridge (NW svalbard) since the last glacial maximum. *Quat. Sci. Rev.* 193, 98–117. doi:10.1016/j.quascirev.2018.06.006

Serov, P., Vadakkepuliyambatta, S., Mienert, J., Patton, H., Portnov, A., Silyakova, A., et al. (2017). Postglacial response of Arctic Ocean gas hydrates to climatic amelioration. *Proc. Natl. Acad. Sci. U. S. A.* 114, 6215–6220. doi:10.1073/pnas.1619288114

Sert, M. F., D'Andrilli, J., Gründger, F., Niemann, H., Granskog, M. A., Pavlov, A. K., et al. (2020). Compositional differences in dissolved organic matter between Arctic cold seeps versus non-seep sites at the Svalbard continental margin and the Barents Sea. *Front. Earth Sci.* 8 (8), 552731. doi:10.3389/feart.2020.552731

Smrzka, D., Feng, D., Himmler, T., Zwicker, J., Hu, Y., Monien, P., et al. (2020). Trace elements in methane-seep carbonates: Potentials, limitations, and perspectives. *Earth. Sci. Rev.* 208, 103263. doi:10.1016/j.earscirev.2020.103263

Smrzka, D., Zwicker, J., Klügel, A., Monien, P., Bach, W., Bohrmann, G., et al. (2016). Establishing criteria to distinguish oil-seep from methane-seep carbonates. *Geology* 44, 667–670. doi:10.1130/G38029.1

Sparrow, K. J., Kessler, J. D., Southon, J. R., Garcia-Tigreros, F., Schreiner, K. M., Ruppel, C. D., et al. (2018). Limited contribution of ancient methane to surface waters of the u.S. Beaufort sea shelf. *Sci. Adv.* 4, eaao4842–8. doi:10.1126/sciadv.aao4842

Suess, E. (2014). Marine cold seeps and their manifestations: Geological control, biogeochemical criteria and environmental conditions. doi:10.1007/s00531-014-1010-0

Suess, E. (2018). "Marine cold seeps: Background and recent advances," in *Hydrocarbons, oils and lipids: Diversity, origin, chemistry and fate* (Cham: Springer International Publishing), 1–21. doi:10.1007/978-3-319-54529-5_27-1

Swart, P. K. (2015). The geochemistry of carbonate diagenesis: The past, present and future. *Sedimentology* 62, 1233–1304. doi:10.1111/sed.12205

Teichert, B. M. A., Eisenhauer, A., Bohrmann, G., Haase-Schramm, A., Bock, B., and Linke, P. (2003). U/Th systematics and ages of authigenic carbonates from Hydrate Ridge, Cascadia Margin: Recorders of fluid flow variations. *Geochim. Cosmochim. Acta* 67, 3845–3857. doi:10.1016/S0016-7037(03)00128-5

Teichert, B. M. A. A., Bohrmann, G., and Suess, E. (2005a). Chemoherms on Hydrate Ridge — unique microbially-mediated carbonate build-ups growing into the water column. *Palaeogeogr. Palaeoclimatol. Palaeoecol.* 227, 67–85. doi:10.1016/j.palaeo.2005.04.029

Teichert, B. M. A., Gussone, N., Eisenhauer, A., and Bohrmann, G. (2005b). Clathrites: Archives of near-seafloor pore-fluid evolution (δ44/40Ca, δ13C, δ18O) in gas hydrate environments. *Geol.* 33, 213–216. doi:10.1130/G21317.1

Vadakkepuliyambatta, S., Bünz, S., Mienert, J., and Chand, S. (2013). Distribution of subsurface fluid-flow systems in the SW Barents Sea. *Mar. Pet. Geol.* 43, 208–221. doi:10.1016/j.marpetgeo.2013.02.007

Vadakkepuliyambatta, S., Chand, S., and Bünz, S. (2017). The history and future trends of ocean warming-induced gas hydrate dissociation in the SW Barents Sea. *Geophys. Res. Lett.* 44, 835–844. doi:10.1002/2016GL071841

Waage, M., Serov, P., Andreassen, K., Waghorn, K. A., and Bünz, S. (2020). Geological controls of giant crater development on the Arctic seafloor. *Sci. Rep.* 10, 1–12. doi:10.1038/s41598-020-65018-9–

Weber, T., Wiseman, N. A., and Kock, A. (2019). Global ocean methane emissions dominated by shallow coastal waters. *Nat. Commun.* 10, 4584. doi:10.1038/s41467-019-12541-7

Whiticar, M. J. (2020). "The biogeochemical methane cycle," in *Hydrocarbons, oils and lipids: Diversity, origin, chemistry and fate* (Cham: Springer International Publishing), 1–78. doi:10.1007/978-3-319-54529-5_5-1

Winsborrow, M. C. M., Andreassen, K., Corner, G. D., and Laberg, J. S. (2010). Deglaciation of a marine-based ice sheet: Late Weichselian palaeo-ice dynamics and retreat in the southern Barents Sea reconstructed from onshore and offshore glacial geomorphology. *Quat. Sci. Rev.* 29, 424–442. doi:10.1016/j.quascirev.2009.10.001

Yao, H., Niemann, H., and Panieri, G. (2020). Multi-proxy approach to unravel methane emission history of an Arctic cold seep. *Quat. Sci. Rev.* 244, 106490. doi:10.1016/j.quascirev.2020.106490

Yao, H., Panieri, G., Lehmann, M. F., Himmler, T., and Niemann, H. (2021). Biomarker and isotopic composition of seep carbonates record environmental conditions in two arctic methane seeps. *Front. Earth Sci.* 8, 1–12. doi:10.3389/feart.2020.570742

Zhang, Y., Jing, H., and Peng, X. (2020). Vertical shifts of particle-attached and free-living prokaryotes in the water column above the cold seeps of the South China Sea. *Mar. Pollut. Bull.* 156, 111230. doi:10.1016/j.marpolbul.2020.111230

Zwicker, J., Smrzka, D., Himmler, T., Monien, P., Gier, S., Goedert, J. L., et al. (2018). Rare Earth elements as tracers for microbial activity and early diagenesis: A new perspective from carbonate cements of ancient methane-seep deposits. *Chem. Geol.* 501, 77–85. doi:10.1016/j.chemgeo.2018.10.010

frontiers | Frontiers in Marine Science

TYPE Review
PUBLISHED 15 December 2022
DOI 10.3389/fmars.2022.1031096

OPEN ACCESS

EDITED BY
Dong Feng,
Shanghai Ocean University, China

REVIEWED BY
Yang Lu,
University of Oslo, Norway
Zhifeng Wan,
Sun Yat-sen University, China

*CORRESPONDENCE
Hailong Lu
hlu@pku.edu.cn

SPECIALTY SECTION
This article was submitted to
Marine Biogeochemistry,
a section of the journal
Frontiers in Marine Science

RECEIVED 29 August 2022
ACCEPTED 14 November 2022
PUBLISHED 15 December 2022

CITATION
Liu H, Zhan L and Lu H (2022)
Mechanisms for upward migration of methane in marine sediments.
Front. Mar. Sci. 9:1031096.
doi: 10.3389/fmars.2022.1031096

Mechanisms for upward migration of methane in marine sediments

Haotian Liu[1,2], Linsen Zhan[2] and Hailong Lu[2]*

[1]College of Engineering, Peking University, Beijing, China, [2]Beijing International Center for Gas Hydrate, School of Earth and Space Sciences, Peking University, Beijing, China

Methane, a non-negligible component of the global carbon budget, could be discharged upward through marine sediments to ocean floor by certain migration mechanisms. Although quite some studies have been conducted, the mechanisms for methane migration have not been well reviewed yet, especially in hydrate-bearing sediments. In this study, methane migration mechanisms are classified into diffusion and advection processes which include water movement, free gas flow, sediment failures, and recently developed gas migration through hydrate channels. The occurrence of natural gas hydrate might affect methane migration in three ways: (1) reducing the permeability of marine sediments and consequently hindering the upward movement of methane either in gas or liquid phase, (2) enhancing the geomechanical strength of marine sediments, which prevents the creation of new pathways for methane escape by sediment failures, and (3) benefiting upward methane migration by constructing hydrate channels at the interface of continuous gas columns. Generally, dissolved methane could hardly break through the gas hydrate stability zone and sulfate-methane transition zone because of the high consumption rate for methane in these two zones. For free methane gas, the capillary force is a strong resistance to free gas flow in porous sediments. However, whether for dissolved methane or free methane gas, discharge along pre-existing fractures or failure surfaces might be considerable. In addition, methane discharge by gas flow through hydrate channels is still hard to constrain. Finally, based on current research uncertainties in constraining the methane flux to the ocean, the research outlook is also addressed. It is suggested that more investigations should be conducted in three aspects: the flow characteristic of high-permeability conduits, the quantitative correlations of geomechanical properties and hydrate distribution, and the occurrence conditions of hydrate channels.

KEYWORDS

diffusion, water movement, free gas flow, sediment failure, hydrate channel, gas hydrate

1 Introduction

Methane is a potent greenhouse gas with a warming potential that is ~23 times stronger than carbon dioxide (Stocker, 2014), and can be generated in marine sediments primarily by biodegradation of organic matters or thermal decomposition of organic matters in depth (Reeburgh, 2007; Timmis et al., 2010; You et al., 2019). The methane would migrate upward through marine sediments, potentially escaping into ocean or even to atmosphere (Liu et al., 2019). Considering the vast area of seafloor, the methane flux across seafloor to the ocean is expected to account for a non-negligible part of the global carbon budget (Dickens, 2003; Weber et al., 2019). For example, Ruppel and Kessler (2017) estimated the global methane flux in the range of 16 to 3200 Tg yr^{-1} based on an assumption that the dissolved methane concentration and the aerobic oxidation rate for methane are both steady. However, it is quite difficult to constrain the methane flux accurately, considering the spatial heterogeneity of marine sediments and the difference in mechanisms for methane transport. That is, different mechanisms for methane transport might dominate in different geological settings, contributing unevenly to the methane flux. The limited data available might also lead to the estimation of the methane flux with a variance of orders of magnitude over different regions or even at different spots in the same region (Linke et al., 1994; Tryon et al., 1999). Moreover, some processes might be involved with methane, e.g., hydrate formation/degradation (Ruppel and Waite, 2020), methane dissolution/exsolution (Sultan et al., 2020), and oxidation of methane (Barnes and Goldberg, 1976), and they could also exert a certain influence on upward methane migration, complicating the estimation of the methane flux. Therefore, it is too arbitrary to obtain the global methane flux by simply extrapolating from the locally-representative data in field surveys. To understand methane migration in marine sediments, clarification on the methane migration mechanisms is required for constraining the methane flux from sediments to the ocean.

In this review, the mechanisms for upward methane migration in gas hydrate systems are summarized, including diffusion and advection, such as water movement, free gas flow, sediment failures, and recently developed gas flow through hydrate channels, with the effects of hydrate formation and anaerobic oxidation on methane. The contribution of each mechanism to the methane flux to the ocean is also qualitatively evaluated. The future research outlook is also addressed based on current research uncertainties in constraining the methane flux to the ocean. This review aims to (1) provide a comprehensive understanding of different methane migration mechanisms associated with gas hydrate systems that can cause methane seepage and (2) point out future research topics that should be strengthened to help constrain the methane flux to the ocean.

2 Migration mechanisms

2.1 Upward methane diffusion

Diffusion, one of the most fundamental mechanisms for mass transfer, is the movement of small particles (e.g., atoms, ions, molecules) from a region with higher concentration to that with lower concentration, driven by a gradient in Gibbs free energy or chemical potential. When one solute distributes unevenly in bulk water, its steady diffusive flux could be obtained from Fick's First Law at the macroscale (Fick, 1855; Atkins and de Paula, 2021),

$$J = -D \nabla c_{aqu}^{CH_4} \tag{1}$$

where J is the diffusive flux (nL^{-2}T^{-1}); D is the diffusion coefficient (L^{2}T^{-1}); $c_{aqu}^{CH_4}$ is the dissolved methane concentration (nL^{-3}). In water saturated porous media, the matters dissolved into pore water could also be transferred by diffusion through throats between grains. Previous studies have indicated that the diffusive flux in porous media J_e could be described approximately by $J_e = -D_e \nabla c_{aqu}^{CH_4}$ similar to Fick's First Law (Perkins and Johnston, 1963). The law is a good tool for calculating the diffusive methane flux according to the measured methane concentration profile. For example, Cao et al. (2021) obtained the diffusive methane flux of five sites in pockmark areas offshore Fujian province ranging from 2.89 – 15.17 × 10^{-2} mmol/(m^{2}yr) by Fick's First Law.

2.1.1 Effective diffusion coefficient

The effective diffusion coefficient D_e in porous media is generally lower than the coefficient D in bulk water, since diffusion in porous media would be weakened by the tortuosity of the flow paths (Ullman and Aller, 1982). This means D_e is dependent on porosity and pore structures (Ullman and Aller, 1982; Iversen and Jørgensen, 1993), besides pressure, temperature, and concentration as in bulk water. According to Iversen and Jørgensen (1993), the effective diffusion coefficient for methane in marine sediments at 4 °C (near the seafloor temperature) lies between 10^{-8} and 10^{-9} m^{2}s^{-1}, which indicates that methane diffusion might be an extremely inefficient way for methane migration in marine sediments.

2.1.2 Concentration gradient of methane

As a consequence of the heterogeneity of methane sources, pressure, temperature, salinity, and lithology (Handa, 1990; Ginsburg and Soloviev, 1997; Brereton et al., 1998; Nole et al., 2016), methane concentration is normally uneven in marine sediments. In the vertical direction, the effects of pressure and temperature are preferentially considered, since the geothermal gradient and the hydrostatic gradient are common in marine sediments.

Methane solubility is the maximum concentration of dissolved methane at a given *P-T* condition, here regarded as the reference value of the methane concentration. Methane solubility could be classified into methane gas solubility and methane hydrate solubility (You et al., 2019). The former refers to the dissolved methane concentration when dissolved methane and free methane gas are at thermodynamic equilibrium. Duan and Weare (1992) suggested that higher methane gas solubility can be obtained at lower temperature and higher pressure. On the other hand, methane hydrate solubility represents the dissolved methane concentration when dissolved methane and methane hydrate are at thermodynamic equilibrium. Methane hydrate solubility increases with temperature and decreases with pressure (Henry et al., 1999).

The vertical temperature and pressure distributions have opposite effects on these two methane solubilities, considering that temperature and pressure both increase with depth. According to previous calculations (Xu and Ruppel, 1999; You et al., 2019), these two solubilities are both sensitive to temperature change in geological systems. That says, methane hydrate solubility increases with depth, while methane gas solubility slightly decreases with depth, as shown in Figure 1.

2.1.3 Contribution of diffusion

Although the upward-decreasing methane hydrate solubility provides a driving force for vertical methane diffusion, the diffusion plays a minor role in transporting methane to the ocean, especially over long distances (Max, 2003; You and Flemings, 2021). According to some field surveys conducted in ocean or lake (Keller and Stallard, 1994; Sauter et al., 2006; Delsontro et al., 2010), methane diffusion only takes a minor

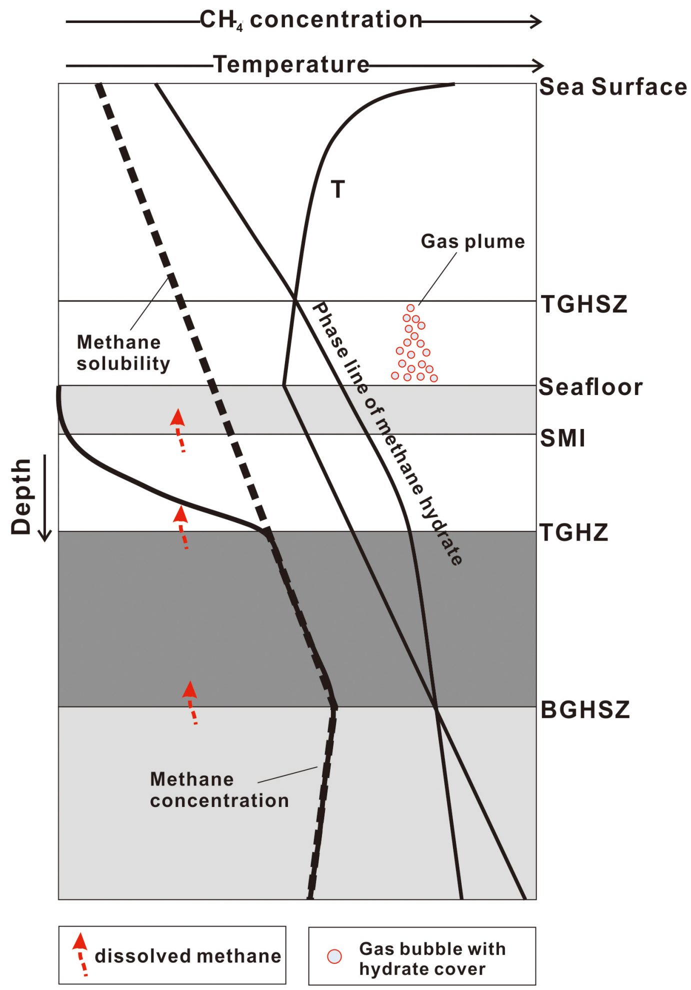

FIGURE 1
Conceptual profile of dissolved methane concentration and solubility [modified from Xu and Ruppel (1999)]. The two solubility curves intersect at the base of gas hydrate stability zone (BGHSZ). TGHSZ, top of gas hydrate stability zone; SMI, sulfate-methane interface; TGHZ, top of gas hydrate zone. Thicknesses of each layer are not to scale.

part of overall methane discharge across seafloor or lake bottom, as the result of the low diffusion coefficient and the low concentration gradient combined. As suggested by Algar et al. (2011a), a timescale of weeks to months would be taken for dissolved methane to pass through tens of centimeters thick sediments based on the Einstein-Smoluchowski equation (Islam, 2004), allowing for the conversion of most dissolved methane into methane hydrate in the gas hydrate stability zone (GHSZ). The upward-decreasing methane hydrate solubility means hydrate formation is even easier in shallower sediments, since the amount of hydrate formation is dependent on the excessive dissolved methane concentration over methane solubility (Ginsburg and Soloviev, 1997), which indicates that GHSZ is a strong barrier for methane diffusion (Xu and Ruppel, 1999). In addition, the methane escaping from GHSZ would be oxidized with sulfate by a process known as sulfate-driven anaerobic oxidation of methane (SD-AOM): $CH_4(aq) + SO_4^{2-}(aq) \rightarrow HCO_3^-(aq) + HS^-(aq) + H_2O$, in which the diffusive methane is usually completely consumed (Barnes and Goldberg, 1976; Reeburgh, 2007; Dale et al., 2009; James et al., 2016; Egger et al., 2018; Mau et al., 2020; De La Fuente et al., 2022). For example, Dale et al. (2008) pointed out that less than 1% of the upward dissolved methane flux could reach the ocean under the restriction of SD-AOM. The SD-AOM communities could even improve their metabolic activities to balance the increase of the methane flux (Nauhaus et al., 2002). The sediment column in which SD-AOM occurs is therefore termed as sulfate-methane transition zone (SMTZ). This means SMTZ is another efficient barrier for methane migration besides GHSZ. Despite the low efficiency of diffusion for methane discharge, diffusion is a universal process for methane migration in marine sediments. A mud layer could be an effective seal for gas bubble motion, but cannot arrest the diffusion of dissolved methane according to previous experiments (Miller, 1980).

2.2 Upward methane advection

Advection is another mechanism for mass transfer by the bulk motion of fluid. In porous media, fluid flow could be affected by porosity and pore structures, besides fluid viscosity and pressure distribution as in free flow. In marine sediments, the vertical advection of the dissolved or free methane might cause methane discharge to the ocean. By pathways and methane phase states, the upward methane advection could be classified into water movement, free gas flow, sediment failures, and gas flow through hydrate channels.

2.2.1 Water movement

The upward water movement in marine sediments could be driven by overpressure gradient, buoyancy, and osmotic pressure. Regardless of driving force, the methane flux could be obtained by the following equation,

$$q_{CH_4} = c_{aqu}^{CH_4} q_{aqu} \tag{2}$$

where $q_{CH4}$is the upward methane flux ($nL^{-2}T^{-1}$); q_{aqu} is the water flux (LT^{-1}), as determined by driving force.

2.2.1.1 Driving force

2.2.1.1.1 Overpressure gradient

In active marine margins, external forces with high sedimentation rates and compaction would induce vertical fluid flow with velocities of several millimeters to 1-2 meters per year (James et al., 2016). The vertical water flux could be calculated according to Darcy's Law (Darcy, 1856; Bear, 1988) as follows,

$$q_{aqu} = -\frac{k}{\mu_w}\left(\frac{\partial P_w}{\partial z} + \rho_w g\right) \tag{3}$$

where q_{aqu} is the water flux (LT^{-1}); k is the permeability (L^2); μ_w is the dynamic water viscosity ($ML^{-1}T^{-1}$); P_w is the water pressure ($ML^{-1}T^{-2}$); P_w is the water density (ML^{-3}); g is the gravitational acceleration (LT^{-2}). The equation shows that the upward water flux is the function of the permeability and overpressure gradient $\partial P_w/\partial z + \rho_w g$ (i.e., the hydrostatic pressure gradient subtracted from the fluid pressure gradient). For example, Dugan and Flemings (2000) suggested that fluid is expelled laterally and vertically upward with an average Darcy velocity of 0.5 mm/yr in New Jersey continental slope through numerical simulation based on Darcy's Law.

The overpressure gradient could be caused by the external loading decrease and the internal pressure increase. The external loading decrease might occur in short-time processes, such as daily tidal variations (Hsu et al., 2013; Sultan et al., 2020) or in geologic-timescale activities like iceberg retreating (Dessandier et al., 2021). Another cause for the genesis of the overpressure gradient is the increase of pore pressure in sediments, which could be generated by physical processes [e.g., disequilibrium compaction in rapid sedimentation (Osborne and Swarbrick, 1997; Dugan and Flemings, 2000; Dugan and Sheahan, 2012), light fluid migration from depth (Osborne and Swarbrick, 1997), fluid aquathermal expansion (Bethke, 1986; Mello et al., 1994), and tectonic movements (Li et al., 2022)], or chemical processes [e.g., diagenesis and hydrocarbon generation (Bethke, 1986; Ma et al., 2021)]. For hydrate-bearing sediments, hydrate dissociation caused by the change of ambient conditions could also pressurize surrounding water, since gas released from hydrate dissociation would expand in pores (Xu and Germanovich, 2006). Additionally, hydrate-bearing sediments could act as good seals for gas migration (Hornbach et al., 2004; Ma et al., 2021). For example, Flemings et al. (2003) suggested that fluid pressure beneath hydrate layers even reaches ~70% of the lithostatic stress in Blake Ridge.

Except for those naturally-occurring overpressure, human activities could also induce localized overpressure. For instance, overpressure in marine sediments might be induced during drilling operations or hydrocarbon production processes, since external fluids are generally injected into marine sediments to ensure smooth drilling or enhance recovery (Dugan and Sheahan, 2012). Therefore, gas hydrate must be carefully developed to avoid man-made large-scale methane leak (Zhang and Zhai, 2015), although it has been viewed as a promising energy source (Boswell and Collett, 2011).

2.2.1.1.2 Buoyancy

When less dense water is surrounded by high-density water, it could rise spontaneously by buoyancy. The water flux could be calculated as follows,

$$q_{aqu} = -\frac{k}{\mu_w}(\Delta\rho g) \tag{4}$$

where $\Delta\rho$ is the density difference between the two fluids (ML^{-3}). For homogeneous sediments, Cardoso and Cartwright (2016) estimated the velocity of upward fluid flow at 0.15m/yr and 0.75m/yr for thermal and solute sources, respectively.

In marine sediments, the buoyancy of water phase can be induced by thermal or solute sources. The former represents the decrease of water density due to heating, while the latter means the density change caused by the diffusion of solutes. These two sources could also occur in gas hydrate formation or dissociation processes. For instance, heat would be released during hydrate formation or less dense fresh water would be released during hydrate dissociation (Cardoso and Cartwright, 2016).

2.2.1.1.3 Osmotic effects

The osmotic effects would cause a flow of water from the dilute solution to the strong solution through semipermeable membranes. Cardoso and Cartwright (2016) proposed that marine sediments could be regarded as a special case of semipermeable media for methane movement, considering the strong absorption of marine sediments for methane molecules. By osmotic pressure, methane-free seawater would move downward through marine sediments to displace methane-saturated pore water upward along high-permeability conduits. Based on field measurements, Cardoso and Cartwright (2016) gave an estimation of the water flux by considering a balance of osmotic and viscous forces as follows,

$$q_{aqu} \sim \frac{2k_f}{a\mu_w}P_o = \frac{2k_f}{a\mu_w}\sigma_0 c_0 RT \tag{5}$$

where k_f is the permeability of high-permeability conduits (L^2); P_o is the osmotic pressure ($ML^{-1}T^{-2}$); σ_0 is the reflection coefficient (1); c_0 is methane solubility (nL^{-3}); R is the universal gas constant ($ML^2T^{-2}n^{-1}K^{-1}$); T is the temperature (K); a is the radius of high-permeability conduits (L).

2.2.1.2 Permeability

The permeability of marine sediments regulates the amount of water that could pass through the overlying sediments to the ocean, reflecting the resistance of sediment grains to free flow. Reagan et al. (2011) suggested that the permeability of marine sediments is a predominant factor controlling methane discharge to the ocean by numerical simulation. The permeability of marine sediments is dependent on porosity, pore structures, compaction degree, cementing types, clay content, with extra hydrate saturation S_h and hydrate morphology for hydrate-bearing sediments (Lijith et al., 2019). According to field surveys, the permeability of marine sediments exhibits a great variance of orders of magnitude, ranging from 10^{-8} m^2 for sands to 10^{-19} m^2 for consolidated muds (Max, 2003; Spinelli et al., 2004). The permeability in hydrate-occurring continental margins also shows variance. For instance, the permeability in production interval is just a few mDs (1 $mD=10^{-15}$ m^2) in China's first production test (Ye et al., 2020), while it is around 10^2 mDs at the Nankai Trough (Konno et al., 2010).

For hydrate-bearing sediments, gas hydrate precipitating in pores increases the resistance to gas/water flow. At the macroscale, the extra resistance is reflected by the reduction of sediment permeability, even by orders of magnitude, as suggested by previous experiments (Kang et al., 2016). Free gas accumulations beneath hydrate-bearing sediments, a typical feature of gas hydrate reservoirs, are widely observed with bottom simulating reflectors (BSRs) indicating hydrate reservoirs (Haacke et al., 2007; Hornbach et al., 2012; Li et al., 2018), which exhibits the seal capacity of hydrate-bearing sediments. The pore habits, spatial distribution, and hydrate saturation are expected to be critical factors for the permeability of hydrate-bearing sediments (Ren et al., 2020). Some widely-used permeability models are classified into theoretical analyses, empirical models, and numerical simulation models, as shown in Table 1. In addition to these prediction models, the actual permeability of hydrate-bearing sediments was also extensively measured by direct flow tests (Kumar et al., 2010; Li et al., 2017; Dai et al., 2019; Shen et al., 2020), numerical simulation combined with computed tomography (CT) images (Zhang et al., 2020; Pan et al., 2021; Sun et al., 2021), and *in situ* measurements with downhole tools (Fujii et al., 2015). Those permeability models in Table 1 are often used as the benchmarks of actual permeability tests. Both the models and the actual measurements indicate that the permeability decreases with hydrate saturation, although the decrease rate varies in different models and measurements.

2.2.1.3 Methane concentration

As mentioned above, methane solubility in pore water could be classified into methane gas solubility and methane hydrate solubility. No matter which type of methane

TABLE 1 Prediction models for water permeability in the presence of gas hydrate.

Type	Model	Formula	Fitting parameter	Reference	Remark
Theoretical analyses	Tokyo	$k(S_h)=k_0(1-S_h)^2$		(Masuda et al., 1997)	Original Tokyo's model
	PCTM	$k(S_h) = k_0[1 - S_h^2 + 2(1 - S_h)^2/lnS_h]$		(Kleinberg et al., 2003)	PF
		$k(S_h)=k_0(1-S_h)^2$		(Kleinberg et al., 2003)	GC
	SCPM	$k(S_h)=k_0(1-S_h)^4$		(Dai and Seol, 2014)	PF
		$k(S_h)=k_0(1-S_h)^2$		(Dai and Seol, 2014)	GC
Empirical model	Tokyo	$k(S_h)=k_0(1-S_h)^N$	N	(Masuda et al., 1997)	
	SDR	$k(S_h) = C\phi^4 T_{2LM}^2$		(Kleinberg et al., 2003)	T_{2LM} is the logarithmic mean value of the T2 distribution
	KGM	$k(S_h) = k_0(1 - S_h)^{n+2}/(1 + S_h^{0.5})^2$	n (Archie saturation exponent)	(Kleinberg et al., 2003)	PF
		$k(S_h)=k_0(1-S_h)^{n+1}$		(Kleinberg et al., 2003)	GC
	LBNL	$k(S_h)=k_0[(\phi(S_h)-\phi_c)/(\phi_0-\phi_c)]^n$	n typically ranging from 2 to 3	(Moridis, 2014)	
Numerical simulation	Modified KGM	$k(S_h)=k_0[(1-S_h)^3/(1+2S_h)^2]$		(Dai and Seol, 2014)	PNM
	Linear regressions	$k(S_h) = k_0[\frac{(1 - S_h)^3}{(1 + 2.094S_h - 6.691S_h^2 + 6.837S_h^3)^2}]$		(Kang et al., 2016)	PF; LBM
		$k(S_h) = k_0[\frac{(1 - S_h)^3}{(1 - 0.543S_h - 0.148S_h^2 + 1.886S_h^3)^2}]$		(Kang et al., 2016)	GC; LBM
		$k(S_h) = \tau_{cr}^{-6} r_{cr}(1 - S_h)^3$		(Hou et al., 2018)	LBM; τ_{cr} is the relative control seepage channel tortuosity; r_{cr} is the relative control flow channel size

PCTM, parallel capillary tube model.
SCPM, simple cubic packing model.
SDR, Schlumberger-Doll Research model.
KGM, Kozeny grain model.
LBNL, Lawrence Berkeley National Laboratory model.
PF, pore-filling.
GC, grain-coating.
PNM, pore network model.
LBM, Lattice Boltzmann method.

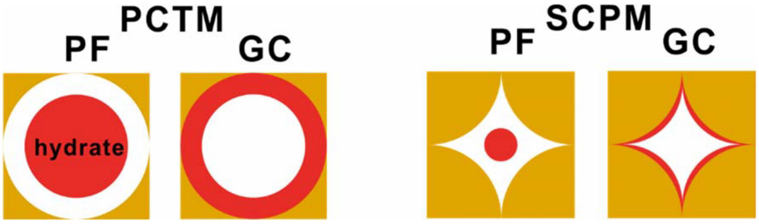

solubility is, it could be predicted accurately according to existing equations of state (Duan and Weare, 1992; Henry et al., 1999). Davie et al. (2004) suggested that methane solubility ranges roughly from 0.05 to 0.2 M (mole per liter) at depths from 0 to 600 meters below seafloor (mbsf) in selected sites.

2.2.1.4 Contribution of water movement

Methane discharge alongside the upward water movement is expected to be of minor importance, since methane solubility is small and the driving force would supposedly dissipate over long migration distance (Max, 2003). Considering that the methane flux is low, GHSZ and SMTZ are still powerful barriers to methane migration (James et al., 2016; You et al., 2019; Ruppel and Waite, 2020), as in the upward methane diffusion. The limited literatures also indicate that the real-time fluid flux across seafloor is low and transient (Tryon et al., 1999; Torres et al., 2002; Sauter et al., 2006).

However, high water flux might occur if fractures, faults, scarps, or other high-permeability pathways exist, accompanied by striking phenomena including cold seeps, mud volcanos, and pockmarks on the seabed (Ma et al., 2021). Linke et al. (1994) measured a fluid velocity as high as 10^5 cm/yr in seep sites, and calculated a methane flux of 120 mmol/(m^2day) on Hydrate Ridge. Stranne et al. (2019) suggested that fracture flow with high velocities could weaken the SD-AOM efficiency by numerical simulation. In addition, polygonal faults developed in fine-grained sediments weaken the seal capacity of marine sediments, providing new pathways for upward water migration (Ma et al., 2021). Berndt (2005) suggested that pipe structures extending from deep polygonal faults are probably the evidence of fluid migration along fault planes.

Human activities are also worrying since these activities might induce more violent increase of fluid pressure than natural processes. It should be noted that when water pressure is high enough to overcome the lithostatic stress, sediments failures (e.g., hydraulic fracturing and fault slips) would occur, facilitating the upward movement of methane (Hornbach et al., 2004; Dugan and Sheahan, 2012).

2.2.2 Free gas flow

Methane bubbles would nucleate if the methane concentration exceeds its solubility. For hydrate-bearing sediments, hydrate can also dissociate into free methane gas and water when *P-T* condition resides out of the gas hydrate stability zone. These methane bubbles would migrate upward by buoyancy, with the possibility of reaching the ocean singly or as a plume. For example, more than 250 gas plumes were observed emitting from the seafloor of the West Spitsbergen margin above the upper limit of GHSZ (Graham, 2009). The free gas flow in porous sediments is composed of three processes: buoyant movement, capillary trapping, and pressure-driven flow.

2.2.2.1 Buoyant movement

When gas bubbles are small enough or flow space is large enough (e.g., fractures), these bubbles could move freely without being deformed by grains in the vertical direction, as methane gas is still buoyant relative to pore water even at large depth (Max, 2003). The upward velocity of gas bubbles v_b (LT^{-1}) could be estimated by the Stoke's law (Zheng and Yapa, 2000),

$$v_b = \frac{g(\rho_w - \rho_g)d^2}{18\mu_w} \tag{6}$$

where ρ_w is the water density (ML^{-3}); ρ_g is the density of gas bubbles (ML^{-3}); d is the diameter of gas bubbles (L). By the equation, the upward velocity of a bubble with a diameter of 5 mm might be as high as 13 m/s (g=9.8 m/s^2, μ_w=10^{-3} kg/(m·s), ρ_w-$\rho_g \approx 10^3$ kg/m^3).

2.2.2.2 Capillary trapping

Except for that occurring in large space like fractures, the free buoyant movement is not supposed to last long, since the upward movement of methane bubbles is accompanied by the expansion of their volumes with the decrease of the surrounding pressure (Mahabadi et al., 2018). When growing to sizes greater than throats, these methane bubbles would be trapped in the pores (i.e., capillary trapping or residual trapping). Normally, the buoyancy exerted on methane bubbles is much smaller than the auxiliary capillary resistance against these bubbles that intend to pass through throats. Accordingly, the maximum height of gas column *H* (L) that overlying sediments can withstand could be calculated by means of Hunt et al. (1988),

$$P_g - P_w = \frac{2\gamma\cos\theta}{r} = (\rho_w - \rho_g)H \tag{7}$$

where P_g and P_w are the gas and water pressure ($ML^{-1}T^{-2}$), respectively; γ is the gas-water interfacial tension (MT^{-2}); θ is the contact angle (1); r is the radius of the narrowest throat (L). The third term of the equation represents the buoyancy exerted on the gas column with a height of *H*. The capillary resistance is inversely proportional to the radius of throats containing gas-water interfaces. The equation can be used to evaluate the sealing capacity of sediments for free gas, e.g., mud with a pore radius of 100 nm can withstand roughly an interconnected gas column of kilometers high (Max, 2003). Those isolated bubbles are supposedly stabilized in the pores, which holds promise for conducting the storage of greenhouse gases in aquifers (Krevor et al., 2015). In GHSZ, hydrate shells can form at the surface of these methane bubbles (Jin et al., 2012; Chen et al., 2017; Lei et al., 2019) and might hinder the upward movement of methane bubbles, since hydrate shells with certain mechanical strength could prevent the deformation of these bubbles that intend to pass through throats, as shown in Figure 2.

However, recent studies indicated that those isolated bubbles trapped in pores are only stable hydrodynamically not thermodynamically. Xu et al. (2019) suggested that gravity induces a vertical chemical potential gradient that could lead to the upward diffusion between two static bubbles, even with the same pressure. Yet, the diffusion is slow and might be negligible unless in a timescale of thousands of years.

2.2.2.3 Pressure-driven flow

When gas supply from depth is abundant, gas accumulates gradually up to its critical height that could penetrate the overlying sediments. The capillary resistance exceeds far the viscous force as gas flow is expected to be very slow, so the most favorable path is the one that connects the largest throats in

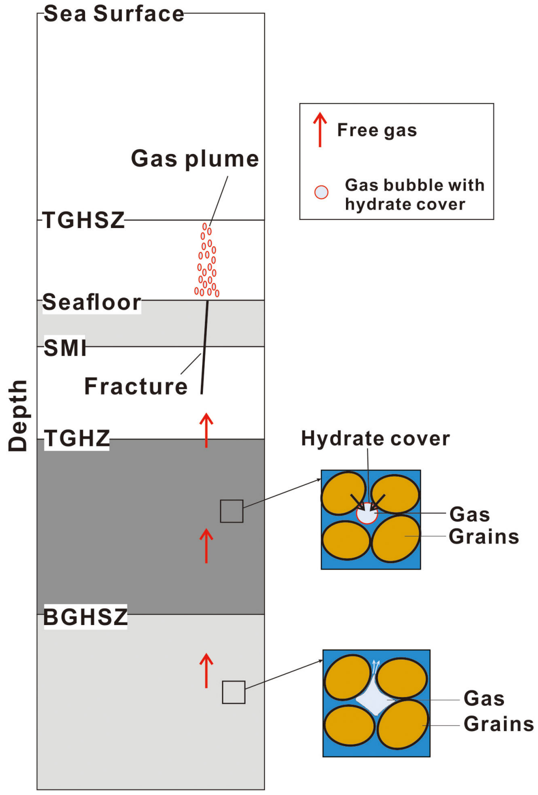

FIGURE 2
Schematics of capillary invasion of free gas bubbles and resistance from hydrate cover to capillary invasion in gas hydrate stability zone [modified from Fauria and Rempel (2011)]. Thicknesses of each layer are not to scale.

sediments (Max, 2003). At the macroscale, the gas flux q_{gas} (LT^{-1}) could be calculated by Darcy's Law in multiphase flow scenarios,

$$q_{gas} = [-\frac{kk_{rg}}{\mu_g}(\frac{\partial P_g}{\partial z} + \rho_g g)] \quad (8)$$

where k_{rg} is the relative permeability of gas phase ranging from 0 ~ 1; μ_g is the gas viscosity ($ML^{-1}T^{-1}$). The pressure gradient can be induced by the density difference between gas and water phase. Etiope (2015) suggested that the continuous gas flow can easily reach the velocities of 10^{-4} to 10^{0} cm/s (observed gas velocities) in less than 0.02 mm wide fractures, faster than the buoyant bubble movement at the same condition. However, in real marine sediments with complex structure, the continuous gas flow is limited by the relative permeability of gas phase k_{rg}.

The relative permeability k_{rg}, often expressed as the function of gas saturation S_g, could be affected by the wettability of grains, pore structures, the ratio of gas viscosity to water viscosity, the capillary curve, the measurement methods, and hydrate saturation S_h for hydrate-bearing sediments (Lijith et al., 2019). The results of Johnson et al. (2011) and Dai et al. (2019) indicated that k_{rg} in hydrate-bearing sediments is lower than the water relative permeability k_{rw} in a large range of S_g, since gas is the non-wetting phase at most time in marine sediments.

Some classical relative permeability models (usually the function of water saturation S_w) for unsaturated soils are used for marine sediments, as shown in Table 2. Jang and Santamarina (2014) suggested Corey's and van Genuchten's models are applicable in hydrate-bearing sediments by numerical simulation. Several correlations have been invoked to describe the effects of gas hydrate on empirical parameters (e.g., n_w, n_g, S_{rw}) in these relative permeability models based on numerical simulation, as shown in Table 2, suggesting lower relative permeability would be obtained at higher hydrate saturation.

2.2.2.4 Contribution of free gas flow

The free gas flow is expected to be of minor importance for methane discharge to the ocean, since isolated methane bubbles would be trapped by the capillary force and consumed gradually by hydrate formation in GHSZ, and continuous free gas flow would be limited by low relative permeability for gas phase.

TABLE 2 Relative permeability models applied in marine sediments and corresponding correlations for fitting parameters.

Model	Formula	$\bar{S}$	Fitting parameters	Reference	Correlations for fitting parameters
Van Genuchten	$k_{rw}=\bar{S}^{0.5}[1-(1-\bar{S}^{1/m})^m]^2$	$\bar{S}=(S_w-S_{rw})/(S_{wmax}-S_{rw})$	S_{rw} S_{wmax} m	(Van Genuchten, 1980)	$\begin{cases} m=m_0(1-0.19S_h) \\ S_{rw}=0.1+0.17S_h \\ S_{wmax}=1-0.7S_h \end{cases}$ (Mahabadi et al., 2016)
Modified Stone	k_{rw}=[(S_w–S_{rw})/(1–S_{rw})]^{n_w}		S_{rw} n_w n_g	(Stone, 1970)	$\begin{cases} n_w=2.4 \text{ avg.} \\ n_g=S_h^{0.38}/1.35 \end{cases}$ (Mahabadi and Jang, 2014)
	k_{rg}=[(S_g–S_{rg})/(1–S_{rw})]^{n_g}				$\begin{cases} n_w=3.0\tilde{\ }3.5 \\ n_g=2+2.6S_h \\ S_{rw}=0.1+0.17S_h \end{cases}$ (Mahabadi et al., 2016)
Corey	$k_{rw}=\bar{S}^4$ $k_{rg}=(1-\bar{S})^2(1-\bar{S}^2)$	$\bar{S}=(S_w-S_{rw})/(1-S_{rg}-S_{rw})$		(Corey, 1954)	

However, if high-permeability conduits are present in marine sediments, the capillary force can drive gas (non-wetting phase) from marine sediments to these conduits, because the capillary force is minor in open space (Bethke et al., 1991). When these methane bubbles pass through GHSZ, hydrate shells might form at water-gas interfaces (Warzinski et al., 2014). Yet, there is limited knowledge about the competition between the fast movement of gas bubbles and hydrate formation. The effects of SD-AOM on methane bubbles are limited, since microbes can only access dissolved methane (James et al., 2016; De La Fuente et al., 2022). However, Regnier et al. (2011) suggested that if pore water reaches methane-undersaturated under the influence of the methane consumption of SD-AOM, part of the free methane gas could re-dissolve and contribute to the flux of dissolved methane accessible to microbes. These methane bubbles could migrate along high-permeability conduits with a high velocity, potentially move across seafloor, and form gas plumes in the water column (Römer et al., 2019). Seabed features linked to gas release, such as pockmarks, mud volcanoes, and cold seeps, reflect gas migration along sub-seabed high-permeability conduits (Sultan et al., 2020). The free gas movement along high-permeability conduits is seen as a dominant methane transport mechanism (Saunders et al., 1999). For example, Torres et al. (2002) observed methane bubbles escaping from subsurface conduits at a velocity of ~1 m/s on Hydrate Ridge.

2.2.3 Sediment failures

Although overpressure is a critical driving force for the upward migration of water or gas phase, the increase of fluid pressure P_f (gas or water pressure) might lead to sediment failures due to the decrease of effective stress σ' (= σ - P_f, assuming Biot's coefficient a =1). Once sediments fail, these failures provide new pathways for methane escape and could be classified into fracture initiation, fault slips, and large-scale submarine landslides according to scale.

Hydrate-bearing sediments can generally resist the occurrence of sediment failures due to the enhancement of gas hydrate on sediment strength. The enhancement from gas hydrate has been widely observed in multiple types of sediments including coarse-grained (Ebinuma et al., 2005; Masui et al., 2005; Yun et al., 2007) or fine-grained sediments (Yun et al., 2007), in laboratory tests (Winters et al., 2007; Yun et al., 2007; Miyazaki et al., 2011), and in *in-situ* measurements (Yun et al., 2006; Sultan et al., 2007), as listed in Table 3. Generally, gas hydrate exists in the form of cementation by interconnecting grains or pore occupation by bearing load, and thus enhances geomechanical strength of sediments (Waite et al., 2009; Lijith et al., 2019; Wu et al., 2020). The effects of gas hydrate could be described from the perspective of hydrate saturation and hydrate morphology. The strength, cohesion (C), stiffness (E), and Poisson's ratio (v) of sediments increase with hydrate saturation, while the internal friction angle Φ s generally insensitive to hydrate saturation (Waite et al., 2009; Lijith et al., 2019; Wu et al., 2020), with several corresponding empirical models listed in Table 4. With respect to the effects of hydrate morphology on the strength of marine sediments, cementing hydrate might have a more striking effect on mechanical properties than pore-filling hydrate, as suggested by previous experiments or numerical simulation (Ebinuma et al., 2005; Masui et al., 2005; Ding et al., 2022). However, the models considering the effects of hydrate morphology are currently rare and should be developed in the future.

2.2.3.1 Fracture initiation

A number of geophysical data indicated that fractures develop commonly in marine sediments (Krabbenhoeft et al., 2013; Plaza-Faverola et al., 2015; Elger et al., 2018; Ma et al., 2021). Except for those interpreted by tectonic activities,

TABLE 3 Summary of experimental or numerical tests on geomechanical properties of hydrate-bearing sediments.

Hydrate type	Sample types	Method	Key findings	Reference
CH_4	Artificial sandy sediments	Triaxial tests	• The shear strength and stiffness of sediments are increased prominently even by a small amount of gas hydrate. • The modes of hydrate occurrence have an important effect on the strength characteristics of the hydrate-saturated specimens.	(Ebinuma et al., 2005)
CH_4	Toyoura sand	Triaxial tests	• The proportional correlation between the shear strength and hydrate saturation degree is obtained.	(Masui et al., 2005)
CH_4	Natural sediments from the Mackenzie Delta; Ottawa sand; Clayey silt	Triaxial tests	• The magnitude of the increase of shear strength is related to hydrate saturation and hydrate cementation characteristics.	(Winters et al., 2007)
CH_4	Toyoura sand; silica sand	Triaxial tests	• The strength and stiffness of hydrate-bearing sediments increase with hydrate saturation and with the effective confining pressure. • The effect of hydrate saturation on Poisson's ratio is minor.	(Miyazaki et al., 2011)
CH_4	Clayey sediments	Triaxial tests	• The strength of the sediments is reduced by hydrate dissociation, and the strength tended to decrease further at the lower confining pressures. • The decrease in strength was mainly affected by the reduction of cohesive force.	(Song et al., 2014)
CO_2	Sand; Silt	Direct shear	• Stress state and hydrate saturation are dominant factors controlling both the stiffness and the strength of hydrate-bearing sediments. • Hydrate contributes mainly the cohesion of hydrate-bearing sediments. The cohesion increases with hydrate saturation. • The internal friction angle has no clear dependence on hydrate saturation.	(Liu et al., 2018)
		Discrete element method (DEM); Biaxial tests	• The shear strength and secant modulus (stiffness) of hydrate-bearing sediments increase with hydrate saturation regardless of the hydrate morphology. • The shear strength is slightly but the secant modulus (stiffness) is significantly influenced by hydrate morphology. The cementing type of hydrate-bearing sediments exhibits the largest secant modulus.	(Ding et al., 2022)
Tetrahydrofuran	Sand; Crushed silt; Precipitated silt; Kaolinite	Triaxial tests	• The stress-strain behavior of hydrate-bearing sediments is dependent of particle size, confining pressure, and hydrate saturation. • The peak strength of the samples increases nonlinearly with hydrate saturation. • Hydrate-bearing sediments exhibit high stiffness at low strains.	(Yun et al., 2007)

most fractures might be associated with overpressure (Daigle and Dugan, 2010; Elger et al., 2018). It should be noted that when gas and liquid phase coexists in marine sediments, gas is always the phase initiating fractures, since the gas phase has higher pressure than the water phase in water-wetting marine sediments (Daigle et al., 2020). If the internal pressure of gas bubbles exceeds their surrounding stress, these bubbles would expand by displacing neighboring grains, with new pathways generated. In a passive margin (i.e., the vertical maximum principal stress σ_1 and the horizontal minimum principal stress σ_3), these secondary fractures would open horizontally and propagate vertically (Daigle et al., 2020), and even evolve

TABLE 4 Several correlations of geomechanical properties and S_h.

Geomechanical parameters	Definition	Empirical correlations with S_h	Reference	Description
C	The component of shear strength of sediments.	$C=a+b(S_h)^2$	(Song et al., 2014; Liu et al., 2018; Lijith et al., 2019)	The cohesion C of hydrate-bearing sediments increases with S_h.
Φ	Reflecting the internal friction between grains during shearing.		(Waite et al., 2009; Song et al., 2014; Liu et al., 2018; Lijith et al., 2019)	The internal friction angle Φ has no clear dependence on S_h.
E	The extent to which sediments resists deformation.	$E/\sigma_3' = a + bS_h^{2.5}$	(Yun et al., 2007; Miyazaki et al., 2011; Song et al., 2014; Liu et al., 2018; Lijith et al., 2019; Ding et al., 2022)	The stiffness E of hydrate-bearing sediments increases significantly with S_h.
v	The ratio between lateral strain and axial strain	0.1~0.3	(Miyazaki et al., 2011)	The effects of S_h on Poisson's ratio are not noticeable.

Note that Lijith et al. (2019) obtained the empirical correlations listed above only by fitting current available data. More experiments need to be conducted to confirm these correlations.

into pipe structures if overpressure is high enough (Elger et al., 2018; Chen et al., 2021).

Previous studies suggested that there exists a critical size V_r (L^3) for gas bubbles in marine sediments by likening marine sediments to linear elastic media (Boudreau et al., 2005; Barry et al., 2010; Algar et al., 2011b; Algar et al., 2011b; Algar et al., 2011a). When reaching their critical sizes, gas bubbles would move upward continuously with the crack propagating vertically. The V_r(L^3) could be calculated as follows (Algar et al., 2011a),

$$V_r = \frac{16(1-v^2)\rho_s g a_r^4}{3E} \tag{9}$$

where v is Poisson's ratio (1); E is Young's modulus ($ML^{-1}T^{-2}$); ρ_s is the bulk density of sediments (ML^{-3}); a_r is the critical half-length of crack (L), which could be calculated as follows (Algar et al., 2011a),

$$a_r = \left(\frac{3K_{IC}\sqrt{\pi}}{10\rho_s g}\right)^{2/3} \tag{10}$$

where K_{IC} is the tensile fracture toughness ($ML^{-1/2}T^{-2}$), inversely proportional to porosity of marine sediments reported by Johnson et al. (2012). Algar et al. (2011a) suggested that the spontaneous rise velocities of gas bubbles in soft sediments are on the order of centimeters per second based on numerical simulation.

Yet, at the macroscale, the mathematical models considering such spontaneous rise of gas bubbles are rare currently. Some researchers employed a simpler tensile failure criterion to consider the fracturing process (Scandella et al., 2011; Jin et al., 2015; Stranne et al., 2017; Liu et al., 2019; Daigle et al., 2020), as shown in Figure 3,

$$P_f > \sigma_3 + T or - T > \sigma' \tag{11}$$

where P_f is the fluid pressure ($ML^{-1}T^{-2}$); σ_3 is the minimum principal stress ($ML^{-1}T^{-2}$), normally horizontal stress in passive margin (Dugan and Sheahan, 2012; Daigle et al., 2020) ($ML^{-1}T^{-2}$); T is the tensile strength ($ML^{-1}T^{-2}$); $\sigma'(= \sigma - P_f)$ is the effective stress ($ML^{-1}T^{-2}$).

The results obtained based on the assumption of tensile failure reproduce the episodic fashion of gas release in nature (Scandella et al., 2011; Stranne et al., 2017). In fact, the occurrence of fracture initiation is related to not only the magnitude of overpressure, but burial depth and stress state (Fauria and Rempel, 2011), clay content (Terzariol et al., 2021), and hydrate saturation. It should be noted that fine-grained sediments cannot guarantee their seal capacity for free gas, since free gas would crack the sediments before reaching the entry pressure, considering that the entry pressure might be higher than its geomechanical strength in fine-grained sediments.

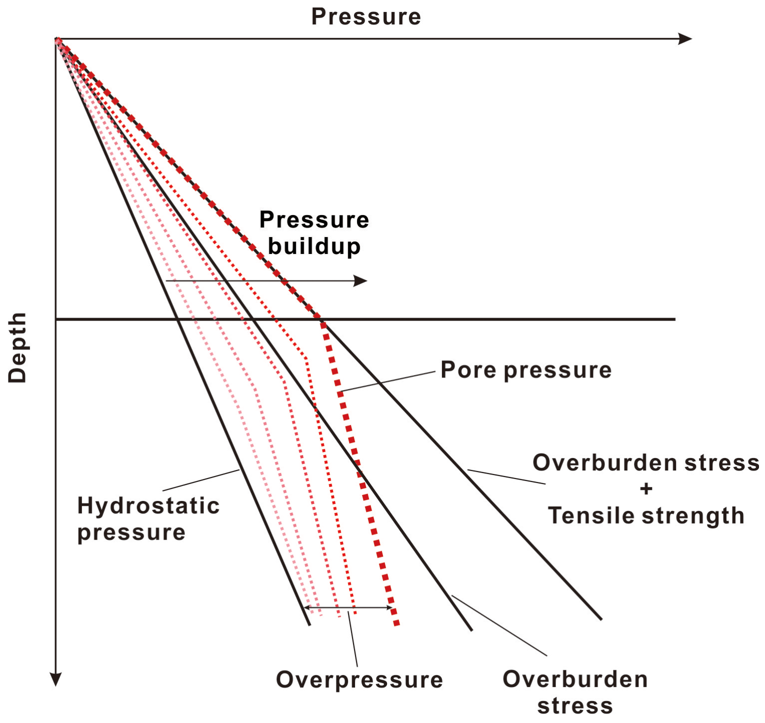

FIGURE 3
Illustration of pressure buildup in marine sediments [modified from Scandella et al. (2011)]. Sediments would be fractured if pore pressure reaches critical stress.

2.2.3.2 Fault slips

Fault slips, essentially shear failures, refer to the phenomena that the hanging wall and foot wall slip along fault planes. Fault slips could therefore be predicted by Mohr-Coulomb (MC) criterion, as shown in Figure 4,

$$\tau_f = C + \sigma'_n tan \quad \Phi \tag{12}$$

where τ_f is the shear stress at failure ($ML^{-1}T^{-2}$); C is the cohesion force ($ML^{-1}T^{-2}$), which is near zero for weak-cementing or non-cementing faults; σ'_n is the normal effective stress ($ML^{-1}T^{-2}$); Φ is the friction angle.

Fault slips could be caused by some abrupt activities such as earthquakes (Ostanin et al., 2013), or slow pressure buildup of gas phase (Hornbach et al., 2004). Hornbach et al. (2004) proposed a model to calculate the critical gas pressure that could trigger fault slips,

$$P_f = \frac{(\sigma_h + \sigma_v)/2 + [(\sigma_h - \sigma_v)/2](cos2\theta - sin2\theta/\mu) + C/\mu}{a} \tag{13}$$

where σ_h and σ_v are the total horizontal stress and vertical stress ($ML^{-1}T^{-2}$), respectively; θ is the fault/fracture angle; μ is the coefficient of sliding friction; a is Biot's coefficient.

2.2.3.3 Submarine landslides

Submarine landslides, essentially shear failures of marine sediments, refer to the downward and outward movement of slope-forming materials along one or several surfaces (Hampton et al., 1996). On a slope scale, landslides are one kind of large-scale seafloor destabilization (Talling et al., 2014). Landslides are

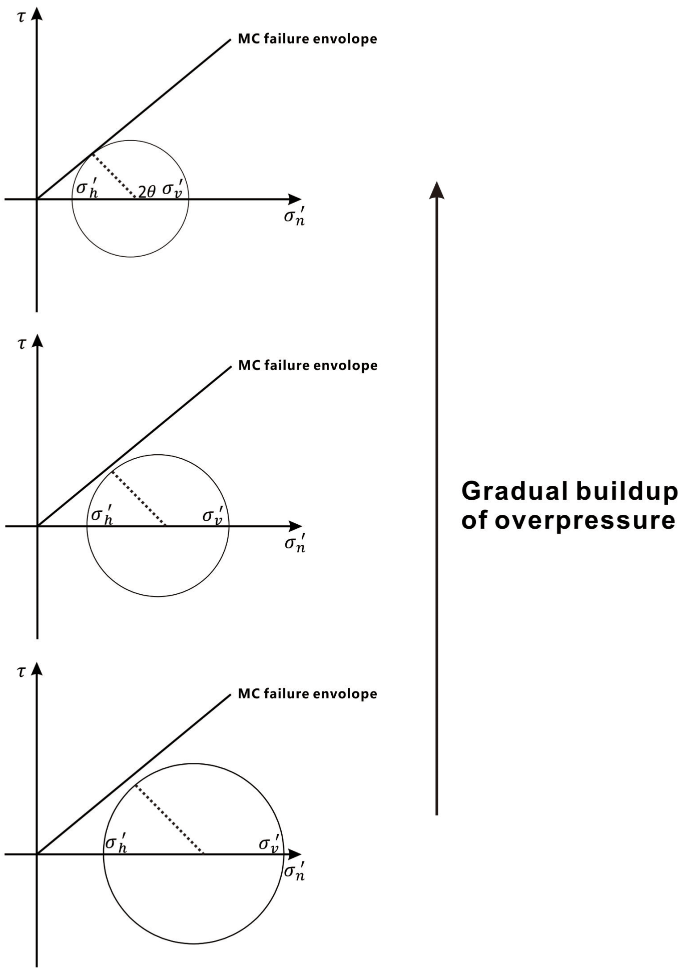

FIGURE 4
Illustration of the occurrence of fault slips, given the fault cohesion is near zero. The process of the gradual buildup of overpressure represent certain scenarios, such as slow gas accumulation beneath hydrate-bearing layers. The increase of overpressure lowers the effective stress and moves the Mohr's circle to the left [modified from Hornbach et al. (2004)]. σ'_n is the effective normal stress; σ'_v and σ'_h are the effective vertical stress and the effective horizontal stress, respectively; τ is the shear stress; θ is the fault angle.

violent ways for methane release, the amount of which is regulated by the amount of free gas beneath sliding surfaces. The safety factor *FS* was proposed to predict potential submarine landslides of slopes,

$$FS = \frac{[(\sigma_v - \rho_f gz)\cos^2\theta - u^*] + C}{(\sigma_v - \rho_f gz)\cos\theta\sin\theta}\tan\phi_f \qquad (14)$$

where θ is the seafloor angle; ϕ_f is the internal angle of friction; u^* is overpressure (P_f - $\rho_f gz$, $ML^{-1}T^{-2}$). The equation provides a relation between the magnitude of overpressure and the potential of slope failures (landslides occur when $FS < 1$). Silver and Dugan (2020) employed the equation to investigate the influence of clay content on submarine slope failure through laboratory experiment and numerical simulation.

Landslides could be caused by the weight increase of overlying water, rapid sedimentation, fluid flow, cyclic wave loading, and earthquakes (Hampton et al., 1996). On continental margins, the dissociation of gas hydrate could also potentially trigger submarine landslides, since hydrate dissociation lowers the geomechanical strength of marine sediments and the released gas reduces the effective stress of marine sediments (e.g., the Storegga slides offshore of Norway reported in Paull et al. (1991) and the Cape Fear slides on the South Carolina continental rise reported in Paull et al. (1996)), as illustrated by Figure 5.

2.2.3.4 Contribution of sediment failures

The methane discharge alongside these sediment failures is expected to be great, since methane escape accompanied by abrupt pressure release is violent in short time. For example, fault slips have been invoked to explain large-scale methane release in paleo-ocean (Hornbach et al., 2004). The methane discharge associated with sediment failures is supposedly episodic most time (Stranne et al., 2017), since pressure buildup is much slower than pressure release. These dynamic processes should be considered in future work for constraining the methane flux to the ocean.

2.2.4 Gas flow through hydrate channels

Based on the phenomena that hydrate covers would form rapidly at the surface of methane bubbles in GHSZ, a new mechanism for methane migration was proposed recently. When gas supply is continuously abundant, hydrate films forming at water-gas interfaces construct tube-like hydrate channels for gas flow (Fu et al., 2020; Meyer et al., 2020), which is termed as the crustal fingering (Fu et al., 2020). Mass transfer across hydrate films is dependent on the diffusion through the films, since hydrate channels separate methane gas from water physically. Given that the diffusion coefficient of methane through hydrate films is as low as 10^{-14} to 10^{-17} m^2/s (Davies et al., 2010), the hydrate channels could construct new pathways for gas flow. These tube-like hydrate channels have been observed in experiments (Katsuki et al., 2007; Jin et al., 2012), numerical simulation (Fu et al., 2018; Fu et al., 2020), and field surveys (Fu et al., 2021). Meyer et al. (2018) proposed a schematic hydrate formation model associated with hydrate channels to explain the reason why the measured hydrate saturation was much lower than that predicted, as shown in Figure 6. Meyer et al. (2020) derived a corresponding mathematical formula of hydrate growth rate R_{CH4} ($nL^{-3}T^{-1}$),

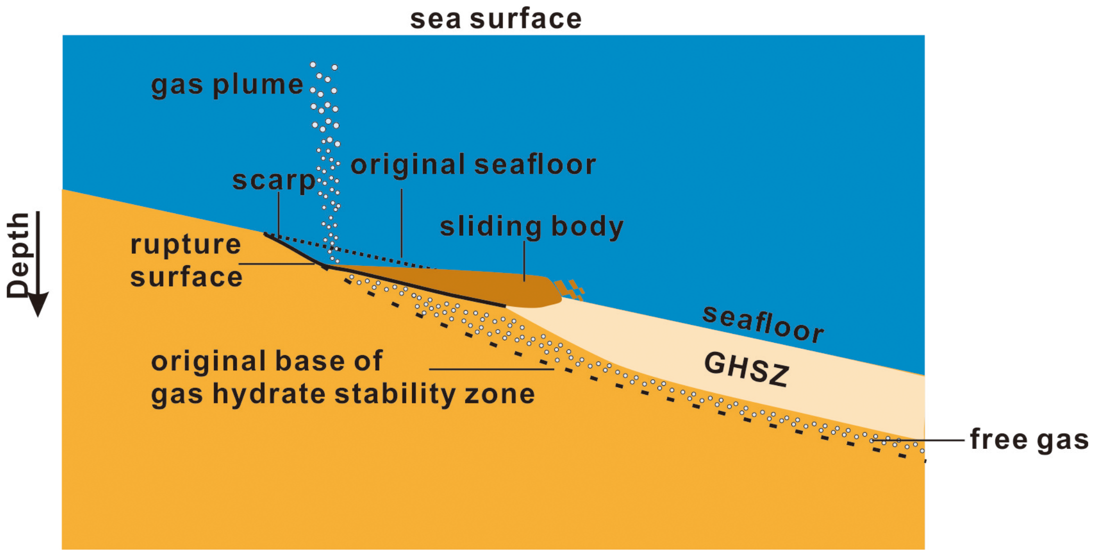

FIGURE 5
Schematic of submarine landslide caused by gas hydrate dissociation [modified from Dickens (2003)].

$$R_{CH4} = \frac{9(1-\varphi)^2 s_g^2}{\varphi S_H r_{grain}^2 M_m} D_m (C_{mg} - C_{mw}) \qquad (15)$$

Where φ is the porosity (1); r_{grain} is the median grain radius (L); M_m is the molecular weight of methane (Mn^{-1}); D_m is the diffusion coefficient of methane through hydrate films (L^2T^{-1}); C_{mg} and C_{mw} are the methane concentrations in methane hydrate in contact with free gas and water (ML^{-3}), respectively.

The recently-recognized mechanism challenges the concept of the seal capacity of hydrate-bearing sediments, since the hydrate channels could protect gas from being consumed and facilitate upward methane migration.

2.2.4.1 Contribution of gas flow through hydrate channels

The hydrate formation rate obtained from the hydrate channel growth model is much slower than that predicted by traditional kinetic equations of hydrate formation proposed by Kim et al. (1987), so this new hydrate formation model could partly explain how methane gas moves through GHSZ. Although the hydrate channels have been observed at seafloor (Fu et al., 2021), more experiments are required to confirm the occurrence of long-distance hydrate channels in the course of methane gas migration through porous sediments. It is still little understood at which condition the channel-assisted gas movement would dominate methane migration, although Fu et al. (2020) suggested that the rate and frequency of gas supply determine whether vertical hydrate channels could occur.

To our current knowledge, we infer that this mechanism might be dominant in the case that gas supply from depth is abundant and continuous. If the long-distance hydrate channels can be constructed, free methane gas might migrate from depth to seafloor. However, it is still hard to constrain how much methane could escape to the ocean through hydrate channels. If the channel-assisted gas movement is proved a widespread mechanism, the effects of hydrate channels need to be incorporated into the macroscopic simulation in future work, which could help constrain the methane flux to the ocean more accurately.

3 Discussion

These mechanisms for methane migration shown in Figure 7 might occur at the same time or in succession. For example, O'hara et al. (1995) suggested water flow could also be driven by the movement of gas bubbles. Fauria and Rempel (2011) observed a transition of the migration mechanism of free gas from capillary invasion at bottom sediments to sediment fracturing at top sediments even within a single invasion episode.

Previous researchers proposed several migration mechanisms to explain the methane source of hydrate formation, e.g., local methane diffusion (Malinverno, 2010), short-range advective migration (Nole et al., 2016), and long-range fluid advection and free gas flow (Wei et al., 2022).

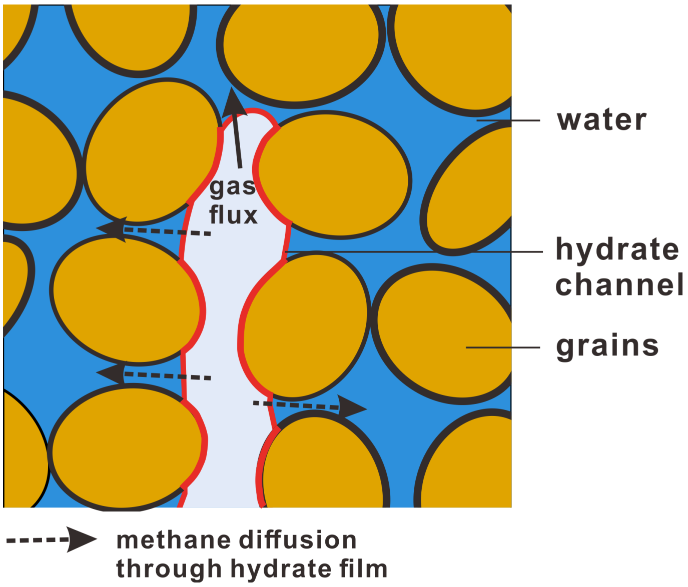

FIGURE 6
Schematic of gas flow through a hydrate channel [modified from Meyer et al. (2020)].

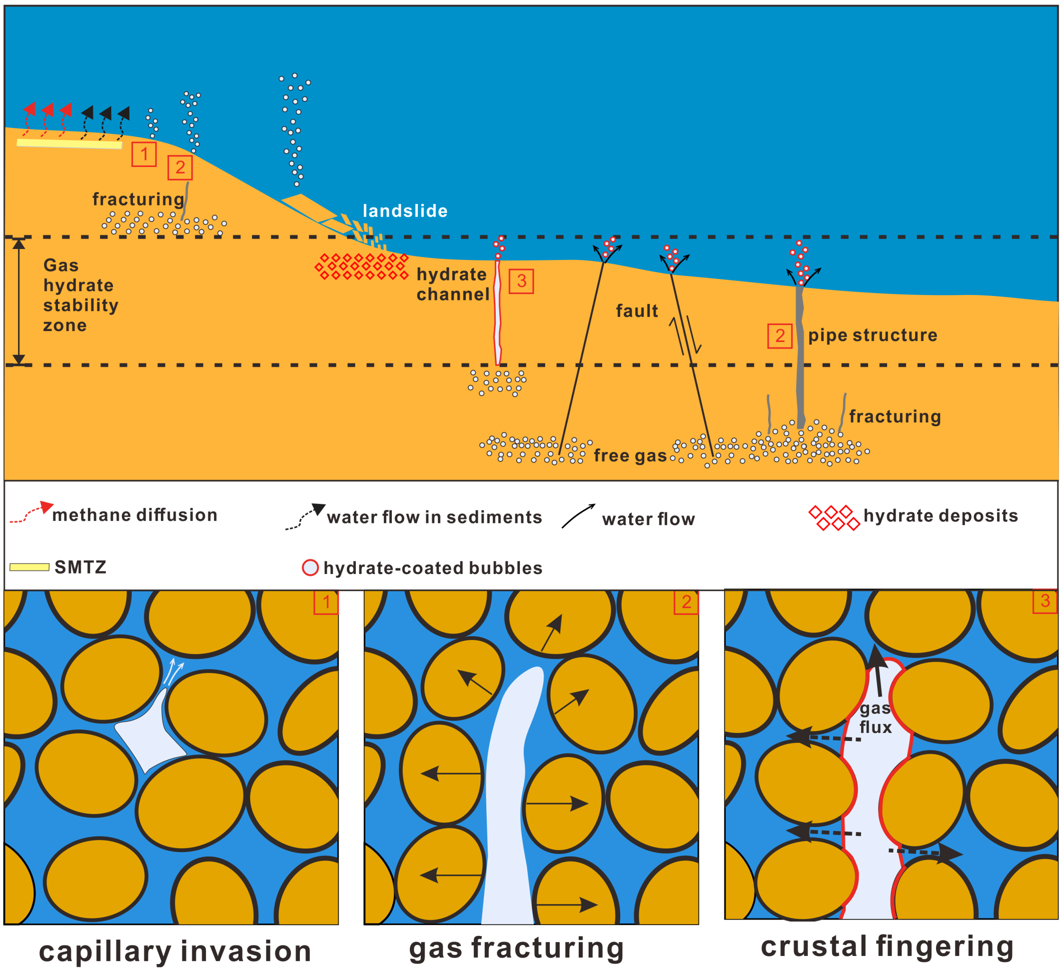

FIGURE 7
A comprehensive illustration of various mechanisms for methane migration [modified from Ma et al. (2021)].

Considering these mechanisms associated with hydrate formation, our study unifies gas hydrate systems, methane migration, and methane seepage. Compared with previous study (James et al., 2016), this study incorporates some mechanisms not mentioned before, such as sediment failures and gas flow through hydrate channels. Here, we provide a comprehensive understanding of different methane migration mechanisms associated with gas hydrate systems that can cause methane seepage.

In gas hydrate systems, in addition to the methane consumption caused by hydrate formation, the presence of gas hydrate could affect methane migration in three ways,

- preventing upward methane migration through water/gas flow by reducing the permeability of marine sediments;
- preventing upward methane migration through sediment failures by enhancing the geomechanical strength of marine sediments;
- benefiting upward methane migration by constructing hydrate channels at the interface of continuous gas columns.

Among these effects, there is an obvious contradiction. The effect of gas hydrate depends on hydrate morphology, methane phase state, and sediment type. The first effect generally occurs in coarse-grained sediments in which gas hydrate occupies pore space without completely blocking flow space for water or methane gas. The second effect commonly occurs in less permeable sediments, typically fine-grained sediments or sediments with hydrate clog where the flow resistance of fluid is higher than critical failure stress. The third effect reflects the dynamic process of hydrate growth, requiring the involvement of methane gas.

4 Conclusions and outlook

As discussed above, methane generated in marine sediments might move upward to the ocean by certain mechanisms. These mechanisms for methane transport could be classified into diffusion and advection which includes water movement, free gas flow, sediment failures, and gas flow through hydrate channels.

- Diffusion is one of the most fundamental mechanisms for methane migration. The diffusive methane flux can be calculated by Fick's law involved with the effective methane diffusion coefficient and the dissolved methane concentration gradient. Due to the high consumption rate for methane in the gas hydrate stability zone and sulfate-methane transition zone, dissolved methane could hardly escape to the ocean by means of diffusion.
- Water movement or free gas flow are closely related to the permeability of marine sediments and the overpressure gradient of gas or liquid phase. Generally, the gas hydrate stability zone and sulfate-methane transition zone could still capture most of the dissolved methane so that few methane could reach the overlying water column by water movement. For free methane gas, marine sediments can hold isolated gas bubbles stably by the capillary force. However, the existence of high-permeability conduits might benefit water and gas migration and thus lead to a higher methane flux to the ocean.
- Sediment failures can generate new pathways for methane escape, acting as another non-negligible mechanism for methane migration. The failure modes include fracture initiation, fault slips, and submarine landslides. The methane discharge alongside sediment failure is episodic sometime, since gas/water pressure buildup is generally much slower than pressure release.
- Gas flow through hydrate channels is one recently-recognized mechanism that can partly explain how methane gas moves through the gas hydrate stability zone, challenging the concept of the seal capacity of hydrate-bearing sediments. However, more investigation is necessary to have a full understanding about the contribution of hydrate channels to the methane flux to the ocean.

As summarized in Table 5, dissolved methane from depth would be depleted in GHSZ and SMTZ and free methane would be arrested by capillary trapping. However, methane migration along preexisting fractures or sediment failure surfaces, might be considerable, since the velocity of methane movement exceeds far the rate of methane consumption (i.e., hydrate formation and methane oxidation). In addition, methane migration through hydrate channels might be ignored by previous researchers.

Although advances have been made about the methane migration mechanisms through marine sediments, further theoretical and experimental studies are necessary to have a better understanding in the following aspects,

(1) Considering that high-permeability conduits in sediments are important pathways for methane seepage, their seepage properties for gas and water flow (e.g., permeability, relative permeability, and capillary curve) are critical inputs for the estimation of the methane flux at the macroscale. However, the studies on seepage properties of these conduits are currently scarce. More experiments should be conducted to clarify the flow characteristics of high-permeability conduits quantitatively.

(2) The geomechanical properties of marine sediments are critical parameters for predicting the occurrence of sediment failures that are important ways for methane release. Although hydrate-bearing sediments exhibit

TABLE 5 Summary of mechanisms for methane transport.

Mass transfer type	Migration mechanism	Methane state	Are there new pathways generated?	Pathways	Main resistance to methane transport	Methane flux to ocean
Diffusion	Methane diffusion	Dissolved methane	N	Sediments	GHSZ and SMTZ	Low
Advection	Water movement	Dissolved methane	N	Sediments	GHSZ and SMTZ	Low
			N	Faults		High
	Free gas flow	Free methane	N	Sediments	GHSZ and Capillary trapping	Low
			N	Faults		High
	Sediment failures	Dissolved methane/ Free methane	Y	Failure surfaces		High
	Crustal fingering	Free methane	Y	Hydrate channels		Uncertain

enhanced geomechanical properties, reliable constitutive models describing the hydrate effect are still rare. More investigations should be focused on the quantitative correlations of geomechanical properties and hydrate distribution including hydrate saturation and morphology.

(3) As a recently-recognized mechanism, gas flow through hydrate channels might constitute a part of the methane flux to the ocean. However, the occurrence of hydrate channels in the course of methane transport is still little known. More experiments should be conducted to confirm the occurrence conditions of hydrate channels.

Author contributions

HLu supervised the study; HLiu wrote the original draft; LZ and HLu contributed to refining the draft. All authors contributed to the article and approved the submitted version.

Funding

This work is supported by the China Geological Survey (grant number: DD20221703).

Conflict of interest

The authors declare that the research was conducted in the absence of any commercial or financial relationships that could be construed as a potential conflict of interest.

Publisher’s note

References

Algar, C. K., Boudreau, B. P., and Barry, M. A. (2011a). Initial rise of bubbles in cohesive sediments by a process of viscoelastic fracture. *J. Geophys. Res.-Solid Earth* 116(B4), B04207. doi: 10.1029/2010jb008133

Algar, C. K., Boudreau, B. P., and Barry, M. A. (2011b). Release of multiple bubbles from cohesive sediments. *Geophys. Res. Lett.* 38(8), L08606. doi: 10.1029/2011gl046870

Atkins, P., and de Paula, J. (2021) *Physical chemistry for the life science*. Available at: https://chem.libretexts.org/@go/page/1392 (Accessed March 7 2022).

Barnes, R., and Goldberg, E. (1976). Methane production and consumption in anoxic marine sediments. *Geology* 4 (5), 297–300. doi: 10.1130/0091-7613(1976)4<297:MPACIA>2.0.CO;2

Barry, M., Boudreau, B., Johnson, B., and Reed, A. (2010). First-order description of the mechanical fracture behavior of fine-grained surficial marine sediments during gas bubble growth. *J. Geophys. Res.: Earth Surf.* 115 (F4), F04029. doi: 10.1029/2010JF001833

Bear, J. (1988). *Dynamics of fluids in porous media* (North Chelmsford: Courier Corporation).

Berndt, C. (2005). Focused fluid flow in passive continental margins. *Philos. Trans. R. Soc. A: Math. Phys. Eng. Sci.* 363 (1837), 2855–2871. doi: 10.1098/rsta.2005.1666

Bethke, C. M. (1986). Inverse hydrologic analysis of the distribution and origin of gulf coast-type geopressured zones. *J. Geophys. Res.: Solid Earth* 91 (B6), 6535–6545. doi: 10.1029/JB091iB06p06535

Bethke, C. M., Reed, J. D., and Oltz, D. F. (1991). Long-range petroleum migration in the Illinois basin. *AAPG Bull.* 75 (5), 925–945. doi: 10.1306/0C9B2899-1710-11D7-8645000102C1865D

Boswell, R., and Collett, T. S. (2011). Current perspectives on gas hydrate resources. *Energy Environ. Sci.* 4 (4), 1206–1215. doi: 10.1039/c0ee00203h

Boudreau, B. P., Algar, C., Johnson, B. D., Croudace, I., Reed, A., Furukawa, Y., et al. (2005). Bubble growth and rise in soft sediments. *Geology* 33 (6), 517–520. doi: 10.1130/G21259.1

Brereton, G. J., Crilly, R. J., and Spears, J. R. (1998). Nucleation in small capillary tubes. *Chem. Phys.* 230 (2-3), 253–265. doi: 10.1016/S0301-0104(98)00052-4

Cao, C., Cai, F., Qi, H. S., Zhao, S. H., and Wu, C. Q. (2021). Differences in the sulfate-methane transitional zone in coastal pockmarks in various sedimentary environments. *Water* 13 (1), 68. doi: 10.3390/w13010068

Cardoso, S. S., and Cartwright, J. H. (2016). Increased methane emissions from deep osmotic and buoyant convection beneath submarine seeps as climate warms. *Nat. Commun.* 7, 13266. doi: 10.1038/ncomms13266

Chen, L.-T., Li, N., Sun, C.-Y., Chen, G.-J., Koh, C. A., and Sun, B.-J. (2017). Hydrate formation in sediments from free gas using a one-dimensional visual simulator. *Fuel* 197, 298–309. doi: 10.1016/j.fuel.2017.02.034

Chen, D., Zhang, G., Dong, D., Zhao, M., and Wang, X. (2021). Widespread fluid seepage related to buried submarine landslide deposits in the northwestern south China Sea. *Geophys. Res. Lett.* 49 (6), e2021GL096584. doi: 10.1029/2021GL096584

Corey, A. T. (1954). The interrelation between gas and oil relative permeabilities. *Producers mon.* 19 (1), 38–41.

Daigle, H., Cook, A., Fang, Y., Bihani, A., Song, W., and Flemings, P. B. (2020). Gas-driven tensile fracturing in shallow marine sediments. *J. Geophys. Res.: Solid Earth* 125, e2020JB020835. doi: 10.1029/2020JB020835

Daigle, H., and Dugan, B. (2010). Origin and evolution of fracture-hosted methane hydrate deposits. *J. Geophys. Res.: Solid Earth* 115 (B11), B11103. doi: 10.1029/2010JB007492

Dai, S., Kim, J., Xu, Y., Waite, W. F., Jang, J., Yoneda, J., et al. (2019). Permeability anisotropy and relative permeability in sediments from the national gas hydrate program expedition 02, offshore India. *Mar. Petrol. Geol.* 108, 705–713. doi: 10.1016/j.marpetgeo.2018.08.016

Dai, S., and Seol, Y. (2014). Water permeability in hydrate-bearing sediments: A pore-scale study. *Geophys. Res. Lett.* 41 (12), 4176–4184. doi: 10.1002/2014GL060535

Dale, A. W., Regnier, P., Van Cappellen, P., Fossing, H., Jensen, J., and Jørgensen, B. (2009). Remote quantification of methane fluxes in gassy marine sediments through seismic survey. *Geology* 37 (3), 235–238. doi: 10.1130/G25323A.1

Dale, A. W., Van Cappellen, P., Aguilera, D. R., and Regnier, P. (2008). Methane efflux from marine sediments in passive and active margins: Estimations from bioenergetic reaction-transport simulations. *Earth Planet. Sci. Lett.* 265 (3-4), 329–344. doi: 10.1016/j.epsl.2007.09.026

Darcy, H. (1856). *Les Fontaines publiques de la ville de Dijon: exposition et application* (Paris: Victor Dalmont).

Davies, S. R., Sloan, E. D., Sum, A. K., and Koh, C. A. (2010). *In situ* studies of the mass transfer mechanism across a methane hydrate film using high-resolution confocal raman spectroscopy. *J. Phys. Chem. C* 114 (2), 1173–1180. doi: 10.1021/jp909416y

Davie, M., Zatsepina, O. Y., and Buffett, B. (2004). Methane solubility in marine hydrate environments. *Mar. geol.* 203 (1-2), 177–184. doi: 10.1016/S0025-3227(03)00331-1

De La Fuente, M., Arndt, S., Marin-Moreno, H., and Minshull, T. A. (2022). Assessing the benthic response to climate-driven methane hydrate destabilisation: State of the art and future modelling perspectives. *Energies* 15 (9), 3307. doi: 10.3390/en15093307

Delsontro, T., McGinnis, D. F., Sobek, S., Ostrovsky, I., and Wehrli, B. (2010). Extreme methane emissions from a Swiss hydropower reservoir: Contribution from bubbling sediments. *Environ. Sci. Technol.* 44 (7), 2419–2425. doi: 10.1021/es9031369

Dessandier, P. A., Knies, J., Plaza-Faverola, A., Labrousse, C., Renoult, M., and Panieri, G. (2021). Ice-sheet melt drove methane emissions in the Arctic during the last two interglacials. *Geology* 49 (7), 799–803. doi: 10.1130/G48580.1

Dickens, G. R. (2003). Rethinking the global carbon cycle with a large, dynamic and microbially mediated gas hydrate capacitor. *Earth Planet. Sci. Lett.* 213 (3-4), 169–183. doi: 10.1016/S0012-821x(03)00325-X

Ding, Y., Qian, A., Lu, H., Li, Y., and Zhang, Y. (2022). DEM investigation of the effect of hydrate morphology on the mechanical properties of hydrate-bearing sands. *Comput. Geotech.* 143, 104603. doi: 10.1016/j.compgeo.2021.104603

Duan, Z., and Weare, J. H. (1992). The prediction of methane solubility in natural-waters to high ionic-strength from 0-Degrees-C to 250-Degrees-C and from 0 bar to 1600 bar - reply. *Geochim. Et Cosmochim. Acta* 56 (12), 4303–4303. doi: 10.1016/0016-7037(92)90271-J

Dugan, B., and Flemings, P. B. (2000). Overpressure and fluid flow in the new Jersey continental slope: Implications for slope failure and cold seeps. *Science* 289 (5477), 288–291. doi: 10.1126/science.289.5477.288

Dugan, B., and Sheahan, T. (2012). Offshore sediment overpressures of passive margins: Mechanisms, measurement, and models. *Rev. Geophys.* 50 (3), RG3001. doi: 10.1029/2011RG000379

Ebinuma, T., Kamata, Y., Minagawa, H., Ohmura, R., Nagao, J., and Narita, H. (2005). "Mechanical properties of sandy sediment containing methane hydrate," In: *Fifth International Conference on Gas Hydrates*. (Trondheim, Norway: Tapir Acad).

Egger, M., Riedinger, N., Mogollon, J. M., and Jorgensen, B. B. (2018). Global diffusive fluxes of methane in marine sediments. *Nat. Geosci.* 11 (6), 421–42+. doi: 10.1038/s41561-018-0122-8

Elger, J., Berndt, C., Rüpke, L., Krastel, S., Gross, F., and Geissler, W. H. (2018). Submarine slope failures due to pipe structure formation. *Nat. Commun.* 9 (1), 1–6. doi: 10.1038/s41467-018-03176-1

Etiope, G. (2015). *Natural gas seepage*. (Cham: Springer Cham). doi: 10.1007/978-3-319-14601-0

Fauria, K. E., and Rempel, A. W. (2011). Gas invasion into water-saturated, unconsolidated porous media: Implications for gas hydrate reservoirs. *Earth Planet. Sci. Lett.* 312 (1-2), 188–193. doi: 10.1016/j.epsl.2011.09.042

Fick, A. (1855). Ueber diffusion. *Annalen der Physik* 170 (1), 59–86. doi: 10.1002/andp.18551700105

Flemings, P. B., Liu, X. L., and Winters, W. J. (2003). Critical pressure and multiphase flow in Blake ridge gas hydrates. *Geology* 31 (12), 1057–1060. doi: 10.1130/G19863.1

Fu, X. J., Cueto-Felgueroso, L., and Juanes, R. (2018). Nonequilibrium thermodynamics of hydrate growth on a gas-liquid interface. *Phys. Rev. Lett.* 120 (14), 144501. doi: 10.1103/PhysRevLett.120.144501

Fujii, T., Suzuki, K., Takayama, T., Tamaki, M., Komatsu, Y., Konno, Y., et al. (2015). Geological setting and characterization of a methane hydrate reservoir distributed at the first offshore production test site on the daini-atsumi knoll in the eastern nankai trough, Japan. *Mar. Petrol. Geol.* 66, 310–322. doi: 10.1016/j.marpetgeo.2015.02.037

Fu, X., Jimenez-Martinez, J., Nguyen, T. P., Carey, J. W., Viswanathan, H., Cueto-Felgueroso, L., et al. (2020). Crustal fingering facilitates free-gas methane migration through the hydrate stability zone. *Proc. Natl. Acad. Sci.* 117 (50), 31660. doi: 10.1073/pnas.2011064117

Fu, X., Waite, W. F., and Ruppel, C. D. (2021). Hydrate formation on marine seep bubbles and the implications for water column methane dissolution. *J. Geophys. Res.-Oceans* 126 (9), e2021JC017363. doi: 10.1029/2021JC017363

Ginsburg, G. D., and Soloviev, V. A. (1997). Methane migration within the submarine gas-hydrate stability zone under deep-water conditions. *Mar. Geol.* 137 (1-2), 49–57. doi: 10.1016/S0025-3227(96)00078-3

Graham, K., and Westbrook, (2009). Escape of methane gas from the seabed along the West spitsbergen continental margin. *Geophys. Res. Lett* 36, L15608. doi: 10.1029/2009GL039191

Haacke, R. R., Westbrook, G. K., and Hyndman, R. D. (2007). Gas hydrate, fluid flow and free gas: Formation of the bottom-simulating reflector. *Earth Planet. Sci. Lett.* 261 (3-4), 407–420. doi: 10.1016/j.epsl.2007.07.008

Hampton, M. A., Lee, H. J., and Locat, J. (1996). Submarine landslides. *Rev. geophys.* 34 (1), 33–59. doi: 10.1029/95RG03287

Handa, Y. P. (1990). Effect of hydrostatic pressure and salinity on the stability of gas hydrates. *J. Phys. Chem.* 94 (6), 2652–2657. doi: 10.1021/j100369a077

Henry, P., Thomas, M., and Ben Clennell, M. (1999). Formation of natural gas hydrates in marine sediments 2. thermodynamic calculations of stability conditions in porous sediments. *J. Geophys. Res.-Solid Earth* 104 (B10), 23005–23022. doi: 10.1029/1999jb900167

Hornbach, M. J., Bangs, N. L., and Berndt, C. (2012). Detecting hydrate and fluid flow from bottom simulating reflector depth anomalies. *Geology* 40 (3), 227–230. doi: 10.1130/g32635.1

Hornbach, M. J., Saffer, D. M., and Holbrook, W. S. (2004). Critically pressured free-gas reservoirs below gas-hydrate provinces. *Nature* 427 (6970), 142–144. doi: 10.1038/nature02172

Hou, J., Ji, Y., Zhou, K., Liu, Y., and Wei, B. (2018). Effect of hydrate on permeability in porous media: Pore-scale micro-simulation. *Int. J. Heat Mass Transf.* 126, 416–424. doi: 10.1016/j.ijheatmasstransfer.2018.05.156

Hsu, S. K., Wang, S. Y., Liao, Y. C., Yang, T. Y. F., Jan, S., Lin, J. Y., et al. (2013). Tide-modulated gas emissions and tremors off SW Taiwan. *Earth Planet. Sci. Lett.* 369, 98–107. doi: 10.1016/j.epsl.2013.03.013

Hunt, J. R., Sitar, N., and Udell, K. S. (1988). Nonaqueous phase liquid transport and cleanup: 1. analysis of mechanisms. *Water Resour. Res.* 24 (8), 1247–1258. doi: 10.1029/WR024i008p01247

Islam, M. (2004). Einstein–Smoluchowski diffusion equation: a discussion. *Physica Scripta* 70 (2-3), 120. doi: 10.1088/0031-8949/70/2-3/008

Iversen, N., and Jørgensen, B. B. (1993). Diffusion coefficients of sulfate and methane in marine sediments: Influence of porosity. *Geochim. Cosmochim. Acta* 57 (3), 571–578. doi: 10.1016/0016-7037(93)90368-7

James, R. H., Bousquet, P., Bussmann, I., Haeckel, M., Kipfer, R., Leifer, I., et al. (2016). Effects of climate change on methane emissions from seafloor sediments in the Arctic ocean: A review. *Limnol. Oceanogr.* 61 (S1), S283–S299. doi: 10.1002/lno.10307

Jang, J., and Santamarina, J. C. (2014). Evolution of gas saturation and relative permeability during gas production from hydrate-bearing sediments: Gas invasion vs. gas nucleation. *J. Geophys. Res.: Solid Earth* 119 (1), 116–126. doi: 10.1002/2013JB010480

Jin, Z. H., Johnson, S. E., and Cook, A. E. (2015). Crack extension induced by dissociation of fracture-hosted methane gas hydrate. *Geophys. Res. Lett.* 42 (20), 8522–8529. doi: 10.1002/2015GL066060

Jin, Y., Konno, Y., and Nagao, J. (2012). Growth of methane clathrate hydrates in porous media. *Energy Fuels* 26 (4), 2242–2247. doi: 10.1021/ef3001357

Johnson, B. D., Barry, M. A., Boudreau, B. P., Jumars, P. A., and Dorgan, K. M. (2012). *In situ* tensile fracture toughness of surficial cohesive marine sediments. *Geo-Marine Lett.* 32 (1), 39–48. doi: 10.1007/s00367-011-0243-1

Johnson, A., Patil, S., and Dandekar, A. J. M. (2011). Experimental investigation of gas-water relative permeability for gas-hydrate-bearing sediments from the mount Elbert gas hydrate stratigraphic test well, Alaska north slope. *Mar. Petrol. Geol.* 28 (2), 419–426. doi: 10.1016/j.marpetgeo.2009.10.013

Kang, D. H., Yun, T. S., Kim, K. Y., and Jang, J. (2016). Effect of hydrate nucleation mechanisms and capillarity on permeability reduction in granular media. *Geophys. Res. Lett.* 43 (17), 9018–9025. doi: 10.1002/2016gl070511

Katsuki, D., Ohmura, R., Ebinuma, T., and Narita, H. (2007). Methane hydrate crystal growth in a porous medium filled with methane-saturated liquid water. *Philos. Mag.* 87 (7), 1057–1069. doi: 10.1080/14786430601021652

Keller, M., and Stallard, R. F. (1994). Methane emission by bubbling from gatun lake, Panama. *J. Geophys. Res.-Atmos.* 99 (D4), 8307–8319. doi: 10.1029/92jd02170

Kim, H., Bishnoi, P. R., Heidemann, R. A., and Rizvi, S. S. (1987). Kinetics of methane hydrate decomposition. *Chem. Eng. Sci.* 42 (7), 1645–1653. doi: 10.1016/0009-2509(87)80169-0

Kleinberg, R., Flaum, C., Griffin, D., Brewer, P., Malby, G., Peltzer, E., et al. (2003). Deep sea NMR: Methane hydrate growth habit in porous media and its relationship to hydraulic permeability, deposit accumulation, and submarine slope stability. *J. Geophys. Res.: Solid Earth* 108 (B10), 2508. doi: 10.1029/2003JB002389

Konno, Y., Oyama, H., Nagao, J., Masuda, Y., and Kurihara, M. (2010). Numerical analysis of the dissociation experiment of naturally occurring gas hydrate in sediment cores obtained at the Eastern nankai trough, Japan. *Energy Fuels* 24 (12), 6353–6358. doi: 10.1021/ef1008727

Krabbenhoeft, A., Bialas, J., Klaucke, I., Crutchley, G., Papenberg, C., and Netzeband, G. L. (2013). Patterns of subsurface fluid-flow at cold seeps: The hikurangi margin, offshore new Zealand. *Mar. Petrol. Geol.* 39 (1), 59–73. doi: 10.1016/j.marpetgeo.2012.09.008

Krevor, S., Blunt, M. J., Benson, S. M., Pentland, C. H., Reynolds, C., Al-Menhali, A., et al. (2015). Capillary trapping for geologic carbon dioxide storage – from pore scale physics to field scale implications. *Int. J. Greenhouse Gas Control* 40, 221–237. doi: 10.1016/j.ijggc.2015.04.006

Kumar, A., Maini, B., Bishnoi, P. R., Clarke, M., Zatsepina, O., and Srinivasan, S. (2010). Experimental determination of permeability in the presence of hydrates and its effect on the dissociation characteristics of gas hydrates in porous media. *J. Petrol. Sci. Eng.* 70 (1-2), 114–122. doi: 10.1016/j.petrol.2009.10.005

Lei, L., Seol, Y., and Myshakin, E. M. (2019). Methane hydrate film thickening in porous media. *Geophys. Res. Lett.* 46 (20), 11091–11099. doi: 10.1029/2019gl084450

Lijith, K. P., Malagar, B. R. C., and Singh, D. N. (2019). A comprehensive review on the geomechanical properties of gas hydrate bearing sediments. *Mar. Petrol. Geol.* 104, 270–285. doi: 10.1016/j.marpetgeo.2019.03.024

Linke, P., Suess, E., Torres, M., Martens, V., Rugh, W., Ziebis, W., et al. (1994). *In situ* measurement of fluid flow from cold seeps at active continental margins. *Deep Sea Res. Part I: Oceanogr. Res. Pap.* 41 (4), 721–739. doi: 10.1016/0967-0637(94)90051-5

Liu, Z., Dai, S., Ning, F., Peng, L., Wei, H., and Wei, C. (2018). Strength estimation for hydrate-bearing sediments from direct shear tests of hydrate-bearing sand and silt. *Geophys. Res. Lett.* 45 (2), 715–723. doi: 10.1002/2017gl076374

Liu, J. L., Haeckel, M., Rutqvist, J., Wang, S. H., and Yan, W. (2019). The mechanism of methane gas migration through the gas hydrate stability zone: Insights from numerical simulations. *J. Geophys. Res.-Solid Earth* 124 (5), 4399–4427. doi: 10.1029/2019jb017417

Li, G., Wu, D.-M., Li, X.-S., Lv, Q.-N., Li, C., and Zhang, Y. (2017). Experimental measurement and mathematical model of permeability with methane hydrate in quartz sands. *Appl. Energy* 202, 282–292. doi: 10.1016/j.apenergy.2017.05.147

Li, J. F., Ye, J. L., Qin, X. W., Qiu, H. J., Wu, N. Y., Lu, H. L., et al. (2018). The first offshore natural gas hydrate production test in south China Sea. *China Geol.* 1 (1), 5–16. doi: 10.31035/cg2018003

Li, C., Zhan, L., and Lu, H. (2022). Mechanisms for overpressure development in marine sediments. *J. Mar. Sci. Eng.* 10 (4), 490. doi: 10.3390/jmse10040490

Mahabadi, N., Dai, S., Seol, Y., Sup Yun, T., and Jang, J. (2016). The water retention curve and relative permeability for gas production from hydrate-bearing sediments: pore-network model simulation. *Geochem. Geophys. Geosyst.* 17 (8), 3099–3110. doi: 10.1002/2016gc006372

Mahabadi, N., and Jang, J. (2014). Relative water and gas permeability for gas production from hydrate-bearing sediments. *Geochem. Geophys. Geosyst.* 15 (6), 2346–2353. doi: 10.1002/2014gc005331

Mahabadi, N., Zheng, X. L., Yun, T. S., van Paassen, L., and Jang, J. (2018). Gas bubble migration and trapping in porous media: Pore-scale simulation. *J. Geophys. Res.-Solid Earth* 123 (2), 1060–1071. doi: 10.1002/2017jb015331

Malinverno, A. (2010). Marine gas hydrates in thin sand layers that soak up microbial methane. *Earth Planet. Sci. Lett.* 292 (3-4), 399–408. doi: 10.1016/j.epsl.2010.02.008

Masuda, Y., Naganawa, S., and Ando, S. (1997). "Numerical calculation of gas production performance from reservoirs containing natural gas hydrates," in *Annual technical conference* (San Antonio, Tex.: Soc. of Petrol. Eng.).

Masui, A., Haneda, H., Ogata, Y., and Aoki, K. (2005). "The effect of saturation degree of methane hydrate on the shear strength of synthetic methane hydrate sediments," In: *Fifth International Conference on Gas Hydrates*. (Trondheim, Norway: Tapir Acad).

Mau, S., Tu, T. H., Becker, M., Ferreira, C. D., Chen, J. N., Lin, L. H., et al. (2020). Methane seeps and independent methane plumes in the south China Sea offshore Taiwan. *Front. Mar. Sci.* 7. doi: 10.3389/fmars.2020.00543

Max, M. D. (2003). *Natural gas hydrate in oceanic and permafrost environments* (Berlin: Springer Science & Business Media).

Ma, G., Zhan, L., Lu, H., and Hou, G. (2021). Structures in shallow marine sediments associated with gas and fluid migration. *J. Mar. Sci. Eng.* 9 (4), 396. doi: 10.3390/jmse9040396

Mello, U. T., Karner, G. D., and Anderson, R. N. (1994). A physical explanation for the positioning of the depth to the top of overpressure in shale-dominated sequences in the gulf coast basin, united states. *J. Geophys. Res.: Solid Earth* 99 (B2), 2775–2789. doi: 10.1029/93JB02899

Meyer, D. W., Flemings, P. B., DiCarlo, D., You, K., Phillips, S. C., and Kneafsey, T. J. (2018). Experimental investigation of gas flow and hydrate formation within the hydrate stability zone. *J. Geophys. Res.: Solid Earth* 123 (7), 5350–5371. doi: 10.1029/2018jb015748

Meyer, D. W., Flemings, P. B., You, K., and DiCarlo, D. A. (2020). Gas flow by invasion percolation through the hydrate stability zone. *Geophys. Res. Lett.* 47 (3), e2019GL084380. doi: 10.1029/2019GL084380

Miller, R. D. (1980). Freezing phenomena in soils. *Appl. Soil phys.* (New York: Acad. Press), 254–299. doi: 10.1016/B978-0-12-348580-9.50016-X

Miyazaki, K., Masui, A., Sakamoto, Y., Aoki, K., Tenma, N., and Yamaguchi, T. (2011). Triaxial compressive properties of artificial methane-hydrate-bearing sediment. *J. Geophys. Res.* 116 (B6), B06102. doi: 10.1029/2010jb008049

Moridis, G. (2014). *User's manual of the TOUGH+ core code v1. 5: A general-purpose simulator of non-isothermal flow and transport through porous and fractured media*. California, United States: Lawrence Berkeley National Laboratory. doi: 10.2172/1165986

Nauhaus, K., Boetius, A., Krüger, M., and Widdel, F. (2002). *In vitro* demonstration of anaerobic oxidation of methane coupled to sulphate reduction in sediment from a marine gas hydrate area. *Environ. Microbiol.* 4 (5), 296–305. doi: 10.1046/j.1462-2920.2002.00299.x

Nole, M., Daigle, H., Cook, A. E., and Malinverno, A. (2016). Short-range, overpressure-driven methane migration in coarse-grained gas hydrate reservoirs. *Geophys. Res. Lett.* 43 (18), 9500–9508. doi: 10.1002/2016gl070096

O'hara, S., Dando, P., Schuster, U., Bennis, A., Boyle, J., Chui, F., et al. (1995). Gas seep induced interstitial water circulation: observations and environmental implications. *Continent. Shelf Res.* 15 (8), 931–948. doi: 10.1016/0278-4343(95)80003-V

Osborne, M. J., and Swarbrick, R. E. (1997). Mechanisms for generating overpressure in sedimentary basins: A reevaluation. *AAPG Bull.* 81 (6), 1023–1041. doi: 10.1306/522B49C9-1727-11D7-8645000102C1865D

Ostanin, I., Anka, Z., di Primio, R., and Bernal, A. (2013). Hydrocarbon plumbing systems above the snøhvit gas field: structural control and implications for thermogenic methane leakage in the hammerfest basin, SW barents Sea. *Mar. Petrol. Geol.* 43, 127–146. doi: 10.1016/j.marpetgeo.2013.02.012

Pan, L., Lei, L., and Seol, Y. (2021). Pore-scale influence of methane hydrate on permeability of porous media. *J. Natural Gas Sci. Eng.* 87, 103758. doi: 10.1016/j.jngse.2020.103758

Paull, C. K., Buelow, W. J., Ussler, W.III, and Borowski, W. S. (1996). Increased continental-margin slumping frequency during sea-level lowstands above gas hydrate–bearing sediments. *Geology* 24 (2), 143–146. doi: 10.1130/0091-7613(1996)024<0143:ICMSFD>2.3.CO;2

Paull, C. K., Ussler, W.III, and Dillon, W. P. (1991). Is the extent of glaciation limited by marine gas-hydrates? *Geophys. Res. Lett.* 18 (3), 432–434. doi: 10.1029/91GL00351

Perkins, T., and Johnston, O. (1963). A review of diffusion and dispersion in porous media. *Soc. Petrol. Eng. J.* 3 (01), 70–84. doi: 10.2118/480-PA

Plaza-Faverola, A., Bünz, S., Johnson, J. E., Chand, S., Knies, J., Mienert, J., et al. (2015). Role of tectonic stress in seepage evolution along the gas hydrate-charged vestnesa ridge, fram strait. *Geophys. Res. Lett.* 42 (3), 733–742. doi: 10.1002/2014gl062474

Reagan, M. T., Moridis, G. J., Elliott, S. M., and Maltrud, M. (2011). Contribution of oceanic gas hydrate dissociation to the formation of Arctic ocean methane plumes. *J. Geophys. Res.: Oceans* 116 (C9), C09014. doi: 10.1029/2011JC007189

Reeburgh, W. S. (2007). Oceanic methane biogeochemistry. *Chem. Rev.* 107 (2), 486–513. doi: 10.1021/cr050362v

Regnier, P., Dale, A. W., Arndt, S., LaRowe, D. E., Mogollon, J., and Van Cappellen, P. (2011). Quantitative analysis of anaerobic oxidation of methane (AOM) in marine sediments: A modeling perspective. *Earth-Sci. Rev.* 106 (1-2), 105–130. doi: 10.1016/j.earscirev.2011.01.002

Ren, X. W., Guo, Z. Y., Ning, F. L., and Ma, S. Z. (2020). Permeability of hydrate-bearing sediments. *Earth-Sci. Rev.* 202, 103100. doi: 10.1016/j.earscirev.2020.103100

Römer, M., Hsu, C.-W., Loher, M., MacDonald, I. R., dos Santos Ferreira, C., Pape, T., et al. (2019). Amount and fate of gas and oil discharged at 3400 m water depth from a natural seep site in the southern gulf of Mexico. *Front. Mar. Sci.* 6. doi: 10.3389/fmars.2019.00700

Ruppel, C. D., and Kessler, J. D. (2017). The interaction of climate change and methane hydrates. *Rev. Geophys.* 55 (1), 126–168. doi: 10.1002/2016rg000534

Ruppel, C. D., and Waite, W. F. (2020). Timescales and processes of methane hydrate formation and breakdown, with application to geologic systems. *J. Geophys. Res.: Solid Earth* 125 (8), e2018JB016459. doi: 10.1029/2018JB016459

Saunders, D. F., Burson, K. R., and Thompson, C. K. (1999). Model for hydrocarbon microseepage and related near-surface alterations. *AAPG Bull.* 83 (1), 170–185. doi: 10.1306/00AA9A34-1730-11D7-8645000102C1865D

Sauter, E. J., Muyakshin, S. I., Charlou, J. L., Schluter, M., Boetius, A., Jerosch, K., et al. (2006). Methane discharge from a deep-sea submarine mud volcano into the upper water column by gas hydrate-coated methane bubbles. *Earth Planet. Sci. Lett.* 243 (3-4), 354–365. doi: 10.1016/j.epsl.2006.01.041

Scandella, B. P., Varadharajan, C., Hemond, H. F., Ruppel, C., and Juanes, R. (2011). A conduit dilation model of methane venting from lake sediments. *Geophys. Res. Lett.* 38 (6), L06408. doi: 10.1029/2011GL046768

Shen, P., Li, G., Li, B., and Li, X. (2020). Coupling effect of porosity and hydrate saturation on the permeability of methane hydrate-bearing sediments. *Fuel* 269, 117425. doi: 10.1016/j.fuel.2020.117425

Silver, M. M. W., and Dugan, B. (2020). The influence of clay content on submarine slope failure: insights from laboratory experiments and numerical models. *Geol. Soc. London Special. Publ.* 500 (1), 301–309. doi: 10.1144/sp500-2019-186

Song, Y., Zhu, Y., Liu, W., Zhao, J., Li, Y., Chen, Y., et al. (2014). Experimental research on the mechanical properties of methane hydrate-bearing sediments during hydrate dissociation. *Mar. Petrol. Geol.* 51, 70–78. doi: 10.1016/j.marpetgeo.2013.11.017

Spinelli, G. A., Giambalvo, E. R., and Fisher, A. T. (2004). "Sediment permeability, distribution, and influence on fluxes in oceanic basement," In *Hydrogeology of the Oceanic Lithosphere with CD-ROM* (Cambridge: Cambridge University Press).

Stocker, T. (2014). Climate change 2013: the physical science basis: Working Group I contribution to the Fifth assessment report of the Intergovernmental Panel on Climate Change. (Cambridge: Cambridge University Press)

Stone, H. (1970). Probability model for estimating three-phase relative permeability. *J. petrol. Technol.* 22 (02), 214–218. doi: 10.2118/2116-PA

Stranne, C., O'Regan, M., and Jakobsson, M. (2017). Modeling fracture propagation and seafloor gas release during seafloor warming-induced hydrate dissociation. *Geophys. Res. Lett.* 44 (16), 8510–8519. doi: 10.1002/2017GL074349

Stranne, C., O'Regan, M., Jakobsson, M., Brüchert, V., and Ketzer, M. (2019). Can anaerobic oxidation of methane prevent seafloor gas escape in a warming climate? *Solid Earth* 10 (5), 1541–1554. doi: 10.5194/se-10-1541-2019

Sultan, N., Plaza-Faverola, A., Vadakkepuliyambatta, S., Buenz, S., and Knies, J. (2020). Impact of tides and sea-level on deep-sea Arctic methane emissions. *Nat. Commun.* 11 (1), 1–10. doi: 10.1038/s41467-020-18899-3

Sultan, N., Voisset, M., Marsset, T., Vernant, A. M., Cauquil, E., Colliat, J. L., et al. (2007). Detection of free gas and gas hydrate based on 3D seismic data and cone penetration testing: An example from the Nigerian continental slope. *Mar. Geol.* 240 (1-4), 235–255. doi: 10.1016/j.margeo.2007.02.012

Sun, J., Dong, H., Arif, M., Yu, L., Zhang, Y., Golsanami, N., et al. (2021). Influence of pore structural properties on gas hydrate saturation and permeability: A coupled pore-scale modelling and X-ray computed tomography method. *J. Natural Gas Sci. Eng.* 88, 103805. doi: 10.1016/j.jngse.2021.103805

Talling, P. J., Clare, M., Urlaub, M., Pope, E., Hunt, J. E., and Watt, S. F. L. (2014). Large Submarine landslides on continental slopes geohazards, methane release, and climate change. *Oceanography* 27 (2), 32–45. doi: 10.5670/oceanog.2014.38

Terzariol, M., Sultan, N., Apprioual, R., and Garziglia, S. (2021). Pore habit of gas in gassy sediments. *J. Geophys. Res.-Solid Earth* 126 (5), e2020JB021511. doi: 10.1029/2020JB021511

Timmis, K. N., McGenity, T., van der Meer, J. R., and de Lorenzo, V. (2010). *Handbook of hydrocarbon and lipid microbiology* (Berlin: Springer).

Torres, M. E., McManus, J., Hammond, D., De Angelis, M., Heeschen, K., Colbert, S., et al. (2002). Fluid and chemical fluxes in and out of sediments hosting methane hydrate deposits on hydrate ridge, OR, I: Hydrological provinces. *Earth Planet. Sci. Lett.* 201 (3-4), 525–540. doi: 10.1016/S0012-821X(02)00733-1

Tryon, M. D., Brown, K. M., Torres, M. E., Tréhu, A. M., McManus, J., and Collier, R. W. (1999). Measurements of transience and downward fluid flow near episodic methane gas vents, hydrate ridge, cascadia. *Geology* 27 (12), 1075–1078. doi: 10.1130/0091-7613(1999)027<1075:MOTADF>2.3.CO;2

Ullman, W. J., and Aller, R. C. (1982). Diffusion-coefficients in nearshore marine-sediments. *Limnol. Oceanogr.* 27 (3), 552–556. doi: 10.4319/lo.1982.27.3.0552

Van Genuchten, M. T. (1980). A closed-form equation for predicting the hydraulic conductivity of unsaturated soils. *Soil Sci. Soc. America J.* 44 (5), 892–898. doi: 10.2136/sssaj1980.03615995004400050002x

Waite, W. F., Santamarina, J. C., Cortes, D. D., Dugan, B., Espinoza, D. N., Germaine, J., et al. (2009). Physical properties of hydrate-bearing sediments. *Rev. Geophys.* 47, RG4003. doi: 10.1029/2008rg000279

Warzinski, R. P., Lynn, R., Haljasmaa, I., Leifer, I., Shaffer, F., Anderson, B. J., et al. (2014). Dynamic morphology of gas hydrate on a methane bubble in water: Observations and new insights for hydrate film models. *Geophys. Res. Lett.* 41 (19), 6841–6847. doi: 10.1002/2014GL061665

Weber, T., Wiseman, N. A., and Kock, A. (2019). Global ocean methane emissions dominated by shallow coastal waters. *Nat. Commun.* 10, 4584. doi: 10.1038/s41467-019-12541-7

Wei, L., Cook, A., and You, K. (2022). Methane migration mechanisms for the green canyon block 955 gas hydrate reservoir, northern gulf of Mexico. *AAPG Bull.* 106 (5), 1005–1023. doi: 10.1306/06022120134

Winters, W. J., Waite, W. F., Mason, D. H., Gilbert, L. Y., and Pecher, I. A. (2007). Methane gas hydrate effect on sediment acoustic and strength properties. *J. Petrol. Sci. Eng.* 56 (1-3), 127–135. doi: 10.1016/j.petrol.2006.02.003

Wu, P., Li, Y., Sun, X., Liu, W., and Song, Y. (2020). Mechanical characteristics of hydrate-bearing sediment: A review. *Energy Fuels* 35 (2), 1041–1057. doi: 10.1021/acs.energyfuels.0c03995

Xu, W., and Germanovich, L. N. (2006). Excess pore pressure resulting from methane hydrate dissociation in marine sediments: A theoretical approach. *J. Geophys. Res.: Solid Earth* 111 (B1), B01104. doi: 10.1029/2004JB003600

Xu, K., Mehmani, Y., Shang, L., and Xiong, Q. (2019). Gravity-induced bubble ripening in porous media and its impact on capillary trapping stability. *Geophys. Res. Lett.* 46 (23), 13804–13813. doi: 10.1029/2019GL085175

Xu, W. Y., and Ruppel, C. (1999). Predicting the occurrence, distribution, and evolution of methane gas hydrate in porous marine sediments. *J. Geophys. Res.-Solid Earth* 104 (B3), 5081–5095. doi: 10.1029/1998jb900092

Ye, J.-L., Qin, X.-W., Xie, W.-W., Lu, H.-L., Ma, B.-J., Qiu, H.-J., et al. (2020). The second natural gas hydrate production test in the south China Sea. *China Geol.* 3 (2), 197–209. doi: 10.31035/cg2020043

You, K., and Flemings, P. B. (2021). Methane hydrate formation and evolution during sedimentation. *J. Geophys. Res.-Solid Earth* 126 (4), e2020JB021235. doi: 10.1029/2020JB021235

You, K., Flemings, P. B., Malinverno, A., Collett, T., and Darnell, K. (2019). Mechanisms of methane hydrate formation in geological systems. *Rev. Geophys.* 57 (4), 1146–1196. doi: 10.1029/2018RG000638

Yun, T. S., Narsilio, G. A., and Carlos Santamarina, J. (2006). Physical characterization of core samples recovered from gulf of Mexico. *Mar. Petrol. Geol.* 23 (9-10), 893–900. doi: 10.1016/j.marpetgeo.2006.08.002

Yun, T. S., Santamarina, J. C., and Ruppel, C. (2007). Mechanical properties of sand, silt, and clay containing tetrahydrofuran hydrate. *J. Geophys. Res.: Solid Earth* 112 (B4), B04106. doi: 10.1029/2006jb004484

Zhang, L., Ge, K., Wang, J., Zhao, J., and Song, Y. (2020). Pore-scale investigation of permeability evolution during hydrate formation using a pore network model based on X-ray CT. *Mar. Petrol. Geol.* 113, 104157. doi: 10.1016/j.marpetgeo.2019.104157

Zhang, Y., and Zhai, W.-D. (2015). Shallow-ocean methane leakage and degassing to the atmosphere: triggered by offshore oil-gas and methane hydrate explorations. *Front. Mar. Sci.* 2. doi: 10.3389/fmars.2015.00034

Zheng, L., and Yapa, P. D. (2000). Buoyant velocity of spherical and nonspherical bubbles/droplets. *J. Hydraul. Eng.* 126 (11), 852–854. doi: 10.1061/(ASCE)0733-9429(2000)126:11(852)

frontiers | Frontiers in Marine Science

TYPE Original Research
PUBLISHED 13 January 2023
DOI 10.3389/fmars.2022.1101599

Marine sediment nitrogen isotopes and their implications for the nitrogen cycle in the sulfate-methane transition zone

Xin Yang[1,2], Yihao Zhang[2,3†], Xiaoming Sun[1,2,3*], Li Xu[1,2*] and TingTing Chen[1,2]

[1]School of Marine Sciences, Sun Yat-sen University, Zhuhai, China, [2]Guangdong Provincial Key Laboratory of Marine Resources and Coastal Engineering, Zhuhai, China, [3]School of Earth Science and Engineering, Sun Yat-sen University, Zhuhai, China

Introduction: Recent work has proposed that the nitrogen isotopes in marine sediments can be impacted by anaerobic oxidation of methane (AOM), since nitrogen uptake by anaerobic methanotrophic archaea (ANME) modifies the nitrogen isotope compositions of bulk sediment. Thus, unraveling the AOM-driven nitrogen cycle in the sulfate-methane transition zone (SMTZ) becomes significant. Additional study of the nitrogen cycle between sediment and interstitial water in SMTZ is needed.

Methods: To better understand the nitrogen cycle in the SMTZ, we analyzed NH4+ concentrations of interstitial water and nitrogen isotopes of sediment in the core GC10 from the southwestern Taiwan Basin in the South China Sea.

Results: The defined SMTZ is located at 560–830 cmbsf, based on methane and sulfate concentrations, as well as TS/TOC ratios, δ13CTIC and δ34S values. In the SMTZ, the NH4+ concentration decreases, the δ15NTN shows a negative excursion, δ15Ndecarb displays a positive excursion.

Discussions: NH4+ concentration decrease is interpreted by sulfate-reducing ammonium oxidation (SRAO). The δ15NTN shows negative excursion, which is most likely interpreted to N2 (δ15N=0‰) released from SRAO that was fixed into marine sediment via ANME nitrogen fixation. The δ15Ndecarb shows a negative correlation with NH4+ concentrations, indicating that it was controlled by organic matter decomposition. In the SMTZ, the methane competes with organic matter for becoming the substrate of sulfate reduction bacteria, which possibly decreases the organic matter degradation rate and causes δ15Ndecarb relative positive excursion. Although δ15Ndecarb is controlled by organic matter degradation, δ15NTN still reveals a negative excursion in the SMTZ. This likely indicates that nitrogen uptake by ANME/AOM microbial consortiums mainly modifies the nitrogen isotope of soluble nitrogen in the SMTZ.

OPEN ACCESS

EDITED BY
Dong Feng,
Shanghai Ocean University, China

REVIEWED BY
Yao Guan,
Ministry of Natural Resources, China
Jiasheng Wang,
China University of Geosciences
Wuhan, China

*CORRESPONDENCE
Xiaoming Sun
eessxm@mail.sysu.edu.cn
Li Xu
xuli22@mail.sysu.edu.cn

†These authors share first authorship

SPECIALTY SECTION
This article was submitted to
Marine Biogeochemistry,
a section of the journal
Frontiers in Marine Science

RECEIVED 18 November 2022
ACCEPTED 15 December 2022
PUBLISHED 13 January 2023

CITATION
Yang X, Zhang Y, Sun X, Xu L and Chen T (2023) Marine sediment nitrogen isotopes and their implications for the nitrogen cycle in the sulfate-methane transition zone. *Front. Mar. Sci.* 9:1101599.
doi: 10.3389/fmars.2022.1101599

Conclusions: This study indicates unique geochemistry processes in SMTZ will modify nitrogen characteristics in sediment/interstitial water, and the latter can serve as a proxy for AOM.

KEYWORDS

cold seep, anaerobic oxidation of methane (AOM), nitrogen isotopes, total organic carbon (TOC), South China Sea

1 Introduction

Methane (CH_4) is a strong greenhouse gas, with 25 times more greenhouse effects than carbon dioxide over 100 years (IPCC, 2007; Ruppel, 2017). Methane is the main component of gas hydrate deposits (Ruppel, 2017). Gas hydrates tend to form in a low-temperature and high-pressure environment with sufficient methane concentrations (Clennell et al., 1999). The continental margin is highly conducive to gas hydrate formation and represents the world's largest gas hydrate reservoirs (Suess, 2010). The buried gas hydrate is unstable, and would decompose due to various processes, such as earthquakes and ocean current circulation (Suess, 2020). Gas hydrate decomposition would generate a methane flow transported from deeper sediments towards the seafloor, which is called methane leakage (Suess, 2020). Methane leakage adds about 0.02 Gt of carbon to the ocean each year (Boetius and Wenzhöfer, 2013). Methane leakage is widely dispersed across the continental margin and has had a major impact on marine carbon cycling and climate over the last geological history (Dickens, 2003; Levin et al., 2016; Ruppel, 2017; Egger et al., 2018; Zhang et al., 2019; Akam et al., 2020; Kim and Zhang, 2022). Most of the methane released is consumed by anaerobic oxidation of methane (AOM) in the shallow sediments and/or anoxic water column, primarily using sulfate as an electron acceptor (Boetius et al., 2000; Reeburgh, 2007). The AOM process will occur at the sulfate methane transition zone (SMTZ), mediated by sulfate reducing bacteria (SRB) and anaerobic methanotrophic archaea (ANME) (Boetius et al., 2000). During this process, authigenic pyrite and carbonate are generated, significantly changing the sediment's geochemical characteristics (Boetius et al., 2000; Peckmann and Thiel, 2004; Lin et al., 2016). At the SMTZ, multiple elements (C, O, N, P, Fe, Mo etc.) undergo unique geochemical turnover (Peckmann et al., 1999; Boetius et al., 2000; Antler et al., 2015; Feng et al., 2018a; Feng et al., 2018b), understanding which is of great significance to tracing methane leakage.

Nitrogen is a fundamental element for life (Jing et al., 2020). Nitrogen is contained in all life (Jing et al., 2020). In the SMTZ, nitrogen experiences complex biogeochemical interactions, and the nitrogen isotope composition of sediments can be modified by ANME or AOM microbial consortiums (Dekas et al., 2009; Ettwig et al., 2010; Dong et al., 2017; Hu et al., 2020). Laboratory culture results have revealed that ANME can mediate nitrogen fixation and ammonia assimilation (Dekas et al., 2009). Recent studies suggest that nitrogen uptake by ANME causes a negative excursion of nitrogen stable isotopes in sediment (Feng et al., 2015; Hu et al., 2020), which can be applied as a proxy for AOM-impacted sediment in settings with or without authigenic carbonates (Hu et al., 2020). Previous studies mainly focused on nitrogen isotopic compositions in sediments or cold-seep organisms (Feng et al., 2015; Hu et al., 2020), whereas similar studies on sediment-interstitial water are rare.

Although ANME could mediate nitrogen fixation and lead to a negative excursion of biomass $\delta^{15}N$, the $\delta^{15}N$ composition in marine sediments could also be affected by both sedimentary input and diagenesis processes (Wehrmann et al., 2011; Robinson et al., 2012; Quan et al., 2013a; Quan et al., 2013b). The $\delta^{15}N$ compositions of marine sediments can be influenced by different nitrogen inputs (Quan et al., 2013b; Quan et al., 2013a; Tesdal et al., 2013). Redox conditions could also influence the $\delta^{15}N$ compositions of marine sediments (Quan et al., 2013b). Nitrate utilization and denitrification can also result in large nitrogen isotope fractionation (up to 30‰) (Freudenthal et al., 2001; Lehmann et al., 2002; Lehmann et al., 2007; Robinson et al., 2012). The diagenesis process would also have an impact on $\delta^{15}N$ of marine sediment (Freudenthal et al., 2001; Lehmann et al., 2002; Robinson et al., 2012). Organic matter degradation includes preferential degradation of amino acids rich in ^{15}N (Nakatsuka et al., 1997) and selective removal of proteins (Macko and Estep, 1984), which could induce $\delta^{15}N$ of organic matter decrease. Therefore, the nitrogen cycle between sediment and interstitial water may be more complicated than previously thought. It is necessary to combine interstitial water data and sediment data to uncover the nitrogen cycle in SMTZ.

In this study, we analyzed the nitrogen concentrations, nitrogen isotopic compositions of marine sediment as well as the NH_4^+ concentration in interstitial water. The object of this study is to understand the mechanism of the nitrogen cycle in SMTZ.

2 Geological setting

The sampling site (core GC10) is located in the southwestern Taiwan basin of the northeastern South China Sea (Figure 1).

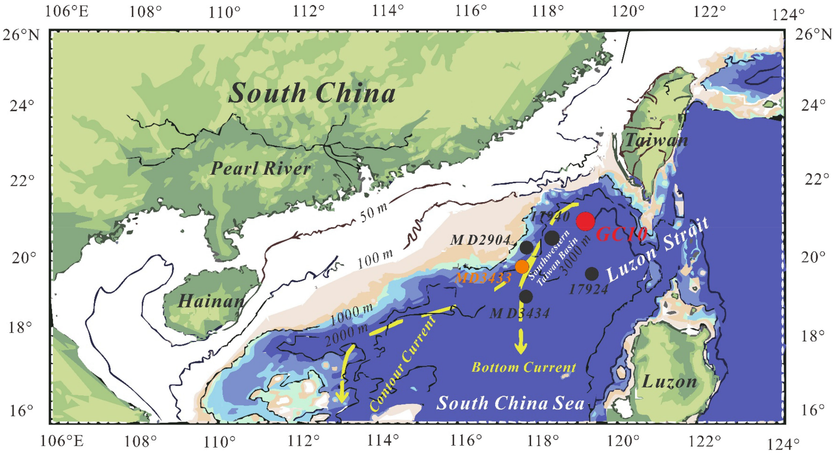

FIGURE 1
Map showing the sampling locations (red spot) (*modified after* Xu et al., 2021).

The basin has a 7 km-thick sediment succession with abundant organic matter and a high geothermal gradient, favoring gas hydrate formation (McDonnell et al., 2000). Moreover, bottom simulating reflectors (BSR) are widely distributed in the basin, indicating buried gas hydrates (McDonnell et al., 2000; Wu et al., 2007). The Jiulong methane reef was discovered in the southwestern Taiwan basin, and gas hydrates were successfully drilled in 2013 (Tong et al., 2013; Lin et al., 2018b). The Jiulong reef represents the world's largest methane-derived authigenic carbonate reef, indicating methane seepage used to be a common process at this site (Zhang et al., 2015). The southwestern Taiwan basin is considered a highly promising gas hydrate exploration target in the South China Sea (Lin et al., 2021).

3 Material and methods

The piston core was collected at site GC10 (21°18.453'N, 119°11.819'E) in the southwestern Taiwan basin in the South China Sea during the "Taiyang" cruise (No. SO177, June, 2004). The water depth at GC10 is 3008 m, and the core is 9.37 m long. The "porridge structure" is present at 9.10–9.20 m depth, likely caused by gas hydrate dissociation (Wu et al., 2010). The sediments are composed mainly of silt and fine-grained clay. After the retrieval, the core was cut into ~10 cm intervals and stored in a cold room (4°C). Samples were packed individually in zip-lock plastic bags and freeze-dried. For elemental and isotopic analyses, the samples were selected at 30 cm intervals, and pulverized with an agate mortar to< 63 µm.

Total sulfur (TS) and total nitrogen (TN) content were measured with a CNS-HO rapid element analyzer at the Guangdong Provincial Key Laboratory of Marine Resources and Coastal Engineering in March 2021. About 30 mg of the sample (mixed with ~30 mg V_2O_5) was transferred to a tin cup (2 mm*8 mm), and then converted to SO_2 and N_2 at 1020°C before being measured by the element analyzer.

Total organic carbon (TOC) and decarbonated nitrogen (N_{decarb}) contents were measured by an elemental analyzer. About 0.2 g of sediment was added into a 15 mL centrifuge tube and acidified by about 15 mL of 10% HCl (excess) for 12 hours, and then washed three times with deionized water. The treated samples were freeze-dried for TOC and N_{decarb} content measurement, with analytical procedures similar to those for the TS and TN measurements.

The TS, TN, TOC, and N_{decarb} isotopes were determined with a continuous flow Thermo Fisher Scientific MAT 253 Plus isotope ratio mass spectrometer at the School of Marine Sciences, Sun Yat-Sen University, in March 2021. About 15 mg of the sample was converted to CO_2, SO_2, N_2 in the elemental analyzer at 1020°C, and then the isotope compositions were measured by the isotope ratio mass spectrometer. N_{other} content was calculated by subtracting N_{decarb} from TN content. N_{other} isotope values were calculated by the simple binary model:

$$\text{ʅ}_{TN} * \text{£}_{TN} = \text{ʅ}_{decarb} * \text{£}_{decarb} + \text{ʅ}_{other} * \text{£}_{other}$$

Where ʅ represents the nitrogen isotope value; £ represents the nitrogen content.

Total inorganic carbon (TIC) isotopes were measured by a Thermo Fisher Scientific MAT 253 Plus isotope ratio mass spectrometer coupled with the Gas Bench II. Bulk sediment (~800 µg) was placed into a clear glass centrifuge tube, and helium gas was applied to flush out atmospheric gases from the tube. About 5 mL of 100% phosphoric acid was added to the tube at room temperature (25°C). In the tube, carbonate in sediments reacted with phosphoric acid for 24 hours, and then the released CO_2 was transported *via* Gas Bench II to be analyzed by the mass spectrometer.

The C, S, and N isotope values were reported with the standard δ notation relative to the Vienna Pee Dee Belemnite (V-PDB), Vienna Canyon Diablo Troilite (V-CDT), and atmospheric nitrogen, respectively. International reference materials for the C, S, and N isotopic data calibration are IAEA-S1 ($\delta^{34}S = -0.30$‰), NBS-18 ($\delta^{13}C = -5.014$‰, $\delta^{18}O = -23.2$‰) and IAEA-600 ($\delta^{13}C$ = -27.771‰, $\delta^{15}N$ = 1.0‰), respectively.

We compiled NH_4^+, methane, and sulfate concentrations from Wu et al. (2010) to reflect the nitrogen cycle and biochemical rate (Wu et al., 2010). Porewater was squeezed from marine sediment after retrieval (Wu et al., 2010). The NH_4^+ concentration of porewater was measured by a spectrophotometer on deck in June 2004 (Wu et al., 2010). Methane and sulfate concentrations were measured by ICP at the Guangzhou Marine Geological Survey in July 2004 (Wu et al., 2010). The precision of porewater is available for numerical simulation and analysis.

In this study, the organic matter degradation rate (R_{POC}), OSR rate, AOM rate, and methanogenesis rate under steady-state were calculated using porewater data and TOC content (Table S1–S4; Figure 2). The geochemistry rate models used in this study were the most well-known and commonly used in AOM-impacted sediment cores (Lehmann et al., 2002; Wehrmann et al., 2011; Meister et al., 2019; Zhang et al., 2019; Akam et al., 2020; Zhang et al., 2021). The parameters used in those models are as close to the study site as possible.

The organic matter degradation rate, R_{POC} (g C g^{-1} yr^{-1}), was calculated based on the most accepted method (Middelburg, 1989; Borowski et al., 1996; Beulig et al., 2017).

$$R_{POC} = POC*\left(0.16*\left(a_0+\frac{x}{v_s}\right)^{-0.95}\right) \qquad (1)$$

Where a_0 is the initial age of organic matter ($a_0 = 6030$ yr BP; Table S1); x (cm) represents the depth below seafloor; v_s is the porewater downward diffusion velocity, in this study, v_s equal to sedimentary rate (cm yr^{-1}) (v_s=25 cm yr^{-1}); POC is the TOC content of sediment.

The rate of AOM (Boetius et al., 2000), R_{AOM} (μmol cm^{-3} yr^{-1}), was calculated based on the most accepted method (Regnier et al., 2011):

$$R_{AOM} = k_{AOM}*\left[SO_4^{2-}\right]*[CH_4] \qquad (2)$$

Where K_{AOM} is the rate constant (k_{AOM}=1, according to Luo et al., 2015); $[SO_4^{2-}]$ and $[CH_4]$ are the concentrations of sulfate and methane in porewater (Table S2).

Based on the previous studies (Middelburg, 1989; Beulig et al., 2017), the rate of methanogenesis was determined as follows:

$$R_{MG} = 0.5*\frac{\rho_s*(1-\varnothing)*10^6}{MW_C*\varnothing}*\frac{[SO_4^{2-}]}{[SO_4^{2-}]+K_{SO_4^{2-}}}*R_{POC} \qquad (3)$$

Where ρ_s is the density of dry sediment (ρ_s =2.5 g/cm^3; according to Luo et al., 2015); $\varnothing$ is the porosity of sediment ($\varnothing$ =0.7; according to Feng et al., 2021); MW_C is the atomic weight of carbon (12 g/mol); $K_{SO_4^{2-}}$ is the Michaelis–Menten constant ($K_{SO_4^{2-}}$ = 0.1).

Age data were compiled to constrain the initial age of organic matter and the sedimentary rate (Table S1). The parameters of models are listed in Table S2 (Table S2).

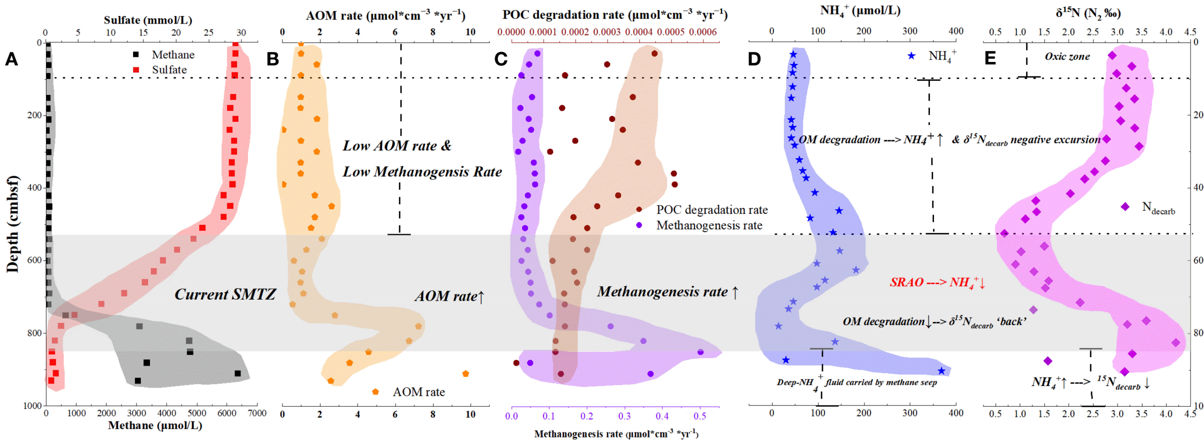

FIGURE 2
Graph for geochemistry rates, NH4+ concentration, and Ndecarb isotope composition. **(A)** Methane and sulfate concentrations in GC10. **(B)** AOM rate of GC10. AOM rate increases in the SMTZ. **(C)** Organic matter degradation rate and methanogenesis rate of GC10. The organic matter degradation rate decreases with depth due to the organic matter's decreased reactivity. The methanogenesis rate increases sharply in the SMTZ. **(D)** NH4+ concentrations of GC10 (Wu et al., 2010). In 0–560 cmbsf, NH4+ concentration increases with depth; in 560-830 cmbsf, NH4+ concentration display a distinct drop; below 830 cmbsf, NH4+ concentration sharply increases. **(E)** δ15Ndecarb shows a negative correlation with NH4+ concentration.

4 Results

4.1 Carbon and sulfur isotope compositions

The $\delta^{13}C_{TIC}$ of sediment from site GC10 is presented in Figure 3D. The $\delta^{13}C_{TIC}$ values vary widely, ranging from -20.89 to 1.03‰, averaging -2.37‰ (n = 32). In 0-420 cmbsf, the $\delta^{13}C_{TIC}$ is relatively stable, averaging 0.19‰ (n = 14). In 440-560 cmbsf, the $\delta^{13}C_{TIC}$ also shows relatively stable values, averaging -3.24‰ (n = 5). Distinct negative $\delta^{13}C_{TIC}$ excursions occur at 630 and 730 cmbsf, which reach -20.33‰ and -20.89‰, respectively. Below 830 cmbsf, the $\delta^{13}C_{TIC}$ of sediment displays relative stability, averaging -0.6‰ (n = 3). The $\delta^{34}S$ of sediment from site GC10 is presented in Figure 3E. Bulk sediment $\delta^{34}S$ varies from -29.36 to 24.20‰, averaging 4.20‰ (n = 32). The $\delta^{34}S$ is stable in 0–100 cmbsf (from 9.27 to 9.69‰; avg. 9.46‰; n = 3), decreases with depth in 100–400 cmbsf (from 9.46 to -27.96‰), and increases with depth in 400–930 cmbsf (from -27.96 to 24.2‰) (Figures 3D, E; Tables 1, 2).

TABLE 1 C-N-S content of core GC10.

Depth (cmbsf)	TOC content (wt%)	TN content (wt%)	Ndecarb content (wt%)	Nother content (wt%)
30-40	0.54	0.15	0.08	0.07
60-70	0.53	0.12	0.08	0.04
80-90	0.39	0.13	0.06	0.07
117-130	0.4	0.11	0.06	0.05
150-160	0.5	0.14	0.08	0.06
167-177	0.43	0.1	0.03	0.07
208-220	0.5	0.14	0.08	0.06
230-242	0.6	0.13	0.08	0.05
260-270	0.37	0.13	0.05	0.08
280-290	0.24	0.12	0.03	0.09
320-330	0.84	0.19	0.11	0.08
350-360	0.87	0.17	0.11	0.06
370-380	0.92	0.19	0.11	0.08
410-420	0.63	0.15	0.08	0.07
429-440	0.53	0.14	0.08	0.06
460-470	0.4	0.15	0.06	0.09
479-490	0.51	0.13	0.08	0.05
520-530	0.43	0.2	0.07	0.13
550-560	0.43	0.13	0.07	0.06
570-580	0.49	0.13	0.08	0.05
605-615	0.31	0.11	0.05	0.06
625-632	0.55	0.06	0.09	–
652-660	0.53	0.12	0.07	0.05
670-680	0.44	0.14	0.06	0.08
710-720	0.46	0.11	0.06	0.05
730-740	0.22	0.08	0.03	0.05
760-770	0.34	0.1	0.04	0.06
775-790	0.49	0.15	0.06	0.09
820-830	0.42	0.12	0.06	0.06

(Continued)

TABLE 1 Continued

Depth (cmbsf)	TOC content (wt%)	TN content (wt%)	Ndecarb content (wt%)	Nother content (wt%)
850-860	0.43	0.12	0.05	0.07
870-880	0.56	0.13	0.06	0.07
900-910	0.51	0.12	0.07	0.05

TABLE 2 C-N-S isotopes of core GC10.

Depth (cmbsf)	$\delta^{13}C_{TIC}$ (V-PDB)	$\delta^{34}S$ (V-CDT)	$\delta^{15}N_{TN}$ (Air N_2)	$\delta^{15}N_{decarb}$ (Air N_2)	TS/TOC
30-40	0.19	9.27	3.56	2.89	0.22
60-70	0.1	9.43	3.02	3.29	0.26
80-90	-0.25	9.69	2.2	2.99	0.2
117-130	1.03	-15.44	2.94	3.18	0.75
150-160	0.69	-9.68	3.06	3.35	0.61
167-177	0.77	-16.47	2.27	3.03	1.13
208-220	0.08	-13.9	2.41	3.06	0.63
230-242	0.07	-13.1	2.52	3.35	0.24
260-270	0.16	-20.05	2.5	2.77	0.52
280-290	0	-16.61	2.92	3.44	1.11
320-330	-0.08	-21.3	2.37	2.75	0.31
350-360	-0.23	-29.36	2.01	2.53	0.32
370-380	-0.37	-27.96	2.6	2.33	0.39
410-420	0.44	-18.43	3.38	2.03	0.66
429-440	-3.2	-7.68	2.47	1.32	0.67
460-470	-3.54	-5.64	2.14	1.34	0.64
479-490	-3.65	-3.62	2.01	1.11	0.41
520-530	-3.02	0.28	3.27	0.68	0.39
550-560	-2.79	-2.82	1.68	1.5	0.6
570-580	-7.11	-2.62	1.15	1.02	0.41
605-615	-2.78	-0.56	0.69	0.91	0.5
625-632	-20.33	-4.19	1.74	1.28	0.71
652-660	-2.1	-9.53	2.1	1.59	0.62
670-680	-1.9	-0.85	1.8	1.52	0.84
710-720	-2.82	7.01	1.6	2.23	1.19
730-740	-20.89	0.18	2.68	1.27	2.32
760-770	-0.22	0.16	0.79	3.59	1.06
775-790	-1.73	-1.19	1.71	3.2	0.65
820-830	-0.42	15.7	1.41	4.2	0.82
850-860	-0.66	14.25	1.3	3.3	0.55
870-880	-0.65	16.66	1.06	1.57	0.54
900-910	-0.49	24.2	1.93	3.15	0.09

4.2 TOC, TN, N_{decarb} and TS contents

The TN and N_{decarb} content of sediment from site GC10 is presented in Figure 4A. The samples have TOC = 0.22–0.92 wt% (avg. 0.49 wt%; n = 32), TN = 0.08–0.2 wt% (avg. 0.13 wt%; n = 32), and N_{decarb} = 0.03–0.11 wt% (avg. 0.07 wt%; n = 32). TOC, TN, and N_{decarb} content display similar trends and vary widely. In 605–632 and 730-770 cmbsf, TOC, TN, and N_{decarb} content present distinct decreases (Figure 4A, Table 1). The samples have TS = 0.04–0.79 wt% (avg. 0.29 wt%; n = 32). In 0-100 cmbsf, TS content displays relatively low values. In 100-560cmbsf, TS content is relatively high and varies widely. TS content shows a significant increase in 560–830 cmbsf (Figure 3C). TS/TOC is less than 0.36 in 0-100 cmbs and higher than 0.36 in 100-930 cmbsf (Figure 3B). TS/TOC displays a significant increase in 560-830 cmbsf.

4.3 TN and N_{decarb} isotopes

The samples have $\delta^{15}N_{TN}$ = 0.69–3.56‰ (avg. 2.16‰; n = 32). In 0-100 cmbsf, the $\delta^{15}N_{TN}$ decreases with depth. In 100-560 cmbsf, the $\delta^{15}N_{TN}$ of sediment is relatively stable. The $\delta^{15}N_{TN}$ exhibits distinct negative excursions in 560-830 cmbsf. $\delta^{15}N_{decarb}$ varies from 0.68 to 4.20‰ (avg. 2.37‰; n = 32). In 0-100 cmbsf, the $\delta^{15}N_{decarb}$ of sediment is relatively stable. In 100-560 cmbsf, the $\delta^{15}N_{decarb}$ decreases with depth. The $\delta^{15}N_{decarb}$ shows positive excursion in 560–830 cmbsf (Figure 4, Table 2).

5 Discussion

5.1 Geological records for AOM

In order to reveal the nitrogen cycle in SMTZ, the SMTZ position of core GC10 must first be constrained. The current SMTZ of core GC10 has been constrained at ~800 cmbsf using porewater methane and sulfate concentrations (Wu et al., 2010). At ~800 cmbsf, methane concentrations rise sharply, whereas sulfate concentrations drop sharply with depth, indicative of the AOM occurrence there (Figures 2, 3). To trace the integral methane seepage dynamics, TS/TOC and the TIC and TS isotopes are also used here to trace the AOM geological record.

5.1.1 TS/TOC indicates AOM in sediment

In the marine sedimentary environment, sulfur comes primarily from pyrite (FeS_2), which is mainly sourced by sulfide from sulfate reduction of organic matter (OSR) and Fe^{2+} from porewater (equations (5), (6), (7), and (8)), thus there is a dependency between the TS and TOC contents (Berner, 1984; Wang et al., 2018b). Because OSR would produce authigenic pyrite, the TS/TOC ratio is less than 0.36 in an oxic setting and larger than 0.36 in an anaerobic environment (Berner, 1984; Li et al., 2016). In the SMTZ, AOM produces additional authigenic pyrite (not dependent on TOC) (Berner, 1984; Li et al., 2016; Wang et al., 2018b), which significantly increases the sediment TS content and TS/TOC ratio (equations (4), (5), (6), (7), and (8)). Therefore, a high TS/TOC ratio is widely used to trace AOM in sediments (van Dongen et al., 2007; Li et al., 2018; Yang et al., 2020; Miao et al., 2021).

$$CH_4 + SO_4^{2-} \rightarrow HS^- + HCO_3^- + H_2O \tag{4}$$

$$2CH_2O + SO_4^{2-} \rightarrow H_2S + 2HCO_3^- \tag{5}$$

$$Fe^{2+} + HS^- \rightarrow FeS + H^+ \tag{6}$$

$$FeS + H_2S \rightarrow FeS_2 + H_2 \tag{7}$$

$$FeS + S_n^{2-} \rightarrow FeS_2 + S_{n-1}^{2-} \tag{8}$$

In core GC10, the TS/TOC ratio is< 0.36 in 0–100 cmbsf, which indicates that the horizon is oxidizing. Below 100 cmbsf, TS/TOC is generally > 0.36, indicative of an anaerobic environment. The sharp TS/TOC increase (reaching 2.32) in 560–830 cmbsf is most likely attributed to the presence of AOM-generated additional authigenic pyrite, thus constraining the SMTZ there (Figure 3B).

5.1.2 TIC isotopes trace authigenic carbonate generated by AOM

The TIC of bulk marine sediment is a mixture of different inorganic carbon sources (Yang et al., 2020). TIC is primarily derived from calcareous nannofossils and authigenic carbonate generated by the seawater dissolved inorganic carbon (DIC) pool ($\delta^{13}C$ = 0 ‰) (Suess, 2014; Consolaro et al., 2015). The carbon isotope composition of calcareous nannofossils varies from -2 to 2‰ in a marine sedimentary environment without methane leakage (Berger, 1970; Panieri et al., 2017), thus the TIC carbon isotope composition varies generally between -2 and 2‰ (Wang et al., 2018b; Feng et al., 2021b; Li et al., 2021). In methane leakage regions, the TIC of bulk marine sediment is composed of calcareous nannofossils and authigenic carbonate generated by special DIC pools (Meister et al., 2019). The potential DIC pools in the methane seepage region include AOM-derived DIC, OSR-derived DIC, and deep-DIC flux (Akam et al., 2020). AOM-derived DIC inherits the ^{13}C depletion from methane (biogenic methane $\delta^{13}C$ less than -50‰) (Peckmann et al., 1999; Peckmann et al., 2004; Peckmann et al., 2009). OSR-derived DIC inherits the ^{13}C depletion from organic matter ($\delta^{13}C$ of marine organic matter varies from -19 to -22‰) (Berner, 1978; Lim et al., 2011). Deep-DIC flux fluxes from methanogenic depths with higher $\delta^{13}C$ values (5 to 24‰) (Meister et al., 2019; Akam et al., 2020). In SMTZ, high alkalinity will convert

7-36% DIC pools into authigenic carbonate (Akam et al., 2020). These DIC pools convert to authigenic carbonate minerals in the sediments and/or overprint foraminiferal shells (Zhuang et al., 2016; Panieri et al., 2017; Bergamin et al., 2019), which significantly changes the TIC carbon isotope compositions of bulk marine sediment, causing TIC ^{13}C depletion. AOM-derived authigenic carbonate typically displays ^{13}C depletion (<–30‰) which mainly mirrors AOM-derived DIC. Because OSR-derived DIC is limited by the reactive organic matter content of sediment, OSR could only generate a small proportion of DIC (Consolaro et al., 2015; Beulig et al., 2017; Feng et al., 2018b; Li et al., 2018; Feng et al., 2021a; Li et al., 2021).

The $\delta^{13}C_{TIC}$ values show clear negative excursions in 560–830 cmbsf (reaching -20.89‰), which indicate a mixture of calcareous nannofossils and authigenic carbonate generated by the AOM-derived DIC pool (Figure 3D). AOM-induced negative excursions of $\delta^{13}C_{TIC}$ also been reported in many AOM-impacted sediment cores (Li et al., 2016; Xie et al., 2019; Hu et al., 2020; Xiong et al., 2020; Yang et al., 2020; Li et al., 2021). Therefore, the SMTZ was constrained at 560–830 cmbsf.

5.1.3 TS isotope reveals AOM impact on core GC10

Organic sulfur, elemental sulfur, and pyrite are all components of sulfur in marine sediment. Because organic sulfur, elemental sulfur, and Fe-sulfides are all metastable (Hofmann et al., 2009; Chen et al., 2016; Lin et al., 2016; Zhang et al., 2018), they are easily converted to pyrite. Pyrite is the most abundant sulfur component in bulk sediments (Berner, 1984). In an anaerobic marine environment, sulfate reduction bacteria preferentially use ^{32}S to generate pyrite when sulfate replenishment is sufficient (Hofmann et al., 2009; Chen et al., 2016; Lin et al., 2016; Zhang et al., 2018). Thus, the pyrite formed by organic matter sulfate reduction (OSR) is ^{34}S-depleted (Borowski et al., 2013; Egger et al., 2015; Beulig et al., 2017). In SMTZ, the consumption rate of sulfates in interstitial water is much higher than the seawater sulfate replenishment rate, resulting in a residual ^{34}S-rich sulfate pool, which eventually precipitates into ^{34}S-rich pyrite *via* AOM (Borowski et al., 2013; Egger et al., 2015; Lin et al., 2016; Lin et al., 2018a). This will generate ^{34}S-rich pyrite in marine sediment (Hofmann et al., 2009; Chen et al., 2016; Lin et al., 2016; Zhang et al., 2018). $\delta^{34}S_{TS}$ displays a similar tendency as $\delta^{34}S_{CRS,}$ as pyrite is the major sulfur source in bulk sediment (Li et al., 2018; Liu et al., 2020; Feng et al., 2021b). $\delta^{34}S_{TS}$ can also indicate the sulfur isotope characteristic of pyrite (Wang et al., 2018b; Yang et al., 2020; Feng et al., 2021b).

In 0–100 cmbsf, $\delta^{34}S_{TS}$ is stable (from 9.27 to 9.69‰; avg. 9.46‰) and TS/TOC is< 0.36 (oxic zone), which were interpreted by disproportionation and reoxidation. Disproportionation and reoxidation of sulfide is most-likely attributed to heavy ^{34}S enrichment of pyrite in surface marine sediment (Lin et al., 2016; Lin et al., 2017). During very early diagenesis, there was an increased availability of easily degradable organic materials, which led to high cellular sulfate reduction rates and declining isotope discrimination (Lin et al., 2016; Lin et al., 2017). This is reflected in the high δ^{34}S values and low pyrite content (Lin et al., 2016; Lin et al., 2017). Such sulfide disproportionation and reoxidation (a high δ^{34}S value and a low pyrite content in shallow surface sediments) have been widely reported in surface sediment from continental margins and cold-seep regions (Borowski et al., 2013; Lin et al., 2017; Lin et al., 2018b). In 100–400 cmbsf, δ^{34}S decreases with depth and TS/TOC is high (> 0.36), which is most likely caused by the addition of OSR-driven ^{34}S-depleted pyrite. In 100-400 cmbsf, OSR is occurring due to the anoxic environment (TS/TOC > 0.36). The rate of OSR is slow enough not to contribute to a sulfate gradient, but strong enough to produce enough isotopically light sulfide in here. It is indicated by the δ^{34}S decrease with depth in 100-400 cmbsf but sulfate concentration is relatively stable. The negative δ^{34}S value of pyrite generated by OSR is also reported in most marine sediments (Berner, 1978; Robinson et al., 2012; Borowski et al., 2013; Li et al., 2016; Lin et al., 2016; Antler et al., 2017; Lin et al., 2018a; Lin et al., 2018b; Lin et al., 2021; Lin et al., 2021). In 400–830 cmbsf, δ^{34}S increases with depth (Figure 3D), which is most likely due to AOM-generated ^{34}S-rich pyrite. The positive excursion of δ^{34}S below the SMTZ (below 830 cmbsf) is most likely caused by the sulfate reduction rate faster than the sulfate replenish rate (Liu et al., 2020). This phenomenon was also observed in many sediment cores in the Bornholm Basin (Liu et al., 2020).

In a word, the SMTZ of GC10 are restricted at 560–830 cmbsf, based on a significantly increased TS/TOC ratio, $\delta^{13}C_{TIC}$ negative excursions, δ^{34}S positive excursions, and methane/sulfate concentration.

5.2 Nitrogen geochemistry and its constraints for nitrogen cycle in SMTZ

5.2.1 Nitrogen geochemistry in interstitial water

We compiled NH_4^+, methane, and sulfate concentrations from Wu et al. (2010) to reflect the nitrogen cycle and biochemical rate (Wu et al., 2010). In the core of GC10, NH_4^+ concentration rises with depth and then falls sharply to the current SMTZ, below which it rises sharply again (Figure 2D). NH_4^+ is a major nitrogen component in interstitial water that is mostly released by organic matter degradation (Laima, 1992; Yang et al., 2010). NH_4^+, as an indicator of organic matter degradation, has been utilized in many continental margin porewater investigations (Nakatsuka et al., 1997; Holmes et al., 1999; Freudenthal et al., 2001; Wehrmann et al., 2011; Robinson et al., 2012; Schrum et al., 2015; Komada et al., 2016). The concentration of NH_4^+ in pore water normally increases with depth in a marine environment without methane seepage, which has been interpreted as organic matter degradation releasing NH_4^+ accumulation in interstitial water (Lehmann et al., 2007; Wehrmann et al., 2011; Robinson et al., 2012; Quan et al., 2013a; Tesdal et al., 2013; Schrum et al., 2015; Akam et al., 2020; Zhang et al., 2021). The laboratory incubation found that organic matter decomposition releases NH_4^+, and NH_4^+ concentration increases with incubation time (Holmes et al., 1999; Freudenthal et al., 2001; Lehmann et al., 2002; Wehrmann et al., 2011). The age of organic matter in marine sediment increases with depth, thus NH_4^+ concentration increases with depth in normal marine environment (Nakatsuka et al., 1997; Holmes et al., 1999; Freudenthal et al., 2001; Wehrmann et al., 2011; Robinson et al., 2012; Schrum et al., 2015; Komada et al., 2016).

In the methane seepage region, the NH_4^+ concentration increases from low values near the seafloor to an interval where the concentration gradients are minimal, followed by a pronounced increase very close to the depth where sulfate values approach zero (Wehrmann et al., 2011; Schrum et al., 2015). In fact, the zone where sulfate values approach zero coincides with the SMTZ lower boundary. Therefore, in the methane seepage region, the NH_4^+ concentration increases with depth, and the concentration gradients are minor in the SMTZ but significantly higher below the SMTZ. The concentration gradients are minimal in the SMTZ, which is interpreted by sulfate-reducing ammonium oxidation and ammonia assimilation into biomass (Wehrmann et al., 2011; Schrum et al., 2015). Sulfate-reducing ammonium oxidation (SRAO) could be illustrated as equation (10) (Schrum et al., 2015). According to computed Gibbs energies, sulfate-reducing ammonium oxidation is energy yielding and metabolically practical (Schrum et al., 2015). The rapid increase in NH_4^+ concentration below SMTZ is interpreted by the upward NH_4^+ flow carried by methane leakage (Wehrmann et al., 2011; Schrum et al., 2015).

$$4NH_4^+ + 4SO_4^{2-} + 5(CH_2O)_n \rightarrow 5CO_2 + 2N_2 + 11H_2O + 4HS^- \quad (10)$$

The whole down-core profile of NH_4^+ concentration for GC10 is similar to most AOM-impacted sediment cores from the Bering Sea Slope, Bay of Bengal and Greenwich Bay (Wehrmann et al., 2011; Schrum et al., 2015). In the oxidation zone of 0-100 cmbsf (TS/TOC< 0.36), the NH_4^+ concentration was stabilized at a low value (average 46.1 µmol/L) most likely due to the release of NH_4^+ from organic matter degradation under oxidative conditions. Organic matter could be degraded by O_2, N, Fe, Mn, and SO_4^{2-}; it depends on the Gibbs energy difference (O_2 < Mn < N < Fe < SO_4^{2-}) (Froelich et al., 1979; Thullner et al., 2007; LaRowe and Van Cappellen, 2011). The lower the Gibbs energy, the more likely the reaction is to happen (Froelich et al., 1979; Thullner et al., 2007; LaRowe and Van Cappellen, 2011). In 0-100 cmbsf, TS/TOC is less than 0.36, indicating an oxidation condition. Because the Gibbs energy of organic matter degradation by O_2 is lower than that of SO_4^{2-}, most organic matter is degraded by O_2 in 0-100 cmbsf. The concentration of NH_4^+ increases with depth in the range of 100-560 cmbsf, which is most likely owing to organic matter age increasing with depth and interstitial water accumulating NH_4^+ produced by organic matter decomposition. In 100-560 cmbsf, TS/TOC is higher than 0.36, indicating an anaerobic condition. Thus, in 100-560 cmbsf, most organic matter is degraded by SO_4^{2-}. The SMTZ (560-830 cmbsf) has a lower NH_4^+ concentration, which is most likely due to NH_4^+ consumption by the SRAO. Below the SMTZ (830-930 cmbsf), NH_4^+ concentration increases sharply (reach to 367.9 µmol/L), accounting for deep NH_4^+ flux upward with methane leakage.

Based on above mentioned, NH_4^+ concentration decreases in the SMTZ which most likely indicate sulfate-reducing ammonium oxidation occurrence there.

5.2.2 Nitrogen geochemistry in marine sediment

In marine sediment, the potential nitrogen sources include nitrogen from particulate organic matter, nitrogen from dissolved organic matter, NO_3^-, exchangeable NH_4^+, and NH_4^+ fixed into clay mineral structures (Macko and Estep, 1984; Karl et al., 1997; Holmes et al., 1999; Lehmann et al., 2007; Martens-Habbena and Qin, 2022). The most abundant nitrogen source in marine sediment is nitrogen from organic matter (Karl et al., 1997; Hong et al., 2013; Tesdal et al., 2013; Komada et al., 2016; Kuypers et al., 2018). Exchangeable NH_4^+ makes up only a modest percentage of nitrogen (<1%) in open ocean sediments with little TOC, but its content will rise in anaerobic environments as interstitial water NH_4^+ concentrations rise and the significant capacity of the clays to absorb NH_4^+ (Freudenthal et al., 2001; Lehmann et al., 2007; Robinson et al., 2012; Hong et al., 2013; Schrum et al., 2015; Martens-Habbena and Qin, 2022). NH_4^+ fixed into clay mineral structures would be a substantial nitrogen pool in marine sediment with low organic matter content, but in environments with high organic matter content, the main nitrogen pool is nitrogen from organic matter (Alshameri et al., 2018).

TN, N_{decarb}, and N_{other} contents are illustrated in Figure 4A. Interesting, TN, N_{decarb}, and N_{other} content display distinct drops in 625-632 and 730-740 cmbsf, which are most likely due to AOM-generating carbonate diluting nitrogen content in sediment. Because $\delta^{13}C_{TIC}$ displays negative excursions in 625-632 and 730-740 cmbsf, indicating that AOM generates a substantial amount of carbonate there. In 625-632 cmbsf, N_{decarb} content even higher than TN content, which also consistent with that carbonate dilute nitrogen content in sediment there. Thus, TN, N_{decarb} and N_{other} contents could be influenced by carbonate dilution and could not reflect nitrogen accumulation.

TN is made up of N_{decarb}, and N_{other} in this study. The nitrogen sources of marine sediment associated with different nitrogen types are depicted in Figure 5. PON, DON, E-AM, NO_3^-, and CFN are all possible nitrogen types for TN. The probable

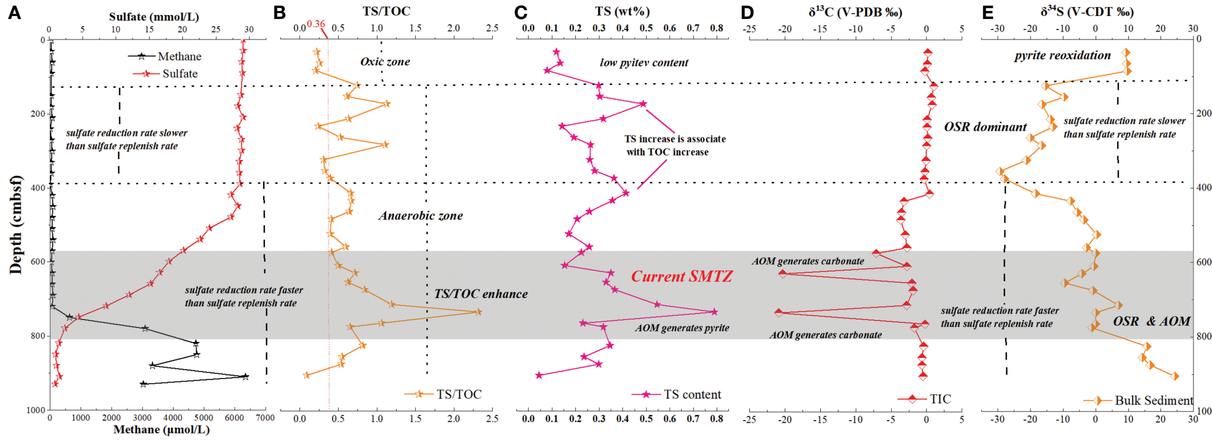

FIGURE 3
Geological records of SMTZ in core GC10. **(A)** Interstitial water data for GC10 (Wu et al., 2010). Methane concentrations rise, and sulfate drops sharply at 560–830 cmbsf, indicating the SMTZ location there. **(B)** TS/TOC of sediments from GC10. TS/TOC enhances at 560–830 cmbsf. **(C)** Total sulfur content for GC10. Total surfur content increases at 560-830 cmbsf, indicating additional pyrite generated by AOM. **(D)** Total inorganic carbon δ13C for sediments, showing negative δ13CTIC excursions at 560–830 cmbsf (reaching -20.89‰), and indicating AOM occurrence here. **(E)** Bulk-sediment δ34S for GC10. δ34S values are positive in 0–100 cmbsf, decrease in 100-400 cmbsf, and variably increase in 400–937 cmbsf.

nitrogen types of N_{decarb} include PON and CFN, while DON, NO_3^- and E-AM are all potential types for N_{other}. E-AM and CFN may not be the majority nitrogen types at site GC10, because site GC10 is a typical methane seep location with substantial organic matter (average TOC content = 0.49 wt%). The majority of nitrogen in GC10 is related to organic matter, since TOC vs TN and TOC vs N_{decarb} in GC10 show a clear positive correlation (Figure 6). This implies that TN and N_{decarb} of sediment in site GC10 are mostly derived from organic matter.

The $\delta^{15}N$ of organic matter is controlled by sedimentary input and early diagenesis (Lehmann et al., 2002; Komada et al., 2016; Chuang et al., 2019; Zhang et al., 2020). a) Sedimentary input. Nitrogen isotopes from various organic matter sources would have varying $\delta^{15}N$ values (Nakatsuka et al., 1997; Freudenthal et al., 2001; Lehmann et al., 2007; Reeburgh, 2007; Robinson et al., 2012). Organic matter $\delta^{15}N$ would vary with different sedimentary inputs. Organic matter would have little $\delta^{15}N$ offset in an area with steady sedimentary input (relatively

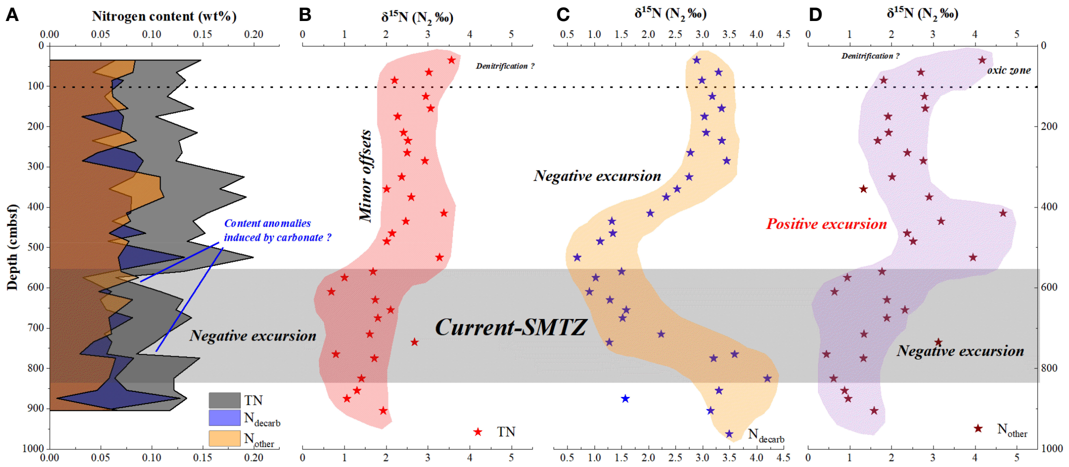

FIGURE 4
Element and isotope compositions of different nitrogen species for GC10. δ15NTN and δ15Nother shows negative excursions in the SMTZ. **(A)** TN, Ndecarb and Nother content;**(B)** TN isotope; **(C)** Ndecarb isotope; **(D)** Nother isotope.

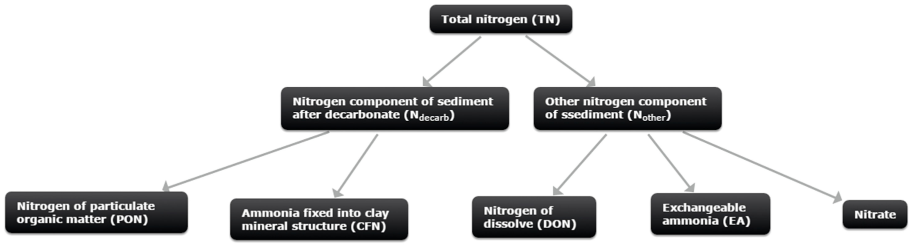

FIGURE 5
Nitrogen composition of marine sediment. Total nitrogen (TN) includes N_{decarb} and N_{other}; N_{decarb} includes nitrogen of particulate organic matter (PON) and amminia fixed into clay minerals structure (CFN); N_{other} includes nitrogen of dissolve organic matter (DON) and exchangeable ammonia, and negligeble nitrate.

stable organic matter source and relatively stable sedimentation rate). b) Early diagenesis. In early diagenesis, a variety of aerobic and anaerobic microbial processes could modify the $\delta^{15}N$ of organic matter (nitrate utilization, denitrification, nitrification, N_2-fixation, organic matter degradation, and sulfate-reducing ammonium oxidation) (Macko and Estep, 1984; Robinson et al., 2012; Komada et al., 2016; Wang et al., 2018a; Akam et al., 2020).

Nitrate utilization, denitrification, and nitrification are all associated with nitrate. Although nitrate utilization and denitrification can result in large nitrogen isotope fractionation (up to 30‰), nitrate is exhausted by denitrification within a few centimeters (Lehmann et al., 2007). Below the seafloor, in anaerobic environment, low nitrate concentration in deep sediment can lead to under-expression of this isotope effect, both at the organism and sediment scales (Lehmann et al., 2007). Thus, the $\delta^{15}N$ of organic matter in deep sediment is less impacted by nitrate utilization, denitrification, and nitrification. N_2-fixation may also result in a negative excursion of sediment $\delta^{15}N$ (Karl et al., 1997), as N_2 has a relatively low nitrogen isotope ($\delta^{15}N$ = 0‰) (Robinson et al., 2012). ANME is a type of N_2-fixation diazotrophic bacteria (Dekas et al., 2009), which could result in the depletion of ^{15}N in sediment (Hu et al., 2020). Organic matter degradation could also modify the nitrogen isotope of sediment (Nakatsuka et al., 1997; Holmes et al., 1999; Freudenthal et al., 2001; Lehmann et al., 2002; Lehmann et al., 2007). Selective loss of specific fractions from total organic matter during degradation could alter the $\delta^{15}N$ of organic matter (Libes and Deuser, 1988; Karl et al., 1997; Nakatsuka et al., 1997; Komada et al., 2016; Meister et al., 2019). Carbohydrates, proteins, and lipids make up organic matter in marine sediment, and degradation of organic matter can change the relative abundance of carbohydrates, proteins, and lipids (Karl et al., 1997; Robinson et al., 2012). This could also change the nitrogen isotope component of organic matter (Karl et al., 1997; Robinson et al., 2012). Organic matter degradation preferential degradation of amino acids (^{15}N-rich) (Nakatsuka et al., 1997) and selective removal of proteins (with relative ^{15}N rich) (Macko and Estep, 1984) which could induce $\delta^{15}N$ of organic matter negative excursion.

The $\delta^{15}N_{TN}$ of sediment displays a relatively high value in 0-100 cmbsf, shows relatively stable values (offset 2‰) in 100-530 cmbsf, and displays a negative excursion in the SMTZ. In 0-100 cmbsf, the $\delta^{15}N_{TN}$ of sediment displays a relatively high value, which is most likely due to denitrification. In an oxic condition, denitrification would make surface marine sediment ^{15}N enriched (Lehmann et al., 2007). In 0-100 cmbsf, TS/TOC<0.36 indicates an oxic environment here, which favors denitrification and sediment ^{15}N enrichment. In 100-530 cmbsf, the $\delta^{15}N_{TN}$ between the fluff layers is relatively steady (Figure 4B), which reflects relatively stable sedimentary input in site GC10. In addition, the nitrogen isotope of sediment from northern South China Sea (site MD3433, that study site is close to our study area) is relatively stable (< 1‰) since 50 ka (Figure 1) (Wang et al., 2018a), which consistent with site GC10 has relatively stable sedimentary input. *In the SMTZ (560-830 cmbsf), the* $\delta^{15}N_{TN}$ of sediment displays a negative excursion, which is most likely due to nitrogen uptake by ANME or AOM microbial consortiums. The $\delta^{15}N_{TN}$ of sediment cores displaying negative excursions in AOM-impacted zones has been observed in many methane seepage regions (Hu et al., 2020). This phenomenon is interpreted by the nitrogen uptake of ANME or AOM microbial consortiums (Hu et al., 2020). However, the nitrogen source in SMTZ is not well understood. Combining with SRAO would consume NH_4^+ and produce N_2 (equation 10) in the SMTZ, the negative excursion of $\delta^{15}N_{TN}$ in the SMTZ likely due to that N_2 generated by SRAO was fixed into marine sediment. There are further studies needed to confirm it.

Interestingly, $\delta^{15}N_{decarb}$ displays a different tendency from $\delta^{15}N_{TN}$.The $\delta^{15}N_{decarb}$ of sediment decreases with depth in 0-530 cmbsf and displays a positive excursion in the SMTZ. In 0-530 cmbsf, the $\delta^{15}N_{decarb}$ of sediment decreases with depth, which is most likely due to organic matter degradation. Organic matter degradation would consume organic matter and release NH_4^+ (Nakatsuka et al., 1997). Organic matter degradation involves preferential degradation of amino acids and selective removal of proteins (with relative ^{15}N rich) (Macko and Estep, 1984), which would induce the $\delta^{15}N$ of particular organic matter decrease. In 0-530 cmbsf, the $\delta^{15}N_{decarb}$ decrease with depth, and NH_4^+ concentration increase with depth, which are consistent with organic matter degradation releasing NH_4^+ and inducing $\delta^{15}N_{decarb}$ decrease. The plot of $\delta^{15}N_{decarb}$ vs NH_4^+ displays a negative correlation (Figure 6B), which is also consistent with it. In the SMTZ, the $\delta^{15}N_{decarb}$ of sediment displays a positive excursion, which is likely due to the organic matter degradation rate decreasing in the SMTZ. In SMTZ, methane competes with organic matter for becoming the substrate of *Sulfate Reduction Bacteria* (Jørgensen et al., 2019), which would decrease the organic matter degradation rate. The AOM rate, methanogenesis rate, and POC (particulate organic carbon) degradation rate are estimated, based on interstitial water *via* numerical simulation calculation. In GC10, the low POC degradation rate in the SMTZ is consistent with $\delta^{15}N_{decarb}$ positive excursion that is possible due to the organic matter degradation rate decrease in the SMTZ.

TN is a mixture of N_{decarb} and N_{other}. TN is derived from both particulate organic matter and soluble organic matter. N_{decarb} only comes from particulate organic matter. The $\delta^{15}N_{decarb}$ of sediment is mainly controlled by organic matter degradation, but the $\delta^{15}N_{TN}$ of sediment reflects the nitrogen fixation and ammonia assimilation influence of ANME/AOM microbial consortiums. This indicates that the nitrogen fixation process and ammonia assimilation of ANME may mainly control the soluble organic nitrogen isotope composition. The calculated $\delta^{15}N_{other}$ shows negative excursions in the SMTZ, which further supports our opinion (Figure 4A). In addition, N_2-fixation induced negative excursion of soluble organic matter $\delta^{15}N$ has been reported in many studies (Karl et al., 1997; Robinson et al., 2012).

5.2.3 Nitrogen cycle model in the SMTZ

Based on $\delta^{15}N_{TN}$, $\delta^{15}N_{decarb}$, TOC content, and NH_4^+ concentration of core GC10, we present a nitrogen cycle model in SMTZ, which is depicted in Figure 7. When SMTZ is positioned in the sediment column, as an anaerobic environment, nitrate will be quickly consumed by denitrification at the sediment surface, and nitrate is absent from the nitrogen cycle in SMTZ. The nitrogen cycle in SMTZ will only be associated with NH_4^+ in interstitial water, nitrogen in sediment, and N_2.

Sulfate-reducing ammonium oxidation (SRAO) would consume NH_4^+ and release N_2 in SMTZ (Schrum et al., 2015). This would induce a decrease in NH_4^+ concentration and an increase in N_2 concentration. In SMTZ, as abundant ANME could mediate N_2-fixation (Boetius et al., 2000; Boetius and Wenzhöfer, 2013; Suess, 2014; Feng et al., 2015; Feng et al., 2018b; Suess, 2020), N_2-fixation rate clearly increased. Diazotrophic bacteria (ANME is one of them) mediating N_2-fixation would cause a decrease in the soluble nitrogen isotope (Karl et al., 1997; Robinson et al., 2012). N_2 released from SRAO would be fixed into sediment *via* soluble organic matter due to ANME N_2-fixation. Because N_2 has a relatively lighter nitrogen isotope ($\delta^{15}N \approx 0$ ‰), the $\delta^{15}N_{TN}$ of sediment would exhibit negative excursion in SMTZ. As to the $\delta^{15}N_{decarb}$ of sediment, it is controlled by organic matter degradation. In SMTZ, methane competes with organic matter, which induce organic matter degradation rate decrease and the $\delta^{15}N_{decarb}$ of sediment displays a positive excursion. This nitrogen cycle model could be modified in the future as more research on the nitrogen cycle in SMTZ is conducted. This study shows that the unique geochemistry processes in SMTZ would modify the nitrogen geochemistry characteristics.

6 Conclusions

(1) Based on the TIC and TS isotopes, TS/TOC, methane and sulfate concentrations of the sediment core GC10

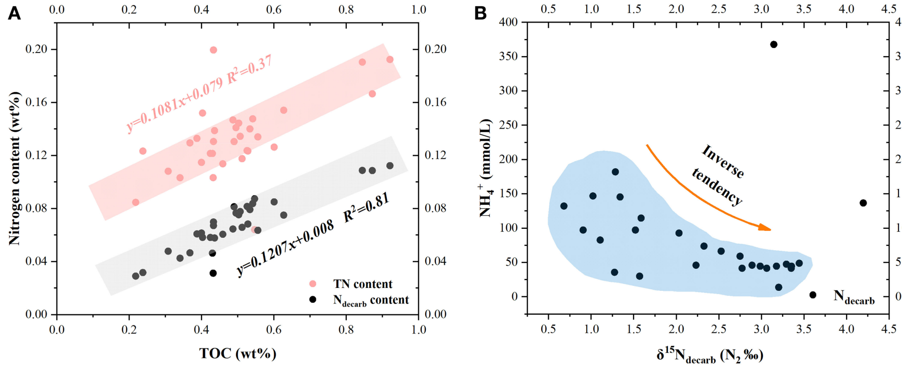

FIGURE 6
Scatter plot for nitrogen contents and isotopes of GC10. TN and N_{decarb} contents increase with TOC content, indicating that nitrogen in sediments mainly comes from organic matter. **(A)** Scatter plots for TOC vs TN and TOC vs N_{decarb}. **(B)** Scatter plot for NH_4^+ vs $\delta^{15}N_{decarb}$.

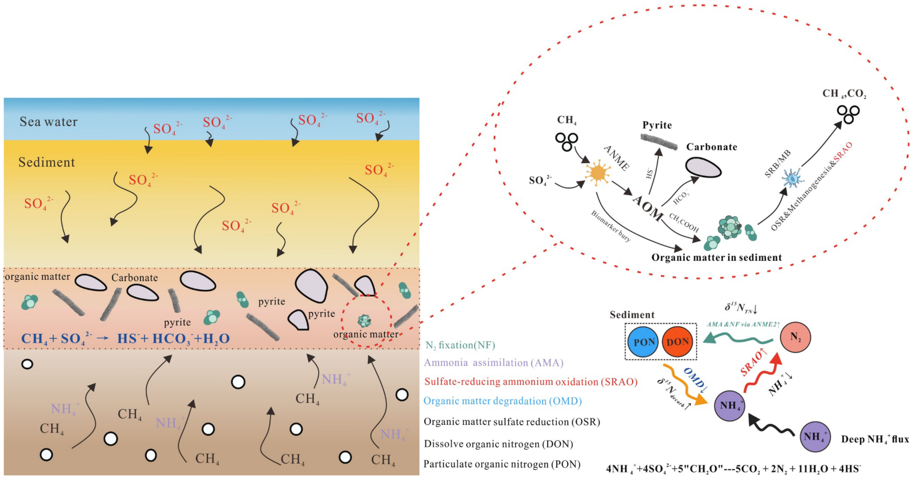

FIGURE 7
Schematic diagram for the nitrogen cycle in SMTZ. The nitrogen cycle in SMTZ is connected with nitrogen in sediment, NH_4^+ in porewater, and N_2 in air. As sulfate-reducing ammonium oxidation (SRAO) would consume NH_4^+, NH_4^+ concentration will decrease in SMTZ. Because ANME is most abundant in SMTZ, the rate of N_2-fixation (mediated by ANME) rises. The dissolve organic nitrogen isotope will decrease as a result of N_2-fixation (ANME mediate), and the $\delta^{15}N_{TN}$ of sediment display negative excursion in SMTZ.

from the southwestern Taiwan basin (South China Sea), the current SMTZ is delineated at 560–830 cmbsf.

(2) In the SMTZ, NH_4^+ concentration decreases due to sulfate-reducing ammonium oxidation. Below the current SMTZ, NH_4^+ concentration increases sharply due to the upward deep- NH_4^+ flux.

(3) The $\delta^{15}N_{decarb}$ variation in core GC10 is most likely due to organic matter degradation. The $\delta^{15}N_{TN}$ displays distinct negative excursions in the SMTZ, which are interpreted as ANME N_2-fixation modifying the soluble nitrogen isotope.

(4) The nitrogen isotope of sediment would experience a negative excursion in SMTZ is most likely due to the release of N_2 caused by sulfate-reducing ammonium oxidation and the regulation of N_2 fixing there by abundant ANME.

Data availability statement

The original contributions presented in the study are included in the article/Supplementary Material. Further inquiries can be directed to the corresponding authors.

Author contributions

XY: Wrote the manuscript. YZ: Analysis of N isotopes. XS: Supervision of the project. LX: Analysis and interpretation of data. TC: Analysis if N content. All authors contributed to the article and approved the submitted version.

Funding

This research was jointly funded by the Natural Science Foundation of China (41876038, 91128101, 41806049) and the Guangdong Special Fund for Economic Development (Marine Economy, GDME-2018D001).

Acknowledgments

We are grateful to Dr. Hongfeng Lu and the Guangzhou Marine Geological Survey for providing samples and valuable suggestions.

Conflict of interest

The authors declare that they have no known competing financial interests or personal relationships that could have appeared to influence the work reported in this paper.

Publisher's note

All claims expressed in this article are solely those of the authors and do not necessarily represent those of their

Supplementary material

The Supplementary Material for this article can be found online at: https://www.frontiersin.org/articles/10.3389/fmars.2022.1101599/full#supplementary-material

References

Akam, S. A., Coffin, R. B., Abdulla, H. A. N., and Lyons, T. W. (2020). Dissolved inorganic carbon pump in methane-charged shallow marine sediments: State of the art and new model perspectives. *Front. Mar. Sci.* 7. doi: 10.3389/fmars.2020.00206

Alshameri, A., He, H., Zhu, J., Xi, Y., Zhu, R., Ma, L., et al. (2018). Adsorption of ammonium by different natural clay minerals: Characterization, kinetics and adsorption isotherms. *Appl. Clay Sci.* 159, 83–93. doi: 10.1016/j.clay.2017.11.007

Antler, G., Turchyn, A. V., Herut, B., and Sivan, O. (2015). A unique isotopic fingerprint of sulfate-driven anaerobic oxidation of methane. *Geology* 43, 619–622. doi: 10.1130/G36688.1

Antler, G., Turchyn, A. V., Ono, S., Sivan, O., and Bosak, T. (2017). Combined 34S, 33S and 18O isotope fractionations record different intracellular steps of microbial sulfate reduction. *Geochim. Cosmochim. Acta* 203, 364–380. doi: 10.1016/j.gca.2017.01.015

Bergamin, L., Di Bella, L., Ferraro, L., Frezza, V., Pierfranceschi, G., and Romano, E. (2019). Benthic foraminifera in a coastal marine area of the eastern ligurian Sea (Italy): Response to environmental stress. *Ecol. Indic.* 96, 16–31. doi: 10.1016/j.ecolind.2018.08.050

Berger, W. H. (1970). Planktonic foraminifera: Selective solution and the lysocline. *Mar. Geol.* 8, 111–138. doi: 10.1016/0025-3227(70)90001-0

Berner, R. A. (1978). Sulfate reduction and the rate of deposition of marine sediments. *Earth Planet. Sci. Lett.* 39, 308. doi: 10.1016/0012-821x(78)90209-1

Berner, R. A. (1984). Sedimentary pyrite formation: An update. *Geochim. Cosmochim. Acta* 48, 605–615. doi: 10.1016/0016-7037(84)90089-9

Beulig, F., Røy, H., Glombitza, C., and Jørgensen, B. B. (2017). Control on rate and pathway of anaerobic organic carbon degradation in the seabed. *Proc. Natl. Acad. Sci. U. S. A.* 115, 367–372. doi: 10.1073/pnas.1715789115

Boetius, A., Ravenschlag, K., Schubert, C. J., Rickert, D., Widdel, F., Gleseke, A., et al. (2000). A marine microbial consortium apparently mediating anaerobic oxidation methane. *Nature* 407, 623–626. doi: 10.1038/35036572

Boetius, A., and Wenzhöfer, F. (2013). Seafloor oxygen consumption fuelled by methane from cold seeps. *Nat. Geosci.* 6, 725–734. doi: 10.1038/ngeo1926

Borowski, W. S., Paull, C. K., and Ussler, W. (1996). Marine pore-water sulfate profiles indicate *in situ* methane flux from underlying gas hydrate. *Geology* 24, 655–658. doi: 10.1130/0091-7613(1996)024<0655:MPWSPI>2.3.CO;2

Borowski, W. S., Rodriguez, N. M., Paull, C. K., and Ussler, W. (2013). Are 34S-enriched authigenic sulfide minerals a proxy for elevated methane flux and gas hydrates in the geologic record? *Mar. Pet. Geol.* 43, 381–395. doi: 10.1016/j.marpetgeo.2012.12.009

Chen, F., Hu, Y., Feng, D., Zhang, X., Cheng, S., Cao, J., et al. (2016). Evidence of intense methane seepages from molybdenum enrichments in gas hydrate-bearing sediments of the northern south China Sea. *Chem. Geol.* 443, 173–181. doi: 10.1016/j.chemgeo.2016.09.029

Chuang, P. C., Yang, T. F., Wallmann, K., Matsumoto, R., Hu, C. Y., Chen, H. W., et al. (2019). Carbon isotope exchange during anaerobic oxidation of methane (AOM) in sediments of the northeastern south China Sea. *Geochim. Cosmochim. Acta* 246, 138–155. doi: 10.1016/j.gca.2018.11.003

Clennell, M., Hovland, M., Booth, J., Hwnry, P., and Winters, W. (1999). Formation of natural gas hydrates in marine sediments: Gas hydrate growth and stability conditioned by host sediment properties. *J. Geophys. Res.* 104, 22,985–23,003. doi: 10.1111/j.1749-6632.2000.tb06842.x

Consolaro, C., Rasmussen, T. L., Panieri, G., Mienert, J., Bünz, S., and Sztybor, K. (2015). Carbon isotope (d13C) excursions suggest times of major methane release during the last 14 kyr in fram strait, the deep-water gateway to the Arctic. *Clim. Past* 11, 669–685. doi: 10.5194/cp-11-669-2015

Dekas, A. E., Poretsky, R. S., and Orphan, V. J. (2009). Deep-Sea archaea fix and share nitrogen in methane-consuming microbial consortia. *Science* 326, 422–426. doi: 10.1126/science.1178223

Dickens, G. R. (2003). Rethinking the global carbon cycle with a large, dynamic and microbially mediated gas hydrate capacitor. *Earth Planet. Sci. Lett.* 213, 169–183. doi: 10.1016/S0012-821X(03)00325-X

Dong, F., Peng, Y., Peckmann, J., Roberts, H., and Duofu, C. (2017). Stable carbon, nitrogen and sulfur isotopes in non-carbonate fractions of cold-seep carbonates. *Geophys. Res. Abstr.* 19, 3402. doi: 10.1130/G38233.1

Egger, M., Rasigraf, O., Sapart, C. J., Jilbert, T., Jetten, M. S. M., Röckmann, T., et al. (2015). Iron-mediated anaerobic oxidation of methane in brackish coastal sediments. *Environ. Sci. Technol.* 49, 277–283. doi: 10.1021/es503663z

Egger, M., Riedinger, N., Mogollón, J. M., and Jørgensen, B. B. (2018). Global diffusive fluxes of methane in marine sediments. *Nat. Geosci.* 11, 421–425. doi: 10.1038/s41561-018-0122-8

Ettwig, K. F., Butler, M. K., Le Paslier, D., Pelletier, E., Mangenot, S., Kuypers, M. M. M., et al. (2010). Nitrite-driven anaerobic methane oxidation by oxygenic bacteria. *Nature* 464, 543–548. doi: 10.1038/nature08883

Feng, D., Cheng, M., Kiel, S., Qiu, J. W., Yang, Q., Zhou, H., et al. (2015). Using bathymodiolus tissue stable carbon, nitrogen and sulfur isotopes to infer biogeochemical process at a cold seep in the south China Sea. *Deep. Res. Part I Oceanogr. Res. Pap.* 104, 52–59. doi: 10.1016/j.dsr.2015.06.011

Feng, J., Li, N., Liang, J., Shang, J., Yang, S., and Wang, H. (2021b). Using multi-proxy approach to constrain temporal variations of methane flux in methane-rich sediments of the southern south China Sea. *Mar. Pet. Geol.* 132, 105152. doi: 10.1016/j.marpetgeo.2021.105152

Feng, D., Peckmann, J., Li, N., Kiel, S., Qiu, J. W., Liang, Q., et al. (2018a). The stable isotope fingerprint of chemosymbiosis in the shell organic matrix of seep-dwelling bivalves. *Chem. Geol.* 479, 241–250. doi: 10.1016/j.chemgeo.2018.01.015

Feng, D., Pohlman, J. W., Peckmann, J., Sun, Y., Hu, Y., Roberts, H. H., et al. (2021a). Contribution of deep-sourced carbon from hydrocarbon seeps to sedimentary organic carbon: Evidence from radiocarbon and stable isotope geochemistry. *Chem. Geol.* 585, 120572. doi: 10.1016/j.chemgeo.2021.120572

Feng, D., Qiu, J. W., Hu, Y., Peckmann, J., Guan, H., Tong, H., et al. (2018b). Cold seep systems in the south China Sea: An overview. *J. Asian Earth Sci.* 168, 3–16. doi: 10.1016/j.jseaes.2018.09.021

Freudenthal, T., Wagner, T., Wenzhöfer, F., Zabel, M., and Wefer, G. (2001). Early diagenesis of organic matter from sediments of the Eastern subtropical Atlantic: Evidence from stable nitrogen and carbon isotopes. *Geochim. Cosmochim. Acta* 65, 1795–1808. doi: 10.1016/S0016-7037(01)00554-3

Froelich, P. N., Klinkhammer, G. P., Bender, M. L., Luedtke, N. A., Heath, G. R., Cullen, D., et al. (1979). Early oxidation of organic matter in pelagic sediments of the eastern equatorial Atlantic: suboxic diagenesis. *Geochim. Cosmochim. Acta* 43, 1075–1090. doi: 10.1016/0016-7037(79)90095-4

Hofmann, A., Bekker, A., Rouxel, O., Rumble, D., and Master, S. (2009). Multiple sulphur and iron isotope composition of detrital pyrite in archaean sedimentary rocks: A new tool for provenance analysis. *Earth Planet. Sci. Lett.* 286, 436–445. doi: 10.1016/j.epsl.2009.07.008

Holmes, M. E., Eichner, C., Struck, U., and Wefer, G. (1999). Reconstruction of surface ocean nitrate utilization using stable nitrogen isotopes in sinking particles and sediments. *Use Proxies Paleoceanogr.* 40, 447–468. doi: 10.1007/978-3-642-58646-0_18

Hong, W. L., Torres, M. E., Kim, J. H., Choi, J., and Bahk, J. J. (2013). Carbon cycling within the sulfate-methane-transition-zone in marine sediments from the ulleung basin. *Biogeochemistry* 115, 129–148. doi: 10.1007/s10533-012-9824-y

Hu, Y., Feng, D., Peng, Y., Peckmann, J., Kasten, S., Wang, X., et al. (2020). A prominent isotopic fingerprint of nitrogen uptake by anaerobic methanotrophic archaea. *Chem. Geol* 558, 119972. doi: 10.1016/j.chemgeo.2020.119972

Group I, Averyt, M, Solomon, S, et al (2007). IPCC, Climate Change : The Physical Science Basis. South African Geographical Journal Being A Record of the Proceedings of the South African Geographical Society. 92, 86–87. doi: 10.1080/03736245.2010.480842

Jørgensen, B. B., Beulig, F., Egger, M., Petro, C., Scholze, C., and Røy, H. (2019). Organoclastic sulfate reduction in the sulfate-methane transition of marine sediments. *Geochim. Cosmochim. Acta* 254, 231–245. doi: 10.1016/j.gca.2019.03.016

Jing, H., Wang, R., Jiang, Q., Zhang, Y., and Peng, X. (2020). Anaerobic methane oxidation coupled to denitrification is an important potential methane sink in deep-sea cold seeps. *Sci. Total Environ.* 748, 142459. doi: 10.1016/j.scitotenv.2020.142459

Karl, D., Letelier, R., Tupas, L., Dore, J., Christian, J., and Hebel, D. (1997). The role of nitrogen fication in biogeochemical cycling in the subtropical north pacific ocean. *Nature* 388, 533–537. doi: 10.1007/b138051

Kim, B., and Zhang, Y. G. (2022). Methane hydrate dissociation across the oligocene–Miocene boundary. *Nat. Geosci.* 15:203-211. doi: 10.1038/s41561-022-00895-5

Komada, T., Burdige, D. J., Li, H. L., Magen, C., Chanton, J. P., and Cada, A. K. (2016). Organic matter cycling across the sulfate-methane transition zone of the Santa Barbara basin, California borderland. *Geochim. Cosmochim. Acta* 176, 259–278. doi: 10.1016/j.gca.2015.12.022

Kuypers, M. M. M., Marchant, H. K., and Kartal, B. (2018). The microbial nitrogen-cycling network. *Nat. Rev. Microbiol.* 16, 263–276. doi: 10.1038/nrmicro.2018.9

Laima, M. J. C. (1992). Extraction and seasonal variation of NH4+ pools in different types of coastal marine sediments. *Mar. Ecol. Prog. Ser.* 82, 75–84. doi: 10.3354/meps082075

LaRowe, D. E., and Van Cappellen, P. (2011). Degradation of natural organic matter: A thermodynamic analysis. *Geochim. Cosmochim. Acta* 75, 2030–2042. doi: 10.1016/j.gca.2011.01.020

Lehmann, M. F., Bernasconi, S. M., Barbieri, A., and McKenzie, J. A. (2002). Preservation of organic matter and alteration of its carbon and nitrogen isotope composition during simulated and *in situ* early sedimentary diagenesis. *Geochim. Cosmochim. Acta* 66, 3573–3584. doi: 10.1016/S0016-7037(02)00968-7

Lehmann, M. F., Sigman, D. M., McCorkle, D. C., Granger, J., Hoffmann, S., Cane, G., et al. (2007). The distribution of nitrate 15N/14N in marine sediments and the impact of benthic nitrogen loss on the isotopic composition of oceanic nitrate. *Geochim. Cosmochim. Acta* 71, 5384–5404. doi: 10.1016/j.gca.2007.07.025

Levin, L. A., Baco, A. R., Bowden, D. A., Colaco, A., Cordes, E. E., Cunha, M. R., et al. (2016). Hydrothermal vents and methane seeps: Rethinking the sphere of influence. *Front. Mar. Sci.* 3. doi: 10.3389/fmars.2016.00072

Libes, S. M., and Deuser, W. G. (1988). The isotope geochemistry of particulate nitrogen in the Peru upwelling area and the gulf of Maine. *Deep Sea Res. Part A Oceanogr. Res. Pap* 35, 517–533. doi: 10.1016/0198-0149(88)90129-X

Li, N., Feng, D., Chen, L., Wang, H., and Chen, D. (2016). Using sediment geochemistry to infer temporal variation of methane flux at a cold seep in the south China Sea. *Mar. Pet. Geol.* 77, 835–845. doi: 10.1016/j.marpetgeo.2016.07.026

Lim, Y. C., Lin, S., Yang, T. F., Chen, Y. G., and Liu, C. S. (2011). Variations of methane induced pyrite formation in the accretionary wedge sediments offshore southwestern Taiwan. *Mar. Pet. Geol.* 28, 1829–1837. doi: 10.1016/j.marpetgeo.2011.04.004

Lin, Z., Sun, X., Lu, Y., Strauss, H., Xu, L., Chen, T., et al. (2018a). Iron isotope constraints on diagenetic iron cycling in the taixinan seepage area, south China Sea. *J. Asian Earth Sci.* 168, 112–124. doi: 10.1016/j.jseaes.2018.01.007

Lin, Z., Sun, X., Peckmann, J., Lu, Y., Xu, L., Strauss, H., et al. (2016). How sulfate-driven anaerobic oxidation of methane affects the sulfur isotopic composition of pyrite: A SIMS study from the south China Sea. *Chem. Geol.* 440, 26–41. doi: 10.1016/j.chemgeo.2016.07.007

Lin, Z., Sun, X., Strauss, H., Eroglu, S., Böttcher, M. E., Lu, Y., et al. (2021). Molybdenum isotope composition of seep carbonates – constraints on sediment biogeochemistry in seepage environments. *Geochim. Cosmochim. Acta* 307, 56–71. doi: 10.1016/j.gca.2021.05.038

Lin, Z., Sun, X., Strauss, H., Lu, Y., Böttcher, M. E., Teichert, B. M. A., et al. (2018b). Multiple sulfur isotopic evidence for the origin of elemental sulfur in an iron-dominated gas hydrate-bearing sedimentary environment. *Mar. Geol.* 403, 271–284. doi: 10.1016/j.margeo.2018.06.010

Lin, Z., Sun, X., Strauss, H., Lu, Y., Gong, J., Xu, L., et al. (2017). Multiple sulfur isotope constraints on sulfate-driven anaerobic oxidation of methane: Evidence from authigenic pyrite in seepage areas of the south China Sea. *Geochim. Cosmochim. Acta* 211, 153–173. doi: 10.1016/j.gca.2017.05.015

Liu, J., Pellerin, A., Antler, G., Kasten, S., Findlay, A. J., Dohrmann, I., et al. (2020). Early diagenesis of iron and sulfur in bornholm basin sediments : the role of near-surface pyrite formation. *Geochim. Cosmochim. Acta* 34, 45–60. doi: 10.1016/j.gca.2020.06.003

Li, N., Yang, X., Peckmann, J., Zhou, Y., Wang, H., Chen, D., et al. (2021). Persistent oxygen depletion of bottom waters caused by methane seepage: Evidence from the south China Sea. *Ore Geol. Rev.* 129:103949. doi: 10.1016/j.oregeorev.2020.103949

Li, N., Yang, X., Peng, J., Zhou, Q., and Chen, D. (2018). Paleo-cold seep activity in the southern south China Sea: Evidence from the geochemical and geophysical records of sediments. *J. Asian Earth Sci.* 168, 106–111. doi: 10.1016/j.jseaes.2017.10.022

Macko, S. A., and Estep, M. L. F. (1984). Microbial alteration of stable nitrogen and carbon isotopic compositions of organic matter. *Org. Geochem.* 6, 787–790. doi: 10.1016/0146-6380(84)90100-1

Martens-Habbena, W., and Qin, W. (2022). Archaeal nitrification without oxygen(The single-cell organism can self-produce oxygen for ammonia oxidation). *Science* 375, 7–9.

McDonnell, S. L., Max, M. D., Cherkis, N. Z., and Czarnecki, M. F. (2000). Tectono-sedimentary controls on the likelihood of gas hydrate occurrence near Taiwan. *Mar. Pet. Geol.* 17, 929–936. doi: 10.1016/S0264-8172(00)00023-4

Meister, P., Liu, B., Khalili, A., Böttcher, M. E., and Jørgensen, B. B. (2019). Factors controlling the carbon isotope composition of dissolved inorganic carbon and methane in marine porewater: An evaluation by reaction-transport modelling. *J. Mar. Syst.* 200, 103227. doi: 10.1016/j.jmarsys.2019.103227

Miao, X., Feng, X., Li, J., and Lin, L. (2021). Tracing the paleo-methane seepage activity over the past 20,000 years in the sediments of qiongdongnan basin, northwestern south China Sea. *Chem. Geol.* 559, 119956. doi: 10.1016/j.chemgeo.2020.119956

Middelburg, J. J. (1989). A simple rate model for organic matter decomposition in marine sediments. *Geochim. Cosmochim. Acta* 53, 1577–1581. doi: 10.1016/0016-7037(89)90239-1

Nakatsuka, T., Handa, N., Harada, N., Sugimoto, T., and Imaizumi, S. (1997). Origin and decomposition of sinking particulate organic matter in the deep water column inferred from the vertical distributions of its δ15N, δ13 and δ14. *Deep Sea Res. Part I Oceanogr. Res. Pap.* 44, 1957–1979. doi: 10.1016/s0967-0637(97)00051-4

Panieri, G., Lepland, A., Whitehouse, M. J., Wirth, R., Raanes, M. P., James, R. H., et al. (2017). Diagenetic mg-calcite overgrowths on foraminiferal tests in the vicinity of methane seeps. *Earth Planet. Sci. Lett.* 458, 203–212. doi: 10.1016/j.epsl.2016.10.024

Peckmann, J., Birgel, D., and Kiel, S. (2009). Molecular fossils reveal fluid composition and flow intensity at a Cretaceous seep. *Geology* 37, 847–850. doi: 10.1130/G25658A.1

Peckmann, J., and Thiel, V. (2004). Carbon cycling at ancient methane-seeps. *Chem. Geol.* 205, 443–467. doi: 10.1016/j.chemgeo.2003.12.025

Peckmann, J., Thiel, V., Reitner, J., Taviani, M., Aharon, P., and Michaelis, W. (2004). A microbial mat of a large sulfur bacterium preserved in a miocene methane-seep limestone. *Geomicrobiol. J.* 21, 247–255. doi: 10.1080/01490450490438757

Peckmann, J., Walliser, O. H., Riegel, W., and Reitner, J. (1999). Signatures of hydrocarbon venting in a middle Devonian carbonate mound (Hollard mound) at the hamar laghdad (Antiatlas, Morocco). *Facies* 40, 281–296. doi: 10.1007/BF02537477

Quan, T. M., Adigwe, E. N., Riedinger, N., and Puckette, J. (2013a). Evaluating nitrogen isotopes as proxies for depositional environmental conditions in shales: Comparing caney and woodford shales in the arkoma basin, Oklahoma. *Chem. Geol.* 360–361, 231–240. doi: 10.1016/j.chemgeo.2013.10.017

Quan, T. M., Wright, J. D., and Falkowski, P. G. (2013b). Co-Variation of nitrogen isotopes and redox states through glacial-interglacial cycles in the black Sea. *Geochim. Cosmochim. Acta* 112, 305–320. doi: 10.1016/j.gca.2013.02.029

Reeburgh, W. S. (2007). *Oceanic methane biogeochemistry* (Irvine, California: Department of Earth System Science, University of California). doi: 10.1021/cr050362v

Regnier, P., Dale, A. W., Arndt, S., LaRowe, D. E., Mogollón, J., and Van Cappellen, P. (2011). Quantitative analysis of anaerobic oxidation of methane (AOM) in marine sediments: A modeling perspective. *Earth-Science Rev.* 106, 105–130. doi: 10.1016/j.earscirev.2011.01.002

Robinson, R. S., Kienast, M., Luiza Albuquerque, A., Altabet, M., Contreras, S., De Pol Holz, R., et al. (2012). A review of nitrogen isotopic alteration in marine sediments. *Paleoceanography* 27:4203. doi: 10.1029/2012PA002321

Ruppel, C. D. (2017). The interaction of climate change and methane hydrates. *Rev. Geophys.* 55, 126–168. doi: 10.1002/2016RG000534

Schrum, H. N., Spivack, A. J., Kastner, M., and D'Hondt, S. (2015). Sulfate-reducing ammonium oxidation: A thermodynamically feasible metabolic pathway in subseafloor sediment. *Geology* 37, 939–942. doi: 10.1130/G30238A.1

Suess, E. (2010). Handbook of hydrocarbon and lipid microbiology. *Handb. Hydrocarb. Lipid Microbiol.* Springer-Verlag Berlin Heidelberg doi: 10.1007/978-3-540-77587-4

Suess, E. (2014). Marine cold seeps and their manifestations: geological control, biogeochemical criteria and environmental conditions. *Int. J. Earth Sci.* 103, 1889–1916. doi: 10.1007/s00531-014-1010-0

Suess, E. (2020). Hydrocarbons, oils and lipids: Diversity, origin, chemistry and fate. *Hydrocarb. Oils Lipids Divers. Orig. Chem. Fate.* Springer International Publishing AG doi: 10.1007/978-3-319-90569-3

Tesdal, J. E., Galbraith, E. D., and Kienast, M. (2013). Nitrogen isotopes in bulk marine sediment: Linking seafloor observations with subseafloor records. *Biogeosciences* 10, 101–118. doi: 10.5194/bg-10-101-2013

Thullner, M., Regnier, P., and Van Cappellen, P. (2007). Modeling microbially induced carbon degradation in redox-stratified subsurface environments: Concepts and open questions. *Geomicrobiol. J.* 24, 139–155. doi: 10.1080/01490450701459275

Tong, H., Feng, D., Cheng, H., Yang, S., Wang, H., Min, A. G., et al. (2013). Authigenic carbonates from seeps on the northern continental slope of the south China Sea: New insights into fluid sources and geochronology. *Mar. Pet. Geol.* 43, 260–271. doi: 10.1016/j.marpetgeo.2013.01.011

van Dongen, B. E., Roberts, A. P., Schouten, S., Jiang, W. T., Florindo, F., and Pancost, R. D. (2007). Formation of iron sulfide nodules during anaerobic oxidation of methane. *Geochim. Cosmochim. Acta* 71, 5155–5167. doi: 10.1016/j.gca.2007.08.019

Wang, X., Li, N., Feng, D., Hu, Y., Bayon, G., Liang, Q., et al. (2018b). Using chemical compositions of sediments to constrain methane seepage dynamics: A case study from haima cold seeps of the south China Sea. *J. Asian Earth Sci.* 168, 137–144. doi: 10.1016/j.jseaes.2018.11.011

Wang, T., Ravelo, A. C., Ren, H., Dang, H., Jin, H., Liu, J., et al. (2018a). Nitrogen isotope variations in the northern south China Sea since marine isotopic stage 3: Reconstructed from foraminifera-bound and bulk sedimentary nitrogen. *Paleoceanogr. Paleoclimatology* 33, 594–605. doi: 10.1029/2018PA003344

Wehrmann, L. M., Risgaard-Petersen, N., Schrum, H. N., Walsh, E. A., Huh, Y., Ikehara, M., et al. (2011). Coupled organic and inorganic carbon cycling in the deep subseafloor sediment of the northeastern Bering Sea slope (IODP exp. 323). *Chem. Geol.* 284, 251–261. doi: 10.1016/j.chemgeo.2011.03.002

Wu, S., Wang, X., Wong, H. K., and Zhang, G. (2007). Low-amplitude BSRs and gas hydrate concentration on the northern margin of the south China Sea. *Mar. Geophys. Res.* 28, 127–138. doi: 10.1007/s11001-007-9020-y

Wu, D., Wu, N., Fu, S., Lian, J., and Hongxiang, G. (2010). Geochemicalcharacteristic of shallow sediments in the gas hydrate distribution area of dongsha, the northern south China Sea. *Mar. Geol. Quat. Geol.* 30, 41–51. doi: 10.3788/HPLPB20102209.2186

Xie, R., Wu, D., Liu, J., Sun, T., Liu, L., and Wu, N. (2019). Evolution of gas hydrates inventory and anaerobic oxidation of methane (AOM) after 40ka in the taixinan basin, south China Sea. *Deep Sea Res. Part I Oceanogr. Res. Pap*, 152:103084. doi: 10.1016/j.dsr.2019.103084

Xiong, P., Lu, H., Xie, X., Zhang, G., Fu, S., Jiang, L., et al. (2020). Geochemical responses and implications for gas hydrate accumulation: Case study from site SHC in shenhu area within northern south China Sea. *Mar. Pet. Geol.* 111, 650–661. doi: 10.1016/j.marpetgeo.2019.06.032

Xu, F., Hu, B., Zhao, J., Liu, X., Xu, K., Xiong, Z., et al. (2021). Provenance and weathering of sediments in the deep basin of the northern south China Sea during the last 38 kyr. *Mar. Geol.* 440, 106602. doi: 10.1016/j.margeo.2021.106602

Yang, T., Jiang, S. Y., Ge, L., Yang, J. H., Wu, N. Y., Zhang, G. X., et al. (2010). Geochemical characteristics of pore water in shallow sediments from shenhu area of south China Sea and their significance for gas hydrate occurrence. *Chin. Sci. Bull.* 55, 752–760. doi: 10.1007/s11434-009-0312-2

Yang, X., Sun, X., Li, D., Lin, Z., Lu, Y., Liang, Y., et al. (2020). Elemental and isotopic response of different carbon components to anaerobic oxidation of methane: A case study of marine sediments in the shenhu region, northern south China Sea. *J. Asian Earth Sci.* 206, 104577. doi: 10.1016/j.jseaes.2020.104577

Zhang, X., Gong, J., Sun, Z., Liao, J., Zhai, B., Wang, L., et al. (2021). Pore-water geochemistry in methane-seep sediments of the makran accretionary wedge off Pakistan: Possible link to subsurface methane hydrate. *Acta Oceanol. Sin.* 40, 23–32. doi: 10.1007/s13131-021-1899-7

Zhang, G., Liang, J., Lu, J., Yang, S., Zhang, M., Holland, M., et al. (2015). Geological features, controlling factors and potential prospects of the gas hydrate occurrence in the east part of the pearl river mouth basin, south China Sea. *Mar. Pet. Geol.* 67, 356–367. doi: 10.1016/j.marpetgeo.2015.05.021

Zhang, M., Lu, H., Guan, H., Liu, L., Wu, D., and Wu, N. (2018). Methane seepage intensities traced by sulfur isotopes of pyrite and gypsum in sediment from the shenhu area, south China Sea. *Acta Oceanol. Sin.* 37, 20–27. doi: 10.1007/s13131-018-1241-1

Zhang, Y., Luo, M., Hu, Y., Wang, H., and Chen, D. (2019). An areal assessment of subseafloor carbon cycling in cold seeps and hydrate-bearing areas in the northern south China Sea. *Geofluids* 2019:2573937. doi: 10.1155/2019/2573937

Zhang, T., Xiao, X., Chen, S., Zhao, J., Chen, Z., Feng, J., et al. (2020). Active anaerobic archaeal methanotrophs in recently emerged cold seeps of northern south China Sea. *Front. Microbiol.* 11:612135. doi: 10.3389/fmicb.2020.612135

Zhuang, C., Chen, F., Cheng, S. H., Lu, H. F., Wu, C., Cao, J., et al. (2016). Light carbon isotope events of foraminifera attributed to methane release from gas hydrates on the continental slope, northeastern south China Sea. *Sci. China Earth Sci.* 59, 1981–1995. doi: 10.1007/s11430-016-5323-7

Frontiers in Marine Science

TYPE Original Research
PUBLISHED 03 February 2023
DOI 10.3389/fmars.2023.1091549

OPEN ACCESS

EDITED BY
Dong Feng,
Shanghai Ocean University, China

REVIEWED BY
Junxi Feng,
Guangzhou Marine Geological Survey,
China
Yuncheng Cao,
Shanghai Ocean University, China

*CORRESPONDENCE
Wanjun Lu
✉ wjlu@cug.edu.cn
Yong Chen
✉ yongchenzy@upc.edu.cn

SPECIALTY SECTION
This article was submitted to
Marine Biogeochemistry,
a section of the journal
Frontiers in Marine Science

RECEIVED 07 November 2022
ACCEPTED 02 January 2023
PUBLISHED 03 February 2023

CITATION
Li H, Lu X, Wang L, Wang W, Li T, Lu W and Chen Y (2023) Dissolution migration of gas, a mechanism to enrich ethane near the BSR and increase upwardly C_1/C_2 ratios in the hydrate-occurring zones: Insight from pore-scale experimental observation. *Front. Mar. Sci.* 10:1091549. doi: 10.3389/fmars.2023.1091549

Dissolution migration of gas, a mechanism to enrich ethane near the BSR and increase upwardly C_1/C_2 ratios in the hydrate-occurring zones: Insight from pore-scale experimental observation

Hui Li[1], Xuekang Lu[1], Lin Wang[2], Wenjing Wang[1], Tianhua Li[1], Wanjun Lu[1]* and Yong Chen[3]*

[1]College of Marine Science and Technology, China University of Geosciences, Wuhan, China, [2]School of Marine Engineering Equipment, Zhejiang Ocean University, Zhoushan, China, [3]School of Geosciences, China University of Petroleum (East China), Qingdao, Shandong, China

Most experiments show that gas hydrates are often enriched in C_{2+} gases relative to the feeding gas source because of fractionation during hydrate crystallization directly from free gases and dissolved gases. However, sediments below and near the base of the gas hydrate stability zone (BGHSZ) in many ocean drilling program (ODP)/International Ocean Discovery Program (IODP) sites are relatively enriched in C_{2+} hydrocarbon gases, compared with the hydrate-occurring zone above. It is still unclear what kind of process causes the abrupt decreases in C_1/C_{2+} ratios with the depth in headspace gas in sediments around seismic bottom-simulating reflector (BSR) and increasing upward C_1/C_2 ratios in the hydrate-occurring zone. To test the "dissolution/migration mechanism" and its links to the enrichment of ethane near the BSR and increasing upward C_1/C_2 ratios in the hydrate-occurring zone, we performed a series of pore-scale experimental observations, simulating the gas dissolution–migration–hydration processes, and investigated the effects of the composition of feeding gases and temperatures on the composition of the hydrate grown under the dissolution–migration mechanism. Hydrates are grown from aqueous fluids supplied by the migration of gases dissolved from the capillary-trapped free gas in a capillary high-pressure optical cell, with different supplying gases (90 mol% CH_4 + 10 mol% C_2H_6, 80 mol % CH_4 + 20 mol% C_2H_6) and a geothermal gradient (temperature from 278.15 to 293.15 K). The gas hydrate structure and composition were determined by quantitative Raman spectroscopy. Our study indicated that (1) under the dissolution–migration–hydration processes, the mole fraction of C_2H_6 in hydrates is depleted compared with gas sources, which confirms that the dissolution–migration of gases is a mechanism to enrich ethane near the BSR; (2) the proportion of C_2H_6 in structure I (sI) or structure II (sII) hydrates decreases with decreasing temperature, and decreasing temperature enlarges the difference of diffusion coefficient between methane and ethane and enhances the gas fractionation during migration, which could cause the increase upwardly C_1/C_2 ratios in the hydrate-occurring zone. A simplified geological model was proposed to explain the variability of hydrate composition with depth in the hydrate-occurring zone and the fractionation of gases near the BSR.

KEYWORDS

gas hydrate composition, gas source, methane and ethane, gas fractionation, Raman spectroscopy

1 Introduction

Natural gas hydrates are ice-like crystallites, formed and preserved in conditions of high pressure and low temperature, which exist extensively in marine sediments at deep-sea continental margins (Hester et al., 2007; Kida et al., 2009; Klapp et al., 2010a), in permafrost areas (Lu et al., 2011; Liu et al., 2016), and in deep lakes (Khlystov et al., 2013).

In natural geological environments, gas hydrates can form three different structures [structure I (sI) or structure II (sII), and H], which contain gas hydrocarbon molecules such as methane (C_1), ethane (C_2), propane (C_3), etc. (Sloan, 2003; Sloan, 2008). Methane is the dominant hydrocarbon gas in these gas hydrates (Hester et al., 2007; Kida et al., 2009; Liu et al., 2015) and ethane is the second most important component (Klapp et al., 2010a), accounting for up to 17% of hydrate composition (Liang et al., 2019).

Hydrates are often enriched in C_{2+} gases relative to void and the pressure core sampler (PCS) gases (Milkov et al., 2004). However, sediments near the base of the gas hydrate stability zone are relatively enriched in C_{2+} hydrocarbon gases (Milkov et al., 2004; Paganoni et al., 2016), leading to an abrupt decrease in C_1/C_{2+} ratios in headspace gas in sediments around the bottom-simulating reflector (BSR), which has been termed the "geochemical BSR" (Whiticar et al., 1995) (Figure 1). In the hydrate-occurring zone, there is a general trend for the ratio of methane to ethane and heavier hydrocarbons (C_1/C_{2+}) to reduce with depth (Milkov et al., 2004; Plaza-Faverola et al., 2017; Wei et al., 2021). As the geochemical processes that occur in the sediments around the depth of the BSR are poorly understood, it is unclear what kind of process could cause ethane enrichment near the BSR and increasing upward C_1/C_2 ratios in the hydrate-occurring zone.

Most experiments show that gas hydrates are often enriched in C_{2+} gases relative to the feeding gas source. Subramanian (Subramanian et al., 2000) studied the influence of feed gas composition, consisting of different mixtures of CH_4 and C_2H_6, on hydrate structure and composition at three-phase equilibrium [aqueous solution of water (L_W)– hydrate (H)–pure vapor phase (V)] conditions and 274.2 K using Raman and nuclear magnetic resonance (NMR) spectroscopic techniques in the laboratory. They found evidence of a change in hydrate structure from sI to sII in between 72.2 and 75 mol% methane in vapor, which was associated with a 20% change in hydrate composition. In addition, they also showed that the ethane component in mixed hydrates was also higher than in original feed gases. Another experiment conducted by Uchida (Uchida et al., 2002) indicated that ethane was enriched in both sI and sII hydrates formed at 150 K and 1–3 MPa. Seo (Seo et al., 2009) found that heavy hydrocarbon molecules of natural gas preferentially occupied large cages of sII hydrates formed by finite methane–ethane–propane–iso-butane gases (CH_4–C_2H_6–C_3H_8–i-C_4H_{10}), resulting in the enrichment of heavy hydrocarbons in the hydrate phase.

Until now, there has been no experimental or numerical simulation work to explain why there are often abrupt decreases in C_1/C_{2+} ratios with depth in headspace gas in sediments around the BSR. Upward migration of gases from the base of the gas hydrate stability zone (BGHSZ) (as well as the corresponding BSR) through the sediment is linked to the concentration of gases in the hydrate-occurring zone. Brown (Brown et al., 1996) proposed a "dissolution–diffusion mechanism": below the BGHSZ, the bubbles trapped in sediments by capillary forces in the free gas zone must continually dissolve, and methane and ethane in solution are transported upward and incorporated into the hydrate layer. Such "dissolution–migration–hydration" processes could happen in most marine environments, especially at sites with a low flux of upward migration near the BGHSZ.

To test the "dissolution–migration–hydration mechanism" and the links to the enrichment of ethane near the BSR and increasing upward C_1/C_2 ratios in the hydrate-occurring zone, we performed a

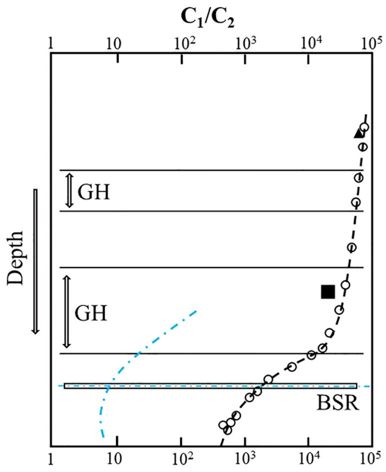

FIGURE 1
Gas fractionation near and above the bottom-simulating reflector (BSR). C_1/C_2 ratio in gas voids (open circles) and PCS gases (black triangles) and C_1/C_2 ratio in hydrates at sites 1,247, ODP Leg 204 (Milkov et al., 2004); blue indicates C_1/C_2 ratio in gas voids at NW Borneo (Paganoni et al., 2016).

series of pore-scale experimental observations, simulating the dissolution–diffusion of gas molecules from a free gas zone and migration in aqueous solution for the growth of hydrate, and studying the fractionation of methane and ethane during the process. The structure and composition of mixed gas hydrates were investigated by *in situ* Raman spectroscopy. The effects of feed gases and temperatures on the composition and structure of the corresponding hydrates were investigated.

2 Experimental section

2.1 Experimental apparatus and materials

A capillary high-pressure optical cell (HPOC) (Lu et al., 2007; Caumon et al., 2014; Ou et al., 2016) in combination with a Linkam CAP500 heating–cooling stage was used to simulate and observe the hydrate growing processes, supplied by gas migration in aqueous solution from the dissolution of free gas. The HPOC was constructed from a fused-silica capillary tube with an outer diameter (OD) of 375 µm, an inner diameter (ID) of 50 µm, and a length of around 25 cm. To prepare the sample, we loaded a section of ultrapure water (about 10 mm in length) into the sealed end of the capillary cell, then connected the other end to the pipeline with the feed gases and pressure pump. The capillary cell was inserted into the sample chamber of the heating–cooling stage for temperature control and Raman spectroscopic measurements, where the temperature could be maintained with an accuracy of ± 0.1 K from 273 to 373 K. The pressure in the cell could be adjusted by the pressure generator and measured by a full-scale pressure gauge (Setra 206 digital pressure transducer with a Datum 2000 manometer, accurate to ± 0.14%). The experimental apparatus has been reported in previous studies. (Lu et al., 2008; Guo et al., 2013; Lu et al., 2013).

The water used was ultra-purified in the laboratory with a resistivity of 18.24 MΩ·cm. Three different mixed CH_4 and C_2H_6 gas cylinders, obtained from Wuhan Iron & Steel Group Gas Co. Ltd, were used and the compositions (5.08 mol% C_2H_6 + 94.92 mol% CH_4, 10.18 mol% C_2H_6 + 89.82 mol% CH_4, and 20.12 mol % C_2H_6 + 79.88 mol% CH_4) were analyzed by gas chromatography before the experiment.

2.2 Experimental procedures and methods

2.2.1 Growing hydrate from aqueous fluids supplied by the migration of gases dissolved from the capillary-trapped free gas

To simulate the dissolution–diffusion of gas molecules from the free gas zone, and migration in an aqueous solution for the growth of hydrate, we used the following procedures. First, the capillary cell (with a section of pure water loaded in its closed end) and pipeline were evacuated. Second, mixed methane and ethane gas were loaded into the pressure line and cell, and then pressurized to 30 MPa by a pressure generator; this pressure was maintained for several days to ensure that the mixed gas diffused into the ultrapure water in the capillary cell. Hydrates were nucleated in the solution near the closed end of the optical cell by placing about 5 mm of the cell in the heating–cooling stage and adjusting the temperature to 243 K for a few minutes. The sample areas of the capillary cell were then warmed to the target temperature (above 273.15 K to avoid possible ice) to ensure the formation of a single hydrate crystal at 30 MPa. During the growth of the hydrate, guest molecules (methane and ethane) were supplied through diffusion in the aqueous phase from the vapor–aqueous solution interface, and the hydrate was grown for 2–5 days (i.e., a minimum of 48 h and maximum of 126 h) to achieve a long column of hydrate for Raman spectroscopic observation (Figure 2).

To investigate the effects of temperature and the feed gas composition on the composition and structure of mixed gas hydrates grown from the solution, experiments were performed at four temperatures, 278.15, 283.15, 288.15, and 293.15 K, at 30 MPa, with two different mixtures of methane and ethane at each temperature and pressure condition.

2.2.2 Determining the hydrate composition *via* the hydrate-dissociated gas columns

The composition of hydrates cannot be determined directly by Raman spectroscopy. In order to acquire the composition of hydrates, the hydrates were heated to 298.15 K at 30 MPa (with a heating rate of 50°C/min) and rapidly dissociated into free gas and water columns (Figure 3). The composition of the hydrate-dissociated gas columns was then measured by Raman spectroscopy in a very short space of time. The average composition of the hydrate-dissociated gas was considered to be the same as the composition of the original hydrate, as the standard deviation between the measured values of composition was small.

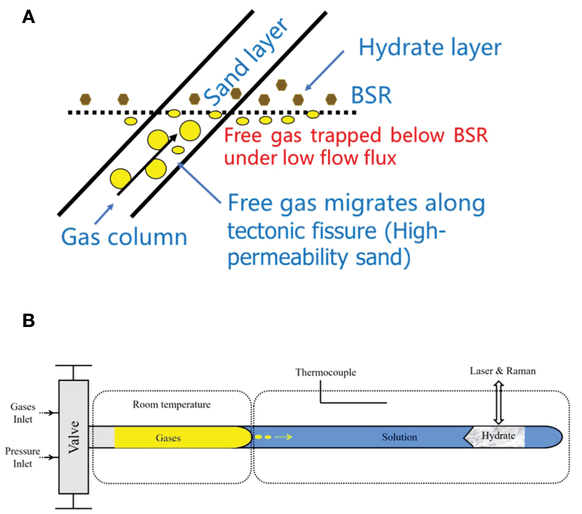

FIGURE 2
The dissolution–migration–hydration process near the bottom-simulating reflector (BSR). **(A)** In a submarine environment, the growth of the hydrate was supplied by guest molecules (i.e., methane and ethane) through diffusion in the aqueous phase from the vapor–aqueous solution interface near the base of the gas hydrate stability zone (BGHSZ). **(B)** Hydrates were grown from aqueous fluids supplied by the gases dissolved from the capillary-trapped free gas in a capillary high-pressure optical cell. Yellow arrows indicate the direction of gas migration. The shadow corner line is the boundary between hydrate and water solution, indicating growth direction.

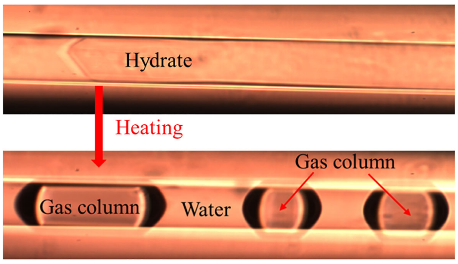

FIGURE 3
Gas column decomposed from hydrate after heating for quantitative Raman spectroscopic study.

2.2.3 Quantitative Raman measurements of mixed methane and ethane gas

Raman scattering cross-sections are related to the specific Raman-active species and may be affected by molecular interactions. Instrumental efficiency varies with the instrumental settings, so Raman spectroscopic measurements and the Raman quantification factor of pure mixed methane and ethane gas with the same instrumental settings was necessary. Raman intensity is positively correlated with the number of molecules, as described in previous works (Lu et al., 2006; Lu et al., 2008). For Raman-active species *a* and *b* in the gas phase, their relative concentrations, X_r (e.g., mole or mol%), are related to their Raman peak area A_S and Raman peak height H_S. The same method was used to estimate hydrate compositions for the CH_4 and CO_2 system (Sum et al., 1997). In this study, the relationship between the peak heights ratio (*HR*) of methane and ethane and mole fraction ratios of the gases at 30 MPa, at temperatures from 278.15 to 298.15 K, was established by the formula:

$$\frac{H_a}{H_b} = (\frac{X_a}{X_b})(\frac{\sigma_a}{\sigma_b})(\frac{\eta_a}{\eta_b}) = (\frac{X_a}{X_b})(\frac{F_a}{F_b}) \qquad (1)$$

$$\frac{X_b}{X_a} = (\frac{H_b}{H_a})(\frac{F_a}{F_b}) \qquad (2)$$

$$X_r = K \cdot (HR) \qquad (3)$$

TABLE 1 Overall nomenclatures in this section.

Nomenclatures	
a	Methane
b	Ethane
H	Raman peak height
X	Mole fraction of component in the gas phase
σ	Raman scattering cross-section
η	Instrumental efficiency
F	Raman quantification factor
X_r	The relative concentrations in the gas phase
K	Coefficient of relative concentrations and Raman peak height ratio
HR	Raman peak height ratio

The specific nomenclatures are shown in Table 1.

2.2.4 Raman spectra collection and calculating the peak area and heights

Raman spectra of hydrate and the dissociation gas were acquired by a JY/Horiba LabRam HR Raman system, using a 532.06 nm [frequency-doubled neodymium-doped yttrium aluminum garnet (Nd : YAG)] laser excitation with an output laser power of approximately 45 mW, at a 20× long-work-distance Olympus objective with a 0.5 numerical aperture, and an 1,800 groove/mm grating with a spectral resolution of about 1 cm^{-1}. Raman shifts were calibrated with the spectrum of the neon emission during the measurement, ranging from 2,720 to 3,080 cm^{-1}, which covers the C–H stretching vibration of methane and Fermi resonance doublet bands of ethane in hydrate s I and s II cages (Klapp et al., 2010a; Klapp et al., 2010b). Peak area and peak heights of CH_4 and C_2H_6 for hydrate were calculated using a Gaussian and Lorentzian function by NGSLabSpec software (Lu et al., 2013; Ou et al., 2015).

3 Results

3.1 Relationship between peak height ratio (*HR*) of methane and ethane and mole fraction ratios of the gases

Figure 4 shows the relationship between the peak height ratio (HR) of methane and ethane and mole fraction ratios of the gases, and the calibration curve for the CH_4 and C_2H_6 system at 30 MPa and different temperatures that was then constructed. All data used in this figure were obtained at 273.15, 278.15, 283.15, 288.15, 293.15, and 298.15 K. The peak HRs of CH_4 and C_2H_6 were well fitted by a linear function of vapor mole fraction ratios ($X(C_2H_6)/X(CH_4)$), with a correlation coefficient over 0.9978, which showed good agreement with the results obtained by Subramanian (Subramanian et al., 2000). The calibration curve was further used to determine the composition of feed gas and the hydrate decomposition gases.

3.2 Raman spectra characteristics and distinguishing sI and sII hydrate

For each hydrate crystal, at least three locations were selected for Raman spectra measurements. Figure 5 shows the corrected representative Raman spectra of the mixed gas hydrates in the regions between 2,800 cm^{-1} and 3,000 cm^{-1} covering the C–H stretching vibrations in hydrates. The Raman spectra are reliable for the identification of hydrate structures (Subramanian et al., 2000), and the measured and assigned Raman band positions of C–H symmetric stretching are listed in Table 2.

Logically, all the Raman characteristic signatures of C–H symmetric stretching for hydrates can be used as the judgment of hydrate structure, but the difference in the Raman shifts characteristics of CH_4 in sI and sII hydrates is very small, with only one difference of wavenumber. Therefore, the Raman stretching

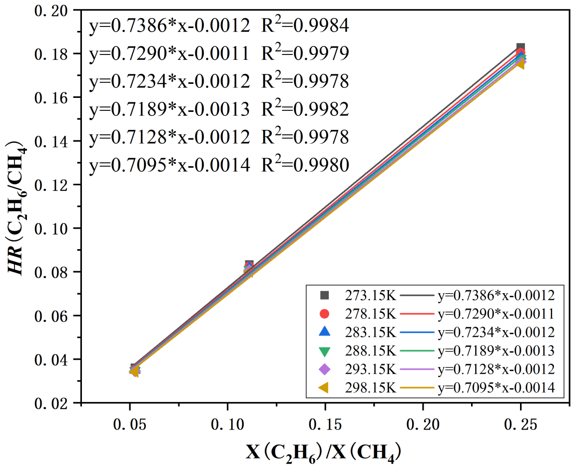

FIGURE 4
Calibration curve for the CH_4 and C_2H_6 system based on vapor mixtures at 30 MPa. The ordinate is the Raman peak height ratios. The abscissa is the mole fraction ratios of CH_4 and C_2H_6 gas. The linear functions' corresponding temperatures are indicated.

vibration band frequencies of C_2H_6 molecules in hydrates can be a useful index for determining the hydrate structures, with four differences of wavenumber (Subramanian et al., 2000). The ratio of the number of large cages (LC) to the number of small cages (SC) in sI and sII hydrates is 3:1 and 1:2, respectively. If all the cages are occupied, the Raman peaks area intensity ratio (PAR) of CH_4 in the LC to SC (I_{MLC}/I_{MSC}) should be 3 and 0.5 for sI and sII hydrates, respectively (Wei et al., 2021). Therefore, the above two Raman spectra characteristics can mutually support the hydrate structures (Klapp et al., 2010b).

Between 2,800 cm^{-1} and 3,000 cm^{-1}, two patterns of Raman spectra can be distinguished. Figure 5A shows the first pattern of Raman spectra, that for hydrate samples A1, A2, A3, A4, and B2. There are two distinct strong peaks for CH_4 and a weak peak (ν_2) for C_2H_6 molecules (at about 2,946 cm^{-1}). The Raman spectra signature (ν_1), located at 2,891 cm^{-1}, was very feeble and could be fitted only with the use of software. Figure 5B shows the second pattern of Raman spectra, that for hydrate samples B1, B3, and B4. In this case, there are two distinct strong peaks for CH_4 molecules and two weak peaks (ν_1 and ν_2) for C_2H_6 molecules (at 2,886 cm^{-1} and 2,942 cm^{-1}, respectively), with lower wavenumbers. Note that the Raman peaks for C_2H_6 molecules located at 2,891 cm^{-1} and 2,946 cm^{-1} are assigned to the C_2H_6 engaged in the large cavities of the sI hydrate, whereas the Raman peaks for the C_2H_6 molecules that occur 2,887 cm^{-1} and 2,942 cm^{-1} were reported by previous researchers to be an indication of C_2H_6 engaged in the large cavities of the sII hydrate (Murshed and Kuhs, 2009; Klapp et al., 2010b; Sum et al., 1997). Therefore, we considered hydrate samples A1, A2, A3, A4, and B2, exhibiting the first pattern of Raman spectra, to be sI hydrates, and hydrate samples B1, B3, and B4, exhibiting the second pattern of Raman spectra, to be sII hydrates. The weak signature of C–H shifts of ethane for sI hydrates might be due to the relatively low cage occupancies of ethane in large cages, which could lead to the deviation of the Raman spectra signature (ν_1) in the fitting procedure. The shapes of the Raman spectra obtained for sII hydrates in this work are consistent with that of the methane and ethane hydrate formed in Monterey Bay (1,024 m, 278 K) (Hester et al., 2006).

In addition, Raman spectra of the ν_1 and ν_2 C–H stretch of C_2H_6 for mixed gas hydrates and Raman PARs of CH_4 in the LC to SC (I_{MLC}/I_{MSC}) are demonstrated in Figure 6, which corresponds to the Raman spectra of the first and second patterns in Figures 5A, B. The Raman peak positions of ethane in C–H regions for sII hydrates were lower than those of ethane for sI hydrates (Table 2). The Raman PARs of CH_4 in the LC to SC (I_{MLC}/I_{MSC}) for hydrate samples A1–A4 and B2 were 3.41, 3.26, 3.11, 3.02, and 3.13, respectively, and I_{MLC}/I_{MSC} for hydrate samples B1, B3, B4, and C1 was 0.41, 0.24, 0.24, and 0.17, respectively. Hence, we concluded that the hydrate samples A1–A4 and B2 were sI hydrates, and hydrate samples B1, B3, B4, and C1 were sII hydrates. The Raman PAR of CH_4 in the LC to SC for sI hydrates (red point in Figure 6) was greater than 3.0, which might be attributed to relatively high occupancies of methane in large cages for sI hydrates. Meanwhile, I_{MLC}/I_{MSC} for sI hydrates decreased from 3.4 to 3.0 with a rise in temperature, which indicated that ethane had a preference to enter the large cages for sI hydrates with increasing temperature. By contrast, I_{MLC}/I_{MSC} for sII hydrates was smaller than 0.5; a reasonable

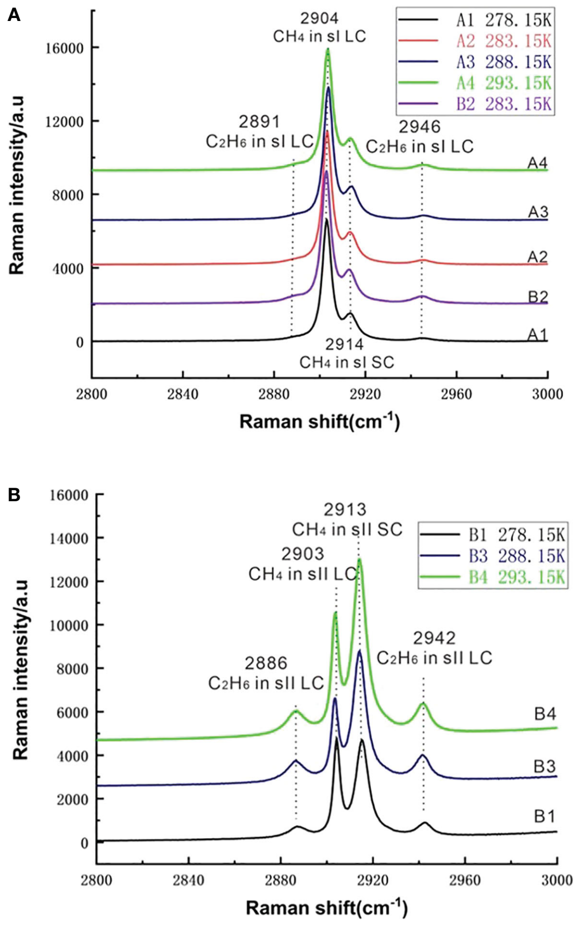

FIGURE 5
Raman spectra of the mixed gas hydrate samples in the regions between 2,800 cm^{-1} and 3,000 cm^{-1}. Sample number and corresponding experimental temperature are marked. **(A)** Raman spectra of the C–H region for structure I (sI) hydrate samples (A1, A2, A3, A4, and B2); and **(B)** Raman spectra of the C–H region for structure II (sII) hydrate samples (B1, B3, and B4).

TABLE 2 Assigned and measured Raman shifts in different hydrates based on literature data.

Component	Cavity type	$v_{measured}$ (cm^{-1})	$v_{literature}$ (cm^{-1})	References
CH_4	sI large cage	2,904	2,905	(Sum et al., 1997)
	sII large cage	2,903	2,904	(Sum et al., 1997)
	sI small cage	2,914	2,915	(Murshed and Kuhs, 2009)
	sII small cage	2,913	2,914	(Murshed and Kuhs, 2009)
C_2H_6	sI large cage	2,891, 2946	2,891, 2,946	(Subramanian et al., 2000)
	sII large cage	2,886, 2,942	2,887, 2,942	(Subramanian et al., 2000)

sI, structure I; sII, structure II.

explanation is that the relatively high cage occupancies of ethane for sII hydrates led to a decrease in the occupancies of methane in large cages, and the small cages were almost fully occupied by methane. From the limited data available for sII hydrate samples, no distinct conclusions could be drawn on the effect of temperature on the I_{MLC}/I_{MSC} for sII hydrates, but it could be seen that there was a significant decrease in I_{MLC}/I_{MSC}, from 0.41 to 0.24, when the temperature changed from 278.15 to 288.15 K, which was probably caused by the decrease in cage occupancies for methane in small cages.

3.3 Cage occupancies of the mixed gas hydrates

We calculated the cage occupancies of hydrates and hydration numbers (Table 3) using Raman spectroscopic analysis (Sum et al., 1997; Subramanian et al., 2000; Kumar et al., 2008). The calculated hydration numbers are in agreement with previously reported values, which range from 5.8 to 6.3 (Ripmeester and Ratcliffe, 1988).

In theory, CH_4 can occupy all the large cavities in all hydrate structures (Sum et al., 1997) whereas C_2H_6 molecules can be included only in large cages (Uchida et al., 2007). In the sI hydrate samples A1–A4 and B2, $\theta_{L-M,sI}$ (CH_4 cage occupancies for sI LC) was equal to, or was close to, $\theta_{S-M,sI}$ (CH_4 cage occupancies for sI SC) and was higher than $\theta_{L-M,sII}$ (CH_4 cage occupancies for sII LC) in sII hydrate samples B1, B3, and B4, which indicated that CH_4 had an advantage over C_2H_6 in the competition for inclusion in the large cage for sI hydrates. In sII hydrate samples B1, B3, and B4, the small cages were almost fully occupied by CH_4, and $\theta_{S-M,sII}$ (CH_4 cage occupancies for sII SC) was higher than $\theta_{S-M,sI}$. Meanwhile, the cage occupancies of C_2H_6 for the sII hydrates samples suggested that $\theta_{L-E,sII}$ (C_2H_6 cage occupancies for sII LC) was also higher than that for sI hydrates, which might be the reason for the weak Raman peaks (ν_1 and ν_2) for C_2H_6 in sI hydrates. This cage occupancies phenomenon could reasonably be explained by the guest-to-cavity ratio proposed by Lederhos et al. (Lederhos et al., 1993). As temperatures increased, the cage occupancies of C_2H_6 gradually increased; the cage occupancies of CH_4 in large cages were the opposite, which can be attributed to the contribution of ethane to cavity stabilization.

3.4 Effect of feeding gas on hydrate composition and structure

Under the dissolution–migration–hydration processes, the feeding gas source components affect both the composition and structure of the hydrates. The sII hydrates were formed only in the experiment in which the feed gas components contained at least 20.12 mol% C_2H_6. With this composition of feed gas, sample B2 formed sI hydrate, and other samples, B1, B3, and B4, all formed sII hydrate. At a constant temperature and pressure, we found that the higher the proportion of C_2H_6 in the feed gas, the higher the concentration of C_2H_6 in the hydrates (Table 3).

An important discovery was that the C_2H_6 concentration in hydrate formed at 30 MPa was depleted compared with the feed gas. For example, in samples A1–A4 and B1–B4, the proportion of C_2H_6 in the hydrates was lower than that in feed gas; methane-to-ethane ratios (C_1/C_2) in hydrates formed in the dissolution–migration–hydration processes were 1.2 to 2.1 times that of the gas source; this contrasts with the findings of previous studies reporting heavy hydrocarbon enrichment in hydrates crystallized directly from free gases (Kumar et al., 2008; Seo et al., 2009).

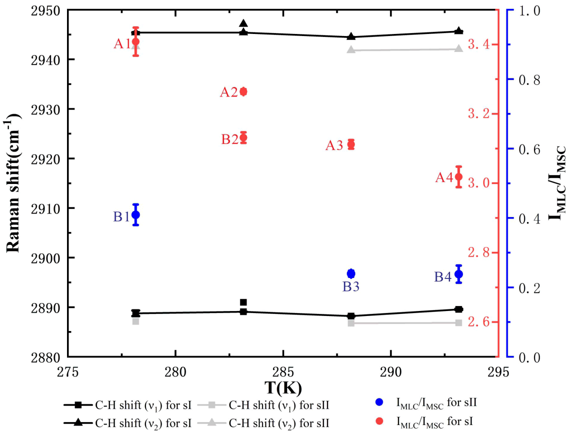

FIGURE 6
Raman spectra of the ν_1 and ν_2 C–H stretch of ethane for mixed hydrates and Raman peaks area intensity ratios (PARs) of CH_4 in the large cages (LC) to small cages (SC) (I_{MLC}/I_{MSC}). Black points and line segments correspond to structure I (sI) hydrate samples A1, A2, A3, A4, and B2. Gray points and line segments correspond to structure II (sII) hydrate samples B1, B3, and B4, with lower wavenumbers. The red dots marked with the sample number correspond to the red coordinate axis on the right, and the blue dots marked with the sample number correspond to the blue coordinate axis on the right.

TABLE 3 | The experimental pressure and temperature, feed gas composition, hydrate structure, hydrate composition, cage occupancies, and hydration number of hydrates in this work.

Trial number	P(MPa)	T (K)	Feed gas composition		STDEV	Hydrate structure	Hydrate phase composition		Methane cage occupancies		Ethane cage occupancies	Hydration number	STDEV
			Methane (mol%)	Ethane (mol%)			Methane (mol%)	Ethane (mol%)	θ_{S-M}	θ_{L-M}	θ_{L-E}		
A1	30.0	278.15	88.19	11.81	0.004369	SI	93.47	6.53	0.8482	0.7868	0.2132	5.98	0.001990
A2	30.0	283.15	88.50	11.50	0.001878	SI	92.54	7.46	0.8680	0.7598	0.2402	5.95	0.001813
A3	30.0	288.15	88.51	11.49	0.001015	SI	92.42	7.58	0.8990	0.7546	0.2454	5.90	0.001152
A4	30.0	293.15	88.20	11.80	0.001437	SI	90.23	9.77	0.8981	0.6980	0.3020	5.90	0.001630
B1	30.0	278.15	78.82	21.18	0.004088	SII	85.43	14.57	0.9089	0.6299	0.3701	6.03	0.006707
B2	30.0	283.15	78.73	21.27	0.001510	SI	88.66	11.34	0.8584	0.6639	0.3361	5.96	0.001405
B3	30.0	288.15	78.58	21.42	0.0007334	SII	82.66	17.34	0.9999	0.4794	0.5206	5.67	0.001807
B4	30.0	293.15	78.67	21.33	0.003145	SII	81.85	18.15	0.9912	0.4645	0.5355	5.70	0.008578

P, pressure; T, temperature; STDEV, standard deviation.

3.5 Effect of temperature on hydrate composition

Under the dissolution–migration–hydration processes, temperature has a significant effect on hydrate composition. For example, by comparing sI hydrate samples A1 (hydrated at 278 K) and A4 (hydrated at 293 K), and sII hydrates B1 (hydrated at 278 K), B3 (hydrated at 288 K), and B4 (hydrated at 293 K), we found that the proportion of C_2H_6 in sI hydrate and sII hydrates increased with temperature by 49.6% and 24.6%, respectively (Table 3). The trend of the proportion of C_2H_6 in hydrate increasing with temperature is consistent with the core data, where temperature increases with the depth under geothermal gradients. For example, core data from samples from the South China Sea show that the C_1/C_2 ratio in hydrates gradually tends toward a low value with depth (Paganoni et al., 2016), and core data in many ocean drilling programs (ODP)/ International Ocean Discovery Program (IODP) sites (Milkov et al., 2004).

4 Discussion

4.1 Processes causing the abrupt decrease in C_1/C_{2+} ratios in sediments occurred around the BSR

As the core geochemical data indicated (Milkov et al., 2004; Paganoni et al., 2016), an abrupt decrease in C_1/C_{2+} ratios in headspace gas in sediments occurred around the BSR, and C_1/C_{2+} ratios in the hydrates, sampled at the South China Sea (Zhang et al., 2019; Wei et al., 2021), tended to be lower at greater depth. Previous researchers have suggested two possible mechanisms to explain this phenomenon. One possible mechanism is the biodegradation of heavy hydrocarbons by microorganisms as sediment depth decreases (Pape et al., 2010), and the other is the addition of content of heavy hydrocarbons in the deep strata (Sassen et al., 2001). Neither mechanism can explain why there was an abrupt decrease in C_1/C_{2+} ratios in headspace gas in sediments occurring around the BSR. There should be a specific process only near the depth around the BSR, and the process should be related to the BGHSZ, the boundary of the hydrate-occurring zone, and the free gas zone. According to our experimental observation, the molar fraction of C_2H_6 in hydrate is depleted compared with gas sources. Gases partitioning occurred throughout the reaction transport process. We propose that the dissolution–migration–hydration of gases is the mechanism that enriches ethane near the BSR.

Paull (Paull et al., 1993) proposed a mechanism by which gas could be concentrated by recycling at the BGHSZ. Progressive burial and subsidence through geologic time shifts the BGHSZ upward, such that deep-seated hydrate decomposes and the free gas zone also shifts upward. Some free gas could rise buoyantly upward (permeating fissures in the overlying hydrate stability layer) and be incorporated into the hydrate layer (Cheng et al., 2020; Bello-Palacios et al., 2022). However, as proposed by Brown (Brown et al., 1996), significant residual free gas remains below the gas hydrate stability zone (GHSZ), trapped there by capillary forces. The bubbles in the lower portion of the free gas zone must continually dissolve, and methane and ethane must be transported in pore fluids. Our experimental observations show that gas fractionation occurred between the hydrate and the gas source under "dissolution–migration–hydration" processes. This may cause a larger C_1/C_{2+} ratio in gas hydrates relative to the residual free gas below the BGHSZ, which causes the abrupt decrease in C_1/C_{2+} ratios in headspace gas in sediments occurring around the BSR.

To test the "dissolution–migration mechanism" and its links to the enrichment of ethane near the BSR and increasing upward C_1/C_2 ratios in the hydrate-occurring zone, our experimental observation simulated these processes in a limited time and space. However, dissolved gas migration and gas hydrate formation in marine sediment usually take place over days, or even hundreds to thousands of years. To study the gas fractionation mechanism during the dissolution–migration–hydration processes, and extend our knowledge to a geologic time and space scale, we first compared the dissolution and diffusion properties of methane and ethane at the typical temperatures and pressures in the GHSZ (Table 4). We then simulated the fractionation during the dissolution–diffusion processes (Figure 7) and at last discussed the fractionation during the hydration.

Dissolution can cause gas fractionation in underwater conditions. Ethane is less soluble than methane at the same temperature and pressure; for example, at 283.15 K and 30 MPa, the solubility of methane and ethane (the mole fraction of gases in the water) is 0.00417 and 0.00132, respectively (Li et al., 2015), which indicates that in the same conditions methane is around 3.2 times more soluble than ethane. For binary-component gas mixtures, the phase equilibrium data and models are very limited. We calculated the C_1/C_2 ratio of methane and ethane in an aqueous solution after dissolution at 30 MPa and at different temperatures with a thermodynamic model (Li et al., 2015): the results show that the C_1/C_2 ratios increased by around 2.3 to 2.5 times in the aqueous solution (Table 4). From these calculations and comparisons, we can see that, under submerged conditions, dissolution causes gas fractionation and increases the C_1/C_2 ratio in aqueous solution approximately 2.3 to 3.2 times relative to the vapor gas source.

Diffusion is a dominated process that causes gas fractionation in the geological system. The dissolution–diffusion of gas in the aqueous phase can be treated as a one-dimensional diffusion process because the gas migrates up from the bottom along the long fluid migration pathway. For ideal solutions, the variation of concentration with time is subject to Fick's second law. The bottom gas concentration, near the BSR, in the aqueous phase is constant (theoretically equal to the solubility of the gas in the water at the specific temperature and pressure). Under infinite boundary conditions along the diffusion path, the dissolution–migration of gas can be calculated by the diffusion model (Lu et al., 2006; Guo et al., 2013). We simulated the dissolution–migration process of a methane–ethane mixture (C_1 = 90%, C_2 = 10%), and calculated the C_1/C_2 ratio at a depth of around 1 m above the BSR under dissolution–diffusion processes at 30 MPa, and 278.15 and 288.15 K. The entire duration of the numerical simulation was 10 days. Figure 7 shows that the dissolution–diffusion process can produce significant ethane depletion compared with the gas source; this results in the ratio of C_1/C_2 increasing by several orders of magnitude with distance upward. Decreasing temperature increases the difference in diffusion coefficient between methane and ethane (Table 4), and increases gas fractionation during the dissolution–migration processes (Figure 7); the numerical simulation results are generally consistent with our experimental observations. Advection of methane-bearing fluids is an important means of gas migration in hydrate-occurring zones. When the pore is under low fluid flux, diffusion is the dominant mechanism that causes gas fractionation, and can be further enhanced by advection. Multi-component, multi-phase transport–reaction processes related to the hydrate formation are a complex issue; we will investigate the effect of such processes (as well as advection) on hydrate formation and gas fractionation in the near future.

Hydration is also a process that causes gas fractionation. Hydrates grown from aqueous solutions usually enrich ethane relative to methane, as well as in submarine conditions. Data from ODP site 1245 show that the C_1/C_2 ratios in the pore solution are around 3.3 to 4.4 times higher than the C_1/C_2 ratios in hydrates for the samples at the depths of 50 to 100 mbsf (Milkov et al., 2004). It is clear that gas fractionation between the aqueous and hydrate phases is affected by the temperature–pressure–salinity conditions and dissolved gas composition. For example, the thermodynamic model developed by Velaga (Velaga et al., 2016) for predicting the aqueous solubility of hydrocarbon mixtures at the two-phase hydrate–liquid water equilibrium shows that the presence of propane in the mixture affects the aqueous solubility of hydrocarbon mixtures at the two-phase hydrate–liquid water equilibrium. More experiments are needed to verify such models.

TABLE 4 Dissolution behavior of gas mixture and diffusion properties of methane and ethane under the typical temperatures in GHSZ.

Temperature (K)	C_1/C_2 ratios in aqueous phase equilibrium with mixed gas vapor		Fractionation degree of dissolution relative to the vapor source		Diffusion coefficient (m^2/s)		Ratio of diffusion coefficient
	0.9 C_1 + 0.1 C_2	0.95 C_1 + 0.05 C_2	0.9 C_1 + 0.1 C_2	0.95 C_1 + 0.05 C_2	Methane	Ethane	
275.15	22.60	45.57	2.51	2.40	7.59 E-10	5.63 E-10	1.35
278.15	22.23	44.86	2.47	2.36	8.55 E-10	6.44 E-10	1.33
283.15	21.72	43.89	2.41	2.31	1.03 E-09	7.87 E-10	1.31
288.15	21.32	43.13	2.37	2.27	1.22 E-09	9.43 E-10	1.29

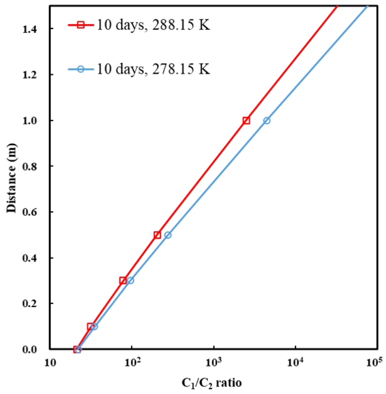

FIGURE 7
The C_1/C_2 ratio along the depth of around 1 m above the bottom-simulating reflector (BSR) under the dissolution–diffusion process of a methane–ethane mixture (90% CH_4 + 10% C_2H_6) at 278.15 and 288.15 K. Diffusion coefficients of gases are listed in Table 4. The entire duration of the numerical simulation was 10 days.

Our study shows that gas fractionation occurring between the hydrate and the gas source under “dissolution–migration–hydration” processes may cause larger C_1/C_{2+} ratios in gas hydrates relative to the residual free gas below the BGHSZ. Such processes cause the abrupt decrease in C_1/C_{2+} ratios in headspace gas in sediments that occur around the BSR (Figure 8).

4.2 Vertical composition variation of hydrates originating from thermogenic gases

Hydrate accumulations originating from thermogenic gases containing heavier hydrocarbons have been found in many regions around the world (Hillman et al., 2017; Plaza-Faverola et al., 2017; Thiagarajan et al., 2020). Under the effect of the formation pressure, the thermogenic gas sources with higher-order hydrocarbons gradually migrate upward into the hydrate stability zones through the preferential transport pathway, which includes gas chimneys, unconformity surfaces, faults, fractures, and sandstone channels, and then form a hydrate layer at the suitable pore sizes (Panieri et al., 2017; Portnov et al., 2021; Liang et al., 2022).

However, not all free gas can be transported into the hydrate stability zone. When the gas pressure cannot overcome the capillary pressure, the gas phase will be trapped in sediments in the free gas zone, and must continually dissolve and be transported upward in solution to be incorporated into the hydrate layer. Our experiments of gas hydrate formation in capillary tubes are highly analogous to the process of natural gas hydration in the pore space in submarine sediments. Gas dissolves and migrates along the capillary pore space through short or long distances, and then forms hydrates. Such “dissolution–migration–hydration” processes result in the percentage of ethane in the hydrate increasing with temperature and depth (Figure 8), especially in sites where thermogenic gas is rapidly transported along a gas chimney and the local geothermal gradient is increased by the warm fluids.

4.3 Implications for estimates of carbons in marine gas hydrate

Previously, the amount of carbon contained in hydrates formed from heavy hydrocarbons, such as ethane, was ignored, resulting in a significant underestimation of the number of carbon resources. Essentially, the estimated amounts of carbon in gas hydrates are constrained by the volume of pore space available for hydrate formation and the gas composition in the hydrate phase (Dickens, 2011; Wallmann et al., 2012), and 1 m^3 of ethane hydrate contains twice the amount of carbon in a similar volume of methane hydrate (Plaza-Faverola et al., 2017).

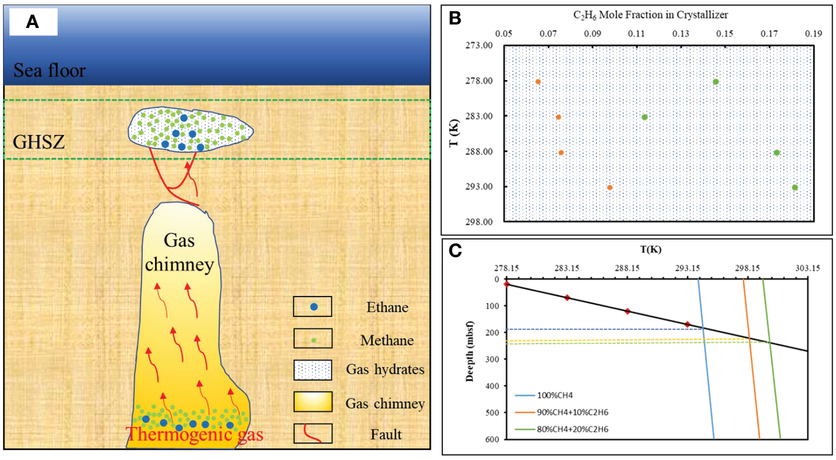

FIGURE 8
A proposed simplified model of the thermogenic dissolved gas hydrate accumulation mechanism. **(A)** Red arrow represents thermogenic gases, red lines indicate faults tectonic, and white represents hydrates. **(B)** The proportion of ethane in hydrates varies with temperature. Orange represents the gas source composition of 90% CH_4 + 10% C_2H_6, green represents the gas source composition of 80% CH_4 + 20% C_2H_6. **(C)** The base of the gas hydrate stability zones was calculated by pure methane, and methane and ethane gases used in this study. The geothermal gradient is calculated by 100°C/km, an average value measured using the Guangzhou Marine Geological Survey (GMGS5) Site W9 (GMGS5-W9) hydrate system with gas chimneys (Liang et al., 2019).

Dissolution–migration of gas near the BSR enriches ethane near the GHSZ; such changes in gas composition could affect the depth of the GHSZ. Our calculation indicates that an increase of 10% in the mole fraction of ethane could deepen the GHSZ thickness by at least 37 m (compared with pure methane hydrate; Figure 8). The higher the proportion of heavier hydrocarbons, the deeper the bottom boundary of the gas hydrate stability zone (Figure 8). Our experiments indicated that the proportion of heavy hydrocarbon in the bottom hydrate (9.77% at 293 K; Table 3) is 49.6% higher than the proportion of heavy hydrocarbon in the top hydrate layer (6.53% at 278 K; Table 3). Assuming 6.53% ethane in the hydrate, this could lead to the amount of carbon per 1 m^3 being underestimated by at least 2.42-fold (considering the 37 m deep thickness of the GHSZ, and comparing with hydrate accumulated from pure methane).

5 Conclusion

We tested the "dissolution–migration mechanism" and its links to the enrichment of ethane near the BSR and increasing upward C_1/C_2 ratios in the hydrate-occurring zone, performed experimental simulations on the gas dissolution–migration–hydration processes, and investigated the effects the composition of feeding gases and temperatures on the composition of hydrates the grown. The main conclusions can be summarized as follows:

Owing to the dissolution–migration–hydration processes, the composition of hydrates differs greatly from the initial supplying gas. Regardless of whether they are type I or II hydrates, the content of methane in hydrates was enriched compared with the gas source, and the proportion of ethane in hydrates was deficient compared with the free gas source. We proposed that the dissolution–migration–hydration of gases is the mechanism that enriches ethane near the BSR, causing the abrupt decrease in C_1/C_{2+} ratios in sediments occurring around the BSR.

Temperature has a significant effect on the composition of hydrates. With the same supply of gas (i.e., the gas source composition remains constant), the proportion of ethane in the hydrates decreased gradually with decreasing temperature, which may cause the spatial variation of hydrate composition within the hydrate stability zone. The ratio of C_1/C_2 in hydrates also increased with decreasing temperature from the base of the gas hydrate stability zone to the seafloor.

Inputs of ethane or heavier hydrocarbons into the gas sources, and the dissolution–migration–hydration mechanism that enriches ethane near the BSR, can increase the depth of the GHSZ. The amount of carbon resources contained in hydrates formed from heavy hydrocarbons, such as ethane, has been significantly underestimated.

Data availability statement

The original contributions presented in the study are included in the article/supplementary material. Further inquiries can be directed to the corresponding authors.

Author contributions

Original draft preparation, HL. Experimental work, HL, XL, TL, and WW. Revision, LW, and WL. Conception and supervision, WL and YC. All authors contributed to the article and approved the submitted version.

Funding

This work was partly supported by the National Natural Science Foundation of China (41876069 and 92058208), and the National Key Research and Development Program of China (2018YFC0310006–04).

Acknowledgments

We are grateful to two reviewers, for their critical reviews and thoughtful comments on the manuscript.

Conflict of interest

The authors declare that the research was conducted in the absence of any commercial or financial relationships that could be construed as a potential conflict of interest.

Publisher's note

References

Bello-Palacios, A., Fotland, P., and Ersland, G. (2022). Modeling the effects of sedimentation on natural occurrences of CH4 hydrates in marine sediments. *Energy Fuels* 36, 3778–3787. doi: 10.1021/acs.energyfuels.1c03611

Brown, K. M., Bangs, N. L., Froelich, P. N., and Kvenvolden, K. A. (1996). The nature, distribution, and origin of gas hydrate in the Chile triple junction region. *Earth Planet. Sci. Lett.* 139, 471–483. doi: 10.1016/0012-821X(95)00243-6

Caumon, M.-C., Robert, P., Laverret, E., Tarantola, A., Randi, A., Pironon, J., et al. (2014). Determination of methane content in NaCl–H2O fluid inclusions by raman spectroscopy. calibration and application to the external part of the central Alps (Switzerland). *Chem. Geol.* 378-379, 52–61. doi: 10.1016/j.chemgeo.2014.03.016

Cheng, C., Jiang, T., Kuang, Z. G., Yang, C. Z., Zhang, C., He, Y. L., et al. (2020). Characteristics of gas chimneys and their implications on gas hydrate accumulation in the shenhu area, northern south China sea. *J. Natural Gas Sci. Eng.* 84, 103629. doi: 10.1016/j.jngse.2020.103629

Dickens, G. R. (2011). Down the rabbit hole: toward appropriate discussion of methane release from gas hydrate systems during the Paleocene-Eocene thermal maximum and other past hyperthermal events. *Climate Past* 7, 831–846. doi: 10.5194/cp-7-831-2011

Guo, H. R., Chen, Y., Lu, W. J., Li, L. L., and Wang, M. H. (2013). *In situ* raman spectroscopic study of diffusion coefficients of methane in liquid water under high pressure and wide temperatures. *Fluid Phase Equilibria* 360, 274–278. doi: 10.1016/j.fluid.2013.09.051

Hester, K. C., Dunk, R. M., White, S. N., Brewer, P. G., Peltzer, E. T., and Sloan, E. D. (2007). Gas hydrate measurements at hydrate ridge using raman spectroscopy. *Geochimica Cosmochimica Acta* 71, 2947–2959. doi: 10.1016/j.gca.2007.03.032

Hester, K. C., White, S. N., Peltzer, E. T., Brewer, P. G., and Sloan, E. D. (2006). Raman spectroscopic measurements of synthetic gas hydrates in the ocean. *Mar. Chem.* 98, 304–314. doi: 10.1016/j.marchem.2005.09.006

Hillman, J. I. T., Cook, A. E., Daigle, H., Nole, M., Malinverno, A., Meazell, K., et al. (2017). Gas hydrate reservoirs and gas migration mechanisms in the terrebonne basin, gulf of Mexico. *Mar. Petroleum Geol.* 86, 1357–1373. doi: 10.1016/j.marpetgeo.2017.07.029

Khlystov, O., De Batist, M., Shoji, H., Hachikubo, A., Nishio, S., Naudts, L., et al. (2013). Gas hydrate of lake baikal: Discovery and varieties. *J. Asian Earth Sci.* 62, 162–166. doi: 10.1016/j.jseaes.2012.03.009

Kida, M., Suzuki, K., Kawamura, T., Oyama, H., Nagao, J., Ebinuma, T., et al. (2009). Characteristics of natural gas hydrates occurring in pore-spaces of marine sediments collected from the Eastern nankai trough, off Japan. *Energy Fuels* 23, 5580–5586. doi: 10.1021/ef900612f

Klapp, S. A., Bohrmann, G., Kuhs, W. F., Murshed, M. M., Pape, T., Klein, H., et al. (2010a). Microstructures of structure I and II gas hydrates from the gulf of Mexico. *Mar. Petroleum Geol.* 27, 116–125. doi: 10.1016/j.marpetgeo.2009.03.004

Klapp, S. A., Murshed, M. M., Pape, T., Klein, H., Bohrmann, G., Brewer, P. G., et al. (2010b). Mixed gas hydrate structures at the chapopote knoll, southern gulf of Mexico. *Earth Planet. Sci. Lett.* 299, 207–217. doi: 10.1016/j.epsl.2010.09.001

Kumar, R., Linga, P., Moudrakovski, I., Ripmeester, J. A., and Englezos, P. (2008). Structure and kinetics of gas hydrates from methane/ethane/propane mixtures relevant to the design of natural gas hydrate storage and transport facilities. *AIChE J.* 54, 2132–2144. doi: 10.1002/aic.11527

Lederhos, J. P., Christiansen, R. L., and Sloan, E. D. (1993). A first order method of hydrate equilibrium estimation and its use with new structures. *Fluid Phase Equilibria* 83, 445–454. doi: 10.1016/0378-3812(93)87049-7

Liang, J., Meng, M., Liang, J., Ren, J., He, Y., Li, T., et al. (2022). Drilling cores and geophysical characteristics of gas hydrate-bearing sediments in the production test region in the shenhu sea, south China sea. *Front. Earth Sci.* 10, 911123. doi: 10.3389/feart.2022.911123

Liang, J., Zhang, W., Lu, J.a., Wei, J., Kuang, Z., and He, Y. (2019). Geological occurrence and accumulation mechanism of natural gas hydrates in the eastern qiongdongnan basin of the south China sea: Insights from site GMGS5-W9-2018. *Mar. Geol.* 418, 106042. doi: 10.1016/j.margeo.2019.106042

Liu, S., Jiang, Z., Liu, H., Pang, S., Xia, Z., Jin, Z., et al. (2016). The natural-gas hydrate exploration prospects of the nayixiong formation in the kaixinling-wuli permafrost, qinghai-Tibet plateau. *Mar. Petroleum Geol.* 72, 179–192. doi: 10.1016/j.marpetgeo.2016.01.022

Liu, C. L., Meng, Q. G., He, X. L., Li, C. F., Ye, Y. G., Zhang, G. X., et al. (2015). Characterization of natural gas hydrate recovered from pearl river mouth basin in south China Sea. *Mar. Petroleum Geol.* 61, 14–21. doi: 10.1016/j.marpetgeo.2014.11.006

Li, J., Zhang, Z., Luo, X., and Li, X. (2015). Modelling of phase equilibria in CH4–C2H6–C3H8–nC4H10–NaCl–H2O systems. *Appl. Geochem.* 56, 23–36. doi: 10.1016/j.apgeochem.2015.02.006

Lu, W. J., Chou, I. M., and Burruss, R. C. (2008). Determination of methane concentrations in water in equilibrium with sI methane hydrate in the absence of a vapor phase by *in situ* raman spectroscopy. *Geochimica Cosmochimica Acta* 72, 412–422. doi: 10.1016/j.gca.2007.11.006

Lu, W. J., Chou, I. M., Burruss, R. C., and Song, Y. C. (2007). A unified equation for calculating methane vapor pressures in the CH4-H2O system with measured raman shifts. *Geochimica Cosmochimica Acta* 71, 3969–3978. doi: 10.1016/j.gca.2007.06.004

Lu, W. J., Chou, I. M., Burruss, R. C., and Yang, M. Z. (2006). *In situ* study of mass transfer in aqueous solutions under high pressures *via* raman spectroscopy: A new method for the determination of diffusion coefficients of methane in water near hydrate formation conditions. *Appl. Spectrosc.* 60, 122–129. doi: 10.1366/000370206776023278

Lu, W. J., Guo, H. R., Chou, I. M., Burruss, R. C., and Li, L. L. (2013). Determination of diffusion coefficients of carbon dioxide in water between 268 and 473 K in a high-pressure capillary optical cell with *in situ* raman spectroscopic measurements. *Geochimica Cosmochimica Acta* 115, 183–204. doi: 10.1016/j.gca.2013.04.010

Lu, Z. Q., Zhu, Y. H., Zhang, Y. Q., Wen, H. J., Li, Y. H., and Liu, C. L. (2011). Gas hydrate occurrences in the qilian mountain permafrost, qinghai province, China. *Cold Regions Sci. Technol.* 66, 93–104. doi: 10.1016/j.coldregions.2011.01.008

Milkov, A. V., Claypool, G. E., Lee, Y.-J., Torres, M. E., Borowski, W. S., Tomaru, H., et al. (2004). Ethane enrichment and propane depletion in subsurface gases indicate gas hydrate occurrence in marine sediments at southern hydrate ridge offshore Oregon. *Organic Geochem.* 35, 1067–1080. doi: 10.1016/j.orggeochem.2004.04.003

Murshed, M. M., and Kuhs, W. F. (2009). Kinetic studies of methane-ethane mixed gas hydrates by neutron diffraction and raman spectroscopy. *J. Phys. Chem. B* 113, 5172–5180. doi: 10.1021/jp810248s

Ou, W. J., Geng, L. T., Lu, W. J., Guo, H. R., Qu, K., and Mao, P. X. (2015). Quantitative raman spectroscopic investigation of geo-fluids high-pressure phase equilibria: Part II. accurate determination of CH4 solubility in water from 273 to 603 K and from 5 to 140 MPa and refining the parameters of the thermodynamic model. *Fluid Phase Equilibria* 391, 18–30. doi: 10.1016/j.fluid.2015.01.025

Ou, W., Lu, W., Qu, K., Geng, L., and Chou, I. M. (2016). *In situ* raman spectroscopic investigation of flux-controlled crystal growth under high pressure: A case study of carbon dioxide hydrate growth in aqueous solution. *Int. J. Heat Mass Transf.* 101, 834–843. doi: 10.1016/j.ijheatmasstransfer.2016.05.082

Paganoni, M., Cartwright, J. A., Foschi, M., Shipp, R. C., and Van Rensbergen, P. (2016). Structure II gas hydrates found below the bottom-simulating reflector. *Geophys. Res. Lett.* 43, 5696–5706. doi: 10.1002/2016GL069452

Panieri, G., Bünz, S., Fornari, D. J., Escartin, J., Serov, P., Jansson, P., et al. (2017). An integrated view of the methane system in the pockmarks at vestnesa ridge, 79°N. *Mar. Geol.* 390, 282–300. doi: 10.1016/j.margeo.2017.06.006

Pape, T., Bahr, A., Rethemeyer, J., Kessler, J. D., Sahling, H., Hinrichs, K. U., et al. (2010). Molecular and isotopic partitioning of low-molecular-weight hydrocarbons during migration and gas hydrate precipitation in deposits of a high-flux seepage site. *Chem. Geol.* 269, 350–363. doi: 10.1016/j.chemgeo.2009.10.009

Paull, C. K., Ussler, W., and III and Borowski, W. S. (1993). Sources of biogenic methane to form marine gas hydrates: *In situ* production or upward migration? *Ann. New York Acad. Sci.* 175, 392–409. doi: 10.2172/10185837

Plaza-Faverola, A., Vadakkepuliyambatta, S., Hong, W. L., Mienert, J., Bunz, S., Chand, S., et al. (2017). Bottom-simulating reflector dynamics at Arctic thermogenic gas provinces: An example from vestnesa ridge, offshore west Svalbard. *J. Geophys. Res. Solid Earth* 122, 4089–4105. doi: 10.1002/2016JB013761

Portnov, A., Cook, A. E., and Vadakkepuliyambatta, S. (2021). Diverse gas composition controls the moby-dick gas hydrate system in the gulf of Mexico. *Geology* 49, 1446–1451. doi: 10.1130/G49310.1

Ripmeester, J. A., and Ratcliffe, C. I. (1988). Low-temperature cross-polarization/magic angle spinning carbon-13 NMR of solid methane hydrates: structure, cage occupancy, and hydration number. *J. Phys. Chem.* - 92, 337–339. doi: 10.1021/j100313a018

Sassen, R., Losh, S. L., Cathles, L., Roberts, H. H., Whelan, J. K., Milkov, A. V., et al. (2001). Massive vein-filling gas hydrate: relation to ongoing gas migration from the deep subsurface in the gulf of Mexico. *Mar. Petroleum Geol.* 18, 551–560. doi: 10.1016/S0264-8172(01)00014-9

Seo, Y., Kang, S.-P., and Jang, W. (2009). Structure and composition analysis of natural gas hydrates: 13C NMR spectroscopic and gas uptake measurements of mixed gas hydrates. *J. Phys. Chem. A* 113, 9641–9649. doi: 10.1021/jp904994s

Sloan, E. D. (2003). Fundamental principles and applications of natural gas hydrates. *Nature* 426, 353–359. doi: 10.1038/nature02135

Sloan, E. D. (2008). Clathrate hydrates of natural gases. *Fuel* 87, 3158–3158. doi: 10.1016/j.fuel.2008.03.028

Subramanian, S., Kini, R. A., Dec, S. F., and Sloan, E. D. (2000). Evidence of structure II hydrate formation from methane+ethane mixtures. *Chem. Eng. Sci.* 55, 1981–1999. doi: 10.1016/S0009-2509(99)00389-9

Sum, A. K., Burruss, R. C., and Sloan, E. D. (1997). Measurement of clathrate hydrates *via* raman spectroscopy. *J. Phys. Chem. B* 101, 7371–7377. doi: 10.1021/jp970768e

Thiagarajan, N., Kitchen, N., Xie, H., Ponton, C., Lawson, M., Formolo, M., et al. (2020). Identifying thermogenic and microbial methane in deep water gulf of Mexico reservoirs. *Geochimica Cosmochimica Acta* 275, 188–208. doi: 10.1016/j.gca.2020.02.016

Uchida, T., Takeya, S., Kamata, Y., Ikeda, I. Y., Nagao, J., Ebinuma, T., et al. (2002). Spectroscopic observations and thermodynamic calculations on clathrate hydrates of mixed gas containing methane and ethane: determination of structure, composition and cage occupancy. *J. Phys. Chem. B* 106, 12426–12431. doi: 10.1021/jp025884i

Uchida, T., Takeya, S., Kamata, Y., Ohmura, R., and Narita, H. (2007). Spectroscopic measurements on binary, ternary, and quaternary mixed-gas molecules in clathrate structures. *Ind. Eng. Chem. Res.* 46, 5080–5087. doi: 10.1021/ie070153w

Velaga, S. C., Levine, J. S., Warzinski, R. P., and Anderson, B. J. (2016). A thermodynamic model to predict the aqueous solubility of hydrocarbon mixtures at two-phase hydrate-liquid water equilibrium. *Fluid Phase Equilibria* 414, 75–87. doi: 10.1016/j.fluid.2015.12.049

Wallmann, K., Pinero, E., Burwicz, E., Haeckel, M., Hensen, C., Dale, A., et al. (2012). The global inventory of methane hydrate in marine sediments: A theoretical approach. *Energies* 5, 2449–2498. doi: 10.3390/en5072449

Wei, J., Wu, T., Zhu, L., Fang, Y., Liang, J., Lu, H., et al. (2021). Mixed gas sources induced co-existence of sI and sII gas hydrates in the qiongdongnan basin, south China Sea. *Mar. Petroleum Geol.* 128, 105024. doi: 10.1016/j.marpetgeo.2021.105024

Whiticar, M. J., Hovland, M., Kastner, M., and Sample, J. C. (1995). Organic geochemistry of gases, fluids, and hydrates at the cascadia margin accretionary margin. *Proc. Ocean Drilling Program Sci. Results*, 146 385–397. doi: 10.2973/odp.proc.sr.146-1.247.1995

Zhang, W., Liang, J. Q., Wei, J. G., Su, P. B., Lin, L., and Huang, W. (2019). Origin of natural gases and associated gas hydrates in the shenhu area, northern south China Sea: Results from the China gas hydrate drilling expeditions. *J. Asian Earth Sci.* 183, 103953. doi: 10.1016/j.jseaes.2019.103953

Frontiers in Marine Science

TYPE Original Research
PUBLISHED 13 March 2023
DOI 10.3389/fmars.2023.1111133

Check for updates

OPEN ACCESS

EDITED BY
Dong Feng,
Shanghai Ocean University, China

REVIEWED BY
Rui Yang,
Qingdao Institute of Marine Geology (QIMG), China
Xiting Liu,
Ocean University of China, China
Claudio Argentino,
UiT The Arctic University of Norway, Norway

*CORRESPONDENCE
Daidai Wu
wudd@ms.giec.ac.cn
Ping Yin
1419685757@qq.com

SPECIALTY SECTION
This article was submitted to Marine Biogeochemistry, a section of the journal Frontiers in Marine Science

RECEIVED 29 November 2022
ACCEPTED 27 February 2023
PUBLISHED 13 March 2023

CITATION
Sun T, Wu D, Wu N and Yin P (2023) The effects of organic matter and anaerobic oxidation of methane on the microbial sulfate reduction in cold seeps. *Front. Mar. Sci.* 10:1111133. doi: 10.3389/fmars.2023.1111133

The effects of organic matter and anaerobic oxidation of methane on the microbial sulfate reduction in cold seeps

Tiantian Sun[1,2], Daidai Wu[3]*, Nengyou Wu[1,2] and Ping Yin[1,2]*

[1]Qingdao Institute of Marine Geology, China Geological Survey, Ministry of Natural Resources, Qingdao, China, [2]Laboratory for Marine Geology, Qingdao National Laboratory for Marine Science and Technology, Qingdao, China, [3]Guangzhou Institute of Energy Conversion, Chinese Academy of Sciences, Guangzhou, China

Cold seep sediments are dominated by intensive microbial sulfate reduction coupled to anaerobic oxidation of methane. However, the contribution proportion between this process and the role of organic matter has remained enigmatic. Here, pore water data combined with PROFILE model, fluxes of sulfate and methane concentration calculated from Fick's first law, and $\delta^{34}S_{SO4}$ and $\delta^{18}O_{SO4}$ of pore water sulfate were studied to reconstruct co-occurring microbial organoclastic sulfate reduction and anaerobic oxidation of methane coupled with sulfate reduction in methane seep sediments collected from South China Sea. The sulfate concentration profiles of C9 and C14 in Qiongdongnan Basin generally show quasilinear depletion with depth. Reaction-transport modeling provided close fits to concentration data. $\delta^{18}O_{SO4}$ and $\delta^{34}S_{SO4}$ increase fastest with sediment depth above 400 cmbsf and slowest below that depth. The values of methane flux are always lower than those of total sulfate reduction of sulfate diffusive flux at GC-10, GC-9, GC-11 and HD319 sites in Taixinan Basin. Besides, positions of sulfate methane transition zone in all study sites are approximately ~400 to 800 centimeters below seafloor. These results showed that microbial sulfate reduction in sediments is mainly controlled by intense anaerobic oxidation of methane, but there is a certain relationship with organic matter metabolism process. This emphasizes that traditional redox order of bacterial respiration is highly simplified, where, in sediments such as these seeps, all of these microbial sulfate reduction processes can occur together with complex couplings between them.

KEYWORDS

methane seepage, anaerobic oxidation of methane, microbial sulfate reduction, Organoclastic Sulfate Reduction, Qiongdongnan Basin, Taixinan Basin

1 Introduction

In the early diagenesis of sediments, pore water in sediment close to the seafloor is rich in sulfate due to the downward diffusion and infiltration of high concentration of sulfate in the ocean. Organoclastic sulfate reduction (OSR): $2(CH_2O) + SO_4^{2-} \rightarrow 2HCO_3^- + H_2S$ (Berner et al., 1985; Boetius et al., 2000) and anaerobic oxidation of methane coupled with sulfate reduction (AOM-SR): $SO_4^{2-} + CH_4 \rightarrow HCO_3^- + HS^- + H_2O$ (Masuzawa et al., 1992; Knittel and Boetius, 2009) are important microbial sulfate reduction (MSR) pathways in sediments, which play a vital role in the sulfur and carbon cycles in marine sediments. Those with highly active organic matter with sulfate reduction occur in the sulfate reduction zone (SRZ). Below the SRZ lies the sulfate-methane transition zone (SMTZ), a zone where methane and sulfate would be exhausted. The upward diffusion of methane in sediment directly controls the gradient of sulfate change in pore water and the depth position of the SMTZ. Generally, the greater the upward diffusion flux of methane, the more intense the AOM reaction, resulting in a shallower SMTZ depth (Borowski et al., 1996; Borowski et al., 1999). Borowski et al. (1999) conducted a systematic study on the change in sulfate concentration in pore water during the Deep Sea Drilling Project (DSDP) and Ocean Drilling Program (ODP) stations on the continental margins around the world and found that the SMTZ depth of most gas hydrate occurrence areas and cold seeps are less than 50 m, with an average of 20 m. In the area where hydrate occurs, the content of SO_4^{2-} in pore water decreases rapidly due to strong AOM, which makes the SMTZ in sediments shallow. Therefore, linear and steep sulfate profile gradients and shallow SMTZ positions are signs of strong methane flux and possible existence of AOM-SR (Borowski et al., 1996; Borowski et al., 2000; Wu et al., 2013).

Most geochemical and microbiological studies point to AOM-SR as the dominant sink for methane (up to 90%) in cold seep sediments (Knittel and Boetius, 2009). However, the proportion of this process has remained enigmatic. For methane seep sediments under different environmental settings, the proportion of sulfate consumed in pore water by OSR and AOM-SR differs. For example, only 50% of sulfate diffused downward from pore water of the Cariaco Trench basin in Venezuela is consumed by AOM (Reeburgh, 1976). 61-89% of the sulfate in the bottom sediments of the Kattegat Strait and Skagrak Strait is consumed by AOM (Jørgensen, 1992). Besides, Egger et al. (2018) conducted a detailed study on sulfate and methane fluxes in the SMTZ from the worldwide. They concluded that OSR consumed more than 40% of sulfate in the SMTZ. Jørgensen et al., (2019b) studied the content of methane and sulfate and their reaction rates in pore water at several sites along the Danish coast and found that about 14-59% of sulfate near the SMTZ was consumed through OSR. These studies have helped demonstrate the important role of OSR in the MSR process within sedimentary systems under the background of methane seeps, even in the presence of AOM. However, many questions remain. There is still enigmatic on the ratio of sulfate consumed by anaerobic oxidation of methane (AOM) and sulfate consumed by organic matter-driven MSR when both processes occur, as well as their influencing control factors.

Separating the contributions of OSR and AOM-SR to the overall sedimentary sulfur cycle has been challenging but has benefited from recent advances in isotope biogeochemistry. Stable carbon isotopes have been vastly used to address these processes. Recently, the sulfur and oxygen isotopes in dissolved sulfate ($\delta^{34}S_{SO4}$ and $\delta^{18}O_{SO4}$) may be a diagnostic tool for tracking the pathways of sulfate reduction by methane or other organic compounds (Böttcher et al., 1998; Gilad et al., 2013; Deusner et al., 2014; Gilad et al., 2014; Chen et al., 2022). Metabolic processes distinguish light and heavy isotopologues, and the gradual enrichment of heavy isotopes observed in the residual sulfate pool can trace this activity. The overall rate of MSR itself is related to the relative chemical balance of the several main intracellular steps, each step is reversible, and the branching points generated in the cell itself will respond to changes in environmental conditions (Wing and Halevy, 2014; Santos et al., 2015). A fast increase in $\delta^{18}O$ of sulfate relative to its $\delta^{34}S$ suggests there is a high rate of back-reaction and equilibration of oxygen isotopes in intermediate-valence-state-sulfur species with water, and thus a slower overall rate of MSR (Chen et al., 2022). Two other processes impact the sulfur isotope fractionation observed in sediments, the disproportionation of external sulfur intermediates and microbial sulfide oxidation, and the observed sulfur isotopic composition of sulfate may be due to a combination of all three processes (Jørgensen et al., 2019a; Pellerin et al., 2019). This relationship has been investigated in pure culture experiments (Canfield et al., 2006), batch culture experiments using natural populations (Stam et al., 2011) and calculated *in situ* using pore fluids profiles (Aharon and Fu, 2000; Gilad et al., 2013). The drilling research of Deep Sea Drilling Project (DSDP) Leg 11 and Leg 76 also shows that methane intensity affects the stable S and O isotope values of sulfate in sedimentary pore water, which often shows a series of geochemical anomalies in depth profiles (Borowski et al., 1996; Borowski et al., 2000).

Here, we compare and analyze the pore water composition and PROFILE model of six sedimentary sites collected from the Qiongdongnan Basin and the Taixinan Basin, respectively, in the South China Sea to study OSR and AOM-SR of two important microbial sulfate reduction in cold seep sediments and the location of SMTZ that can be used to indicate the intensity of methane seepage. Sulfate and methane concentration gradients into SMTZ are used to estimate sulfate reduction rates and AOM rates. Combined with $\delta^{34}S_{SO4}$ and $\delta^{18}O_{SO4}$ of pore water sulfate to help evaluate whether OSR accounts for a certain proportion during AOM-SR process. We provide strong evidence for the co-existence of OSR and AOM under the background of cold seeps, and propose that the intensity of methane seepage significantly influence mechanisms on the $\delta^{34}S_{SO4}$ and $\delta^{18}O_{SO4}$ of pore water. In the process of microbial sulfate reduction, $\delta^{34}S_{SO4}$ and $\delta^{18}O_{SO4}$ in the residual sulfate are also affected by the disproportionation of external sulfur intermediates and the oxidation of microbial sulfide.

2 Study area

The South China Sea is one of the largest marginal seas in the low-latitude area of the Western Pacific Ocean. It is located at the intersection of Eurasian plate, Pacific plate and India-Australia plate (Taylor and Hayes, 1983). There are various structural landforms or geological bodies on the continental slope, such as deep troughs, submarine plateaus, continental slope platforms, steep submarine slopes and submarine valleys. From the seismic profile of gas hydrate distribution areas in the typical passive continental margin, most of the seafloors are developed with abundant faults and/or fold structures, and the hydrate enrichment zone is primarily concentrated in the sedimentary layer near or above the major faults (Hu et al., 2020). The study area includes two areas in the northern slope of the South China Sea (Qiongdongnan and Taixinan), with the water depth ranging from ~700 to ~ 2000 meters (see Figure 1). According to the survey of marine resources, clear undersea simulated reflectors (BSRs) have been found in Xisha Trough, Taixinan Basin, Shenhu and Dongsha areas, Qiongdongnan Basin, which to a large extent indicates that there are huge potential sources of natural gas hydrates in the northern South China Sea (Yao, 1998).

The GC-9, GC-10, GC-11 and HD319 sites are located in the Taixinan basin in the southwest of Taiwan Province (Figure 1). The abundant terrestrial clastic rocks derived from Southern China and the Indochina Peninsula have resulted in Neogene sediment deposits up to ~10 km thick at the center of Taixinan Basin. The thick stratigraphic deposits and intense hydrocarbon generation and expulsion processes of the deep source kitchens have led to high fluid activity, forming a series of NE-trending basin that are rich in oil and gas, with widely distributed mud volcanoes, mud diapirs, gas chimneys, and submarine cold seeps (Schnürle et al., 2011). Moreover, gas seepages and associated cold seeps have been confirmed *via* multibeam profiles and *in situ* ROV observations. During the R/V SONNE 177 cruise in 2007, a widely distributed seep carbonate crust called Jiulong Methane Reef was found in the deep waters of the Taixinan Basin, indicating extensive paleo-methane seep events in this area (Suess et al., 2005; Han et al., 2008).

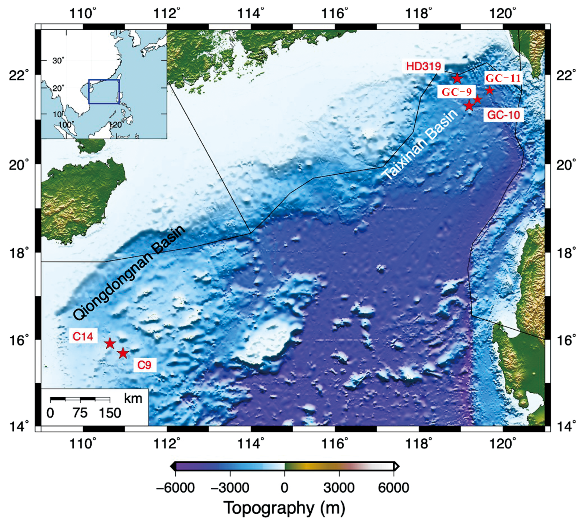

FIGURE 1
Map of study sites and locations in the northern South China Sea. Rectangle boxes denote study areas, which includes the Qiongdongnan basin and Taixinan basin.

Sites C9 and C14 are located in southwest Qiongdongnan Basin (Figure 1). The Qiongdongnan Basin, located on the northwestern continental slope of the SCS, contains a Cenozoic sedimentary succession of up to 12 km in thickness and is suggested to have great hydrocarbon and gas hydrate potential (Zhu et al., 2009; Shi et al., 2013; Zhang et al., 2018). A large number of seabed pockmarks, mounds and acoustic blanking reflections related to submarine fluid flow together with indicators of shallow gas hydrate occurrence have been reported in the western Qiongdongnan Basin (Sun et al., 2011; Luo et al., 2014). In 2015, "Haima cold seeps" were discovered in the southern Qiongdongnan Basin during ROV surveys launched by the Guangzhou Marine Geological Survey. Piston and push coring processes also recovered gas hydrates and authigenic carbonate rocks from subsurface sediments at seepage sites in the Qiongdongnan Basin (Liang et al., 2017).

3 Materials and methods

3.1 Data

This study primarily utilized public and published data; reference sources are provided for all the data. The concentration of major components (SO_4^{2-}, Ca^{2+}, DIC) and ^{34}S isotope value of sulfate in pore water in the Qiongdongnan Basin is from the data of Luo et al. (2013), while the ^{18}O isotope value of sulfate is from the data of Luo et al. (2014); The concentration of CH_4 and major components (SO_4^{2-}, Ca^{2+}, H_2S, TA, Sr^{2+}, Mg^{2+}, Ba^{2+}, Mn^{2+}) in pore water in the Taixinan Basin is from the data of Wu et al. (2010); Wu et al. (2013). However, these data have not previously been used for the same purpose as this study. The number of complete datasets available is limited, and only four are listed here. The geographic locations of the six sampling sites are shown in the figure (Figure 1). Names and coordinates of all sites are given in Table 1 together with other key parameters (water depth, core length, and references).

3.2 Numerical modeling

The measured concentration gradient of pore water was used to calculate the net production or net consumption rate of the primary elements (SO_4^{2-}, CH_4, Ca^{2+}, H_2S, DIC) in the sediment pore water from the four stations (stations C9, C14, GC-10, and HD319) and the resulting vertical flux. SMTZ is a zone with unclear boundaries, especially on the continental shelf sediments rich in organic matter. It usually occurs within a few meters of shallow surface sediments. The methane profile extends to the sulfate reduction zone (Schmaljohann, 1996; Piker et al., 1998; Jørgensen et al., 2004). In this study, a reaction transport model was used to determine the depth range when the net methane consumption rate (AOMR) and sulfate reduction rate (SRR) increase. It was assumed that the

TABLE 1 Coordinates, water depth and core length at the sediment stations sampled on the northern South China Sea; bsf is below sea floor.

Station	Latitude	Longitude	Core length	Water depth	References from
	(N)	(E)	(cm bsf)	(m bsf)	
C9	15°41.032′	110°57.246′	760	829	(Luo et al., 2014)
C14	15°54.507′	110°38.607′	670	840	(Luo et al., 2014)
GC-10	21°18′27″	119°11′49″	937	3008	(Wu et al., 2010)
GC-9	21°18′27″	119°11′50″	850	3009	(Wu et al., 2013)
GC-11	21°18′29″	119°11′58″	730	3008	(Wu et al., 2013)
HD319	21°54′48″	118°54′47″	730	1730	(Wu et al., 2010)

Sampling method and survey ship description: GC, gravity coring (Taiyang), HD, large gravity piston coring (Haiyang IV).

system is in a stable state and only diffuses through molecules. This condition is consistent with the diffusion around the sediment SMTZ. The standard boundary condition used is the concentration of the main components in the pore water. These combined depth intervals were used to define the biogeochemical processes at the upper and lower boundaries of SMTZ and its surroundings, and are compared with the measured data.

The one-dimensional numerical model software PROFILE proposed by Berg et al. (1998) was used for simulation. The software first divides the sediment into any number of equally spaced blocks, and each block has a constant reaction rate. By selecting the simplest reaction rate distribution, the least square method was used to fit the best concentration curve of the data. The model conducts the F test for different solutes, ensuring the continuity of flux between regions and providing the solute flux.

According to previous research (Luo et al., 2013), sites C9 and C14 within 100 cmbsf are mainly controlled by OSR. Therefore, one-dimensional reaction-transport modeling of the pore water sulfate concentration profiles in Qiongdongnan was developed to estimate the net rates of sulfate reduction in subsurface sediments using the software PROFILE (Berg et al., 1998). The reaction rate was calculated in volume units of sediment per day (nmol cm^{-3} d^{-1}). The net reaction and net consumption per square meter per day during the interval are calculated in mmol m^{-2} d^{-1} based on the volume ratio within the interval of a determined depth. Considering the oxygen enrichment of the bottom seawater at these sites in this study, there may be biological disturbances in Taixinan Basin. Therefore, an unsteady-state scenario at GC-10, GC-9, GC-11 and HD319 sites can be supported by Fick's first law. This procedure assumed that sulfate transport only occurs *via* molecular diffusion. The assumption is largely consistent with the study sites where subsurface sediments are dominantly affected by sulfate or methane diffusion instead of advection as usually seen at methane seeps (Hu et al., 2020). Calibration of the diffusive coefficient with tortuosity was after the equation of Boudreau (1997). Here, the diffusion coefficient of sediment was calculated according to the porosity using the empirical equation of Iversen and Jørgensen (1993): $D_s = D_{sw}/[1 + 3(1-\Phi)]$.

The diffusion flux J was obtained by Fick's first law according to the pore water concentration profile (Schulz, 2006): $J = -\Phi D_s (dC/dx)$.

Here, Φ refers to the sediment porosity, set as 0.75 under stable conditions, see Wang et al. (2000). Ds is the diffusion coefficient of the whole sediment package after curve correction, C is the concentration of components in pore water, x is depth, and dc/dx is the vertical concentration gradient. This study assumed that the average pH value of sediment for all research stations was 7.5, and the bottom water temperature was uniformly set as 5 °C (refer to (Jin and Wang, 2010). The diffusion coefficients D_{SW} (m^2s^{-1}) of pore water components (SO_4^{2-}, CH_4, Ca^{2+}, DIC) at the relevant temperature and salinity were taken from Schulz (2006) and corrected for the set temperature and salinity. The D_{SW} values (m^2s^{-1}) of CH_4, SO_4^{2-}, and Ca^{2+} were 9.0 $x10^{-10}$, $5.7x10^{-10}$, and $4.3x10^{-10}$, respectively. For DIC, according to the set temperature of 5°C, the D_{SW} values of CO_3^{2-} and HCO_3^- were $5.04x10^{-10}$ and $6.09x10^{-10}$ respectively. The effective diffusion coefficients were $5.4x10^{-10}$ and $5.565x10^{-10}$, respectively.

4 Results and discussion

4.1 Microbial sulfate reduction in the pore water

We analysed 6 sediment cores, including 4 in Taixinan and 2 in Qiongdongnan, and all the geochemical data are shown in Table S1. The concentration profiles of SO_4^{2-}, CH_4, TA, DIC, H_2S and Ca^{2+}, Sr^{2+}, Mg^{2+}, $Mn^{2+}$and Ba^{2+} in the pore water of stations C9 and C14 in the Qiongdongnan Basin and GC-9, GC-10, GC-11 and HD319 in the Taixinan Basin are shown in Figure 2. The sulfate concentration profiles of C9 and C14 in Qiongdongnan Basin generally show quasilinear depletion with depth (Figure 2). Ca^{2+} concentration profiles in Qiongdongnan decreases sharply and then decreases slowly with depth. In contrast, DIC concentration profiles in Qiongdongnan generally increased with depth. Reaction-transport modeling provided close fits to the concentration data (Figure 2), which can be used to identify AOM and quantify the rates of AOM-SR (e.g., Jørgensen et al., 2019b).

Dissolved sulfate is the main electron acceptor available for the oxidation of organic matter and methane, and it is mainly supplied by diffusion from, or burial of, overlying seawater. Especially in the 0-100 cmbsf, rapid SO_4^{2-} consumption rates and concave-down

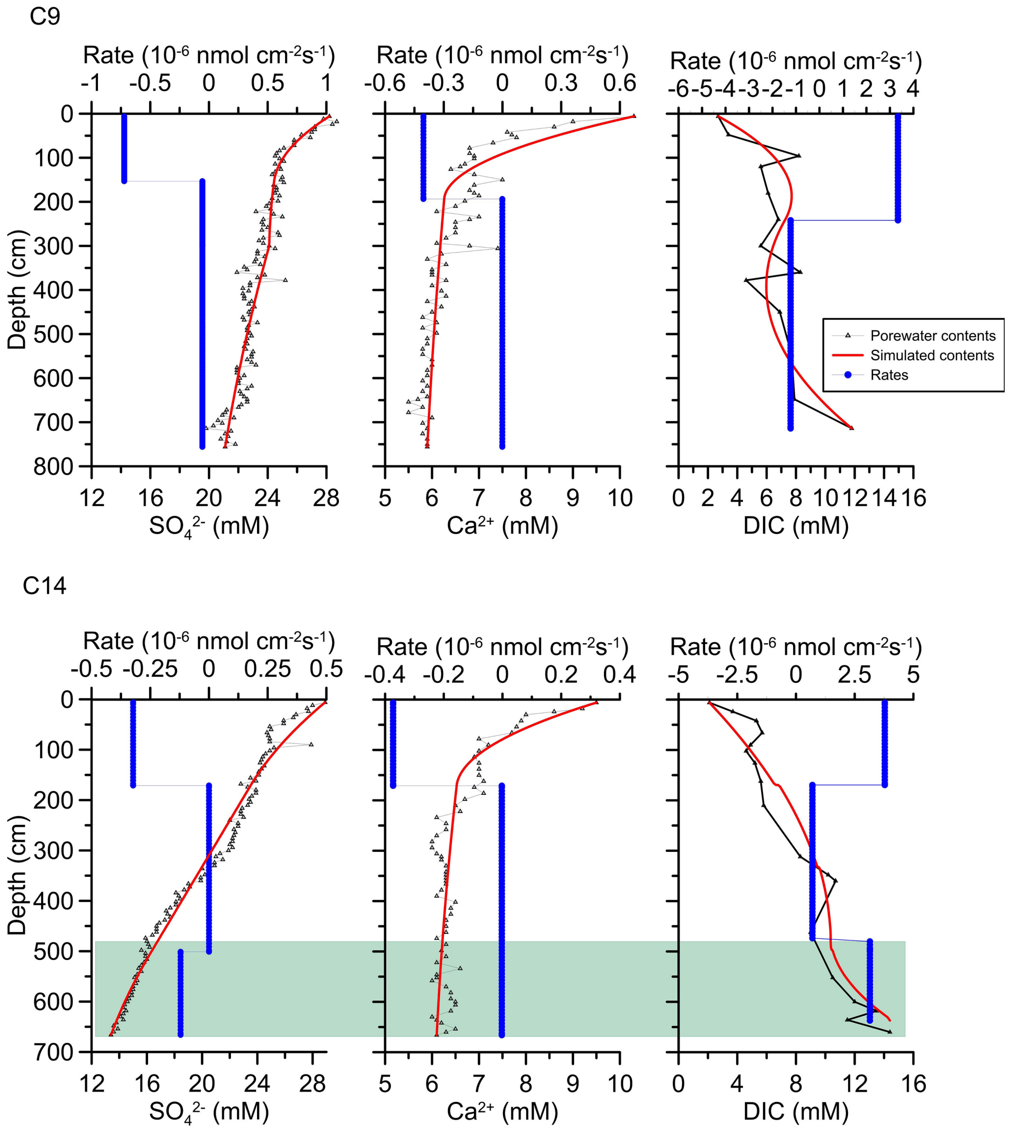

FIGURE 2

Depth profiles of pore water geochemical data for C9 and C14 sites. Black triangle with line indicates the measured concentration, red line represents the simulated concentration based on PROFILE model, and the blue line represents the net (production or consumption) reaction rate. Green shadow indicates the sulfate-methane transition zone.

curvatures at C9 and C14 sites, indicating that the microbial sulfate reduction is dominated by OSR in the uppermost sediments (Borowski et al., 1996; Hu et al., 2015; Miao et al., 2022). Jørgensen et al. (2001) showed that OSR was the most active in near-surface sediments, which was due to the high unstable organic load and sulfate flux at the sediment-water interface. Therefore, simulated OSR rates of C9 and C14 sites are $0.7*10^{-6}$ nmol cm^{-2} s^{-1} and $0.3*10^{-6}$ nmol cm^{-2} s^{-1} (Figure 2), which is relatively fast within 0-100 cmbsf. With easily degradable organic matter and sulfate being consumed, sulfate reduction rate declines, thereby resulting in less steep slopes for sulfate concentrations below 100 cmbsf. However, pore water concentration profiles of SO_4^{2-} and DIC and their reaction rate of the two sites are different below 500 cmbsf. The gradually increasing DIC concentration and slowly decrease in SO_4^{2-} consumption at C9 site are predominantly in response to OSR. For C14 site, SO_4^{2-} concentration display approximate linear decline below 500 cmbsf, and is accompanied by distinct increasing DIC concentration. Moreover, the sulfate reduction rate is $0.1*10^{-6}$ nmol cm^{-2} s^{-1} and DIC production reaction rate is $3.15*10^{-6}$ nmol cm^{-2} s^{-1} below 500 cmbsf. Compared with the sulfate reduction rate dominated by OSR at the bottom of C9 ($0.06*10^{-6}$ nmol cm^{-2} s^{-1}), it indicates that there may be additional sulfate consumption reaction and DIC production reaction at the bottom of C14. Previous studies suggested that OSR and AOM-SR co-occurrence in sediments can also result in a nearly linear change in the sulfate concentration profile (Malinverno and Pohlman, 2011). Considering the study area in Qiongdongnan Basin is located in pockmark area, it is speculated that there is probably dominated by OSR and AOM-SR in the study sites of Qiongdongnan Basin. Based on the reaction equations of OSR and AOM-SR, Luo et al. (2013) distinguished the types of sulfate reduction reaction by using the diagram of the produced DIC versus consumed sulfate ratios after correcting for carbonate precipitation. Their results showed that the ratios were close to 2:1 at the bottom of C9, while were between 1.6:1 and 1:1 at the bottom of C14. Combined with the simulated rate data, it further suggests that MSR of C9 are predominantly in response to OSR, whereas the sulfate reduction below 500 cmbsf of C14 is affected by AOM-SR. The main sulfate reduction process of C14 is caused by varying proportions of contributions from OSR and AOM-SR. But due to the diversity of methane seepages activities, such as methane seepage activity in dormancy or declining period, some discriminant MSR (OSR or AOM-SR) proxies and the boundary between OSR and AOM-SR are missing in indicating certain methane seepages activities (Miao et al., 2022).

Sulfate concentration profiles at GC-10, GC-9, GC-11 and HD319 sites in Taixinan Basin do not follow the general trend of quasi-linear decrease. In the GC-10 site (Figure 3), SO_4^{2-} concentrations display near-seawater value above 400 cmbsf, and then approximately linearly decreases to the lower level at 750 cmbsf, where H_2S and TA reach the maximum value. Below 750 cmbsf, H_2S and TA gradually decreased while methane increased sharply. Based on the above indicators, It can be seen that the specific depth of the SMTZ in GC-10 to be approximately 700-800 cmbsf (Borowski et al., 1996). Similarly, the characteristics of

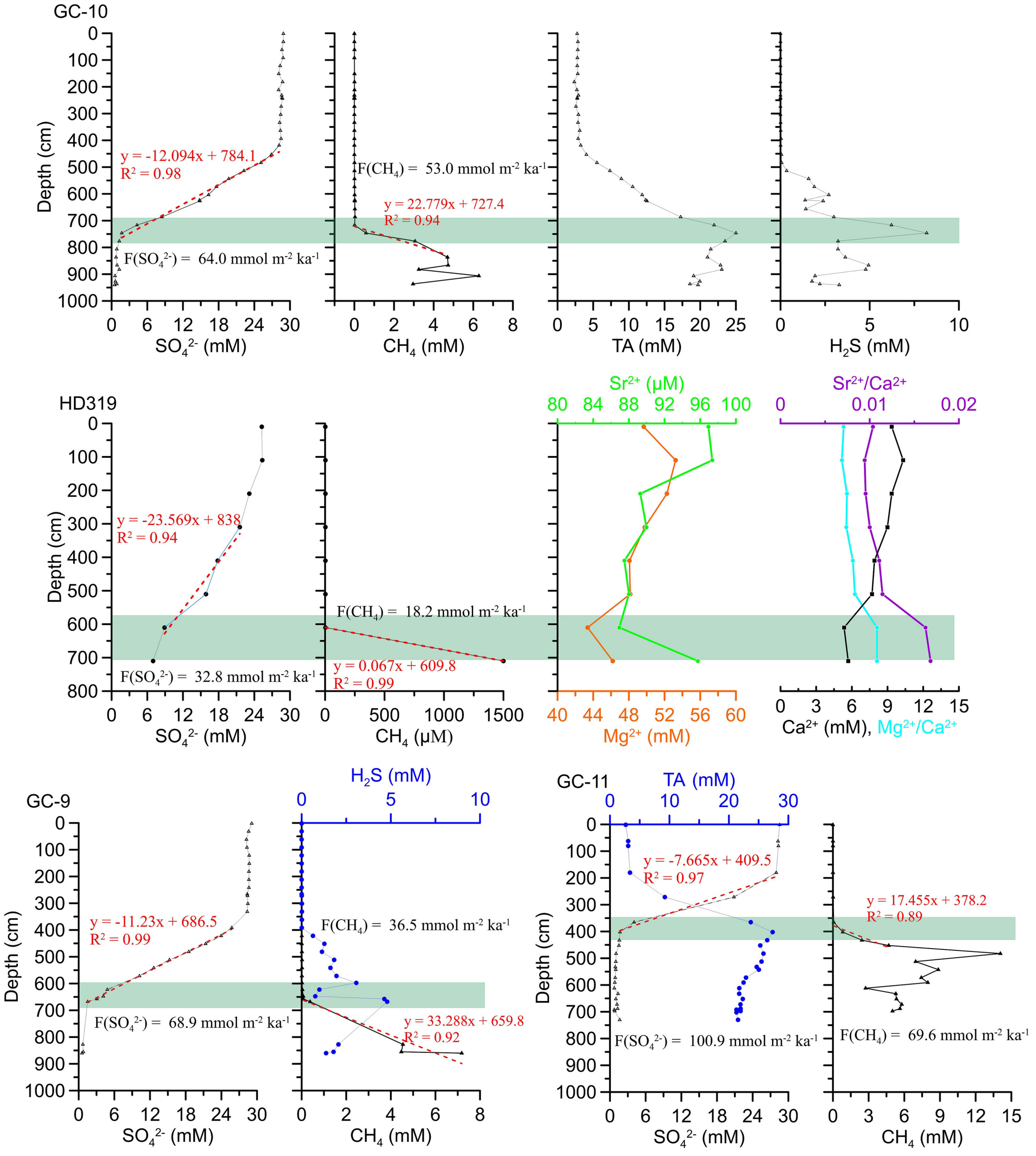

FIGURE 3
Depth profiles of pore water geochemical data for GC-9, GC-10, GC-11 and HD319 sites. Red dotted line represents CH_4 or SO_4^{2-} concentration linear fitting curve entering the sulfate-methane transition zone. Green shadow indicates sulfate-methane transition zone.

methane, SO_4^{2-}, H_2S and TA in pore water of stations GC-9 and GC-11 also have similar characteristics (Figure 3), it can be said that the SMTZ of GC-9 and GC-11 are 600-700 cmbsf and 350-450 cmbsf respectively. The SO_4^{2-} curve of pore water at HD319 site presents a convex up curve above 300 cmbsf and then basically quasilinearly decline with depth. It's similar to those metal ions (Ca^{2+}, Sr^{2+} and Mg^{2+}) concentration profiles at HD319 site, which all come from the overlying seawater. Also metal ions reached at low points at ~ 600 cmbsf where methane starts to increase sharply, indicating that SMTZ at HD319 is around ~ 600 cmbsf. Methane seepage provides nutrient components for anaerobic methanotrophic archaea and associated sulfate-reducing bacteria in marine sediments. The ascending methane is largely consumed at the SMTZ, producing peak concentration of DIC and total alkalinity by AOM-SR (Hu et al., 2019). In methane seep environments, pore water concentration depth profiles in shallow sediments often exhibit negative anomalies of Ca^{2+}, Mg^{2+} and Sr^{2+} concentrations, and these concentration changes can be used to identify the mineralogy of the carbonate which has currently precipitated from solution (Nöthen and Kasten, 2011). The rapid consumption of Ca^{2+}, Mg^{2+} and Sr^{2+} (Figure 2) and pore water Sr^{2+}/Ca^{2+} and Mg^{2+}/Ca^{2+} weight ratios increase within SMTZ in HD319 are most likely due to high-Mg calcite precipitation (Mazzini et al., 2006). In the present study, distinctly shallower SMTZs are observed at the ~400-800 cmbsf, which may further support high Mg-calcite precipitation in shallow sediments of four study sites in Taixinan Basin. This observation confirms that these sites are affected by methane intensities and the AOM process increases sulfate consumption, resulting in the net (production or consumption) of the main components in pore water.

Although Borowski et al. (Borowski et al., 1996; Borowski et al., 1999) showed that the change of sulfate content was mainly affected by AOM, the change of organic matter content in sediment had little effect on the gradient of sulfate concentration. Attentively, there is still sulfate concentration at the bottom of GC-10, GC-9, GC-11 and HD319 sites in Taixinan Basin, indicating that sedimentary columns contain a transition zone where methane and sulfate coexist, which is attributed to the kinetic factors of active intermediates involved in sulfide reoxidation back to sulfate (Dale et al., 2009; Holmkvist et al., 2011). Therefore, the anaerobic oxidation of methane consumes sulfate, with a stoichiometry of 1:1, thereby competing with OSR. Methane concentration gradients below the SMTZ can be used to estimate AOM rates, while sulfate concentration gradient entering SMTZ can be used to estimate sulfate reaction rate. The risk of underestimating AOM rates exists by using methane concentration gradients due to the rapid decrease in pressure. Nevertheless, in order to avoid the factors of methane escape as much as possible, studies of only some sites from limited area of the South China Sea have carefully reported methane concentration data, our GC-10, GC-9, GC-11 and HD319 sites included. Consequently, the attempt to use methane concentration gradients to constrain AOM rates is still common in the South China Sea (Chen et al., 2017; Hu et al., 2020). In all the sites from Taixinan Basin, obvious discrepancy between sulfate fluxes and methane fluxes calculated from Fick's first law are shown in Figure 2. Based on fluxes of sulfate and methane, it can be seen that the values of methane flux are always lower than those of total sulfate reduction of sulfate diffusive flux. In contrast to previous studies in similar environments, OSR was not negligible. It can be seen that the steeper the sulfate concentration gradient, the lower the sulfate reduction rate and the smaller the methane flux. This is consistent with the conclusion that methane flux plays an important role in controlling sulfate consumption in the previous study of cold seep areas (Borowski et al., 2000; Yang et al., 2010; Wu et al., 2013), and also indirectly shows the reliability of our calculation results. Therefore, it can be said that sulfate consumption is not only due to AOM in seep sediments affected by methane seepage, but also probably has related to OSR buried in the sediments.

4.2 Coupled sulfur and oxygen isotope compositions of sulfate

MSR process is characterized by complex multi-step evolution (Gilad et al., 2013) (Figure 4). First sulfate-reducing bacteria ingest sulfate and the sulfate is activated with adenosine triphosphate (ATP) to form Adenosine 5' Phosphosulfate (APS); next, the APS is reduced to SO_3^{2-}, and finally the SO_3^{2-} is reduced to H_2S and eliminate it from their cells. The S isotope fractionation effect ($\epsilon^{34}S = \delta^{34}SSO4 - \delta^{34}SH2S$) generated in MSR process mainly depends on two factors: (1) the original sulfur isotope ratio of reactants participating in each reaction step; and (2) the degree of each reversible reaction also plays a key role, due to all reactions occurring in cells are reversible during those series of processes (Rees, 1973; Brunner et al., 2005; Gilad et al., 2013; Gilad et al., 2014). During MSR (including OSR and AOM-SR), sulfate-reducing bacteria selectively preferentially ingest the lighter ^{32}S in sulfate, resulting in obvious sulfur isotope fractionation. This reaction forms H_2S with lower ^{34}S isotope values, resulting in the residual sulfate with higher ^{34}S isotope values (Canfield, 2001; Böttcher et al., 2006; Deusner et al., 2014). In addition, previous studies also noted a relationship between the magnitude of the sulfur isotope fractionation and the sulfate reduction rate (Aharon and Fu, 2000; Stam et al., 2011; Gilad et al., 2013; Bradbury et al., 2021; Chen et al., 2022). In all these studies, higher sulfur isotope fractionation corresponded to slower sulfate reduction rates.

To better understand the control mechanisms affecting two MSR processes (OSR, AOM-SR), this study further analyzed S and O isotopes ($\delta^{18}O_{SO4}$ vs. $\delta^{34}S_{SO4}$) of dissolved sulfate at C9 and C14 in

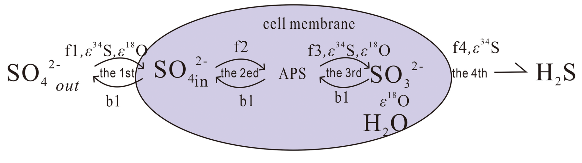

FIGURE 4
Schematic diagram showing the steps during the bacterial sulfate reduction. Arrows fi (i=1,2,3) represent the forward reaction while bi (i=1,2,3) represent the backward reactions during this process. $\epsilon^{34}s$ and $\epsilon^{18}o$ are isotope fractionation effects for sulfur and oxygen. Modified after (Fotherby et al., 2021).

Qiongdongnan basin. $\delta^{18}O_{SO4}$ and $\delta^{34}S_{SO4}$ increase fastest with sediment depth above 400 cmbsf and slowest below that depth (Figures 5A, B). They increase linearly from close to the seawater values [$\delta^{34}S_{SO4}$ = +21.24‰, (Tostevin et al., 2014); $\delta^{18}O_{SO4}$ = +8.7‰, (Johnston et al., 2014)]. Over the two sites there is a similar increase in $\delta^{18}O_{SO4}$ and $\delta^{34}S_{SO4}$; as mentioned above this slope has been linked to the overall cell-specific rate of MSR, suggesting a similar rate in sediments above 400 cmbsf. However, there is a different rate in sediments below 400 cmbsf at C9 and C14. It appears that $\delta^{34}S_{SO4}$ may increase slightly faster than $\delta^{18}O_{SO4}$ at C14 site. Moreover, we noted that the cross plot of $\delta^{18}O_{SO4}$ vs. $\delta^{34}S_{SO4}$ comes out of the apparent linear phase (Figure 5B: The pink shadow area), where the $\delta^{18}O_{SO4}$ values change slowly as the $\delta^{34}S_{SO4}$ values continue to increase. As for C9 site, the $\delta^{18}O_{SO4}$ and $\delta^{34}S_{SO4}$ values covary, and into the equilibration phase (Figure 5B: The gray shadow area).

According to the above discussion, the relative enrichment of $\delta^{18}O_{SO4}$ and $\delta^{34}S_{SO4}$ values is affected by different sulfate reduction rates and reaction mechanisms (such as OSR and AOM). The faster the sulfate reduction rate, the more constrained the O exchange process between the sulfur intermediate (SO_3^{2-}) and the surrounding water intracellularly (H_2O), resulting in an enrichment of O isotopes less than that of S isotopes. Therefore, the slope of the S-O isotope growth curve appears lower in the $\delta^{18}O_{SO4}/\delta^{34}S_{SO4}$ ratios mapping below 400 cmbsf (Figure 5) (Böttcher et al., 1998; Aharon and Fu, 2000; Gilad et al., 2013; Gilad et al., 2014). Predecessors (Gilad et al., 2014; Tostevin et al., 2014; Antler et al., 2015; Chen et al., 2022) compared and analyzed the pore water data of strong methane seeps (methane in excess) and in typical sedimentary environments (methane diffusion limited). They found that the slope of the sulfate S-O isotope curve in cold seeps ($\delta^{18}O_{SO4}/\delta^{34}S_{SO4}$ ratio) is far lower than the normal sedimentary environment, so it can be used to indicate whether the sedimentary environment is rich in methane fluids.

Take C14 site as an example, the steep slope is consistent with a normal sedimentary environment above 400 cmbsf (Figure 5B), further illustrating the primary role of OSR. Based on previous research results, it can be said that H_2S is produced during MSR or simple sulfide and other sulfur intermediates in the sediments occur, reoxidation of sulfide occurs and is disproportionation to reproduce sulfate again, accompanied by O isotope exchange with water intracellularly, resulting in significant positive correlations of $\delta^{18}O_{SO4}$ vs. $\delta^{34}S_{SO4}$ (Thamdrup et al., 1993; Böttcher et al., 2001; Chen et al., 2022). Although the $\delta^{18}O_{SO4}$ and $\delta^{34}S_{SO4}$ values below 400 cmbsf are similar to the isotope model in the methane diffusion environment (Figure 5B) (Gilad et al., 2014; Antler et al., 2015; Chen et al., 2022), the O isotopes of pore water sulfate do not significantly change with depth. Balci et al. (2007) suggested that the sulfate formed by the oxidation of pyrites in the sediment under the aerobic environment has a relatively stable O isotope value (about 5 ‰). Besides, if iron oxides are encountered during disproportionation, the sulfate generated in this process is more enriched with ^{18}O (Böttcher et al., 2001). Therefore, it is speculated that the constraint of $\delta^{18}O_{SO4}$ vs. $\delta^{34}S_{SO4}$ below 400 cmbsf at C14 may be dominated by OSR and AOM-SR. Faster MSR limits the exchange of O atoms between sulfur intermediates and the surrounding water intracellularly, and inhibits the growth of O isotopes. This conclusion indicates that in the recession or dormancy period of methane seepage, organic matter and residual methane fluids may jointly constraint the consumption of sulfate in pore water.

The two sites C9 and C14 in Qiongdongnan basin, have a large difference in the apparent sulfur isotope fractionation as evidenced by the change in $\delta^{34}S_{SO4}$; often when using the change in the isotopic composition of pore fluid to resolve the sulfur isotope fractionation factor during MSR, Rayleigh distillation is used (Rudnicki et al., 2001; Breukelen and Prommer, 2008). When the apparent sulfur isotope fractionation is calculated using this simple closed-system Rayleigh fractionation approach, significantly different sulfur isotope fractionation factors are calculated for sites C9 and C14 (Figure 6; C14 at -32‰ and C9 at -44.5‰). This feature may be related to

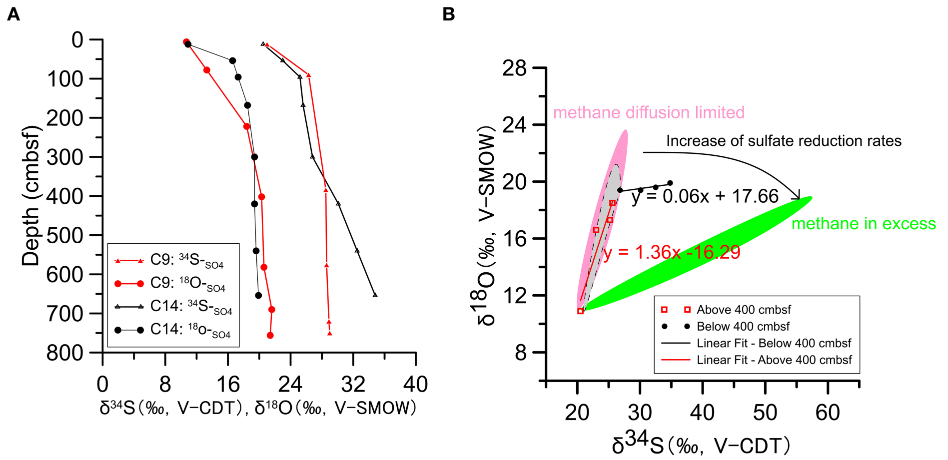

FIGURE 5

(A) S and O isotopic composition of sulfate in pore water at stations C9 and C14. **(B)** The $\delta^{18}O_{sulfate}$ versus $\delta^{34}S_{sulfate}$ data from pore water sulfate for studies sites. The lines represent the general increasing trends of pore water sulfate in a $\delta^{18}O_{sulfate}$ versus $\delta^{34}S_{sulfate}$ plot, which are based on the environmental pore water data. The pink and green shadows for "methane diffusion limited" and "methane in excess" environments, while the gray shadow for possible trend of $\delta^{18}O_{sulfate}$ versus $\delta^{34}S_{sulfate}$ at station C9.

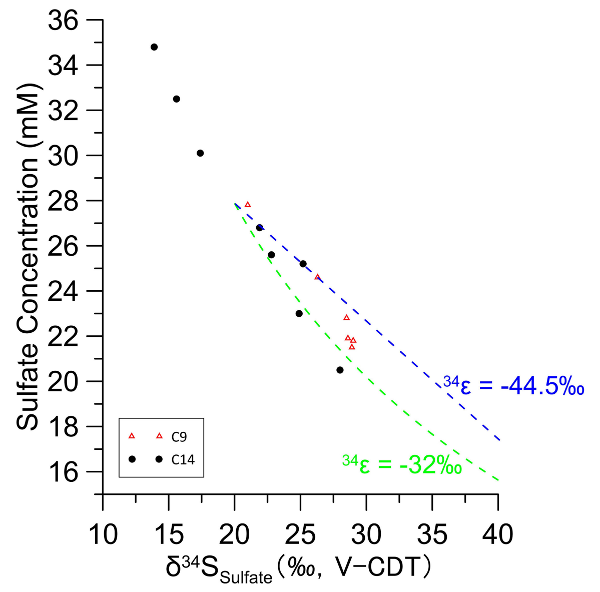

FIGURE 6
The increase in the sulfur isotope composition of sulfate as a function of the decrease in pore fluid sulfate concentrations.

different MSR processes at the bottom of the two sites. The deeper part of C14 is related to weak methane seepage, which accelerates the MSR rate. On the contrary, with the higher sulfate reduction rate at C14 site, metabolizable organic matter and weakly diffusion methane has a more significant impact on the apparent or observed sulfur isotope fractionation. Whereas the lower rate of OSR at C9 site may lower the impact methane diffusion has on the apparent evolution of the sulfur isotopic composition of the pore fluid.

In conclusion, the sulfur and oxygen isotope compositions of sulfate in pore water show that in addition to the oxidation of H_2S and the disproportionation of S intermediates, organoclastic sulfate reduction also play an important role in sulfur isotope fractionation. Evidence from Rayleigh fractionation approach shows that the sulfur and oxygen isotopes in the residual sulfate pool between organoclastic sulfate reduction and anaerobic oxidation of methane are significantly different, which are mainly affected by sulfate reduction rate and sulfur disproportionation in different degrees. These results highlight a role for organic matter during microbial sulfate reduction in cold seeps.

4.3 Influence of methane seepages on MSR

The results showed that most of the sulfate in the study area is consumed in the SMTZ, and all SMTZs except the C9 station are shallow (600-800 cmbsf). Studies by Jiang et al. (2005), Fang and Chu (2008), Yang et al. (2010) and suggested that the SMTZ position in the northern South China Sea is about 10 mbsf. The SMTZs in this study are consistent with previous studies (Borowski et al., 1996; Borowski et al., 2000; Wu et al., 2013; Miao et al., 2022). These shallow SMTZ indicate that there are relatively stable high fluxes of methane in the sediment, which enables the mutual consumption of sulfate and methane to continue. AOM existence sustained by intense methane seepages in the cold seep sediments, which may be affected by decomposition of the underlying natural gas hydrates (Liu et al., 2012). Recent studies have shown that methane seepage flux is unstable in both time and space, and is closely related to the decomposition and reformulation of natural gas hydrates (Teichert et al., 2003; Lin et al., 2016). Zhang et al. (2019) used the reaction transport model to study the spatial distributions of different biogeochemical processes in different sea areas of the South China Sea, which showed that methane flux was unevenly distributed and the rate of organic matter degradation in Qingdongnan basin was slightly higher than those in the Taixinan area. This may be related to underlying gas hydrates (Wu et al., 2013). All of this seem that OSR did occur in our sediments. The discrepancy in fluxes of sulfate and methane calculated from Fick's first law also supports occurrence of OSR at our study sites. Previous studies also showed that the ratio of sulfate flux to methane flux in SMTZ is 1.4:1 rather than 1:1. This means that about 40% of sulfate in SMTZ is consumed through OSR (Berelson et al., 2005; Lin et al., 2017; Egger et al., 2018).

A simplified model (Figure 7) shows how microbial sulfate reduction (OSR and AOM-SR) affects sulfur and oxygen isotope compositions of residual sulfate in pore water. (a) In a marine sedimentary environment, the reaction process dominated by OSR controls the stable growth and change in the S and O isotopes in residual sulfate. In addition to the OSR process with organic matter as the matrix, H_2S re-oxidation and biological disproportionation also play an essential role in the sulfur fractionation, thus accelerating the exchange of oxygen isotopes in the reaction process, leading to the rapid growth of O isotopes. (b) With low levels of methane, the sulfur and oxygen isotopes in the residual sulfate pool are controlled by the combined OSR and AOM-SR. Due to weak anaerobic oxidation of methane, sulfate reduction rate is slower and the sulfur disproportionation is significant at sulfate-methane transition zone. (c) During strong methane seepages, microbial sulfate reduction in sediments is mainly controlled by intense anaerobic oxidation of methane, but there is a certain relationship with organic matter metabolism process. The intense AOM results in a faster sulfate reduction rate and a less degree fractionation of sulfur and oxygen isotopes. In conclusion, the S and O isotopic enrichment relationship of sulfate in pore water can effectively judge and study different biogeochemical processes in sediments. In particular, it is necessary to distinguish different MSR mechanisms affected by intensity of methane seepages. Nonetheless, to what extent the impact of organic matter from cold seep sediments on the S and O isotopes in residual sulfate remains to be investigated.

5 Conclusions

This paper used pore water data combined with PROFILE model and fluxes of methane and sulfate in Qiongdongnan and Taixinan basins to conduct a geochemical study of the sites to further clarify miarobial sulfate reduction process related to OSR and AOM-SR under the background of methane seepages. Our results suggest that SMTZ positions in all study sites are roughly ~600 to 800 cmbsf,

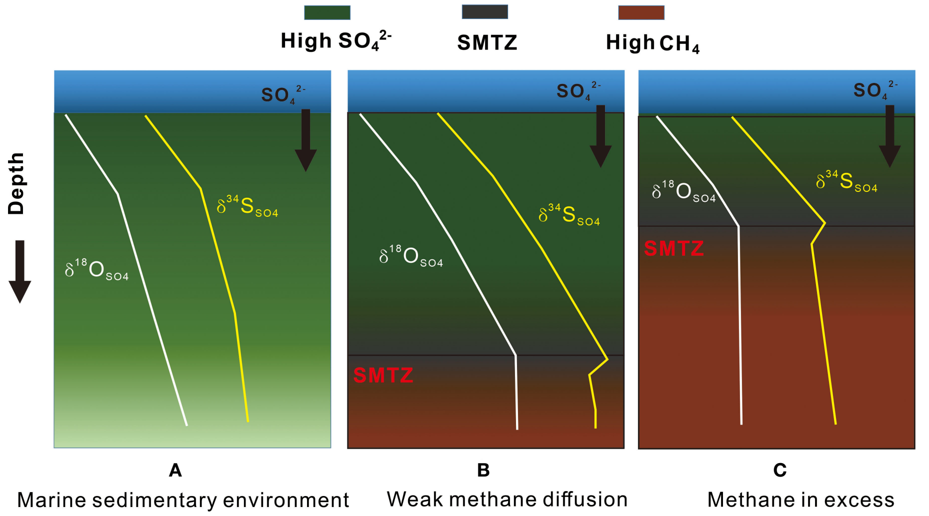

FIGURE 7
Variations of $\delta^{18}O_{SO4}$ and $\delta^{34}S_{SO4}$ with depth. **(A)** represents the normal marine sedimentary environment without methane impact; **(B)** represents the sedimentary environment with weak methane diffusion; **(C)** represents the sedimentary environment with methane in excess.

which is relatively shallower compared to international SMTZs in cold seeps. The values of methane flux are always lower than those of total sulfate reduction of sulfate diffusive flux. Combined with $\delta^{34}S_{SO4}$ vs. $\delta^{18}O_{SO4}$ of residual sulfate, it can be said that the coexistence of OSR and AOM-SR in methane seep sediments in Qiongdongnan. Beyond the intensity of methane seepages, the presence of OSR to a greater extent results in affecting the microbial sulfate reduction rate, and thus causing fractionation of sulfur and oxygen isotopes in residual sulfate pool. This emphasizes that the traditional redox order of bacterial respiration is highly simplified, where, in sediments such as these seeps, all of these processes can occur together with complex couplings between them. Nonetheless, further studies remain to be investigated.

Data availability statement

The datasets presented in this study can be found in online repositories. The names of the repository/repositories and accession number(s) can be found in the article/Supplementary Material.

Author contributions

TS designed and wrote the manuscript and analyzed the modeled data related to the pore water. DW designed the study and provided pore water data in Taixinan Basin. PY and NW helped to revise the manuscript and give some useful suggestions. All authors contributed to the article and approved the submitted version.

Funding

This work was financially supported by the Postdoctoral Foundation of Qingdao (Grant QDBSH20220202138), the China Geological Survey Project (NO. DD20190276) and the Fund of Ministry of Science and Technology (Nos 2013FY112200 and 2019YFE0127200).

Acknowledgments

We are grateful to the editors and reviewers for their constructive comments on our manuscript.

Conflict of interest

The authors declare that the research was conducted in the absence of any commercial or financial relationships that could be construed as a potential conflict of interest.

The reviewer RY declared a shared affiliation with the authors TS, NW, PY to the handling editor at the time of review.

Publisher's note

Supplementary material

The Supplementary Material for this article can be found online at: https://www.frontiersin.org/articles/10.3389/fmars.2023.1111133/full#supplementary-material

References

Aharon, P., and Fu, B. (2000). Microbial sulfate reduction rates and sulfur and oxygen isotope fractionations at oil and gas seeps in deepwater gulf of Mexico. *Geochimica Cosmochimica Acta* 64, 233–246. doi: 10.1016/S0016-7037(99)00292-6

Antler, G., Turchyn, V., Herut, B., and Sivan, O. (2015). A unique isotopic fingerprint of sulfate-driven anaerobic oxidation of methane. *Geology* 43 (7), 619–622. doi: 10.1130/G36688.1

Balci, N., Shanks, W., Mayer, B., and Mandernack, K. (2007). Oxygen and sulfur isotope systematic of sulfate produced by bacterial and abiotic oxidation of pyrite. *Geochimica Cosmochimica Acta* 71, 3796–3811. doi: 10.1016/j.gca.2007.04.017

Berelson, W., Prokopenko, M., Sansone, F., Graham, A., McManus, J., and Bernhard, J. (2005). Anaerobic diagenesis of silica and carbon in continental margin sediments: Discrete zones of TCO_2 production'. *Geochimica Cosmochimica Acta* 69, 4611–4629. doi: 10.1016/j.gca.2005.05.011

Berg, P., Risgaard-Petersen, N., and Rysgaard, Søren (1998). Interpretation of measured concentration profiles in sediment pore water. *Limnol. Oceanogr.* 13, 395–411. doi: 10.4319/lo.1998.43.7.1500

Berner, R., de Leeuw, J., Spiro, B., Murchison, D., and Eglinton, G. (1985). Sulphate reduction, organic matter decomposition and pyrite formation [and discussion]. *Philos. Trans. R. Soc. A: Mathematical Phys. Eng. Sci.* 315, 25–38. doi: 10.1098/rsta.1985.0027

Boetius, A., Ravenschlag, K., Schubert, J.C., Rickert, D., and Widdel, F. (2000). A marine microbial consortium apparently mediating anaerobic oxidation of methane. *Nature* 407, 623–629. doi: 10.1038/35036572

Borowski, W., Paull, C., and Ussler, B. (1999). Global and local variations of interstitial sulfate gradients in deep-water, continental margin sediments: Sensitivity to underlying methane and gas hydrates. *Mar. Geology* 159, 131–154. doi: 10.1016/S0025-3227(99)00004-3

Borowski, W., Hoehler, T., Alperin, M., Rodriguez, N., and Paull, C. (2000). Significance of anaerobic methane oxidation in methane-rich sediments overlying the Blake ridge gas hydrates. *Proc. Ocean Drilling Program: Sci. Results* 164, 87–99. doi: 10.2973/odp.proc.sr.164.214.2000

Borowski, W., Paull, C., and Ussler, B. (1996). Marine pore-water sulfate profiles indicate *in situ* methane flux from underlying gas hydrate. *Geology* 24, 655–658. doi: 10.1130/0091-7613(1996)024<0655:MPWSPI>2.3.CO;2

Böttcher, M. E. (1998). Manganese (II) partitioning during experimental precipitation of rhodochrosite–calcite solid solutions from aqueous solutions. *Mar. Chem.* 62, 287–297. doi: 10.1016/S0304-4203(98)00039-5

Böttcher, M., Boetius, A., and Rickert, D. (2006). *Sulfur isotope fractionation during microbial sulfate reduction associated with anaerobic methane oxidation*. European Geosciences Union. doi: 1607-7962/gra/EGU06-A-10040

Böttcher, M. E., Brumsack, H. J., and Lange, G. (1998). Sulfate reduction and related stable isotope (^{34}S, ^{18}O) variations in interstitial waters from the Eastern Mediterranean. In A. H. F. Robertson, K.-C. Emeis, C. Richter and A. Camerlenghi *Proccedings of the Ocean Drlling Program, Leg 160.* (Eastern Mediterranean. College Station, TX: Ocean Drilling Program). 365–373. doi: 10.2973/odp.proc.sr.160.002.1998

Böttcher, M., Thamdrup, Bo, and Vennemann, T. (2001). Oxygen and sulfur isotope fractionation during anaerobic bacterial disproportionation of elemental sulfur. *Geochimica Cosmochimica Acta* 65, 1601–1609. doi: 10.1016/S0016-7037(00)00628-1

Boudreau, B. P. (1997). Diagenetic models and their implementation. *Springer*. doi: 10.1007/978-3-642-60421-8

Bradbury, H. J., Turchyn, A. V., Bateson, A., Antler, G., Fotherby, A., Druhan, J. L., et al. (2021). The carbon-sulfur link in the remineralization of organic carbon in surface sediments. *Front. Earth Sci.* 9, 652960. doi: 10.3389/feart.2021.652960

Breukelen, B., and Prommer, H. (2008). Beyond the Rayleigh equation: Reactive transport modeling of isotope fractionation effects to improve quantification of biodegradation. *Environ. Sci. Technol.* 42, 2457–2463. doi: 10.1021/es071981j

Brunner, B., Bernasconi, S., Kleikemper, J., and Schroth, M. (2005). A model for oxygen and sulfur isotope fractionation in sulfate during bacterial sulfate reduction processes. *Geochimica Cosmochimica Acta* 69, 4773–4785. doi: 10.1016/j.gca.2005.04.017

Canfield, D. (2001). Isotope fractionation by natural populations of sulfate-reducing bacteria. *Geochimica Cosmochimica Acta* 65, 1117–1124. doi: 10.1016/S0016-7037(00)00584-6

Canfield, D., Olesen, C., and Cox, R. (2006). Temperature and its control of isotope fractionation by a sulfate-reducing bacterium. *Geochimica Cosmochimica Acta* 70, 548–561. doi: 10.1016/j.gca.2005.10.028

Chen, T., Strauss, H., Fang, Y., Lin, Z., Sun, X., Liu, J., et al. (2022). Sulfur and oxygen isotope records of sulfate-driven anaerobic oxidation of methane in diffusion-dominated marine sediments. *Front. Earth Sci.* 10, 862333. doi: 10.3389/feart.2022.862333

Chen, N.-C., Yang, T. F., Hong, W.-L., Chen, H.-W., Chen, H.-C., Hu, C.-Y., et al. (2017). Production, consumption, and migration of methane in accretionary prism of southwestern Taiwan. *Geochemistry Geophysics Geosystems* 18 (8), 2970–2989. doi: 10.1002/2017GC006798

Dale, A., Regnier, P., Van Cappellen, P., Fossing, H., Jensen, Jørn, and Jørgensen, Bo (2009). Remote quantification of methane fluxes in gassy marine sediments through seismic survey. *Geology* 37, 235–238. doi: 10.1130/G25323A.1

Deusner, C., Holler, T., Arnold, G. L., Bernasconi, S. M., Formolo, M. J., and Brunner, B. (2014). Sulfur and oxygen isotope fractionation during sulfate reduction coupled to anaerobic oxidation of methane is dependent on methane concentration. *Earth Planetary Sci. Lett.* 399, 61–73. doi: 10.1016/j.epsl.2014.04.047

Egger, M., Riedinger, N., Mogollón, J., and Jørgensen, Bo (2018). Global diffusive fluxes of methane in marine sediments. *Nat. Geosci.* 11, 421–425. doi: 10.1038/s41561-018-0122-8

Fang, Y., and Chu, F. (2008). The relationship of sulfate-methane interface,the methane flux and the underlying gas hydrate. *Mar. Sci. Bull.* 10, 28–37.

Fotherby, A., Bradbury, H., Antler, G., Sun, X., Druhan, J., and Turchyn, A. (2021). Modelling the effects of non-steady state transport dynamics on the sulfur and oxygen isotope composition of sulfate in sedimentary pore fluids. *Front. Earth Sci.* 8. doi: 10.3389/feart.2020.587085

Gilad, A., Turchyn, A., Herut, B., Davies, A., Rennie, V., and Sivan, O. (2014). Sulfur and oxygen isotope tracing of sulfate driven anaerobic methane oxidation in estuarine sediments. *Estuarine Coast. Shelf Sci.* 142, 4–11. doi: 10.1016/j.ecss.2014.03.001

Gilad, A., Turchyn, A., Rennie, V., Herut, B., and Sivan, O. (2013). Coupled sulfur and oxygen isotope insight into bacterial sulfate reduction in the natural environment. *Geochimica Cosmochimica Acta* 118, 98–117. doi: 10.1016/j.gca.2013.05.005

Han, X., Suess, E., Huang, Y., Wu, N., Bohrmann, G., Su, X., et al. (2008). Jiulong methane reef: Microbial mediation of seep carbonates in the south China Sea. *Mar. Geology* 249, 243–256. doi: 10.1016/j.margeo.2007.11.012

Holmkvist, L., Kamyshny, A., Vogt, C., Vamvakopoulos, K., Ferdelman, T., and Jørgensen, Bo (2011). Sulfate reduction below the sulfate–methane transition in black Sea sediments. *Deep Sea Res. Part I: Oceanographic Res. Papers* 58, 493–504. doi: 10.1016/j.dsr.2011.02.009

Hu, Yu, Feng, D., Liang, Q., Xia, Z., Chen, L., and Chen, D. (2015). Impact of anaerobic oxidation of methane on the geochemical cycle of redox-sensitive elements at cold-seep sites of the northern south China Sea. *Deep Sea Res. Part II: Topical Studies in Oceanography* 122, 84–94. doi: 10.1016/j.dsr2.2015.06.012

Hu, Y., Feng, D., Peckmann, J., Gong, S., Liang, Q., Wang, H., et al. (2020). The impact of diffusive transport of methane on pore-water and sediment geochemistry constrained by authigenic enrichments of carbon, sulfur, and trace elements: A case study from the shenhu area of the south China Sea. *Chem. Geology* 553, 119805. doi: 10.1016/j.chemgeo.2020.119805

Hu, Y., Liang, Q., Chen, L., Feng, D., Yang, S., Liang, J., et al. (2019). Pore fluid compositions and inferred fluid flow patterns at the haima cold seeps of the south China Sea. *Mar. Petroleum Geology* 103, 29–40. doi: 10.1016/j.marpetgeo.2019.01.007

Iversen, N., and Jørgensen, B. (1993). Diffusion coefficients of sulfate and methane in marine sediments: Influence of porosity. *Geochimica Cosmochimica Acta* 57, 571–578. doi: 10.1016/0016-7037(93)90368-7

Jørgensen, N. (1992). Methane-derived carbonate cementation of Holocene marine sediments from kattegat, Denmark. *Continental Shelf Res.* 12, 1209–1218. doi: 10.1016/0278-4343(92)90080-4

Jørgensen, B., Beulig, F., Egger, M., Petro, C., Scholze, C., and Røy, H. (2019b). Organoclastic sulfate reduction in the sulfate-methane transition of marine sediments. *Geochimica Cosmochimica Acta* 254, 231–245. doi: 10.1016/j.gca.2019.03.016

Jørgensen, Bo B., Böttcher, M. E., Lüschen, H., Neretin, L. N., and Volkov., I. I. (2004). Anaerobic methane oxidation and a deep H2S sink generate isotopically heavy sulfides in black Sea sediments. *Geochimica Cosmochimica Acta* 68, 2095–2118. doi: 10.1016/j.gca.2003.07.017

Jørgensen, Bo B., Findlay, A. J., and Pellerin, André (2019a). The biogeochemical sulfur cycle of marine sediments. *Front. Microbiol.* 10, 1–27. doi: 10.3389/fmicb.2019.00849

Jørgensen, Bo B., Weber, A., and Zopfi, J. (2001). 'Sulfate reduction and anaerobic methane oxidation in black Sea sediments. *Deep Sea Res. Part I: Oceanographic Res. Papers* 48, 2097–2120. doi: 10.1016/S0967-0637(01)00007-3

Jiang, S. Y., Yang, T., Xue, Z. C., Yang, J. H., Ling, H. F., Wu, N., et al. (2005). Chlorine and sulfate concentrations in pore waters from marine sediments in the north margin of the south China Sea and their implications for gas hydrate exploration. *Geoscience* 19 (1), 45–54. doi:1000-8527(2005)01-0045-10

Jin, C., and Wang, J. (2010). A preliminary study of the gas hydrate stability zone in the south China Sea. *Acta Geologica Sinica-English Edition* 76, 423–428. doi: 10.1111/j.1755-6724.2002.tb00095.x

Johnston, D. T., Gill, B. C., Masterson, A., Beirne, E., Casciotti, K. L., Knapp, A. N., et al. (2014). Placing an upper limit on cryptic marine sulphur cycling. *Nature* 513, 530–533. doi: 10.1038/nature13698

Knittel, K., and Boetius, A. (2009). Anaerobic oxidation of methane: Progress with an unknown process. *Annu. Rev. Microbiol.* 63, 311–334. doi: 10.1146/annurev.micro.61.080706.093130

Liang, Q., Hu, Y., Feng, D., Peckmann, J., Chen, L., Yang, S., et al. (2017). Authigenic carbonates from newly discovered active cold seeps on the northwestern slope of the south China Sea: Constraints on fluid sources, formation environments, and seepage dynamics. *Deep Sea Res. Part I: Oceanographic Res. Papers* 124, 31–41. doi: 10.1016/j.dsr.2017.04.015

Lin, Z., Lu, Y., Xu, L., Gong, J., Lu, H., Teichert, B., et al. (2016). Stable isotope patterns of coexisting pyrite and gypsum indicating variable methane flow at a seep site of the shenhu area, south China sea'. *J. Asian Earth Sci.* 123, 213–223. doi: 10.1016/j.jseaes.2016.04.007

Lin, Z., Strauss, H., Lu, Y., Gong, J., Xu, L., Lu, H., et al. (2017). Multiple sulfur isotope constraints on sulfate-driven anaerobic oxidation of methane: Evidence from authigenic pyrite in seepage areas of the south China Sea. *Geochimica Cosmochimica Acta* 211, 153–173. doi: 10.1016/j.gca.2017.05.015

Liu, C., Ye, Y., Meng, Q.-G., He, X., Lu, H., Zhang, J., et al. (2012). The characteristics of gas hydrates recovered from shenhu area in the south China Sea. *Mar. Geology* 307-310, 22–27. doi: 10.1016/j.margeo.2012.03.004

Luo, M., Chen, L., Tong, H., Yan, W., and Chen, D. (2014). Gas hydrate occurrence inferred from dissolved cl– concentrations and δ18O values of pore water and dissolved sulfate in the shallow sediments of the pockmark field in southwestern xisha uplift, northern south China Sea. *Energies* 7, 3886–3899. doi: 10.3390/en7063886

Luo, M., Chen, L., Wang, S., Yan, W., Wang, H., and Chen, D. (2013). Pockmark activity inferred from pore water geochemistry in shallow sediments of the pockmark field in southwestern xisha uplift, northwestern south China Sea. *Mar. Petroleum Geology* 48, 247–259. doi: 10.1016/j.marpetgeo.2013.08.018

Malinverno, A., and Pohlman, J. (2011). Modeling sulfate reduction in methane hydrate-bearing continental margin sediments: Does a sulfate-methane transition require anaerobic oxidation of methane? *Geochemistry Geophysics Geosystems* 12, 1525–2027. doi: 10.1029/2011GC003501

Masuzawa, T., Handa, N., Kitagawa, H., and Kusakabe, M. (1992). Sulfate reduction using methane in sediments beneath a bathyal "cold seep" giant clam community off hatsushima island, sagami bay, Japan. *Earth Planetary Sci. Lett.* 110, 39–50. doi: 10.1016/0012-821X(92)90037-V

Mazzini, A., Henrik, S., Martin, H., and Sverre, P. (2006). Comparison and implications from strikingly different authigenic carbonates in a Nyegga complex pockmark, G11, Norwegian Sea. *Marine Geology* 231, 89–102.

Miao, X., Liu, X., Li, Q., Li, A., Cai, F., Kong, F., et al. (2022). Porewater geochemistry indicates methane seepage in the Okinawa Trough and its implications for the carbon cycle of the subtropical West Pacific. *Palaeogeogr. Palaeoclimatol. Palaeoecol.* 607, 111266. doi: 10.1016/j.palaeo.2022.111266

Nöthen, K., and Sabine, K. (2011). Reconstructing changes in seep activity by means of pore water and solid phase Sr/Ca and Mg/Ca ratios in pockmark sediments of the Northern Congo Fan. *Marine Geology* 287, 1–13.

Pellerin, A., Gilad, A., Holm, S., Findlay, A., Crockford, P., Turchyn, A., et al. (2019). Large Sulfur isotope fractionation by bacterial sulfide oxidation. *Sci. Adv.* 5 (7), 1–6. doi: 10.1126/sciadv.aaw1480

Piker, L., Schmaljohann, R., and Imhoff, J. (1998). Dissimilatory sulfate reduction and methane production in gotland deep sediments (Baltic Sea) during a transition period from oxic to anoxic bottom water. *Aquat. Microbial Ecol.* 14, 183–193. doi: 10.3354/ame014183

Reeburgh, W. S. (1976). Methane consumption in cariaco trench waters and sediments. *Earth Planetary ence Lett.* 28, 337–344. doi: 10.1016/0012-821X(76)90195-3

Rees, C. E. (1973). Steady-state model for sulfur isotope fractionation in bacterial reduction processes. *Geochimica Cosmochimica Acta* 37, 1141–1162. doi: 10.1016/0016-7037(73)90052-5

Rudnicki, M., Elderfield, H., and Spiro, B. (2001). Fractionation of sulfur isotopes during bacterial sulfate reduction in deep ocean sediments at elevated temperatures. *Geochimica Cosmochimica Acta* 65, 777–789. doi: 10.1016/S0016-7037(00)00579-2

Santos, A., Venceslau, S., Grein, F., Leavitt, W., Dahl, C., Johnston, D., et al. (2015). A protein trisulfide couples dissimilatory sulfate reduction to energy conservation. *Science* 350 (6267), 1541–1545. doi: 10.1126/science.aad3558

Schmaljohann, R. (1996). Methane dynamics in the sediment and water column of Kiel harbour (Baltic Sea). *Mar. Ecology-progress Ser.* 131, 263–273. doi: 10.3354/meps131263

Schnürle, P., Liu, C.-S., Lin, A. T., and Lin, S. (2011). Structural controls on the formation of BSR over a diapiric anticline from a dense MCS survey offshore southwestern Taiwan. *Mar. Petrol. Geol.* 28 (10), 1932–1942. doi: 10.1016/j.marpetgeo.2010.12.004

Schulz, H. D. (2006). "Quantification of early diagenesis: dissolved constituents in pore water and signals in the solid phase," in *Marine geochemistry* (Springer).

Shi, W., Xie, Y., Wang, Z., Li, X., and Tong, C. (2013). Characteristics of overpressure distribution and its implication for hydrocarbon exploration in the qiongdongnan basin. *J. Asian Earth Sci.* 66, 150–165. doi: 10.1016/j.jseaes.2012.12.037

Stam, M., Mason, P. R. D., Laverman, A., Pallud, C., and Van Cappellen, P. (2011). 34S/ 32S fractionation by sulfate-reducing microbial communities in estuarine sediments. *Geochimica Et Cosmochimica Acta - GEOCHIM COSMOCHIM Acta* 75, 3903–3914. doi: 10.1016/j.gca.2011.04.022

Suess, E., Huang, Y. Y., and Wu, N. (2005). "Cruise report SO177, sino-German cooperative project, south China Sea," in *Distribution, formation and effect of methane & gas hydrate on the environment*. Available at: http://store.pangaea.de/documentation/Reports/SO177.pdf.

Sun, Q., Wu, S., Hovland, M., Luo, P., Lu, Y., and Qu, T. (2011). The morphologies and genesis of mega-pockmarks near the xisha uplift, south China Sea. *Mar. Petroleum Geology* 28, 1146–1156. doi: 10.1016/j.marpetgeo.2011.03.003

Taylor, B., and Hayes, D. E. (1983). Origin and history of the south China Sea basin. *Tectonic Geologic Evol. Southeast Asian Seas Islands: Part 2* 27, 23–56. doi: 10.1029/GM027p0023

Teichert, B., Eisenhauer, A., Bohrmann, G., Haase - Schramm, A., Bock, B., and Linke, P. (2003). U/Th systematics and ages of authigenic carbonates from hydrate ridge, cascadia margin: Recorders of fluid flow variations. *Geochimica Cosmochimica Acta* 67 (20), 3845–3857. doi: 10.1016/S0016-7037(03)00128-5

Thamdrup, B. O., Finster, K., Hansen, J. Würgler, and Bak, F. (1993). Bacterial disproportionation of elemental sulfur coupled to chemical reduction of iron or manganese. *Appl. Environ. Microbiol.* 59, 101–108. doi: 10.1128/aem.59.1.101-108.1993

Tostevin, R., Turchyn, A., Farquhar, J., Johnston, D., Eldridge, D., Bishop, J., et al. (2014). Multiple sulfur isotope constraints on the modern sulfur cycle. *Earth Planetary Sci. Lett.* 396, 14–21. doi: 10.1016/j.epsl.2014.03.057

Wang, P., Prell, W. L., and Blum, P. (2000). Initial reports. *Proc. Ocean Drill. Prog.*, 184.

Wing, B., and Halevy, I. (2014). Intracellular metabolite levels shape sulfur isotope fractionation during microbial sulfate respiration. *Proc. Natl. Acad. Sci. United States America* 111, 18116–18125. doi: 10.1073/pnas.1407502111

Wu, D., Wu, N., Fu, S., Liang, J., and Guan, H. (2010). Geochemical characteristics of shallow sediments in the gas hydrate distribution area of dongsha, the northern south China Sea. *Mar. Geology Quaternary Geology* 30, 41–51.

Wu, D., Wu, N., Zhang, M., Guan, H., Fu, S., and Yang, R. (2013). Relationship of sulfate-methane tnterface (SMI), methane fluux and the underlying gas hydrate in dongsha area, northern south China Sea. *Earth Science- J. China Univ. Geosciences* 38, 1309–1320.

Yang, T., Jiang, S.-Y., Ge, L., Yang, J., Wu, N., Zhang, G., et al. (2010). Geochemical characteristics of pore water in shallow sediments from shenhu area of south China Sea and their significance for gas hydrate occurrence. *Chin. Sci. Bull.* 55, 752–760. doi: 10.1007/s11434-009-0312-2

Yao, B. (1998). Preliminary study on gas hydrate in the northern continental margin of the south china sea. *Mar. Geology Quaternary Geology* 18, 11–18. doi: 10.16562/j.cnki.0256-1492.1998.04.002

Zhang, W., Liang, J., Su, P., Wei, J., Gong, Y., Lin, L., et al. (2018). Distribution and characteristics of mud diapirs, gas chimneys, and bottom simulating reflectors associated with hydrocarbon migration and gas hydrate accumulation in the qiongdongnan basin, northern slope of the south China Sea. *Geological J.* 54, 1–18. doi: 10.1002/gj.3351

Zhang, P., Zuraida, R., Rosenthal, Y., Holbourn, A., Kuhnt, W., and Xu, J. (2019). Geochemical characteristics from tests of four modern planktonic foraminiferal species in the Indonesian throughflow region and their implications. *Geosci. Front.* 10, 505–516. doi: 10.1016/j.gsf.2018.01.011

Zhu, W., Huang, B., Mi, L., Wilkins, R., Fu, N., and Xiao, X. (2009). Geochemistry, origin and deep-water exploration potential of natural gases in the pearl river mouth and qiongdongnan basins, south China Sea. *Aapg Bull. - AAPG Bull.* 93, 741–776. doi: 10.1306/02170908099

Frontiers in Marine Science

TYPE Review
PUBLISHED 24 April 2023
DOI 10.3389/fmars.2023.1157879

EDITED BY
Dong Feng,
Shanghai Ocean University, China

REVIEWED BY
Jiasheng Wang,
China University of Geosciences Wuhan, China
Sui Wan,
South China Sea Institute of Oceanology (CAS), China

*CORRESPONDENCE
Hailong Lu
✉ hlu@pku.edu.cn

SPECIALTY SECTION
This article was submitted to Marine Biogeochemistry, a section of the journal Frontiers in Marine Science

RECEIVED 03 February 2023
ACCEPTED 06 April 2023
PUBLISHED 24 April 2023

CITATION
Lu Y, Yang H, Huang B, Liu Y and Lu H (2023) Foraminifera associated with cold seeps in marine sediments. *Front. Mar. Sci.* 10:1157879. doi: 10.3389/fmars.2023.1157879

Foraminifera associated with cold seeps in marine sediments

Yinghan Lu[1], Hailin Yang[1], Baoqi Huang[2], Yujia Liu[3] and Hailong Lu[1]*

[1]Beijing International Center for Gas Hydrate, School of Earth and Space Sciences, Peking University, Beijing, China, [2]Key Laboratory of Orogenic Belts and Crustal Evolution, Ministry of Education (MOE), School of Earth and Space Sciences, Peking University, Beijing, China, [3]School of Marine Science, Nanjing University of Information Science and Technology, Nanjing, China

Cold seep foraminifera have attracted considerable attention as they provide valuable insights into the study of cold seeps. This study provides a comprehensive overview of the manifestations of foraminifera in cold seep environments and methane seepage activities. Certain taxa of benthic foraminifera, such as *Uvigerina*, *Bolivina*, *Bulimina*, *Chilostomella*, *Globobulimina*, *Nonionella*, *Melonis*, *Epistominella*, *Cibicidoides*, and *Globocassidulina*, are known to inhabit geochemical conditions induced by methane-rich environments and may feed on associated methanotrophic microbial communities. Secondary mineralization on foraminifera shells is a widespread manifestation in seep sediments, and alters the microstructure, elementary composition, and isotopic signatures of foraminifera. On one hand, the precipitation of secondary authigenic Mg-rich, Mn-rich, Sr-rich, and Ba-rich calcite coatings have been observed on microfossils. On the other hand, micron-sized crystal pyrite and gypsum aggregates can also grow on the foraminifera walls. The negative $\delta^{13}C$ and positive $\delta^{18}O$ anomalies in both planktonic and benthic foraminifera from seep-associated sediments can serve as proxies for tracing past seepage activities, either in their live form or being adulterated by methane-derived authigenic carbonate after deposition. Seeping activities are recognized with a significant impact on benthic foraminifera, and the presence of cold seep-related species and significant isotopic anomalies in shells can be used to reconstruct past methane seepage events. Intensive methane seepage tends to suppress benthic foraminifera populations, while moderate intensity seepage may lead to a thriving benthic foraminiferal community, with hypoxia-enduring taxa such as *Uvigerina*, *Melonis*, and *Bulimina* being predominant. In contrast, oxygen-loving epibenthic taxa such as *Cibicidoides* often occur in areas of low methane flux. Compared to planktonic foraminifera, the single species of benthic foraminifera can provide a more comprehensive record of seepage evolution. Live benthic specimens are preferred for *in-situ* seep studies, while the superimposition of secondary minerals on the original shells should not be ignored when observing dead individuals. The significance of the evolution of methane seepage, changes in environmental parameters of the living habitat, and species sensitivity in cold seeps are emphasized in explaining the variation in foraminiferal assemblages and fluctuations in stable isotopes.

KEYWORDS

cold seep, marine foraminifera, methane seepage, species composition, secondary mineralization, stable isotopes

1 Introduction

Marine cold seeps, frequently observed in the vicinity of active and passive continental margin slopes, have been linked to the destabilization of gas hydrate reservoirs (Ceramicola et al., 2018; Suess, 2020). Variations in sea level increase in bottom water temperature, tectonic activity, and fluctuations in deposition rates can trigger instability in gas hydrate reservoirs and lead to repeated episodes of methane seepage (Karstens et al., 2018; Wallmann et al., 2018; Ketzer et al., 2020; Suess, 2020; Sultan et al., 2020). The seep fluids often saturate the pore water with hydrocarbon gases, an essential process of methane oxidation in methane-charged sediments *via* the action of anaerobic oxidation of methane (AOM, Eq. 1, Caldwell et al., 2008; Knittel and Boetius, 2009). This process is performed by a consortium of anaerobic methane-oxidizing archaea (ANME) and sulfate-reducing bacteria (SRB) (Knittel and Boetius, 2009). The AOM and methane aerobic oxidation processes (Eq. 2, Paull et al., 2005; Reeburgh, 2007) generate carbon dioxide (CO_2) and hydrogen sulfide (H_2S), which, in turn, resulting in local acidic and anoxic conditions (Niewöhner et al., 1998; Aharon and Fu, 2000; Joye et al., 2010). Elevated carbonate alkalinity promoted by AOM results in the formation of authigenic carbonate minerals. Typically, methane-derived authigenic carbonate (MDAC) is a universal mineral indicator in seep areas and is primarily composed of acicular aragonite, high-Mg calcite, and dolomite (Boetius et al., 2000; Judd et al., 2007; Naehr et al., 2007; Buckman et al., 2020; Judd et al., 2020). However, in some cases, Fe- and Mn-carbonates may also be present (Suess, 2020). Meanwhile, a direct consequence of such stressful conditions is the occurrence of symbolic benthic seep communities. Tube worms, clams, mussels, and microbial mats, are indicator organisms to survive in seep ecological environments (Suess, 2020), and these organisms may provide carbon and energy *via* AOM (Boetius et al., 2000). Implications are that the association of methane fluids, authigenic minerals, and benthic biota has been regarded as a biogeochemical footprint to identify cold seeps.

$$CH_4 + SO_4{}^{2-} \rightarrow HCO_3{}^{-} + HS^{-} + H_2O \tag{1}$$

$$CH_4 + 2O_2 \rightarrow CO_2 + 2H_2O \tag{2}$$

Foraminifera, single-celled eukaryotes widely distributed in seawater and deep-sea sediments, have been established as a crucial micro-paleontological foundation for the study of paleoceanography and paleoclimatology (Jorissen, 1992; Schiebel et al., 2018). Environmental information can be obtained through the examination of foraminifera assemblage on a macro-scale, and as well as shell elements and isotopic compositions on a micro scale (Gooday, 1994; Kucera, 2007; Ravelo and Hillaire-Marcel, 2007; Pawlowski and Holzmann, 2008; Schiebel et al., 2018). In recent decades, evidence of deep-sea benthic foraminifera in seep areas has been discovered (e.g. Brooks et al., 1991; Sen Gupta and Aharon, 1994; Martin et al., 2010), and growing interests begins to focus on the identification of seep environments and methane seepage activities *via* foraminifera research. Apparently, cold seep foraminifera have been served as archives of seep activity, and differences in foraminiferal assemblages, secondary minerals alteration on the shells, and isotopic compositions between seep and non-seep areas can be detected.

The community assemblage of benthic foraminifera (composition, abundance, diversity, and dominant species) have been recognized as an advantageous indicator for the identification of cold seep environments. Data from different oceanic basins spread across the Pacific Rim shelf (Bernhard and Reimers, 1991; Hill et al., 2003; Heinz et al., 2005; Khusid et al., 2006; Zhou et al., 2009; Chen et al., 2010; Martin et al., 2010; Xiang et al., 2012; Saeidi Ortakand et al., 2016; Pan et al., 2018; Xin et al., 2020; Zhou et al., 2020; Li et al., 2021), the North and east Atlantic (Jones, 1993; Sen Gupta and Aharon, 1994; Sen Gupta et al., 1997; Rathburn et al., 2000; Bernhard et al., 2001; Rathburn et al., 2003; Robinson et al., 2004; Bhaumik and Gupta, 2005; Panieri, 2005; Bhaumik and Gupta, 2007; Lobegeier and Sen Gupta, 2008; Panieri and Gupta, 2008; Wilfert et al., 2015), the North Indian Ocean (Erbacher and Nelskamp, 2006), the Arctic marginal seas (Dessandier et al., 2019; Melaniuk, 2021), and Mediterranean (Panieri, 2003; Panieri, 2006) demonstrate the opportunism of benthic foraminifera associates with cold seep habitats (Figure 1). Some benthic foraminifera, including endobenthic taxa such as *Uvigerina, Bolivina, Bulimina, Chilostomella, Globobulimina, Nonionella* and *Melonis*, as well as epibenthic taxa such as *Epistominella, Cibicidoides* and *Globocassidulina*, are known to withstand methane- and sulfide-enriched seepage conditions. However, no seep-endemic species have been reported to date, as these taxa are well-documented in normal marine environments as well. It should be noted that benthic foraminiferal assemblages (e.g., abundance and diversity) are not congruent in these cold seep areas on a global scale and are influenced by multiple factors. Despite the absence of consistent global patterns in seep benthic foraminiferal assemblages, their sensitive response to seepage environments provides valuable evidence for identifying past methane seepage events (Bhaumik and Gupta, 2007; Zhou et al., 2009; Pan et al., 2018; Li et al., 2021).

Visible changes in the primary microstructure and elemental composition of seep foraminifera due to diagenetic alteration have been obtained through diversified macro-scale observations. This phenomenon has been described by Electron Probe Micro Analysis (EPMA) (Panieri et al., 2017), Energy Dispersive Spectrometer (EDS) (Schneider et al., 2017; Dessandier et al., 2020; Zhou et al., 2020; Miao et al., 2021), Scanning Electron Microscopy (SEM) (Fontanier et al., 2014; Consolaro et al., 2015; Panieri et al., 2017; Schneider et al., 2017; Wan et al., 2018; Dessandier et al., 2020; Zhou et al., 2020; Miao et al., 2021), Transmission Electron Microscopy (TEM) (Panieri et al., 2017), and Electron Back Scatter Diffraction (EBSD) (Panieri et al., 2017). However, the current understanding from *in-situ* observations of seep foraminifera may be deficient, as better micro-observations of specimens after visible diagenetic alteration were just from active seep sites of the Arctic Ocean (Consolaro et al., 2015; Panieri et al., 2017; Schneider et al., 2017; Dessandier et al., 2020), the Atlantic Ocean (Merinero et al., 2008; Fontanier et al., 2014; Dessandier et al., 2020), the South China Sea (Wan et al., 2018; Zhou et al., 2020), and fossil seep sites of the Greenland Sea (Millo et al., 2005), the Barents Sea (Argentino et al., 2021), the Oregon Washington coast and Vancouver Island (Torres et al., 2010). In these methane-charged sediments, the geochemical

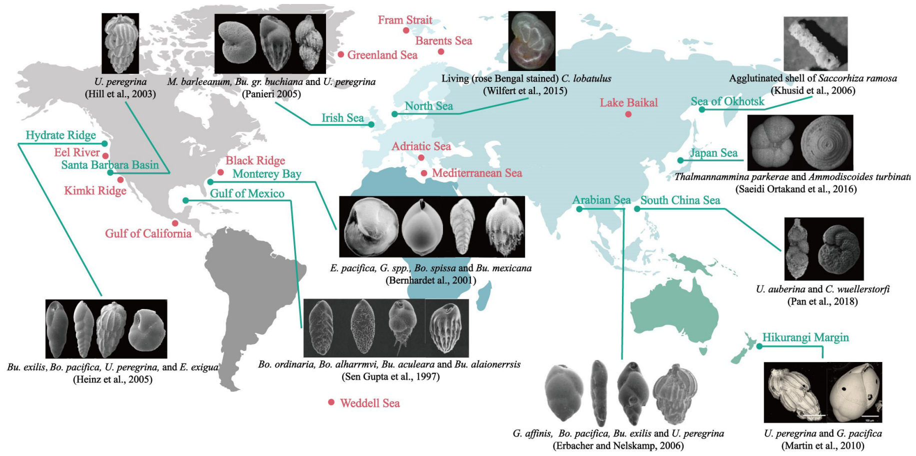

FIGURE 1
Foraminifera associated with the cold seeps in the world. The research areas, where isotopic analyses and/or species studies have already been carried out, are denoted by filled circles, among which green filled symbols indicate the sites with the community composition determined and electron microscopy images or optical microscope images of typical benthic foraminifera given next to them. As for the locations of the red dots, no foraminifera photographs are found, but it is certain that foraminifera related studies were involved. Please refer to Appendix Table 1 for relevant references.

cycles of elements are interconnected with authigenic minerals such as carbonate, pyrite, and gypsum (Ritger et al., 1987; Tribovillard et al., 2006; McQuay et al., 2008; Griffith and Paytan, 2012; Large et al., 2017; Smrzka et al., 2020). Available observations indicate that foraminifera shell components are significantly influenced by seep authigenic mineral precipitation, as evidenced by the formation of authigenic Mg-, Sr-, Mn-, and Ba-rich carbonate coatings, and the micron-sized euhedral gypsum and pyrite growth on the exterior and interior walls of seep foraminifera.

Currently, isotopic signals recorded in foraminifera tests are an ideal index for identifying methane release from cold seeps. The isotopic composition of seawater, including both the pore water in seafloor sediments and the upper water body, undergoes significant changes as a result of the reformative processes of seepage fluids and methane-related biogeochemical processes, making the observation of low δ^{13}C and high δ^{18}O anomalies recorded by foraminifera shells to be widely considered as a marker of methane release at cold seeps (Li et al., 2010; Martin et al., 2010; Panieri et al., 2012). So far, the isotopic composition analysis of foraminifera has revealed the occurrence of methane-release events from various cold seep environments, including the Gulf of California (Keigwin, 2002), the Santa Barbara Basin (Kennett et al., 2000; Hill et al., 2003; Cannariato and Stott, 2004), the Black Ridge (Bhaumik and Gupta, 2007), the Cascadia margin (Hill et al., 2004; Li et al., 2010), the Peru shelf margin (Wefer et al., 1994), the West Svalbard continental margin (Panieri et al., 2014), the Norwegian continental margin (Hill et al., 2012), the Greenland Sea (Smith et al., 2001; Millo et al., 2005), the Fram Strait (Consolaro et al., 2015), the Mediterranean Sea (Panieri et al., 2012), the Japan Sea (Ohkushi et al., 2005; Uchida et al., 2008), the South China Sea (Lei et al., 2012; Wang et al., 2013; Chang et al., 2015; Zhuang et al., 2016), and the Weddell Sea (Thomas et al., 2002) (Figure 1). Additionally, the application of the isotopic composition analysis of foraminifera has enabled the interpretation of previous methane-release events in various geological settings, including the Northern Apennines (Italy) (Panieri et al., 2009), Western Washington State (USA) (Martin et al., 2007), and the Sunda arc (Indonesia) (Wiedicke and Weiss, 2006). Consequently, reconstructions of methane fluxes and the historical evolution of seepage can be performed through the analysis of fluctuations in foraminifera isotopic ratios (Kennett et al., 2000; Li et al., 2010; Wang et al., 2013; Panieri et al., 2014; Consolaro et al., 2015; Zhuang et al., 2016; Zhou et al., 2020).

While multiple proxies based on cold seep foraminifera offer insights into contemporaneous seep areas and seep activities during geological history, certain issues remain unresolved. For example, the selection of scientifically valuable cold seep-related benthic foraminifera species, the mechanism of the foraminifera community assembly response to dynamic seeping activities, and the explanation of fluctuations in foraminifera isotopic values. Additionally, the ability of foraminifera to fully assimilate seawater or pore water methane-derived carbon during biomineralization, and the differing information recorded by living and fossil, planktonic and benthic foraminifera in cold seep areas also contribute to the uncertainty in interpreting the results. Meanwhile, there still have difficulty in distinguishing the stable isotope signatures between primary biogenic calcite and secondary authigenic calcite precipitate driven by AOM on dead specimens. Thus, while the approach of identifying cold seep environments through multiple foraminifera proxies offers significant potential, the influence of mixed interference from other factors necessitates further research to resolve these knowledge gaps.

2 Species composition of benthic foraminifera

2.1 Seep-related benthic foraminifera

Benthic foraminifera are widely recognized as valuable indicators of cold seep activities in the seafloor sediment community. In general, the superficial seep sediments exhibit high methane fluxes (up to 90 mmol m^{-2} d^{-1}; Hill et al., 2004), sulfide concentrations (up to 63 mmol m^{-2} d^{-1}; Heinz et al., 2005), and total organic carbon content (up to 4%; Bhaumik and Gupta, 2005). The stressful microhabitat of active cold seepages presents a challenge for foraminifera to survive. Numerous studies have investigated the responses of benthic foraminiferal assemblages to seep activity in various seep areas, including the Hydrate Ridge (Torres et al., 2003; Hill et al., 2004; Heinz et al., 2005), the Eel River (Rathburn et al., 2000), the Santa Barbara Basin (Hill et al., 2003), the Kimki Ridge (McGann and Conrad, 2018), the Peru shelf margin (Wefer et al., 1994), the Japan Sea (Uchida et al., 2008; Saeidi Ortakand et al., 2016), the Sea of Okhotsk (Khusid et al., 2006), the South China Sea (Zhou et al., 2009; Xiang et al., 2012; Pan et al., 2018; Xin et al., 2020), the Blake Ridge (Robinson et al., 2004; Bhaumik and Gupta, 2005; Bhaumik and Gupta, 2007), the Gulf of Mexico (Sen Gupta and Aharon, 1994; Sen Gupta et al., 1997; Robinson et al., 2004), the Monterey Bay (Bernhard et al., 2001; Rathburn et al., 2003; Martin et al., 2004), the Irish Sea (Panieri, 2005), the North Sea (Wilfert et al., 2015), the Mediterranean Sea (Panieri, 2003; Panieri, 2006), the Adriatic Sea (Panieri, 2003; Panieri, 2006), the Arabian Sea (Erbacher and Nelskamp, 2006), the Arctic shelf margin (Dessandier et al., 2019; Melaniuk, 2021), and the New Zealand shelf margin (Martin et al., 2010). The distribution of benthic foraminifera in seep sediments is remarkably skewed toward adjacent non-seep-affected environments, which suggests that some organisms may opportunistic to adapt to the challenging geochemical conditions brought by methane seepages (Jones, 1993; Bernhard et al., 2001; Panieri, 2005; Bhaumik and Gupta, 2007; Burkett et al., 2016; Dessandier et al., 2019). In these cold seep areas, the foraminifera assemblage is largely hyaline perforate calcitic or aragonitic species, while imperforate porcelaneous and coarsely agglutinated taxa are infrequent. Some hyaline taxa, such as *Uvigerina*, *Bolivina*, *Bulimina*, *Chilostomella*, *Globobulimina*, *Nonionella*, *Melonis*, *Epistominella*, *Cibicidoides*, and *Globocassidulina* have been considered as seep-related species due to their higher adaptation to the high organic, low oxygen, reducing conditions, and hypoxia environments rich in CH_4 and H_2S commonly found in cold seep environments (Appendix Table 1). However, evidence suggests that these foraminifera may not be restricted to the seep environments (e.g. Sen Gupta et al., 1997; Rathburn et al., 2000; Bernhard et al., 2001).

Typically, endobenthic benthic foraminifera exhibit superior tolerance to the harsh conditions of methane seeps, these methane-loving taxa include *Uvigerina*, *Bolivina*, *Bulimina*, *Chilostomella*, *Globobulimina*, *Nonionella*, and *Melonis*. *Uvigerina* has been observed to be adaptable to high organic matter, low oxygen, and methane-rich conditions and is likely specialized in methane-oxidizing bacteria (Sen Gupta and Aharon, 1994; Rathburn et al., 2000; Bernhard et al., 2001; Torres et al., 2003). *Bolivina* is associated with dysoxic bottom waters due to high methane emissions and is known to be resistant to anoxia and sulfide toxicity (Sen Gupta et al., 1997; Hill et al., 2003; Bhaumik and Gupta, 2005). *Bulimina* is commonly found in seep sediments with high organic matter content (Rathburn et al., 2000; Rathburn et al., 2003; Martin et al., 2004; Wiedicke and Weiss, 2006; Zhou et al., 2009; Xin et al., 2020). *Chilostomella* is noted to tolerate hypoxia and hostile environments rich in methane and hydrogen sulfide (Corliss, 1985; Pan et al., 2018). *Globobulimina* is frequently found in Pacific and Atlantic methane seep areas (Sen Gupta et al., 1997; Rathburn et al., 2000; Rathburn et al., 2003; Hill et al., 2004; Martin et al., 2004; Bhaumik and Gupta, 2007). And food supply provided by microbial mats appears to facilitate the survival of *Melonis* in high-latitude methane-rich environments (Panieri, 2005; Dessandier et al., 2019; Melaniuk, 2021). These hypoxia-tolerant benthic foraminifera are often abundant in methane-rich sediments and serve as proxies for tolerance to stressful seep environments.

However, there are exceptions where densities of a few oxygen-loving epibenthic taxa increase in certain cold seep areas, such as *Epistominella*, *Cibicidoides*, and *Globocassidulina*. *Epistominella* has been observed to be dominant taxa in seep areas of the North Sea (Jones, 1993), the Monterey Bay (Bernhard et al., 2001; Rathburn et al., 2003), the Gulf of Mexico (Robinson et al., 2004), the northern Adriatic Sea (Panieri, 2006), the Hydrate Ridge (Heinz et al., 2005), and the Santa Barbara Basin (Hill et al., 2003). *Cibicidoides* has been found in methane-rich bottom waters of the South China Sea (Pan et al., 2018; Xin et al., 2020), the Hydrate Ridge (Torres et al., 2003; Hill et al., 2004), the Gulf of Mexico (Robinson et al., 2004), and the Vestnesa Ridge (Melaniuk et al., 2022). In some cases, like the East Greenland slope (Smith et al., 2001; Millo et al., 2005), the Blake Ridge (Bhaumik and Gupta, 2005), the Northern North Sea (Wilfert et al., 2015), the Vestnesa Ridge (Dessandier et al., 2019), the Margin of Eastern New Zealand (Martin et al., 2010), and the South China Sea (Zhou et al., 2009; Xiang et al., 2012), *Cibicidoides* also holds a larger advantage. Meanwhile, *Globocassidulina* is dominant in methane seep sediments associated with oxygen depletion and organic-rich conditions (Sen Gupta and Aharon, 1994; Rathburn et al., 2000; Panieri and Gupta, 2008; Zhou et al., 2009). Previous studies have indicated that these benthic foraminifera commonly attach to the wall of the worm tubes and live a few centimeters to tens of centimeters above the bottom sediments (Mackensen et al., 2006; Lobegeier and Sen Gupta, 2008;

Rathburn et al., 2009). This attached lifestyle is likely to allow them to escape extreme seep habitats (Gupta et al., 2007).

2.2 Benthic foraminiferal assemblages

Many studies have taken emphasized on the distinction in benthic foraminiferal assemblages between seep and non-seep habitats (Rathburn et al., 2000; Bernhard et al., 2001; Panieri, 2003; Torres et al., 2003; Wiedicke and Weiss, 2006; Dessandier et al., 2019; Li et al., 2021), and environmental parameters such as microhabitat conditions and seepage activities are known to play a crucial role in the survival of these organisms (Figure 2).

Overall, benthic foraminifera are commonly found in a range of seep ecosystems, such as clam beds, microbial mats, mud volcanoes, pockmarks, and algal reefs (Appendix Table 1). The preference of benthic foraminifera for specific seep microhabitats is influenced by substrate type, oxygen level, and total organic carbon content. Fine-grained sediments rich in clay and mud, typically charged with methane, are abundant in endobenthic taxa (e.g. Bhaumik and Gupta, 2005; Zhou et al., 2009; Xin et al., 2020). While epibenthic benthic foraminifera tend to inhabit in coarse and hard areas, such as algal reefs or environments precipitated with carbonate nodules (e.g. Panieri, 2006; Xiang et al., 2012) (Figure 2D). In general, habitats with high oxygen (O_2) levels and low carbon dioxide (CO_2) concentrations are conducive to the survival of foraminifera, as a decrease in O_2 and an increase in CO_2 can limit their survival or symbiotic existence (Herguera et al., 2014). Agglutinate foraminifera thrive in microhabitats with adequate O_2 levels and high CO_2 concentrations, while the growth of calcareous foraminifera is limited in these conditions (Herguera et al., 2014). During periods of high methane flux and anoxic conditions associated with active seepages, endobenthic benthic foraminifera tend to predominate, while with a decrease in seepage activity and an increase in O_2 levels, epibenthic taxa gradually become dominant (Zhou et al., 2009; Pan et al., 2018). In addition, benthic foraminifera have also been found to show sensitivity to the organic flux to the sea floor (Abu-Zied et al., 2008). In seep areas, organic matter can provide additional food sources for foraminifera, and foraminifera with food tendencies, such as *Cibicidoides*, *Bulimina*, *Uvigerina*, *Nonionella*, and *Melonis*, have been observed (Wefer et al., 1994; Torres et al., 2003; Dessandier et al., 2019; Xin et al., 2020). Compared to non-seep sites, the significantly lower abundance of agglutinate foraminifera (approximately 10% of the total) in seep sites suggests that they may not be well adapted to the seep geochemical environment (Zhou et al., 2009; Martin et al., 2010; Wilfert et al., 2015; Dessandier et al., 2019). There are, however, exceptions, such as the dominance of agglutinate taxa in the Sea of Okhotsk Deryugin seep area (Khusid et al., 2006).

What's more, the point is that the benthic foraminiferal communities in cold seep environments are strongly affected by seepage activities. Studies have shown variable results in terms of foraminiferal abundance in seep areas (from several to thousands per 10 cm^3), with reports of both decreased (e.g. Panieri, 2003; Bhaumik and Gupta, 2007; McGann and Conrad, 2018; Dessandier et al., 2019), increased (e.g. Rathburn et al., 2000; Torres et al., 2003; Wiedicke and Weiss, 2006), as well as no significant differences from non-seepage sites (e.g. Bernhard et al., 2001; Rathburn et al., 2003). Although seep environments are known to be harmful to the survival of benthic foraminifera (Dickens et al., 1995; Dickens et al., 1997; McConnaughey et al., 1997; Bernhard and Bowser, 1999), recent studies suggest that the relationship between seepage activities and benthic foraminifera abundance is more complex (Figure 2). Foraminifera are generally thought to prefer an aerobic methane environment with low methane flux, but the bacteria that flourished during the period of moderate-flux methane seepage may provide a food source for benthic foraminifera, resulting in higher

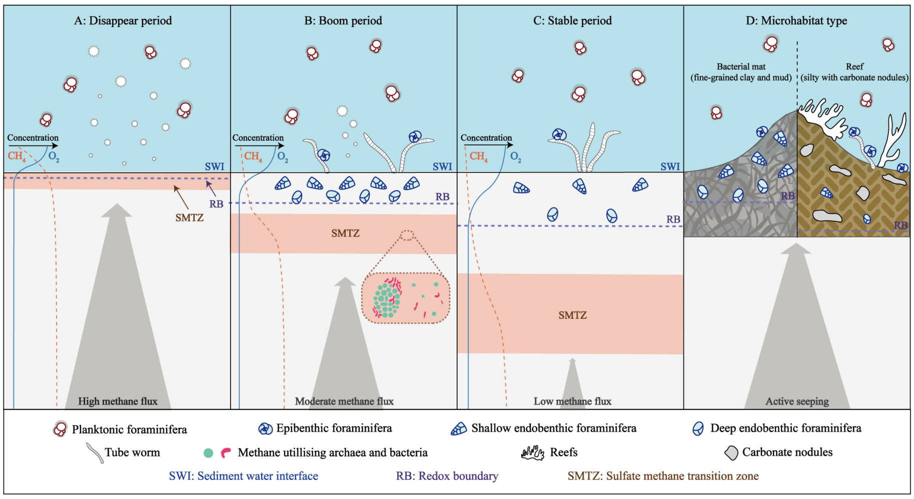

FIGURE 2
Living foraminiferal assemblages associated with methane seepages (after Borowski et al., 1996; Consolaro et al., 2015; Li et al., 2021). **(A)** Disappear period of benthic foraminifera during times of high methane flux. **(B)** Boom period of benthic foraminifera during times of moderate methane flux. **(C)** Stable period of benthic foraminifera during times of low methane flux. **(D)** Benthic foraminiferal assemblages in different seep microhabitats.

abundance (Figure 2B, Li et al., 2021). The poisonous sulfidic environment during high-methane flux periods will lead to the death of the foraminifera, while the benthic foraminifera community in low-methane flux periods may be similar to that of the normal marine sediments (Figure 2, Consolaro et al., 2015; Li et al., 2021; Melaniuk et al., 2022). Additionally, the density of living foraminifera is related to the thickness of microbial mats, with higher taxa observed in thicker mats due to a greater food supply (Robinson et al., 2004). The depth distribution of benthic foraminifera is also influenced by redox conditions in methane-rich sediments. Typically, the redox boundary is close to the sediment-water interface and may be lower than 1 cm (Sen Gupta and Aharon, 1994). which restricts the distribution of living foraminifera within 0.5-3 cm below the sediments, where they are primarily hypoxia-tolerant epibenthic species (Rathburn et al., 2000; Erbacher and Nelskamp, 2006; Melaniuk, 2021).

3 Micro-observation of foraminifera shells

3.1 Authigenic carbonate coatings

The precipitation of authigenic calcite is an anticipated process due to the typically intense AOM and inherent saturation of $CaCO_3$ in seep-associated sediments (Figure 3A). Authigenic Mg-calcite overgrowth is the dominant form of secondary mineral coatings observed on the macroscopic tests of foraminifera, with a contribution to the shell weight reaching up to 58 wt% (Millo et al., 2005; Schneider et al., 2017; Wan et al., 2018). This microcrystalline Mg-calcite overgrowth may overlay the whole foraminifera surface and is structurally identical to the primary biogenic calcite (Panieri et al., 2017). As diagenetic alteration intensifies, the precipitation of MDAC on the shell is cumulatively added. The shell surfaces from "glassy" to "translucent," and even "fuzzy," eventually forming a solid inorganic carbonate crust, which results in the loss of the shell's smooth surface texture, with both the interior and exterior walls covered and thicken (Schneider et al., 2017). The "glassy" shells under biomineralization processes usually show low magnesium content below 0.2 wt% $MgCO_3$ (Blackmon and Todd, 1959; Bentov and Erez, 2006), whereas in modern active seep sites the Mg/Ca ratios of benthic foraminifera tests can higher than 10 mmol/mol (Panieri et al., 2017; Wan et al., 2018). Furthermore, diagenesis-altered benthic foraminifera tests from ancient seep sites have been reported to exhibit spots with high Mg (*Cassidulina neoteretis, Cassidulina reniforme*, and *Melonis barleeanum*, Argentino et al., 2021), and the Mg/Ca ratios could up to 69 mmol/mol (*Globobulimina pacifica*, Torres et al., 2010). The elevated Mg content of original shells is considered to benefit from Mg-rich interlayers with Mg/Ca ratios even reaching 220 mmol/mol (Panieri et al., 2017) (Figure 3B). To some extent, the increasing Mg/Ca ratio of altered foraminifera shells reflects the heightened activity of AOM and authigenic carbonate precipitation, which in turn signifies changes in the activities of seepage (e.g. Torres et al., 2003; Li et al., 2010).

Secondary mineralization can also be traced with the use of Sr, Mn, and Ba content of foraminifera. Sr and Mn are typical elements to determine the extent of alteration associated with meteoric diagenesis, as Mn can be incorporated into carbonate while Sr will separate from carbonate during diagenetic alteration (Kaufman and Knoll, 1995). The Sr/Ca of benthic foraminifera in seep areas is usually around 1 mmol/mol, but individual tests could reach up to 36.48 mmol/mol (Torres et al., 2010), which may be related to the precipitation of Sr-rich aragonite (Tesoriero and Pankow, 1996; Fontanier et al., 2014).

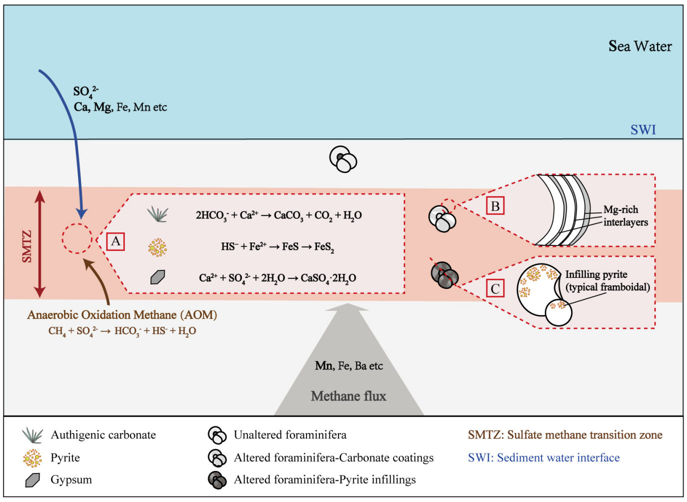

FIGURE 3
Authigenic secondary minerals precipitation and their alteration to foraminifera shells in seep-associated sediments. **(A)** Typical authigenic secondary minerals precipitation, and the equations utilized to depict this process are derived from the works of Berner (1982); Borowski et al. (2013); Liu et al. (2018), and Miao et al. (2021). **(B)** Altered foraminifera coated with high-Mg carbonate interlayers. **(C)** Altered foraminifera infilled with authigenic pyrites.

The Mn/Ca ratio of foraminifera in case of natural calcification ranges from 0.05 to 0.3 mmol/mol (Klinkhammer et al., 2009), while the Mn/Ca ratio of benthic foraminifera in seep-associated sediments can exceed 1 mmol/mol, or even up to 12 mmol/mol (Torres et al., 2010). Moreover, foraminifera modified by cold seeps in high latitudes display spots of high Ba content under EDS images (Dessandier et al., 2020). These trace elements can mask microbial shells by incorporating carbonates after the alteration of diagenesis and may play an important role in seep elemental cycling.

3.2 Self-shaped crystal growth

An association of authigenic gypsum with pyrite tends to occur within the sulfate-methane transition zone (SMTZ), which also marks the methane seepage events (Figure 3A; Lin et al., 2016a, b; Zhou et al., 2020; Dantas et al., 2022). The fluid released by natural gas hydrate decomposition or seepage carries dissolved barium (Ba^{2+}) (Hu et al., 2014), resulting in a higher Ba content in bottom water and usually precipitated in the form of gypsum ($CaSO_4{\cdot}2H_2O$) in surface sediments (Pierre, 2017). Macroscopic observations of gypsum in methane-charged sediments reveal rhombic, bladed, lenticular, or trapezoidal shapes (Kocherla, 2013; Lin et al., 2016a). By now, crystal growth of gypsum microcrystals on foraminifera shells in the seep sediments of the Nansha Trough (Zhou et al., 2020) and the Santos Basin (Dantas et al., 2022) has been observed.

Pyrite (FeS_2) is a ubiquitous sulfide mineral in marine sediments and plays a crucial role in the global Fe-S cycle (Berner, 1985). In cold seep environments, the formation of pyrite is closely linked to the presence of methane upwelling, as hydrogen sulfide produced by AOM action may be the main electron donor for pyrite formation (Schippers and Jorgensen, 2002; Zhang M. et al., 2018). Framboidal pyrite, which forms *via* authigenic crystallization, is known as the typical morphology in methane-charged sediments (Peckmann et al., 2001; Lin et al., 2016b). Additionally, pyrite may also precipitate in bacterial forms, such as spheroids, rod-chains, and worm-like structures (Chen et al., 2006). Pyrite infill in foraminifera chambers is not extraordinary and typically exhibits framboids and aggregates forms (Figure 3C). In recent years, numerous studies have reported the presence of pyrite infillings in foraminifera shells from various cold seep sites, including the western Svalbard (Panieri et al., 2017), the Haima seep (Miao et al., 2021), the Nansha Trough (Zhou et al., 2020), the South China Sea (Zhuang et al., 2016), and the Gulf of Cadiz (Merinero et al., 2008). From another perspective, many trace elements can incorporate into the pyrite structure as solid solution or as sulfide/metal microinclusions (e.g. As, Cu, Zn, Pb, Sb, Mo, Ag, Cd, Mn, Hg, Au). or directly through ionic substitution (e.g. Ni^{2+}, Co^{2+}, Cu^{2+}, Se^{2-}, Te^{2-}) (Large et al., 2017), These pyrite-filling aggregates can influence the elemental composition of foraminifera shells, but the quantification of trace element cycling processes remains challenging due to a lack of relevant findings.

4 Isotope anomalies of foraminifera

4.1 Negative carbon-isotope anomalies

It is generally believed that the apparent lack of ^{13}C in foraminifera shells is invoked as an indicator of methane seepages. There have been published that use foraminifera carbon isotopic signatures to reconstruct ancient seepages and variable methane fluxes (e.g. Consolaro et al., 2015; Panieri et al., 2016; Zhou et al., 2020). During the destabilization of hydrate reservoirs, large amounts of ^{13}C-depleted methane are released and anaerobically consumed when they reach the seafloor (Ruppel and Kessler, 2017; Egger et al., 2018). Carbon isotope signals will be conveyed into the pore water dissolved inorganic carbon (DIC) pool in the form of HCO_3^- *via* AOM (Ussler and Paull, 2008). And by so doing, benthic foraminifera often have low $\delta^{13}C$ values by incorporating ^{13}C-depleted DIC during calcification (Hill et al., 2003; Rathburn et al., 2003). Given that AOM mainly occurs within the SMTZ near the top of the sediments, the carbon isotope deficit is most pronounced in this region (e.g. Torres et al., 2003; Ussler and Paull, 2008).

Most carbon isotopic composition of benthic foraminifera shells, both living and fossil, from methane seepage environments have been observed to range from 3‰ to -22‰ PDB, with one exception of -35.7‰ PDB (Martin et al., 2010), in contrast, the isotopic composition of ancient seep specimens have been observed to be lower than -50‰ PDB (Appendix Table 2, Figure 4). Methane in gas hydrates can have a variety of sources, such as thermogenic, biogenic or a mixture, with a typical carbon isotope value of methane ranging from -30% to -110% PDB, and typically lower than -60% PDB (Sackett, 1978; Kvenvolden, 1993; Whiticar, 1999). The carbon isotope of pore water DIC ($\delta^{13}C_{DIC}$) in normal marine sediments is typically between -1 and 1‰ PDB (Tagliabue and Bopp, 2008), but can become lower than -45‰ PDB when corporate by methane-derived carbon (Rathburn et al., 2003; Torres et al., 2003). Apart from that, the carbon isotope of authigenic carbonate ($\delta^{13}C_{carbonate}$) precipitates related to methane oxidation processes is commonly lower than -40‰ PDB (Whiticar, 1999). Although carbon isotopic values of benthic foraminifera ($\delta^{13}C_{BF}$) in seep sediments exhibit discernable negative shifts compared to those living in normal marine sedimentary environments (-1 to 1‰ PDB, McCorkle et al., 1990), the shifts still remain far from the magnitude observed in $\delta^{13}C_{DIC}$ or $\delta^{13}C_{carbonate}$ influenced by methane (Figure 4). Overall, most bulk values of $\delta^{13}C_{BF}$ have been observed to be concentrated between 0‰ and -16‰ PDB, which suggests a disequilibrium between $\delta^{13}C_{BF}$ and methane-derived $\delta^{13}C_{DIC}$.

Planktonic foraminifera living in the upper water column are generally considered to be isolated from the light carbon isotope signals from methane seepage, due to processes such as AOM in sediments, diffusion, and dissolution in seawater, as well as consumption by methanotrophic microbes (Damm et al., 2005;

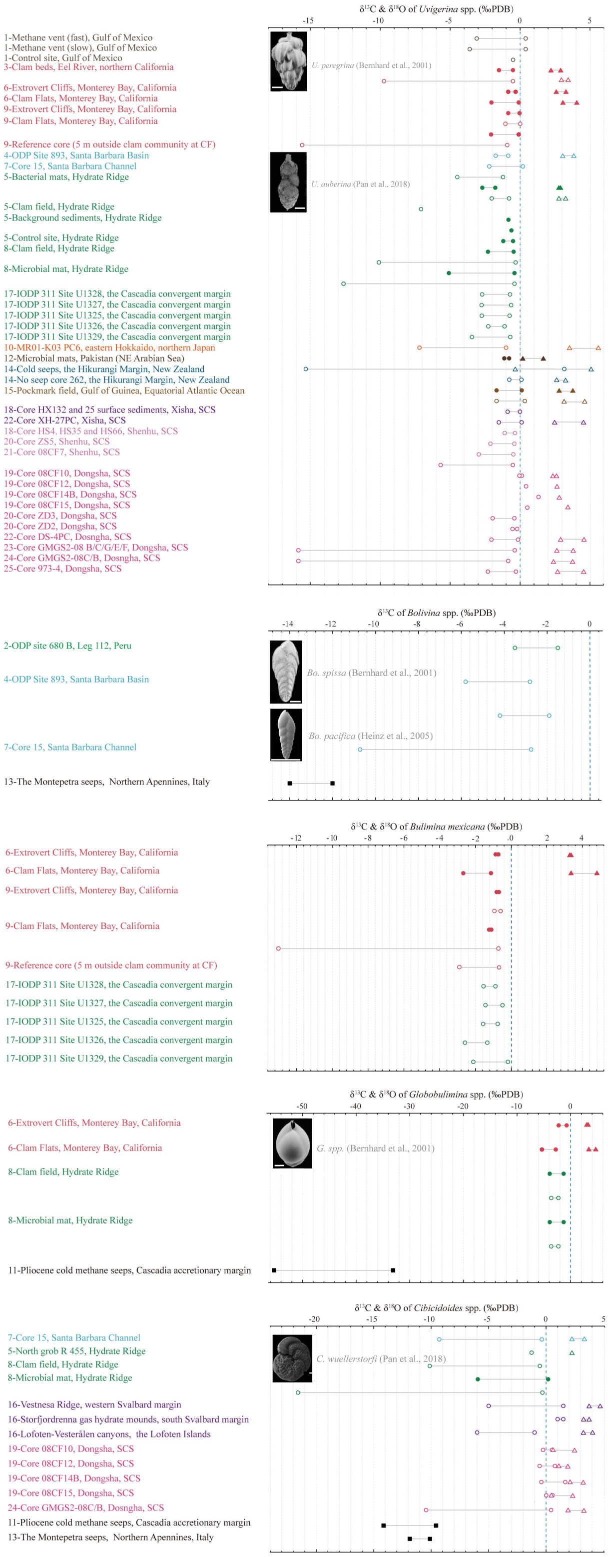

FIGURE 4

Summary of carbon and oxygen isotopic records of benthic foraminifera in seep sediments. The most commonly adopted endobenthic species (*Uvigerina* spp., *Bolivina* spp., *Bulimina mexicana*, and *Globobulimina* spp.) and epibenthic species (*Cibicidoides* spp.) are selected. $\delta^{13}C$ values of live and dead benthic specimens are represented by solid dots and open circles, respectively. Similarly, $\delta^{18}O$ values are represented by triangles. The black square represents the $\delta^{13}C$ results of ancient seep samples. The solid gray line in the middle of two symbols represents the fluctuation range of the isotopic value, but it does not mean continuous change. Dotted blue line is a guide for the normal marine average $\delta^{13}C_{BF}$ value, which is selected as 0‰ PDB here. Please refer to Appendix Table 2 for data sources.

Steinle et al., 2015; Ruppel and Kessler, 2017; Egger et al., 2018). Despite this, several studies have reported the occurrence of simultaneous negative shifts in both $\delta^{13}C_{BF}$ and carbon isotopic values of planktonic foraminifera ($\delta^{13}C_{PF}$), which could potentially be indicative of methane emissions. For example, Kennett et al. (2000) observed that $\delta^{13}C_{PF}$ of the Santa Barbara Basin sediments changed over the past 6000 years, but this change was not significant (higher than -3.5‰). Additionally, Hill et al. (2012) found that methane venting not only had an impact on the isotopic composition of benthic foraminifera, but also caused significant negative shifts in the $\delta^{13}C_{PF}$ of *Neogloboquadrina pachyderma* in the Nyegga pockmark field. Zhuang et al. (2016) pointed out that the $\delta^{13}C_{PF}$ of *Globigerinoides ruber* was depleted (as low as -5.68‰ PDB), but not to the same extent as the benthic foraminifera *Uvigerina peregrina*, which was depleted as low as -15.85‰ PDB. McGann and Conrad (2018) found the same lower $\delta^{13}C$ peaks in both benthic and planktonic tests, which may provide the evidence of methane releases large enough to influence the water column. Zhou et al. (2020) determined two major paleo-methane seepage events according to anomalously $\delta^{13}C_{PF}$ shifts of *Globigerinoides ruber* from seep sediments in the South China Sea. Although benthic foraminifera generally exhibit more obvious shifts in isotopic composition, there are also instances where $\delta^{13}C_{PF}$ shifts are significantly depleted (e.g. Smith et al., 2001; Ohkushi et al., 2005). In these cases, careful analysis and consideration of the potential impact of secondary environmental factors on the death of planktonic foraminifera shells is necessary.

4.2 Positive oxygen-isotope anomalies

The high $\delta^{18}O$ values of foraminifera are also considered as evidence of seep activity due to the release of large amounts of ^{18}O-rich water molecules during hydrate decomposition (Hesse and Harrison, 1981; Davidson et al., 1983; Matsumoto and Borowski, 2000). This process occurs deeper than SMTZ, thus its influence extends deeper than the record of ^{13}C depletion (Dessandier et al., 2020). Positive $\delta^{18}O$ shifts have been observed in the shells of both living and fossil benthic foraminifera at modern seeps in various locations, such as the South China Sea (Chang et al., 2015), the Barents Sea (Mackensen et al., 2006), the Hikurangi Margin of eastern New Zealand (Martin et al., 2010), the Niger delta (Fontanier et al., 2014), and core records from the Cascadia Margin of northeastern Pacific (Li et al., 2010), the Weddell Sea of Southern Ocean (Thomas et al., 2002), and the Western Mediterranean Sea (Panieri et al., 2012). These shifts of oxygen isotope of benthic foraminifera ($\delta^{18}O_{BF}$), which range from 0‰ to 4.5‰ PDB in bulk analyses, are positively correlated with the period of methane emission but not remarkable compared to $\delta^{13}C_{BF}$ in the same tests (Appendix Table 2).

The oxygen isotope of planktonic foraminifera ($\delta^{18}O_{PF}$) is of critical importance on detecting abnormal climate events since the last glacial period. The marine oxygen isotope record (MIS) has been constructed based on this proxy, which largely reflects the expected changes in paleotemperature (Broecker and Van Donk, 1970; Schiebel et al., 2018). As a result, the $\delta^{18}O_{PF}$ is frequently used to infer both paleotemperature changes and sea-level changes that may have induced methane discharge (Smith et al., 2001; Thomas et al., 2002; Hill et al., 2003). Although some clues of seepage can be detected through $\delta^{18}O_{PF}$ tests, it is more likely to be represented by the carbonate deposits precipitated by AOM rather than the original calcification record (e.g. Dessandier et al., 2020).

Compared to $\delta^{13}C$ records, the $\delta^{18}O$ signatures of foraminifera are less informative of methane seepages, leading to a lack of correlation between $\delta^{13}C$ and $\delta^{18}O$ views. Three main factors contribute to this phenomenon. Firstly, there may not be a clear synergy between $\delta^{18}O_{BF}$ and $\delta^{13}C_{BF}$, as $\delta^{18}O_{BF}$ is more prone to isotopic equilibrium zero-point rather than reflecting $\delta^{18}O$ values in surrounding water bodies (McCorkle et al., 1990). Secondly, $\delta^{18}O_{PF}$ is highly sensitive to temperature changes, which is often used to reconstruct seawater temperature. It has been shown that $\delta^{18}O_{BF}$ becomes heavier with deeper water depth (lower temperature) (Sen Gupta and Aharon, 1994; Cheng et al., 2005; Erbacher and Nelskamp, 2006; Chang et al., 2015). Finally, the post-depositional alteration to dead individuals during the burial process, such as the precipitation of authigenic carbonates, cannot be disregarded and is difficult to measure.

4.3 Influencing factors

The carbon and oxygen isotopes of foraminifera are primarily influenced by vital effects, ecological preferences and environmental parameters such as pH and temperature *in vivo* (Duplessy et al., 1970; Zahn et al., 1986; Bemis et al., 1998; Barras et al., 2010). However, it is also important to consider the secondary environmental impacts on the shells of dead individuals. In the context of cold seep research, the interpretation of the carbon and oxygen stable isotope values of foraminifera shells remains a subject of controversy and can be summarized into five aspects.

4.3.1 External input of organic matter

Since pore water $\delta^{13}C$ is often a negative shift due to the decomposition of organic matter in sediments, making $\delta^{13}C_{DIC}$ is closely related to organic carbon fluxes from the overlying seawater (McCorkle et al., 1990). In a previous study, Stott et al. (2002) posited that sedimentation of photosynthetically produced organic matter in the upper water column led to the release of HCO_3^- into pore water through anaerobic oxidation (Eq. 3), which ultimately resulted in a negative shift in $\delta^{13}C_{BF}$. In low-seepage or non-seepage environments, the anaerobic oxidation of organic carbon was found to be the primary factor affecting the $\delta^{13}C_{BF}$ (Chang et al., 2015). On the other hand, some studies have shown that there may not be a direct relationship between the organic carbon content and the $\delta^{13}C$ of foraminifera in areas with high methane flux, as the $\delta^{13}C_{BF}$ is primarily influenced by methane seepage (Wefer et al., 1994; Chen et al., 2007).

$$2(CH_2O) + SO_4^{\ 2-} \rightarrow H_2S + 2HCO_3^{\ -} \tag{3}$$

Despite previous assumptions, some studies have uncovered that the carbon and oxygen isotope fluctuations of benthic foraminifera may not necessarily support the presence of methane release events, but rather demonstrate stronger correlations with the glacial-interglacial cycle during the Quaternary period. For instance, Hill et al. (2012) found that the $\delta^{18}O_{BF}$ and $\delta^{18}O_{PF}$ in a pockmark of the Storegga Slide complex demonstrated a clear transition between glacial and deglacial stages. In Site 973-4 of the South China Sea, benthic foraminifera *Uvigerina* spp. failed to record a methane-derived signature during the last sea-level lowstand, but instead reflected an increase in organic carbon input during the ice age (-2.26‰ PDB during Last Glacial Maximum, Zhang M et al., 2018). Additionally, the $\delta^{13}C_{PB}$ of *Pulleniatina obliquiloculata* showed a positive shift (0.25-1.25‰ PDB) during the seepage period, although the source of short-term light carbon remains uncertain (Zhang B et al., 2018). Similar observations were made in the Shenhu area (Chen et al., 2010) and the Adriatic Sea (Panieri, 2006), where the stable isotope records of foraminifera were deemed to be independent of methane seepages.

4.3.2 Biochemical processes by foraminifera

The carbon and oxygen isotope signals of foraminifera are influenced by various vital activities, including predation, metabolism, and symbionts. During their lifespan, benthic foraminifera exhibit restricted incorporation of ^{13}C depleted methane-derived carbon (Herguera et al., 2014). Spero and Lea (1996) found that food uptake accounted for 8% to 15% of the $\delta^{13}C_{PF}$ in *Globigerina bulloides*. Additionally, metabolic processes may mix depleted $\delta^{13}C$ into foraminifera shells (Erez, 1978; Grossman, 1987; Herguera et al., 2014). Bacteria thriving in methane-influenced environments, such as Beggiatoa (Panieri, 2006), may provide food for benthic foraminifera, and these microbes have a distinct light carbon isotope composition (Jiasheng et al., 2007). Some taxa incorporate the carbon derived from methane into their shells *via* predation and/or the incorporation of ambient DIC (Bernhard and Reimers, 1991; Panieri, 2006; Melaniuk et al., 2022). Recent studies suggest that benthic foraminifera species, such as *Uvigerina peregrina* (Bernhard et al., 2001; Torres et al., 2003), *Nonionella auris* (Wefer et al., 1994), and *Melonis barleeanus* (Dessandier et al., 2019) could record light $\delta^{13}C$ values by feeding on methanotrophic bacteria and/or incorporating surrounding DIC (Melaniuk et al., 2022).

Apart from this, the presence of symbiotic bacteria within the foraminifera body may have a significant impact on the isotopic signals of living species. The symbiotic relationship between foraminifera and their endosymbiotic bacteria has been noted by several studies (e.g. Bernhard et al., 2001; Barbieri and Panieri, 2004). Despite the recent discovery of chemoautotrophic symbionts in some living seep-related species in 2010, the positive staining reaction of these endobionts with Rose Bengal raises questions about the reliability of isotopic signals produced by living foraminifera (Bernhard et al., 2010). This highlights the need to further investigate the influence of symbiotic bacteria on the isotopic composition of living foraminifera.

4.3.3 Microhabitat preference and species-specific vital effects

Studies have consistently shown that the analysis of seep activity is often performed by comparing isotopic records obtained from the same species or taxa of foraminifera. This is because the sensitivity of foraminifera to their microhabitat plays a crucial role in the interpretation of seepage intensity (Zahn et al., 1986; McCorkle et al., 1990; McGann and Conrad, 2018). The shallow infaunal species, such as *Uvigerina peregrina*, are known to reflect the isotopic signature of the pore water below the sediment-water interface, while deep infaunal species, such as *Globobulimina pacifica*, record the isotopic signature in the depth of dissolved oxygen concentration near zero, in contrast, epifaunal species, such as *Cibicidoides wuellerstorfi*, primarily record the bottom water above the sediment-water interface (McCorkle et al., 1990; Keigwin, 1998; McGann and Conrad, 2018). Similarly, planktonic foraminifera, such as *Globigerinoides ruber*, *Neogloboquadrina dutertrei* and *Pulleniatina obliquiloculata*, mainly record seawater information corresponding to the depth of their living environments (Hemleben et al., 1989). It is suggested that benthic individuals are more likely to *in-situ* record isotopic signals from seep environments compared to their planktonic counterparts, and therefore may have recorded the excursion prior to the latter (Thomas et al., 2002; Martin et al., 2004).

The vital effect refers to the difference in isotopic fractionation between different species of foraminifera, as well as between juveniles and adults of the same species, due to biological processes, such as metabolism. This effect has been shown to result in fluctuations of ~1-2‰ $\delta^{13}C$ values within a single specimen (Rathburn et al., 2000; Rathburn et al., 2003; Panieri, 2006; Melaniuk et al., 2022). Corliss (1985) proposed that reduced absorption of ^{12}C during low-productivity periods leads to the depletion of ^{13}C and lower carbon isotope values of foraminifera. Rathburn et al. (2003) pointed out that different species of benthic foraminifera exhibit distinct ranges of isotope fluctuations, but results from a single species have the potential to be valuable in evaluating methane seepage, assuming no carbonate diagenesis. McGann and Conrad (2018) observed $\delta^{13}C$ depletion in benthic foraminifera from the Kimki Ridge seep, however, multiple fluctuations were evident among species living above or below the water-sediment interface and in shallow or deep sediments. Additionally, the shell size of planktonic foraminifera has also been proposed as a factor in paleoenvironment reconstruction, with a size of 270-320 μm being suggested as most suitable by Spero and Lea (1996). However, Dessandier et al. (2020) found no significant effect of shell size on the results of stable isotope tests in seep environments. While the mechanisms of microhabitat preference and species-specific vital effects are still unclear, it is widely acknowledged that signals from the same species can provide valuable information in investigating and interpreting cold seep environments.

4.3.4 Methane seepage activities

It can be stated that the $\delta^{13}C$ values of benthic foraminifera reflect ambient methane concentration to some extent, serving as an indicator of the intensity of methane seepages. Previous studies have demonstrated that a significant negative shift in foraminifera $\delta^{13}C$ values is commonly associated with high-efficiency AOM during periods of intense methane release (e.g. Millo et al., 2005; Uchida et al., 2008; Consolaro et al., 2015; McGann and Conrad, 2018). On the other hand, normal marine $\delta^{13}C$ values may be observed during periods of no or low methane seepage, where AOM cannot affect the shallow pore water DIC and living foraminifera (Sen Gupta and Aharon, 1994; Chen et al., 2007). However, the relationship between methane seepage intensity and foraminifera activity is complex and not straightforward. A recent study thought that foraminifera communities tend to thrive and actively incorporate methane-derived carbon during periods of moderate seepage, whereas high methane discharge could result in the death of foraminifera and secondary signals begin to superimpose (Melaniuk et al., 2022). Additionally, it should be considered that the growth of foraminifera shells is not continuous and that methane seepage events in geological history are dynamic and transient (Thatcher et al., 2013), making it challenging to discern short-term or rapid methane emissions through shell samples (Dessandier et al., 2020).

To explain the mismatch between δ^{13}C values of benthic foraminifera and pore water DIC, a lot of research has made the efforts. Early research suggested that periods of excessive methane flux have the potential to induce foraminiferal migration, thereby leading to an imbalance carbon isotope records between the biogenic carbonate and pore water DIC (Bernhard and Bowser, 1999). Another explanation is that the extreme circumstance of active AOM may inhibit the metabolism of foraminifera (Sen Gupta and Aharon, 1994). From the results of methane seepage-emulating culture experiments, it is true that methane release can continue to affect the isotopic composition of deep-sea benthic foraminifera (Wollenburg et al., 2015). As for the variability of foraminifera isotopic values, the mixing of different methane sources (e.g. thermogenic and biogenic) with DIC and marine organic carbon seems to be the most plausible explanation (Martin et al., 2007). Despite numerous studies addressing this discrepancy, there remains a lack of clarity regarding the mechanism by which foraminifera fail to record equivalent DIC signals in seep areas.

4.3.5 Methane-derived authigenic carbonate (MDAC) secondary overgrowth

It has been confirmed that MDAC can capture methane-derived ^{13}C-depleted (may lower than 60 ‰ PDB) and ^{18}O-enriched signatures (may higher than 8.9 ‰ PDB) from seep environments (Naehr et al., 2007; Feng et al., 2018; Buckman et al., 2020). Foraminifera fossil shells in sediments are susceptible to MDAC secondary overgrowth after diagenetic alteration, which will obscure the original information contained in the shells (e.g. Torres et al., 2003; Millo et al., 2005; Martin et al., 2007; Sexton and Wilson, 2009; Panieri et al., 2012; Edgar et al., 2013; Consolaro et al., 2015). Both planktonic and benthic foraminifera shells can be affected by this process, especially in deep sediments and specimens from ancient cold seep locations (Figure 5).

Indeed, the extreme values in stable isotopes of both benthic and planktonic foraminifera tests are believed to show an information superimposition by secondary overgrowth of MDAC (e.g. Martin et al., 2010; Fontanier et al., 2014; Panieri et al., 2014). These altered shells possess highly variable and extremely depleted δ^{13}C signals, ranging from -1.6‰ to -55.3‰ PDB (Torres et al., 2003; Hill et al., 2004; Martin et al., 2007; Uchida et al., 2008; Panieri et al., 2009; Martin et al., 2010; Fontanier et al., 2014; Panieri et al., 2016), and false positive shifts in δ^{18}O, ranging from 1.5‰ to 5.3‰ PDB (Ohkushi et al., 2005; Uchida et al., 2008; Naehr et al., 2009; Dessandier et al., 2020).

To quantify the relative amount of MDAC overgrowth on foraminifera shells, Schneider et al. (2017) introduced a formula

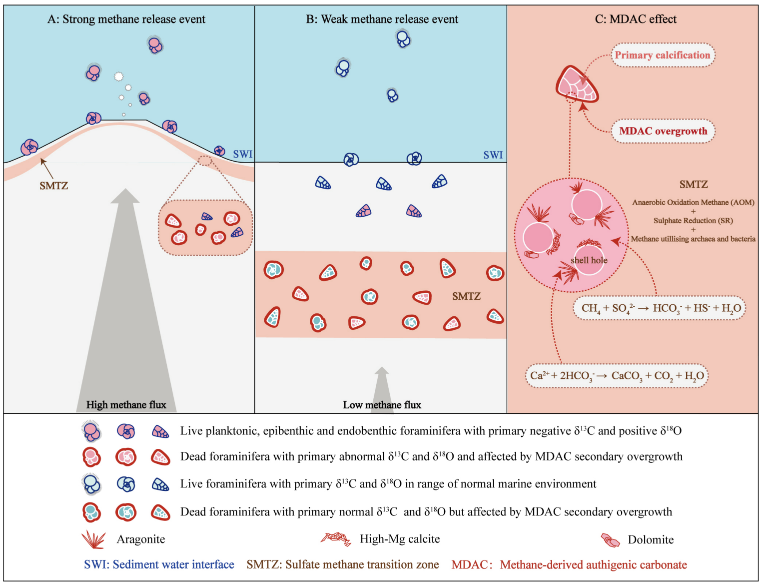

FIGURE 5
Impact on foraminifera stable isotopic signatures from methane seepage intensity and the MDAC-covered coating. **(A)** Impact during high methane flux period. **(B)** Impact during low methane flux period. **(C)** Zoom schematic of the MDAC-covered coating on foraminifera shell.

that takes into account the primary calcification and secondary overgrowth of MDAC (Eq. 4). This method is on the basis that the $\delta^{13}C$ of foraminifera is composed of two segments: the primary calcification and the secondary overgrowth of MDAC (Figure 5C). Results based on this formula indicate that in the Vestnesa Ridge seep sediments, the $\delta^{13}C_{BF}$ signals of *Cassidulina neoteretis* were remarkably mixed by MDAC with a contribution ranging from 55-58% (Schneider et al., 2017). Similarly, in the South China Sea, where seepage activity is relatively weak, MDAC-coupled $\delta^{13}C$ signals were found to contribute 20-30% in benthic specimens (*Uvigerina peregrina* and *Cibicidoides* spp.) and 11-20% in planktonic specimens (*Globigerinoides ruber* and *Pulleniatina obliquiloculata*) (Wan et al., 2018)

$$\begin{aligned}&\mathrm{weight}_{\mathrm{MDAC}}(\%)\\&=(\delta^{13}C_{\text{bulk-foram}}-\delta^{13}C_{\text{pristine-foram}})/(\delta^{13}C_{\mathrm{MDAC}}\\&\quad-\delta^{13}C_{\text{pristine-foram}})\times 100 \qquad (4)\end{aligned}$$

$\delta^{13}C_{\text{bulk-foram}}$ represents the $\delta^{13}C$ of 15 to 28 individual foraminifera, $\delta^{13}C_{\text{pristine-foram}}$ represents assumed $\delta^{13}C$ of pristine foraminifera, and $\delta^{13}C_{\mathrm{MDAC}}$ represents an average $\delta^{13}C$ of some MADC samples.

Notice that the presence of MDAC on foraminifera shells obscure the original information of primary biomass shells, proper cleaning procedures may necessary to obtain the raw isotopic signals. Three cleaning protocols have been established for now, including the use of methanol proposed by Chen et al. (2005), a comprehensive chemical method designed by Barker et al. (2003), and an acid-leaching approach by Millo et al. (2005) and Uchida et al. (2008). The high contribution rates of the MDAC coating to the results may emphasize the importance of properly distinguishing primary and secondary signals in foraminifera shell tests. Results from these procedures revealed that MDAC can dominate up to 10-20% of the $\delta^{13}C$ signals in foraminifera shells from Quaternary sediments in the Southwest Greenland Sea (Millo et al., 2005), and can contribute up to 22% for planktonic foraminifera and 15% for benthic foraminifera in sediments from Hokkaido, Japan (Uchida et al., 2008). Despite attempts to remove MDAC coatings through leaching experiments, negative $\delta^{13}C$ and positive $\delta^{18}O$ values persisted, suggesting that both primary calcification and secondary overgrowth contribute to the excursions of isotopic signatures in foraminifera shells (Panieri et al., 2012; Consolaro et al., 2015). It can be concluded that seepage signatures can be achieved through both primary calcification and secondary overgrowth of MDAC. And by so, foraminifera calcite could still able to exhibit visible excursions in $\delta^{13}C$ even after cleaning by a standard method, and major ancient methane release events or modern seep environments could be identified (e.g. Millo et al., 2005; Wan et al., 2018; Zhou et al., 2020).

However, the altered specimens may difficult to identify *via* light microscopy, and there still remains arduous to selectively eliminate MDAC from the unaltered shells through the process of exhaustive cleaning (Panieri et al., 2017), making the cleaning process to be a subject of debate. Several publications show specimens with pristine microstructures free from secondary mineral overgrowths in methane-charged sediments (Hill et al., 2003; Hill et al., 2004; Martin et al., 2007), and the stable isotopic composition of foraminiferal shells may be not significantly affected by authigenic calcite precipitates (Hill et al., 2004; Mackensen et al., 2006; Panieri et al., 2012). To mitigate the influence of secondary minerals on isotope results, some studies have opted to focus exclusively on specimens that are well-preserved, with complete individuals and distinct rims or bright surfaces (e.g. Fontanier et al., 2014; Zhuang et al., 2016; McGann and Conrad, 2018). However, the effort might somewhat limited since the secondary coatings may thin or infill the interior shell walls (e.g. Torres et al., 2003; Hill et al., 2004; Hill et al., 2012). Typically, the diagenetic alteration of foraminifera calcite is comparatively less problematic in benthic as opposed to planktic foraminifera (Uchida et al., 2008; Edgar et al., 2013). There are indeed reports to reconstruct ancient seepage history by distinguishing negative excursions in untreated benthic foraminiferal $\delta^{13}C$ (e.g. Hill et al., 2012; Panieri et al., 2014; Panieri et al., 2016). Additionally, the negative $\delta^{13}C$ values of planktonic foraminifera tests buried in seep environments are largely believed to be amplified by diagenetic overprinting with MDAC during methane seepage, rather than a true signal of biogenic carbonates (e.g. Cannariato and Stott, 2004; Ohkushi et al., 2005; Hill et al., 2012; Consolaro et al., 2015; Wan et al., 2018). Incidentally, almost all of the extreme isotopic values reported in prior studies were obtained from dead specimens that appear to have undergone post-depositional alteration (e.g. Torres et al., 2003; Hill et al., 2004; Millo et al., 2005; Martin et al., 2010). However, it is undeniable that the remarkably depleted $\delta^{13}C$ values of altered foraminifera indirectly confirm the formation of authigenic carbonates in proximity to the shift of the SMTZ and the associated alteration in past methane release events.

5 Summary

(1) The presence of specific types and assemblages of benthic foraminifera in cold seep sediments reflects the micro-environmental conditions associated with dynamic methane seepages. Despite significant research efforts, the endemic species of benthic foraminifera in seep environments remain to be identified. The dominated assemblages are typically hyaline, some taxa may able to thrive in seep areas due to their high tolerance to the challenging conditions and/or feed on associated methanotrophic microbial communities. These benthic foraminifera, including endobenthic taxa such as *Uvigerina*, *Bolivina*, *Bulimina*, *Chilostomella*, *Globobulimina*, *Nonionella*, and *Melonis*, as well as epibenthic taxa such as *Epistominella*, *Cibicidoides*, and *Globocassidulina*, provide valuable opportunities to study the seep environments.

(2) The assemblage patterns of benthic foraminifera in cold seep environments are found to be inconsistent and influenced by various environmental factors, such as

seepage activity, oxygen levels, total organic carbon content, substrate type, and microhabitat conditions. In areas of high seeping intensity, hypoxia-tolerant endobenthic species tend to dominate the community within the sediments closest to the seafloor. Meanwhile, agglutinate taxa may experience survival difficulties in these harsh conditions. In contrast, when seepage intensity decreases and environmental conditions become less harsh, oxygen-loving epibenthic species may become abundant. It is expected that benthic foraminifera communities will experience maximal flourishing during periods of moderate seepage intensity, where food supplies are abundant and conditions are more favorable for microbial growth.

(3) In methane-charged sediments, a pristine shell of foraminifera may undergo widespread alteration by secondary mineralization after the death of the organisms. It can be inferred that foraminifera shells buried in seep-associated sediments may exhibit overprinting signals of secondary authigenic carbonate-bound (Mg, Sr, Mn, Ba) coatings and the growth of gypsum and pyrite microcrystals. The alteration of secondary mineralization to seep foraminifera reveals a magnesium, barium, and strontium incorporation in carbonates formed within SMTZ, and the appearance of gypsum and pyrite shows a typical signature of cold seep environments. Typically, the degrees of secondary mineralization may be served as a valuable proxy for the intensity of AOM and associated post-depositional alteration during methane seepages.

(4) The detection of abnormal negative $\delta^{13}C$ and positive $\delta^{18}O$ values in foraminifera shells is considered a unique fingerprinting of methane release events. Benthic foraminifera, which live above or below the surface of seafloor sediments, are known to be reliable recorders of methane-derived light carbon isotopes and heavy oxygen isotopes released from hydrate decomposition. While this isotopic imprinting may also be observed in planktonic foraminifera tests which are likely to have been altered by methane-derived authigenic carbonate.

(5) The variations in $\delta^{13}C$ and $\delta^{18}O$ signatures preserved in foraminifera shells may reflect the influence of external organic matter inputs, biochemical processes, microhabitat parameters, seeping activities, and post-burial secondary authigenic carbonate overgrowth. To minimize these uncertainties, it is advisable to use live foraminifera to study modern cold seep activities, as they provide the best record of *in situ* isotopic data. Benthic species are preferable to planktonic individuals as they are thought to have a higher potential to capture methane-derived light carbon isotopes and heavy oxygen isotopes. To effectively evaluate the evolutionary history of a seepage, the isotopic results of a single species must be considered in conjunction with other geological and environmental data. Cleaning protocols can be utilized before stable isotopic analyses to distinguish the signals originating from primary biogenic calcite and secondary carbonate coatings. Foraminifera whether after strict cleaning procedures, or selected under microscopic to minimize authigenic contamination, or in their original state, cannot completely eliminate the influence of secondary carbonate isotopes signals, but all have the potential to exhibit a response to the cold seep environments.

Author contributions

YHL: Data collection, Writing original draft; HY: Data collection, Writing–review and editing; BH and YJL: Writing–review and editing; HL: Conceptualization, Supervision, Writing–review and editing. BH supervised the study; YHL wrote the original draft; HY, HL, and YJL contributed to refining the draft. All authors contributed to the article and approved the submitted version.

Conflict of interest

The authors declare that the research was conducted in the absence of any commercial or financial relationships that could be construed as a potential conflict of interest.

Publisher's note

Supplementary material

The Supplementary Material for this article can be found online at: https://www.frontiersin.org/articles/10.3389/fmars.2023.1157879/full#supplementary-material

APPENDIX TABLE 1
Summary of cold seeps benthic foraminiferal assemblages.

APPENDIX TABLE 2
Summary of stable isotopic records of cold seep related benthic foraminifera.

References

Abu-Zied, R. H., Rohling, E. J., Jorissen, F. J., Fontanier, C., Casford, J. S., and Cooke, S. (2008). Benthic foraminiferal response to changes in bottom-water oxygenation and organic carbon flux in the eastern Mediterranean during LGM to recent times. *Mar. Micropaleontol* 67 (1-2), 46–68. doi: 10.1016/j.marmicro.2007.08.006

Aharon, P., and Fu, B. (2000). Microbial sulfate reduction rates and sulfur and oxygen isotope fractionations at oil and gas seeps in deepwater gulf of Mexico. *Geochimica Cosmochimica Acta* 64 (2), 233–246. doi: 10.1016/s0016-7037(99)00292-6

Argentino, C., Waghorn, K. A., Vadakkepuliyambatta, S., Polteau, S., Bünz, S., and Panieri, G. (2021). Dynamic and history of methane seepage in the SW barents Sea: new insights from leirdjupet fault complex. *Sci. Rep.* 11 (1), 1–13. doi: 10.1038/s41598-021-83542-0

Barbieri, R., and Panieri, G. (2004). How are benthic foraminiferal faunas influenced by cold seeps? evidence from the Miocene of Italy. *Palaeogeography Palaeoclimatol Palaeoecol.* 204 (3-4), 257–275. doi: 10.1016/S0031-0182(03)00730-2

Barker, S., Greaves, M., and Elderfield, H. (2003). A study of cleaning procedures used for foraminiferal Mg/Ca paleothermometry. *Geochemistry Geophysics Geosystems* 4 (9), 1–20. doi: 10.1029/2003gc000559

Barras, C., Duplessy, J., Geslin, E., Michel, E., and Jorissen, F. J. (2010). Calibration of $\delta^{18}O$ of cultured benthic foraminiferal calcite as a function of temperature. *Biogeosciences* 7 (4), 1349–1356. doi: 10.5194/bg-7-1349-2010

Bemis, B. E., Spero, H. J., Bijma, J., and Lea, D. W. (1998). Reevaluation of the oxygen isotopic composition of planktonic foraminifera: experimental results and revised paleotemperature equations. *Paleoceanography* 13 (2), 150–160. doi: 10.1029/98PA00070

Bentov, S., and Erez, J. (2006). Impact of biomineralization processes on the mg content of foraminiferal shells: a biological perspective. *Geochemistry Geophysics Geosystems* 7 (1), 1–11. doi: 10.1029/2005GC001015

Berner, R. A. (1982). Burial of organic carbon and pyrite sulfur in the modern ocean: its geochemical and environmental significance. *Am. J. Sci.* 282 (4), 451–473. doi: 10.2475/ajs.282.4.451

Berner, R. A. (1985). Sulphate reduction, organic matter decomposition and pyrite formation. *Philos. Trans. R. Soc. London. Ser. A Math. Phys. Sci.* 315 (1531), 25–38. doi: 10.1098/rsta.1985.0027

Bernhard, J. M., and Bowser, S. S. (1999). Benthic foraminifera of dysoxic sediments: chloroplast sequestration and functional morphology. *Earth-Science Rev.* 46 (1-4), 149–165. doi: 10.1016/S0012-8252(99)00017-3

Bernhard, J. M., Buck, K. R., and Barry, J. P. (2001). Monterey Bay cold-seep biota: assemblages, abundance, and ultrastructure of living foraminifera. *Deep Sea Res. Part I* 48 (10), 2233–2249. doi: 10.1016/s0967-0637(01)00017-6

Bernhard, J. M., Martin, J. B., and Rathburn, A. E. (2010). Combined carbonate carbon isotopic and cellular ultrastructural studies of individual benthic foraminifera: 2. toward an understanding of apparent disequilibrium in hydrocarbon seeps. *Paleoceanography* 25 (4), 1–12. doi: 10.1029/2009PA001846

Bernhard, J. M., and Reimers, C. E. (1991). Benthic foraminiferal population fluctuations related to anoxia: Santa Barbara basin. *Biogeochemistry* 15 (2), 127–149. doi: 10.1007/BF00003221

Bhaumik, A. K., and Gupta, A. K. (2005). Deep-sea benthic foraminifera from gas hydrate-rich zone, Blake ridge, Northwest Atlantic (ODP hole 997A). *Curr. Sci.* 88 (12), 1969–1973. doi: 10.1016/j.rsma.2021.101949

Bhaumik, A. K., and Gupta, A. K. (2007). Evidence of methane release from Blake ridge ODP hole 997A during the plio-pleistocene: benthic foraminifer fauna and total organic carbon. *Curr. Sci.* 92 (2), 192–199. Available at: https://www.jstor.org/stable/24096688.

Blackmon, P. D., and Todd, R. (1959). Mineralogy of some foraminifera as related to their classification and ecology. *J. Paleontol* 33 (1), 1–15.

Boetius, A., Ravenschlag, K., Schubert, C. J., Rickert, D., Widdel, F., Gieseke, A., et al. (2000). A marine microbial consortium apparently mediating anaerobic oxidation of methane. *Nature* 407 (6804), 623–626. doi: 10.1038/35036572

Borowski, W. S., Paull, C. K., and Ussler, W.III (1996). Marine pore-water sulfate profiles indicate in situ methane flux from underlying gas hydrate. *Geology* 24 (7), 655–658. doi: 10.1130/0091-7613(1996)024<0655:mpwspi>2.3.co;2

Borowski, W. S., Rodriguez, N. M., Paull, C. K., and Ussler, I. I. I. (2013). Are ^{34}S-enriched authigenic sulfide minerals a proxy for elevated methane flux and gas hydrates in the geologic record? *Mar. Petroleum Geology* 43, 381–395. doi: 10.1016/j.marpetgeo.2012.12.009

Broecker, W. S., and Van Donk, J. (1970). Insolation changes, ice volumes, and the O^{18} record in deep-sea cores. *Rev. Geophysics* 8 (1), 169–198. doi: 10.1029/rg008i001p00169

Brooks, J. M., Field, M. E., and Kennicutt, M. C.II (1991). Observations of gas hydrates in marine sediments, offshore northern California. *Mar. Geology* 96 (1-2), 103–109. doi: 10.1016/0025-3227(91)90204-H

Buckman, J., Donnelly, T., Jiang, Z., Lewis, H., and Ruffell, A. (2020). Methane derived authigenic carbonate (MDAC) aragonite cemented quaternary hardground from a methane cold seep, rathlin basin, northern Ireland: $\delta^{13}C$ and $\delta^{18}O$ isotopes, environment, porosity and permeability. *Geosciences* 10 (7), 255. doi: 10.3390/geosciences10070255

Burkett, A. M., Rathburn, A. E., Elena Pérez, M., Levin, L. A., and Martin, J. B. (2016). Colonization of over a thousand cibicidoides wuellerstorfi (foraminifera: schwager 1866) on artificial substrates in seep and adjacent off-seep locations in dysoxic, deep-sea environments. *Deep Sea Res. Part I* 117, 39–50. doi: 10.1016/j.dsr.2016.08.011

Caldwell, S. L., Laidler, J. R., Brewer, E. A., Eberly, J. O., Sandborgh, S. C., and Colwell, F. S. (2008). Anaerobic oxidation of methane: mechanisms, bioenergetics, and the ecology of associated microorganisms. *Environ. Sci. Technol.* 42 (18), 6791–6799. doi: 10.1021/es800120b

Cannariato, K. G., and Stott, L. D. (2004). Evidence against clathrate-derived methane release to Santa Barbara basin surface waters? *Geochemistry Geophysics Geosystems* 5 (5), 1–9. doi: 10.1029/2003GC000600

Ceramicola, S., Dupré, S., Somoza, L., and Woodside, J. (2018). "Cold seep systems," in *Submarine geomorphology*. Eds. A. Micallef, S. Krastel and A. Savini (Switzerland: Springer Geology. Springer, Cham), 367–387. doi: 10.1007/978-3-319-57852-1_19

Chang, Z., Fang, C., Sihai, C., Hongfeng, L., Yang, Z., and Guanghu, L. (2015). Stable isotopic characteristics and their influencing factors of benthic foraminifera in the prospective gas hydrate area from the northern south China Sea since the last glacial. *Quaternary Sci.* 35 (2), 422–432. doi: 10.11928/j.issn.1001-7410.2015.02.17

Chen, D. F., Feng, D., Su, Z., Song, Z. G., Chen, G. Q., and Cathles, L. M. (2006). Pyrite crystallization in seep carbonates at gas vent and hydrate site. *Materials Sci. Engineering: C* 26 (4), 602–605. doi: 10.1016/j.msec.2005.08.037

Chen, D. F., Huang, Y. Y., Yuan, X. L., and Cathles, III, L.M. (2005). Seep carbonates and preserved methane oxidizing archaea and sulfate reducing bacteria fossils suggest recent gas venting on the seafloor in the northeastern south China Sea. *Mar. petroleum Geology* 22 (5), 613–621. doi: 10.1016/j.marpetgeo.2005.05.002

Chen, F., Su, X., Lu, H., Chen, C., Zhou, Y., Cheng, S., et al. (2007). Carbon stable isotopic composition of benthic foraminifers from the north of the south China Sea: indicator of methane-rich environment. *Mar. Geology Quaternary Geology* 27 (4), 1–7. doi: 10.1016/j.palaeo.2006.10.002

Chen, F., Zhou, Y., Su, X., Lu, H., Liu, G., and Zhuang, C. (2010). Benthic foraminifera and stable isotopic composition of gas hydrate-bearing sediments from shenhu area in the northern south China Sea. *Mar. Geology Quaternary Geology* 30 (2), 1–8. doi: 10.3724/SP.J.1140.2010.02001

Cheng, X., Huang, B., Jian, Z., Zhao, Q., Tian, J., and Li, J. (2005). Foraminiferal isotopic evidence for monsoonal activity in the south China Sea: a present-LGM comparison. *Mar. Micropaleontol* 54 (1-2), 125–139. doi: 10.1016/j.marmicro.2004.09.007

Consolaro, C., Rasmussen, T. L., Panieri, G., Mienert, J., Bünz, S., and Sztybor, K. (2015). Carbon isotope ($\delta^{13}C$) excursions suggest times of major methane release during the last 14 kyr in fram strait, the deep-water gateway to the Arctic. *Climate Past* 11 (4), 669–685. doi: 10.5194/cp-11-669-2015

Corliss, B. H. (1985). Microhabitats of benthic foraminifera within deep-sea sediments. *Nature* 314 (6010), 435–438. doi: 10.1038/314435a0

Damm, E., Mackensen, A., Budéus, G., Faber, E., and Hanfland, C. (2005). Pathways of methane in seawater: plume spreading in an Arctic shelf environment (SW-spitsbergen). *Continental Shelf Res.* 25 (12-13), 1453–1472. doi: 10.1016/j.csr.2005.03.003

Dantas, R. C., Hassan, M. B., Cruz, F. W., and Jovane, L. (2022). Evidence for methane seepage in south Atlantic from the occurrence of authigenic gypsum and framboidal pyrite in deep-sea sediments. *Mar. Petroleum Geology* 142, 105727. doi: 10.1016/j.marpetgeo.2022.105727

Davidson, D. W., Leaist, D. G., and Hesse, R. (1983). Oxygen-18 enrichment in the water of a clathrate hydrate. *Geochimica Cosmochimica Acta* 47 (12), 2293–2295. doi: 10.1016/0016-7037(83)90053-4

Dessandier, P., Borrelli, C., Kalenitchenko, D., and Panieri, G. (2019). Benthic foraminifera in Arctic methane hydrate bearing sediments. *Front. Mar. Sci.* 6. doi: 10.3389/fmars.2019.00765

Dessandier, P., Borrelli, C., Yao, H., Sauer, S., Hong, W., and Panieri, G. (2020). Foraminiferal $\delta^{18}O$ reveals gas hydrate dissociation in Arctic and north Atlantic ocean sediments. *Geo-Marine Lett.* 40 (4), 507–523. doi: 10.1007/s00367-019-00635-6

Dickens, G. R., Castillo, M. M., and Walker, J. C. (1997). A blast of gas in the latest Paleocene: simulating first-order effects of massive dissociation of oceanic methane hydrate. *Geology* 25 (3), 259–262. doi: 10.1130/0091-7613(1997)025<0259:abogit>2.3.co;2

Dickens, G. R., O'Neil, J. R., Rea, D. K., and Owen, R. M. (1995). Dissociation of oceanic methane hydrate as a cause of the carbon isotope excursion at the end of the Paleocene. *Paleoceanography* 10 (6), 965–971. doi: 10.1029/95pa02087

Duplessy, J. C., Lalou, C., and Vinot, A. C. (1970). Differential isotopic fractionation in benthic foraminifera and paleotemperatures reassessed. *Science* 168 (3928), 250–251. doi: 10.1126/science.168.3928.250

Edgar, K. M., Pälike, H., and Wilson, P. A. (2013). Testing the impact of diagenesis on the $\delta^{18}O$ and $\delta^{13}C$ of benthic foraminiferal calcite from a sediment burial depth transect in the equatorial pacific. *Paleoceanography* 28 (3), 468–480. doi: 10.1002/palo.20045

Egger, M., Riedinger, N., Mogollón, J. M., and Jørgensen, B. B. (2018). Global diffusive fluxes of methane in marine sediments. *Nat. Geosci.* 11 (6), 421–425. doi: 10.1038/s41561-018-0122-8

Erbacher, J., and Nelskamp, S. (2006). Comparison of benthic foraminifera inside and outside a sulphur-oxidizing bacterial mat from the present oxygen-minimum zone off Pakistan (NE Arabian Sea). *Deep Sea Res. Part I: Oceanographic Res. Papers* 53 (5), 751–775. doi: 10.1016/j.dsr.2006.02.003

Erez, J. (1978). Vital effect on stable-isotope composition seen in foraminifera and coral skeletons. *Nature* 273 (5659), 199–202. doi: 10.1038/273199a0

Feng, D., Qiu, J., Hu, Y., Peckmann, J., Guan, H., Tong, H., et al. (2018). Cold seep systems in the south China Sea: an overview. *J. Asian Earth Sci.* 168, 3–16. doi: 10.1016/j.jseaes.2018.09.021

Fontanier, C., Koho, K. A., Goñi-Urriza, M. S., Deflandre, B., Galaup, S., Ivanovsky, A., et al. (2014). Benthic foraminifera from the deep-water Niger delta (Gulf of guinea): assessing present-day and past activity of hydrate pockmarks. *Deep Sea Res. Part I: Oceanographic Res. Papers* 94, 87–106. doi: 10.1016/j.dsr.2014.08.011

Gooday, A. J. (1994). The biology of deep-sea foraminifera: a review of some advances and their applications in paleoceanography. *Palaios* 9 (1), 14–31. doi: 10.2307/3515075

Griffith, E. M., and Paytan, A. (2012). Barite in the ocean–occurrence, geochemistry and palaeoceanographic applications. *Sedimentology* 59 (6), 1817–1835. doi: 10.1111/j.1365-3091.2012.01327.x

Grossman, E. L. (1987). Stable isotopes in modern benthic foraminifera; a study of vital effect. *J. Foraminiferal Res.* 17 (1), 48–61. doi: 10.2113/gsjfr.17.1.48

Gupta, B. K. S., Smith, L. E., and Lobegeier, M. K. (2007). Attachment of foraminifera to vestimentiferan tubeworms at cold seeps: refuge from seafloor hypoxia and sulfide toxicity. *Mar. Micropaleontol* 62 (1), 1–6. doi: 10.1016/j.marmicro.2006.06.007

Heinz, P., Sommer, S., Pfannkuche, O., and Hemleben, C. (2005). Living benthic foraminifera in sediments influenced by gas hydrates at the cascadia convergent margin, NE pacific. *Mar. ecology. Prog. Ser. (Halstenbek)* 304, 77–89. doi: 10.3354/meps304077

Hemleben, C., Spindler, M., and Anderson, O. R. (1989). Modern planktonic foraminifera. *Springer New York NY*. 363, 77–89. doi: 10.1007/978-1-4612-3544-6

Herguera, J. C., Paull, C. K., Perez, E., Ussler, W.III, and Peltzer, E. (2014). Limits to the sensitivity of living benthic foraminifera to pore water carbon isotope anomalies in methane vent environments. *Paleoceanography* 29 (3), 273–289. doi: 10.1002/2013PA002457

Hesse, R., and Harrison, W. E. (1981). Gas hydrates (clathrates) causing pore-water freshening and oxygen isotope fractionation in deep-water sedimentary sections of terrigenous continental margins. *Earth planetary Sci. Lett.* 55 (3), 453–462. doi: 10.1016/0012-821X(81)90172-2

Hill, T. M., Kennett, J. P., and Spero, H. J. (2003). Foraminifera as indicators of methane-rich environments: a study of modern methane seeps in Santa Barbara channel, California. *Mar. Micropaleontol* 49 (1-2), 123–138. doi: 10.1016/S0377-8398(03)00032-X

Hill, T. M., Kennett, J. P., and Valentine, D. L. (2004). Isotopic evidence for the incorporation of methane-derived carbon into foraminifera from modern methane seeps, hydrate ridge, northeast pacific. *Geochimica Cosmochimica Acta* 68 (22), 4619–4627. doi: 10.1016/j.gca.2004.07.012

Hill, T. M., Paull, C. K., and Critser, R. B. (2012). Glacial and deglacial seafloor methane emissions from pockmarks on the northern flank of the storegga slide complex. *Geo-Marine Lett.* 32 (1), 73–84. doi: 10.1007/s00367-011-0258-7

Hu, Y., Feng, D., Peckmann, J., Roberts, H. H., and Chen, D. (2014). New insights into cerium anomalies and mechanisms of trace metal enrichment in authigenic carbonate from hydrocarbon seeps. *Chem. Geology* 381 (14), 55–66. doi: 10.1016/j.chemgeo.2014.05.014

Jiasheng, W., Wang, Y., and Li, Q. (2007). Potential contributions of extremophiles to hydrocarbon resources in marine extreme environments: a review. *Front. Earth Sci. China* 1 (4), 444–451. doi: 10.1007/s11707-007-0055-9

Jones, R. W. (1993). "Preliminary observations on benthonic foramininera associated with biogenic gas seep in the north Sea". in *Applied Micropalaeontology*. Eds. D. G. Jenkins (Dordrecht: Springer), 69–91. doi: 10.1007/978-94-017-0763-3_3

Jorissen, F. J. (1992). Ecology and palaeoecology of benthic foraminifera. *Palaeogeography Palaeoclimatol Palaeoecol.* 95 (3–4), 349–350. doi: 10.1016/0031-0182(92)90153-V

Joye, S. B., Bowles, M. W., Samarkin, V. A., Hunter, K. S., and Niemann, H. (2010). Biogeochemical signatures and microbial activity of different cold-seep habitats along the gulf of Mexico deep slope. *Deep Sea Res. Part II: Topical Stud. Oceanography* 57 (21-23), 1990–2001. doi: 10.1016/j.dsr2.2010.06.001

Judd, A., Croker, P., Tizzard, L., and Voisey, C. (2007). Extensive methane-derived authigenic carbonates in the Irish Sea. *Geo-Marine Lett.* 27, 259–267. doi: 10.1007/s00367-007-0079-x

Judd, A., Noble-James, T., Golding, N., Eggett, A., Diesing, M., Clare, D., et al. (2020). The croker carbonate slabs: extensive methane-derived authigenic carbonate in the Irish Sea–nature, origin, longevity and environmental significance. *Geo-Marine Lett.* 40 (4), 423–438. doi: 10.1007/s00367-019-00584-0

Karstens, J., Haflidason, H., Becker, L. W. M., Berndt, C., Rüpke, L., Planke, S., et al. (2018). Glacigenic sedimentation pulses triggered post-glacial gas hydrate dissociation. *Nat. Commun.* 9 (1), 635. doi: 10.1038/s41467-018-03043-z

Kaufman, A. J., and Knoll, A. H. (1995). Neoproterozoic variations in the c-isotopic composition of seawater: stratigraphic and biogeochemical implications. *Precambrian Res.* 73 (1-4), 27–49. doi: 10.1016/0301-9268(94)00070-8

Keigwin, L. D. (1998). Glacial-age hydrography of the far northwest pacific ocean. *Paleoceanography* 13 (4), 323–339. doi: 10.1029/98PA00874

Keigwin, L. D. (2002). Late pleistocene-Holocene paleoceanography and ventilation of the gulf of California. *J. Oceanography* 58 (2), 421–432. doi: 10.1023/A:1015830313175

Kennett, J. P., Cannariato, K. G., Hendy, I. L., and Behl, R. J. (2000). Carbon isotopic evidence for methane hydrate instability during quaternary interstadials. *Science* 288 (5463), 128–133. doi: 10.1126/science.288.5463.128

Ketzer, M., Praeg, D., Rodrigues, L. F., Augustin, A., Pivel, M. A. G., Rahmati-Abkenar, M., et al. (2020). Gas hydrate dissociation linked to contemporary ocean warming in the southern hemisphere. *Nat. Commun.* 11 (1), 3788–3789. doi: 10.1038/s41467-020-17289-z

Khusid, T. A., Domanov, M. M., and Svininnikov, A. M. (2006). Species composition and distribution of foraminifers in the deryugin basin (Sea of Okhotsk). *Biol. Bull.* 33 (2), 172–178. doi: 10.1134/S1062359006020129

Klinkhammer, G. P., Mix, A. C., and Haley, B. A. (2009). Increased dissolved terrestrial input to the coastal ocean during the last deglaciation. *Geochemistry Geophysics Geosystems* 10 (3), 1–11. doi: 10.1029/2008GC002219

Knittel, K., and Boetius, A. (2009). Anaerobic oxidation of methane: progress with an unknown process. *Annu. Rev. Microbiol.* 63, 311–334. doi: 10.1146/annurev.micro.61.080706.093130

Kocherla, M. (2013). Authigenic gypsum in gas-hydrate associated sediments from the East coast of India (Bay of Bengal). *Acta Geologica Sinica-English Edition* 87 (3), 749–760. doi: 10.1111/1755-6724.12086

Kucera, M. (2007). Chapter six planktonic foraminifera as tracers of past oceanic environments. *Developments Mar. geology* 1, 213–262. doi: 10.1016/S1572-5480(07)01011-1

Kvenvolden, K. A. (1993). Gas hydrates–geological perspective and global change. *Rev. geophysics* 31 (2), 173–187. doi: 10.1029/93RG00268

Large, R. R., Mukherjee, I., Gregory, D. D., Steadman, J. A., Maslennikov, V. V., and Meffre, S. (2017). Ocean and atmosphere geochemical proxies derived from trace elements in marine pyrite; implications for ore genesis in sedimentary basins. *Economic geology Bull. Soc. Economic Geologists* 112 (2), 423–450. doi: 10.2113/econgeo.112.2.423

Lei, H., Cao, C., Ou, W., Gong, C., and Shi, C. (2012). Carbon and oxygen isotope characteristics of foraminiferan from northern south China Sea sediments and their significance to late quaternary hydrate decomposition. *J. Cent. South Univ.* 19 (6), 1728–1740. doi: 10.1007/s11771-012-1200-5

Li, N., Feng, D., Wan, S., Peckmann, J., Guan, H., Wang, X., et al. (2021). Impact of methane seepage dynamics on the abundance of benthic foraminifera in gas hydrate bearing sediments: new insights from the south China Sea. *Ore Geology Rev.* 136, 104247. doi: 10.1016/j.oregeorev.2021.104247

Li, Q., Wang, J., Chen, J., and Wei, Q. (2010). Stable carbon isotopes of benthic foraminifers from iodp expedition 311 as possible indicators of episodic methane seep events in a gas hydrate geosystem. *Palaios* 25 (10), 671–681. doi: 10.2307/40865499

Lin, Q., Wang, J., Algeo, T. J., Su, P., and Hu, G. (2016a). Formation mechanism of authigenic gypsum in marine methane hydrate settings: evidence from the northern south China Sea. *Deep Sea Res. Part I: Oceanographic Res. Papers* 115, 210–220. doi: 10.1016/j.dsr.2016.06.010

Lin, Q., Wang, J., Algeo, T. J., Sun, F., and Lin, R. (2016b). Enhanced framboidal pyrite formation related to anaerobic oxidation of methane in the sulfate-methane transition zone of the northern south China Sea. *Mar. Geology* 379 (1), 100–108. doi: 10.1016/j.margeo.2016.05.016

Liu, X., Li, A., Dong, J., Zhuang, G., Xu, F., and Wan, S. (2018). Nonevaporative origin for gypsum in mud sediments from the East China Sea shelf. *Mar. Chem.* 205 (20), 90–97. doi: 10.1016/j.marchem.2018.08.009

Lobegeier, M. K., and Sen Gupta, B. K. (2008). Foraminifera of hydrocarbon seeps, gulf of Mexico. *J. Foraminiferal Res.* 38 (2), 93–116. doi: 10.1175/JTECH2026.1

Mackensen, A., Wollenburg, J., and Licari, L. (2006). Low $\delta^{13}C$ in tests of live epibenthic and endobenthic foraminifera at a site of active methane seepage. *Paleoceanography* 21 (2), 1–12. doi: 10.1029/2005PA001196

Martin, J. B., Day, S. A., Rathburn, A. E., Perez, M. E., Mahn, C., and Gieskes, J. (2004). Relationships between the stable isotopic signatures of living and fossil foraminifera in Monterey bay, California. *Geochemistry Geophysics Geosystems* 5 (4), 1–25. doi: 10.1029/2003GC000629

Martin, R. A., Nesbitt, E. A., and Campbell, K. A. (2007). Carbon stable isotopic composition of benthic foraminifera from pliocene cold methane seeps, cascadia accretionary margin. *Palaeogeography Palaeoclimatol Palaeoecol.* 246 (2-4), 260–277. doi: 10.1016/j.palaeo.2006.10.002

Martin, R. A., Nesbitt, E. A., and Campbell, K. A. (2010). The effects of anaerobic methane oxidation on benthic foraminiferal assemblages and stable isotopes on the hikurangi margin of eastern new Zealand. *Mar. Geology* 272 (1-4), 270–284. doi: 10.1016/j.margeo.2009.03.024

Matsumoto, R., and Borowski, W. S. (2000). Gas hydrate estimates from newly determined oxygen isotopic fractionation (αGH-IW) and $\delta^{18}O$ anomalies of the interstitial waters: leg 164, Blake ridge. *Proc. ODP Sci. Results* 164, 59–66. doi: 10.2973/odp.proc.sr.164.206.2000

McConnaughey, T. A., Burdett, J., Whelan, J. F., and Paull, C. K. (1997). Carbon isotopes in biological carbonates: respiration and photosynthesis. *Geochimica Cosmochimica Acta* 61 (3), 611–622. doi: 10.1016/S0016-7037(96)00361-4

McCorkle, D. C., Keigwin, L. D., Corliss, B. H., and Emerson, S. R. (1990). The influence of microhabitats on the carbon isotopic composition of deep-sea benthic foraminifera. *Paleoceanography* 5 (2), 161–185. doi: 10.1029/PA005i002p00161

McGann, M., and Conrad, J. E. (2018). Faunal and stable isotopic analyses of benthic foraminifera from the southeast seep on kimki ridge offshore southern California, USA. *Deep Sea Res. Part II* 150, 92–117. doi: 10.1016/j.dsr2.2018.01.011

McQuay, E. L., Torres, M. E., Collier, R. W., Huh, C., and McManus, J. (2008). Contribution of cold seep barite to the barium geochemical budget of a marginal basin. *Deep Sea Res. Part I* 55 (6), 801–811. doi: 10.1016/j.dsr.2008.03.001

Melaniuk, K. (2021). Effectiveness of fluorescent viability assays in studies of arctic cold seep foraminifera. *Front. Mar. Sci.* 8. doi: 10.3389/fmars.2021.587748

Melaniuk, K., Sztybor, K., Treude, T., Sommer, S., and Rasmussen, T. L. (2022). Influence of methane seepage on isotopic signatures in living deep-sea benthic foraminifera, 79° n. *Sci. Rep.* 12 (1) 1169. doi: 10.1038/s41598-022-05175-1

Merinero, R., Lunar, R., Martinez-Frias, J., Somoza, L., and Diaz-del-Rio, V. (2008). Iron oxyhydroxide and sulphide mineralization in hydrocarbon seep-related carbonate submarine chimneys, gulf of cadiz (SW Iberian peninsula). *Mar. Petroleum Geology* 25 (8), 706–713. doi: 10.1016/j.marpetgeo.2008.03.005

Miao, X., Feng, X., Liu, X., Li, J., and Wei, J. (2021). Effects of methane seepage activity on the morphology and geochemistry of authigenic pyrite. *Mar. Petroleum Geology* 133, 105231. doi: 10.1016/j.marpetgeo.2021.105231

Millo, C., Sarnthein, M., Erlenkeuser, H., and Frederichs, T. (2005). Methane-driven late pleistocene $\delta^{13}C$ minima and overflow reversals in the southwestern Greenland Sea. *Geology* 33 (11), 873–876. doi: 10.1130/G21790.1

Naehr, T. H., Birgel, D., Bohrmann, G., MacDonald, I. R., and Kasten, S. (2009). Biogeochemical controls on authigenic carbonate formation at the chapopote "asphalt volcano", bay of campeche. *Chem. Geology* 266 (3-4), 390–402. doi: 10.1016/j.chemgeo.2009.07.002

Naehr, T. H., Eichhubl, P., Orphan, V. J., Hovland, M., Paull, C. K., Ussler, W.III, et al. (2007). Authigenic carbonate formation at hydrocarbon seeps in continental margin sediments: a comparative study. *Deep Sea Res. Part II* 54 (11-13), 1268–1291. doi: 10.1016/j.dsr2.2007.04.010

Niewöhner, C., Hensen, C., Kasten, S., Zabel, M., and Schulz, H. D. (1998). Deep sulfate reduction completely mediated by anaerobic methane oxidation in sediments of the upwelling area off Namibia. *Geochimica cosmochimica Acta* 62 (3), 455–464. doi: 10.1016/S0016-7037(98)00055-6

Ohkushi, K., Ahagon, N., Uchida, M., and Shibata, Y. (2005). Foraminiferal isotope anomalies from northwestern pacific marginal sediments. *Geochemistry Geophysics Geosystems* 6 (4), 1–15. doi: 10.1029/2004gc000787

Pan, M., Wu, D., Yang, F., Sun, T., Wu, N., and Liu, L. (2018). Geochemical sedimentary evidence from core 973-2 for methane activity near the jiulong methane reef in the northern south China Sea. *Interpretation* 6 (1), 163–174. doi: 10.1190/int-2017-0001.1

Panieri, G. (2003). Benthic foraminifera response to methane release in an Adriatic Sea pockmark. *Rivista Italiana di Paleontologia e Stratigrafia* 109 (3), 549–562. doi: 10.13130/2039-4942/5523

Panieri, G. (2005). Benthic foraminifera associated with a hydrocarbon seep in the rockall trough (NE Atlantic). *Geobios* 38 (2), 247–255. doi: 10.1016/j.geobios.2003.10.004

Panieri, G. (2006). Foraminiferal response to an active methane seep environment: a case study from the Adriatic Sea. *Mar. Micropaleontol* 61 (1-3), 116–130. doi: 10.1016/j.marmicro.2006.05.008

Panieri, G., Camerlenghi, A., Cacho, I., Cervera, C. S., Canals, M., Lafuerza, S., et al. (2012). Tracing seafloor methane emissions with benthic foraminifera: results from the ana submarine landslide (Eivissa channel, Western Mediterranean Sea). *Mar. Geology* 291-294 (1), 97–112. doi: 10.1016/j.margeo.2011.11.005

Panieri, G., Camerlenghi, A., Conti, S., Pini, G. A., and Cacho, I. (2009). Methane seepages recorded in benthic foraminifera from Miocene seep carbonates, northern Apennines (Italy). *Palaeogeography Palaeoclimatol Palaeoecol.* 284 (3-4), 271–282. doi: 10.1016/j.palaeo.2009.10.006

Panieri, G., Graves, C. A., and James, R. H. (2016). Paleo-methane emissions recorded in foraminifera near the landward limit of the gas hydrate stability zone offshore western Svalbard. *Geochemistry Geophysics Geosystems* 17 (2), 521–537. doi: 10.1002/2015GC006153

Panieri, G., and Gupta, B. K. S. (2008). Benthic foraminifera of the Blake ridge hydrate mound, western north Atlantic ocean. *Mar. Micropaleontol* 66 (2), 91–102. doi: 10.1016/j.marmicro.2007.08.002

Panieri, G., James, R. H., Camerlenghi, A., Westbrook, G. K., Consolaro, C., Cacho, I., et al. (2014). Record of methane emissions from the West Svalbard continental margin during the last 23.500 yrs revealed by $\delta^{13}C$ of benthic foraminifera. *Global Planetary Change* 122, 151–160. doi: 10.1016/j.gloplacha.2014.08.014

Panieri, G., Lepland, A., Whitehouse, M. J., Wirth, R., Raanes, M. P., James, R. H., et al. (2017). Diagenetic mg-calcite overgrowths on foraminiferal tests in the vicinity of methane seeps. *Earth Planetary Sci. Lett.* 458 (15), 203–212. doi: 10.1016/j.epsl.2016.10.024

Paull, C. K., Ussler, W., Lorenson, T., Winters, W., and Dougherty, J. (2005). Geochemical constraints on the distribution of gas hydrates in the gulf of Mexico. *Geo-Marine Lett.* 25 (5), 273–280. doi: 10.1007/s00367-005-0001-3

Pawlowski, J., and Holzmann, M. (2008). Diversity and geographic distribution of benthic foraminifera: a molecular perspective. *Biodiversity Conserv.* 17 (2), 317–328. doi: 10.1007/s10531-007-9253-8

Peckmann, J., Reimer, A., Luth, U., Luth, C., Hansen, B. T., Heinicke, C., et al. (2001). Methane-derived carbonates and authigenic pyrite from the northwestern black Sea. *Mar. geology* 177 (1-2), 129–150. doi: 10.1016/S0025-3227(01)00128-1

Pierre, C. (2017). Origin of the authigenic gypsum and pyrite from active methane seeps of the southwest African margin. *Chem. Geology* 449 (20), 158–164. doi: 10.1016/j.chemgeo.2016.11.005

Rathburn, A. E., Levin, L. A., Held, Z., and Lohmann, K. C. (2000). Benthic foraminifera associated with cold methane seeps on the northern California margin: ecology and stable isotopic composition. *Mar. Micropaleontol* 38 (3-4), 247–266. doi: 10.1016/S0377-8398(00)00005-0

Rathburn, A. E., Levin, L. A., Tryon, M., Gieskes, J. M., Martin, J. B., Pérez, M. E., et al. (2009). Geological and biological heterogeneity of the Aleutian margin, (1965–4822 m). *Prog. Oceanography* 80 (1-2), 22–50. doi: 10.1016/j.pocean.2008.12.002

Rathburn, A. E., Pérez, M. E., Martin, J. B., Day, S. A., Mahn, C., Gieskes, J., et al. (2003). Relationships between the distribution and stable isotopic composition of living benthic foraminifera and cold methane seep biogeochemistry in Monterey bay, California. *Geochemistry Geophysics Geosystems* 4 (12), 1–28. doi: 10.1029/2003gc000595

Ravelo, A. C., and Hillaire-Marcel, C. (2007). Chapter eighteen the use of oxygen and carbon isotopes of foraminifera in paleoceanography. *Developments Mar. geology* 1, 735–764. doi: 10.1016/S1572-5480(07)01023-8

Reeburgh, W. S. (2007). Oceanic methane biogeochemistry. *Chem. Rev.* 107 (2), 486–513. doi: 10.1021/cr050362v

Ritger, S., Carson, B., and Suess, E. (1987). Methane-derived authigenic carbonates formed by subduction-induced pore-water expulsion along the Oregon/Washington margin. *Geological Soc. America Bull.* 98 (2), 147–156. doi: 10.1130/0016-7606(1987)98<147:MACFBS>2.0.CO;2

Robinson, C. A., Bernhard, J. M., Levin, L. A., Mendoza, G. F., and Blanks, J. K. (2004). Surficial hydrocarbon seep infauna from the Blake ridge (Atlantic ocean 2150 m) and the gulf of Mexico (690–2240 m). *Mar. Ecol.* 25 (4), 313–336. doi: 10.1111/j.1439-0485.2004.00034.x

Ruppel, C. D., and Kessler, J. D. (2017). The interaction of climate change and methane hydrates. *Rev. Geophysics* 55 (1), 126–168. doi: 10.1002/2016RG000534

Sackett, W. M. (1978). Carbon and hydrogen isotope effects during the thermocatalytic production of hydrocarbons in laboratory simulation experiments. *Geochimica Cosmochimica Acta* 42 (6), 571–580. doi: 10.1016/0016-7037(78)90002-9

Saeidi Ortakand, M., Hasegawa, S., Matsumoto, R., and Matsuda, H. (2016). Correlating biostratigraphy and palaeoceanographic changes during late quaternary at cold seeps with gas hydrate-free areas of the Japan Sea using foraminifera paleoecology. *Island Arc* 25 (1), 55–71. doi: 10.1111/iar.12131

Schiebel, R., Smart, S. M., Jentzen, A., Jonkers, L., Morard, R., Meilland, J., et al. (2018). Advances in planktonic foraminifer research: new perspectives for paleoceanography. *Rev. Micropaléontologie* 61 (3-4), 113–138. doi: 10.1016/j.revmic.2018.10.001

Schippers, A., and Jorgensen, B. B. (2002). Biogeochemistry of pyrite and iron sulfide oxidation in marine sediments. *Geochimica et cosmochimica acta* 66(1), 85–92. doi: 10.1016/S0016-7037(01)00745-1

Schneider, A., Crémière, A., Panieri, G., Lepland, A., and Knies, J. (2017). Diagenetic alteration of benthic foraminifera from a methane seep site on vestnesa ridge (NW Svalbard). *Deep Sea Res. Part I* 123, 22–34. doi: 10.1016/j.dsr.2017.03.001

Sen Gupta, B. K., and Aharon, P. (1994). Benthic foraminifera of bathyal hydrocarbon vents of the gulf of Mexico: initial report on communities and stable isotopes. *Geo-Marine Lett.* 14 (2), 88–96. doi: 10.1007/BF01203719

Sen Gupta, B. K., Platon, E., Bernhard, J. M., and Aharon, P. (1997). Foraminiferal colonization of hydrocarbon-seep bacterial mats and underlying sediment, gulf of Mexico slope. *J. Foraminiferal Res.* 27 (4), 292–300. doi: 10.2113/gsjfr.27.4.292

Sexton, P. F., and Wilson, P. A. (2009). Preservation of benthic foraminifera and reliability of deep-sea temperature records: importance of sedimentation rates, lithology, and the need to examine test wall structure. *Paleoceanography* 24 (2), 1–14. doi: 10.1029/2008PA001650

Smith, L. M., Sachs, J. P., Jennings, A. E., Anderson, D. M., and DeVernal, A. (2001). Light $\delta^{13}C$ events during deglaciation of the East Greenland continental shelf attributed to methane release from gas hydrates. *Geophysical Res. Lett.* 28 (11), 2217–2220. doi: 10.1029/2000GL012627

Smrzka, D., Feng, D., Himmler, T., Zwicker, J., Hu, Y., Monien, P., et al. (2020). Trace elements in methane-seep carbonates: potentials, limitations, and perspectives. *Earth-Science Rev.* 208, 103263. doi: 10.1016/j.earscirev.2020.103263

Spero, H. J., and Lea, D. W. (1996). Experimental determination of stable isotope variability in globigerina bulloides: implications for paleoceanographic reconstructions. *Mar. Micropaleontol* 28 (3-4), 231–246. doi: 10.1016/0377-8398(96)00003-5

Steinle, L., Graves, C. A., Treude, T., Ferré, B., Biastoch, A., Bussmann, I., et al. (2015). Water column methanotrophy controlled by a rapid oceanographic switch. *Nat. Geosci.* 8 (5), 378–382. doi: 10.1038/NGEO2420

Stott, L. D., Bunn, T., Prokopenko, M., Mahn, C., Gieskes, J., and Bernhard, J. M. (2002). Does the oxidation of methane leave an isotopic fingerprint in the geologic record? *Geochemistry Geophysics Geosystems* 3 (2), 1–16. doi: 10.1029/2001gc000196

Suess, E. (2020). "Marine cold seeps: background and recent advances," in *Hydrocarbons, oils and lipids: diversity, origin, chemistry and fate. handbook of hydrocarbon and lipid microbiology*. Eds. H. Wilkes (Cham: Springer), 747–767. doi: 10.1007/978-3-319-90569-3_27

Sultan, N., Plaza-Faverola, A., Vadakkepuliyambatta, S., Buenz, S., and Knies, J. (2020). Impact of tides and sea-level on deep-sea Arctic methane emissions. *Nat. Commun.* 11 (1), 5087. doi: 10.1038/s41467-020-18899-3

Tagliabue, A., and Bopp, L. (2008). Towards understanding global variability in ocean carbon-13. *Global biogeochemical cycles* 22 (1), 1–13. doi: 10.1029/2007GB003037

Tesoriero, A. J., and Pankow, J. F. (1996). Solid solution partitioning of Sr^{2+}, Ba^{2+}, and Cd^{2+} to calcite. *Geochimica Cosmochimica Acta* 60 (6), 1053–1063. doi: 10.1016/0016-7037(95)00449-1

Thatcher, K. E., Westbrook, G. K., Sarkar, S., and Minshull, T. A. (2013). Methane release from warming-induced hydrate dissociation in the West Svalbard continental margin: timing, rates, and geological controls. *J. Geophysical Res.* 118 (1), 22–38. doi: 10.1029/2012JB009605

Thomas, D. J., Zachos, J. C., Bralower, T. J., Thomas, E., and Bohaty, S. (2002). Warming the fuel for the fire: evidence for the thermal dissociation of methane hydrate during the Paleocene-Eocene thermal maximum. *Geology* 30 (12), 1067–1070. doi: 10.1130/0091-7613(2002)030<1067:WTFFTF>2.0.CO;2

Torres, M. E., Martin, R. A., Klinkhammer, G. P., and Nesbitt, E. A. (2010). Post depositional alteration of foraminiferal shells in cold seep settings: new insights from flow-through time-resolved analyses of biogenic and inorganic seep carbonates. *Earth Planetary Sci. Lett.* 299 (1-2), 10–22. doi: 10.1016/j.epsl.2010.07.048

Torres, M. E., Mix, A. C., Kinports, K., Haley, B., Klinkhammer, G. P., McManus, J., et al. (2003). Is methane venting at the seafloor recorded by $\delta^{13}C$ of benthic foraminifera shells? *Paleoceanography* 18 (3), 1–7. doi: 10.1029/2002PA000824

Tribovillard, N., Algeo, T. J., Lyons, T., and Riboulleau, A. (2006). Trace metals as paleoredox and paleoproductivity proxies: an update. *Chem. Geology* 232 (1-2), 12–32. doi: 10.1016/j.chemgeo.2006.02.012

Uchida, M., Ohkushi, K., Kimoto, K., Inagaki, F., Ishimura, T., Tsunogai, U., et al. (2008). Radiocarbon-based carbon source quantification of anomalous isotopic foraminifera in last glacial sediments in the western north pacific. *Geochemistry Geophysics Geosystems* 9 (4), 1–26. doi: 10.1029/2006GC001558

Ussler, W.III, and Paull, C. K. (2008). Rates of anaerobic oxidation of methane and authigenic carbonate mineralization in methane-rich deep-sea sediments inferred from models and geochemical profiles. *Earth Planetary Sci. Lett.* 266 (3-4), 271–287. doi: 10.1016/j.epsl.2007.10.056

Wallmann, K., Riedel, M., Hong, W. L., Patton, H., Hubbard, A., Pape, T., et al. (2018). Gas hydrate dissociation off Svalbard induced by isostatic rebound rather than global warming. *Nat. Commun.* 9 (1), 83. doi: 10.1038/s41467-017-02550-9

Wan, S., Feng, D., Chen, F., Zhuang, C., and Chen, D. (2018). Foraminifera from gas hydrate-bearing sediments of the northeastern south China Sea: proxy evaluation and application for methane release activity. *J. Asian Earth Sci.* 168, 125–136. doi: 10.1016/j.jseaes.2018.04.036

Wang, S., Yan, B., and Yan, W. (2013). Tracing seafloor methane emissions with benthic foraminifera in the baiyun sag of the northern south China Sea. *Environ. Earth Sci.* 70 (3), 1143–1150. doi: 10.1007/s12665-012-2201-2

Wefer, G., Heinze, P., and Berger, W. H. (1994). Clues to ancient methane release. *Nature* 369, 282–282. doi: 10.1038/369282a0

Whiticar, M. J. (1999). Carbon and hydrogen isotope systematics of bacterial formation and oxidation of methane. *Chem. Geology* 161 (1-3), 291–314. doi: 10.1016/S0009-2541(99)00092-3

Wiedicke, M., and Weiss, W. (2006). Stable carbon isotope records of carbonates tracing fossil seep activity off Indonesia. *Geochemistry Geophysics Geosystems* 7 (11), 1–22. doi: 10.1029/2006GC001292

Wilfert, P., Krause, S., Liebetrau, V., Schönfeld, J., Haeckel, M., Linke, P., et al. (2015). Response of anaerobic methanotrophs and benthic foraminifera to 20 years of methane emission from a gas blowout in the north Sea. *Mar. Petroleum Geology* 68, 731–742. doi: 10.1016/j.marpetgeo.2015.07.012

Wollenburg, J. E., Raitzsch, M., and Tiedemann, R. (2015). Novel high-pressure culture experiments on deep-sea benthic foraminifera–evidence for methane seepage-related $\delta^{13}C$ of cibicides wuellerstorfi. *Mar. Micropaleontol* 117, 47–64. doi: 10.1016/j.marmicro.2015.04.003

Xiang, R., Fang, L., Chen, Z., Zhang, L., Yan, W., and Chen, M. (2012). Carbon isotope of benthic foraminifera and its implications for cold seepage in the southwestern area off Dongsha islands, South China Sea. *Marine Geology & Quaternary Geology* 32(4), 17–24. doi: 10.3724/SP.J.1140.2012.04017

Xin, S., Ying, Q., Fang, C., Shengxiong, Y., Yang, Z., Hongpeng, C., et al. (2020). Deep sea benthic foraminifera from the taixinan basin and changes of their cold seep microhabitats during the past 50000 years. *Earth Sci. Front.* 27 (6), 255. doi: 10.13745/j.esf.sf.2020.6.13

Zahn, R., Winn, K., and Sarnthein, M. (1986). Benthic foraminiferal $\delta^{13}C$ and accumulation rates of organic carbon: uvigerina peregrina group and cibicidoides wuellerstorfi. *Paleoceanography* 1 (1), 27–42. doi: 10.1029/PA001i001p00027

Zhang, M. Z. M., Lu, H. L. H., Guan, H. G. H., Liu, L. L. L., Wu, D. W. D., and Wu, N. W. N. (2018). Methane seepage intensities traced by sulfur isotopes of pyrite and gypsum in sediment from the shenhu area, south China Sea. *Acta Oceanologica Sin.* 37 (7), 20–27. doi: 10.1007/s13131-018-1241-1

Zhang, B., Pan, M., Wu, D., and Wu, N. (2018). Distribution and isotopic composition of foraminifera at cold-seep site 973-4 in the dongsha area, northeastern south China Sea. *J. Asian Earth Sci.* 168, 145–154. doi: 10.1016/j.jseaes.2018.05.007

Zhou, Y., Chen, F., Su, X., Liu, G., and Chen, C. (2009). Benthic foraminifera communities in methane-rich environment showed by core hd319 in dongsha sea area of the south China Sea. *Mar. Geology Quaternary Geology* 29 (3), 1–8. doi: 10.3724/SP.J.1140.2009.03001

Zhou, Y. A., Di, P. B. C. D., Li, N. B. C. D., Chen, F. A., Su, X. F., and Zhang, J. A. (2020). Unique authigenic mineral assemblages and planktonic foraminifera reveal dynamic cold seepage in the southern south China sea. *Minerals* 10 (3), 275. doi: 10.3390/min10030275

Zhuang, C., Chen, F., Cheng, S., Lu, H., Wu, C., Cao, J., et al. (2016). Light carbon isotope events of foraminifera attributed to methane release from gas hydrates on the continental slope, northeastern south China Sea. *Sci. China Earth Sci.* 59 (10), 1981–1995. doi: 10.1007/s11430-016-5323-7

frontiers | Frontiers in Marine Science

TYPE Original Research
PUBLISHED 30 June 2023
DOI 10.3389/fmars.2023.1140549

OPEN ACCESS

EDITED BY
Davide Oppo,
University of Louisiana at Lafayette,
United States

REVIEWED BY
Renbiao Tao,
Center for High Pressure Science and
Technology Advanced Research, China
Zhifeng Wan,
Sun Yat-sen University, China
Jinan Guan,
Chinese Academy of Sciences (CAS), China
Shuanshi Fan,
South China University of Technology,
China

*CORRESPONDENCE
Yuncheng Cao
yccao@shou.edu.cn

RECEIVED 09 January 2023
ACCEPTED 13 June 2023
PUBLISHED 30 June 2023

CITATION
Zhu Z, Cao Y, Zheng Z, Wu N and Chen D (2023) A model to predict the thermodynamic stability of abiotic methane-hydrogen binary hydrates in a marine serpentinization environment. *Front. Mar. Sci.* 10:1140549. doi: 10.3389/fmars.2023.1140549

A model to predict the thermodynamic stability of abiotic methane-hydrogen binary hydrates in a marine serpentinization environment

Zhiwei Zhu[1], Yuncheng Cao[1]*, Zihan Zheng[1], Nengyou Wu[2] and Duofu Chen[1]

[1]Shanghai Engineering Research Center of Hadal Science and Technology, College of Marine Sciences, Shanghai Ocean University, Shanghai, China, [2]The Key Laboratory of Gas Hydrate, Ministry of Natural Resources, Qingdao Institute of Marine Geology, Qingdao, Shandong, China

Abiotic methane (CH_4) and hydrogen (H_2), which are produced during marine serpentinization, provide abundant gas source for hydrate formation on ocean floor. However, previous models of CH_4−H_2 hydrate formation have generally focused on pure water environments and have not considered the effects of salinity. In this study, the van der Waals−Platteeuw model, which considered the effects of salinity on the chemical potentials of CH_4, H_2, and H_2O, was applied in a marine serpentinization environment. The model uses an empirical formula and the Peng−Robinson equation of state to calculate the Langmuir constants and fugacity values, respectively, of CH_4 and H_2, and it uses the Pitzer model to calculate the activity coefficients of H_2O in the CH_4−H_2−seawater system. The three-phase equilibrium temperature and pressure predicted by the model for CH_4−H_2 hydrates in pure water demonstrated good agreement with experimental data. The model was then used to predict the three-phase equilibrium temperature and pressure for CH_4−H_2 hydrates in a NaCl solutions, for which relevant experimental data are lacking. Thus, this study provides a theoretical basis for gas hydrate research and investigation in areas with marine serpentinization.

KEYWORDS

serpentinization, hydrogen gas, methane gas, gas hydrate, phase equilibrium

1 Introduction

Natural gas hydrates are crystalline solids formed from a mixture of water and gases. Natural gas hydrates are not only a new clean energy resource, but also have an important role in environmental effects and marine hazard assessment (Wan et al., 2022). The microstructure comprises cavities (hosts) formed by water molecules through hydrogen bonding and gas molecules (guests) trapped inside (Dendy Sloan and Koh, 2007). Typical gas molecules include methane (CH_4), ethane, propane, and carbon dioxide, which can be biotic or abiotic in origin. Serpentinization, which primarily occurs at mid-ocean ridges and fore-arc systems, plays an important role in producing abiotic gases (Holm et al., 2015). Serpentinization is the hydration of olivine and orthopyroxene minerals, the main constituents of ultramafic rocks, creating a reducing chemical environment characterized by high H_2 concentrations. The general reaction equation is: $6[Mg_{1.8}Fe_{0.2}SiO_4] + 7H_2O \rightarrow 3[Mg_3Si_2O_5(OH)_4] + Fe_3O_4 + H_2$. Excess H_2 reduces CO_2 dissolved in water to CH_4 and low-molecular-weight hydrocarbons through Fischer-Tropsch type (FTT) reactions, The general reaction equation is: $CO_{2aq} + [2 + (m/2n)]H_2 \rightarrow (1/n)C_nH_m + 2H_2O$ (Proskurowski et al., 2008). The ultraslow-spreading ridges in the Fram Strait between the North Atlantic Ocean and Arctic Ocean are a typical serpentinization area with bottom simulating reflectors (BSRs) in their seismic profiles, which is characteristic of CH_4 hydrate development (Rajan et al., 2012; Johnson et al., 2015). In addition to CH_4, serpentinization produces substantial amounts of H_2 (Coveney et al., 1987; McCollom and Bach, 2009). The formation of hydrates from H_2 has been a well-explored research topic in recent years. Experimental studies have shown that the pressure required to form stable H_2 hydrates is hundreds of times higher than that of CH_4 hydrates under the same low-temperature conditions (Dyadin et al., 1999; Mao et al., 2002). However, the pressure required to form H_2 hydrates can be effectively reduced by mixing in a small amount of a second guest molecule such as tetrahydrofuran (THF) (Hashimoto et al., 2006). Similar to THF, CH_4 can be used as a thermodynamic promoter to stabilize H_2 hydrate formation, and it is small enough to afford H_2 a higher occupancy in hydrate cages compared to THF (Matsumoto et al., 2014). This effect of the second guest molecule may allow CH_4–H_2 hydrates to form from the abundance of abiotic CH_4 and H_2 produced by serpentinization. To confirm this possibility, the three-phase (hydrate, liquid, and vapor) equilibrium conditions require to be determined for the formation of CH_4–H_2 hydrates in a serpentinization environment.

Researchers have experimentally measured the phase equilibrium conditions for forming CH_4–H_2 hydrates at various molar fraction ratios. Holder et al. (1983) measured the phase equilibrium conditions for the formation of H_2-rich gas hydrates at temperatures of<282.3 K and concluded that hydrate formation is strongly dependent upon the gas composition. Zhang et al. (2000) used the pressure search method to measure the phase equilibrium conditions for hydrate formation from H_2 and hydrocarbon gas mixtures in pure water. They considered temperature and pressure ranges of 274.3–278.2 K and 3.72–6.63 MPa, respectively, and H_2 molar fractions of 22.13 and 36.18 mol%. Their results suggested that increasing H_2 molar fractions was not conducive to the formation of CH_4–H_2 hydrates. Measurements by Chen et al. (2002) demonstrated that the pressure range for CH_4–H_2 hydrate formation at H_2 molar fractions of 22–70 mol% and a temperature of 274.15 K was 3.72–9.67 MPa. Skiba et al. (2007) used differential thermal analysis to investigate the phase equilibrium of CH_4–H_2 hydrates at H_2 molar fractions of 0–70 mol% and a pressure of up to 250 MPa. Their results suggested that the decomposition temperature of the formed hydrate decreased as the H_2 concentration in the initial gas mixture increased. Pang et al. (2012) injected gas or gas mixtures into an equilibrium cell containing an appropriate amount of water and at a constant pressure. They nucleated and decomposed hydrates by adjusting the temperature, where the equilibrium temperature was defined as the point at which hydrates appeared to melt for the second time. The phase equilibrium conditions for CH_4–H_2 hydrates were measured for H_2 molar fractions of 5–66 mol%. Li et al. (2022) used the isochoric pressure-search method to measure the phase equilibrium conditions for CH_4–H_2 hydrates in the temperature range of 274.24–287.43 K at H_2 molar fractions of 22 and 80 mol%. Additionally, Researchers have established several models to obtain a wider range of phase equilibrium data. Skiba et al. (2007) obtained the coefficients of the equation $T(^\circ C) = A + B \times P + C \times P^2 + D \times P^3 + E \times \ln P(P, MPa)$ by fitting the experimental data using the method of least squares. The equation demonstrated good agreement with the experimental results of pure CH_4 hydrates and initial gas mixtures with H_2 molar fractions of<40 mol%. However, the difference between the predicted values and experimental results considerably widened when the H_2 molar fractions was >40 mol%. Pang et al. (2012) used the Ng–Robinson model (Ng and Robinson, 1976) to establish a model that can predict the three-phase equilibrium conditions for the formation of CH_4–H_2 hydrates at different gas molar fractions. Li et al. (2022) used the Chen–Guo model (Chen and Guo, 1998) to establish a model that can predict the three-phase equilibrium conditions for the formation of multi-component mixtures from different molar fractions of H_2 with one or more hydrocarbons.

The abovementioned models can accurately predict the three-phase equilibrium conditions for the formation of multi-component gas hydrates from H_2 in a pure water system. However, salinity can inhibit hydrate formation, and currently available models cannot accurately predict the three-phase equilibrium conditions for CH_4–H_2 hydrates in a marine serpentinization environment. Although various abiotic and microbially mediated reactions affect the chemical compositions of pore waters in serpentinization surface sediments, resulting in some differences in major and trace elements, the pore water ions are still dominated by NaCl and are generally similar in species to those found in the upper layers of ocean water (Hulme et al., 2010). For example, The Ocean Drilling Program Site 1200, located on the South Chamorro Seamount, has highly permeable and strongly alkaline (pH 12.5) in the deep pore water compared to other serpentinization areas. The contents of chloride, magnesium, and calcium ions are lower while the alkalinity and contents of sodium, potassium, sulfate, and light hydrocarbon ions are significantly higher compared with the upper layers of ocean water. The content of sodium and chloride ions in this region are above 500mmol/kg, potassium and sulfate ions are 10-20mmol/kg, while magnesium and calcium ions are less than 5mmol/kg. Therefore, sodium and chloride ions are still the leading components, and Na/Cl can reach a maximum of 1.2 (Salisbury et al., 2002). The effects of alkalinity and other ions on hydrate formation are essentially negligible compared with the effects of sodium and chloride ions.

Thus, a thermodynamic model that can predict the three-phase equilibrium conditions for the formation of CH_4–H_2 hydrates in both pure water and a sodium chloride (NaCl) solution is required. In this study, the van der Waals–Platteeuw thermodynamic model of classical adsorption theory was used to establish a thermodynamic model that can accurately predict the temperature and pressure conditions for the three-phase equilibrium of CH_4–H_2 hydrates in a marine serpentinization environment. The model incorporates the molecular potential energy model to consider the effects of temperature, pressure, and salinity. The performance of the model was evaluated by comparison with experimental data in the literature.

2 Thermodynamic model of gas hydrates

At phase equilibrium, the chemical potential or fugacity of each component in the system is identical in various phases. Water has low volatility and is not compatible with hydrocarbons, and therefore it generally accounts for a low proportion of the vapor and liquid phases of hydrocarbons. Therefore, the chemical potentials of water in the hydrate and liquid phases can be selected as the constraints. If water is selected as the reference component, the phase equilibrium constraint is given by

$$\mu_w^H = \mu_w^L \tag{1}$$

where μ_w^H is the chemical potential of water in the hydrate phase (J/mol) and μ_w^L is the chemical potential of water in the liquid phase (J/mol).

If the chemical potential of water in the hypothetical empty hydrate lattice is selected as the intermediate state, the constraints are given by

$$\Delta\mu_w^H = \mu_w^\beta - \mu_w^H = \mu_w^\beta - \mu_w^L = \Delta\mu_w^L \tag{2}$$

where μ_w^β is the chemical potential of water in the hypothetical empty hydrate lattice (J/mol). $\Delta\mu_w^H$ is the difference between the chemical potentials of water in the empty hydrate and hydrate phases (J/mol). $\Delta\mu_w^L$ is the difference between the chemical potentials of water in the empty hydrate and liquid phases (J/mol).

Determining the structural type for CH_4–H_2 hydrates is crucial in this approach, but the thermodynamic properties of CH_4–H_2 hydrates are currently not well understood. From the available studies, pure H_2 hydrates tend to naturally form Structure II (Mao et al., 2002). However, as the initial molar fractions of CH_4 increases, there is a higher likelihood that Structure I will become more favorable (Grim et al., 2012). Based on the dependence of hydrate structure on thermodynamic and kinetic conditions, the hydrate structure of the CH_4 + H_2 mixed system is dependent on several factors: structure induction, driving force of hydrate independent nucleation, composition of gas mixture, pressure, and formation period (Matsumoto et al., 2014; Gao et al., 2022). Considering the pressure and gas composition in the serpentinization area, Structure I was finally chosen as the calculation standard. $\Delta\mu_w^H$ can be calculated as per the statistical mechanics model proposed by van der Waals and Platteeuw (2007):

$$\Delta\mu_w^H = RT\sum_i \nu_i \ln(1+\sum_{j=1} C_{ij} f_j) \tag{3}$$

where R is the universal gas constant (8.314 J/mol/K), T is the temperature (K), ν_i is the number of type i cages in each water molecule (Table 1), C_{ij} is the temperature-dependent Langmuir constant of the gas component j in type i cavities, and f_j is the fugacity of the gas component j in the hydrate phase (MPa).

The Langmuir constant is a critical parameter of the van der Waals–Platteeuw model and depends on the chemical potential for the interaction between guest and water molecules. For Structure I hydrates, the Langmuir constants of CH_4 and H_2 are calculated from the empirical equations fitted by Sun and Duan (2007) and Klauda and Sandler (2003), respectively.

$$C_{ij}(T) = e^{A_{ij}+\frac{B_{ij}}{T}} \tag{4}$$

$$C_{ij}(T) = e^{A_{ij}+\frac{B_{ij}}{T}+\frac{D_{ij}}{T^2}} \tag{5}$$

where the values of A, B, and D are given in Table 2.

Another important aspect of an accurate thermodynamic model is calculating the fugacity of the gas component. When three phases coexist in equilibrium, the fugacity values of gas j in the hydrate, liquid water, and vapor phases are identical:

$$f_j^H = f_j^L = f_j^V \tag{6}$$

where the superscripts H, L, and V indicate the hydrate, liquid, and vapor phases, respectively. In this study, the fugacity values of CH_4 and H_2 in the vapor phase were calculated using the equation of state for gas mixtures proposed by Peng and Robinson (1970). $\Delta\mu_w^L$ can be calculated by using the equations proposed by Holder et al. (1980):

$$\frac{\Delta\mu_w^L}{RT} = \frac{\Delta\mu_w^0}{RT_0} - \int_{T_0}^{T}\frac{\Delta h_w}{RT^2}dT + \int_0^P \frac{\Delta V_w}{RT}dp - \ln(\alpha_w) \tag{7}$$

TABLE 1 Values of ν_i in two types of hydrate cages.

Structure	Type I	Type II
Small cage	1/23	2/17
Large cage	3/23	1/17

TABLE 2 Calculated parameters of Langmuir constant.

Parameters	CH_4 hydrate		H_2 hydrate	
	Small cage	Large cage	Small cage	Large cage
A	-24.02799	-22.68305	-21.6228	-20.2942
B	3134.7529	3080.3857	1020.2356	966.9431
D			31948.65	-11765.04

$$\Delta h_w = \Delta h_w^0 + \int_{T_0}^{T} \Delta C_{pw} dT \tag{8}$$

$$\Delta C_{pw} = \Delta C_{pw}^0 + b(T - T_0) \tag{9}$$

where $\Delta \mu_w^0$ is the difference between the reference chemical potentials of water in the empty hydrate and ice phases at the reference temperature T_0 (generally 273.15 K) and zero pressure (J/mol). Δh_w is the difference between the molar enthalpies of the empty hydrate lattice and liquid or ice phase of pure water (J/mol). ΔV_w is the difference between the molar volumes of the empty hydrate lattice and the liquid or ice phase of pure water (m^3/mol). α_w is the water activity. ΔC_{pw} is the difference between the molar heat capacities of the empty hydrate lattice and liquid or ice phase of pure water (J/mol/K). Table 3 presents the above parameters.

To calculate the three-phase equilibrium pressure at a given temperature T, the molar fractions of H_2 (mol%), and salinity (mol/kg), the initial pressure P_1 is estimated first. Then, $\Delta \mu_w^H$ and $\Delta \mu_w^L$ are calculated and compared at P_1. If the absolute difference between $\Delta \mu_w^H$ and $\Delta \mu_w^L$ is sufficiently small, then the pressure can be considered the equilibrium pressure P under the above conditions. Otherwise, the pressure is modified, then $\Delta \mu_w^H$ and $\Delta \mu_w^L$ are calculated at the modified pressure. The abovementioned processes are repeated by using Newton's method or dichotomy until the equilibrium pressure is determined. If the absolute difference between $\Delta \mu_w^H$ and $\Delta \mu_w^L$ is less than 1×10^{-2}, then the iteration is terminated, and an equilibrium pressure is obtained with a deviation of<0.1%.

2.1 Fugacity calculation

As described above, the fugacity values of CH_4 and H_2 can be calculated by using the equation of state for gas mixtures proposed by Peng and Robinson (1970):

$$P = \frac{RT}{v - b} - \frac{a(T)}{v(v + b) + b(v - b)} \tag{10}$$

Equation 11 presents rules by which Equation 10 can be rearranged in the form of Equation 12:

$$A = \frac{aP}{R^2T^2}; B = \frac{bP}{RT}; Z = \frac{Pv}{RT} \tag{11}$$

TABLE 3 Thermodynamically relevant parameters of Structure I hydrate at T_0 =273.15 K.

Parameters	Type I
$\Delta \mu_w^0$	1202
Δh_w^0 (T≥273.15)	1300
Δh_w^0 (T<273.15)	-4709.5
ΔC_{pw} (T≥273.15)	-38.12 + 0.141×(T-T$_0$)
ΔC_{pw} (T<273.15)	0.565 + 0.002×(T-T$_0$)

$$Z^3 - (1 - B)Z^2 + (A - 3B^2 - 2B)Z - (AB - B^2 - B^3) = 0 \tag{12}$$

where R is the universal gas constant (8.314 J/mol/K), v is the gas molar volume, a is a measure of the intermolecular attraction, and b is a constant related to the gas molecule size. The values of a and b at the critical point can be obtained as per the critical properties of gases:

$$T_r = \frac{T}{T_c}; a(T_c) = 0.45724\frac{R^2T_c^2}{P_c}; b(T_c) = 0.07780\frac{RT_c}{P_c}; Z_c = 0.307 \tag{13}$$

$$a(T) = a(T_c) \cdot \alpha(T_r, w); b(T) = b(T_c) \tag{14}$$

$$\sqrt{\alpha(T_r, w)} = 1 + \kappa(1 - \sqrt{T_r}) \tag{15}$$

$$\kappa = 0.37464 + 1.54226\omega - 0.26992\omega^2 \tag{16}$$

where κ is a constant characteristic of each substance. where the critical temperature T_c of H_2 is 33.2 K, the critical pressure P_c is 1.3 MPa, and the acentric factor ω is −0.216. The critical temperature T_c of CH_4 is 190.4 K, the critical pressure P_c is 4.6 MPa, and the acentric factor ω is 0.012. The above method is followed when calculating pure gases, but certain rules should be followed when calculating gas mixtures. The mixing rule is as follows:

$$\begin{gathered} a = \sum_i \sum_j x_i x_j a_{ij} \\ b = \sum_i x_i b_i \\ a_{ij} = (1 - \delta_{ij})\sqrt{a_i}\sqrt{a_j} \end{gathered} \tag{17}$$

In eq 17, x is the initial molar fractions of component i and component j in the gas mixture. δ_{ij} is an empirically determined binary interaction coefficient characterizing the binary formed by component i and component j. The value δ_{ij} is 0.9035 between component H_2 and component CH_4 (Matsumoto et al., 2014). As per the state parameters and mixing rule of CH_4 and H_2, the critical values of a and b can be calculated by Equation 17. Then, the fugacity coefficients f_k of H_2 and CH_4 can be calculated from the following equation:

$$\ln\frac{f_k}{x_k P} = \frac{b_k}{b}(Z - 1) - \ln(Z - B) - \frac{A}{2\sqrt{2}B} \times \left(\frac{2\sum_i x_i a_{ik}}{a} - \frac{b_k}{b}\right) \ln\left(\frac{Z + 2.414B}{Z - 0.414B}\right) \tag{18}$$

2.2 Water activity calculation

The water activity a_w in Equation 7 is calculated using the Pitzer model (Pitzer, 1975). The relationship between a_w and the permeability coefficient ϕ is denoted by the following equation:

$$\ln a_w = -\frac{M_W}{1000}\left(\sum_i m_i\right)\phi \tag{19}$$

where M_W is the molecular weight of water. m_i is the molality of solute i, which can be cations, anions, or neutral substances. ϕ is the permeability coefficient, which was first proposed by Pitzer and Silvester (Pitzer and Silvester, 1976) and was eventually rearranged by Harvie et al. (1984) and Felmy and Weare (1986) to obtain:

$$\begin{aligned}(\sum_i m_i)(\phi - 1) = 2\Bigg\{ & -\frac{A^{\phi}I^{1.5}}{1+1.2I^{1.5}} + \sum_c\sum_a m_c m_a (B^{\phi}_{ca} + ZC_{ca}) \\ & + \sum\sum_{c<c'} m_c m_{c'}(\Phi^{\phi}_{cc'} + \sum_a m_a \psi_{cc'a}) + \sum\sum_{a<a'} m_a m_{a'}(\Phi^{\phi}_{aa'} + \sum_c m_c \psi_{aa'c}), \\ & + \sum_n\sum_c m_n m_c \lambda_{nc} + \sum_n\sum_a m_n m_a \lambda_{na} + \sum_n\sum_c\sum_a m_n m_c m_a \zeta_{nca}\Bigg\}\end{aligned} \quad (20)$$

where I is the ionic strength. The subscripts c, a, and n are cations, anions, and neutral substances, respectively. The summation index, c, denotes the sum over all cations in the system. The double summation index, c< c', denotes the sum over all distinguishable pairs of dissimilar cations. Analogous definitions apply to the summation indices for anions. A^{ϕ} is one-third of the Debye–Hückel limiting slope. B^{ϕ}, Φ^{ϕ}, and λ are measurable combinations of the second virial coefficient. C, ψ, and ζ are measurable combinations of the third virial coefficient.

The second virial coefficients B^{ϕ}_{ca} and $\Phi^{\phi}_{cc'}$ are functions of the ionic strength, and the third virial coefficients C_{ca} and $\psi_{cc'a}$ are assumed independent of the ionic strength. Duan and Sun (2006) described the equations for calculating the above parameters in detail. Because gas hydrates in an aqueous solution of electrolytes exist in equilibrium at low temperatures of -25 to 25°C, the relevant parameters determined by Spencer et al. (1990) were selected. The temperature-dependent ion interaction parameters in the Pitzer model are expressed as follows (The values of c_1-c_6 can be found in the paper of Spencer et al. (1990)):

$$Par(T) = c_1 + c_2 T + \frac{c_3}{T} + c_4 \ln T + c_5 T^2 + c_6 T^3. \quad (21)$$

The effect of pressure on activity coefficients at a specific temperature should be included in the theoretical calculation. However, Monnin (1990) reported that the effect of pressure on the activity of water is small and can be ignored. Duan and Sun (2006) also confirmed this result from temperature- and pressure-dependent parameters for aqueous NaCl solutions. Thus, this model will neglect the effect of pressure on water activity.

The second virial coefficient λ_{ni} and third virial coefficient ζ_{nij} are the interactions between ions and neutral substances (Duan and Sun (2006)). λ_{CH_4-i} and ζ_{CH_4-ij} have been determined by the CH_4 solubility model established by Duan and Mao (2006), and λ_{H_2-i} and ζ_{H_2-ij} have been determined by the H_2 solubility model established by Zhu et al. (2022). Duan and Sun (2006) set λ_{CH_4-Cl} to zero and fitted λ_{CH_4-Na} and $\zeta_{CH_4-Na-Cl}$ based on the solubility of CH_4 in an aqueous NaCl solutions. All interaction parameters between CH_4 and monovalent and divalent cations can be approximated as λ_{CH_4-Na} and $2\lambda_{CH_4-Na}$, respectively. λ_{H_2-Cl}, λ_{H_2-Na}, and $\zeta_{H_2-Na-Cl}$ are treated by the same method, where all interaction parameters between H_2 and monovalent and divalent cations approximated as λ_{H_2-Na} and $2\lambda_{H_2-Na}$, respectively.

$$\begin{aligned}\lambda_{CH_4-Na} = & -0.81222036 + 0.10635172 \times 10^{-2} T + 0.18894036 \times 10^{3} \tfrac{1}{T} \\ & +0.44105635 \times 10^{-4} P - 0.4679771810^{-10} P^2 T\end{aligned} \quad (22)$$

$$\begin{aligned}\lambda_{H_2-Na} = & -7.68559552 + 1.91233146 \times 10^{-2} T + 1.04890475 \times 10^{3} \tfrac{1}{T} - 1.52746819 \times 10^{-5} T^2 \\ & + 1.59803686 \times 10^{-4} P - 19.2667249 \tfrac{P}{T^2} - 47.5822792 \tfrac{1}{P} + 0.472712503 \tfrac{T}{P} \\ & - 1.56750050 \times 10^{-3} \tfrac{T^2}{P} + 1.73272315 \times 10^{-6} \tfrac{T^3}{P}\end{aligned} \quad (23)$$

$$\zeta_{CH_4-Na-Cl} = -0.29903571 \times 10^{-2} \quad (24)$$

$$\zeta_{H_2-Na-Cl} = -1.44839161 \times 10^{-2} \quad (25)$$

In summary, Equation 19 and 20 form the fundamental equations of the model for predicting the stability of gas hydrates in an aqueous solution of electrolytes. All parameters in these equations have been assessed by researchers. The phase equilibrium data for gas hydrate formation in an aqueous solution of electrolytes should not be adjusted before use.

3 Results and discussion

At present, only experimental data of CH_4–H_2 hydrates in pure water are available. In this study, 60 data points were collected for H_2 molar fractions of 4.55%–80.00%. The model was used to predict the pressure necessary to form CH_4–H_2 hydrates at a specific temperature. The model predictions in pure water were confirmed against experimental data from the literature, and deviations of the predicted results from the experimental data were tabulated (Table 4). The minimum and maximum mean absolute percentage errors (MAPEs) between the predicted results and experimental data were 0.86% and 18.03%, respectively. MAPE was >10.00% only at H_2 molar fractions of 36.18% and 65.90%.

To confirm the prediction accuracy of the model, the pressures for forming CH_4–H_2 hydrates at temperatures of 274.15–293.15 K were calculated at different H_2 molar fractions (Figure 1). The three-phase equilibrium pressure increased with the temperature regardless of the initial H_2 molar fractions. For example, when the H_2 molar fractions was 33.85%, the three-phase equilibrium pressures were 4.59, 7.71, 13.56, 25.40, and 43.37 MPa at temperatures of 274.15, 279.15, 284.15, 289.15, and 293.15 K, respectively. The calculated pressure increments were 3.13, 5.85, 11.84, and 17.97 MPa, respectively. These results suggest that the pressure does not increase linearly with temperature. The experimental data obtained by Zhang et al. (2000) corresponded to H_2 molar fractions of 22.13% and 36.18%; these were lower than those obtained by Li et al. (2022) and Pang et al. (2012) of 20.00% and 33.85%, respectively. The model predictions were greater than the above experimental data when the H_2 molar fractions were 22.13% and 36.18%. Notably, the error increased with the H_2 molar fractions, which is consistent with the results of other researchers (Pang et al., 2012; Ma et al., 2013; Wang et al., 2015). In general, the conventional equation of state cannot accurately calculate the phase equilibrium properties because of the quantum properties of H_2 molecules, and the parameters of the equation of state of H_2 molecules may be specifically regressed (Deiters, 2013; Privat and Jaubert, 2013).

The model can predict the three-phase equilibrium conditions for CH_4–H_2 hydrates in NaCl solutions of different concentrations,

TABLE 4 Errors occurring when model predicts conditions for hydrate formation in pure water.

References	The H_2 molar fractions	T(K)	P (MPa)	N^a	MAPE (%)
Zhang et al. (2000)	22.13%	274.30-278.20	3.72-5.34	5	8.28%
	36.18%	274.30-278.20	4.46-6.63	5	10.41%
Chen et al. (2002)	22.00%	274.15	3.72	1	3.29%
	36.00%	274.15	4.46	1	6.52%
	47.00%	274.15	5.47	1	5.92%
	58.00%	274.15	6.89	1	6.74%
	70.00%	274.15	9.67	1	6.51%
Pang et al. (2012)	4.55%	274.45-291.45	3.11-20.51	8	3.82%
	28.03%	275.75-288.45	4.68-20.52	7	3.67%
	33.85%	274.35-287.55	4.51-20.73	7	1.42%
	41.90%	273.85-285.35	5.33-20.64	8	9.27%
	65.90%	274.35-279.95	11.19-20.41	4	18.03%
Li et al. (2022)	20.00%	276.4-287.43	4.69-7.69	8	0.86%
	80.00%	274.24-276.12	16.38-20.81	3	8.83%

for which relevant experimental data are lacking. To consider the effects of solution ions on the three-phase equilibrium of CH_4–H_2 hydrates, four initial H_2 molar fractions were selected: 4.55%, 20.00%, 28.03%, and 33.85%. Then, the three-phase equilibrium conditions were calculated for the formation of CH_4–H_2 hydrates from H_2 in pure water and in 0.1, 0.55, and 1 mol/kg NaCl solutions at temperatures of 274.15–293.15 K. Figure 2 plots the results with experimental data. Figure 2A shows that the three-phase equilibrium pressures for the formation of CH_4–H_2 hydrates at temperatures of 274.15, 283.15, and 293.15 K were 3.06, 7.73, and 27.3 MPa, respectively, in pure water; 3.15, 7.98, and 28.45 MPa, respectively, in the 0.1 mol/kg NaCl solutions; 3.49, 9.04, and 33.62 MPa, respectively, in the 0.55 mol/kg NaCl solutions; and 3.88, 10.33, and 39.94 MPa, respectively, in the 1 mol/kg NaCl solutions. Compared with pure water, the 1 mol/kg NaCl solutions increased the three-phase equilibrium pressures at 274.15, 283.15, and 293.15 K by 0.82, 2.60, and 12.67 MPa, respectively. This suggests that the three-phase equilibrium pressure increases with the temperature as well as the NaCl concentration. Note that experimental data are still required to verify the accuracy of the model in NaCl solutions, but the trend of the effect of NaCl solutions on the phase equilibrium of CH_4-H_2 hydrates is the same as that of pure methane hydrate.

At the same temperature, the equilibrium pressure of CH_4–H_2 hydrates is associated with the initial molar fractions of CH_4 and H_2. Four temperatures were selected to calculate the three-phase equilibrium pressures for hydrate formation with initial H_2 molar fractions of 10–80mol%: 274.15, 280.15, 286.15, and 293.15 K. Figure 3 plots the results with experimental data obtained by Chen et al. (2002). Figure 3A shows that the three-phase equilibrium pressures at initial H_2 molar fractions of 10%, 35%, 60%, and 80% were 3.28, 4.67, 7.72, and 15.23 MPa, respectively. Based on these results, the model was used to calculate the three-phase equilibrium pressures of CH_4–H_2 hydrates in 0.1, 0.55, and 1 mol/kg NaCl solutions. At the above H_2 molar fractions, the three-phase equilibrium pressures were 3.36, 4.79, 7.92, and 15.60 MPa, respectively, in the 0.1 mol/kg NaCl solutions; 3.73, 5.33, 8.83, and 17.34 MPa, respectively, in the 0.55 mol/kg NaCl solutions; and

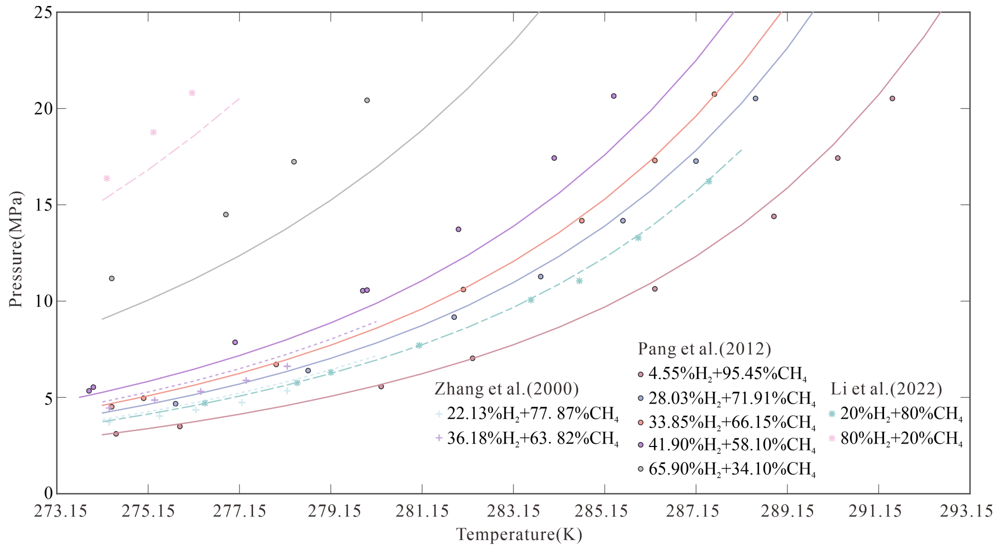

FIGURE 1
Comparison between model-predicted results and experimental data in pure water.

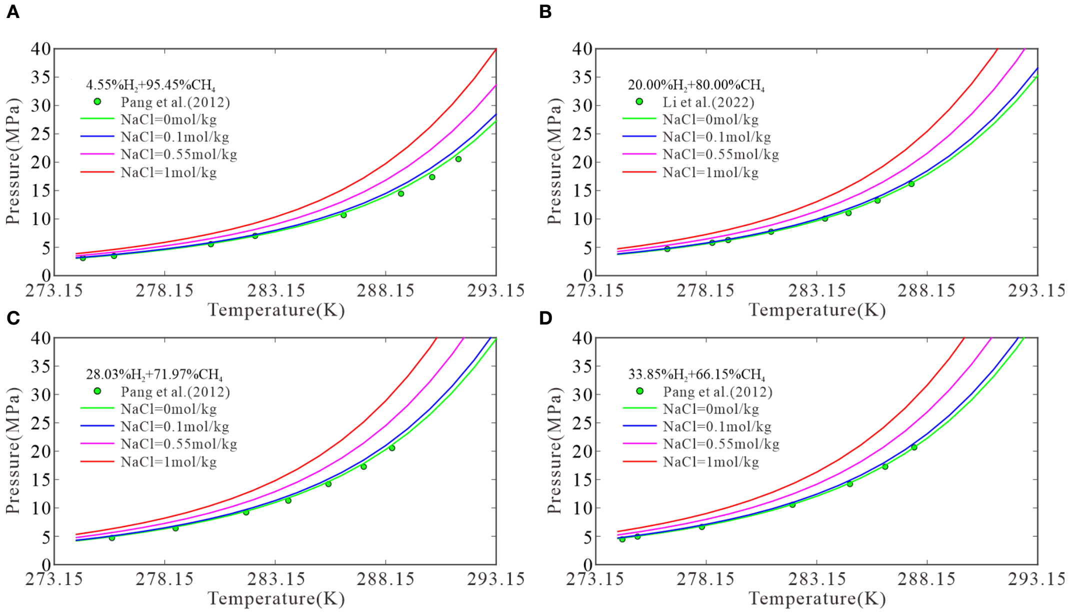

FIGURE 2
The model predictions at H_2 molar fractions of 4.55 **(A)**, 20.00 **(B)**, 28.03 **(C)**, and 33.85 mol% **(D)**.

4.15, 5.96, 9.87, and 19.32 MPa, respectively, in the 1 mol/kg NaCl solutions. Figure 3A shows that the model predictions were consistent with experimental data in pure water. The three-phase equilibrium pressure for the formation of CH_4–H_2 hydrates was low when the initial molar fractions of CH_4 was high and increased with the H_2 content until H_2 was dominant. Then, the pressure increased to a value that cannot be reached under natural conditions. Figures 3B–D show similar trends. A higher H_2 content resulted in more demanding conditions for hydrate formation in submarine sediments, particularly in serpentinization areas.

4 Conclusions

A thermodynamic model was established based on classical adsorption theory, the van der Waals theory, and the molecular

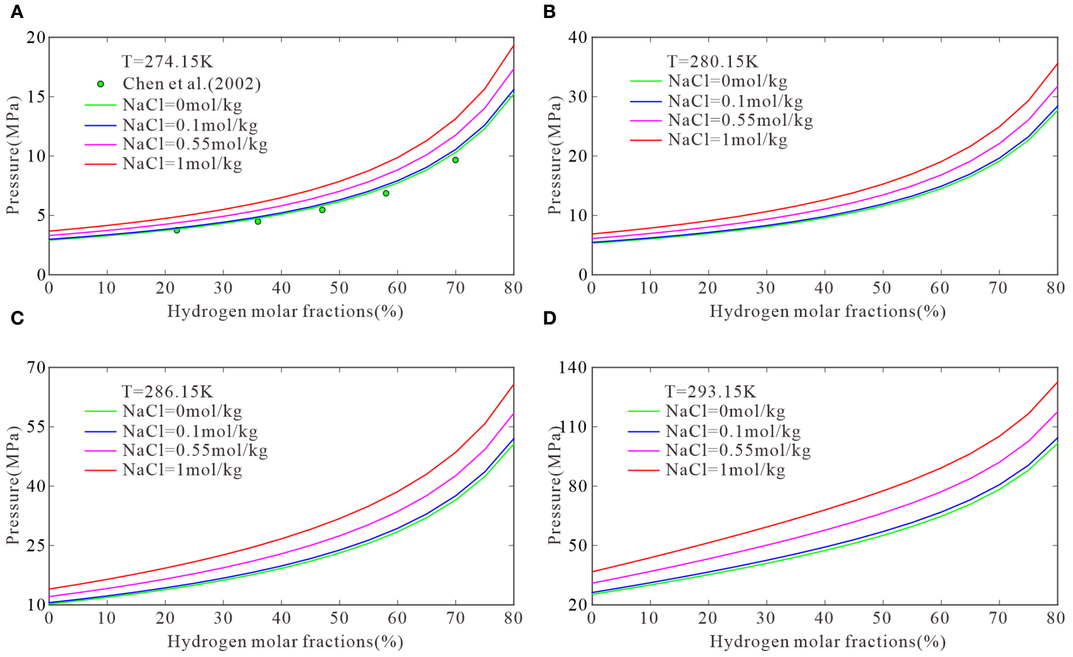

FIGURE 3
The model predictions when temperatures are 274.15 **(A)**, 280.15 **(B)**, 286.15 **(C)**, and 293.15 K **(D)**.

potential model to predict the three-phase (hydrate, liquid, and vapor) equilibrium temperature and pressure for the formation of CH_4–H_2 hydrates at different molar fractions of CH_4 and H_2. The model predictions were consistent with recent experimental data of CH_4–H_2 hydrates, and the proposed model demonstrated its superiority to previously established models in terms of temperature and pressure ranges as well as prediction accuracy. Moreover, the model can consider the effects of salinity on the hydrate stability. The model predictions indicated that the pressure necessary for the formation of CH_4–H_2 hydrates in saltwater increases with the temperature, NaCl concentration, and H_2 molar fractions when other conditions remain unchanged. In the sedimentary layers of serpentinization areas, the combined effects of the temperature, NaCl concentration, and H_2 molar fractions on the formation of CH_4–H_2 hydrates should be comprehensively considered. This study thus provides a theoretical basis for identifying CH_4–H_2 hydrates on ocean floor in marine areas.

Data availability statement

Publicly available datasets were analyzed in this study. This data can be found here: https://gashydrates.nist.gov/.

Author contributions

ZWZ: Conceptualization, investigation, methodology, software and writing—original draft. YC: Conceptualization, software, funding acquisition, writing-review and editing. ZHZ: methodology, software. NW: writing-review. DC: writing-review and funding acquisition. All authors contributed to the article and approved the submitted version.

Funding

This study is financially supported by the National Natural Science Foundation of China (No. 41776050, No. 41776080, and No. 91858208).

Conflict of interest

The authors declare that the research was conducted in the absence of any commercial or financial relationships that could be construed as a potential conflict of interest.

Publisher's note

References

Chen, G.-J., and Guo, T.-M. (1998). A new approach to gas hydrate modelling. *Chem. Eng. J.* 71 (2), 145–151. doi: 10.1016/S1385-8947(98)00126-0

Chen, G. J., Sun, C.-Y., and Guo, T. M. (2002). *A new technique for separating (hydrogen + methane) gas mixtures using hydrate technology*. In: Proceedings of the 4th International Conference on Gas Hydrates. (Yokohama, Japan), pp. 1016–1020.

Coveney, R. M.Jr., Goebel, E. D., Zeller, E. J., Dreschhoff, G. A. M., and Angino, E. E. (1987). Serpentinization and the origin of hydrogen gas in Kansas1. *AAPG. Bull.* 71 (1), 39–48. doi: 10.1306/94886D3F-1704-11D7-8645000102C1865D

Deiters, U. K. (2013). Comments on the modeling of hydrogen and hydrogen-containing mixtures with cubic equations of state. *Fluid. Phase. Equilibria.* 352, 93–96. doi: 10.1016/j.fluid.2013.05.032

Dendy Sloan, E., and Koh, C. (2007). *Clathrate hydrates of natural gases, third edition.* (CRC Press). 20074156.

Duan, Z., and Mao, S. (2006). A thermodynamic model for calculating methane solubility, density and gas phase composition of methane-bearing aqueous fluids from 273 to 523 K and from 1 to 2000 bar. *Geochim. Cosmochim. Acta* 70 (13), 3369–3386. doi: 10.1016/j.gca.2006.03.018

Duan, Z., and Sun, R. (2006). A model to predict phase equilibrium of CH4 and CO2 clathrate hydrate in aqueous electrolyte solutions. *Am. Mineralog.* 91 (8-9), 1346–1354. doi: 10.2138/am.2006.2017

Dyadin, Y. A., Larionov, E. G., Manakov, A. Y., Zhurko, F. V., Aladko, E. Y., Mikina, T. V., et al. (1999). Clathrate hydrates of hydrogen and neon. *Mendeleev. Commun.* 9 (5), 209–210. doi: 10.1070/MC1999v009n05ABEH001104

Felmy, A. R., and Weare, J H J G E C A. (1986). The prediction of borate mineral equilibria in natural waters: application to searles lake, California. *Geochimica et Cosmochimica Acta*50, 12, 2771–2783. doi: 10.1016/0016-7037(86)90226-7

Gao, J., Sun, Q., Xu, Z., Zhang, Y., Wang, Y., Guo, X., et al. (2022). Modelling the hydrate formation condition in consideration of hydrates structure transformation. *Chem. Eng. Sci.* 251, 117487. doi: 10.1016/j.ces.2022.117487

Grim, R. G., Kerkar, P. B., Shebowich, M., Arias, M., Sloan, E. D., Koh, C. A., et al. (2012). Synthesis and characterization of sI clathrate hydrates containing hydrogen. *J. Phys. Chem. C.* 116 (34), 18557–18563. doi: 10.1021/jp307409s

Harvie, C. E., Møller, N., and Weare, J. H. (1984). The prediction of mineral solubilities in natural waters: the Na-K-Mg-Ca-H-Cl-SO4-OH-HCO3-CO3-CO2-H2O system to high ionic strengths at 25°C. *Geochimica et Cosmochimica Acta* 48, 4, 723–751. doi: 10.1016/0016-7037(84)90098-X

Hashimoto, S., Murayama, S., Sugahara, T., Sato, H., and Ohgaki, K. (2006). Thermodynamic and raman spectroscopic studies on H2 + tetrahydrofuran +water and H2+ tetra-n-butyl ammonium bromide +water mixtures containing gas hydrates. *Chem. Eng. Scie.* 61 (24), 7884–7888. doi: 10.1016/j.ces.2006.09.039

Holder, G. D., Corbin, G., and Papadopoulos, K. D. (1980). Thermodynamic and molecular properties of gas hydrates from mixtures containing methane, argon, and krypton. *Ind. Eng. Chem. Fundamentals.* 19 (3), 282–286. doi: 10.1021/i160075a008

Holder, G. D., Stephenson, J. L., Joyce, J. J., John, V. T., Kamath, V. A., and Malekar, S. (1983). Formation of clathrate hydrates in hydrogen-rich gases. *Ind. Eng. Chem. Process. Design. Dev.* 22 (1), 170–171. doi: 10.1021/i200020a029

Holm, N. G., Oze, C., Mousis, O., Waite, J. H., and Guilbert-Lepoutre, A. (2015). Serpentinization and the formation of H2 and CH4 on celestial bodies (Planets, moons, comets). *Astrobiology* 15 (7), 587–600. doi: 10.1089/ast.2014.1188

Hulme, S., Wheat, C., Fryer, P., and Mottl, M. (2010). Pore water chemistry of the Mariana serpentinite mud volcanoes: a window to the seismogenic zone. *Geochem. Geophys. Geosyst. - GEOCHEM. GEOPHYS. GEOSYST.* 11, Q01X09. doi: 10.1029/2009GC002674

Klauda, J., and Sandler, S. (2003). Phase behavior of clathrate hydrates: a model for single and multiple gas component hydrates and multiple gas component hydrates *Chem. Engin. Sci.* 58(1), 27–41. doi: 10.1016/S0009-2509(02)00435-9

Johnson, J. E., Mienert, J., Plaza-Faverola, A., Vadakkepuliyambatta, S., Knies, J., Bünz, S., et al. (2015). Abiotic methane from ultraslow-spreading ridges can charge Arctic gas hydrates. *Geology* 43 (5), 371–374. doi: 10.1130/G36440.1

Li, X., Fan, S., Wang, Y., Li, G., Wang, S., Lang, X., et al. (2022). Hydrate phase equilibrium of hydrogen-natural gas blends: experimental study and thermodynamic modeling. *Fluid. Phase. Equilibria.* 556. doi: 10.1016/j.fluid.2022.113417

Ma, Q.-L., Chen, G.-J., Sun, C.-Y., Yang, L. -Y., and Liu, B. (2013). Predictions of hydrate formation for systems containing hydrogen. *Fluid. Phase. Equilibria.* 358, 290–295. doi: 10.1016/j.fluid.2013.08.019

Mao, W. L., Mao, H.-k., Goncharov, A. F., Struzhkin, V. V., Guo, Q., Hu, J., et al. (2002). Hydrogen clusters in clathrate hydrate. *Science* 297 (5590), 2247–2249. doi: 10.1126/science.1075394

Matsumoto, Y., Grim, R. G., Khan, N. M., Sugahara, T., Ohgaki, K., Sloan, E. D., et al. (2014). Investigating the thermodynamic stabilities of hydrogen and methane binary gas hydrates. *J. Phys. Chem. C.* 118 (7), 3783–3788. doi: 10.1021/jp411140z

McCollom, T. M., and Bach, W. (2009). Thermodynamic constraints on hydrogen generation during serpentinization of ultramafic rocks. *Geochim. Et. Cosmochim. Acta* 73 (3), 856–875. doi: 10.1016/j.gca.2008.10.032

Monnin, C. (1990). The influence of pressure on the activity coefficients of the solutes and on the solubility of minerals in the system Na-Ca-Cl-So4-H2o to 200°C and 1 kbar and to high nacl concentration. *Geochim. Cosmochim. Acta* 54, 3265–3282. doi: 10.1016/0016-7037(90)90284-R

Ng, H. J., and Robinson, D. B. (1976). The measurement and prediction of hydrate formation in liquid hydrocarbon-water systems. *Ind.eng.chem.fundam* 15 (4), 293–298. doi: 10.1021/i160060a012

Pang, J., Ng, H.-J., Zuo, J., Zhang, D., Ma, Q., and Chen, G. (2012). Hydrogen gas hydrate–measurements and predictions. *Fluid. Phase. Equilibria.* 316, 6–10. doi: 10.1016/j.fluid.2011.12.006

Peng, D. Y., and Robinson, D. B. (1970). A new two-constant equation of state. *Ind. Eng. Chem. Fundamentals.* 15 (1), 3069–3078. doi: 10.1021/i160057a011

Pitzer, K. S. (1975). Thermodynamics of electrolytes. v. effects of higher-order electrostatic terms. *J. Solution. Chem.* 4 (3), 249–265. doi: 10.1007/BF00646562

Pitzer, K. S., and Silvester, L. F. (1976). Thermodynamics of electrolytes. VI. weak electrolytes including H3PO4. *J. Solution. Chem.* 5 (4), 269–278. doi: 10.1007/BF00645465

Privat, R., and Jaubert, J.-N. (2013). Classification of global fluid-phase equilibrium behaviors in binary systems. *Chem. Eng. Res. Design.* 91 (10), 1807–1839. doi: 10.1016/j.cherd.2013.06.026

Proskurowski, G., Lilley, M. D., Seewald, J. S., Fruh-Green, G. L., Olson, E. J., Lupton, J. E., et al. (2008). Abiogenic hydrocarbon production at lost city hydrothermal field. *Science* 319 (5863), 604–607. doi: 10.1126/science.1151194

Rajan, A., Mienert, J., Bünz, S., and Chand, S. (2012). Potential serpentinization, degassing, and gas hydrate formation at a young (<20 ma) sedimented ocean crust of the Arctic ocean ridge system. *J. Geophys. Res.: Solid. Earth* 117 (B3). doi: 10.1029/2011JB008537

Salisbury, M. H., Shinohara, M., Richter, C., Araki, E., Barr, S. R., D'Antonio, M., et al. (2002). *Proceedings of the ocean drilling program, initial reports*, Vol. 195.

Skiba, S. S., Larionov, E. G., Manakov, A. Y., et al. (2007). Investigation of hydrate formation in the system H2–CH4–H2O at a pressure up to 250 MPa. *J. Phys. Chem. B.* 111 (38), 11214–11220. doi: 10.1021/jp072821x

Spencer, R. J., Møller, N., and Weare, J. H. (1990). The prediction of mineral solubilities in natural waters: a chemical equilibrium model for the Na-k-. doi: 10.1016/0016-7037(90)90354-N

Sun, R., and Duan, Z. (2007). An accurate model to predict the thermodynamic stability of methane hydrate and methane solubility in marine environments. *Chem. Geol.* 244 (1-2), 248–262. doi: 10.1016/j.chemgeo.2007.06.021

Waals, J. H. V. D., and Platteeuw, J. C. (2007). "Clathrate solutions," in *Advances in chemical physics*. Prigogine (Ed.). 1–57. doi: 10.1002/9780470143483.ch1

Wan, Z.-F., Zhang, W., Ma, C., Liang, J.-Q., Li, A., Meng, D.-J., et al. (2022). Dissociation of gas hydrates by hydrocarbon migration and accumulation-derived slope failures: an example from the south China Sea. *Geosci. Front.* 13 (2), 101345. doi: 10.1016/j.gsf.2021.101345

Wang, X.-H., Qin, H.-B., Dandekar, A., et al. (2015). Hydrate phase equilibrium of H2/CH4/CO2 ternary gas mixtures and cage occupancy percentage of hydrogen molecules. *Fluid. Phase. Equilibria.* 403, 160–166. doi: 10.1016/j.fluid.2015.06.020

Zhang, S. -X., Chen, G. -J., Ma, C. -F., Yang, L., and Guo, T. -M. (2000). Hydrate formation of hydrogen + hydrocarbon gas mixtures. *J. Chem. Eng. Data.* 45 (5), 908–911. doi: 10.1021/je000076a

Zhu, Z., Cao, Y., Zheng, Z., and Chen, D. (2022). An accurate model for estimating H2 solubility in pure water and aqueous NaCl solutions. *Energies* 15 (14). doi: 10.3390/en15145021

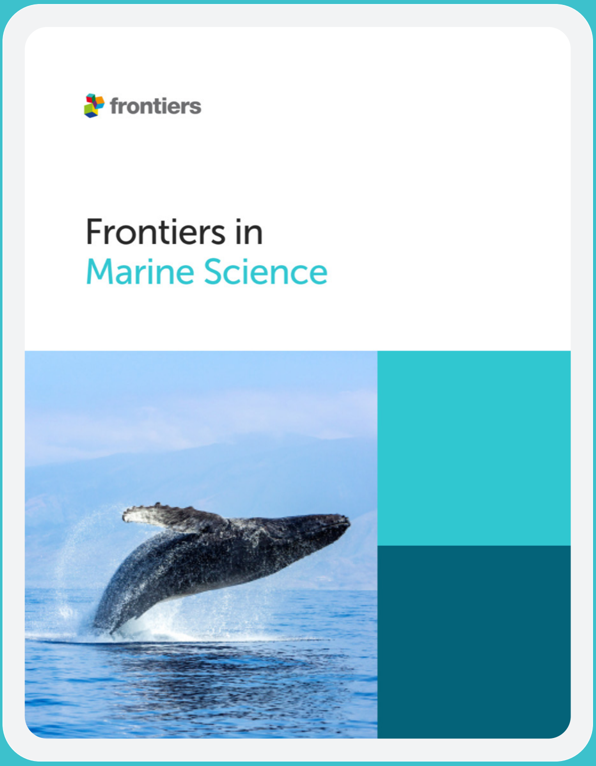

frontiers

Frontiers in
Marine Science

Frontiers

Avenue du Tribunal-Fédéral 34
1005 Lausanne, Switzerland
frontiersin.org

Contact us

+41 (0)21 510 17 00
frontiersin.org/about/contact